UNIVERSITY OF READING.

NEUTRON SCATTERING AND MODELLING STUDIES OF THE ATOMIC AND MAGNETIC STRUCTURE OF THE METALLIC GLASS Dy_7Ni_3 AND OF THE ATOMIC STRUCTURE AND DYNAMICS OF VITREOUS B_2O_3.

by

Alex C. Hannon M.A. (Oxon)

A thesis submitted to the
University of Reading
for the degree of
Doctor of Philsophy
1989

J.J. Thomson Physical Laboratory
Department of Physics
University of Reading
Whiteknights
Reading RG6 2AF
England

QUOTATIONS.

'...the preparation and study of amorphous solids owe rather less to science and rather more to art than does the study of crystalline materials.'

J.S.Blakemore (BLAKEMORE, 1969).

'Crystals are rigid and inflexible, whereas amorphous materials possess variability, changeability and possibility. We are at the door of a new age, just looking through a tiny gap. I have seen only a small area but I think that the room on the other side is very large. The twentieth century is the crystal age, but the next age will be the amorphous age.'

Y.Kuwano (BELL and JOHSTONE, 1985).

ABSTRACT.

The partial correlation functions of amorphous Dy_7Ni_3 have been measured. Modelling the static disorder leads to interatomic distances and coordination numbers. A modelling study of the atomic structure has been performed. It is concluded that a distorted trigonal prismatic model shows the greatest potential.

The magnetic structure factor of Dy_7Ni_3 has been studied. A Fourier-transformation approach shows that the moments are on the Dy ions only, that the nearest neighbour interaction is ferromagnetic in character and suggests that magnetic anisotropy is small.

The magnetic form factor for Dy^{3+} in Dy_7Ni_3 has been measured. The unpaired 4f-electrons of Dy^{3+} are more highly localised than predicted by a Hartree-Fock calculation. An additional low-Q contribution to the form factor was observed which may be due to a conduction electron polarisation. The Dy moment is close to the free-ion value.

A SANS study shows that the Dy_7Ni_3 samples are highly homogeneous apart from surface defects. Also the evolution of magnetic correlations has been observed by SANS. The Lorentzian-plus-Lorentzian-squared lineshape is appropriate above 35K but not below. The deduced spin correlation lengths indicate $D_0/J_0 \sim 0.023$.

Inelastic neutron scattering has been used to measure the vibrational density of states of vitreous-B_2O_3 over its full energy-range with medium resolution and in the region of the boroxol ring breathing mode with high resolution. The boroxol ring breathing mode contributes only a small feature to the density of states. Thus it is accentuated in the Raman spectrum.

Vibrational density of states calculations have been performed for B_2O_3 structural models. By comparison with the neutron data and the Raman isotopic substitution data it is shown that the triangular BO_3 network contains a high proportion of boroxol rings. A Born-force model with a force constant ratio of 0.2 gives good consistency with experiment, but with evidence for a more sophisticated force model.

NB An informative summary of this thesis may be found in the final Chapter.

ACKNOWLEDGEMENTS.

I should like to thank Adrian Wright for supervising me for most of the work that is described in this thesis. It was he who provided the initial inspiration for much of the work, as well as the samples, diffraction analysis programs and much invaluable advice. Thanks are also due to John Blackman for his inspiring advice on the numerical calculations of vibrational properties. I am also grateful to Roger Sinclair of Harwell Laboratory for helping with all of the experimental work described in this thesis. My fellow students Alix Clare and David Grimley deserve special mention for their tolerant friendliness which helped me stay sane, in spite of everything.

I should like to thank Argonne National Laboratory for providing experimental time on their Intense Pulsed Neutron Source for my experiments on B_2O_3. Thanks are due to many people at Argonne, but I should especially like to thank David Price for inviting me back to perform a complete analysis of my data and for cooking a splendid Thanksgiving dinner. I am grateful to the Institut Laue Langevin for providing experimental time and assistance for my experiments on Dy_7Ni_3. Thanks are due to Harwell Laboratory for awarding me a CASE studentship, and for the provision of experimental facilities which expanded my general experience of neutron scattering.

I should also like to thank Micky Atzmon (now at Harvard) and Bill Johnson of Caltech for preparing my Dy_7Ni_3 samples. Micky Atzmon also deserves special mention for measuring the density of Dy_7Ni_3 so very quickly, and for allowing me to sleep on his floor in Pasadena. Thanks are also due to E.Foster of Harwell Laboratory for isotopic analysis of my B_2O_3 sample.

I am grateful to the Reading University Computer Centre for allowing me to use their excellent Amdahl computer to analyse my experimental data and to perform my numerical calculations. Special thanks are due to Alan Thornton, Neal Curran and Hilary Vines for tackling the strange errors that always seemed to plague me, and to all of the operators for coping with so many plots which they always tried hard to produce correctly.

Thanks are also due to the following people for encouraging me to complete this thesis: My family and relatives, Charis Burridge, Bob Cywinski, Paul Davies, Archie Eaglesham, Lynn Gladden, Carmen Goodwin, Mark Hagen, Nick Harwood, Steve Hull, Sue Kilcoyne, Mike Lea-Wilson, Dan and Pat Montague, Mario Paoli, Tim Shaw, Alan Soper, Sherman Susman, Andy Tipping, Popi Trohidou, Norimasa Umesaki, Mary Vrtis and Gavin Williams (plus anyone else who I have forgotten in my absent-mindedness!). Also I am grateful to the Rutherford Appleton Laboratory for the use of their facilities which assisted in the completion of this thesis.

Lastly I should like to thank the Science and Engineering Research Council for providing me with (just enough!) money to keep the wolf from the door, for purchasing my Dy_7Ni_3 samples, for providing me with my neutron beam time and for funding the first two of my three trips to Argonne Laboratory.

NEUTRON SCATTERING AND MODELLING STUDIES OF THE ATOMIC AND MAGNETIC STRUCTURE OF THE METALLIC GLASS Dy_7Ni_3 AND OF THE ATOMIC STRUCTURE AND DYNAMICS OF VITREOUS B_2O_3.

CHAPTER 1.

INTRODUCTION.

Glassy materials have been known to man and made use of for many centuries. Prior to this century all the known glasses were oxide glasses and their main use was in optical applications. Since then there has been a great increase in the variety of amorphous solids, in the number of methods of preparation of amorphous solids and in the applications for which these materials are used. As amorphous solids become increasingly important technologically, so it becomes more important to understand their basic properties. However, at present these basic properties are not at all well understood. Amorphous solids are described in general in chapter two of this thesis.

The technique that has been used for all the experimental work described in this thesis is neutron scattering. This is one of the most successful and widely used of modern experimental techniques and neutron scattering has found application in many areas of physics, chemistry, biology and engineering. An introduction to neutron scattering is given in chapters three and four together with a development of the theoretical results needed for the neutron scattering experiments described in later chapters of the thesis.

This thesis is concerned in particular with the metallic glass Dy_7Ni_3. Amorphous metals were discovered in 1960 and have since been shown to have useful mechanical and magnetic properties. However, our understanding of the atomic and magnetic structure of amorphous metals is still limited and must be greatly advanced if their especial properties are to be fully utilised. To this end the approach of the work reported in this thesis has been to make a detailed study of one particular metallic glass, Dy_7Ni_3. The atomic and the magnetic correlations in Dy_7Ni_3 have been studied, both at short range and at long range, and these studies are reported in chapters six to eleven.

The second amorphous solid dealt with in this thesis is vitreous B_2O_3. This oxide glass has been known for a long time and its atomic short range order would seem to be well understood. However, the intermediate range order in B_2O_3 is still a matter of controversy and measurements of the atomic vibrations have been made as a means of obtaining valuable experimental evidence relating to this question. Also calculations of the dynamics of B_2O_3 have been performed for several structural models, and the results of these are considered in conjunction with the experimental data. The work on B_2O_3 is described in chapters twelve to fifteen.

CHAPTER 2

AMORPHOUS SOLIDS.

2.1 INTRODUCTION.

As yet there are no universally accepted definitions of the terms 'amorphous' and 'glass' and hence it is worthwhile to define what they mean in this thesis. The definition of the term amorphous adopted here is as follows: An amorphous material is a phase of condensed matter which has a non-crystalline atomic structure. Thus amorphous materials do not possess the atomic long range order (LRO) characteristic of a crystal. That is to say they are not periodic. This has the practical consequence that an amorphous material can be identified by its diffraction pattern which does not contain Bragg peaks but rather is a smoothly varying function in reciprocal space. Note that the term amorphous applies to both solids and liquids, but does not apply to the recently discovered quasi-crystalline materials (SHECHTMAN, BLECH, GRATIAS and CAHN, 1984) which are thought to possess long range orientational order but not long range positional order.

The properties of an amorphous solid can be strongly dependent on the method of preparation (see for example WRIGHT, SINCLAIR and LEADBETTER, 1985) and this has resulted in a narrower, more specific definition of the term glass. The definition adopted in this thesis is as follows: A glass is an amorphous solid which has been prepared by quenching from the melt. The term vitreous is taken to have a meaning identical to that of the term glassy.

An important property of amorphous solids is that they are generally isotropic. That is to say their macroscopic properties are generally found to be independent of the orientation of the sample. This is a consequence of the disordered non-crystalline atomic structure. However, preparation methods which involve a degree of anisotropy can result in exceptions to this general property of macroscopic isotropy. For example thin films formed by thermal evaporation can sometimes be produced with a columnar structure (LEAMY, GILMER and DIRKS, 1980).

2.2 PREPARATION METHODS.

In order to produce an amorphous solid the material must be solidified in such a manner that crystallisation is prevented from occurring. The conventional preparation method is melt quenching. This involves cooling the molten form of the material sufficiently quickly to preclude crystal nucleation and growth. For an easy glass-former, such as B_2O_3, the glassy phase can be produced simply by using an oven to heat a crucible of the material above its melting point and then allowing it to cool to room temperature. The rate of cooling for this procedure is of order $1Ks^{-1}$. However, for glasses which are relatively far from thermodynamic equilibrium, notably metallic glasses, it is necessary to use a special technique where a much greater cooling rate is achieved. The original method used for preparing metallic glasses was splat cooling in which small drops of liquid metal are either projected at a copper sheet or smashed between a hammer and anvil. Nowadays either melt spinning or melt extraction is used. In the melt spinning technique ingots of the metal are melted in a quartz tube by an r.f. heating coil and a stream of the molten metal is forced through a hole in the bottom of the tube by a blast of inert gas (figure 2.1). The jet hits a rapidly rotating copper wheel and is thus cooled at a rate of ~$10^6 Ks^{-1}$ or greater. This results in a long, thin, ribbon of the metallic glass of thickness up to about 30μm. In the melt extraction technique a rapidly spinning copper disc removes liquid from a reservoir producing fine wires. Neither of these techniques is able to produce material in bulk form. However, recent studies (ATZMON, UNRUH, POLITIS and JOHNSON, 1985) have shown that bulk material may be produced from melt-spun ribbons by a process of repeated cold rolling.

Another method for producing amorphous solids with the starting material in the liquid state is the sol-gel process. This method starts with a solution which then forms a multicomponent gel by a process of polymerisation, finally forming a three dimensional (3D) network. The solvent is then driven off by heat, and densification occurs with the amorphous solid as the final result. Amorphous solids prepared by the sol-gel process can be made very pure, and they are found to be very similar to glasses.

There is a number of techniques which can be used to produce thin films of amorphous solid, most of which involve the vapour phase as the starting material. The problem with all of these techniques is that the final product cannot be made very pure, and for most of them there is little control over the composition. However, they do have the advantage that the estimated effective cooling rate, ~$10^9 Ks^{-1}$, is higher than for any other method. In the thermal evaporation technique a starting compound is vaporised and a thin film is deposited from the vapour onto a substrate.

The substrate is held at a low temperature so that the mobility of the adatoms is low and hence crystallisation is prevented from occurring. The technique of sputtering is similar to thermal evaporation except that atoms are removed from the starting compound by ion bombardment. In the case of glow-discharge decomposition an r.f. field produces a plasma in a low pressure gas, chemical decomposition of the gas takes place and a solid film is deposited on a substrate. The technique of chemical vapour deposition is similar to glow-discharge decomposition except that decomposition of the vapour relies on thermal energy. Thin films of amorphous solids may also be produced by electrolytic deposition.

The methods discussed above are the main ones used for producing amorphous solids. However, there is a number of less important techniques which will be discussed briefly: The technique of irradiation uses a starting material which is already in the solid state. A crystalline sample of the material is bombarded with ionising radiation (high energy neutrons, electrons or ions) and structural damage occurs which results in an amorphous solid. Amorphisation can also occur as a result of mechanical processes. In the case of shear amorphisation the simple act of grinding can render amorphous an originally crystalline material. Amorphisation can also be caused by shock-wave transformation where it is thought that the shock-wave front from an explosion produces local melting. There are also certain chemical reactions which can result in the formation of an amorphous solid.

2.3 CLASSIFICATION OF AMORPHOUS SOLIDS.

Amorphous solids can be classified according to the type of bonding that occurs between the atoms (ELLIOTT, 1983). It should be pointed out that in a real solid more than one type of bonding can contribute. However, one type of bonding will generally predominate and so such a classification is still worthwhile.

2.3.1 COVALENT BONDING.

The group of glasses which has been known for by far the longest is the oxide glasses and these are often termed 'conventional glasses'. Prime examples of oxide glasses are SiO_2 and B_2O_3. Glasses made from the oxide of just one element are known as single component glasses, and these can generally only be made at the stoichiometric composition. However, multicomponent oxide glasses (ie. made from the oxides of more than one element) form over a wide range of compositions. Multicomponent glasses which contain non-glass-forming oxides in addition to glass-forming oxides can also be made and these are termed modified glasses (eg Na_2O-SiO_2). More recently it has been discovered that amorphous solids can be formed by binary systems involving the chalcogen elements sulphur, selenium or tellurium, and these materials are known as chalcogenides. It should be noted that even though oxygen is a chalcogen, oxides and chalcogenides are always considered as two separate classes of amorphous solid. Arsenic sulphide and germanium selenide are typical examples of chalcogenides. These can be made over a wide range of non-stoichiometric composition, and also form a large number of multicomponent glasses involving one or more chalcogens and one or more other elements. Monatomic amorphous solids are formed by sulphur, selenium and phosphorus. WRIGHT and LEADBETTER (1976) have given an extensive review of structural studies of covalently bonded amorphous solids.

2.3.2 IONIC BONDING.

The largest class of amorphous solids in which ionic bonding predominates is the halide glasses. $ZnCl_2$ and BeF_2 have been known to form amorphous solids for some time. More recently there have been a number of studies of fluoroberyllate glasses. These are multicomponent glasses containing fluorine, beryllium and one or more other elements from the first two groups of the periodic table. There have also been studies of heavy metal fluoride glasses such as BaF_2-ZrF_4, and of oxyhalide glasses such as PbO-$PbCl_2$ (WRIGHT, GRIMLEY, SINCLAIR, RAO and RAO, 1985). Halide based glasses are currently of technological interest for both optical fibres and high power lasers for fusion reactors. WRIGHT (1986) has recently reviewed diffraction studies of the structure of halide glasses. Another class of amorphous solid in which ionic bonding predominates is the nitrate glasses. Glass formation only occurs in systems containing two or more nitrates, such as KNO_3-$Ca(NO_3)_2$.

2.3.3 METALLIC BONDING.

A discussion of metallic amorphous solids is delayed until Chapter 6 where a much more extensive review of this class of amorphous solids is given.

2.3.4 VAN DER WAALS BONDING.

Polymers with a regular molecular structure usually crystallise on cooling. However, the extent of crystallisation is limited by irregularities in the molecular structure and irregular polymers tend to form amorphous solids on cooling. For example ordinary polystyrene, which is nearly atactic, is amorphous. The forces which link the chains of polymers are Van der Waals' forces.

2.3.5 HYDROGEN BONDING.

Whilst the bonding in the oxide glasses described in section 2.3.1 is predominantly covalent, there are amorphous solids containing oxygen which are believed to owe their existence to the presence of hydrogen bonds. Potassium bisulphate glass ($KHSO_4$) is thought to be such a solid. If water vapour is condensed on a very cold surface it forms an amorphous solid and there is also a number of aqueous solutions which form amorphous solids much more readily, an example being a solution of LiCl.

2.4 GLASS FORMATION.

The process of glass formation may be described qualitatively by considering the volume-temperature behaviour for a typical glass-former as shown in figure 2.2. If the liquid is slowly cooled from the point A so that thermal equilibrium is maintained it will crystallise at the melting temperature T_m with an abrupt and appreciable reduction in volume. Further cooling results in volume reduction along CD. However, if the liquid is sufficiently rapidly cooled the system follows the path BE and crystallisation does not occur at T_m. A liquid which is at a temperature below its melting point T_m (and is still a liquid) is known as a supercooled liquid. Further cooling of the supercooled liquid results in a relatively gradual change in slope of the V-T curve at the point E. The region over which the change of slope occurs is termed the glass transition temperature T_g. At temperatures below T_g the system is in an effectively solid non-crystalline state known as a glass. Since the glass transition is a continuous transition extending over a range of temperatures, T_g is not well defined and JONES (1971) has defined the fictive temperature T_f as the temperature of the intersection of the extrapolated liquid and glass curves. However, even T_f is not a well defined temperature for a particular material as it is found to vary with the rate of cooling of the supercooled liquid; the faster the rate of cooling, the higher T_f and T_g are found to be.

Whilst thermodynamic variables such as volume and entropy are found to be continuous through the glass transition with a change of slope, derivative variables such as the specific heat at constant pressure c_p (figure 2.3) show a discontinuity. Thus it would appear that the glass transition is a second order phase transition. However, the relatively large variation of the transition temperature suggests that the glass transition is not a genuine thermodynamic phase transition. Figure 2.3 also shows c_p for the crystalline phase of the same material. This exhibits a singularity at the melting point T_m due to the latent heat of melting. No such latent heat singularity accompanies the glass transition. Note also that the specific heats of the glassy and crystalline phases are essentially the same.

Perhaps the clearest approach to the phenomenon of the glass transition and the glassy state concerns relaxation processes. If a glass is maintained at a temperature just below its glass transition temperature it is found that eventually it relaxes to metastable equilibrium at a point on the extrapolated supercooled liquid line (ADKINS, 1975). However, as a glass-former is cooled relaxation times rise dramatically and this is manifested as a sharp (but continuous) increase in viscosity. The relaxation times for the atoms to rearrange into the (metastable) equilibrium configuration (the supercooled liquid) become much larger than the timescale of any experimental probe (ie. of the order of years to the age of the universe), the atoms are frozen in position and so the glass is effectively solid. The glass transition may thus be regarded as occurring at a temperature for which relaxation times become large in comparison with the experimental timescale. The glassy state may then be regarded as an effectively metastable state which is in effect a solid but is not the equilibrium configuration. In principal a glass will relax to the (metastable) equilibrium configuration (the supercooled liquid), but the relaxation times involved are so very long that the glassy state is a phase of matter worthy of consideration in its own right. This enables a clear distinction to be drawn between the glassy state and the supercooled liquid; the supercooled liquid is a (metastable) equilibrium configuration in which the atoms do not have fixed equilibrium positions, whereas the glass is an effectively metastable non-equilibrium configuration in which the atoms vibrate about equilibrium positions which are fixed on normal timescales. Thus the glass transition occurs between two clearly different phases of matter. The ideas presented above provide a clear explanation of the observation that the faster a glass-former is cooled, the higher T_g is found to be, since a faster quench rate means that relaxation processes become frozen out at a higher temperature.

Another approach to the glass transition is to consider the entropy involved. The specific heat c_p is given by;

$$c_p = T\left(\frac{\partial S}{\partial T}\right)_p \tag{2.4.1}$$

yielding;

$$S_2 - S_1 = \int_{T=T_1}^{T=T_2} c_p \; d(\ln T) \tag{2.4.2}$$

Hence integrating c_p with respect to lnT gives the entropy directly. Following this the specific heats shown in figure 2.3 may be integrated from zero temperature up to a finite temperature T to obtain the excess entropy ΔS shown in figure 2.4 . The excess entropy is defined as;

$$\Delta S = (S_{liquid} - S_{crystal}) \tag{2.4.3}$$

where S_{liquid} and $S_{crystal}$ are the entropies of the supercooled liquid and of the crystal. At T_m the excess entropy of the supercooled liquid is S_m, the entropy of melting (of the crystal). As the temperature of the supercooled liquid is reduced below T_m the excess entropy ΔS decreases until T_g is reached when solidification (to a glass) occurs and ΔS becomes essentially zero. However, if the temperature of the supercooled liquid is reduced more slowly then the glass transition occurs at a lower value of T_g. This raises the question of what would happen if it were feasible to cool the supercooled liquid more and more slowly without limit. If ΔS is extrapolated to lower temperatures (figure 2.4) then it becomes zero at a temperature T_0 and then becomes negative. This leads to what is known as the 'entropy crisis' (KAUZMANN, 1948) - according to the extrapolation of the ΔS curve it could be possible to obtain a supercooled liquid of lower entropy than the crystal if the cooling were sufficiently slow. Such a situation is physically unacceptable and in practice is always avoided by the occurrence of the glass transition. The temperature T_0 has thus been interpreted as a hypothetical ideal glass transition temperature and it sets a lower limit on any real T_g. Real values of T_g are always greater than T_0 because of the mediation of kinetic (relaxation) effects. However, the existence of an ideal limiting glass transition temperature suggests that the existence of glasses is not dependent purely on kinetic phenomena.

At present there exists no wholly successful theoretical treatment of the glass transition. The unification of the thermodynamic and kinetic aspects of the glass transition is perhaps one of the most formidable problems of condensed matter physics. The best-known and most general theoretical picture of the glass transition is the free volume model of TURNBULL and COHEN (1961; 1970). In this model each molecule has associated with it a free volume which may be defined as the region of space accessible to its centre of mass without movement of the other molecules. The free volume may either be localised such that the molecule cannot exchange neighbours and can only execute oscillatory solid-like motion, or it may be delocalised such that the molecule can exchange neighbours by a diffusive excursion. The model assumes that no free energy is required for redistributing free volume among the molecules so that the free volume v_f of each molecule fluctuates with the continual redistribution of the total free volume V_f. A liquid undergoes a glass transition when V_f is reduced to a critical level below which there is inadequate room for molecular manoeuvrability and macroscopic fluidity. Thus the glass transition occurs when the free volume is sufficiently excluded from the system.

For mixtures (binary, ternary etc.) it is found that the range of composition over which a glass may be formed (the glass-forming region) is located around a deep eutectic in the phase diagram (see figure 6.4 for an example of a phase diagram of a binary system). This may be understood as follows; the range of temperature over which the melt is both thermodynamically ($T<T_m$) and kinetically ($T>T_g$) capable of crystallising is much less at the eutectic composition than at any other composition. This is simply because T_m has its minimum at the eutectic composition. Hence if a melt at the eutectic composition is cooled rapidly it is less at risk of crystallising than at any other composition and this explains why the glass-forming region is located around a deep eutectic.

2.5 THE ATOMIC STRUCTURE OF AMORPHOUS SOLIDS.

2.5.1 THEORIES OF ATOMIC STRUCTURE.

Whilst amorphous solids do not exhibit LRO it is found that they do exhibit local order. This may be seen to be a consequence of the fact that the interatomic distances do not sink below some minimum value (ie. the local order arises from the forces between the atoms). The study of the atomic structure of amorphous solids is thus concerned with the characterisation of local order.

Probably the first theory of the atomic structure of amorphous solids was the crystallite theory of LEBEDEV (1921) and later RANDALL, ROOKSBY and COOPER (1930). This theory envisages an amorphous solid as an assembly of very small crystallites whose linear dimensions are of order 10Å to 20Å. In such a model the lack of LRO arises from the random arrangement of the crystallites with respect to each other. However, the early diffraction experiments of WARREN (1937; 1940) showed that discrete crystallites are not present; it was shown that the crystallites would have to be about the same size as a single unit cell in order to account for the large breadth of the peaks of the diffraction patterns of glasses. This is at variance with the whole idea of crystallinity which is one of regular repetition. (A single unit cell does not constitute a crystal.) Futhermore such small crystallites would imply that a large proportion of the material is composed of inter-crystallite regions and the crystallite theory does not address the nature of these regions at all. As was first pointed out by WARREN and BISCOE (1938), such a structure would lead to a large amount of small angle scattering and this is not observed for conventional glassy materials (eg. SiO_2). More recently PORAI-KOSHITS (1958) formulated the modern crystallite theory in which well ordered regions (~crystallites) are separated by relatively disordered regions, and various versions of the theory still reappear occasionally (GOODMAN, 1982; HOSEMAN, 1985).

The most widely accepted theory for the atomic structure of amorphous solids in which directional covalent bonding predominates is the continuous random network (CRN) theory. This was originally developed from ZACHARIASEN's (1932) empirical rules for oxide glass formation. Zachariasen argued that, since glasses and crystals have the same interatomic forces, the tendency to minimum internal energy results in similar bonding configurations in both phases. It was then assumed that the oxygen polyhedra found in oxide crystals would also occur in glasses, but in glasses these would connect together in a random way so as to result in a non-periodic structure. In this way a CRN is constructed in which the atoms are subject to the constraint that their separations are not less than a normal bond length and thus the internal energy is kept low. The four rules proposed by Zachariasen for the formation of an oxide glass A_nO_m are as follows:

1. An oxygen atom may not be linked to more than two A atoms.
2. The number of oxygen atoms around an A atom must be small (three or four).
3. Oxygen polyhedra share corners with each other, but not faces or edges.
4. At least three corners of each oxygen polyhedron must be shared, or a 3D network will not be obtained.

There are exceptions to these rules (For example, edge-sharing tetrahedra are generally thought to occur in $SiSe_2$ (GLADDEN and ELLIOTT, 1987)) and they should not be regarded as absolute. However, they provide a useful framework for understanding the atomic structure of oxide glasses in terms of a CRN, and can also be easily extended to encompass other covalently bonded materials.

A glass whose atomic structure is described well by a CRN is B_2O_3, and a two-dimensional (2D) analogue of B_2O_3 is used in figures 2.5 to 2.8 to illustrate the ideas presented above. The oxygen polyhedron in these figures is an AO_3 triangle with an A atom at the centre and oxygen atoms at the vertices. Figure 2.5 shows a 2D A_2O_3 crystal, and figure 2.6 shows the atomic structure of a 2D A_2O_3 glass according to the crystallite theory. Figure 2.7 shows a 2D A_2O_3 CRN. The triangular structural unit of the crystal is retained in the CRN structure, and the lack of LRO arises from the distribution of angles between adjacent triangles. The continuous nature of a CRN should be emphasised: In a perfect CRN there are no unsatisfied bonds and a sample may be regarded as a single macromolecule with connections all the way from one side to the other. One may view a CRN as a crystal with an infinitely large unit cell containing an infinite number of atoms.

Of course the idea of a CRN presented above is an idealisation. In a real material there will be dangling (ie. unsatisfied) bonds, vacancies, voids and possibly some kind of line defects.

Figure 2.8 illustrates the atomic structure according to the CRN theory of a modified glass made from glass-forming A_2O_3 and non-glass-forming XO. Each XO unit breaks one of the bridging bonds formed by an oxygen atom between two of the triangular AO_3 structural units, resulting in a pair of non-bridging oxygen atoms each bonded to only one A atom. The non-bridging oxygen atoms carry a negative charge which is compensated by the positive charge of the X cation. The overall result is that the connectivity of the network is reduced and hence the X cation is known as a network modifier. This theory of the atomic structure of a modified glass provides a simple physical interpretation of the observation that the addition of network modifier material to a glass-former results in a rapid decrease of such quantities as viscosity and melting point. If sufficient network modifier is added to a glass-former the network connectivity is completely destroyed and the resultant structure is known as an invert glass.

Single component oxide glasses normally occur only at the stoichiometric composition defined by the 8-N rule (which states that the coordination number of an atom with N valence electrons is given by 8-N). For such systems bonding only occurs between unlike atoms and the application of the CRN theory is straightforward. However, single component chalcogenide glasses occur over a wide range of non-stoichiometric composition and hence there must be some bonding between like atoms. The application of the CRN theory is thus more involved since the degree of chemical ordering must be considered. The two extreme cases (BETTS, BIENENSTOCK and OVSHINSKY, 1970) are the chemically ordered network (CON) and the random covalent network (RCN). The CON has the maximum possible number of unlike atom bonds. Meanwhile the RCN has no preferential ordering and the distribution of bond types is purely statistical, determined only by the atomic coordination numbers and the composition. Most chalcogenide glasses are thought to have an atomic structure well described by a CON.

It is customary to make a division of the local order in covalent amorphous solids into two regimes. The first involves shorter range atomic correlations and is thus related to the basic structural unit of the CRN. This regime is termed short range order (SRO). The second regime involves atomic correlations over distances greater than the size of the basic structural unit and is termed intermediate range order (IRO). A prototypical example of IRO is the planar boroxol ring of three triangular BO_3 units thought to occur in B_2O_3, and this forms the basis of the study reported in Chapters 12 to 15.

In addition to the CRN theory and the microcrystallite theory discussed above, the literature contains a number of other theories of the atomic structure of covalently bonded amorphous solids. Noteworthy examples are as follows: The amorphon model of GRIGOROVICI and MANAILA (1969) which is a network model for Ge or Si composed of a mixture of diamond-like units and regular dodecahedra; the polytetrahedral model of GASKELL (1975) which is a model for Ge or Si based upon polytetrahedral units containing five tetrahedra; and PHILLIPS' (1981) raft model for $GeSe_2$ which involves crystalline layers terminated by Se-Se 'wrong' bonds. Generally such approaches have agreed less well with the experimental data than the CRN theory. However, in some specific cases an alternative theory has been found to be more appropriate. For example DANIEL, LEADBETTER, WRIGHT and SINCLAIR (1979) have shown that vapour-deposited arsenic sulphide is well described by a partially polymerised molecular model, arising from the presence of As_4S_4 molecules in the vapour.

For amorphous solids in which highly directional covalent bonding is not the predominant form of bonding the CRN theory is probably not appropriate. In the case of amorphous metals a random close packing (RCP) of hard spheres has been widely used to model the atomic structure. However, it is not yet clear how the chemical ordering found in many amorphous metals arises. The atomic structure of amorphous metals is discussed in more detail in Chapter 6. In the case of polymer glasses, the chain molecules of which are linked to each other by Van der Waals' forces, the structure is best described by the random coil model of FLORY (1975).

2.5.2 THE CHARACTERISATION OF ATOMIC STRUCTURE.

One of the simplest structural properties of an amorphous solid is the density. A successful model of the atomic structure must reproduce the density of the real material and this provides a very important constraint on model structures.

To characterise the SRO of an amorphous solid as completely as possible one must consider how the atoms are distributed about each other. Since amorphous solids are isotropic a measurement of the atomic structure can only yield information on how the atoms are distibuted as a function of distance and not on any directional dependence. Thus a useful function for characterising SRO is the radial distibution function (RDF) $n(r)$ where $n(r)dr$ is the number of atoms at distances in the range $(r,r+dr)$ from an origin atom, averaged over all possible origin atoms. Alternatively one may consider the pair distribution function (or radial density function) $g(r)$ which gives the directionally averaged atomic number density at a distance r from an origin atom, averaged over all possible origin atoms. Clearly these two functions are related;

$$n(r)dr = 4\pi r^2 dr\, g(r) \qquad (2.5.1)$$

The symbol $g(r)$ is used here to be consistent with the Van Hove $G(\underline{r},t)$ correlation function formalism introduced in section 3.3.4 . The function which is most appropriate for diffraction measurements of SRO and is used in the work described in this thesis (see Chapters 7 and 8) is the total correlation function t(r) defined by;

$$t(r) = 4\pi r g(r) \qquad (2.5.2)$$

In the case of a polyatomic material the correlation function may be separated into partial correlations functions giving the distribution of one particular type of atom about another particular type of atom. Thus the partial density function $g_{AB}(r)$ gives the average density of B atoms at a distance r from an A atom. For example in the case of Dy_7Ni_3 there are three unique partial correlation functions describing correlations between the following three pairs of atoms: Dy-Dy, Dy-Ni and Ni-Ni. Such a separation into partial correlation functions is generally ascribed to FABER and ZIMAN (1964).

It follows that the best criterion for assessing a model of the atomic structure of an amorphous solid is a comparison of the partial correlation functions of the model with those of the real material. The nearest neighbour coordination numbers may be derived from the partial correlation functions and these can be particularly useful in understanding the atomic structure. Other quantities than the partial correlation functions can provide additional information for assessing a particular structural model. In particular studies of the atomic vibrations as discussed in Chapter 5 and Chapters 13 to 15 can be most useful. Also magnetic resonance signals and extended X-ray absorption fine structure (EXAFS) have been found to be useful.

2.5.3 METHODS OF MODELLING ATOMIC STRUCTURE.

The aim in the modelling of the atomic structure of an amorphous solid is to identify the local arrangement giving rise to the observed SRO (ie. the basic structural unit in the case of a CRN) and also to determine how the IRO arises. A commonly used method for testing various structural ideas has been to construct a cluster model containing of order 1000-2000 atoms and to compare this with experiment. The first such model was that constructed by BELL and DEAN (1970) for SiO_2. These models are constructed according to structural ideas under consideration either by hand using 'ball and stick' type pieces, or by using a computer to generate the atomic coordinates. Usually the model is then relaxed by means of an appropriate interatomic potential so as to minimise the strain energy. In the case of covalently bonded materials the appropriate potential is the KEATING (1966) potential which contains both bond-stretch terms and so-called bond-bend terms (see Chapter 5). The correlation function $t^m(r)$ calculated directly from a model must be corrected for the finite size of the model. MASON (1968) has given the finite size correction factor for a spherical model of diamter L as;

$$t^m(r) = \left(\frac{r-L}{L}\right)^2 \left(\frac{r+2L}{2L}\right) t(r) \qquad (2.5.3)$$

where t(r) is the correlation function for an infinite system of which the model is a representative sample. Of course the correlation function $t^m(r)$ of a spherical model of diameter L is zero for r>L. Modelling techniques have been found to be most useful in characterising the SRO and IRO in amorphous solids and a review of their use for CRN structures is given by ELLIOTT (1983).

It is frequently found that the basic structural unit in an amorphous solid is the same as the basic structural unit in the corresponding crystalline material. Hence LEADBETTER and WRIGHT (1972) have given a method, known as the quasi-crystalline model (not to be confused with the quasi-crystalline materials mentioned in section 2.1), for comparing the SRO in a suitable crystal with the experimentally measured partial correlation functions. This model considers a single crystal sphere with diameter of order 15Å embedded in a homogeneous matrix of the same average density and averaged over all orientations. Thus qualitative comparisons can be made between the SRO and sometimes the IRO of an amorphous solid and a suitable crystal. However, the model does not provide a method for fully characterising the atomic structure.

A rather different approach to structural modelling is the application of Monte Carlo and molecular dynamics (MD) computer simulation techniques. The Monte Carlo technique starts with a cluster of perhaps 1000 atoms, chooses a small random atomic displacement and accepts or rejects the displacement according to some criterion. RENNINGER, RECHTIN and AVERBACH (1974) have performed such a study on the As_xSe_{1-x} system where the criterion which was used was a comparison of the RDF with experiment. An alternative criterion is the minimisation of the strain energy according to an appropriate interatomic potential. The MD technique operates by solving the equations of motion for a cluster of up to about 1000 atoms. A simple interatomic potential is assumed and the atomic trajectories are followed over several thousand time steps, each one typically of order 10^{-15}s. The atomic speeds are progressively reduced and thus the computer liquid is cooled through the glass transition. The advantage of MD over Monte Carlo methods is that dynamic properties can be studied and hence vibrational properties can be predicted in addition to structural properties. Also the glass transition itself can be studied. However, the problem with the technique is that it requires a large amount of computer time with the result that simulated quench rates, of order $10^{12}Ks^{-1}$, are far too high. Also the interatomic potential must be very simple so as to yield reasonable computation times and all the studies so far have used non-directional (ie. ionic or Van der Waals') potentials. Despite this, studies of oxide glasses have been more successful than might have been expected. For example both SOULES (1980) and AMINI, MITRA and HOCKNEY (1981) found planar triangular BO_3 in studies of B_2O_3 using an ionic interatomic potential (see Chapter 12 for further discussion of this).

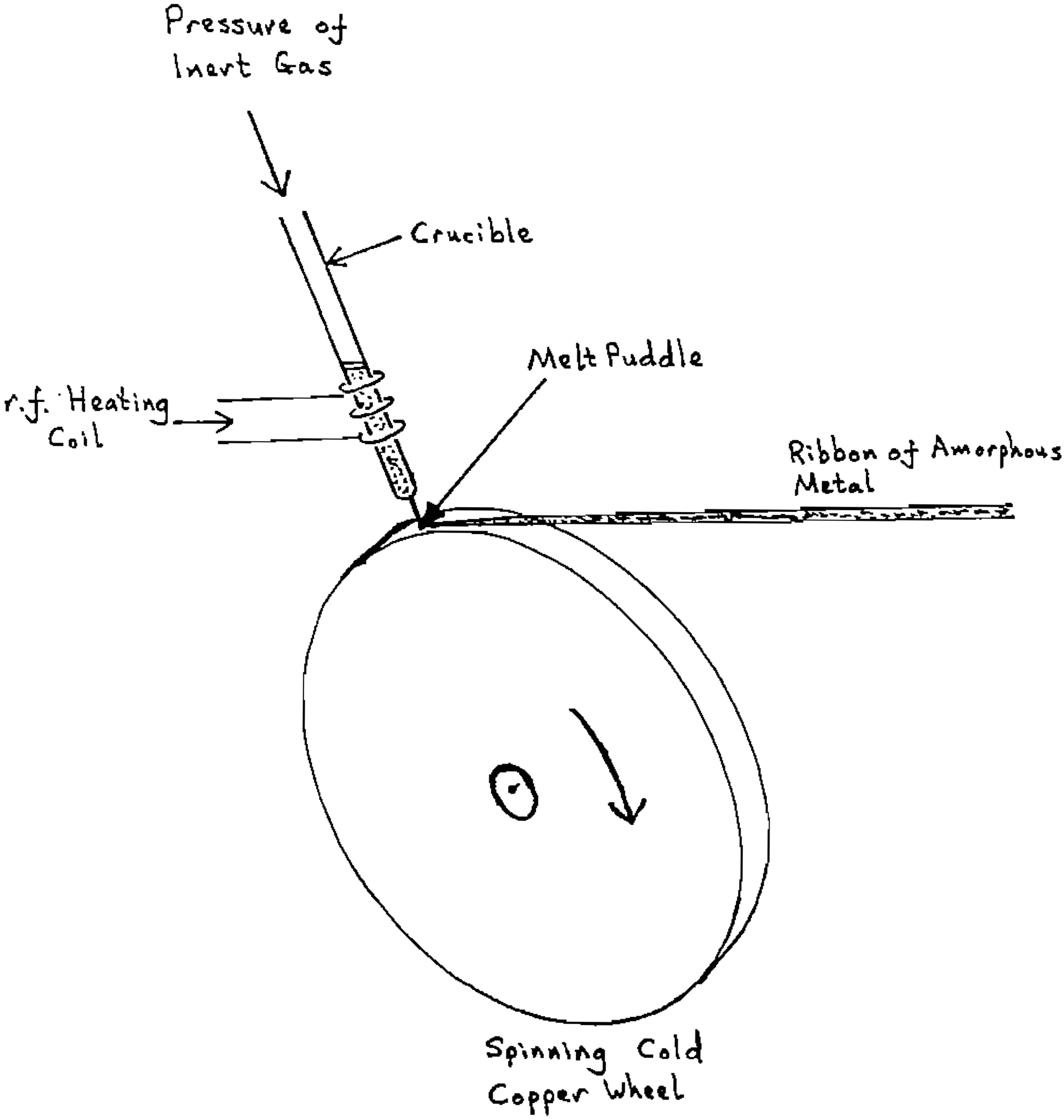

Figure 2.1

The Melt-Spinning Process.

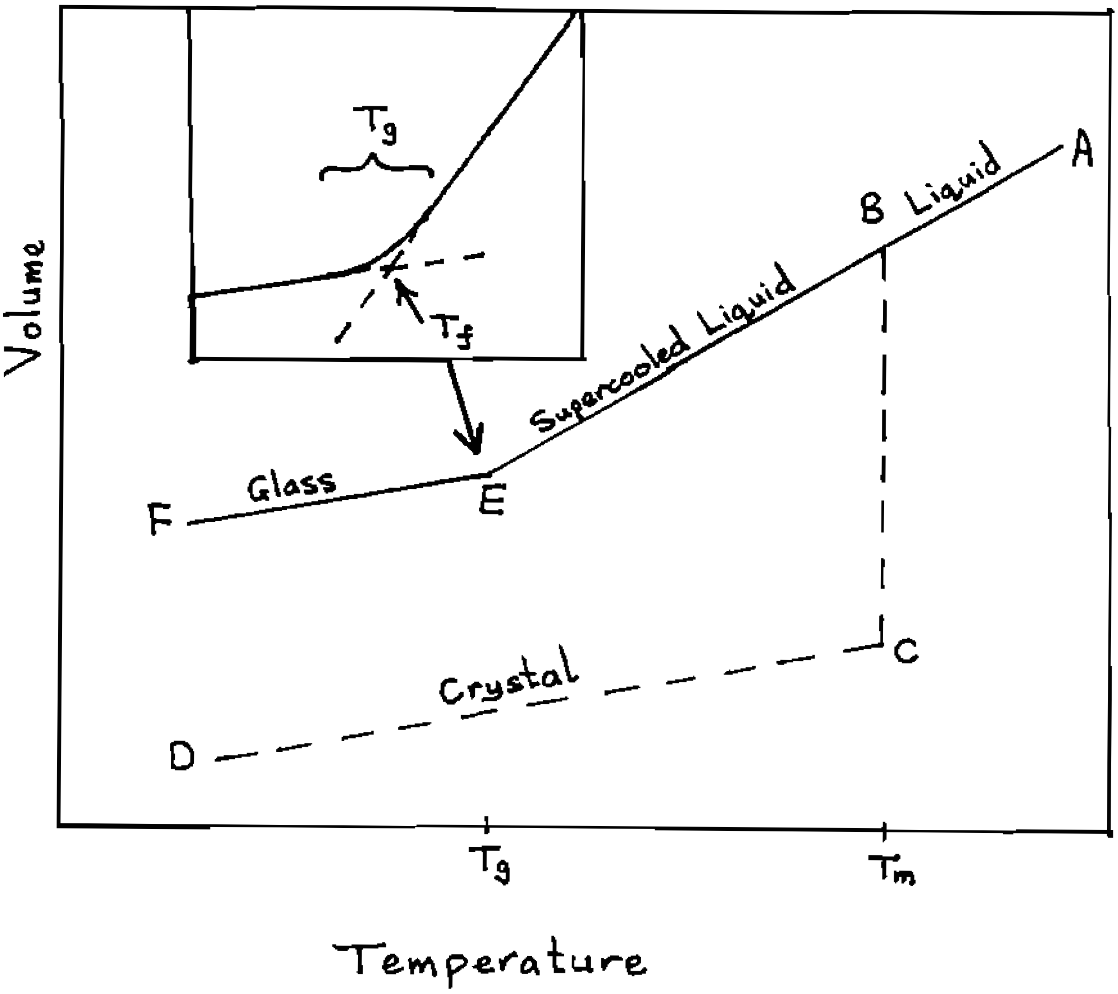

Figure 2.2 V-T Diagram for a Typical Glass-Former.

{after CLARE (1986)}

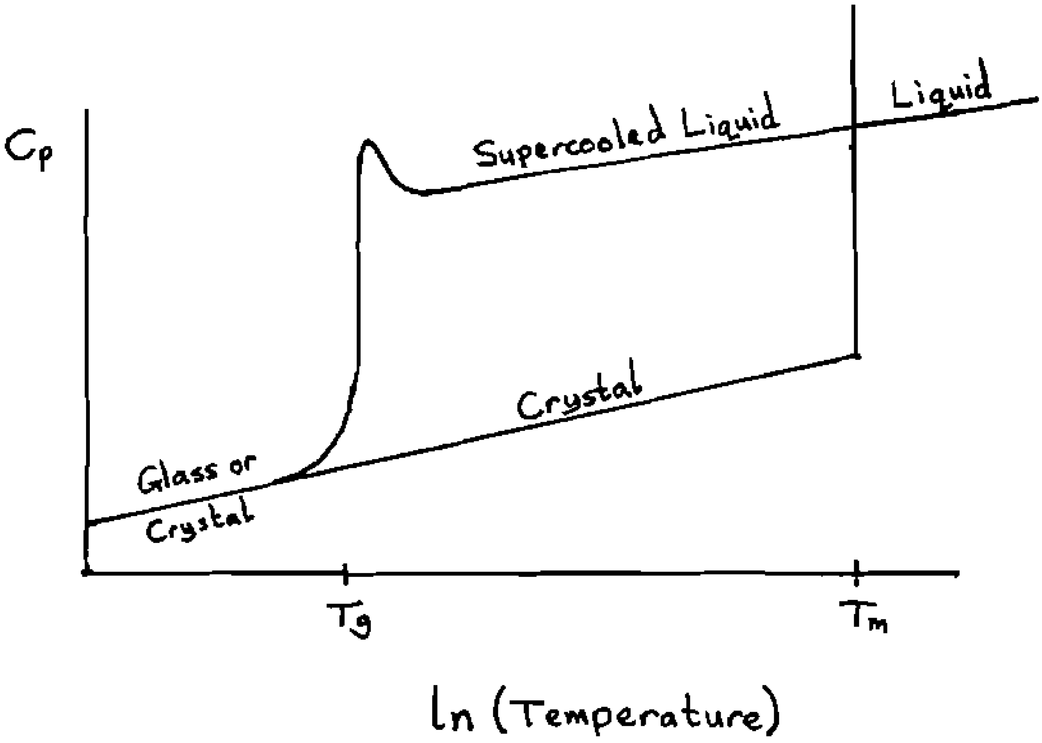

Figure 2.3 The Specific Heat c_p of a Typical Glass-Former.

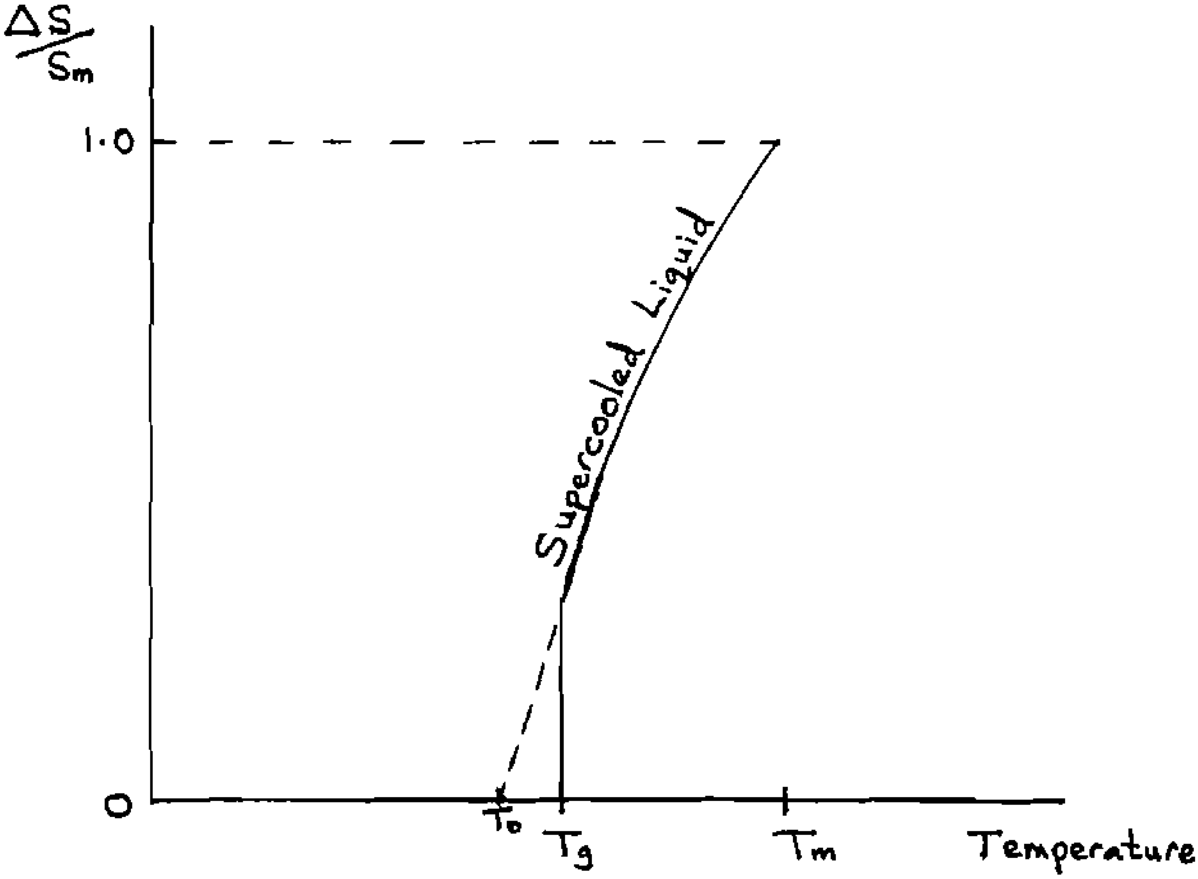

Figure 2.4 The Excess Entropy of a Typical Glass-Forming Supercooled Liquid.

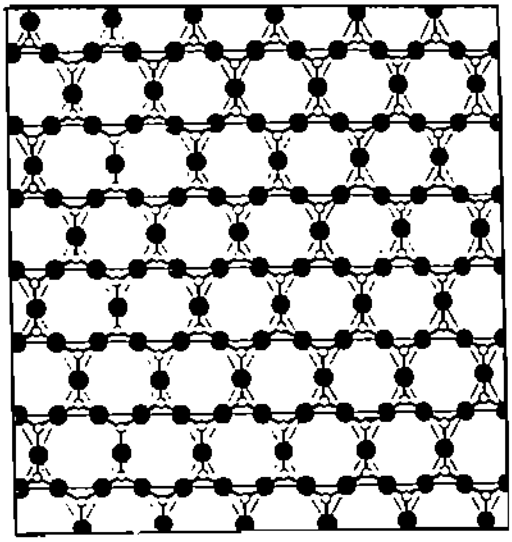

Figure 2.5

A 2D A_2O_3 Crystal.

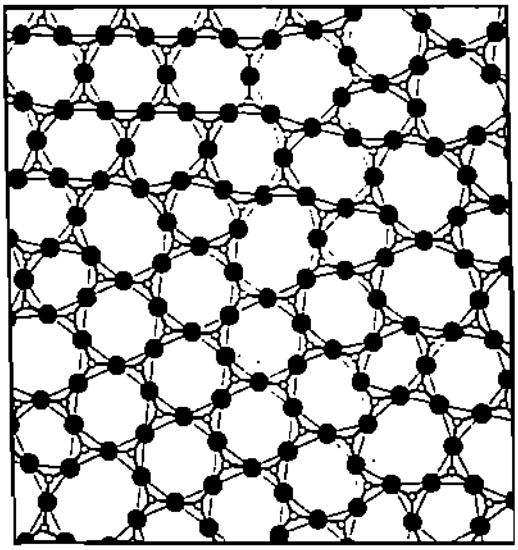

Figure 2.6

A 2D A_2O_3 Glass According to the Crystallite Theory.

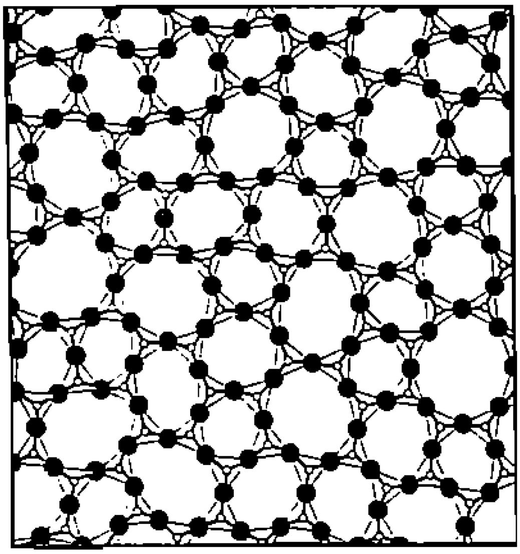

Figure 2.7

A 2D A_2O_3 Glass According to the CRN Theory.

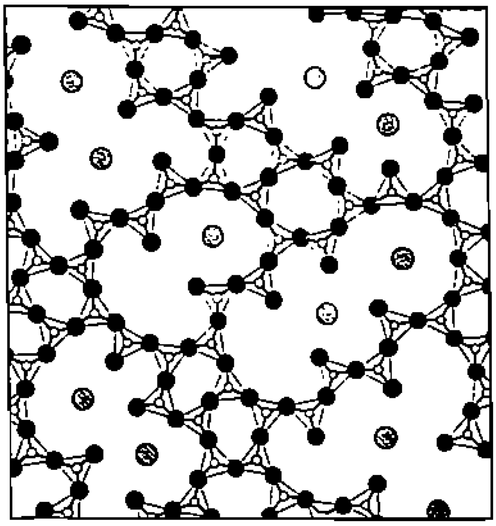

Figure 2.8

A 2D Modified Glass A_2O_3-XO According to the CRN Theory (XO=Modifier).

CHAPTER 3

THE BASIC THEORY OF THERMAL NEUTRON SCATTERING.

3.1 INTRODUCTION.

3.1.1 THE NEUTRON AND NEUTRON SOURCES.

The neutron is a sub-atomic particle which was discovered in 1932 by CHADWICK. The basic properties of the neutron are summarised in table 3.1;

Mass (GOLDMAN, 1972)	1.0086658 amu
Charge	0
Spin	1/2
Magnetic Dipole Moment	$\mu_n = -1.913\mu_N$

Table 3.1

There are two methods which are used for producing thermal neutrons for neutron scattering experiments. These are the nuclear reactor and the pulsed accelerator source. A nuclear reactor produces highly energetic neutrons by the fission of uranium 235 nuclei. The neutrons then undergo collisions within an array of light atoms (for example D_2O) known as a moderator, and the experimental neutron beams are obtained from beam holes which view the moderator. The neutron flux thus obtained is in thermal equilibrium with the moderator, and shows a peak at an energy which depends on the moderator temperature.

A pulsed neutron source operates by accelerating pulsed bursts of charged particles (either protons or electrons) to a high energy. (Of course neutrons cannot be accelerated since they have no charge.) The accelerated particles are then fired into a target and neutrons are produced by a reaction between the particles and the target nuclei (spallation in the case of protons, and bremsstrahlung followed by (γ,n) in the case of electrons). The neutrons produced by these reactions are highly energetic and, as with a reactor, they are thermalised within a moderator. The experimental neutron beams are obtained from beam holes which view the moderator.

See KOSTORZ and LOVESEY (1979) for a description of the reactor source of neutrons at the Institut Laue Langevin and see CARPENTER, LANDER and WINDSOR (1984) for a description of pulsed neutron sources.

3.1.2 THE USE OF NEUTRONS IN CONDENSED MATTER PHYSICS.

There are two interactions which can give rise to the scattering of neutrons by a sample. The first of these is the nuclear force between a neutron and the nuclei of the sample. These nuclear forces are very short range ($\sim 10^{-15}$m), operating over much shorter distances than interatomic distances ($\sim 10^{-10}$m). The second interaction is that between the magnetic moment of the neutron and the unpaired electrons of magnetic atoms. Both of these interactions are relatively weak with the result that neutron scattering experiments are intensity limited and require long counting times. The weakness of these interactions has the advantage that the penetration depth of neutrons in matter is very long and so a neutron scattering experiment samples the bulk properties of the scattering system. This is to be contrasted with the case of X-rays where the scattering is due to the electromagnetic interaction between a photon and the electrons in the scattering system. The electromagnetic interaction is a relatively strong interaction and generally X-rays only penetrate the surface of the scattering system. Thus an X-ray experiment does not sample the bulk properties of the scattering system.

The neutron scattering power of atoms varies haphazardly across the periodic table, unlike the X-ray scattering power which increases steadily with atomic number Z. Thus neutrons are particularly well suited to observing light atoms, especially hydrogen, which are virtually 'invisible' to X-rays. Also neutrons are well suited to systems with elements of similar Z since the contrast in neutron scattering power is generally much greater than the contrast in X-ray scattering power. Furthermore the neutron scattering power of an element can be altered by isotopic substitution so that it is possible to change the contrast between two elements for a neutron scattering experiment.

In the field of thermal neutrons the velocity $2200ms^{-1}$ is often taken as a standard. This corresponds to an energy of 25.3meV, a temperature of 293K (equating kT to energy) and a de Broglie wavelength of 1.798Å. Thus the mass of the neutron is such that thermal neutron wavelengths are of the order of interatomic distances in condensed matter and interference occurs in a thermal neutron scattering experiment which yields information on the atomic structure. The mass of the neutron also leads to a thermal neutron energy which is of the order of the energy of many excitations in condensed matter (eg the phonon spectrum of vitreous B_2O_3 extends from 0meV to 200meV). It follows that inelastic scattering of neutrons (scattering processes which involve the creation or annihilation of an excitation in the scattering system) results in a large fractional change in the neutron energy and accurate information on the energies of excitations can be obtained. The interaction between the magnetic moment of the neutron and the unpaired electrons of atoms enables magnetic systems to be studied with neutrons. The distribution of magnetic moments can be studied by elastic (where elastic means that energy is not transferred between neutron and sample) magnetic scattering, and magnetic excitations can be studied by inelastic (where inelastic means that energy is transferred between neutron and sample) magnetic scattering. Also the ability to determine the state of polarisation of a neutron beam can be of use in studying magnetic systems.

The first experimental demonstrations of the diffraction of neutrons by crystalline materials were performed by MITCHELL AND POWERS (1936) using a radium-beryllium neutron source and by HALBAN AND PREISWERK (1936). The first neutron diffractometer was built at Argonne National Laboratory by ZINN (1947). Nowadays, with the advent of sources dedicated to producing beams for neutron scattering experiments, the applications of neutron scattering to the study of condensed matter physics are many and varied. They may conveniently be divided into two classes: diffraction where energy analysis is not performed, and inelastic scattering where energy analysis is performed.

In a powder diffraction experiment the scattering is measured as a function of momentum transfer between the neutrons and the sample, and by a process of profile refinement a detailed knowledge of the crystal structure can be obtained. A similar technique is also used to study the atomic structure of amorphous materials, and this forms a major part of the work reported in this thesis (Chapters 7 and 9). Single crystals may also be studied using a diffractometer with a large area detector so that the Bragg spots may be observed. A further type of diffraction that is used is small angle neutron scattering (SANS). This technique involves the observation of scattering at very small momentum transfers and yields information on large structures in a sample (tens or hundreds of Ångstroms). An example of the use of SANS is reported in Chapter 10. Another type of diffractometer is used to measure the reflection of neutrons and this is very useful in the study of thin films and layers.

The dispersion relations of excitations in condensed matter can be measured using a neutron spectrometer (the reactor version of which is known as a triple axis spectrometer) which measures the scattering as a function of vector momentum transfer and energy transfer. Also the density of excitation states may be studied using an inelastic scattering time-of-flight spectrometer (see Section 13.1). Diffusion-type processes can be studied by use of a quasi-elastic scattering spectrometer which enables the exchange of small amounts of energy between neutron and sample to be measured with high resolution. The momentum distributions of atoms, and hence the potential wells which they experience, may be probed by use of an inelastic scattering spectrometer which enables large energy transfers between neutron and sample to be observed.

For much more detailed information about the applications of neutron scattering and neutron scattering instruments the reader is referred to the following reviews: KOSTORZ and LOVESEY (1979), WINDSOR (1981), ILL (1983), CARPENTER, LANDER and WINDSOR (1984), AXE and NICKLOW (1985) and ISIS (1988).

3.1.3 THERMAL NEUTRON SCATTERING CROSS-SECTIONS.

In a typical thermal neutron scattering experiment a monochromatic beam of neutrons of energy E and flux Φ is incident on a sample of N atoms known as the scattering system. Neutrons are scattered out of the beam by the scattering system and the total scattering cross-section is defined as;

$$\sigma_{total} = \frac{\text{(Total number of neutrons scattered per unit time)}}{N\ \Phi} \tag{3.1.1}$$

One may consider the variation with direction of the neutron scattering and the relevant experimental quantity is then the differential cross-section, defined as;

$$\frac{d\sigma}{d\Omega} = \frac{\begin{Bmatrix}\text{Number of neutrons scattered per unit time into}\\ \text{the small solid angle } d\Omega \text{ in the direction } (\theta,\phi)\end{Bmatrix}}{N\ \Phi\ d\Omega} \tag{3.1.2}$$

where polar coordinates with the polar axis along the incident beam are used. If E′ is the scattered energy of a neutron then $\varepsilon = E-E'$ is the energy transferred to the sample and one may further consider the variation with energy of the neutron scattering. The relevant experimental quantity is the partial differential cross-section, defined as;

$$\frac{d^2\sigma}{d\Omega d\varepsilon} = \frac{\begin{Bmatrix}\text{Number of neutrons scattered per unit time}\\ \text{into the solid angle } d\Omega \text{ in the direction } (\theta,\phi)\\ \text{with final energy in the range } E-\varepsilon \text{ to } E-(\varepsilon+d\varepsilon)\end{Bmatrix}}{N\ \Phi\ d\Omega\ d\varepsilon} \tag{3.1.3}$$

3.2 THE MASTER FORMULA.

If the interaction potential V between a neutron and the scattering system is treated as a small perturbation then, by use of Fermi's Golden Rule (the Born Approximation), one eventually obtains 'the master formula' (MARSHALL AND LOVESEY, 1971) from which all of neutron scattering theory may be derived. This gives the cross-section representing the sum of all processes in which the neutron changes from a state with momentum $\hbar\underline{k}$ to a state with momentum $\hbar\underline{k}'$ as;

$$\left(\frac{d^2\sigma}{d\Omega d\varepsilon}\right)_{\underline{k}\to\underline{k}'} = \frac{1}{N}\frac{k'}{k}\left(\frac{m}{2\pi\hbar^2}\right)^2 \sum_{\lambda\sigma} p_\lambda p_\sigma \sum_{\lambda'\sigma'} \left|\left\langle \underline{k}'\lambda'\sigma' \middle| V \middle| \underline{k}\,\lambda\,\sigma \right\rangle\right|^2 \delta(E_\lambda - E_{\lambda'} + E - E') \tag{3.2.1}$$

where $|\lambda\rangle$ and $|\lambda'\rangle$ denote initial and final states of the scattering system with energies E_λ and $E_{\lambda'}$ respectively. σ and σ' are the initial and final neutron spin. p_λ denotes the probability that the scattering system is in the state $|\lambda\rangle$, and p_σ denotes the probability distribution of the polarisation of the incident neutrons. m is the neutron mass. Excellent expositions of the quantum mechanics leading to this expression have been given by SQUIRES (1978) and PRICE AND SKÖLD (1986).

3.3 NUCLEAR SCATTERING.

3.3.1 SCATTERING LENGTH AND FERMI PSEUDO-POTENTIAL.

In the case of nuclear scattering the range of the nuclear force interaction between a nucleus and a neutron is very small in comparison with thermal neutron wavelengths. Hence nuclei can be treated as point-like scattering centres which give rise to an isotropic scattered neutron wave (ie only s-wave scattering is considered). The wavefunction of a neutron scattered by a single nucleus at the origin is thus expressed as;

$$\psi_{sc} = -\frac{b}{r}\exp(ik'r) \tag{3.3.1}$$

where b is a constant depending on the potential which describes the interaction between the neutron and the nucleus. Thus the value of b depends on the particular nuclide and the spin state of the neutron-nucleus system. b is in units of length and is generally known as the scattering length. The scattering length is positive for most isotopes, but there are a few isotopes with negative values. A positive scattering length corresponds to a phase change of π between the scattered wave and the incident wave. Usually the thermal neutron scattering length may be taken as real and energy independent, but at energies near an absorption resonance it becomes complex and energy dependent.

In order to describe the interaction between a neutron and an assembly of nuclei the interaction potential is expressed as:

$$V(\underline{r}) = \frac{2\pi\hbar^2}{m}\sum_{j=1}^{N} b_j\ \delta(\underline{r}-\underline{R}_j) \tag{3.3.2}$$

an expression known as the Fermi pseudo-potential. The summation is taken over the the N nuclei whose position vectors and scattering lengths are $\underline{R}_j$ and b_j respectively. The Fermi pseudo-potential is not the true potential which really operates between a neutron and the nuclei of a scattering system. In fact it is not even correct to use perturbation methods for the scattering of a neutron by nuclei because the true interaction potential is too strong. The justification for the use of the Fermi pseudo-potential and the Born approximation is that together they give isotropic s-wave scattering for a single nucleus (equation (3.3.1)) - a result which is known to be correct.

The scattering length defined in equation (3.3.1) relates to a fixed nucleus and is sometimes known as the bound atom scattering length. If the nucleus (mass M) is free then the scattering must be treated in the centre-of-mass frame of reference which involves replacing the neutron mass m by the reduced mass μ $(=mM/(m+M))$ of the nucleus-neutron system. However, since the potential is the same whether the nucleus is fixed or free, equation (3.3.2) shows that the bound atom scattering length b should be replaced by the free atom scattering length $(\mu/m)b$.

The use of the Fermi pseudo-potential in the master formula (3.2.1) eventually results in the following expression;

$$\frac{d^2\sigma}{d\Omega d\varepsilon} = \frac{1}{N}\frac{k'}{k}\frac{1}{2\pi\hbar}\sum_{jj'} b_j b_{j'} \int_{-\infty}^{\infty} \left\langle \exp(-i\underline{Q}.\underline{R}_j(0))\exp(i\underline{Q}.\underline{R}_{j'}(t)) \right\rangle \exp(-i\omega t)dt \tag{3.3.3}$$

The summations j and j′ are taken over the nuclei of the scattering system. The angular brackets denote a thermal average at the temperature T of the scattering system, and t is of course time. The energy transfer (ie energy transferred to the scattering system) is defined as;

$$\hbar\omega = \varepsilon = E - E' \tag{3.3.4}$$

Similarly the momentum transfer, or scattering vector as it is also known, is defined as;

$$\hbar\underline{Q} = \hbar\underline{k} - \hbar\underline{k}' \qquad (3.3.5)$$

Thus the energy transfer ε and scattering vector $\underline{Q}$ are the two variables which specify the interaction of a neutron with the scattering system. If $\varepsilon=0$ the interaction is termed elastic, and if $\varepsilon\neq0$ the interaction is termed inelastic. It should be noted that $\underline{R}_j(0)$ and $\underline{R}_{j'}(t)$ in (3.3.3) are Heisenberg operators.

3.3.2 DISTINCT AND SELF SCATTERING.

For convenience one may define;

$$\left\langle j,j'\right\rangle = \frac{1}{N}\frac{k'}{k}\frac{1}{2\pi\hbar}\int_{-\infty}^{\infty}\left\langle \exp(-i\underline{Q}.\underline{R}_j(0))\exp(i\underline{Q}.\underline{R}_{j'}(t))\right\rangle \exp(-i\omega t)dt \qquad (3.3.6)$$

Equation (3.3.3) may thus be rewritten as;

$$\frac{d^2\sigma}{d\Omega d\varepsilon} = \sum_{jj'} b_j b_{j'} \left\langle j,j'\right\rangle \qquad (3.3.7)$$

Let N_l be the number of atoms of element l in the scattering system. Equation (3.3.7) can then be divided into two parts;

$$\frac{d^2\sigma}{d\Omega d\varepsilon} = \sum_{\substack{ll'\\ l\neq l'}} \sum_{j=1}^{N_l} \sum_{j'=1}^{N_{l'}} b_j b_{j'} \left\langle j,j'\right\rangle + \sum_{l} \sum_{j=1}^{N_l} \sum_{j'=1}^{N_l} b_j b_{j'} \left\langle j,j'\right\rangle \qquad (3.3.8)$$

where the summations l and l' are taken over elements and the summations j and j' are now over the nuclei of one element only. This expression may be simplified with respect to the scattering length values. The approach is to average the cross-section over all possible distributions of scattering length, assuming that there is no correlation between the scattering length values of nuclei of the same element. This assumption is true in all but a very few special cases. The averaging process may be thought of as calculating the cross-section for a very large number of scattering systems, identical in nuclear positions and motions, one with each possible distribution of b_j values, and taking an average. Since the number of nuclei in any real scattering system is extremely large ($\sim 10^{24}$) it is statistically extremely likely that the true cross-section is very close to this averaged value. Equation (3.3.8) thus becomes;

$$\frac{d^2\sigma}{d\Omega d\varepsilon} = \sum_{\substack{ll' \\ l\neq l'}} \sum_{j=1}^{N_l} \sum_{j'=1}^{N_{l'}} \overline{b_j b_{j'}} \left\langle j,j' \right\rangle + \sum_{l} \sum_{j=1}^{N_l} \sum_{j'=1}^{N_l} \overline{b_j b_{j'}} \left\langle j,j' \right\rangle \tag{3.3.9}$$

For the first of these two terms the indices j and j' never refer to the same nucleus. Hence $\overline{b_j b_{j'}}$ may be replaced by $\bar{b}_l \bar{b}_{l'}$, where $\bar{b}_l$ denotes the average value of b for all the nuclei of element l in the scattering system. For the second term of (3.3.9) one may make the same substitution for terms with $j\neq j'$. For terms with $j=j'$, however, $\overline{b_j b_{j'}}$ must be replaced with $\overline{b_l^{\,2}}$, the average square scattering length for all the nuclei of element l in the scattering system. Thus equation (3.3.9) becomes;

$$\frac{d^2\sigma}{d\Omega d\varepsilon} = \sum_{\substack{ll' \\ l\neq l'}} \bar{b}_l \bar{b}_{l'} \sum_{j=1}^{N_l} \sum_{j'=1}^{N_{l'}} \left\langle j,j' \right\rangle + \sum_{l} \bar{b}_l^{\,2} \sum_{j=1}^{N_l} \sum_{\substack{j'=1 \\ j\neq j'}}^{N_l} \left\langle j,j' \right\rangle + \sum_{l} \overline{b_l^{\,2}} \sum_{j=1}^{N_l} \left\langle j,j \right\rangle$$

$$= \sum_{ll'} \bar{b}_l \bar{b}_{l'} \sum_{j=1}^{N_l} \sum_{\substack{j'=1 \\ j\neq j'}}^{N_{l'}} \left\langle j,j' \right\rangle + \sum_{l} \overline{b_l^{\,2}} \sum_{j=1}^{N_l} \left\langle j,j \right\rangle \tag{3.3.10}$$

where $j\neq j'$ indicates that the indices j and j' are not allowed to refer to the same nucleus.

It follows that the cross-section naturally divides into two parts;

$$\frac{d^2\sigma}{d\Omega d\varepsilon} = \left(\frac{d^2\sigma}{d\Omega d\varepsilon}\right)^D + \left(\frac{d^2\sigma}{d\Omega d\varepsilon}\right)^S \qquad (3.3.11)$$

where;

$$\left(\frac{d^2\sigma}{d\Omega d\varepsilon}\right)^D = \frac{1}{N}\frac{k'}{k}\frac{1}{2\pi\hbar}\sum_{ll'}\bar{b}_l\bar{b}_{l'}\sum_{j=1}^{N_l}\sum_{\substack{j'=1\\ j\neq j'}}^{N_{l'}}\int_{-\infty}^{\infty}\left\langle\exp(-i\underline{Q}.\underline{R}_j(0))\exp(i\underline{Q}.\underline{R}_{j'}(t))\right\rangle\exp(-i\omega t)dt \qquad (3.3.12)$$

$$\left(\frac{d^2\sigma}{d\Omega d\varepsilon}\right)^S = \frac{1}{N}\frac{k'}{k}\frac{1}{2\pi\hbar}\sum_{l}\overline{b_l^2}\sum_{j=1}^{N_l}\int_{-\infty}^{\infty}\left\langle\exp(-i\underline{Q}.\underline{R}_j(0))\exp(i\underline{Q}.\underline{R}_j(t))\right\rangle\exp(-i\omega t)dt \qquad (3.3.13)$$

The cross-section defined in equation (3.3.12) is known as the distinct cross-section and that defined in equation (3.3.13) is known as the self cross-section. This separation of the cross-section into off-diagonal and diagonal terms is due to PLACZEK (1952). The distinct scattering cross-section relates to correlations between the positions of one nucleus at time zero and a second different nucleus at time t. The self scattering cross-section relates to correlations between the positions of the same nucleus at different times. Correlations between nuclear positions are discussed in more detail in section 3.3.4.

At this stage it is useful to define the distinct and self partial scattering functions;

$$S^D_{ll'}(\underline{Q},\omega) = \frac{1}{N_l}\frac{1}{2\pi}\sum_{j=1}^{N_l}\sum_{\substack{j'=1\\ j\neq j'}}^{N_{l'}}\int_{-\infty}^{\infty}\left\langle\exp(-i\underline{Q}.\underline{R}_j(0))\exp(i\underline{Q}.\underline{R}_{j'}(t))\right\rangle\exp(-i\omega t)dt \qquad (3.3.14)$$

$$S^{S}_{l}(\underline{Q},\omega) = \frac{1}{N_l}\,\frac{1}{2\pi}\sum_{j=1}^{N_l}\int_{-\infty}^{\infty}\Big\langle \exp(-i\underline{Q}.\underline{R}_j(0))\exp(i\underline{Q}.\underline{R}_j(t))\Big\rangle \exp(-i\omega t)\,dt \qquad (3.3.15)$$

Substituting in (3.3.12) and (3.3.13) gives;

$$\left(\frac{d^2\sigma}{d\Omega d\varepsilon}\right)^{D} = \frac{k'}{k}\,\frac{1}{\hbar}\sum_{ll'} c_l\,\bar{b}_l\bar{b}_{l'}\,S^{D}_{ll'}(\underline{Q},\omega) \qquad (3.3.16)$$

$$\left(\frac{d^2\sigma}{d\Omega d\varepsilon}\right)^{S} = \frac{k'}{k}\,\frac{1}{\hbar}\sum_{l} c_l\,\overline{b_l^{2}}\,S^{S}_{l}(\underline{Q},\omega) \qquad (3.3.17)$$

where c_l , the composition variable for element l, is defined by;

$$c_l = N_l \,/\, N \qquad (3.3.18)$$

The scattering function is incorrectly referred to by some authors as the scattering law. An alternative equivalent formalism for the distinct and self scattering which is favoured particularly by chemists working in the field (WRIGHT, 1974) is;

$$N\left(\frac{d^2\sigma}{d\Omega d\varepsilon}\right)^{D} = N_u\,\frac{k'}{k}\,\frac{1}{\hbar}\sum_{j}\sum_{k}\bar{b}_j\bar{b}_k\,S^{D}_{jk}(\underline{Q},\omega) \qquad (3.3.19)$$

$$N\left(\frac{d^2\sigma}{d\Omega d\varepsilon}\right)^{S} = N_u\,\frac{k'}{k}\,\frac{1}{\hbar}\sum_{j}\overline{b_j^{2}}\,S^{S}_{j}(\underline{Q},\omega) \qquad (3.3.20)$$

where all j summations are taken over the individual atoms in a composition unit, and k summations are taken over atom types. N_u is the number of composition units in the scattering system. In fact the exact definitions of many of the functions discussed in this Chapter vary greatly, and a difference in coefficients between an equation in this thesis and an equation in another author's work is probably just a symptom of this.

3.3.3 COHERENT AND INCOHERENT SCATTERING.

An alternative formalism for subdividing the cross-section is that of coherent and incoherent scattering. This formalism is of more widespread use than that of distinct and self scattering, but is not as appropriate to the study of amorphous materials. Equation (3.3.10) may be recast by adding and subtracting a term $\sum_{l} \bar{b}_l^{\,2} \sum_{j=1}^{N_l} \left\langle j,j' \right\rangle$;

$$\frac{d^2\sigma}{d\Omega d\varepsilon} = \sum_{ll'} \bar{b}_l \bar{b}_{l'} \sum_{j=1}^{N_l} \sum_{j'=1}^{N_{l'}} \left\langle j,j' \right\rangle + \sum_{l} \left(\overline{b_l^{\,2}} - \bar{b}_l^{\,2} \right) \sum_{j=1}^{N_l} \left\langle j,j \right\rangle \tag{3.3.21}$$

The cross-section can then be divided into two parts;

$$\frac{d^2\sigma}{d\Omega d\varepsilon} = \left(\frac{d^2\sigma}{d\Omega d\varepsilon}\right)^{coh} + \left(\frac{d^2\sigma}{d\Omega d\varepsilon}\right)^{inc} \tag{3.3.22}$$

where;

$$\left(\frac{d^2\sigma}{d\Omega d\varepsilon}\right)^{coh} = \frac{1}{N}\frac{k'}{k}\frac{1}{2\pi\hbar} \sum_{ll'} \bar{b}_l \bar{b}_{l'} \sum_{j=1}^{N_l} \sum_{j'=1}^{N_{l'}} \int_{-\infty}^{\infty} \left\langle \exp(-i\underline{Q}.\underline{R}_j(0)) \exp(i\underline{Q}.\underline{R}_{j'},(t)) \right\rangle \exp(-i\omega t)dt \tag{3.3.23}$$

$$\left(\frac{d^2\sigma}{d\Omega d\varepsilon}\right)^{inc} = \frac{1}{N}\frac{k'}{k}\frac{1}{2\pi\hbar} \sum_{l} \left(\overline{b_l^{\,2}} - \bar{b}_l^{\,2} \right) \sum_{j=1}^{N_l} \int_{-\infty}^{\infty} \left\langle \exp(-i\underline{Q}.\underline{R}_j(0)) \exp(i\underline{Q}.\underline{R}_j(t)) \right\rangle \exp(-i\omega t)dt \tag{3.3.24}$$

The cross-section defined in equation (3.3.23) is known as the coherent scattering cross-section, and that defined in equation (3.3.24) is known as the incoherent scattering cross-section. Coherent and incoherent partial scattering functions are defined as follows;

$$S^{coh}_{ll'}(\underline{Q},\omega) = \frac{1}{N_l}\,\frac{1}{2\pi}\sum_{j=1}^{N_l}\;\sum_{j'=1}^{N_{l'}}\int_{-\infty}^{\infty}\left\langle \exp(-i\underline{Q}.\underline{R}_j(0))\exp(i\underline{Q}.\underline{R}_{j'}(t))\right\rangle \exp(-i\omega t)\,dt \tag{3.3.25}$$

$$S^{inc}_{l}(\underline{Q},\omega) = S^{S}_{l}(\underline{Q},\omega) \tag{3.3.26}$$

Note that the equivalence of the incoherent and self partial scattering functions in no way implies an equivalence of the incoherent and self cross-sections. Substituting $S^{coh}_{ll'}(\underline{Q},\omega)$ and $S^{inc}_{l}(\underline{Q},\omega)$ in (3.3.23) and (3.3.24) gives;

$$\left(\frac{d^2\sigma}{d\Omega d\varepsilon}\right)^{coh} = \frac{k'}{k}\,\frac{1}{\hbar}\sum_{ll'} c_l\;\bar{b}_l\bar{b}_{l'}\;S^{coh}_{ll'}(\underline{Q},\omega) \tag{3.3.27}$$

$$\left(\frac{d^2\sigma}{d\Omega d\varepsilon}\right)^{inc} = \frac{k'}{k}\,\frac{1}{\hbar}\sum_{l} c_l\left(\overline{b_l^{\,2}} - \bar{b}_l^{\,2}\right) S^{inc}_{l}(\underline{Q},\omega) \tag{3.3.28}$$

Examination of (3.3.14) and (3.3.25) shows that;

$$S^{coh}_{ll'}(\underline{Q},\omega) = S^{D}_{ll'}(\underline{Q},\omega) + \delta_{ll'}\,S^{S}_{l}(\underline{Q},\omega) \tag{3.3.29}$$

The average scattering length $\bar{b}_l$ for element l is termed the coherent scattering length. Similarly one may define an incoherent scattering length for the element l;

$$(b^{inc}_l)^2 = \overline{b_l^{\,2}} - \bar{b}_l^{\,2} \tag{3.3.30}$$

By a simple rearrangement;

$$\begin{aligned}(b^{inc}_l)^2 &= \overline{b_l^{\,2}} + \bar{b}_l^{\,2} - 2\bar{b}_l^{\,2}\\ &= \frac{1}{N}\sum_{j=1}^{N_l} b_j^{\,2} + \bar{b}_l^{\,2} - 2\bar{b}_l\,\frac{1}{N}\sum_{j=1}^{N_l} b_j\end{aligned}$$

$$= \frac{1}{N} \sum_{j=1}^{N_1} \left(b_j^2 + \bar{b}_1^2 - 2\bar{b}_1 b_j \right)$$

$$= \frac{1}{N} \sum_{j=1}^{N_1} \left(b_j - \bar{b}_1 \right)^2$$

$$= \overline{(b - \bar{b})^2} \qquad (3.3.31)$$

Thus the incoherent scattering length is the root mean square deviation of the scattering length from the mean value, and the coherent and incoherent scattering cross-sections may be interpreted as follows: The coherent scattering is the scattering that would be obtained from a scattering system for which all nuclei of element 1 had a scattering length of $\bar{b}_1$. The incoherent scattering meanwhile arises from the random distribution of deviations of the scattering length from the mean value for each element. The coherent scattering involves correlations between the positions of nuclei at different times and hence gives interference effects. The incoherent scattering only involves correlations between the positions of the same nucleus at different times and does not give interference effects.

There are two factors which give rise to incoherent scattering. These are spin incoherence and isotopic incoherence. Spin incoherence is due to the fact that a neutron and a nucleus of spin I can form two different compound nuclei of spin $I\pm\frac{1}{2}$; the amplitude of the neutron wave scattered by the nucleus, and thus the scattering length is generally different for the two different compound nuclei. There are $(2I+1\pm1)$ states associated with spin $I\pm\frac{1}{2}$ and it follows statistically that for a single isotope i;

$$\bar{b}_i = (2I+1)^{-1} \left[(I+1)b_i^+ + Ib_i^- \right] \qquad (3.3.32)$$

$$\overline{b_i^2} = (2I+1)^{-1} \left[(I+1)(b_i^+)^2 + I(b_i^-)^2 \right] \qquad (3.3.33)$$

where the superscripts + and - indicate respectively the scattering lengths for the I+½ and the I-½ compound nuclei which are formed between the isotope i nucleus and the neutron. This assumes that the neutrons are not polarised and that the nuclear spins are oriented at random. Note also that in the case of zero nuclear spin (I=0) there is no spin incoherence. Isotopic incoherence arises as a result of the presence of more than one isotope of a particular element. For an element l;

$$\bar{b}_l = \sum_i f_i \bar{b}_i \qquad (3.3.34)$$

$$\overline{b_l^2} = \sum_i f_i \overline{b_i^2} \qquad (3.3.35)$$

where f_i is the abundance of the isotope i. Obviously equations (3.3.30) to (3.3.35) may be combined to evaluate the coherent and incoherent scattering lengths for an element l.

3.3.4 VAN HOVE CORRELATION FUNCTIONS.

The formalism for describing scattering in terms of a generalised pair distribution function in space and time was first developed by VAN HOVE (1954a). The generalised pair distribution function, or Van Hove correlation function as it is often known, is defined as;

$$G(\underline{r},t) = \frac{1}{N} \sum_{j=1}^{N} \sum_{j'=1}^{N} \int \left\langle \delta(\underline{r}'-\underline{R}_j(0))\ \delta(\underline{r}'+\underline{r}-\underline{R}_{j'}(t)) \right\rangle d\underline{r}' \qquad (3.3.36)$$

where the summations are over all atoms in the scattering system. The pair correlation function may then be divided into distinct and self partial correlation functions;

$$G(\underline{r},t) = \sum_{ll'} c_l \, G^D_{ll'}(\underline{r},t) + \sum_{l} c_l \, G^S(\underline{r},t) \tag{3.3.37}$$

where;

$$G^D_{ll'}(\underline{r},t) = \frac{1}{N_l} \sum_{\substack{j=1 \\ j\neq j'}}^{N_l} \sum_{j'=1}^{N_{l'}} \int \left\langle \delta(\underline{r}'-\underline{R}_j(0)) \; \delta(\underline{r}'+\underline{r}-\underline{R}_{j'}(t)) \right\rangle d\underline{r}' \tag{3.3.38}$$

$$G^S_l(\underline{r},t) = \frac{1}{N_l} \sum_{j=1}^{N_l} \int \left\langle \delta(\underline{r}'-\underline{R}_j(0)) \; \delta(\underline{r}'+\underline{r}-\underline{R}_j(t)) \right\rangle d\underline{r}' \tag{3.3.39}$$

(Note that all integrals without limits are assumed to be over the whole range of the variable concerned.) Replacing the second delta function of (3.3.38) with its integral representation gives;

$$G^D_{ll'}(\underline{r},t) = \frac{1}{N_l} \sum_{\substack{j=1 \\ j\neq j'}}^{N_l} \sum_{j'=1}^{N_{l'}} \int \left\langle \delta(\underline{r}'-\underline{R}_j(0)) \left[\frac{1}{(2\pi)^3} \int \exp(-i\underline{Q}.(\underline{r}'+\underline{r}-\underline{R}_{j'}(t)))d\underline{Q}\right] \right\rangle d\underline{r}'$$

$$= \frac{1}{N_l} \frac{1}{(2\pi)^3} \sum_{\substack{j=1 \\ j\neq j'}}^{N_l} \sum_{j'=1}^{N_{l'}} \int \exp(-i\underline{Q}.\underline{r}) \left\langle \exp(-i\underline{Q}.\underline{R}_j(0) \; \exp(i\underline{Q}.\underline{R}_{j'}(t)) \right\rangle d\underline{Q} \tag{3.3.40}$$

Similarly for the self correlation function;

$$G^S_l(\underline{r},t) = \frac{1}{N_l} \frac{1}{(2\pi)^3} \sum_{j=1}^{N_l} \int \exp(-i\underline{Q}.\underline{r}) \left\langle \exp(-i\underline{Q}.\underline{R}_j(0) \; \exp(i\underline{Q}.\underline{R}_j(t)) \right\rangle d\underline{Q} \tag{3.3.41}$$

From (3.3.40) one obtains;

$$\int G^{D}_{ll'}(\underline{r},t)\ \exp(i\underline{Q}'.\underline{r})\ d\underline{r} =$$

$$\frac{1}{N}\ \frac{1}{(2\pi)^3} \sum_{j=1}^{N_l} \sum_{j'=1}^{N_{l'}} \iint \exp(i(\underline{Q}'-\underline{Q}).\underline{r})\ d\underline{r} \left\langle \exp(-i\underline{Q}.\underline{R}_j(0)\ \exp(i\underline{Q}.\underline{R}_{j'}(t)) \right\rangle d\underline{Q}$$

$$= \frac{1}{N_l}\ \frac{1}{(2\pi)^3} \sum_{\substack{j=1 \\ j\neq j'}}^{N_l} \sum_{j'=1}^{N_{l'}} \int (2\pi)^3\ \delta(\underline{Q}'-\underline{Q}) \left\langle \exp(-i\underline{Q}.\underline{R}_j(0)\ \exp(i\underline{Q}.\underline{R}_{j'}(t)) \right\rangle d\underline{Q}$$

$$= \frac{1}{N_l} \sum_{\substack{j=1 \\ j\neq j'}}^{N_l} \sum_{j'=1}^{N_{l'}} \left\langle \exp(-i\underline{Q}'.\underline{R}_j(0)\ \exp(i\underline{Q}'.\underline{R}_{j'}(t)) \right\rangle \qquad (3.3.42)$$

Similarly for the self correlation function;

$$\int G^{S}_{l}(\underline{r},t)\ \exp(i\underline{Q}.\underline{r})\ d\underline{r} = \frac{1}{N_l} \sum_{j=1}^{N_l} \left\langle \exp(-i\underline{Q}'.\underline{R}_j(0)\ \exp(i\underline{Q}'.\underline{R}_j(t)) \right\rangle \qquad (3.3.43)$$

Substituting this result in (3.3.14) gives;

$$S^{D}_{ll'}(\underline{Q},\omega) = (1/2\pi) \iint G^{D}_{ll'}(\underline{r},t)\ \exp(i(\underline{Q}.\underline{r}-\omega t))\ d\underline{r}\ dt \qquad (3.3.44)$$

Thus $S^{D}_{ll'}(\underline{Q},\omega)$ and $G^{D}_{ll'}(\underline{r},t)$ form a Fourier transform pair and;

$$G^{D}_{ll'}(\underline{r},t) = (1/(2\pi)^3) \iint S^{D}_{ll'}(\underline{Q},\omega)\ \exp(-i(\underline{Q}.\underline{r}-\omega t))\ d\underline{Q}\ d\omega \qquad (3.3.45)$$

Similarly;

$$S^{S}_{l}(\underline{Q},\omega) = (1/2\pi) \iint G^{S}_{l}(\underline{r},t)\ \exp(i(\underline{Q}.\underline{r}-\omega t))\ d\underline{r}\ dt \qquad (3.3.46)$$

and;

$$G^{S}_{l}(\underline{r},t) = (1/(2\pi)^3) \iint S^{S}_{l}(\underline{Q},\omega)\ \exp(-i(\underline{Q}.\underline{r}-\omega t))\ d\underline{Q}\ d\omega \qquad (3.3.47)$$

Substituting (3.3.44) in (3.3.16) and (3.3.46) in (3.3.17) finally gives the distinct and self cross-sections in terms of the correlation functions as;

$$\left(\frac{d^2\sigma}{d\Omega d\varepsilon}\right)^D = \frac{k'}{k}\,\frac{1}{2\pi\hbar}\sum_{ll'} c_l\,\bar{b}_l\bar{b}_{l'}\iint G^D_{ll'}(\underline{r},t)\,\exp(i(\underline{Q}.\underline{r}-\omega t))\,d\underline{r}\,dt \tag{3.3.48}$$

$$\left(\frac{d^2\sigma}{d\Omega d\varepsilon}\right)^S = \frac{k'}{k}\,\frac{1}{2\pi\hbar}\sum_{l} c_l\,\overline{b_l^{\,2}}\iint G^S_{l}(\underline{r},t)\,\exp(i(\underline{Q}.\underline{r}-\omega t))\,d\underline{r}\,dt \tag{3.3.49}$$

Equations (3.3.48) and (3.3.49) show that the neutron scattering cross-section for nuclear scattering is directly related to the partial pair correlation functions. Thus a measurement of the nuclear cross-section yields information about the pair correlation functions and hence information about the relative positions and motions of the nuclei. Note that it is only for a sample with a single scattering length (ie a monatomic sample with just one zero spin isotope present) that the cross-section is directly related to the pair correlation function rather than a combination of the distinct and self partial correlation functions.

The physical meaning of the pair correlation functions may be explained by use of a particle density operator;

$$\rho_l(\underline{r},t) = \sum_{j=1}^{N_l} \delta(\,\underline{r} - \underline{R}_j(t)\,) \tag{3.3.50}$$

where $\rho_l(\underline{r},t)$ is the number density of nuclei of element l at position $\underline{r}$ at time t. Suppose there is an l nucleus at position $\underline{r}'$ at time t=0. The number of nuclei of element l′ which at time t are $\underline{r}$ away in the volume $\delta\underline{r}$ is $\rho_{l'}(\underline{r}'+\underline{r},t)\delta\underline{r}$. Averaging this number over all l nuclei gives the average number of l′ nuclei in a volume $\delta\underline{r}$ which is $(\underline{r},t)$ away from an l nucleus as $(1/N_l)\int\rho_l(\underline{r}',0)\rho(\underline{r}+\underline{r}',t)d\underline{r}'\delta\underline{r}$. If $\delta\underline{r}$ is allowed to become infinitesimal then this expression may be interpreted as the probability that a volume $d\underline{r}$ which is $(\underline{r},t)$ away from an l nucleus contains an l′ nucleus.

Substituting (3.3.50) in equations (3.3.38) and (3.3.39) yields;

$$G^D_{ll'}(\underline{r},t) = \frac{1}{N_l}\int\left\langle \rho'_l(\underline{r}',0)\ \rho_{l'}(\underline{r}'+\underline{r},t)\right\rangle d\underline{r}' \qquad (3.3.51)$$

$$G^S_l(\underline{r},t) = \frac{1}{N_l}\int\left\langle \rho_l(\underline{r}',0)\ \rho_l(\underline{r}'+\underline{r},t)\right\rangle d\underline{r}' \qquad (3.3.52)$$

where the prime of ρ' is used to imply that terms for which $l=l'$ have been omitted from the summation. The partial pair correlation functions may thus be interpreted as follows:

$G^D_{ll'}(\underline{r},t)d\underline{r}$ is the thermally averaged probability that, given a nucleus of element l at some position $\underline{r}'$ at time t=0, a nucleus of element l′ (but not the same nucleus even if $l'=l$) is in the volume $d\underline{r}$ at position $\underline{r}'+\underline{r}$ at time t, averaged over all the nuclei of element l.

$G^S_l(\underline{r},t)d\underline{r}$ is the thermally averaged probability that, given a nucleus of element l at some position $\underline{r}'$ at time t=0, the same nucleus is in the volume $d\underline{r}$ at position $\underline{r}'+\underline{r}$ at time t, averaged over all the nuclei of element l.

3.4 MAGNETIC SCATTERING.

The purpose of this section is to introduce the theory of the magnetic scattering of neutrons by unpaired electrons in the scattering system. The potential describing the magnetic interaction between a neutron and an electron of momentum $\underline{p}$ may be shown (SQUIRES, 1978) by use of standard electromagnetism to be;

$$V(\underline{r}) = -(\mu_0/4\pi)\gamma\mu_N 2\mu_B\ \underline{\sigma}.[\ \mathrm{curl}\ (\underline{s}\times\underline{\hat{r}}/r^2) + (1/\hbar)p\times\underline{\hat{r}}/r^2\ ] \tag{3.4.1}$$

where γ=1.9132 and μ_N (=$e\hbar/2m_p$) and μ_B (=$e\hbar/2m_e$) are the nuclear and Bohr magnetons. m_p and m_e are respectively the proton and electron rest masses. $\underline{\sigma}$ is the Pauli spin operator for the neutron with eigenvalues of a component of ±1 . $\underline{s}$ is the spin angular momentum operator for the electron with eigenvalues of a component of ±1/2 . $\underline{r}$ is the vector from the electron to the neutron. Note that a proper treatment of this problem would require the use of the Dirac equation (HALPERN and JOHNSON, 1939).

Summing the potential (3.4.1) over all the unpaired electrons in the scattering system and using the master formula (3.2.1) eventually results in the following expression;

$$\frac{d^2\sigma}{d\Omega d\varepsilon} = \frac{1}{N}\frac{k'}{k}\ (\gamma r_0)^2\ \frac{1}{2\pi\hbar}\sum_{jj'} f_j^*(\underline{Q})\ f_{j'}(\underline{Q}) \int_{-\infty}^{\infty} \left\langle \underline{\mu}_{j\perp}(0)\ .\ \underline{\mu}_{j'\perp}(t) \right\rangle$$
$$\left\langle \exp(-i\underline{Q}.\underline{R}_j(0))\ \exp(i\underline{Q}.\underline{R}_{j'}(t)) \right\rangle \exp(-i\omega t)\ dt \tag{3.4.2}$$

where r_0 is the classical electron radius;

$$r_0 = (\mu_0/4\pi)\ (e^2/m_e) \tag{3.4.3}$$

and where $\underline{\mu}_j$ is the magnetic moment in units of μ_B of the j^{th} ion;

$$\underline{\mu}_j = (1/2)\ g_j\ \underline{S}_j \tag{3.4.4}$$

where $\underline{S}_j$ may be spin, total angular momentum $\underline{J}$ or some effective spin in the case of a partially quenched orbital angular momentum. $\underline{\mu}_{j\perp}$ is the vector component of $\underline{\mu}_j$ perpendicular to $\underline{Q}$ (or the projection of $\underline{\mu}_j$ on the diffraction plane as it is sometimes known). $f_j(\underline{Q})$ is the magnetic form factor of the j^{th} ion as discussed below. The magnetic scattering may be seen from equation (3.4.2) to depend on the magnetic fluctuations in the system in a way analogous with the dependence of the nuclear scattering on the density fluctuations in the system. However, it should be noted that the correlation function for atomic positions still enters into the magnetic cross-section so that magnetic scattering is sensitive to atomic structure and dynamics as well as magnetic behaviour.

In the derivation of equation (3.4.2) it is assumed that the incident neutron beam is unpolarised, that the magnetic electrons are localised on ions at positions $\underline{R}_j$ and that the electronic moments have negligible effect on interatomic forces. A detailed derivation of this result may be found in SQUIRES (1978), PRICE and SKÖLD (1986) or DE GENNES (1963).

Comparison of equation (3.4.2) with equation (3.3.3) shows that the characteristic scattering length per electron for magnetic scattering is $\gamma r_0 = 0.539 \times 10^{-14}$m, and thus under suitable conditions magnetic scattering can be of the same order of magnitude as nuclear scattering.

The magnetic form factor $f_j(\underline{Q})$ of the j^{th} ion is defined by;

$$f_j(\underline{Q}) = \int g_{mj}(\underline{r}) \exp(i\underline{Q}.\underline{r})\, d\underline{r} \qquad (3.4.5)$$

where $g_{mj}(\underline{r})$ is the normalised density of the unpaired electrons in the j^{th} ion;

$$g_{mj}(\underline{r}) = g_{+j}(\underline{r}) - g_{-j}(\underline{r}) \tag{3.4.6}$$

where $g_{+j}(\underline{r})$ and $g_{-j}(\underline{r})$ are the charge densities of the two spin states of the electrons of the j^{th} ion. Since $g_{mj}(\underline{r})$ is normalised, it follows that;

$$f_j(0) = 1 \tag{3.4.7}$$

$f_j(\underline{Q})$ thus represents the Fourier transform of the spatial distribution of the magnetic moment $\underline{\mu}_j$ about the centre of the j^{th} ion. $\gamma r_o f_j(\underline{Q})$ is the magnetic equivalent of the nuclear scattering length b_j , and hence the magnetic scattering length depends on $\underline{Q}$ which is due to the extended spatial distribution of an unpaired electron. This is to be contrasted with the case of nuclear scattering where the scattering centres are effectively point-like and the scattering length is independent of $\underline{Q}$.

Equation (3.4.5) shows that a measurement of the magnetic form factor of an ion provides a probe of the unpaired electron distribution for that ion. If the distribution of unpaired electrons is isotropic then $g_{mj}(\underline{r})=g_{mj}(r)$, a function of the magnitude of $\underline{r}$ only. In this case equation (3.4.5) leads to;

$$4\pi r g_{mj}(r) = (2/\pi) \int Q f_j(Q) \sin(rQ)\, dQ \tag{3.4.8}$$

The formalism for Fourier transforms involving isotropic distributions is considered in much greater detail in section 4.1 which considers nuclear diffraction from amorphous solids which are generally isotropic. (Equations (3.4.5) and (3.4.8) are analogous to the equations (4.1.4) and (4.1.30) which will be introduced in section 4.1 for nuclear scattering and the function $4\pi r g_{mj}(r)$ is analogous to the function D(r) for nuclear scattering. However, in the case of the unpaired electron distribution there is no average density term equivalent to $T^o(r)$.)

CHAPTER 4

THE THEORY OF THERMAL NEUTRON SCATTERING FROM AMORPHOUS SOLIDS.

4.1 NUCLEAR DIFFRACTION FROM AMORPHOUS SYSTEMS.

4.1.1 THE STATIC APPROXIMATION.

In a diffraction experiment no energy analysis is performed. That is to say all neutrons are detected, regardless of final energy. Thus the cross-section measured in a diffraction experiment (ignoring the energy dependence of the efficiency of a neutron detector) is;

$$\frac{d\sigma}{d\Omega} = \int_p \left(\frac{d^2\sigma}{d\Omega d\varepsilon}\right) d\varepsilon \tag{4.1.1}$$

where p denotes that the integral is performed along a path in $\underline{Q}$-ε space dictated by the experimental arrangement. In the case of a reactor source a diffraction experiment is performed with a fixed incident energy and a detector which counts at different scattering angles 2θ. Hence the path p is one of constant scattering angle. In the case of a pulsed source a diffraction experiment is performed by using different incident energies at different times, keeping the detector at fixed scattering angle and detecting neutrons as a function of time. The path p is thus a path of constant time.

In the static approximation it is assumed that the incident energy E is large compared with the excitation energies ε of the scattering system. In this case for all possible scattering events $E' \approx E$, $k' \approx k$ and the scattering triangle (3.3.5) gives;

$$Q = |\underline{Q}| \simeq Q_0 = 2k\sin\theta = \frac{4\pi\sin\theta}{\lambda} \tag{4.1.2}$$

where Q_0 is the magnitude of the scattering vector for elastic scattering and 2θ is the scattering angle. That is to say, for all possible scattering events along the integration path p the scattering vector $\underline{Q}$ may be approximated by the elastic value $\underline{Q}_0$ where p crosses the $\underline{Q}$-axis. Thus the integration path p may be approximated by a line of constant $\underline{Q} = \underline{Q}_0$ $(Q_0=4\pi\sin\theta/\lambda)$.

Integrating equation (3.3.48) in the static approximation gives the distinct cross-section as;

$$\frac{d\sigma^D}{d\Omega_{sa}} = \frac{1}{2\pi} \sum_{ll'} c_l \bar{b}_l \bar{b}_{l'} \iint G^D_{ll'}(\underline{r},t) \exp(i\underline{Q}.\underline{r}) \int_{-\infty}^{E/\hbar} \exp(-i\omega t)\, d\omega\, d\underline{r}\, dt \tag{4.1.3}$$

Since in the static approximation E is large compared with the excitation energies $\hbar\omega$ of the scattering system the energy integral of (4.1.3) covers the whole energy range over which the double differential cross-section is non-zero and so the upper limit may be replaced by ∞ . Thus the energy integral is just the integral representation of the delta function $2\pi\delta(t)$;

$$\frac{d\sigma^D}{d\Omega_{sa}} = \sum_{ll'} c_l \bar{b}_l \bar{b}_{l'} \iint G^D_{ll'}(\underline{r},t) \exp(i\underline{Q}.\underline{r})\, \delta(t)\, d\underline{r}\, dt$$

$$= \sum_{ll'} c_l \bar{b}_l \bar{b}_{l'} \int G^D_{ll'}(\underline{r},0) \exp(i\underline{Q}.\underline{r})\, d\underline{r} \tag{4.1.4}$$

Similarly;

$$\frac{d\sigma^S}{d\Omega}_{sa} = \sum_{l} c_l \, \overline{b_l}^2 \int G_l^S(\underline{r},0) \exp(i\underline{Q}.\underline{r}) \, d\underline{r} \tag{4.1.5}$$

Thus the cross-section for a diffraction experiment depends upon the instantaneous partial pair correlation functions, the $G_{ll'}^D(\underline{r},0)$ and $G_l^S(\underline{r},0)$. (This is to be contrasted with the case of elastic scattering where the cross-section depends on the time averaged correlation functions $G_{ll'}^D(\underline{r},\infty)$ and $G_l^S(\underline{r},\infty)$ - see section 4.4.2 .) The measurement of the cross-section in a diffraction experiment gives a 'snapshot' of the atomic positions (it is customary to discuss 'atomic' positions and 'atomic' structure, even though it is really the nuclear positions that are involved). At t=0 the Heisenberg operators $\underline{R}_j(0)$ and $\underline{R}_{j'}(0)$ commute and equations (3.3.38) and (3.3.39) become;

$$G_{ll'}^D(\underline{r},0) = \frac{1}{N_l} \sum_{\substack{j=1 \\ j\neq j'}}^{N_l} \sum_{j'=1}^{N_{l'}} \left\langle \delta(\underline{r}+\underline{R}_j(0)-\underline{R}_{j'}(0)) \right\rangle = g_{ll'}(\underline{r}) \tag{4.1.6}$$

$$G_l^S(\underline{r},0) = \delta(\underline{r}) \tag{4.1.7}$$

where $g_{ll'}(\underline{r})$ is known as the static partial pair-distribution function. These are the functions that are used to describe the instantaneous structure of the sample. Following the interpretation of the generalised partial pair correlation functions presented in section 3.3.4, the static partial pair correlation function may be interpreted as follows: $g_{ll'}(\underline{r})d\underline{r}$ is the thermally averaged probability that at a particular time a volume $d\underline{r}$ which is $\underline{r}$ away from an l atom contains an l' atom. Amorphous materials may generally be taken to be isotropic with the result that the $g_{ll'}(\underline{r})$ depends only on $r=|\underline{r}|$;

$$g_{ll'}(\underline{r}) = g_{ll'}(r) \tag{4.1.8}$$

An amorphous solid has no long range order. Hence there can be no correlation between atomic positions at large separations and the probability that an l′ atom is found in a volume $d\underline{r}$ at a large distance from an l atom depends simply on the macroscopic density of l′ atoms;

$$\lim_{r\to\infty} g_{ll'}(r) = g^{\circ}_{l'} \tag{4.1.9}$$

where;

$$g^{\circ}_{l'} = N_{l'}/V = c_{l'}N/V = c_{l'}g^{\circ} \ , \tag{4.1.10}$$

V is the volume of the sample and g° is the total macroscopic atomic number density. Using equation (4.1.6);

$$g_{l'l}(-\underline{r}) = \frac{1}{N_{l'}} \sum_{j=1}^{N_l} \sum_{\substack{j'=1 \\ j\neq j'}}^{N_{l'}} \left\langle \delta(-\underline{r}+\underline{R}_{j'}(0)-\underline{R}_j(0)) \right\rangle \tag{4.1.11}$$

Using the relation $\delta(-x)\equiv\delta(x)$ then gives;

$$g_{l'l}(-\underline{r})\ N_{l'} = g_{ll'}(\underline{r})\ N_l \tag{4.1.12}$$

In the case of an (isotropic) amorphous solid (4.1.8) shows that the direction of $\underline{r}$ is irrelevant and so;

$$g_{l'l}(r)/g_{ll'}(r) = N_l/N_{l'} = c_l/c_{l'} = g^{\circ}_l/g^{\circ}_{l'} \tag{4.1.13}$$

Using equations (4.1.4) to (4.1.7) the total diffraction cross-section can be expressed as a function of elastic scattering vector $\underline{Q}_{\circ}$;

$$I_{sa}(\underline{Q}_o) = \frac{d\sigma}{d\Omega}_{sa} = I^{S}_{sa} + \sum_{l}\sum_{l'} c_l\, \bar{b}_l \bar{b}_{l'} \int g_{ll'}(\underline{r}) \exp(i\underline{Q}_o\cdot\underline{r})\, d\underline{r} \tag{4.1.14}$$

where;

$$I^{S}_{sa} = \sum_{l} c_l\, \overline{b_l^{2}} \tag{4.1.15}$$

Following equation (4.1.9) it is useful to define a correlation function which represents the deviations of the pair distibution function from the macroscopic density;

$$g'_{ll'}(\underline{r}) = g_{ll'}(\underline{r}) - g^{\circ}_{l'} \tag{4.1.16}$$

Substituting this in equation (4.1.14) gives;

$$I_{sa}(\underline{Q}_o) = I^{S}_{sa} + \sum_{l}\sum_{l'} c_l\, \bar{b}_l \bar{b}_{l'} \left\{ \int g'_{ll'}(\underline{r}) \exp(i\underline{Q}_o\cdot\underline{r}) d\underline{r} + g^{\circ}_{l'} \int \exp(i\underline{Q}_o\cdot\underline{r}) d\underline{r} \right\} \tag{4.1.17}$$

The last of these terms is just a delta function;

$$I^{\circ}(\underline{Q}_o) = (2\pi)^{3}\, \delta(\underline{Q}_o) \sum_{ll'} c_l\, \bar{b}_l \bar{b}_{l'}\, g^{\circ}_{l'} \tag{4.1.18}$$

This delta function is the only Bragg scattering from an amorphous material since it is the only delta function in the diffraction cross-section. It is indistinguishable from the unscattered beam and is experimentally inaccessible. Hence the distinct cross-section measured in a diffraction experiment is;

$$\begin{aligned} i_{sa}(\underline{Q}_o) &= I_{sa}(\underline{Q}_o) - I^{\circ}(\underline{Q}_o) - I^{S}_{sa} \\ &= \sum_{l}\sum_{l'} c_l\, \bar{b}_l \bar{b}_{l'} \int g'_{ll'}(\underline{r}) \exp(i\underline{Q}_o\cdot\underline{r})\, d\underline{r} \end{aligned} \tag{4.1.19}$$

For an amorphous material equation (4.1.8) may be used with the result that the two angular integrals of (4.1.17) may be performed. The cross-section is then a function of the magnitude Q_0 of $\underline{Q}_0$ and does not depend on the direction of $\underline{Q}_0$;

$$i_{sa}(Q_0) = \sum_{l}\sum_{l'} c_l\, \bar{b}_l \bar{b}_{l'}\, (4\pi/Q_0) \int_0^\infty r\, g'_{ll'}(r) \sin(Q_0 r)\, dr \tag{4.1.20}$$

At this stage it is convenient to introduce correlation functions of the form;

$$t_{ll'}(r) = 4\pi r g_{ll'}(r) = d_{ll'}(r) + t^{\circ}_{l'}(r) \tag{4.1.21}$$

$$d_{ll'}(r) = 4\pi r(\, g_{ll'}(r) - g^{\circ}_{l'}\,) = 4\pi r g'_{ll'}(r) \tag{4.1.22}$$

$$t^{\circ}_{l'}(r) = 4\pi r g^{\circ}_{l'} \tag{4.1.23}$$

Equation (4.1.20) then becomes;

$$Q_0 i_{sa}(Q_0) = \sum_{l}\sum_{l'} c_l\, \bar{b}_l \bar{b}_{l'} \int_0^\infty d_{ll'}(r) \sin(Q_0 r)\, dr \tag{4.1.24}$$

One may define total correlation functions;

$$D(r) = \sum_{ll'} c_l\, \bar{b}_l \bar{b}_{l'}\, d_{ll'}(r) \tag{4.1.25}$$

$$T(r) = \sum_{ll'} c_l\, \bar{b}_l \bar{b}_{l'}\, t_{ll'}(r) \tag{4.1.26}$$

Substituting in these two equations from (4.1.10), (4.1.21) and (4.1.23) gives;

$$T(r) = D(r) + T^{\circ}(r) \tag{4.1.27}$$

where;

$$T^{\circ}(r) = 4\pi r g^{\circ} \left(\sum_{l} c_{l} \bar{b}_{l} \right)^{2} \qquad (4.1.28)$$

Equation (4.1.24) then becomes;

$$Q_{\circ} i_{sa}(Q_{\circ}) = \int_{0}^{\infty} D(r) \sin(Q_{\circ} r)\, dr \qquad (4.1.29)$$

which may be Fourier transformed to give;

$$D(r) = (2/\pi) \int_{0}^{\infty} Q_{\circ} i_{sa}(Q_{\circ}) \sin(r Q_{\circ})\, dQ_{\circ} \qquad (4.1.30)$$

Hence in the static approximation the correlation function D(r) is related to the distinct scattering by a Fourier sine transform, and the purpose of a diffraction experiment on an amorphous solid is to measure D(r).

4.1.2 THE PLACZEK CORRECTION.

In the previous section the cross-section for a diffraction experiment is calculated by integrating the double differential cross-section along a line of constant Q and ignoring the effect of detector efficiency. The result of these approximations is that the integral of equation (4.1.1) is not carried out correctly over the inelastic region and corrections must be made to the static approximation results before the Fourier transform of equation (4.1.30) is performed. A method for making such corrections which essentially involves a Taylor's expansion of the scattering function $S(Q,\omega)$ about $Q_{\circ}$ was originally developed by PLACZEK (1952). A similar method is followed here except that instead of the 1/v detector efficiency considered by Placzek a general expression for any functional form of the detector efficiency is obtained and then a particular expression for an exponential detector efficiency is derived. A 1/v form is not an adequate approximation for the correct exponential form, as has been discussed by JOHNSON, WRIGHT and SINCLAIR (1983).

If detector efficiency is taken into account then the effective cross-section measured in a diffraction experiment is;

$$\frac{d\sigma}{d\Omega}_{eff} = I(Q_o) = \int_p f(k') \left(\frac{d^2\sigma}{d\Omega d\varepsilon}\right) d\varepsilon \tag{4.1.31}$$

where f(k') is the efficiency of the detector at final neutron wavevector k', p is the relevant integration path in Q-ε space for the experimental arrangement used and the elastic scattering vector Q_o ($=4\pi\sin\theta/\lambda$) is a convenient variable for specifying the scattering angle 2θ. Substituting from equations (3.3.16) and (3.3.17) for the double differential cross-section gives;

$$\frac{d\sigma^D}{d\Omega}_{eff} = i(Q_o) = \sum_{ll'} c_l \bar{b}_l \bar{b}_{l'} \int_p f(k') \frac{k'}{k} S^D_{ll'}(Q,\omega)\, d\omega \tag{4.1.32}$$

$$\frac{d\sigma^S}{d\Omega}_{eff} = I^S(Q) = \sum_{l} c_l \overline{b_l^2} \int_p f(k') \frac{k'}{k} S^S_l(Q,\omega)\, d\omega \tag{4.1.33}$$

If the incident energy E is much larger than any of the excitation energies of the sample then the integrand of equation (4.1.31) is only non-zero over a range of energies for which ε<<E. In this limit the integrand may be expanded in powers of ε/E and the expressions (4.1.32) and (4.1.33) are evaluated for a reactor instrument as follows:

The integration path p may be obtained by squaring equation (3.3.5);

$$\begin{aligned} Q^2 &= k^2 + k'^2 - 2kk'\cos(2\theta) \\ &= 2k^2 - (\varepsilon/E)k^2 + (1-(\varepsilon/E))^{1/2}(Q_o^2 - 2k^2) \end{aligned} \tag{4.1.34}$$

Expanding the $(1-(\varepsilon/E))^{1/2}$ term according to the binomial theorem gives the path p as;

$$Q^2 - Q_o^2 = -(Q_o^2/2)(\varepsilon/E) + ((2k^2-Q_o^2)/8)(\varepsilon/E)^2 + \ldots \quad (4.1.35)$$

The integration path p is shown in figure 4.1 together with the constant Q path used in the static approximation. Taylor's theorem may be used to express a scattering function $S(Q,\omega)$ at a point on the path p ((ω,Q_p) in figure 4.1) in terms of its value and derivatives at $Q=Q_o$ and the same ω (the point (ω,Q_o) in figure 4.1) by expanding in powers of $\Delta=Q^2-Q_o^2$;

$$S(Q,\omega)_p = S(Q_o,\omega) + \Delta\, S^1(Q_o,\omega) + (\Delta^2/2!)\, S^2(Q_o,\omega) + \ldots \quad (4.1.36)$$

where;

$$S^m(Q_o,\omega) = \left| \partial^m S(Q,\omega)/\partial(Q^2)^m \right|_{Q=Q_o} \quad (4.1.37)$$

The k'/k factor of equations (4.1.32) and (4.1.33) may also be expanded in powers of (ε/E);

$$k'/k = (E'/E)^{1/2} = (1-(\varepsilon/E))^{1/2} = 1 - (\varepsilon/E)/2 - (\varepsilon/E)^2/8 - \ldots \quad (4.1.38)$$

The efficiency $f(k')$ of the detector may be expanded about the incident wavevector k according to Taylor's theorem;

$$\begin{aligned} f(k') &= f_0 + (k'-k)f_1 + (k'-k)^2 f_2/2! + \ldots \\ &= f_0 - f_1 k(\varepsilon/E)/2 + (f_2k^2-f_1k)(\varepsilon/E)^2/8 + \ldots \end{aligned} \quad (4.1.39)$$

where;

$$f_n = [d^n f(k')/dk'^n]_{k'=k} \quad (4.1.40)$$

At this stage it is useful to define the n^{th} moment $S_n(Q)$ of a scattering function $S(Q,\omega)$ as follows;

$$S_n(Q) = \int_{-\infty}^{\infty} \omega^n \, S(Q,\omega) \, d\omega \tag{4.1.41}$$

The zeroth moment is often known as the structure factor. As explained in section 4.1.1 the upper limit of the integral in equation (4.1.31) may be set to ∞ if the incident energy is large, and combining equations (4.1.41), (4.1.39), (4.1.38), (4.1.36) and (4.1.35) then eventually gives (YARNELL, KATZ, WENZEL and KOENIG, 1973) the integral of a scattering function along the path p as;

$$\begin{aligned}\int_p f(k')(k'/k)S(Q,\omega)d\omega = f_0[\ & S_0(Q_o) - (\hbar/2E)\{\ (1+kf_1/f_0)S_1(Q_o) + Q_o^2 S_1^1(Q_o)\ \} \\ & - (\hbar^2/8E^2)\{\ (1-kf_1/f_0-k^2f_2/f_0)S_2(Q_o) - (Q_o^2+2k^2+2Q_o^2kf_1/f_0)S_2^1(Q_o) \\ & - Q_o^4 S_2^2(Q_o)\} + \ldots\ ]\end{aligned} \tag{4.1.42}$$

with;

$$S_n^m(Q_o) = \int_{-\infty}^{\infty} \omega^n \, [\partial^m S(Q,\omega)/\partial(Q^2)^m]_{Q=Q_o} \, d\omega \tag{4.1.43}$$

The first few moments of the distinct and self scattering functions have been calculated by PLACZEK (1952) for a system in which the interactions between the atoms depend only on the atomic positions and not on the atomic momenta;

$$S^D_{ll',0}(Q) = \int_0^{\infty} G^D_{ll'}(\underline{r},0) \exp(i\underline{Q}.\underline{r}) \, d\underline{r} \tag{4.1.44}$$

$$S^D_{ll',1}(Q) = 0 \tag{4.1.45}$$

$$S^{D}_{ll',2}(Q) = \frac{\hbar^{2}Q^{4}}{4M_{l}M_{l'}}\, S^{D}_{ll',0}(Q) + \frac{1}{M_{l}M_{l'}} \left\langle \exp(i\underline{Q}\cdot\underline{r})\ (\underline{p}_{l}\cdot\underline{Q})\ (\underline{p}_{l'}\cdot\underline{Q}) \right\rangle \qquad (4.1.46)$$

$$S^{S}_{l,0}(Q) = \int_{0}^{\infty} G^{S}_{l}(\underline{r},0)\ \exp(i\underline{Q}\cdot\underline{r})\ d\underline{r} = 1 \qquad (4.1.47)$$

$$S^{S}_{l,1}(Q) = \hbar Q^{2}/2M_{l} \qquad (4.1.48)$$

$$S^{S}_{l,2}(Q) = \hbar^{2}Q^{4}/4M_{l}^{2} + 2\bar{K}_{l}Q^{2}/3M_{l} \qquad (4.1.49)$$

where M_l is the mass of an l atom, $\bar{K}_l$ is the average kinetic energy of an l atom and $\underline{p}_l$ is the momentum of an l atom.

Since the first moment of the distinct scattering function is zero and the second moment cannot be calculated in practice (since it depends on a detailed knowledge of the dynamics of the system) a correction can only be applied to the self scattering cross-section. Substituting (4.1.47), (4.1.48) and (4.1.49) in (4.1.42) gives (JOHNSON, WRIGHT and SINCLAIR, 1983) the corrected self scattering as;

$$I^{S}(Q_{o}) = \sum_{l} c_{l}\ \overline{b_{l}^{2}}\ f_{0}\ [\ 1 - 4C_{1}\sin^{2}\theta/\mu l + 16C_{2}\sin^{4}\theta/\mu_{l}^{2} - 8C_{3}\bar{K}_{l}\sin^{2}\theta/3\mu_{l}E_{o}$$
$$+ (1/2\mu_{l})\ (4\sin^{2}\theta/\mu_{l} + 2\bar{K}_{l}/3E_{o}) + \ldots\ ] \qquad (4.1.50)$$

where;

$$\mu_{l} = M_{l}/m \qquad (4.1.51)$$

$$C_{1} = 1 + k_{o}f_{1}/2f_{0} \qquad (4.1.52)$$

$$C_{2} = (\ 3 + 5k_{o}f_{1}/f_{0} + k_{o}^{2}f_{2}/f_{0}\ )\ /\ 8 \qquad (4.1.53)$$

$$C_{3} = -\ (\ 3k_{o}f_{1}/f_{0} + k_{o}^{2}f_{2}/f_{0}\ )\ /\ 4 \qquad (4.1.54)$$

The $\sin\theta$ factors arise from the substitution $Q_{o}=2k\sin\theta$ and the μ_l terms from the substitution $\hbar^{2}k^{2}=2mE$. The static approximation results of section

4.1.1 may then be used with $I^S(Q_o)$ replacing I^S_{sa} and $i(Q_o)$ replacing $i_{sa}(Q_o)$.

For a neutron detector in which the first stage of the detection process involves an element with a 1/v absorption cross-section the k dependence of the efficiency takes the form;

$$f(k) = 1 - \exp(-\gamma/k) \qquad (4.1.55)$$

where γ is a constant. The quantities f_1/f_0 and f_2/f_0 then become;

$$f_1/f_0 = -(\gamma/k_o^2) \exp(-\gamma/k_o) \; / \; (1 - \exp(-\gamma/k_o)) \qquad (4.1.56)$$

$$f_2/f_0 = (\gamma/k_o^3) \; (2 - \gamma/k_o) \exp(-\gamma/k_o) \; / \; (1 - \exp(-\gamma/k_o)) \qquad (4.1.57)$$

Of course neutron scattering diffractometers for amorphous materials should be designed to minimise the Placzek corrections (high incident energy and low scattering angles).

4.1.3 TERMINATION OF THE FOURIER INTEGRAL.

Equation (4.1.30) shows that the correlation function D(r) is related to the distinct scattering $i(Q_o)$ times Q_o by a Fourier sine transform. However, in practice it is only possible to measure the scattering up to some finite elastic momentum transfer Q_{max}, and not to infinity. For example, in a reactor experiment there is a maximum angle $2\theta_{max}$ at which scattering can be measured (with an absolute limit of $2\theta_{max}$=180°). Hence for real experimental data the integral of equation (4.1.30) cannot be performed with the given limits, but only with the upper limit replaced by Q_{max}. This is equivalent to multiplying the cross-section by a modification function $M(Q_o)$ which is a step function cutting off at $Q_o=Q_{max}$. The resultant correlation function is;

$$D'(r) = (2/\pi) \int_0^\infty Q_0 i(Q_0)\, M(Q_0)\, \sin(rQ_0)\, dQ_0 \qquad (4.1.58)$$

The convolution theorem (SPIEGEL, 1974) may be re-phrased to state that the Fourier transform of the product of the Fourier transforms of two functions is equal to the convolution of the two functions. $Q_0 i(Q_0)$ is the Fourier transform of $D(r)$ (see equation (4.1.29)) and so $D'(r)$ may be identified as the convolution of $D(r)$ and the Fourier transform of $M(Q_0)$;

$$D'(r) = \int_0^\infty D(r')\, [\, P(r-r') - P(r+r')\,]\, dr' \qquad (4.1.59)$$

where r' is a dummy variable and;

$$P(r) = (1/\pi) \int_0^\infty M(Q_0) \cos(rQ_0)\, dQ_0 \qquad (4.1.60)$$

Since $M(Q_0)$ is a step function, $P(r)$ has a strong oscillatory component which extends over quite a large range of r on either side of the main peak. This leads to spurious features in the correlation function, known as 'termination ripples', which are usually reduced by using some sort of damping function for $M(Q_0)$.

The modification function used in this work is that due to LORCH (1969);

$$\begin{aligned} M(Q_0) &= \sin(\Delta r Q_0)/\Delta r Q_0 \quad . \quad Q_0 \le Q_{max} \\ &= 0 \qquad\qquad\qquad\quad Q_0 > Q_{max} \end{aligned} \qquad (4.1.61)$$

where;

$$\Delta r = \pi/Q_{max} \qquad (4.1.62)$$

A detailed discussion of modification functions has been given by WASER and SCHOMAKER (1953). The function $P(r)$ is known as the real space peak function, and use of the Lorch modification function results in a peak function of height $0.1876Q_{max}$ and full width at half maximum (FWHM) $5.437/Q_{max}$. The Lorch function is preferrable to the artificial temperature factor $\exp(-BQ^2)$ used by some authors since the latter is discontinuous at $Q_0=Q_{max}$. The effect of the Lorch function is to greatly reduce termination ripples, although at the expense of some real space resolution (the step function modification function has $FWHM \simeq 3.8/Q_{max}$). The real space resolution of a measured correlation function is determined by Q_{max} and thus a diffraction experiment should be performed to as high a value of Q_{max} as possible. This is generally the most important consideration for the resolution of a diffraction experiment on an amorphous material, and instruments should be designed to enable the scattering to be measured to as high a momentum transfer as possible. Other methods of overcoming the restricted Q-range covered by experimental data include the maximum entropy method (ROOT, EGELSTAFF and NICKEL, 1986) and the Monte Carlo method (SOPER, 1988).

4.1.4 THE EFFECT OF ATOMIC VIBRATIONS FOR DIFFRACTION.

The effect for diffraction of the thermal motions of the nuclei may be elucidated by expressing the position of the j^{th} nucleus in the form;

$$\underline{R}_j(t) = \underline{R}_j + \underline{u}_j(t) \qquad (4.1.63)$$

where $\underline{R}_j$ is the equilibrium position of the nucleus (it is now assumed that the scattering system is a solid such that the concept of an equilibrium position is meaningful) and $\underline{u}_j(t)$ represents the displacement of the nucleus from equilibrium. This notation is chosen to be consistent with that used in Chapter 5 which discusses atomic vibrations.

In the static approximation the total diffraction cross-section may be expressed in the following form by combining equation (4.1.14) and equation (3.3.42);

$$I(\underline{Q}) = I^S + \sum_{ll'} c_l \bar{b}_l \bar{b}_{l'} \frac{1}{N_l} \sum_{j=1}^{N_l} \sum_{\substack{j'=1 \\ j\neq j'}}^{N_{l'}} \left\langle \exp(-i\underline{Q}.\underline{R}_j(0)) \exp(i\underline{Q}.\underline{R}_{j'}(0)) \right\rangle \qquad (4.1.64)$$

Use of equation (4.1.63) then yields;

$$I(\underline{Q}) = I^S + \sum_{ll'} c_l \bar{b}_l \bar{b}_{l'} \frac{1}{N_l} \sum_{j=1}^{N_l} \sum_{\substack{j'=1 \\ j\neq j'}}^{N_{l'}} \exp(-i\underline{Q}.(\underline{R}_j-\underline{R}_{j'})) \left\langle \exp(-i\underline{Q}.(\underline{u}_j(0)-\underline{u}_{j'}(0))) \right\rangle \qquad (4.1.65)$$

It may be shown (see Appendix E of SQUIRES (1978)) that in the harmonic approximation;

$$< \exp\zeta > = \exp(<\zeta^2>/2) \qquad (4.1.66)$$

where ζ is a displacement variable. Using this result in equation (4.1.65) gives;

$$I(\underline{Q}) = I^S + \sum_{ll'} c_l \bar{b}_l \bar{b}_{l'} \frac{1}{N_l} \sum_{j=1}^{N_l} \sum_{\substack{j'=1 \\ j\neq j'}}^{N_{l'}} \exp(-i\underline{Q}.(\underline{R}_j-\underline{R}_{j'})) \exp(-(W_j+W_{j'}))$$

$$\exp < \underline{Q}.\underline{u}_j(0)\ \underline{Q}.\underline{u}_{j'}(0) > \qquad (4.1.67)$$

where;

$$2W_j = < (\underline{Q}.\underline{u}_j(0))^2 > \qquad (4.1.68)$$

If it is then assumed that W_j is the same for all the atoms of an element l then equation (4.1.67) becomes;

$$I(\underline{Q}) = I^S + \sum_{ll'} c_l \bar{b}_l \bar{b}_{l'} \frac{1}{N_l} \exp(-W_{ll'}) \sum_{j=1}^{N_l} \sum_{\substack{j'=1 \\ j \neq j'}}^{N_{l'}} \exp(-i\underline{Q}.(\underline{R}_j - \underline{R}_{j'}))$$

$$\exp < \underline{Q}.\underline{u}_j(0)\ \underline{Q}.\underline{u}_{j'}(0) > \qquad (4.1.69)$$

where;

$$W_{ll'} = W_l + W_{l'} \qquad (4.1.70)$$

The term $\exp(-W_{ll'})$ is known as the Debye-Waller factor, and it is this term which represents the effect of atomic vibrations for scattering. For an isotropic system;

$$W_l = Q^2 \langle u_l^2 \rangle / 6 \qquad (4.1.71)$$

where $\langle u_l^2 \rangle$ is the average square displacement from equilibrium for one atom of element l. For an isotropic system the mean square displacement of an atom in a particular direction α is given by;

$$\langle u_{l\alpha}^2 \rangle = \langle u_l^2 \rangle / 3 \qquad (4.1.72)$$

If it is assumed that there is no correlation between atomic motions then the mean square deviation from equilibrium of the bond length for the bond between an atom of element l and an atom of element l′ is;

$$\begin{aligned} \langle u_{ll'}^2 \rangle &= \langle u_{l\alpha}^2 \rangle + \langle u_{l'\alpha}^2 \rangle \\ &= (\langle u_l^2 \rangle + \langle u_{l'}^2 \rangle) / 3 \qquad (4.1.73) \end{aligned}$$

On the assumption of small displacements the exponential factor of equation (4.1.69) may be expanded;

$$\exp \langle \underline{Q}.\underline{u}_j(0)\ \underline{Q}.\underline{u}_{j'}(0) \rangle = 1 + \langle \underline{Q}.\underline{u}_j(0)\ \underline{Q}.\underline{u}_{j'}(0) \rangle + (1/2) \langle \underline{Q}.\underline{u}_j(0)\ \underline{Q}.\underline{u}_{j'}(0) \rangle^2 + \ldots \qquad (4.1.74)$$

As is discussed in section 4.4 the first term (unity) of this (multiphonon) expansion corresponds to elastic scattering whilst the succeeding terms correspond to inelastic processes. In the static approximation inelastic processes are effectively ignored and hence the appropriate expression for the static approximation is obtained by taking just the elastic term of equation (4.1.74), leading to;

$$I(\underline{Q}) = I^S + \sum_{ll'} c_l\ \bar{b}_l \bar{b}_{l'} \exp(-W_{ll'}) \int g_{ll'}^{eq}(\underline{r}) \exp(i\underline{Q}.\underline{r})d\underline{r} \qquad (4.1.75)$$

where the equilibrium partial pair-distribution function $g_{ll'}^{eq}(\underline{r})$ is defined according to;

$$\int g_{ll'}^{eq}(\underline{r}) \exp(i\underline{Q}.\underline{r})\, d\underline{r} = \sum_{j=1}^{N_l} \sum_{\substack{j'=1 \\ j \neq j'}}^{N_{l'}} \exp(-i\underline{Q}.(\underline{R}_j - \underline{R}_{j'})) \qquad (4.1.76)$$

Note that the Debye-Waller factor cannot be ignored in the same way as the exponential of equation (4.1.74) since it applies for all processes including elastic scattering. Equation (4.1.75) may be corrected for the neglection of inelastic processes using the Placzek correction as detailed in section 4.1.2 .

For diffraction (total scattering) the self scattering term I^S does not involve a Debye-Waller factor. This is to be contrasted with the case of elastic scattering (see section 4.4) for which the self scattering term does involve a Debye-Waller factor (MILDNER and WRIGHT, 1980).

The effect of thermal motions may be included in the expression (4.1.24) for diffraction from an amorphous solid as follows;

$$Qi(Q) = \sum_{l}\sum_{l'} c_l \bar{b}_l \bar{b}_{l'} \exp(-W_{ll'}) \int_0^{\infty} d^{eq}_{ll'}(r) \sin(Qr)\, dr \tag{4.1.77}$$

Comparison with equation (4.1.58) shows that the Debye-Waller factor $\exp(-W_{ll'})$ plays a mathematical role entirely analogous to that of the modification function M(Q). Hence equations (4.1.59) and (4.1.60) may be adapted to yield (WRIGHT and SINCLAIR, 1985);

$$d_{ll'}(r) = \left(\frac{3}{2\pi\langle u^2_{ll'}\rangle}\right) \int_0^{\infty} d^{eq}_{ll'}(r') \left[\exp\left(-\left(\frac{(r-r')^2}{2\langle u^2_{ll'}\rangle}\right)\right) - \exp\left(-\left(\frac{(r+r')^2}{2\langle u^2_{ll'}\rangle}\right)\right)\right] dr' \tag{4.1.78}$$

Thus in the harmonic approximation the effect in real-space of thermal motion is a Gaussian broadening of the partial correlation functions d(r) and t(r) (the convolution of equation (4.1.78) does not affect $t^{0}(r)$ since this is proportional to r).

4.2 MAGNETIC DIFFRACTION FROM AMORPHOUS SOLIDS.

4.2.1 SCATTERING FROM A PARAMAGNET.

The cross-section for the scattering of unpolarised neutrons by an ideal paramagnet in zero magnetic field can be calculated from equation (3.4.2). For this calculation it is useful to make the following substitution;

$$\langle \underline{\mu}_{j\perp}(0) \cdot \underline{\mu}_{j',\perp}(t)\rangle = \sum_{\alpha\beta} (\delta_{\alpha\beta} - \hat{Q}_\alpha \hat{Q}_\beta)\langle \mu_{j\alpha}(0)\mu_{j',\beta}(t)\rangle \tag{4.2.1}$$

where α and β are taken over the three Cartesian directions x, y and z and $\hat{\underline{Q}}$ is a unit vector in the $\underline{Q}$ direction. Since the magnetic moments of the ions of a paramagnet are randomly oriented there is no internal magnetic field and thus a change in orientation of a particular moment does not change the energy of the system. Hence the magnetic moment operators $\underline{\mu}_j$ commute with the Hamiltonian of the system and the magnetic moment matrix element in (3.4.2) is time-independent;

$$\langle \mu_{j\alpha}(0)\mu_{j',\beta}(t)\rangle = \langle \mu_{j\alpha}\mu_{j',\beta}\rangle \tag{4.2.2}$$

For a paramagnet there is no correlation between the moments of different ions and so;

$$\langle \mu_{j\alpha}\mu_{j',\beta}\rangle = \langle \mu_{j\alpha}\rangle \; \langle \mu_{j',\beta}\rangle = 0 \quad \text{if } j \neq j' \tag{4.2.3}$$

Thus only $\langle \mu_{j\alpha}\mu_{j\beta}\rangle$ terms contribute to the cross-section. Consider such a term for which $\alpha \neq \beta$. Each allowed value of $\mu_{j\alpha}$ is equally likely and so it is only necessary to consider just one $\mu_{j\alpha}$ value. For this fixed value of $\mu_{j\alpha}$ the expectation value of $\mu_{j\beta}$ is zero with the result that;

$$\langle \mu_{j\alpha}\mu_{j\beta}\rangle = 0 \quad \text{if } \alpha \neq \beta \tag{4.2.4}$$

Hence only $\langle \mu_{j\alpha}{}^2\rangle$ terms contribute to the cross-section. Since the three vector components of a moment are equivalent in a paramagnet;

$$\langle \mu_{j\alpha}{}^2\rangle = (1/3) \langle \mu_{jx}{}^2 + \mu_{jy}{}^2 + \mu_{jz}{}^2 \rangle = (1/3) \langle \underline{\mu}_j{}^2\rangle \tag{4.2.5}$$

Combining equations (4.2.2) to (4.2.5) gives;

$$\langle \mu_{j\alpha}(0)\mu_{j',\beta}(t)\rangle = \delta_{jj'}\ \delta_{\alpha\beta}\ (1/3)\ \langle \underline{\mu}_j^{\,2}\rangle \tag{4.2.6}$$

Substituting this result in (4.2.1) yields;

$$\begin{aligned}\langle \underline{\mu}_{j\perp}(0)\ \cdot\ \underline{\mu}_{j',\perp}(t)\rangle &= \delta_{jj'}\ \sum_{\alpha}\ (\ 1 - \hat{Q}_{\alpha}^{\,2}\ )\ (1/3)\ \langle \underline{\mu}_j^{\,2}\rangle \\ &= \delta_{jj'}\ (2/3)\ \langle \underline{\mu}_j^{\,2}\rangle \end{aligned} \tag{4.2.7}$$

Equation (3.4.2) then gives the cross-section for a paramagnet as;

$$\frac{d^2\sigma^{P}}{d\Omega d\varepsilon} = \frac{1}{N}\frac{k'}{k}\ (\gamma r_o)^2\ \frac{1}{2\pi\hbar}\ \sum_j |f_j(\underline{Q})|^2\ \frac{2}{3}\ \langle \underline{\mu}_j^2\rangle \int_{-\infty}^{\infty} \langle\ \exp(-i\underline{Q}.(\underline{R}_j(0)-\underline{R}_j(t)))\ \rangle\ \exp(-i\omega t)\ dt \tag{4.2.8}$$

Substituting from equation (3.3.43) gives;

$$\frac{d^2\sigma^{P}}{d\Omega d\varepsilon} = \frac{k'}{k}\ (\gamma r_o)^2\ \frac{1}{2\pi\hbar}\ \sum_l c_l\ |f_l(\underline{Q})|^2\ \frac{2}{3}\ \langle \underline{\mu}_l^2\rangle \iint G_l^S(\underline{r},t)\ \exp(-i(\underline{Q}.\underline{r}-\omega t))\ d\underline{r}\ dt \tag{4.2.9}$$

Comparison with equation (3.3.49) shows that the cross-section for a paramagnet is essentially the same as the self scattering cross-section for nuclear scattering, the only difference being the replacement of $\overline{b^2}$ with $(\gamma r_o)^2\ |f_l(\underline{Q})|^2\ (2/3)\ \langle\underline{\mu}_l\rangle^2$.

4.2.2 MAGNETIC CORRELATION FUNCTIONS.

Following VAN HOVE (1954b) one may define magnetic correlation functions which are analagous to the nuclear correlation functions defined in section 3.3.4 ;

$$\Gamma(\underline{r},t) = (1/N)\ \sum_{jj'}\ \langle \underline{\mu}_{j\perp}(0)\ \cdot\ \underline{\mu}_{j',\perp}(t)\rangle \int \langle\ \delta(\underline{r}'-\underline{R}_j(0))\ \delta(\underline{r}'+\underline{r}-\underline{R}_{j'}(t))\rangle\ d\underline{r}' \tag{4.2.10}$$

Note that the vector properties of magnetism result in a correlation function which depends on the direction of measurement and strictly Γ is also a function of $\hat{\underline{Q}}$.

4.2.3 THE QUASISTATIC APPROXIMATION.

Integrating equation (3.4.2) in the static approximation (in the field of magnetic scattering this approximation is known as the quasistatic approximation, but it is essentially the same as the static approximation described in section 4.1.1) gives the cross-section for magnetic diffraction as;

$$\frac{d\sigma^{M}}{d\Omega} = \frac{d\sigma^{MD}}{d\Omega} + \frac{d\sigma^{MS}}{d\Omega} \qquad (4.2.11)$$

where;

$$\frac{d\sigma^{MD}}{d\Omega} = i^{M}(Q) = (\gamma r_{o})^{2} \sum_{ll'} c_{l}\, f_{l}^{*}(\underline{Q})\, f_{l'}(\underline{Q}) \int \Gamma_{ll'}^{D}(\underline{r},0) \exp(i\underline{Q}.\underline{r})\, d\underline{r} \qquad (4.2.12)$$

$$\frac{d\sigma^{MS}}{d\Omega} = (\gamma r_{o})^{2} \sum_{l} c_{l}\, |f_{l}(\underline{Q})|^{2} \int \Gamma_{l}^{S}(\underline{r},0) \exp(i\underline{Q}.\underline{r})\, d\underline{r} \qquad (4.2.13)$$

where the distinct and self partial magnetic correlation functions are defined in exactly the same way as the nuclear correlation functions.

4.2.4 MAGNETIC SELF SCATTERING.

The instantaneous partial magnetic self correlation function is;

$$\Gamma_l^S(\underline{r},0) = (1/N_l)\ \delta(\underline{r}) \sum_{j=1}^{N_l} \langle \underline{\mu}_{j\perp}^2 \rangle \tag{4.2.14}$$

(see equations (4.2.10) and (4.1.7)). For an amorphous solid the property of isotropy yields the result;

$$\Gamma_l^S(\underline{r},0) = \frac{2}{3} \langle \underline{\mu}_l^2 \rangle\ \delta(\underline{r}) \tag{4.2.15}$$

(see equation (4.2.7). Substitution in (4.2.13) gives;

$$\frac{d\sigma^{MS}}{d\Omega} = \frac{2}{3} (\gamma r_o)^2 \sum_l c_l\ |f_l(\underline{Q})|^2 \langle \underline{\mu}_l^2 \rangle \tag{4.2.16}$$

Comparison with the results of section 4.2.1 shows that for diffraction in the static approximation the magnetic self scattering is equivalent to the total scattering from the same system of moments in the paramagnetic state. This is a general result for an amorphous solid in zero field. In principle the paramagnetic scattering diffraction cross-section should be corrected for inelasticity in the same way as for nuclear self scattering (see section 4.1.2). However, this is not done in practice because such a correction requires a precise knowledge of the moments of the scattering function and in the case of magnetic scattering such a knowledge does not exist. Paramagnetic scattering differs in form from nuclear self scattering because of the form factor. Whereas for nuclear diffraction the self scattering is almost level with a small droop due to inelasticity, the diffraction from a paramagnet shows a strong fall-off from its maximum value at Q=0 and tends to zero at high Q (~10Å^{-1}).

4.2.5 MAGNETIC DISTINCT SCATTERING.

The instantaneous partial magnetic distinct correlation function is;

$$\Gamma^{D}_{ll'}(\underline{r},0) = \frac{1}{N_l} \sum_{j=1}^{N_l} \sum_{\substack{j'=1 \\ j\neq j'}}^{N_{l'}} \langle\delta(\underline{r}+\underline{R}_j(0)-\underline{R}_{j'}(0))\rangle \sum_{\alpha\beta} (\delta_{\alpha\beta}-\hat{Q}_\alpha\hat{Q}_\beta)\langle\mu_{j\alpha}(0)\mu_{j'\beta}(0)\rangle \qquad (4.2.17)$$

where equation (4.2.1) has been used to express the magnetic moment matrix element and $j\neq j'$ indicates that the summation is only over distinct pairs of atoms.

In the case of nuclear scattering the equivalent equation to (4.2.12) (equation (4.1.4)) can be Fourier transformed so that the real-space correlation function may be obtained. However, equation (4.2.12) cannot be Fourier transformed in the general case since $\Gamma^{D}_{ll'}(\underline{r},0)$ is actually a function of $\hat{\underline{Q}}$ as well as $\underline{r}$. The distinct magnetic diffraction cross-section may be cast in a more tractable form by following the approach of BLECH and AVERBACH (1964). (Note that the paper by BLECH and AVERBACH contains misprints in several key equations which are corrected here.) Following equations (4.2.12) and (4.2.17) the distinct magnetic diffraction cross-section may be expressed as;

$$i^{M}(Q) = (\gamma r_{o})^{2} \sum_{ll'} c_l\, f^{*}_{l}(\underline{Q})\, f_{l'}(\underline{Q})\, (1/N_l) \sum_{jj'} \eta_{jj'} \qquad (4.2.18)$$

where the symbol $\eta_{jj'}$ is defined for convenience as;

$$\eta_{jj'} = \int \langle\delta(\underline{r}+\underline{R}_j(0)-\underline{R}_{j'}(0))\rangle \sum_{\alpha\beta} (\delta_{\alpha\beta}-\hat{Q}_\alpha\hat{Q}_\beta)\, \langle\mu_{j\alpha}(0)\mu_{j'\beta}(0)\rangle \exp(i\underline{Q}.\underline{r})\, d\underline{r} \qquad (4.2.19)$$

The magnetic part of $\eta_{jj'}$ may conveniently be evaluated for a typical atom pair jj' by making the following choice of axes (see figure 4.2): x is chosen to be in the interatomic direction $\underline{d}_{jj'}=\underline{R}_{j'}-\underline{R}_{j}$ and y and z are chosen so that $\mu_{jz}=0$. The angles ϕ and θ are then chosen to define the direction $\hat{\underline{Q}}$ in this coordinate system as shown in figure 4.2 . $\eta_{jj'}$ may then be shown to be;

$$\eta_{jj'} = \int \langle\mu_{jx}\mu_{j'x}\sin^2\phi+\mu_{jy}\mu_{j'y}(1-\sin^2\phi\cos^2\theta)-\sin\phi\cos\phi\cos\theta(\mu_{jx}\mu_{j'y}+\mu_{jy}\mu_{j'x})$$
$$-\sin\phi\cos\phi\cos\theta\mu_{jx}\mu_{j'z}-\sin^2\phi\cos\theta\sin\theta\mu_{jy}\mu_{j'z}\rangle\ \langle\delta(\underline{r}+\underline{R}_j-\underline{R}_{j'})\rangle\ \exp(i\underline{Q}\cdot\underline{r})d\underline{r} \tag{4.2.20}$$

Performing the angular integrals and assuming macroscopic isotropy (ie. the results do not apply to a magnetised ferromagnet) by averaging over all orientations eventually yields the distinct cross-section as;

$$i^M(Q) = (\gamma r_o)^2 \sum_{ll'} c_l\ f_l^*(Q)\ f_{l'}(Q) \int \left[\Delta^i_{ll'}(r)\ \frac{\sin(Qr)}{Q} + \Delta^a_{ll'}(r)\ (1/Q^2r) \left(\frac{\sin(Qr)}{Qr} - \cos(Qr) \right) \right] dr \tag{4.2.21}$$

where;

$$\Delta^i_{ll'}(r) = (4\pi r/N_l) \sum_{j=1}^{N_l} \sum_{\substack{j'=1\\ j\neq j'}}^{N_{l'}} \langle\delta(r+R_j-R_{j'})\rangle\ \langle\underline{\mu}_{j\perp}\cdot\underline{\mu}_{j'\perp}\rangle \tag{4.2.22}$$

$$\Delta^a_{ll'}(r) = (4\pi r/N_l) \sum_{j=1}^{N_l} \sum_{\substack{j'=1\\ j\neq j'}}^{N_{l'}} \langle\delta(r+R_j-R_{j'})\rangle\ (\ 2\langle\mu_{j\parallel}\cdot\mu_{j'\parallel}\rangle - \langle\underline{\mu}_{j\perp}\cdot\underline{\mu}_{j'\perp}\rangle\ ) \tag{4.2.23}$$

where $\parallel$ and $\perp$ indicate components of the moments parallel and perpendicular to the $\underline{d}_{jj'}$ vector respectively. The superscripts i and a are used to denote magnetic isotropy and anisotropy respectively, as is discussed below. If it is assumed that all the $\Delta^a_{ll'}(r)=0$ then equation (4.2.21) reduces to;

$$Qi^M(Q) = (\gamma r_o)^2 \sum_{ll'} c_l \, f^*_l(Q) \, f_{l'}(Q) \int \Delta^i_{ll'}(r) \sin(Qr) \, dr \tag{4.2.24}$$

In this case the partial correlation functions $\Delta^i_{ll'}(r)$ play a role analogous to that of the functions $d_{ll'}(r)$ in nuclear scattering (equation (4.1.24)) and they are related to the distinct scattering cross-section by a Fourier transformation. The $\Delta(r)$ functions may also be expressed (WRIGHT, 1980a) in the form;

$$\Delta^i_{ll'}(r) = t_{ll'}(r) \, a_{ll'}(r) \tag{4.2.25}$$

$$\Delta^a_{ll'}(r) = t_{ll'}(r) \, b_{ll'}(r) \tag{4.2.26}$$

where;

$$a_{ll'}(r) = \overline{\langle \underline{\mu}_{l\perp} \cdot \underline{\mu}_{l'\perp} \rangle} \tag{4.2.27}$$

$$b_{ll'}(r) = 2\overline{\langle \mu_{l\parallel} \cdot \mu_{l'\parallel} \rangle} - \overline{\langle \underline{\mu}_{l\perp} \cdot \underline{\mu}_{l'\perp} \rangle} \tag{4.2.28}$$

where the bar indicates the average value of the function at the separation r. Of course the functions $a_{ll'}(r)$ and $b_{ll'}(r)$ cannot be defined in terms of microscopic variables independently of the nuclear correlation functions $t_{ll'}(r)$. The assumption that all $\Delta^a_{ll'}(r)=0$ is equivalent to;

$$2\overline{\langle \mu_{l\parallel} \cdot \mu_{l'\parallel} \rangle} = \overline{\langle \underline{\mu}_{l\perp} \cdot \underline{\mu}_{l'\perp} \rangle} \qquad \text{for all } r \text{ and all } l \text{ and } l' \tag{4.2.29}$$

Hence equation (4.2.24) applies when there is no correlation between the magnetic moment directions and that of the interatomic direction vector $\underline{d}_{ll'}$, ie. the distinct cross-section may be Fourier transformed to obtain a real-space correlation function in the case where there is no local magnetic anisotropy (thus the superscripts of $\Delta^{i}_{ll'}(r)$ and $\Delta^{a}_{ll'}(r)$ indicate microscopic magnetic isotropy and anisotropy respectively).

4.2.6 FOURIER TRANSFORMATION OF MAGNETIC DIFFRACTION DATA.

There are additional complications in the Fourier transformation of magnetic diffraction data, as opposed to nuclear diffraction data, due to the magnetic form factor f(Q). The situation is analogous to that of X-ray diffraction with the X-ray atomic scattering factor replaced by the magnetic form factor. The X-ray atomic scattering factor arises from all the electrons in an atom whereas the magnetic form factor arises only from a few unpaired (magnetic) electrons in outer orbitals. Hence the magnetic form factor falls off more rapidly with Q than the X-ray atomic scattering factor. The effect of the magnetic form factor is to restrict real space resolution.

For a sample with a single magnetic species for which the magnetic anisotropy is negligible equation (4.2.24) becomes;

$$Qi^{M}(Q) = (\gamma r_{o})^{2}\, c_{M}\, f^{2}(Q) \int \Delta^{i}(r) \sin(Qr)\, dr \qquad (4.2.30)$$

where c_M is the number concentration of magnetic ions. By analogy with equations (4.1.29) and (4.1.30) for nuclear diffraction;

$$\Delta i_{(r)} = \frac{2}{\pi} \frac{1}{c_{M}(\gamma r_{o})^{2}} \int \frac{Qi^{M}(Q)}{f^{2}(Q)} \sin(rQ)\, dQ \qquad (4.2.31)$$

The Q-dependence of the magnetic form factor is the cause of the essential difference between magnetic diffraction and nuclear diffraction. In order to obtain the correlation function $\Delta^{i}(r)$ which relates to nuclear positions the experimental data must be divided by $f^2(Q)$ before Fourier transformation. One may also define a distribution function given by the direct Fourier transformation of $Qi^{M}(Q)$;

$$\Delta_f^i(r) = (2/\pi)\ (1/c_M(\gamma r_0)^2)\ \int Qi^M(Q)\sin(rQ)\,dQ \qquad (4.2.32)$$

$\Delta_f^i(r)$ is the magnetic equivalent of FINBAK's (1949) electronic distribution function for X-rays (ie. $\Delta_f^i(r)$ is a correlation function for unpaired electrons in different ions, whereas $\Delta^i(r)$ relates to the atomic positions as with the nuclear correlation function d(r)). Since the magnetic electrons of an atom are more widely distributed than the nucleus the function $\Delta_f^i(r)$ is broader than the function $\Delta^i(r)$. Hence the process of dividing by $f^2(Q)$ to obtain $\Delta^i(r)$ (as in equation (4.2.31)) is known as 'sharpening' (PATTERSON, 1935).

Provided that the experimental data extends to a reasonably high Q_{max} the Fourier transformation of equation (4.2.32) does not require a modification function (see section 4.1.3) since the effect of the magnetic form factor is to cause $i^M(Q)$ to fall off rapidly as Q increases. In effect $f^2(Q)$ behaves as a modification function. However, as a result of the process of sharpening a modification function is required for the Fourier transformation of equation (4.2.31) in the same way as for nuclear diffraction.

4.3 SMALL ANGLE NEUTRON SCATTERING.

The term small angle scattering (SAS) is conventionally taken to refer to diffraction in the regime for which the momentum transfer Q is small compared with the first peak Q_1 of the structure factor (or the smallest reciprocal lattice vector in the case of a crystal). Since the range of Q covered in a SAS experiment is small compared with that covered in a conventional diffraction experiment (a so-called wide angle scattering experiment) it follows that the range of r covered in a SAS experiment is large compared with that covered in a conventional diffraction experiment. Thus a SAS experiment is suitable for studying structures which are large compared with interatomic distances in condensed matter. In practice the range of Q accessible to small angle neutron scattering (SANS) diffractometers extends at most from a few thousandths of an inverse Ångstrom ($Å^{-1}$) to perhaps one inverse Ångstrom. Thus the technique is suitable for studying structures with dimensions of tens or hundreds of Ångstroms. For length scales of this order of magnitude the individual scattering centres in condensed matter are not resolved. Hence the correlation function formalism developed previously is not appropriate and the theory of SANS may be developed by commencing with an equation deduced before the introduction of correlation functions. Integrating equation (3.3.23) in the static approximation yields the coherent differential cross-section as;

$$\frac{d\sigma^{coh}}{d\Omega} = \frac{1}{N} \left| \sum_{j=1}^{N} \bar{b}_j \exp(i\underline{Q}.\underline{R}_j) \right|^2 \qquad (4.3.1)$$

where the j-summation is over all atoms, $\bar{b}_j$ is the coherent scattering length appropriate to atom j and the time-dependence of the $\underline{R}_j$ and the thermal averaging have been taken as implicit. Since the SANS regime is concerned with length scales which are large in comparison with the separation of the discrete scattering centres it is appropriate to introduce a continuous scattering length density;

$$\rho_b(\underline{r}) = \sum_l \bar{b}_l \; \rho_l(\underline{r},0) \qquad (4.3.2)$$

where $\rho_l(\underline{r},t)$ is defined by equation (3.3.50). Equation (4.3.1) then becomes;

$$\frac{d\sigma}{d\Omega}^{coh} = \frac{1}{N} \left| \int \rho_b(\underline{r}) \exp(i\underline{Q}.\underline{r}) \, d\underline{r} \right|^2 \qquad (4.3.3)$$

It is convenient to separate $\rho_b(\underline{r})$ into an average value ρ_b^o and a term $\rho_b'(\underline{r})$ representing fluctuations about the average value;

$$\rho_b(\underline{r}) = \rho_b^o + \rho_b'(\underline{r}) \qquad (4.3.4)$$

The contribution to the coherent differential cross-section (4.3.3) due to the average density ρ_b^o is proportional to $\delta(\underline{Q})$ (cf. equation (4.1.18)) and for Q>0 the coherent differential cross-section is given by;

$$\frac{d\sigma}{d\Omega}^{coh} = \frac{1}{N} \left| \int \rho_b'(\underline{r}) \exp(i\underline{Q}.\underline{r}) \, d\underline{r} \right|^2 \qquad (4.3.5)$$

Thus a SANS experiment enables fluctuations in the scattering length density over distances of order tens or hundreds of Ångstroms to be observed. In the case of a perfectly homogeneous sample there is no SANS.

For a given scattering length distribution the cross-section may be evaluated by application of equation (4.3.5). However, it is generally not possible to determine $\rho_b(\underline{r})$ from the measured cross-section since the available range of Q is not usually adequate for the Fourier transformation methods introduced in section 4.1 to be used. Hence the approach used to analyse SANS measurements is generally to fit a model function to the reciprocal-space data.

In the limit Ql<<1 , where l is the characteristic length over which the scattering length density varies (the particle size), one may use the Guinier approximation (GUINIER, 1939). In this approximation the coherent differential cross-section for a sample with N_p particles of homogeneous scattering length density ρ_{bp} embedded in a matrix of homogeneous scattering length density ρ_{bm} is given by;

$$\frac{d\sigma^{coh}}{d\Omega} = (V_p^2N_p^2/N)\ (\rho_{bp}-\rho_{bm})^2\ \exp(-Q^2R_G^2/3) \tag{4.3.6}$$

where R_G is the radius of gyration;

$$R_G^2 = \int_{V_p} (r^2/V_p)\ d\underline{r} \tag{4.3.7}$$

with the integration over the volume V_p of a particle. In the limit where Ql>>1 one may use the Porod approximation (POROD, 1951) which predicts a coherent differential cross-section for the same sample given by;

$$\frac{d\sigma^{coh}}{d\Omega} = (2\pi A_pN_p/N)\ (\rho_{bp}-\rho_{bm})^2\ Q^{-4} \tag{4.3.8}$$

where A_p is the surface area of a particle.

In the case of magnetic scattering the coherent differential cross-section may be obtained by integrating equation (4.1.2) in the static approximation;

$$\frac{d\sigma^{coh}}{d\Omega} = \frac{1}{N}(\gamma r_o)^2 \left| \sum_{j=1}^{N} \underline{\mu}_{j\perp} \exp(i\underline{Q}.\underline{R}_j) \right|^2 \tag{4.3.9}$$

where the form factor $f_j(\underline{Q})$ has been omitted since it is effectively unity in the SANS regime (equation (4.1.7)). One may introduce a continuous magnetisation density;

$$\underline{M}(\underline{r}) = \sum_{j=1}^{N} \underline{\mu}_j \ \delta(\underline{r}-\underline{R}_j) \tag{4.3.10}$$

so that the coherent differential cross-section is given by;

$$\frac{d\sigma^{coh}}{d\Omega} = \frac{1}{N}(\gamma r_o)^2 \left| \underline{M}_{\perp}(\underline{Q}) \right|^2 \tag{4.3.11}$$

where $\underline{M}_{\perp}(\underline{Q})$ is the component of the Fourier transform of the magnetisation density perpendicular to $\underline{Q}$;

$$\underline{M}(\underline{Q}) = \int \underline{M}(\underline{r}) \exp(i\underline{Q}.\underline{r}) \, d\underline{r} \tag{4.3.12}$$

If the magnetisation density $\underline{M}(\underline{r})$ is homogeneous then $\underline{M}(\underline{Q})$ is proportional to $\delta(\underline{Q})$ and there is no observable SANS. However, if there are fluctuations in the magnetisation density then these may be observed by SANS, just as with fluctuations in the scattering length density. Hence SANS is a technique by which the onset of magnetic order may be observed.

For a more complete discussion of the theory of SANS the reader is referred to the Chapter by KOSTORZ (1979).

4.4 NUCLEAR INELASTIC SCATTERING IN THE INCOHERENT APPROXIMATION.

4.4.1 MULTIPHONON EXPANSION.

To elucidate the effect of atomic vibrations for nuclear inelastic scattering the substitution of equation (4.1.63) is used in equations (3.3.14) and (3.3.15);

$$S^{D}_{ll'}(Q,\omega) = \frac{1}{2\pi N_l} \sum_{j=1}^{N_l} \sum_{\substack{j'=1 \\ j\neq j'}}^{N_{l'}} \int_{-\infty}^{\infty} \exp(-i\underline{Q}.(\underline{R}_j-\underline{R}_{j'}))\left\langle \exp(-i\underline{Q}.(\underline{u}_j(0)-\underline{u}_{j'}(t)))\right\rangle \exp(-i\omega t)\, dt \tag{4.4.1}$$

$$S^{S}_{l}(Q,\omega) = \frac{1}{2\pi N_l} \sum_{j=1}^{N_l} \int_{-\infty}^{\infty} \left\langle \exp(-i\underline{Q}.(\underline{u}_j(0)-\underline{u}_j(t)))\right\rangle \exp(-i\omega t)\, dt \tag{4.4.2}$$

where the scattering functions have been expressed as a function of the magnitude of $\underline{Q}$ only since they must be isotropic for an amorphous solid. Using the harmonic approximation result of equation (4.1.66);

$$S^{D}_{ll'}(Q,\omega) = \frac{1}{2\pi N_l} \sum_{j=1}^{N_l} \sum_{\substack{j'=1 \\ j\neq j'}}^{N_{l'}} \int_{-\infty}^{\infty} \exp(-i\underline{Q}.(\underline{R}_j-\underline{R}_{j'}))\, \exp< \underline{Q}.\underline{u}_j(0)\ \underline{Q}.\underline{u}_{j'}(t) > \times \exp(-W_{ll'})\, \exp(-i\omega t)\, dt \tag{4.4.3}$$

$$S_1^S(Q,\omega) = \frac{1}{2\pi N_1} \sum_{j=1}^{N_1} \int_{-\infty}^{\infty} \exp\langle\, \underline{Q}.\underline{u}_j(0)\ \underline{Q}.\underline{u}_j(t) \,\rangle \exp(-W_{11}) \exp(-i\omega t)\, dt \tag{4.4.4}$$

where the Debye-Waller factor $\exp(-W_{11'})$ is as defined in section 4.1.4 . On the assumption of small displacements $\underline{u}_j$ the exponential containing the displacements may be expanded;

$$\exp \langle\, \underline{Q}.\underline{u}_j(0)\ \underline{Q}.\underline{u}_{j'}(t) \,\rangle = 1 + \langle\, \underline{Q}.\underline{u}_j(0)\ \underline{Q}.\underline{u}_{j'}(t) \,\rangle + (1/2) \langle\, \underline{Q}.\underline{u}_j(0)\ \underline{Q}.\underline{u}_{j'}(t) \,\rangle^2 + \ldots \tag{4.4.5}$$

The scattering functions may then be expressed in a form known as the multiphonon expansion;

$$S^{D/S}(Q,\omega) = S^{D/S,el}(Q,\omega) + \sum_{p=1}^{\infty} S^{D/S,p}(Q,\omega) \tag{4.4.6}$$

where $S^{D/S,el}(Q,\omega)$ corresponds to the first term of the expansion (4.4.5) and $S^{D/S,p}(Q,\omega)$ corresponds to the p+1th term of (4.4.5).

4.4.2 ELASTIC SCATTERING.

The first terms of the multiphonon expansion are;

$$S_{11'}^{D,el}(Q,\omega) = \frac{1}{N_1} \sum_{j=1}^{N_1} \sum_{\substack{j'=1 \\ j\neq j'}}^{N_{1'}} \exp(-i\underline{Q}.(\underline{R}_j-\underline{R}_{j'})) \exp(-W_{11'})\ \delta(\omega) \tag{4.4.7}$$

and;

$$S_1^{S,el}(Q,\omega) = \exp(-W_{11})\ \delta(\omega) \tag{4.4.8}$$

where it has been assumed that atomic thermal motions are uncorrelated (WRIGHT and SINCLAIR, 1985). The delta-function $\delta(\omega)$ in equations (4.4.7) and (4.4.8) indicate that these terms represent elastic scattering. The nature of elastic scattering may be elucidated by use of the following separation;

$$G(\underline{r},t) = G(\underline{r},\infty) + G'(\underline{r},t) \tag{4.4.9}$$

where $G(\underline{r},t)$ is any correlation function of the type introduced in section 3.3.4 (see equation (3.3.36)), $G(\underline{r},\infty)$ (TURCHIN, 1965) is the time-averaged part of $G(\underline{r},t)$ and $G'(\underline{r},t)$ is the time-dependent part. The corresponding scattering function $S(\underline{Q},\omega)$ is related to $G(\underline{r},t)$ by a double Fourier transformation (see for example equation (3.3.44));

$$\begin{aligned} S(\underline{Q},\omega) &= (1/2\pi) \iint G(\underline{r},t) \exp(i(\underline{Q}.\underline{r}-\omega t))\, d\underline{r}\, dt \\ &= \int G(\underline{r},\infty) \exp(i\underline{Q}.\underline{r})\, d\underline{r}\ \delta(\omega) + \iint G'(\underline{r},t) \exp(i(\underline{Q}.\underline{r}-\omega t))\, d\underline{r}\, dt \end{aligned} \tag{4.4.10}$$

The first of these terms represents elastic scattering whilst the second represents inelastic scattering. In fact the inelastic term is not zero at $\omega=0$, but it is completely overwhelmed by the elastic term. Equation (4.4.10) shows that the elastic scattering is determined by the time-averaged correlation function $G(\underline{r},\infty)$. This is to be contrasted with the case of total scattering, discussed in section 4.1, which is determined by the instantaneous correlation function $G(\underline{r},0)$. It is also apparent that the elastic self scattering is modulated by a Debye-Waller factor term, unlike the total self scattering (see section 4.1.4).

From equations (3.3.16) and (3.3.17) the elastic cross-section may be derived;

$$\frac{d\sigma^{el}}{d\Omega} = \sum_{ll'} c_l \bar{b}_l \bar{b}_{l'} S^{D,el}_{ll'}(Q) + \sum_{l} c_l \overline{b_l^2} S^{S,el}_{l}(Q) \qquad (4.4.11)$$

Using equation (4.1.73) and equations (4.4.7) and (4.4.8);

$$\frac{d\sigma^{el}}{d\Omega} = I(Q) - I^{S}(Q) + \sum_{l} c_l \overline{b_l^2} \exp(-W_{ll}) \qquad (4.4.12)$$

Strictly equation (4.4.12) is only correct in the limit that all inelastic scattering is incoherent (PRICE and CARPENTER, 1987), ie. correlations in the thermal motions of the atoms have been ignored (WRIGHT and SINCLAIR, 1985).

4.4.3 NORMAL MODES.

In the harmonic approximation the displacements $\underline{u}_j$ may be expressed in terms of a sum over the 3N normal modes of the scattering system (see Appendix G of SQUIRES (1978));

$$\underline{u}_j(t) = \sum_{s=1}^{3N} (\hbar/2M_j\omega_s)^{1/2} \left(\underline{e}_j^{s} \exp(-i\omega_s t)\, a_s + \underline{e}_j^{s*} \exp(i\omega_s t)\, a_s^{+} \right) \qquad (4.4.13)$$

where M_j is the mass of the j^{th} atom, ω_s is the angular frequency of the mode s and $\underline{e}_j^{s}$ is the polarisation vector in this mode for the j^{th} atom (including the wavevector dependence). a_s and a_s^{+} are the annihilation and creation operators for the mode s. Substitution of equation (4.4.13) in the second term of equation (4.4.6) yields;

$$S^{D,1}_{ll'}(Q,\omega) = \frac{1}{2N_l} \sum_{\substack{j=1\\ j\neq j'}}^{N_l} \sum_{j'=1}^{N_{l'}} \exp(-i\underline{Q}.(\underline{R}_j-\underline{R}_{j'}))\, \exp(-W_{ll'}) \times$$

$$\sum_{s=1}^{3N} \frac{\hbar}{\omega_s\sqrt{(M_l M_{l'})}} (\underline{Q}.\underline{e}^s_j)^\star \, (\underline{Q}.\underline{e}^s_{j'}) \, [\langle n_s\rangle\delta(\omega+\omega_s) + \langle n_s+1\rangle\delta(\omega-\omega_s)]$$

(4.4.14)

and;

$$S^{S,1}_{l}(Q,\omega) = \frac{1}{2N_l} \sum_{j=1}^{N_l} \exp(-W_{ll}) \sum_{s=1}^{3N} \frac{\hbar}{\omega_s M_l} |\underline{Q}.\underline{e}^s_j|^2 \, [\langle n_s\rangle\delta(\omega+\omega_s) + \langle n_s+1\rangle\delta(\omega-\omega_s)]$$

(4.4.15)

where $\langle n_s\rangle$ is the population factor for the mode s given by;

$$\langle n_s\rangle = \frac{1}{\exp(\hbar\omega_s/k_BT)-1} \qquad (4.4.16)$$

The δ-functions of the p=1 terms indicate that these terms represent the annihilation or creation of one normal mode of the sample (ie. a phonon). In a similar way it is found that the p^{th} terms of equation (4.4.6) represent p-phonon scattering, and collectively the terms for which p>1 represent multiphonon scattering. The p^{th} term may be seen to vary as $(\hbar Q^2/2M\omega)^p$ so that these terms become decreasingly significant as p increases (typically $(\hbar Q^2/2M\omega)\sim0.05$), and generally introduce a relatively smooth and low background under the one-phonon structure.

4.4.4 INCOHERENT APPROXIMATION.

A frequently used approximation in the analysis of scattering from amorphous and polycrystalline materials is the incoherent approximation. This assumes that when equation (4.4.14) is averaged over a significant range of Q, the interference effects arising from the phase factor $\exp(-i\underline{Q}.(\underline{R}_j-\underline{R}_{j'}))$ cancel out so that the distinct scattering function averages to zero. This assumption may be accounted for by considering the amplitude-dependent factor $(\underline{Q}.\underline{e}_j^s)^*(\underline{Q}.\underline{e}_{j'}^s)$. In the approximation that there is no correlation between the motions of atoms the directions of $\underline{e}_j^s$ and $\underline{e}_{j'}^s$ are unrelated so that;

$$(\underline{Q}.\underline{e}_j^s)^* \; (\underline{Q}.\underline{e}_j^s) = (Qe_j^s)^2 \; \delta_{jj'} \; / \; 3 \tag{4.4.17}$$

This is analogous to the case of an ideal paramagnet (equation (4.2.6). Equation (4.4.17) shows that in the limit of totally uncorrelated atomic motions the distinct scattering function of equation (4.4.14) is zero. Thus it follows that the distinct scattering function is sensitive to correlations between the motions of atoms and hence it is by use of the distinct inelastic scattering that phonon dispersion relations may be measured. In practice, as has been shown by CARPENTER and PRICE (1985), the distinct scattering function is not zero and consequently the cross-section measured in an inelastic scattering experiment is averaged over a range of Q so that the distinct contribution (which oscillates about zero) averages to zero. The Q-averaged cross-section may then be interpreted in terms of the self scattering function alone.

The vibrational density of states (VDOS) may be defined to be (see Chapter 5);

$$g'(\omega) = \sum_{s=1}^{3N} \delta(\omega-\omega_s) \; / \; 3N \tag{4.4.18}$$

Note that for convenience the normalisation of this definition of the VDOS differs from that used in Chapters 5 and 14. Using the expression for $g'(\omega)$ in equation (4.4.15) yields the phonon creation part of the one phonon partial self scattering function as;

$$S_l^{S,+1}(Q,\omega) = \exp(-W_{ll}) \frac{\hbar}{2\omega M_l} 3\overline{|\underline{Q}\cdot\underline{e}_l|^2} \langle n+1\rangle g'(\omega) \tag{4.4.19}$$

where p=+1 has been used to denote phonon creation and the bar of the amplitude-dependent factor indicates an average over all modes at frequency ω. Thus the self inelastic scattering provides a means by which $g'(\omega)$ may be measured.

At this stage it is useful to define a total (ie. not partial) self scattering function, since this is the function which is addressed experimentally (see equation (3.3.17));

$$S^S(Q,\omega) = \sum_l c_l \overline{b_l^2} S_l^S(Q,\omega) \tag{4.4.20}$$

The one phonon creation part of this is;

$$S^{S,+1}(Q,\omega) = \frac{\hbar Q^2}{2\omega} \langle n+1\rangle g'(\omega) \sum_l c_l \overline{b_l^2} \frac{1}{M_l} \exp(-W_{ll}) 3\overline{|\hat{\underline{Q}}\cdot\underline{e}_l|^2} \tag{4.4.21}$$

Experimentally it is useful to define a generalised density of states (CARPENTER and PELIZZARI, 1975) $G(Q,\omega)$ by;

$$S^{S,+1}(Q,\omega) = \exp(-2\overline{W}) (\hbar Q^2/2\overline{M}\omega) \langle\overline{b^2}\rangle \langle n+1\rangle G(Q,\omega) \tag{4.4.22}$$

where;

$$\overline{M}^{\,-1} = \sum_{l} c_l \, M_l^{-1} \tag{4.4.23}$$

$$\overline{\langle b^2 \rangle} = \sum_{l} c_l \, \overline{b_l^2} \tag{4.4.24}$$

$$\overline{W} = Q^2 \, \overline{\langle u^2 \rangle} \, / \, 6 \tag{4.4.25}$$

$$\overline{\langle u^2 \rangle} = \sum_{l} c_l \, \langle u_l^2 \rangle \tag{4.4.26}$$

In the incoherent approximation;

$$G(Q,\omega) = g'(\omega) \sum_{l} \overline{b_l^2} \, \overline{M} \exp(-2W_l) \; 3\overline{|\hat{\underline{Q}}\cdot\underline{e}_l|^2} \, / \, (\, \overline{\langle b^2 \rangle} \, M_l \exp(-2\overline{W}) \,) \tag{4.4.27}$$

and the effective VDOS measured in an experiment is;

$$g_{eff}(\omega) = \int_{Q_1}^{Q_2} G(Q,\omega) \, dQ \, / \, (Q_2 - Q_1) \tag{4.4.28}$$

A problem associated with the use of the incoherent approximation is that there is no simple means of assessing whether the distinct scattering has actually averaged to zero. Recently PRICE and CARPENTER (1987) have suggested that it may be possible to use the information which is present in the distinct scattering (and which is discarded in the incoherent approximation) to obtain useful information about the network dynamics of amorphous solids. However, at present very little work has been done to either model or measure the wavevector dependence of the phonon spectra of amorphous solids.

In the case of a sample for which all atoms are equivalent (the so-called Bravais lattice) the amplitude factor $\overline{|\hat{\underline{Q}}\cdot\underline{e}_1|^2}$ of equation (4.4.27) may be set to one because of the orthonormality of the basis vectors of the normal modes. Thus in this case a direct measurement of $g'(\omega)$ is obtained. This simplification cannot be made for a polyatomic sample and hence equation (4.4.27) shows that an incoherent approximation analysis of inelastic neutron scattering data yields an effective amplitude-weighted VDOS. However, provided that the amplitudes of vibration do not vary sharply with energy which would be unreasonable, $g_{eff}(\omega)$ yields a good experimental approximation to $g'(\omega)$.

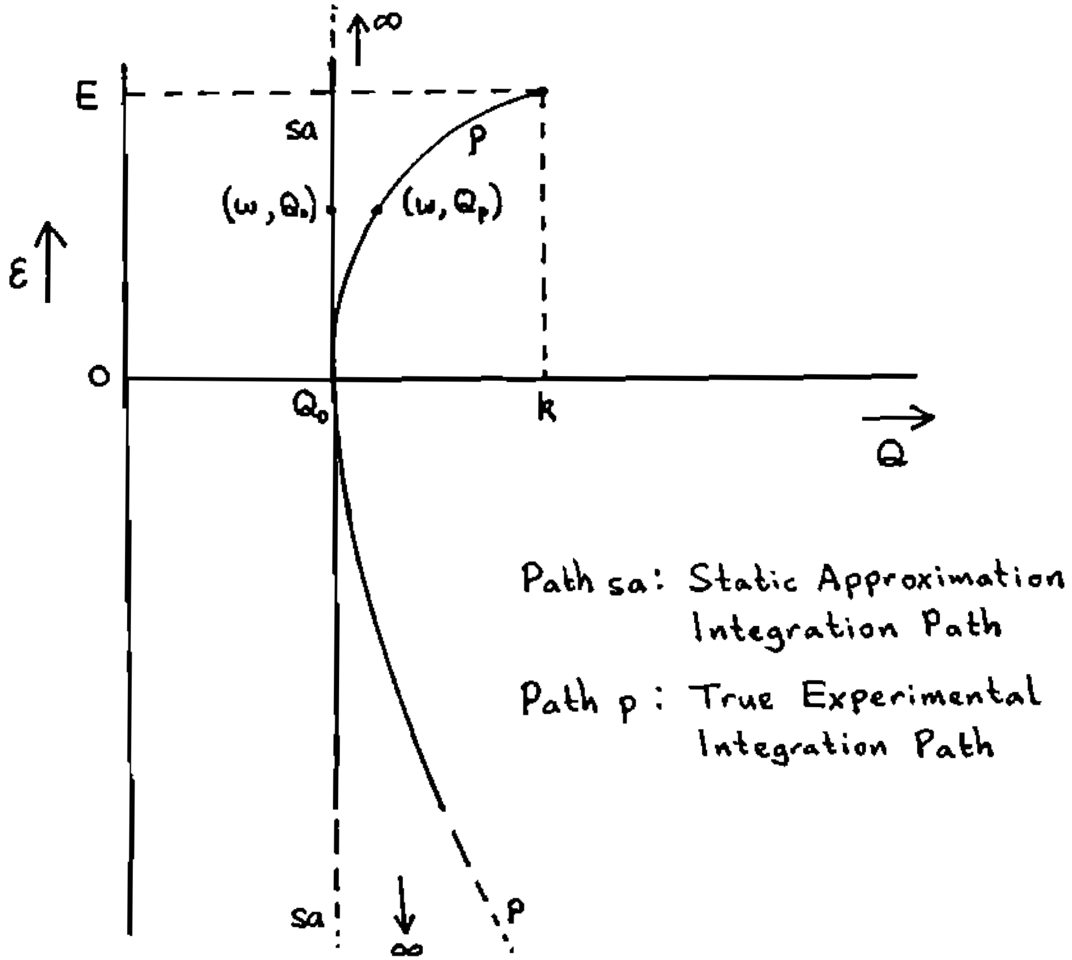

Figure 4.1

Detector Integration Paths in Q-ε Space for Diffraction from an Amorphous Material.

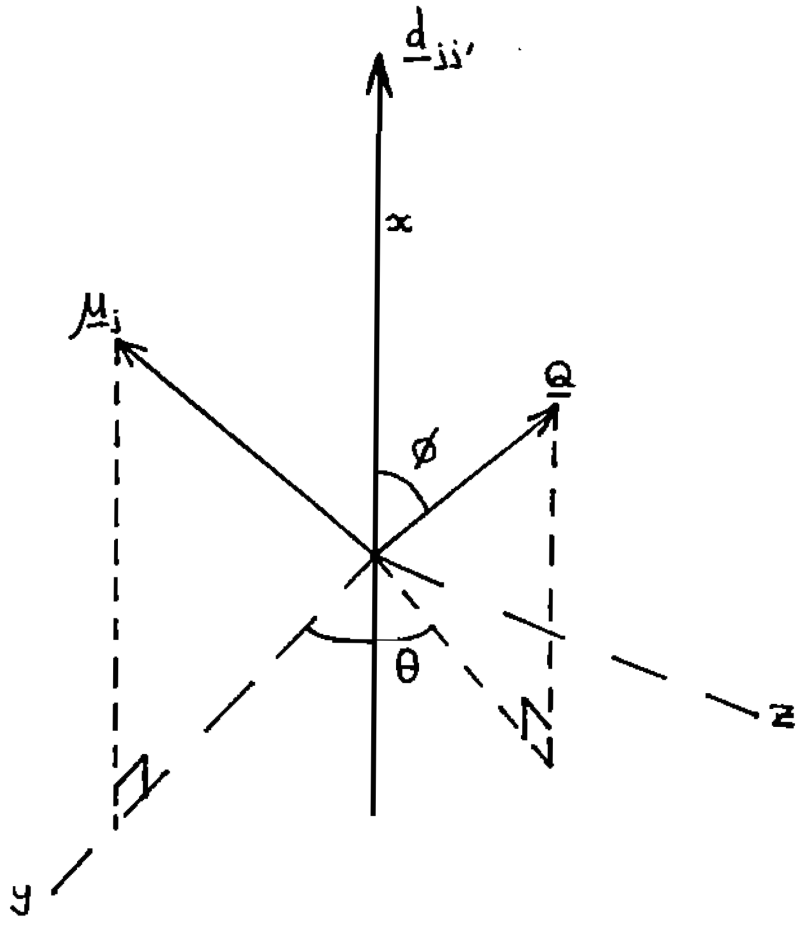

Figure 4.2

Definition of Coordinates for Evaluation of Distinct Magnetic Diffraction Cross-Section.

CHAPTER 5

NETWORK DYNAMICS - INTRODUCTION AND THEORY.

5.1 INTRODUCTION.

The study of atomic vibrations in crystalline materials, known as lattice dynamics, is now a fairly well understood subject. It is the purpose of this chapter to introduce the equivalent field of study for amorphous materials with a CRN structure, a subject which is termed 'network dynamics.'

As discussed in chapter 2 an amorphous solid may be regarded as a crystal with an infinite unit cell. Thus for an amorphous solid the first zone in the Brillouin scheme becomes the point $\mathbf{q}=0$ and the wavevector $\mathbf{q}$ is not useful in classifying the vibrational modes. The concepts of Brillouin zones and phonon dispersion curves lose their meaning (see LEADBETTER (1973) for further discussion of this topic) and the important quantity for describing vibrational excitations in amorphous solids is the vibrational density of states (VDOS). The VDOS $g(\omega)$ is defined so that $g(\omega)d\omega$ is the number of modes with angular frequency in the range $(\omega,\omega+d\omega)$.

The experimental technique most widely used for observing vibrational excitations in amorphous solids is Raman scattering. However, caution must be exercised in the interpretation of Raman spectra since the signal is not simply related to the VDOS (there is a matrix element involving the polarisability of the modes which cannot easily be determined). Vibrational excitations may also be observed by means of inelastic neutron scattering, infrared absorption (IR), tunnelling spectroscopy and electron energy loss spectroscopy. Inelastic neutron scattering is the best technique for a detailed study of the VDOS of an amorphous solid over a significant energy range since the inelastic neutron scattering signal is related to the VDOS in a relatively simple and clear way.

As is shown in sections 5.2 and 5.3 the VDOS of a solid depends on the interatomic forces and the atomic coordinates and masses. Since the masses are known and the forces are fairly well understood the dependence on atomic coordinates may be taken advantage of and used as a probe of SRO and IRO in amorphous solids. In this way measurements of the vibrational properties of an amorphous solid provide complementary structural information to the results obtained from diffraction.

WEAIRE and ALBEN (1972) have pointed out that the phonon spectra of amorphous Si and Ge are in fact very similar to a broadened version of the VDOS of the corresponding crystalline phase. Since the SRO is similar in both phases (see section 2.5.1), this suggests that it is the SRO which essentially determines the VDOS and then the broadening (and lack of Van Hove singularities) for the amorphous phase is due to disorder. Earlier calculations by DEAN and BACON (1963) have shown that the modes of two-component disordered chains are strongly localised at intermediate and high energies. In 1973 THORPE showed that the general form of the VDOS of tetrahedral materials can be accounted for by considering the vibrational characteristics of a single structural unit (ie. one tetrahedron). More recently GALEENER, BARRIO, MARTINEZ and ELLIOTT (1984) have shown that regular rings in a network can have vibrational modes which are decoupled from the rest of the network. These modes produce anomalously narrow features in a vibrational spectrum which consists otherwise of broad bands and thus vibrational spectroscopy provides a probe of IRO in amorphous solids. Information about IRO obtained from vibrational spectra is especially useful since IRO is much more difficult to deduce from diffraction data than is SRO. So far most of the calculations relating to vibrational excitations of amorphous solids have been for tetrahedrally coordinated materials.

There is a number of ways of calculating the VDOS of a CRN structure. These may be divided into analytic approaches and direct numerical calulations. Analytic methods are limited in the sense that they cannot produce a calculation of the whole VDOS for a realistic structure and force model. However, they are still of considerable value as they can provide a physical explanation of many of the salient features of the VDOS such as the general positions of bands and the occurrence of the sharp lines associated with regular IRO structures. (See for example SEN and THORPE (1977), GALEENER (1979), AGRAWAL (1985) and GALEENER (1985).) Direct numerical methods rely on the use of a computer to solve a very large number of equations derived from a ball-and-stick model of the type described in section 2.5.3 . There are several techniques for performing such a calculation, as is discussed below.

The earliest work relating to the vibrational excitations of disordered solids was that performed in the 1960s on two-component disordered chains. This work was useful in indicating some of the general ideas required to understand vibrational excitations in amorphous solids, especially localisation, but it does not provide results which can be directly related to real materials. In particular it is not possible to reproduce the full effect of 3D topological disorder in a one-dimensional (1D) model. DEAN (1972) has given as extensive review of this work.

The first investigation of the atomic vibrations for a realistic structural model was that of BELL, BIRD and DEAN (1968) who calculated the VDOS for SiO_2, GeO_2 and BeF_2 from a tetrahedrally coordinated ball-and-stick model. The calculation method was based upon a use of the negative eigenvalue theorem (NET) (DEAN and MARTIN, 1960) to determine the distribution of the eigenvalues of the dynamical matrix (see section 5.2) and a discussion of this method is delayed until chapter 14 since the same method was used for the calculations reported in this thesis. The calculations were found to agree moderately well with observed vibrational spectra. In later work BELL and DEAN (1972) calculated the eigenvectors in addition to the eigenvalues. It was shown that the modes are fairly extended at low energies (for long wavelengths the material is effectively a continuum and the disordered structure is not important) but show a tendency to greater localisation with increasing energy. The localisation was found to be most accentuated near the band edges, as is also generally found to be the case for electronic states. ALBEN, WEAIRE, SMITH and BRODSKY (1975) have performed similar calculations of the vibrational spectra for Si and Ge. The results were found to compare favourably with Raman and IR data.

Another technique for calculating the VDOS from a ball-and-stick model is the recursion method, developed for vibrational calulations by MEEK

(1976). In this method the local density of states (ie. the density of states weighted by the amplitude squared of each mode at one particular atom) is calculated by terminating a series of recursion relations after a finite number and then averaging over perhaps ten of the central atoms of the model. MEEK calculated the VDOS for elemental tetrahedral models and compared the results with optical spectra for Ge, yielding information about the proportion of odd- and even-membered rings in the network. The recursion method has also been used by DAVIS, WRIGHT, DORAN and NEX (1979) who computed the VDOS for models of As, showing that the best model is one with no constraint on ring order. The VDOS of a ball-and-stick model may also be obtained by the equation of motion method, a review of which has been given by BEEMAN and ALBEN (1977). This method involves following the behaviour with time of a central portion of a model after the atoms have been given random initial displacements. BEEMAN and ALBEN studied the vibrational excitations for four-coordinated (Ge-like), three-coordinated (As-like) and two-coordinated (Se-like) elemental amorphous semiconductors and a reasonable agreement with optical data was obtained.

A potential problem involved in a calculation of the VDOS for a ball-and-stick model is that the surface atoms can be expected to contribute highly localised 'defect' modes to the VDOS. This is undesirable since the aim is to model the VDOS of the bulk material. In the case of the recursion method and the equation of motion method this problem is overcome by only using the atoms in a central portion of the model to calculate the VDOS. Another approach is the 'cluster-Bethe-lattice' method (LAUGHLIN and JOANNOPOULOS, 1977), originally developed by JOANNOPOULOS and YNDURAIN (1974) for calculations of the electronic density of states. In this method an appropriate Bethe-lattice is grafted onto each of the unsatisfied surface atoms. A Bethe-lattice, or Cayley tree as it is otherwise known, is an infinitely branching (ie. no rings) network of atoms. LAUGHLIN and JOANNOPOULOS (1977) have used the cluster-Bethe-lattice method to investigate the relation between vibrational excitations and SRO in SiO_2. BARRIO, GALEENER and MARTINEZ (1984) have shown that also a Bethe-lattice alone can be useful in understanding vibrational excitations of a network. Another problem with finite sized ball-and-stick models is that there is a minimum wavelength for which the VDOS can be calculated.

5.2 THE EIGENVALUE EQUATION.

The theoretical background to VDOS calculations is developed here in detail in order that the equations may be expressed in a form particularly suited to the computations described in Chapter 14. It is found that a notation based upon sub-matrices and outer products (see Appendix A) is most appropriate. In the following analysis it is assumed that the Born-Oppenheimer approximation, or adiabatic approximation as it is otherwise known, can be made. That is to say it is assumed that it is a good approximation to express the potential energy as a function of nuclear coordinates only and not of electronic coordinates.

Consider a disordered system of N atoms. Clearly the energy eigenvalues are of prime importance in characterising the vibrational properties of such a system. It can be shown that, in the harmonic approximation, it is possible to derive the eigenvalues of the system purely by considering the classical problem (DEAN, 1972), and this is done as follows:

Denote the equilibrium position of the i^{th} atom by $\underline{R}_i$, and let it suffer a small displacement $\underline{u}_i$. If it is assumed that the motions of the atoms are coupled by harmonic forces, then the most general expression for the equation of motion of the i^{th} atom is;

$$\ddot{\underline{u}}_i = - \sum_{j=1}^{N} \underline{\underline{v}}_{ij}\, \underline{u}_j \tag{5.2.1}$$

where the sub-matrix $\underline{\underline{v}}_{ij}$ is a 3x3 matrix (for a 3D model) whose elements depend upon the masses of the atoms i and j, the force constant(s) describing the interaction between i and j, and the relative positions of i and j. The double dot indicates a double differentiation with respect to time and the double underline indicates a matrix. At this stage it is convenient to make a transformation from the coordinates $\underline{u}_i$ to normal coordinates $\underline{e}_i$, defined by;

$$\underline{e}_i = m_i^{-1/2}\, \underline{u}_i \tag{5.2.2}$$

Equation (5.2.1) then becomes;

$$\ddot{\underline{e}}_i = - \sum_{j=1}^{N} \underline{\underline{w}}_{ij}\, \underline{e}_j \tag{5.2.3}$$

in which the sub-matrix $\underline{\underline{w}}_{ij}$ is termed the dynamical sub-matrix. Equation (5.2.3) describes a set of coupled equations which can be expressed in matrix form as;

$$\ddot{\underline{y}} = - \underline{\underline{W}}\, \underline{y} \qquad (5.2.2)$$

where $\underline{y}$ is a column matrix whose elements are the $\underline{e}_i$ and the dynamical matrix $\underline{\underline{W}}$ is a 3Nx3N matrix whose elements are the $\underline{\underline{w}}_{ij}$. Note that as a consequence of the transformation to normal coordinates and Newton's Third Law of Motion $\underline{\underline{\mathbf{W}}}$ is a symmetric matrix ($W_{ij} = W_{ji}$). Thus the purpose of the transformation to normal coordinates is to cast $\underline{\underline{\mathbf{W}}}$ in symmetric form which is of considerable advantage for calculations.

Substituting the Fourier transform $\underline{\mathbf{y}}(t)=(2\pi)^{-1/2}\int\tilde{\underline{\mathbf{y}}}(\omega')\exp(-i\omega t)d\omega'$ (all integrals in this section are assumed to be over the whole range of the relevant variable) and taking the derivative inside the integral gives;

$$-(2\pi)^{-1/2} \int \omega'^{2} \tilde{\underline{\mathbf{y}}}(\omega') \exp(-i\omega' t) \, d\omega' = -(2\pi)^{-1/2} \underline{\underline{\mathbf{W}}} \int \tilde{\underline{\mathbf{y}}}(\omega') \exp(-i\omega' t) d\omega' \tag{5.2.5}$$

Taking the scalar product $\int......\exp(i\omega t)dt$ then gives;

$$\int \omega'^{2} \tilde{\underline{\mathbf{y}}}(\omega') \int \exp(-i(\omega'-\omega)t) \, d\omega' \, dt = \underline{\underline{\mathbf{W}}} \int \tilde{\underline{\mathbf{y}}}(\omega') \int \exp(-i(\omega'-\omega)t) \, d\omega' \, dt \tag{5.2.6}$$

Using the integral definition of the delta function $\int\exp(-i(\omega'-\omega)t)dt=2\pi\delta(\omega'-\omega)$ this becomes;

$$2\pi \int \omega'^{2} \tilde{\underline{\mathbf{y}}}(\omega') \, \delta(\omega'-\omega) \, d\omega' = 2\pi \, \underline{\underline{\mathbf{W}}} \int \tilde{\underline{\mathbf{y}}}(\omega') \, \delta(\omega'-\omega) \, d\omega' \tag{5.2.7}$$

$$\underline{\underline{\mathbf{W}}} \, \tilde{\underline{\mathbf{y}}} = \omega^{2} \, \tilde{\underline{\mathbf{y}}} \tag{5.2.8}$$

Thus the frequencies of the normal modes of the system are given by the eigenvalues of the dynamical matrix $\underline{\underline{\mathbf{W}}}$. The VDOS of the N atom system may then be defined to be (THORPE, 1976);

$$g(\omega) = \sum_{s} \delta(\omega-\omega_{s}) \tag{5.2.9}$$

where the summation is taken over the eigenvalues ω_s from equation (5.2.8). Hence a calculation of the distribution of the eigenvalues of $\underline{\underline{\mathbf{W}}}$ yields the

VDOS of the system.

In order to calculate the VDOS of a system its dynamical matrix $\underline{\underline{V}}$ must first be calculated. The dynamical sub-matrices $\underline{\underline{v}}_{ij}$ depend upon the interatomic forces and the atomic coordinates and masses. The atomic masses are known and the dependence on the atomic coordinates is the basic principle which underlies the purpose of these studies. The idea of interatomic forces is fairly well understood and they are discussed in the next section.

5.3 INTERATOMIC FORCES.

All the force models discussed in this section are harmonic since the calculation method used in Chapter 14 is only suitable for a system described by harmonic forces, as is the case with virtually all methods. The true forces in solids are not harmonic (as evidenced by the phenomenon of thermal expansion for example), but it has been found that many properties can be explained very well by models using harmonic forces. However, DE LEEUW and THORPE (1985) have recently suggested that the long range Coulomb force between atoms (ions) may in fact be required to understand fully the VDOS of some glasses. Coulomb forces cannot be directly included in a harmonic force model. Most calculations in the literature consider only topological disorder and ignore any possibility of a variation of force constants from site to site, resulting from differences in atomic environment. However, this may not always be an adequate approximation and this issue is discussed further in Chapter 14.

5.3.1 CENTRAL FORCES.

The simplest model for describing the forces between the atoms in a solid is that of central forces. In this model forces operate only along the interatomic direction and are proportional to the relative displacement from equilibrium along that direction. Whilst central forces can be useful in providing a qualitative understanding of atomic motions, they are too simplistic for use in a VDOS calculation. If the VDOS of a system is calculated using only central forces it is found that a large number of modes occur in a delta function at the origin, ie with zero energy. This may be understood as follows (THORPE, 1976): For an N atom system there are 3N degrees of freedom. Central forces may be thought of as a constraint on the system involving keeping all the N_b bonds fixed in length (eg $N_b = 6N/5$ for B_2O_3). It can be shown that these constraints are linearly independent and so there are $3N-N_b$ degrees of freedom left (9N/5 for B_2O_3). This means that there must be $3N-N_b$ zero energy eigenvalues. Detailed calculations by WEAIRE and ALBEN (1972) and the author confirm this.

The equations for central forces are not given here since they may easily be obtained from those for Born forces in section 5.3.2 by setting the force constants λ_{ij}^{nc} to zero.

5.3.2 BORN FORCES.

In the BORN (1914) force model a small non-central term is added to the central force expression and this overcomes the instability discussed in section 5.3.1 . The non-central force between two atoms is taken to be proportional to the relative vector displacement of the two atoms perpendicular to the interatomic direction, and the central force is as described above. This force model has been most successful in forming a quantitative understanding of the vibrational and related properties of solids. However, the Born force model has the theoretical drawback that it is not rotationally invariant. That is to say, a macroscopic rotation of the whole sample does not leave the potential energy according to the Born force model unchanged. (Note that a VDOS calculation based upon a force model which does satisfy the requirements of invariance yields six zero energy eigenvalues corresponding to translation and rotation in each of the three Cartesian directions.)

Let i and j be two atoms whose equilibrium positions are $\underline{\mathbf{R}}_i$ and $\underline{\mathbf{R}}_j$, and let $\underline{\mathbf{d}}_{ij}$ ('the bond' - see figure 5.1a) be the vector from the equilibrium position of atom i to the equilibrium position of atom j;

$$\underline{\mathbf{d}}_{ij} = \underline{\mathbf{R}}_j - \underline{\mathbf{R}}_i \qquad (5.3.1)$$

Let the atoms suffer small displacements $\underline{\mathbf{u}}_i$ and $\underline{\mathbf{u}}_j$ (u_i, $u_j \ll d_{ij}$) from equilibrium. $\underline{\mathbf{u}}_i$ may be decomposed (see figure 5.1b) into a component $u_{i\parallel}$ parallel to $\underline{\mathbf{d}}_{ij}$ and a component $\underline{\mathbf{u}}_{i\perp}$ perpendicular to $\underline{\mathbf{d}}_{ij}$;

$$u_{i\parallel} = \underline{\mathbf{u}}_i \cdot \underline{\mathbf{d}}_{ij} \; / \; d_{ij} \qquad (5.3.2)$$

$$\underline{\mathbf{u}}_{i\perp} = \underline{\mathbf{u}}_i - u_{i\parallel} \, \hat{\underline{\mathbf{d}}}_{ij} \qquad (5.3.3)$$

where $\hat{\underline{\mathbf{d}}}_{ij}$ is the unit vector in the direction of $\underline{\mathbf{d}}_{ij}$;

$$\hat{\underline{\mathbf{d}}}_{ij} = \underline{\mathbf{d}}_{ij} / d_{ij} \qquad (5.3.4)$$

Let λ_{ij}^{c} be the force constant for the central force between these two atoms. The central force on atom i due to atom j has magnitude;

$$F^{c}_{ij} = \lambda^{c}_{ij}\,(u_{j\parallel} - u_{i\parallel}) \qquad (5.3.5)$$

This force is in the direction $\hat{\underline{d}}_{ij}$;

$$\underline{F}^{c}_{ij} = \lambda^{c}_{ij}\,(\, u_{j\parallel} - u_{i\parallel}\,)\,\hat{\underline{d}}_{ij} \qquad (5.3.6)$$

Similarly let λ^{nc}_{ij} be the force constant for the non-central force between the two atoms. The non-central force on atom i due to atom j is;

$$\underline{F}^{nc}_{ij} = \lambda^{nc}_{ij}\,(\, \underline{u}_{j\perp} - \underline{u}_{i\perp}\,) \qquad (5.3.7)$$

Using (5.3.3);

$$\underline{F}^{nc}_{ij} = \lambda^{nc}_{ij}\,[\,(\underline{u}_j - u_{j\parallel}\,\hat{\underline{d}}_{ij}) - (\underline{u}_i - u_{i\parallel}\,\hat{\underline{d}}_{ij})\,] \qquad (5.3.8)$$

The total force on atom i due to atom j is then;

$$\begin{aligned}\underline{F}_{ij} &= \underline{F}^{c}_{ij} + \underline{F}^{nc}_{ij}\\ &= \lambda^{c}_{ij}\,(u_{j\parallel} - u_{i\parallel})\,\hat{\underline{d}}_{ij} + \lambda^{nc}_{ij}\,[\,(\underline{u}_j - u_{j\parallel}\,\hat{\underline{d}}_{ij}) - (\underline{u}_i - u_{i\parallel}\,\hat{\underline{d}}_{ij})\,]\\ &= (\lambda^{c}_{ij} - \lambda^{nc}_{ij})\,(u_{j\parallel} - u_{i\parallel})\,\hat{\underline{d}}_{ij} + \lambda^{nc}_{ij}\,(\underline{u}_j - \underline{u}_i) \qquad (5.3.9)\end{aligned}$$

Using (5.3.3) and (5.3.4) this becomes;

$$\underline{F}_{ij} = [(\lambda^{c}_{ij} - \lambda^{nc}_{ij})/d_{ij}^{\,2}]\,(\underline{u}_j\cdot\underline{d}_{ij} - \underline{u}_i\cdot\underline{d}_{ij})\,\underline{d}_{ij} + \lambda^{nc}_{ij}\,(\underline{u}_j - \underline{u}_i) \qquad (5.3.10)$$

By use of equation (A.1) this may be expressed in a form suitable for evaluation of the dynamical sub-matrices $\underline{\underline{V}}_{ij}$;

$$\underline{F}_{ij} = [((\lambda^{c}_{ij} - \lambda^{nc}_{ij})/d_{ij}^{\,2})\,\underline{d}_{ij}\underline{d}_{ij} + \lambda^{nc}_{ij}\,]\,(\underline{u}_j - \underline{u}_i) \qquad (5.3.11)$$

The set of forces (5.3.10) is equivalent to a potential given by;

$$V = \sum_{ij} [((\lambda^{c}_{ij} - \lambda^{nc}_{ij})/4d_{ij}^{2})((\underline{u}_i-\underline{u}_j).\underline{d}_{ij})^2 + (\lambda^{nc}_{ij}/4)(\underline{u}_i-\underline{u}_j)^2] \qquad (5.3.12)$$

where both summations are taken over all the N atoms of the sample. Summing (5.3.11) over all atoms j and using Newton's Second Law of Motion gives the total force on atom i as;

$$m_i\ddot{\underline{u}}_i = \underline{F}_i = \sum_{\substack{j=1 \\ j\neq i}}^{N} \underline{F}_{ij} \qquad (5.3.13)$$

In principle the summation over j must be taken over all the other N-1 atoms of the sample in order to obtain the force on atom i. However, in any practical calculation the summation must be restricted, quite possibly to just nearest neighbours, if it is to be manageable.

Comparing with equation (5.2.3) gives the dynamical sub-matrices for a system described by Born forces as;

$$\underline{\underline{\mathbf{v}}}_{ii} = (1/m_i) \sum_{\substack{j=1 \\ j\neq i}}^{N} [((\lambda^{c}_{ij} - \lambda^{nc}_{ij})/d_{ij}^{2})\ \underline{\mathbf{d}}_{ij}\underline{\mathbf{d}}_{ij} + \lambda^{nc}_{ij}\ \underline{\underline{\mathbf{I}}}\ ] \qquad (5.3.14)$$

$$\underline{\underline{\mathbf{v}}}_{ij} = -\sqrt{(1/m_i m_j)}\ [((\lambda^{c}_{ij} - \lambda^{nc}_{ij})/d_{ij}^{2})\ \underline{\mathbf{d}}_{ij}\underline{\mathbf{d}}_{ij} + \lambda^{nc}_{ij}\ \underline{\underline{\mathbf{I}}}\ ] \quad \text{for } j\neq i \qquad (5.3.15)$$

where $\underline{\underline{\mathbf{I}}}$ is the appropriate unit matrix.

From equations (5.3.14) and (5.3.15) it can be seen that the dynamical sub-matrices depend upon the atomic coordinates (through the $\underline{\mathbf{d}}_{ij}$) and masses m_i and the interatomic forces (through the λ^{c}_{ij} and λ^{nc}_{ij}) as stated previously.

4.3.3 KEATING FORCES.

In 1966 KEATING developed a force model which is rotationally invariant. This model consists of a central force term together with another term which is often (incorrectly) referred to as a 'bond-bend' force. The expressions given by Keating are for the specific case of diamond, which is tetrahedrally coordinated, but those given here are suitable for any coordination. The potental energy of a system described by the Keating force model is;

$$V = \sum_{ij} \frac{3\alpha}{16 d_{ij}^2} \left(\underline{r}_{ij}^2 - \underline{d}_{ij}^2 \right)^2 + \sum_{i(j,j')} \frac{3\beta}{8 d_{ij} d_{ij'}} \left(\underline{r}_{ij} \cdot \underline{r}_{ij'} - \underline{d}_{ij} \cdot \underline{d}_{ij'} \right)^2 \qquad (5.3.17)$$

where $\underline{r}_{ij}$ is the vector from atom i to atom j, α and β are force constants, the i summations are taken over all atoms, the j summation is over all neighbours of i and the (j,j') summation is taken over all distinct pairs of neighbours of i. The total force on atom i may be shown to be;

$$\underline{F}_i = \sum_{j} \frac{3\alpha}{d_{ij}^2} (\underline{d}_{ij}\underline{d}_{ij}) (\underline{u}_j - \underline{u}_i) + \sum_{\substack{jj' \\ j'>j}} \frac{3\beta}{4 d_{ij} d_{ij'}} \Big((\underline{d}_{ij'}\underline{D}_{ij'j}) \underline{u}_j + (\underline{d}_{ij}\underline{D}_{ij'j}) \underline{u}_{j'}$$

$$- (\underline{D}_{ij'j}\underline{D}_{ij'j}) \underline{u}_i \Big) + \sum_{\substack{jk \\ k \neq i}} \frac{3\beta}{4 d_{ij} d_{jk}} \Big((\underline{D}_{jki}\underline{d}_{jk}) \underline{u}_j + (\underline{d}_{ij}\underline{d}_{jk}) \underline{u}_k - (\underline{d}_{jk}\underline{d}_{jk}) \underline{u}_i \Big) \qquad (5.3.18)$$

where the k summation is over neighbours of j other than i (see figure 5.1c) and the vector $\underline{D}_{ijk}$ is defined by;

$$\underline{D}_{ijk} = \underline{d}_{ij} + \underline{d}_{ik} \qquad (5.3.19)$$

The dynamical sub-matrices appropriate to the Keating force model may be shown to be;

$$\underline{w}_{ii} = \frac{1}{m_i}\left(\sum_{j} \frac{3\alpha}{d_{ij}^{2}} \underline{d}_{ij}\, \underline{d}_{ij} + \sum_{\substack{jj' \\ j'>j}} \frac{3\beta}{4d_{ij}d_{ij'}} \underline{D}_{ij'j}\, \underline{D}_{ij'j} + \sum_{\substack{jk \\ k\neq i}} \frac{3\beta}{4d_{ij}d_{jk}} \underline{d}_{jk}\, \underline{d}_{jk} \right) \qquad (5.3.20)$$

$$\underline{w}_{ij} = \frac{-1}{\sqrt{(m_i m_j)}}\left(\frac{3\alpha}{d_{ij}^{2}} \underline{d}_{ij}\, \underline{d}_{ij} + \sum_{\substack{j' \\ j'\neq j}} \frac{3\beta}{4d_{ij}d_{ij'}} \underline{d}_{ij'}\, \underline{D}_{ijj'} + \sum_{\substack{k \\ k\neq i}} \frac{3\beta}{4d_{ij}d_{jk}} \underline{D}_{jki}\, \underline{d}_{jk} \right) \qquad (5.3.21)$$

$$\underline{w}_{ik} = \frac{-1}{\sqrt{(m_i m_k)}} \sum_{j} \frac{3\beta}{4d_{ij}d_{jk}} \underline{d}_{ij}\, \underline{d}_{jk} \qquad (5.3.22)$$

where the j summation of (5.3.22) is taken over common neighbours of i and k.

Despite the apparent simplicity of the Keating potential (5.3.17), equations (5.3.20), (5.3.21) and (5.3.22) show clearly that a VDOS calculation based upon Keating forces is very much more complicated than a calculation based upon Born forces. In 1975 ALBEN, WEAIRE, SMITH and BRODSKY showed that calculations for amorphous Si and Ge based upon Born forces yield results which are essentially identical to those obtained using Keating forces. Similarly LAUGHLIN and JOANNOPOULOS (1978) have shown that for a cluster-Bethe-lattice calculation for SiO_2 the simpler Born force model is in most respects an execellent approximation for the more realistic Keating force model. It seems reasonable to assume that this is also the case with other rotationally invariant force models, such as the valence force fields which stem from the work of SCHACHTSCHNEIDER and SNYDER (1963), and so it is concluded that for a VDOS calculation the Born force model is adequate.

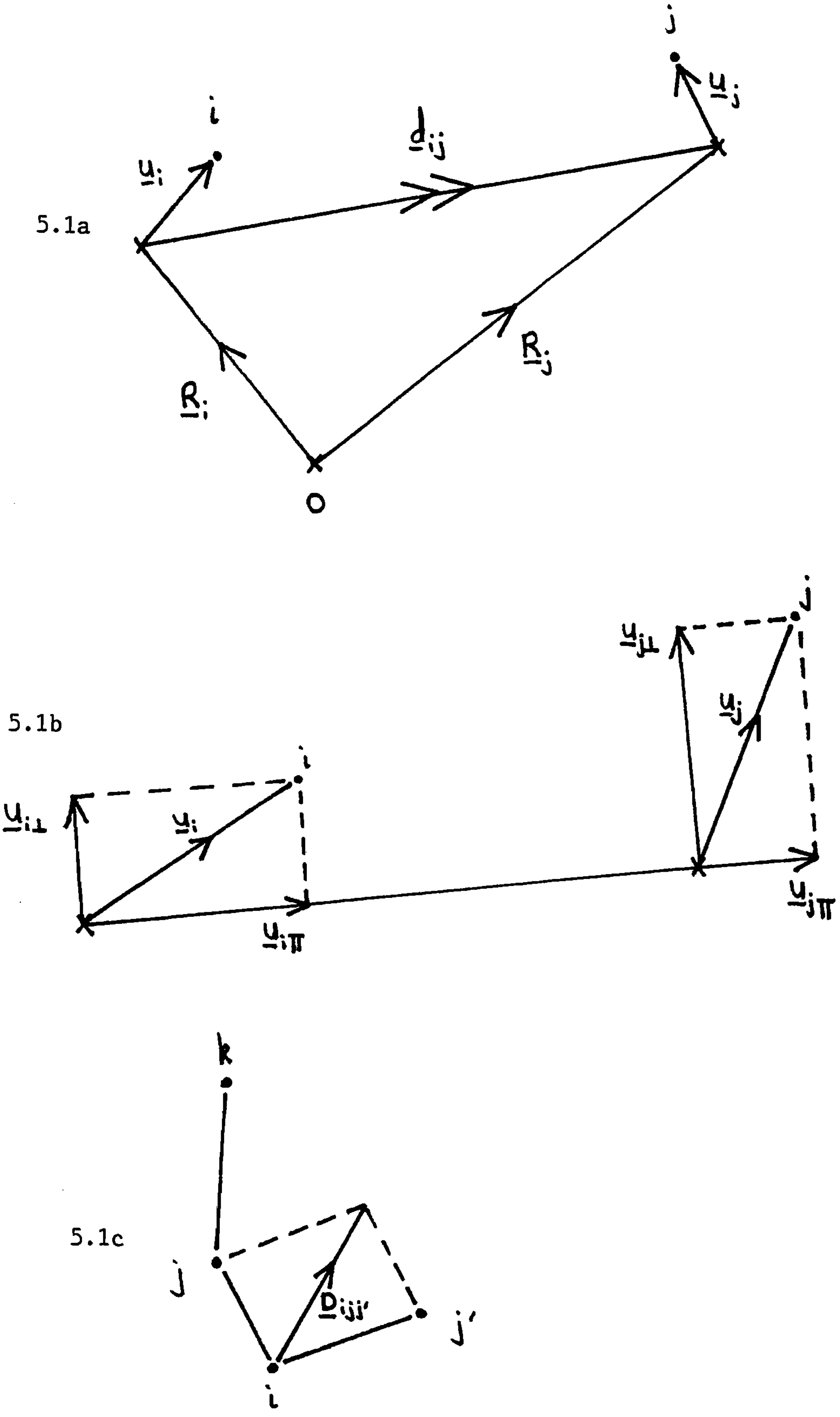

Figure 5.1 Definition of Vectors for the Theory of Network Dynamics.

CHAPTER 6

Dy7Ni3 - INTRODUCTION.

6.1 AMORPHOUS METALS - AN INTRODUCTION.

6.1.1 INTRODUCTION.

In 1960 an exciting new form of matter was discovered (KLEMENT, WILLENS and DUWEZ) during a study of the rapid cooling of a molten alloy of gold and silicon. It was found that if the alloy was cooled sufficiently quickly the resulting solid did not exhibit any regular crystal structure, and yet it did have some of the other properties normally associated with metals such as a high electrical conductivity. Previously it had been thought that directional covalent bonding was a prerequisite for the avoidance of crystallisation from the melt, but this discovery showed this not to be the case. This was the first observation of a metallic glass and subsequent research has shown there to be a wide variety of such materials: Some elemental metals, such as Ni, may be produced in amorphous form, although there is some question as to their purity. Amorphous metallic alloys can also be made, either from combinations of metallic elements alone or from combinations of metallic elements and metalloid elements (Si, B, P or C). Most structural studies have concentrated on binary alloys (ie. two elements) since these offer greater hope of being understood than multicomponent systems. Of particular interest for the present work are rare earth-late transition metal (RE-TL) alloys, such as $Gd_{18}Co_{82}$ (nb. for alloys the subscripts refer to atomic percentages and do not have structural significance). The largest number of structural studies have been on transition metal-metalloid (T-M) alloys, such as $Ni_{76}P_{24}$, with a smaller number of studies on early transition metal-late transition metal (TE-TL) alloys, such as $Ni_{60}Nb_{40}$. Amorphous binary alloys which combine alkali earth elements with other metallic elements have also been studied (eg. $Mg_{70}Zn_{30}$).

(Note that in the above the division of the periodic table between early and late transition metals is taken to be between Mn and Fe.)

6.1.2 PROPERTIES.

The properties of a material are highly dependent upon its atomic structure (e.g. the form of the electron energy bands), and so it is not surprising that amorphous metals have properties which are significantly different from their crystalline counterparts. The electromagnetic properties, for example, are rather different from those of crystalline metals, and these have excited considerable interest. Amorphous metals have somewhat higher electrical resistivities than crystalline metals, and the temperature dependence of the resistivity is rather low. Furthermore, the sign of the temperature coefficient of electrical resistivity can be changed with the addition of impurities to yield a positive, zero or negative value close to or below room temperature. Thus one application of these materials is as standard resistors. Amorphous metals have extremely high Hall coefficients which is of application in magnetic field sensors. It is the magnetic properties of amorphous metals that have generated the greatest volume of research activity. The coercivities of these alloys are generally very low due to the homogeneity of the material (there are no grain boundaries to impede motion of domain walls). The main area of large scale application in the immediate future seems to be as transformer cores. Such cores have much lower power losses than conventional crystalline Fe-Si cores; the higher resistivity reduces heat losses due to eddy currents, and the low coercivity results in low hysteresis losses. It has been established that magnetic anisotropy can be present in amorphous metals (depending on the history of the sample), and also magnetic bubbles have been observed in some alloys which may prove to be useful for high density data storage. The soft magnetic properties of amorphous metals have also been utilised in tape heads and hi-fi pick-ups. Amorphous metals have superconducting properties which may prove useful, particularly in superconducting electromagnets. They are hard and strong, and yet ductile (unlike hard, strong crystals which are generally brittle). Some of them are highly corrosion resistant, and this property may well be exploited in protective coatings for products such as machine parts. Unlike crystals, amorphous metals do not show work-hardening. Some of them behave as catalysts which are more effective than their crystalline equivalent. On a more general note, the continuously variable composition of amorphous metals makes for greater ease of design of materials with desirable properties. Amorphous metals also have relatively cheap production costs compared to traditional metals. (The properties described above are discussed more comprehensively in recent general reviews by CHAUDHARI and TURNBULL (1978), GRANT and McKIM (1982), GIBBS (1983) and DUGDALE, PAVUNA and RHODES (1984).)

6.1.3 ATOMIC STRUCTURE.

To understand the properties of amorphous metals it is necessary to understand their atomic structure. Diffraction experiments are the most important structural probe of materials, and any structural model must be compared with the diffraction data. Density measurements also provide an important test of structural models.

For many amorphous metals the most prominent peaks in the interference function occur close to Bragg peaks of the corresponding crystalline phase and so microcrystalline models for the atomic structure (see section 2.5.1) have an obvious attraction. These models involve misoriented microcrystals with diameters averaging 5 to 10 atomic spacings. However, the problem of how the atoms are arranged in the intercrystalline regions is usually ignored, and there is considerable difficulty in fitting experimental scattering data, in particular the relative sharpness of the first peak of the interference function (CARGILL, 1975). Models involving abrupt structural discontinuities have generally been found to be unsatisfactory and will not be dicussed further.

A somewhat more satisfactory approach to modelling atomic arrangements in amorphous metals is based on structures formed by the random close packing (RCP) of spheres. The study of RCPs of a single size of hard sphere was pioneered by BERNAL (1959, 1964) as an attempt to model simple liquids. A number of hand-built models were constructed with a single size of sphere, the largest and most accurate of which was built by FINNEY (1970) and contained nearly 8000 spheres. The method used to construct these models was to fill a bag with a large number of ball bearings in such a way that firstly there were no regular crystalline regions ('random') and secondly that there were no holes large enough to contain another sphere ('close'). The balls were then glued into position and their coordinates measured (BERNAL, CHERRY, FINNEY and KNIGHT, 1970). More recently RCPs of single-sized spheres have also been constructed by computer (see CARGILL, 1981, and references contained therein). The topology of a RCP of spheres can be described in terms of the holes between the spheres. These holes may be considered to be approximately regular polyhedra (since they are defined by the contacts between single-sized spheres) and BERNAL (1960) has pointed out that there are only five polyhedra small enough not to admit another sphere into their interior. The term 'canonical holes' has been used for these five polyhedra and they are as follows: the tetrahedron, the half-octahedron, the tetragonal dodecahedron, the trigonal prism and the Archimedean anti-prism (see figure 6.1). Alternatively the topology of a RCP may be described in terms of Wigner-Seitz cells (known as Voronoi polyhedra in this context).

In 1964 COHEN and TURNBULL suggested a RCP of hard spheres as a prototype for the structure of monatomic amorphous metals. DAVIES and GRUNDY (1971, 1972) have performed electron diffraction on nominally pure films of Ni, Co, Au and Ag. The data were compared in real-space with FINNEY's (1970) RCP of hard spheres model and it was concluded that the structures of these films are the atomic equivalentof the RCP structure. However, there is a serious unresolved problem in that the hard sphere diameter required to fit the RCP distribution function to the experimental RDFs in the region beyond the first peak was 5% smaller than the average nearest neighbour spacing indicated by the position of the first peak of the experimental RDFs.

In 1970 CARGILL proposed the use of a single sphere size RCP model to describe the structure of T-M alloys, with the two types of atom distributed at random. The argument was based upon the fact that the 12-coordinated Goldschmidt radii for many of the metal-metalloid pairs are very similar. It was shown that the total RDF for this model reproduced the experimental RDF for $Ni_{76}P_{24}$ derived from X-ray diffraction remarkably well, including the split second peak which is a common characteristic of most T-M alloys. However, there are several problems with this model, the most serious of which is that chemical ordering is now known to occur in T-M alloys (see below) and such a phenomenon is not included in the model. Also there are problems with the nearest neighbour distance, coordination number and density.

Chemical ordering was first observed in a T-M alloy by SADOC and DIXMIER (1976) who measured the partial distribution functions for $Co_{80}P_{20}$ by a combined use of neutron diffraction, X-ray diffraction and polarised neutron diffraction. It was found that there are no metalloid-metalloid near neighbours in this alloy. The measurement of partial distribution functions has proved to be of great value in the study of SRO in amorphous metals since, unlike conventional glasses, there tends to be considerable overlap of nearest neighbour peaks in real-space. The partial functions can be separated experimentally by techniques such as isotopic substitution neutron diffraction (see section 6.4.1), combined use of diffraction with different types of radiation and isomorphous substitution. Subsequent to the work of SADOC and DIXMIER (1976) the partial correlation functions have been measured for a number of T-M alloys at a range of compositions and it is found that these alloys exhibit a very strong degree of chemical ordering with an avoidance of metalloid-metalloid contact (SPAEPEN and GARGILL, 1985).

A modification of CARGILL's (1970) single sphere size RCP model for the structure of T-M alloys was proposed by POLK (1970) in which the metal atoms are arranged in a RCP structure with the metalloid atoms occupying the larger holes inherent in the random packing. This modification has the advantage that chemical ordering is now included in the model, and also the proportion of metalloid atoms required to stabilise the structure (~20%) is predicted correctly. However, subsequent calculations (CARGILL, 1975) have shown that in fact the holes in a RCP are not as large as originally thought and there is insufficient volume to accept any but the very smallest type of metalloid atoms. Despite this, the interstitial model for metalloid positioning still appears attractive and there have been several attempts at generating binary RCP models with two sizes of atom, and with no adjacent metalloid atoms (for example see BOUDREAUX and GREGOR, 1977). There have also been attempts to improve RCP models by relaxing the structure (see section 2.5.3) using a Lennard-Jones potential to simulate the predominantly non-directional character of metallic bonding, leading to a type of model known as a RCP of soft spheres (see for example CARGILL, 1981). However, this approach has not been obviously any more successful for T-M alloys.

More recently GASKELL (1979) has proposed an alternative approach to the modelling of the atomic structure of T-M alloys which is rather different to that described above. Many crystalline T_3M alloys consist of packings of MT_6 trigonal prisms (figure 6.2), and it is suggested that it may be possible to describe amorphous T_4M alloys in terms of trigonal prismatic structural units. In order to model the structure of amorphous Pd_4Si a hand-built trigonal prismatic model was constructed. The prisms were connected together by sharing triangle edges with connected prisms having opposite orientations (see figure 6.2) as is found in cementite Fe_3C (Pd_3Si is isostructural with Fe_3C). A trigonal prism was added to the model (starting with a single seed trigonal prism) by placing a single T atom in half-octahedral configuration over the square face of a prism. This then defines the triangular base for the next prism and so on. A random arrangment was obtained by choosing shared edges essentially at random. The M atoms were added at the computation stage. Note that as ELLIOTT (1983) has pointed out one of the major differences of the trigonal prismatic model compared to the RCP of spheres model is that the RCP has a wide variety of coordination polyhedra whereas the trigonal prismatic model has a well-defined structural unit reminiscent of the CRN approach to the modelling of conventional glasses. GASKELL's (1979) model was relaxed using a Lennard-Jones (LJ) potential, although it was found to be necessary to use a very slightly artificial potential so that the trigonal prismatic coordination was maintained. The reciprocal-space and real-space total (ie. not partial) functions for the model were compared with those for Pd_4Si and the agreement obtained was found to be remarkably good for this type of work. A later comparison (GASKELL, 1981) with approximate experimental Pd-Pd and Pd-Si pair distribution functions shows reasonably good agreement at low and medium r, though with some discrepancies at high r. GASKELL

(1981) has also suggested that whilst the Fe_3C type triangle edge sharing arrangement may be relevant to binary alloys with very different atom sizes, the Fe_3P type triangle edge sharing arrangement (figure 6.2) can be expected to be more relevant when the atoms are of a similar size. Also GARDNER and COWLAM (1985) have concluded from a study of the partial functions of amorphous $Ni_{64}B_{36}$ that when there is not a crystal phase of the same stoichiometry as the T-M amorphous phase it may be appropriate to consider crystal phases of both lower and higher metalloid concentration as prototype structures. GELLATLY and FINNEY (1982) have performed a radical plane analysis (a generalisation of Voronoi polyhedra for a multicomponent system) of the GASKELL (1979) model from which they conclude that after relaxation very few of the M atoms still have a trigonal prismatic coordination polyhedron. However, this analysis does not enable a distinction to be drawn between the T atoms in a trigonal prism and half-octahedrally positioned T atoms and it is not clear how much significance can be attached to this result. Possibly the simple LJ potential is unsuitable for the relaxation of such models. A second trigonal prismatic modelling study with a rather different approach has been performed by DUBOIS, GASKELL and LeCAËR (1985). These workers observed that the layered structure of Fe_3C (see section 8.4) can be described in terms of twinning planes. A hypothetical T_4M lattice was proposed which is based upon the Fe_3C lattice with the addition of half-octahedrally positioned metal atoms which are not included in any trigonal prisms. A model for amorphous $Ni_{80}B_{20}$ was constructed by hand with several domains based on this structure and with the twinning planes of each domain in a different direction. The relative twinning plane directions of the domains were chosen so that the common boundary involved only limited strain with boundary atoms conforming to the constraints imposed by at least one set of twinning planes. The prisms were connected together either by triangle edge sharing as in F_3C, by the sharing of a single vertex or via a half-octahedrally positioned metal atom. The model was relaxed with a LJ potential and the partial correlation functions $d_{ll'}(r)$ calculated. A comparison was performed with the measured partial correlation functions of $Ni_{81}B_{19}$ (LAMPARTER, SPERL, STEEB and BLÉTRY, 1982) and reasonable agreement was found. The analysis performed by DUBOIS, GASKELL and LeCAËR (1985) is discussed further in section 8.3.2 .

It is only recently that the structure of metal-metal alloys has received much attention. The partial functions have now been measured for several metal-metal alloys, mostly TE-TL alloys, and the degree of chemical ordering has been found to vary to a much greater extent than for T-M alloys. $Cu_{57}Zr_{43}$ (MIZOGUCHI, KUDO, IRISAWA, WATANABE, NIIMURA, MISAWA and SUZUKI, 1978; LAMPARTER, STEEB and GRALLATH, 1983), $Be_{37.5}Ti_{62.5}$ (LEE, ETHERINGTON and WAGNER, 1985) and possibly $Ni_{35}Zr_{65}$ (LEE, ETHERINGTON and WAGNER, 1984; LEE, JOST, WAGNER and TANNER, 1985; MIZOGUCHI, YODA, AKUTSU, YAMADA, NISHIOKA, SUEMASA and WATANABE, 1985) have been shown to be disordered chemically whilst $Ni_{40}Ti_{60}$ (FUKUNAGA, WATANABE and SUZUKI, 1984), $Be_{43}Zr_{57}$ (MARET, SOPER, ETHERINGTON and WAGNER, 1984), $Ni_{63.7}Zr_{36.3}$ (LEFEBVRE, QUIVY, BIGOT, CALVAYRAC and BELLISSENT, 1985) and $Ni_{62}Nb_{38}$ (SVÁB, MÉSZÁROS, KONCZOS, ISHMAEV, ISAKOV, SADIKOV CHERNYSHOV, 1988) have been shown to be at least partially ordered chemically. Thus far there appear to have been virtually no attempts to interpret the SRO of metal-metal alloys beyond a calculation of nearest neighbour distances, coordination numbers and chemical short range order (CSRO) parameters (see section 8.1.3), and a cursory comparison of the values obtained with related crystals. Hopefully now that the partial functions have been measured for a number of metal-metal alloys there will be a greater effort to model their atomic structure.

There have been several structural studies of sputtered TL-rich RE-TL films: CARGILL (1974, 1975) has performed X-ray diffraction on $Gd_{36}Fe_{64}$ and $Gd_{18}Co_{82}$, RHYNE, PICKART and ALPERIN (1974) have performed neutron diffraction on $TbFe_2$ and FELDMAN, CARTER, SKELTON and FORESTER (1978) have performed X-ray diffraction on $SmFe_2$. The structures of these alloys appear to be essentially the same with a RDF whose first maximum consists of three distinct contributions. These may be interpreted in terms of nearest neighbour contacts between each of the three possible pairs of atoms and the positions of the peaks are in good agreement with the Goldschmidt radii. The identification of the nearest neighbour peaks appears to be confirmed by the calculations of O'LEARY (1975) who has obtained approximate partial correlation functions for $TbFe_2$ by combining the nuclear and magnetic neutron diffraction data for $TbFe_2$ and the X-ray diffraction data for $GdFe_2$ (ignoring the peak function differences between these three different types of diffraction). There is thus no evidence for strong chemical ordering in TL-rich RE-TL alloys. CARGILL (1974, 1975), O'LEARY (1975) and FELDMAN, CARTER, SKELTON and FORESTER (1978) have compared their experimental nearest neighbour distances and coordination numbers with those for the related cubic Laves phase $RE\text{-}TL_2$ crystal. The nearest neighbour distances were found to be roughly similar whilst the coordination numbers were found to differ significantly. CARGILL and KIRKPATRICK (1976) and CARGILL (1981) have compared the diffraction data for Gd_xCo_{1-x} alloys with computer generated sphere packing models. These were generated for two sizes of sphere with a requirement for tetrahedral configurations. The relaxed models show qualitative agreement with the experimental data in both real-space and reciprocal-space. However the model densities are unrealistically low.

There has been only one structural study of RE-rich RE-TL alloys reported in the literature. MARET, CHIEUX, HICTER, ATZMON and JOHNSON (1985, 1987) have measured both the Faber-Ziman and Bhatia-Thornton partial functions (see section 7.3.8) for $Y_{67}Ni_{33}$ and $Y_{67}Cu_{33}$. (Strictly yttrium is not a RE but its chemical properties are very similar to those of RE elements.) For the Ni alloy three neutron diffraction experiments making use of the isotopic substitution method were performed and partial functions of high accuracy were obtained. In the case of the Cu alloy two isotopic substitution neutron diffraction experiments and one X-ray diffraction experiment were performed and the partial functions obtained were much less accurate. The CSRO parameter shows a strong chemical ordering in $Y_{67}Ni_{33}$ and a tendency towards random mixing of both constituents in $Y_{67}Cu_{33}$. The interpretation of the data for these two alloys is discussed in more detail in Chapter 11 together with the interpretation of the present work on Dy_7Ni_3.

6.2 MAGNETIC ORDER IN AMORPHOUS RE-TL ALLOYS.

6.2.1 THE OBSERVATION OF MAGNETIC SRO IN AMORPHOUS RE-TL ALLOYS.

The study of magnetic SRO in amorphous solids by neutron diffraction is a much less well developed subject than either the study of atomic SRO in amorphous solids by diffraction or the study of magnetic order in crystals by neutron diffraction. The early measurements of magnetic SRO in amorphous solids by neutron diffraction have been reviewed by WRIGHT (1980). Virtually all workers in this field have ignored the $\gamma^a(r)$ magnetic anisotropy term in the cross-section and have Fourier transformed the experimental data according to equation (4.2.24) to obtain a real-space correlation function. The only exceptions to this are NÄGELE, KNORR, PRANDL, CONVERT and BUEVOZ (1978) and RAINFORD, CORNELIUS, KILCOYNE and MOHAMMED (1988) who have analysed magnetic neutron diffraction data from amorphous solids by least squares fitting of equation (4.2.21) with the magnetic ions divided into shells as for a crystalline powder (BLECH and AVERBACH, 1964).

There have been very few neutron diffraction studies of magnetic SRO in amorphous rare earth-transition metal alloys. The first such measurement was made by RHYNE, PICKART and ALPERIN (1972; 1973) who isolated the magnetic structure factor for sputtered $TbFe_2$ in the magnetically ordered state by performing a difference between the diffraction pattern measured at high and low temperatures (thus ignoring the change with temperature of the nuclear scattering - see section 4.1.4). The magnetic structure factor was Fourier transformed according to equation (4.2.24) and it was shown that the resultant real-space correlation function could be understood qualitatively in terms of a ferrimagnetic ordering similar to that in crystalline $TbFe_2$. RAINFORD, CORNELIUS, KILCOYNE and MOHAMMED (1988) have used the same temperature-difference technique to isolate the magnetic structure factor in the region of the first peak ($\sim Q_1$) for several melt-spun amorphous alloys. A least squares method was used to fit equation (4.2.21) to the difference patterns, again ignoring the change in the nuclear scattering given by the Debye-Waller factor (and also thermal expansion). For Tb_2Fe evidence was found for long range ferromagnetic correlations. (Note that the Tb-Fe system contains two magnetic species and so it might be expected to exhibit a more complicated magnetic order than the Dy-Ni system which contains only one magnetic species - see section 6.2.2 .) For $(Tb_{0.6}Y_{0.4})_2Ni$ and $(Tb_{0.6}Y_{0.4})_2Cu$ the correlations were found to extend only to nearest neighbours and to be markedly anisotropic. BOUCHER, CHIEUX, CONVERT, TOURBOT and TOURNARIE (1985, 1986) have isolated the magnetic structure factor in the region of Q_1 for sputtered $TbCu_{3.54}$ at a number of temperatures also by using the temperature-difference technique (and ignoring the change with temperature of the nuclear scattering). The magnetic structure factors obtained are very similar to that obtained by RAINFORD, CORNELIUS, KILCOYNE and MOHAMMED (1988) for $(Tb_{0.6}Y_{0.4})_2Ni$. The anisotropy term $\gamma^a(r)$ (equation (4.2.23)) was ignored and the data were Fourier transformed to yield a real-space magnetic correlation function which was related to the nuclear Tb-Tb partial correlation function. However, the interpretation of the results is not clear because of the nuclear heterogeneity of the sample and also the complicated heterogeneous magnetic structure which was postulated ('seedy' magnetic order). (Note that the Dy-Cu system has a single magnetic species as with the Dy-Ni system.) BOUCHER, LIÉNARD, REBOUILLAT and SCHWEIZER (1979a) have performed a study of the magnetic correlations in sputtered $ErCo_2$. Polarised neutrons and polarisation analysis were used to isolate the coherent magnetic scattering, thus avoiding any potential problem due to the change in the nuclear scattering with temperature. However, the drawback of this technique is that the statistical accuracy of the final data is extremely poor. The data was interpreted in terms of a sperimagnetic structure (see section 6.2.2) in which the cobalt moments are parallel whilst the erbium moments are opposed to the cobalt moments but strongly connected to their local easy magnetisation axes. Evidence was found for a correlation between the local easy magnetisation axes; depending on the direction of the anisotropy axes relative to the cobalt moments the ordering between erbium first neighbour moments may be ferromagnetic, antiferromagnetic or at random.

6.2.2 RANDOM ANISOTROPY MAGNETISM.

The only previous study of any type of amorphous $Dy_{1-x}Ni_x$ with the composition variable x in the region of 0.3 is that of BUSCHOW (1980) in which the magnetic properties of several amorphous $RE_{69}Ni_{31}$ (x=0.31) alloys were studied. Following the work of LIÉNARD and REBOUILLAT (1978) which shows that Ni ions in $Y_{1-x}Ni_x$ lose their moments below x=0.83, the magnetic properties of these alloys can be regarded as resulting almost exclusively from the magnetic moments on the RE ions. The temperature dependence of the magnetisation in these alloys was interpreted by BUSCHOW (1980) as being typical of that observed in ferromagnetic materials. The inverse susceptibilty showed a linear temperature dependence at temperatures in excess of the ordering temperature, yielding an asymptotic Curie temperature θ_p=35K for $Dy_{69}Ni_{31}$, with $Gd_{69}Ni_{31}$ showing the highest asymptotic temperature. It was found that at 4.2K saturation of the magnetisation was reached for $Gd_{69}Ni_{31}$ at a field of about 10kOe, whilst for the other alloys saturation was not reached at 4.2K in the maximum field available. The moment M measured at 4.2K in a field of 18kOe was analysed on the assumption of a collinear arrangement of rare earth ion moments. It was found that for $Gd_{69}Ni_{31}$ the moment per RE corresponded to the free ion value, but for the other alloys the moment per RE was far below the free ion value. The uniqueness of the behaviour of the Gd alloy provides the key to determining the type of magnetism operating in these alloys since of the REs only Gd is an S-state ion : An S-state ion does not experience anisotropy due to the crystal field of the neighbouring ions whereas all ions with non-zero orbital angular momentum do experience such anisotropy. Thus the appropriate model for discussing magnetic ordering in Dy_7Ni_3 is that of random anisotropy magnetism (RAM).

The RAM model was introduced (HARRIS, PLISCHKE and ZUCKERMANN, 1973) to describe the magnetic order behaviour of amorphous alloys containing RE ions with non-zero orbital angular momentum. This model is defined by a Hamiltonian which may be generalised to;

$$H = - \sum_{ij} J_{ij} \underline{S}_i . \underline{S}_j - \sum_i D_i (\underline{n}_i . \underline{S}_i)^2 \tag{6.2.1}$$

where $\underline{S}_i$ is the total angular momentum at site i. The first term represents exchange interactions and the exchange interaction parameter J_{ij} may vary from site to site due to fluctuations in exchange interactions as described by the RKKY interaction (RUDERMAN and KITTEL, 1954). The second term represents disorder in the single-ion anisotropy axes: $\underline{n}_i$ is a unit vector in the random easy-axis direction for site i and D_i is the strength of the anisotropy interaction for the i^{th} site.

The magnetic structures which can occur in systems described by the so-called HPZ (HARRIS, PLISCHKE and ZUCKERMANN, 1973) Hamiltonian (6.2.1) are still the subject of much discussion. There have been several theoretical studies (AHARONY, 1975; HARRIS, 1980; PELCOVITS, PYTTE and RUDNICK, 1978, 1982) indicating that ferromagnetism (ie. magnetic LRO) is impossible for a RAM system in less than four dimensions. CHUDNOVSKY and SEROTA (1982; 1983) have given a theory for the RAM problem in both the small and large (D_0/J_0) limits (D_0 and J_0 being the mean values of D_i and of J_{ij} for nearest neighbours). The magnetic structure is found to depend on the parameter Λ_r;

$$\Lambda_r = (D_0/J_0)\ (R_c/a)^2 \qquad (6.2.2)$$

where a is the atomic spacing and R_c is the spatial correlation of easy-axes (in the region of 3a to 5a for amorphous solids). In particular CHUDNOVSKY and SEROTA (1982; 1983) show that in 3D the spin correlation length is given by;

$$\xi \simeq \Lambda_r^{-2}\ R_c \qquad (6.2.3)$$

(see also IMRY and MA, 1975 and ALBEN, BECKER and CHI, 1978). Thus the magnitude of the local anisotropy to exchange ratio (D_0/J_0) governs the magnetic order occurring in a particular RAM system. In such a system the magnetisation can wander in direction to gain from local variations in the easy-axis direction and if (D_0/J_0) is large the bulk properties have much in common with spin glasses (SG). COEY and READMAN (1973) have introduced the term 'speromagnet' (SM) to denote SG-like magnetic structures that result from single-ion anisotropy to distinguish them from SGs which occur due to competing exchange interactions. In the case of very small (D_0/J_0)

the magnetic properties may be difficult to distinguish from a multi-domain ferromagnet. Figure 6.3 shows a phase-diagram given recently by SELLMYER and NAFIS (1985) for RAM systems. CHUDNOVSKY and SEROTA (1982; 1983) have predicted a new type of magnetic structure, the correlated speromagnet (CSM, the nomenclature suggested by SELLMYER and NAFIS (1985) is followed here) which may occur for smaller (D_0/J_0). A CSM exhibits a smooth rotation of the magnetisation over a ferromagnetic correlation length and has a net magnetisation of zero. The CSM is different from a multi-domain ferromagnet in that the rotation of the magnetisation is smooth with no sharp domain walls. The term 'asperomagnet' has been introduced (REBOUILLAT, LIÉNARD, COEY, ARRESE-BOGGIANO and CHAPPERT, 1977) to denote a magnetic structure in which the moments are locked in various orientations but with some orientations more likely than others. (In a speromagnet all orientations are equally likely.) An asperomagnet has a spontaneous magnetisation and can be thought of as a random ferromagnet. Also the term 'sperimagnet' has been introduced (COEY, CHAPPERT and WANG, 1976) to denote a system with two magnetic species in which the moments of at least one of the magnetic species are locked into random orientations.

Small angle neutron scattering (SANS) may be used as a method of studying magnetic order, providing information which is complementary to that obtained by conventional 'wide-angle' neutron diffraction (see section 6.2.1). Conventional neutron diffraction yields information about magnetic correlations over distances of the order of the nearest neighbour distance (~1-10Å) whereas SANS gives information about magnetic correlations extending over larger distances (~10-1000Å). The first amorphous RE-TL alloys to be studied by SANS were $TbFe_2$ and YFe_2 (PICKART, RHYNE and

ALPERIN, 1974). For $TbFe_2$ an intense, strongly temperature-dependent small angle component was observed, accompanied by a 'weak divergence' near the magnetisation-determined critical temperature T_c. Above T_c the lineshape was found to be closely Lorentzian;

$$I(Q) = \frac{A}{Q^2 + \kappa^2} \tag{6.2.4}$$

where κ $(\equiv\xi^{-1})$ is the inverse correlation length and A is a constant. Fits to the data yielded a correlation length which did not appear to diverge at T_c (as would be the case for a ferromagnet) but reached a maximum of about 70Å. The lineshape for $TbFe_2$ below T_c was not well understood, although an analysis in terms of an adaptation of Porod's law (equation (4.3.8)) assuming $I(Q)\propto Q^{-2.4}$ suggested that fluctuations are frozen in at T_c with the correlation length remaining constant below T_c. In the case of YFe_2 the lineshape was found to be Lorentzian at all temperatures. The correlation length obtained by fitting the data did not exceed about 11Å at any temperature and later work (FORESTER, KOON, SCHELLENG and RHYNE, 1979) suggests that YFe_2 behaves as a concentrated SG.

Subsequent SANS studies of amorphous RE-TL alloys have nearly all been performed with $RE\text{-}Fe_2$ alloys and other related alloys. $HoFe_2$ (PICKART, RHYNE and ALPERIN, 1975), $Tb_{1.8}Fe_{98.2}$ (PICKART, ALPERIN and RHYNE, 1977) and $NdFe_2$ (ALPERIN, PICKART and RHYNE, 1978) have all been found to exhibit anomalous SANS behaviour below T_c similar to that observed in $TbFe_2$. PICKART (1977) has analysed the results of a second SANS experiment on $TbFe_2$ at very low Q using Guinier's law (equation (4.3.6)). A radius of gyration for the magnetic clusters of order 800Å was derived - a result which is at variance with the other work on $TbFe_2$. $GdFe_2$ (PICKART, RHYNE and ALPERIN, 1975) has been found to have a broad hump in the SANS at temperatures in the region of T_c with no anomalous low temperature component. Gd is an S-state ion which is not expected to experience anisotropy due to the crystal field and $GdFe_2$ appears to be a conventional ferrimagnet for which the ideas of RAM are not relevant. RHYNE, PICKART and ALPERIN (1978) have also studied SANS from $TmFe_2$ which they interpret as being similar to YFe_2, although there are some differences between the spectra of the two alloys. A SANS study of $ErCo_2$ (BOUCHER, LIÉNARD, REBOUILLAT and SCHWEIZER, 1979b) found evidence for two different regimes in the SANS lineshape with a Q^{-2} law at low Q and a Q^{-3} law at higher Q. This was interpreted in terms of the model for the magnetic structure of $ErCo_2$ (BOUCHER, LIÉNARD, REBOUILLAT and SCHWEIZER, 1979a) discussed in section 6.2.1 .

The understanding of the anomalous low temperature SANS component was advanced in 1984 by RHYNE and GLINKA who showed that the lineshape of $TbFe_2$ below T_c could be represented by the sum of a Lorentzian and a Lorentzian squared (LL^2);

$$I(Q) = \frac{A}{Q^2 + \kappa^2} + \frac{B}{(Q^2 + \kappa^2)^2} \qquad (6.2.5)$$

where A and B are constants. The use of a LL^2 lineshape was stimulated by the general result that the critical scattering from crystalline systems with random fields has a LL^2 lineshape (see for example YOSHIZAWA, COWLEY, SHIRANE, BIRGENAU, GUGGENHEIM and IKEDA, 1982). AHARONY and PYTTE (1983) have discussed the LL^2 scattering curve from a theoretical point of view.

The Lorentzian squared term in (6.2.5) is due to static cluster scattering whilst the Lorentzian term can contain contributions from both residual critical scattering and from finite wavelength spin waves (SPANO and RHYNE, 1985). Subsequently it has been found that the SANS below T_c for $Tb_{75}Fe_{25}$, Tb_2Fe_{98} and $NdFe_2$ can also be represented by a LL^2 lineshape (SPANO and RHYNE, 1985; RHYNE, 1985b). The correlation length ξ obtained from these measurements is very low at high temperatures, rises to a maximum close to T_c and then at low temperatures falls to a constant value in the region 50→100Å. The divergence near T_c becomes stronger as the RE concentration is increased. BARBARA, DIENY, LIÉNARD, REBOUILLAT, BOUCHER and SCHWEIZER (1985) have also attempted to re-analyse the earlier SANS measurements on $ErCo_2$ (BOUCHER, LIÉNARD, REBOUILLAT and SCHWEIZER, 1979b) in terms of a LL^2 lineshape. It appears that the correlation length is of order several hundred Ångstroms, but too large in comparison with the experimental data to be precisely determined. BOUCHER, CHIEUX, CONVERT, TOURBOT and TOURNARIE (1985, 1986) have performed a SANS study of the magnetic order in a heterogeneous sample of amorphous $TbCu_{3.54}$. The magnetic order appears to be determined by the atomic domains in the material and the authors term this 'seedy' magnetic order. There have also been several studies of the field-dependence of the SANS from RE-TL alloys (BOUCHER, LIÉNARD, REBOUILLAT and SCHWEIZER, 1979b; RHYNE and GLINKA, 1984; RHYNE, 1985a, 1985b, 1986). It appears that the field drives the system closer to being a ferromagnet in which the larger spin clusters join to form a near infinite percolating cluster. The smaller residual clusters produce a super-paramagnetic like response (BURKE, CYWINSKI and RAINFORD, 1978) from which may be derived transverse and longitudinal correlation lengths.

Whilst there has been only one previous study of $Dy_{1-x}Ni_x$ with $x\approx0.3$ (BUSCHOW, 1980), there have been several studies of the magnetism occurring for larger values of x. $Dy_{21}Ni_{79}$ (x=0.79) has been studied by Mössbauer spectroscopy and magnetisation measurements (ARRESE-BOGGIANO, CHAPPERT, COEY, LIÉNARD and REBOUILLAT, 1976; REBOUILLAT, LIÉNARD, COEY, ARRESE-BOGGIANO and CHAPPERT, 1977) from which it was concluded that the magnetic structure is asperomagnetic. The Ni moment was found to be very small whilst the Dy moment was found to be close to the free ion value $10.6\mu_B$. The Dy-Dy exchange appears to be positive and very much weaker than the single-ion anisotropy so that the Dy moment directions are strongly correlated with the direction of the crystal field gradient. A value of 47K was obtained for T_c.

There have also been a number of studies (DIENY and BARBARA, 1985, 1986; FILLIPI, DIENY and BARBARA, 1985; BARBARA and DIENY, 1985; BARBARA, COUACH and DIENY, 1987; SOUSA, MOREIRA, AMARAL, AMADO, BRAGA, BARBARA, DIENY and FILIPPI, 1987) of alloys in the series $Dy_zGd_{1-z}Ni$ (approximate Ni concentration) in which the magnetisation, a.c.susceptibility and resistivity have been measured. The anisotropy in $DyNi_{1.32}$ (x=0.57) was found to be large and a value $(D_o/J_o)=0.95\pm0.30$ was determined. A SG transition was observed in the Dy-rich alloys and the spin freezing temperature T_f was found to decrease with increasing Dy concentration. For $DyNi_{1.32}$ T_f was about 13.9K. At low termperatures the real component of susceptibilty was shown to be proportional to $(J_o/D_o)^{3.9\pm0.5}$, strongly suggesting that the critical dimensionality of RAM systems is equal to four.

Finally it remains to suggest that the ideas of RAM may to some extent apply to all amorphous magnets, and not just to RE-TL alloys. For example recent inelastic neutron scattering measurements for $Fe_{83}B_{17}$ (COWLEY, CUSSEN and COWLAM, 1988) indicate that the magnetically ordered state for this alloy is not an ideal collinear ferromagnet, but rather that it involves a distribution of Fe moment directions.

6.3 THE OBJECTIVES OF THIS STUDY.

From the above it is clear that there is a real need to understand the structure of amorphous metals and that there is still a great deal of progress to be made. The purpose of this investigation is to perform a detailed study of one particular amorphous metallic alloy, rather than a cursory study of the structure of a large number of different alloys as has been done by other workers in the past. The alloy Dy_7Ni_3 was chosen for this study because of its particularly advantageous neutron scattering properties, as discussed in section 6.4 . Different neutron techniques yielding information about atomic and magnetic structure at both short and long range have been used so as to characterise this particular alloy as completely as possible.

6.4 THE PARTICULAR ADVANTAGES OF Dy7Ni3 AS A SAMPLE FOR NEUTRON SCATTERING.

6.4.1 SEPARATION OF PARTIAL ATOMIC CORRELATION FUNCTIONS.

As discussed in section 4.1, a neutron diffraction experiment on an amorphous solid yields a measurement of the atomic structure in the form of a correlation function T′(r). T′(r) is the convolution of the true correlation function T(r) with the peak function P(r) defined by the Q_{max} of the experiment (see section 4.1.3). As shown by equation (4.1.26), T′(r) is a weighted sum of m(m+1)/2 independent partial correlation functions, where m is the number of elements in the solid;

$$T'(r) = \sum_{ll'} c_l \, \bar{b}_l \bar{b}_{l'} \, t'_{ll'}(r) \tag{6.4.1}$$

where the summations l and l′ are both over the elements in the sample. For the binary alloy Dy_7Ni_3 equation (6.4.1) becomes;

$$T'(r) = 0.7 \, \bar{b}^2_{Dy} t'_{DyDy}(r) + 0.3 \, \bar{b}^2_{Ni} t'_{NiNi}(r) + 1.4 \, \bar{b}_{Dy} \bar{b}_{Ni} t'_{DyNi}(r) \tag{6.4.2}$$

where equation (4.1.13) has been used to relate the two (non-independent) unlike-atom partial correlation functions;

$$t'_{NiDy}(r) = \left(\frac{0.7}{0.3}\right) t'_{DyNi}(r) \tag{6.4.3}$$

Clearly a measurement of the partial correlation functions will provide more information on the atomic structure than will a single measurement of T′(r). Now the coherent neutron scattering length of an element $\bar{b}$ can be altered by changing the isotopic composition, and this makes it possible to determine the partial correlation functions by measuring T′(r) several times with different values of $\bar{b}$ and solving the resultant simultaneous equations. (It is assumed that the effect of the change in isotopic composition on the atomic structure is negligible. This is a reasonable assumption since the atomic structure is determined by the electronic properties of the atoms.) In the case of a binary alloy there are three partial correlation functions, and T′(r) must be measured for three different isotopic compositions to determine them. This technique, known as the isotopic substitution method, was first employed by ENDERBY, NORTH and EGELSTAFF (1966) to obtain the three partial structure factors for liquid Cu_6Sn_5. Subsequently it has been used by various authors to study a wide range of amorphous samples. However, the differences in scattering length are often small, and the scattering lengths themselves are not known very accurately. Also, the solution of equation (6.4.1) to obtain the partial correlation functions involves combinations of differences such that errors can rapidly build up. Thus there are frequently large uncertainties in published determinations of partial structure factors. Clearly it would be much better if the individual partial correlation functions could be obtained by direct measurement, without the need to resort to combinations of differences. This can be achieved for samples containing certain elements by use of the double null isotopic substitution technique (WRIGHT, HANNON, SINCLAIR, JOHNSON and ATZMON, 1984).

Whilst most elements have only isotopes with positive neutron scattering lengths, there are a few (H,Li,Ti,Cr,Ni,Cd,Sm,Dy and W) which have at least one stable isotope with a negative scattering length and at least one stable isotope with a positive scattering length. Thus it is possible to set $\bar{b}$ to zero for one of these elements by use of a suitable isotopic composition. When this is done for one element of a binary system, equation (6.4.1) shows that a diffraction experiment yields a direct measurement of the like-atom partial correlation function for the other element. This technique, known as the null technique, has previously been used to study a number of amorphous systems.

The double null technique involves the study of a binary system for which both elements can have $\bar{b}$ set to zero. Both like-atom partial correlation functions can be obtained by direct measurement, and the unlike-atom partial correlation function can be obtained by subtracting the other two from the correlation function obtained for a sample containing the natural elements.

For this investigation of Dy_7Ni_3 four samples were made :

$^{N}Dy_7{}^{N}Ni_3$, $^{N}Dy_7{}^{0}Ni_3$, $^{0}Dy_7{}^{N}Ni_3$ and $^{0}Dy_7{}^{0}Ni_3$,

where the superscript N denotes the natural isotopic composition, and the superscript 0 denotes an isotopic composition resulting in a coherent nuclear scattering length ($\bar{b}$) of zero. The diffraction experiments performed on these samples to investigate atomic structure are described in chapter 7.

As discussed above there are frequently large uncertainties in published determinations of partial functions. This may be understood by considering the matrix equation which must be inverted to determine the partial functions for a binary alloy;

$$\begin{pmatrix} {}^{1}T'(r) \\ {}^{2}T'(r) \\ {}^{3}T'(r) \end{pmatrix} = \underline{\underline{A}} \begin{pmatrix} t'_{11}(r) \\ t'_{22}(r) \\ t'_{12}(r) \end{pmatrix} \qquad (6.4.4)$$

where $^{n}T'(r)$ is the correlation function measured in the n^{th} diffraction experiment and $\underline{\underline{A}}$ is a 3x3 matrix whose components may be calculated from equation (4.1.26). To determine the partial correlation functions the matrix $\underline{\underline{A}}$ must be inverted. If the differences in scattering length between experiments are small then, no matter how accurately the scattering lengths are known, the equations (6.4.4) will be ill-conditioned. In this case the fractional errors in the partial functions will be much greater than the fractional errors in the data for one of the experiments n. However, for the diffraction experiments on Dy_7Ni_3 these problems were almost completely avoided since both of the like-atom partial functions were determined directly without the need for matrix inversion. Hence there was no increase in fractional error for the like-atom functions and only the unlike-atom functions have a greater fractional error than in the initial measurements. LIVESEY and GASKELL (1982) have proposed that TURING's number (1948) T should be used as a figure of merit for isotopic substitution experiments. T gives an upper limit on the factor by which the fractional error in the partial functions exceeds the fractional error in the measurements and LIVESEY and GASKELL (1982) have shown that it is given approximately by;

$$T \simeq |A|_E \, |A^{-1}|_E \qquad (6.4.5)$$

where the Euclidean norm;

$$|A|_E = \Big(\sum_{ij} A_{ij}{}^2 \Big)^{1/2} \qquad (6.4.6)$$

MARET (1986) has computed the value of T for a number of isotopic substitution experiments and a value of 5.9 was obtained for the present experiment. The average of the values reported by MARET (1986) is 79.0 and the value for the present experiment is the second lowest. Thus the experiment on Dy_7Ni_3 is one of the most well-conditioned isotopic substitution experiments. (Note that the precise value of T depends on the exact definition of the partial functions and MARET (1986) has used a different definition to that in this thesis.) However, the value of T is not important for the measurement of the like-atom partial functions of Dy_7Ni_3 since these are measured directly, and it is only relevant for the measurement of the unlike-atom partial functions.

6.4.2 SEPARATION OF MAGNETIC SCATTERING.

The fourth sample $^0Dy_7{}^0Ni_3$, which has no coherent nuclear scattering at all, was used because Dy_7Ni_3 is a magnetic material and there is a magnetic contribution to the neutron scattering as well as the nuclear contribution. With this sample it was possible to measure the magnetic component of the total scattering without the usual interference from the coherent nuclear scattering. This is useful for comparison with theoretical calculations of the magnetic form factor (see section 11.2). A good measurement of the magnetic scattering is also important for the investigation of atomic structure since the magnetic scattering must be subtracted from the diffraction data before the correlation functions can be extracted. The $^0Dy_7{}^0Ni_3$ sample was also used to study the magnetic ordering occurring at low temperatures in Dy_7Ni_3. This sample is ideally suited for such measurements since the usual problem of temperature changes in the nuclear scattering making it difficult to separate the magnetic scattering from the nuclear scattering is avoided due to the lack of coherent nuclear scattering (see section 9.2 for further discussion of this point). These experiments are described in chapter 9. The $^0Dy_7{}^0Ni_3$ and $^NDy_7{}^NNi_3$ samples have also been used in a small angle neutron scattering (SANS) study of long range magnetic correlations at low temperatures and structural inhomogeneities in Dy_7Ni_3. As with the conventional neutron diffraction experiments the almost unique neutron scattering properties of these

		(a)	(b)	(c)	(c)	(c)
Nominal Isotope	Isotope	Atomic Percent	Mass Excess $/10^{-3}$amu	Coherent Scattering Length $/10^{-12}$cm	Scattering Cross-Section /barns	Absorption Cross-Section (1Å)/barns
^{60}Ni	^{58}Ni	0.81	-64.664	14.4	26.1	2.558
	^{60}Ni	99.08	-69.220	2.8	0.99	1.613
	^{61}Ni	0.05	-68.950	7.6	9.3	1.390
	^{62}Ni	0.07	-71.660	-8.7	9.5	8.064
			-77.5	0.289	1.204	1.625
^{62}Ni	^{58}Ni	0.38	-64.664	14.4	26.1	2.558
	^{60}Ni	0.52	-69.220	2.8	0.99	1.613
	^{61}Ni	0.13	-68.950	7.6	9.3	1.390
	^{62}Ni	98.70	-71.660	-8.7	9.5	8.064
	^{64}Ni	0.27	-72.04	-0.38	0.018	0.845
			-93.1	-0.851	9.493	7.981
^{162}Dy	^{160}Dy	0.11	-74.77	6.7	5.6	31.142
	^{161}Dy	3.10	-73.03	10.3	16.6	316.984
	^{162}Dy	92.39	-73.16	-1.4	0.25	107.886
	^{163}Dy	3.33	-71.23	5.0	3.3	72.295
	^{164}Dy	1.07	-70.80	49.4	307	1473.699
			-51.6	-0.0272	4.147	128.119

Table 6.1

NB Isotopes not shown were present in insignificant concentrations.

Sources of Numerical Data.

(a) ORNL Isotopic Analysis

(b) GOLDMAN, 1972.

(c) SEARS, 1986.

samples are advantageous in discriminating between nuclear and magnetic scattering.

6.5 SAMPLE PREPARATION.

Zero coherent nuclear scattering length dysprosium (^{0}Dy) and nickel (^{0}Ni) were obtained in the form of the metal from Oak Ridge National Laboratory (ORNL), USA. The ^{0}Dy was manufactured by mixing 0.0755g of natural dysprosium (^{N}Dy) with 4.6945g of nominal ^{162}Dy, and the ^{0}Ni was manufactured by mixing 0.569g of nominal ^{60}Ni with 0.201g of nominal ^{62}Ni. The complete isotopic analysis of the nominal isotopes provided by ORNL is shown in table 6.1, together with the neutron scattering properties of the individual isotopes. Table 6.2 shows the figures used in the calculation of the neutron scattering properties of the elements used in the samples;

Element	Nominal Isotope	Weight /g	Atomic Weight /amu	Coherent Scattering Length $/10^{-12}$cm	Scattering Cross-Section /barns	Absorption Cross-Section (1Å)/barns
^{N}Ni	-	-	58.71	1.03	18.5	2.497
^{N}Dy	-	-	162.50	1.69	90.4	517.185
^{0}Ni	^{60}Ni	0.569	59.9225	0.289	1.204	1.625
	^{62}Ni	0.201	61.9069	-0.851	9.493	7.981
		0.770	60.4405	-0.0087	3.368	3.284
^{0}Dy	^{162}Dy	4.6945	161.9484	-0.0272	4.147	128.119
	^{N}Dy	0.0755	162.50	1.69	90.4	517.185
		4.770	161.9571	0.000018	5.513	134.279

Table 6.2

Within the accuracy of a neutron scattering experiment (0.1% at best) the deviations from zero of the calculated coherent nuclear scattering lengths of the ^{0}Dy and ^{0}Ni used in these experiments are not significant.

Only very small quantities (2.5g→3.0g) of each isotopically substituted sample were made owing to the great expense of the isotopically substituted material. The scattering of neutrons from such small samples is low, but this has the advantage that corrections to the data for absorption, self-shielding and multiple scattering are relatively small.

The weights of dysprosium and nickel in each sample were such that x in $Dy_{1-x}Ni_x$ was almost exactly 0.3 . In fact the precise value of x varied between 0.30068 and 0.30080. The value x=0.3 was chosen because the phase diagram of the Dy-Ni system (figure 6.4) has a deep eutectic at about this composition, and it is generally found that the glass-forming region for an amorphous metallic alloy is ced around a deep eutectic (see section 2.4). The precise value of x for this deep eutectic of the Dy-Ni system is x=0.31 (ZHENG and WANG,1982).

The samples were manufactured at Caltech, USA by M.Atzmon and W.L.Johnson, using a melt-spinner. All the samples were manufactured in as identical a manner as possible, so as to minimise differences in structure due to variations in preparation conditions. Prior to spinning the samples were melted several times in a levitation furnace to ensure homogeneity. Each isotopically substituted sample was spun in two batches. The ribbons were spun into an inert gas atmosphere so as to avoid oxidation. This gives a faster quench rate than spinning into vacuum. After manufacture the samples were sealed in glass ampoules with helium, and subsequent to the first neutron scattering experiments they were kept in an evacuated desiccator. This was to keep contact with air to a minimum to avoid any possibility of the surface of the samples becoming oxidised.

A dial thickness measuring gauge was used to measure the thickness of the ribbons. The thickness was found to be of order 20μm, but there was quite a large variation (~±6μm). This value agrees with that obtained from measuring the transmission of neutrons on the D17 instrument at ILL (see Chapter 10). The average width of the ribbons ${}^{0}Dy_7{}^{0}Ni_3$ was 1.5mm. The average width of all the other ribbons was 0.9mm. The density of the ribbons was determined to be $8.59gcm^{-3}\pm1.5\%$ ($8.59gcm^{-3} \equiv 0.03938$ atoms $Å^{-3}$) by Archimedes' method using toluene (ATZMON, 1986).

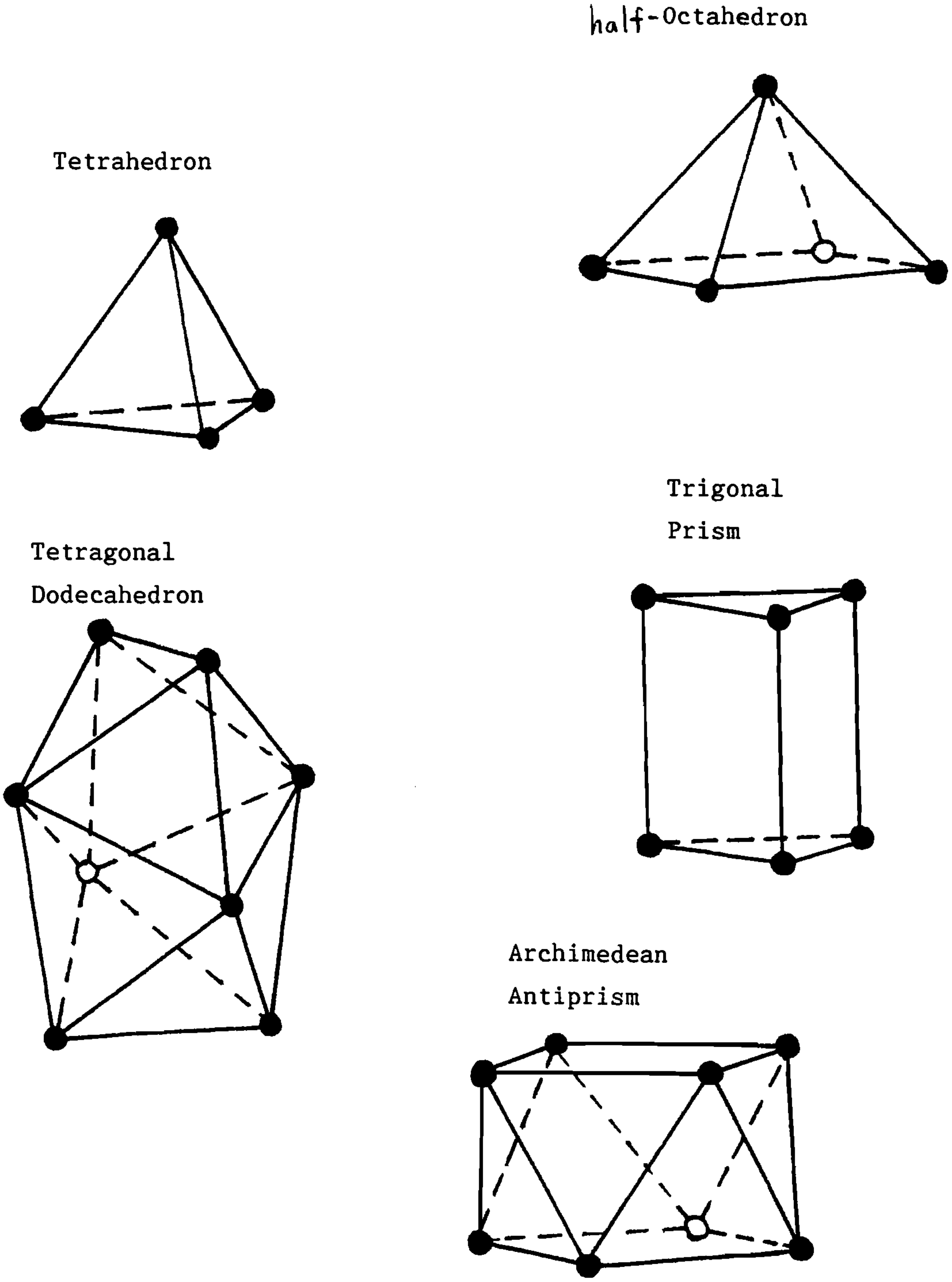

Figure 6.1 The Five Canonical (Bernal) Holes in a RCP of Hard Spheres.

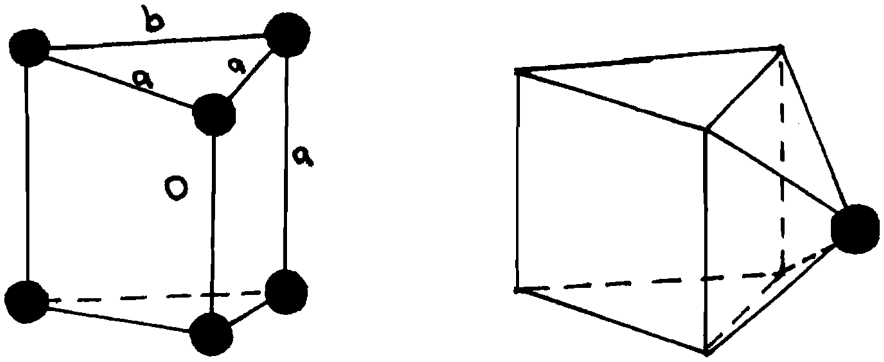

A MT_6 Trigonal Prism.

A Half-octahedrally Positioned Atom.

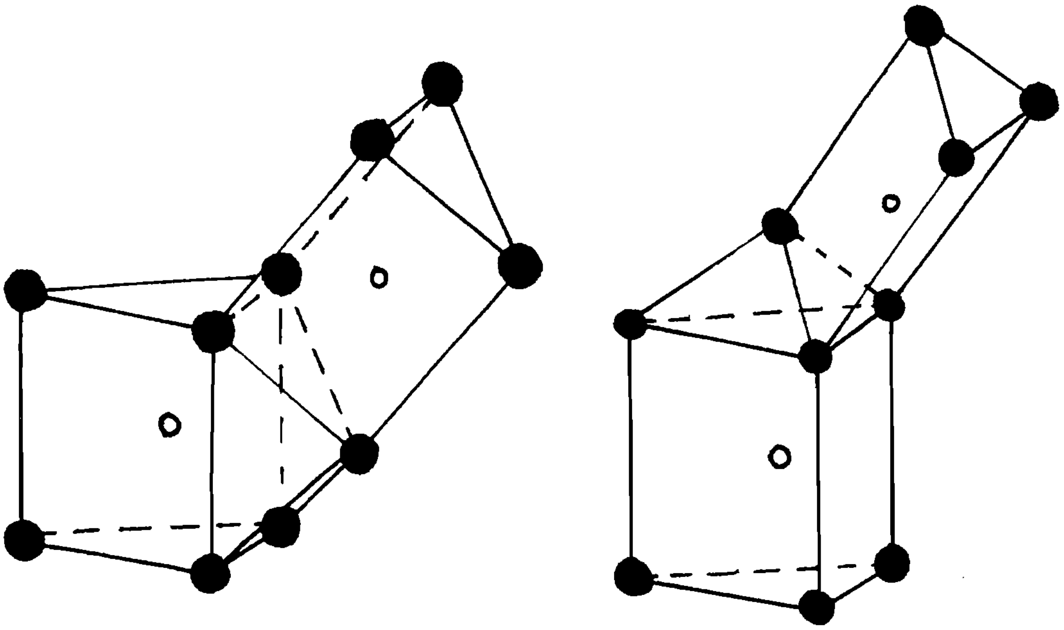

The Fe_3C Triangle Edge Sharing Arrangement.

The Fe_3P Triangle Edge Sharing Arrangement.

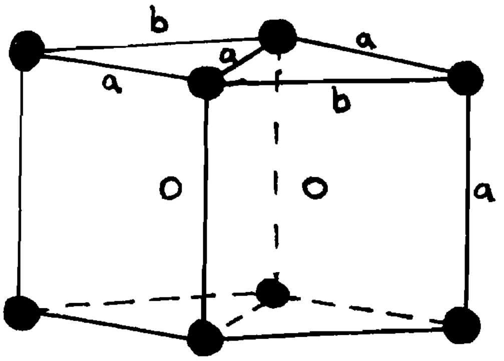

The Dy_3Ni_2 Square Face Sharing Arrangement.

Figure 6.2 Trigonal Prismatic Atomic Configurations.

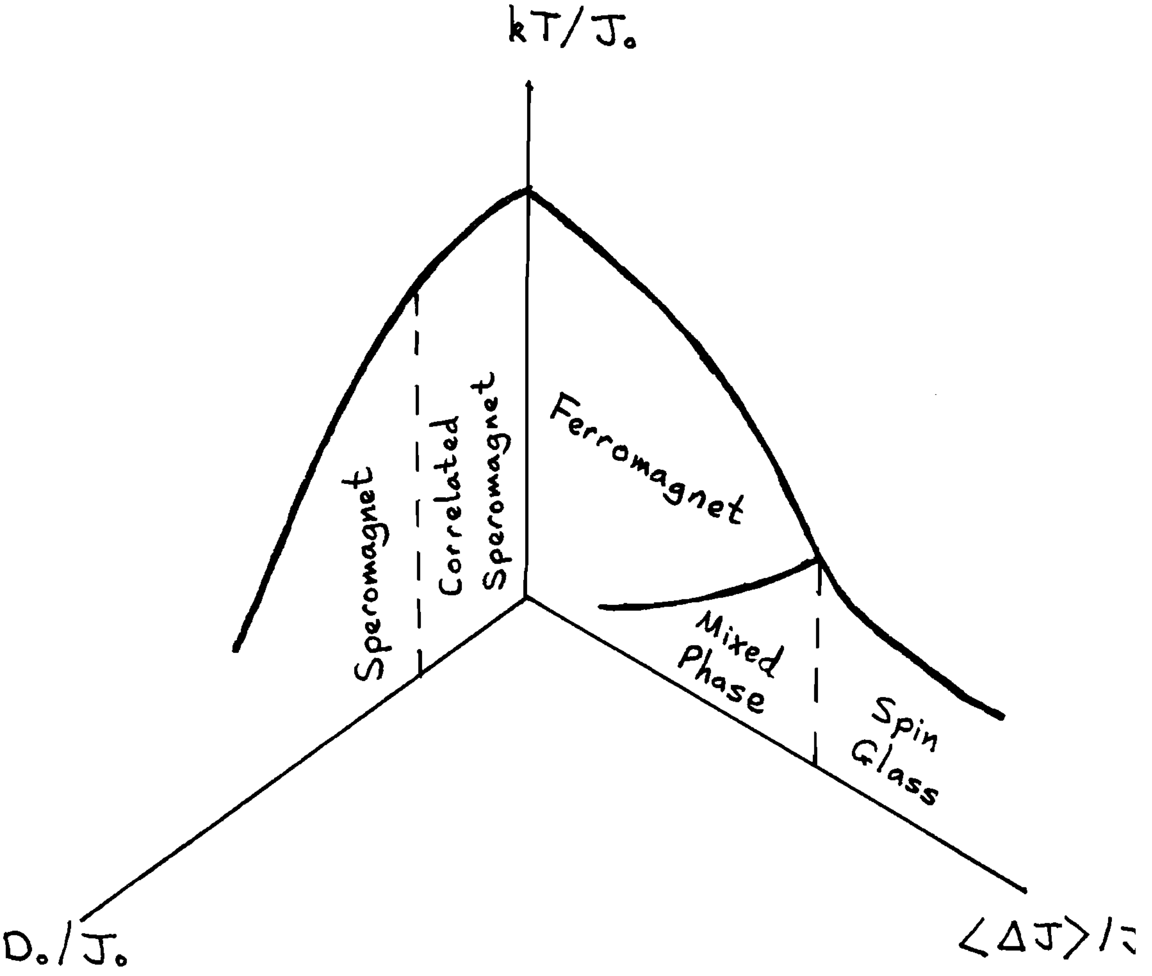

Figure 6.3 A Phase Diagram for RAM Systems {after SELLMYER and NAFIS (1985)}.

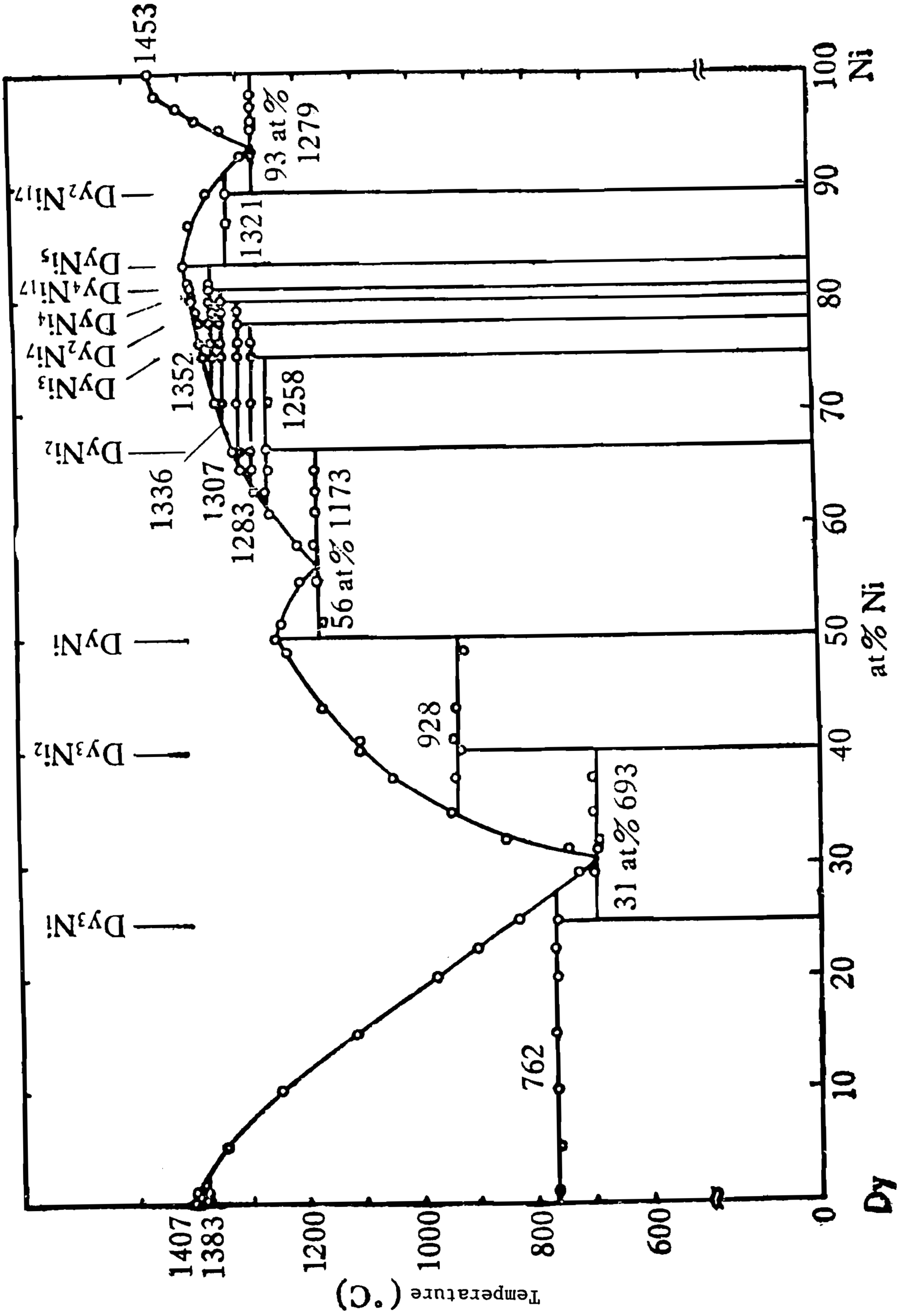

Figure 6.4 The Phase Diagram of the Dy-Ni System (ZHENG and WANG, 1982).

CHAPTER 7

DIFFRACTION STUDIES OF THE ATOMIC STRUCTURE OF Dy7Ni3.

7.1 NEUTRON DIFFRACTOMETERS.

The atomic structure of Dy_7Ni_3 was studied using the neutron diffractometers D4 and D2 at the Institut Laue Langevin (ILL) Grenoble. The main reason for the use of two spectrometers was one of scheduling of experiments, the D2 experiment being performed first.

7.1.1 THE TWIN-AXIS LIQUIDS DIFFRACTOMETER D4.

The twin-axis neutron diffractometer D4 (I.L.L., 1983), illustrated in figure 7.1 , is designed for structural investigations of disordered materials. It provides a very wide range of momentum transfer ($0.2<Q<22Å^{-1}$ with $\lambda=0.5Å$) so as to give high real space resolution, and has a high flux at the sample position so that a high count rate and hence high statistical accuracy is obtained.

The incident neutrons for D4 are obtained from the H8 beam hole on the reactor at ILL. This beam hole views the hot source ($10dm^3$ of graphite at 2000K) so that a high flux at low wavelengths is obtained. Thus a low wavelength can be used for the experiment, which results in a high Q_{max} and hence high real space resolution. A silicon filter removes fast neutrons from the incident beam. This is followed by two diaphragms which define the beam before entering the monochromator drum.

The instrument offers a choice of two 20cmX18cm copper monochromating crystals, and these are contained within a lead drum. One is cut to reflect from the [200] planes, and the other is cut to reflect from the [220] planes. The wavelength is continuously variable, but the instrument is only equipped with second order decontamination filters for 0.5Å (obtained from the [200] crystal) and 0.7Å (the [220] crystal), and so in practice one of these two wavelengths is generally used. These filters are placed at the entrance to the sample chamber. Between the monochromator and the $\lambda/2$ filter are a beam monitor and a set of slits. The purpose of the monitor is to take into account fluctuations in beam intensity. The slits are used to further define the beam.

The sample is enclosed in a fixed vacuum vessel. This is a stainless steel drum with a thin aluminium window where the neutron beam enters. At the height of the detectors there is a thin aluminium strip which extends over the angular range covered by the detectors. Inside the sample chamber, above and below the strip, there are boron carbide slats which define the vertical range of the detectors and prevent scattering from the sample chamber. The sample itself is mounted on a height adjustable platform and two boron carbide flags fixed to this platform define the beam height at the sample. At a wavelength of 0.7Å the flux at the sample is about 4×10^{7} neutrons $cm^{-2}s^{-1}$. The maximum beam size at the sample is 7cm by 2cm.

The instrument has two identical 64 wire ^{3}He multidetectors with a gas pressure of 15 bars and a detection area of about 16cm by 7cm. The detectors can be set at any chosen distance from the sample, but they are constructed so as to give 0.1° angular steps between wires with a sample-detector distance of 1.5m. An evacuated beam tube is placed between each detector and the sample tank and the detectors are shielded against external background. The whole instrument is situated on a polished marble floor and the detectors rest on pads through which compressed air is directed to move them.

7.1.2 THE TWIN-AXIS POWDER DIFFRACTOMETER D2.

D2 (I.L.L., 1983) is a high flux twin-axis diffractometer (figure 7.2) situated on the H11 thermal neutron beam tube at the high flux reactor at the ILL. The monochromation arrangement is set up to provide three alternative wavelengths: The [311] reflection from a germanium crystal is used to provide 1.22Å at which wavelength the maximum flux is obtained. A wavelength of 0.9Å can be obtained from a [111] germanium reflection. This wavelength is generally used for amorphous materials as it gives the best real space resolution. The [111] reflection from a copper crystal is used to provide a wavelength of 2.5Å and this wavelength gives the best Q resolution.

A number of different items of ancillary sample environment equipment are available incuding a special cryostat with a vanadium tail and cadmium shielding which can achieve temperatures in the range 1.6K to 300K. The flux at the sample is about 7×10^{7} neutrons $cm^{-2}s^{-1}$ at a wavelength of 1.22Å. The maximum beam size at the sample is 5cm by 1.8cm.

The detector on D2 is a 64 wire multidetector containing ^{3}He at a pressure of 10 bars. The wires are separated by 2.54mm and the detector is

72.5cm from the centre of the sample. Thus the angle between wires is 0.2° and the detector covers an angular range of 12.8°. Scattering can be measured at angles from 2° to 130°. The useful detector height is 8cm.

7.2 EXPERIMENTAL PROCEDURE.

7.2.1 THE PERFORMANCE OF A NEUTRON DIFFRACTION EXPERIMENT ON AN AMORPHOUS MATERIAL USING A REACTOR SOURCE.

As shown in section 4.1.1 the ultimate purpose of a neutron diffraction experiment on an amorphous material is to determine the real space correlation function D(r) or T(r) (these two functions only differ by the average density term $T^{\circ}(r)$). In order to achieve this the distinct diffraction cross-section $i(Q_0)$ is the quantity which must be measured. As shown in section 4.1.3 $i(Q_0)$ must be measured to as high a maximum elastic momentum transfer Q_{max} as possible. This is achieved by using incident neutrons of relatively high energy and making measurements to as high a scattering angle 2θ as possible. The experiment should also be designed to minimise the experimental corrections which must be applied to the data. To minimise the extent of the Placzek inelasticity correction discussed in section 4.1.2 incident neutrons of high energy should be used and measurements should be made at low angles. The absorption correction and the multiple scattering correction can also be minimised by careful design of the geometry of the sample to avoid them becoming excessive.

In order to position the sample the centre of the incident neutron beam must first be located. This is achieved by use of a specially adapted polaroid camera together with a cadmium marker (cadmium has a very high thermal neutron absorption cross-section and hence appears black on the photograph). The incident neutron wavelength λ and also the absolute zero of scattering angle, $2\theta_0$, for the spectrometer are calibrated by use of a polycrystalline sample. A crystal whose lattice spacing is precisely known and which has well separated Bragg peaks at suitable d-spacings should be used. Nickel powder is generally found to be ideal. As well as measuring the scattering from the sample, measurements should also be made without the sample (but with empty sample-can if used). This enables the background contribution to the scattering to be determined so that it can be subtracted from the signal measured with the sample in place. A run should also be performed with a perfect absorber with the same geometry as the sample so that components in the background which are sample-dependent can be taken into account. Cadmium is usually used for this purpose. In order to normalise the data a run should also be performed on a sample which only scatters incoherently. Vanadium is generally used for this purpose since natural vanadium has a coherent scattering cross-section of 0.0184 barns and an incoherent scattering cross-section of 5.187 barns. To a good approximation the scattering from vanadium is totally featureless and so it is an ideal material for normalising the data to remove the effects of detector efficiency and effective solid angle. Also, since the vanadium cross-sections and average atomic kinetic energy are well-known, the scattering from a vanadium sample can be calculated according to equation (4.1.50) and hence the vanadium run can be used to achieve an absolute normalisation of the sample run.

A very low efficiency detector is used in the incident beam as a monitor so that the data may be normalised to the total neutron flux incident on the sample. The time spent counting on a sample should be determined according to the required statistical accuracy, the estimated error on a point of N counts being $N^{1/2}$. The time spent on the background run should be such that the errors on the normalised background and sample runs are equal since this optimises the statistical accuracy of the background-subtracted data.

Once an absolute normalisation of the data has been achieved, corrections should be made for absorption, self-shielding and multiple scattering to yield a corrected diffraction pattern I(Q). The real-space correlation function may then be obtained from I(Q) by following the steps illustrated in figure 7.3 . The theory behind this process is presented in section 4.1 .

In the experiments described in this Chapter a cadmium run was not performed. This is because previous experience with the diffractometers D4 and D2 has shown that a cadmium correction cannot be satisfactorily performed (WRIGHT, 1987). The instruments are situated relatively close to the reactor and this problem is probably due to fast neutrons to which cadmium is almost transparent. However, with the geometry of these instruments the magnitude of the sample-dependent background components can be expected to be very small with the result that the lack of a cadmium correction is not a severe problem. There is also a problem with the vanadium runs on these instruments and this is discussed in section 7.3.1 .

7.2.2 MOUNTING OF SAMPLES.

The ribbons of amorphous Dy_7Ni_3 were cut into pieces of length 10-11cm which were then sanded to remove any small crystallites which might have formed on the surface. Scotch 3M tape was used to bind the ends of the pieces of ribbon to form approximately cylindrical samples of estimated diameter 7mm and the samples were mounted on the spectrometer in a cadmium-shielded aluminium G-clamp. Table 7.1 gives the number of pieces of ribbon in each sample and also the effective density ρ′ calculated on the assumption of a 7mm diameter cylinder;

	$^NDy_7{}^NNi_3$	$^NDy_7{}^0Ni_3$	$^0Dy_7{}^NNi_3$	$^0Dy_7{}^0Ni_3$
Number of Ribbons	90	25	43	38
$\rho'/10^{-3}$ atoms $Å^{-3}$	1.6577	0.79201	0.46047	1.1665

Table 7.1

7.2.3 D4 EXPERIMENT.

Initially D4 was used with a nominal incident neutron wavelength of 0.5Å (Q_{max}~$22Å^{-1}$) and a sample-detector distance of 1.5m . A detector efficiency file was created by running with a large vanadium rod and counting with each wire at the same angle in turn. This file was used to correct the raw data so that the purpose of the later vanadium runs was only to perform an absolute normalisation and to correct for any geometrical variation in effective counting efficiency. Nickel powder was run in a 7mm diameter nickel can to calibrate the instrument. The calibration was performed with the low angle detector only since the angle encoders for the two detectors were set to be consistent with each other. Scans were performed through the [111], [200] and [220] reflections. A quadratic function was fitted to the background for each peak and this fit was subtracted from the data. The peak positions were then taken to be at the centre of gravity of the result, rather than at the centre of a fitted Gaussian since the resolution function of D4 is not symmetrical. The angles of the three peaks together with their widths were used as input to a least squares fitting program to yield the results shown in table 7.2;

Diffractometer	λ/Å	$2\theta_0$
D4	0.49748	-0.12112
	0.70311	-0.08877
D2	0.92438	0.0

Table 7.2

The calibration was based on a lattice parameter for Ni at 20°C of $a_0=3.52387\pm0.00008$Å (JETTE and FOOTE, 1935).

A run to measure the diffraction pattern of a sample was performed as follows: The detectors were placed at the desired angles and neutrons were counted for a preset number of monitor counts. The low angle detector was moved by 1.5° between such scans so that each angle was covered by four or five detector wires whilst the high angle detector was moved by 1.0° between scans so that each angle was covered by up to six or seven wires since some of the wires in this detector did not work. Three extra scans were performed at the angular limits so that a reasonably uniform coverage was achieved. About five runs were performed on each sample, where one run consists of a set of scans covering the whole angular range of the instrument. The angular range covered by each detector is given in table 7.3 together with the detector constant γ (see equation (4.1.55));

	D4 low angle detector	D4 high angle detector	D2
2θ	1.5° → 88.6°	68.1° → 128.3°	3.4° → 124.0°
$\gamma/\text{Å}^{-1}$	21.5384	17.9199	6.276

Table 7.3

Runs were performed on the $^{N}Dy_7{}^{N}Ni_3$ sample and on the background and the data obtained are shown in figure 7.4 . There did not appear to be any structure beyond about 12Å^{-1} and so it was decided to change the neutron wavelength to 0.7Å ($Q_{max}\sim15\text{Å}^{-1}$) to take advantage of the increased incident flux at higher neutron energy. Nickel scans were performed at the new wavelength, yielding the calibration values shown in table 7.2 . Runs were performed on the $^{N}Dy_7{}^{N}Ni_3$, $^{N}Dy_7{}^{0}Ni_3$ and $^{0}Dy_7{}^{N}Ni_3$ samples (figures 7.4 to 7.6) and also on a 0.477cm diameter vanadium rod and on the background. The experimental time allocated was not sufficient to allow a measurement of the diffraction pattern of the $^{0}Dy_7{}^{0}Ni_3$ sample. In retrospect the decision to change wavelength was a mistake because the difference in count rates was not that great, and a neutron wavelength of 0.5Å would have given greater real space resolution. Also the change in wavelength meant that the $^{N}Dy_7{}^{N}Ni_3$ sample had to be run twice and there was not time to run the $^{0}Dy_7{}^{0}Ni_3$ sample which, when run on D2, gave a signal at higher Q than had been expected. The Q-ranges covered in the experiments described above, as calculated from the calibration values in table 7.2, are given in table 7.4;

Diffractometer	λ/Å	Experimental Q-range/Å^{-1}	Q-range Used/Å^{-1}
D4	0.49748	0.36 → 22.70	0.48 → 22.70
	0.70311	0.26 → 16.08	0.48 → 15.60
D2	0.92438	0.48 → 11.90	0.48 → 11.90

Table 7.4

7.2.4 D2 EXPERIMENT.

The experiment on D2 was performed with an incident neutron wavelength of 0.9309Å according to the calibration performed by ILL staff and the detector angle encoder was set so that the values were absolute with regard to the straight-through beam. However, a subsequent comparison with the data obtained from D4 showed a slight inconsistency between the Q-scales of the two instruments which appeared to be due to a small wavelength error. Hence a 0.7% correction was made yielding an incident neutron wavelength of 0.92438Å for D2.

A detector efficency file was created using a vanadium sample in a similar way to that used on D4. Runs were performed on all four Dy_7Ni_3 samples (figures 7.4 to 7.7) as well as a background (empty G-clamp) run and a vanadium run. The runs on D2 were performed in a similar manner to those on D4. Single background runs were performed between samples to check for any variation in the background but none was found. Runs were also performed on the $^0Dy_7{}^0Ni_3$ sample in a cryostat to study the magnetic SRO at low temperatures and these are discussed in Chapter 9.

7.3 DATA ANALYSIS.

7.3.1 DATA REDUCTION AND CORRECTION.

All the runs on a particular sample were added together and normalised to the monitor counts. In the case of one D4 run a slight correction was required due to an intermittently noisy wire. The relevant background data were then subtracted from the data for each sample. For D4 the data from the high angle detector were joined to the data from the low angle detector. This was achieved by multiplying the high angle detector data by a scaling factor given by the average value of the ratio of the data from the two detectors in the overlap region. There is a potential problem with joining the data from the two D4 detectors in that they are filled to different ^{3}He gas pressures and thus have different detector constants (see table 7.3). Hence the form of the self scattering is different for the two detectors (see equation (4.1.50)) and ideally the data for each detector should be analysed separately until the self scattering has been subtracted. However, in the case of Dy_7Ni_3 the atomic masses (m_{Dy}~163amu and m_{Ni}~59amu) are sufficiently high that this problem can be ignored : A calculation showed that the maximum difference in the magnitude of the Placzek correction (equation (4.1.50)) for the two detectors is less than 0.1%. Hence the error involved in joining the data from the two detectors before subtraction of the self scattering is not significant.

The vanadium data from both instruments were found to slope downwards from low angle to high angle by about 9% whereas equation (4.1.50) predicts a slope of about 5% using the quoted detector efficiencies. One possible explanation for an excessively high vanadium slope is that the vanadium rod could be impure with a small hydrogen content. The high incoherent cross-section and light mass of hydrogen would then have the effect of adding a significant and highly sloping contribution to the self scattering. However, the same vanadium rod as used in this experiment has been run satisfactorily on many other instruments (WRIGHT, 1987) and hence the anomalous vanadium slope on D2 and D4 must be attributed to the instruments. A slope of 9% cannot be explained by an error in detector efficiency since even an infinite detector constant γ does not result in such a large slope. In fact the cause of the anomalously high vanadium slope on these instruments is not known at present. It would seem that there may be a variation with 2θ of the solid angle subtended at the sample by the detector. However, as is discussed below the effect appears to be sample-dependent, and so the correct explanation is probably more complicated and involves some undesirable component of the scattered beam such as multiply scattered neutrons. One aspect which these instruments share and is not commonly found elsewhere is the 64-wire multidetector, although it is not clear how this might lead to the observed effect. It is suggested that the addition of a soller collimator in front of the detector to prevent neutrons not travelling in the scattering plane from being detected might improve the situation. The effect of normalising a sample run with a vanadium run of incorrect slope is to produce a large anomalous peak below about 1Å in the real space correlation function $T'(r)$ (ie. after Fourier transformation). Such a peak is very obvious since, apart from termination ripples and statistical fluctuations which are very much smaller, $T'(r)$ should be zero in this region. CLARE (1986) has performed a detailed investigation of this vanadium normalisation problem using D4 data taken at the same time as the Dy_7Ni_3 data : The gradient of the vanadium data was adjusted to minimise the size of the low-r normalisation error peak. (This method is based on the zero-ripple technique of LORCH (1969).) It was found that the excess fall-off observed in the vanadium data did not occur at all in the sample data. Hence the sample data was finally normalised by integration methods without any use of the vanadium data. A similar analysis was attempted for the Dy_7Ni_3 data but this did not prove to be feasible because of the additional complication of magnetic scattering. The finding of CLARE (1986) was followed and the measured vanadium data was not used to normalise the data for Dy_7Ni_3. Instead an absolute normalisation was achieved by using the calculated self scattering to scale the data (see section 7.3.4). The final raw data points (after the corrections described in section 7.3.3) are shown in figures 7.4 to 7.7 .

7.3.2 SMOOTHING OF THE DATA.

The next stage of the analysis was to smooth the background-subtracted data and to use the resultant fit to interpolate from data with a constant angle interval to points equally spaced in Q. The purpose of this is to provide data which is suitable for direct numerical Fourier transformation and also to reduce the effect of statistical errors. A least-squares cubic spline program (DIXON, WRIGHT and HUTCHINSON, 1977) was used to perform the smoothing of the data. At high Q where points are most dense and the features in I(Q) are smallest the spline tended to follow the noise. Thus it was found to be necessary to add points in threes before splining to obtain a good fit at high Q, the purpose of the procedure being to obtain the line of best fit to the raw data points. The two splines were joined at a suitable point where they were identical over an extended range. Even after this procedure it was necessary to slightly correct some of the fits in the region close to Q_{max} by hand. There appeared to be a systematic error at the very high Q end of the 0.7Å D4 data for all three samples measured (using the 0.5Å data as a guide) and hence the last 0.48Å^{-1} of these spectra was discarded. Figures 7.4 to 7.7 show the final fits to the data.

An additional complication encountered whilst smoothing the data was that the diffraction patterns of the $^{N}Dy_7{}^{N}Ni_3$ and $^{N}Dy_7{}^{0}Ni_3$ samples had a number of relatively small Bragg peaks. These Bragg peaks are easily differentiated from the amorphous diffraction pattern since they are much sharper. They are due to a small concentration of phase-separated crystallites being present in the samples. Clearly Bragg peaks are undesirable since it is the amorphous phase that is of interest and they were removed from the diffraction patterns by drawing a smooth extrapolation of the amorphous diffraction pattern underneath them (as shown in figures 7.4 and 7.5). An attempt was made to index the Bragg peaks obtained, but without much success. There were indications that possibly more than one crystal phase was present, and of the ten crystalline compounds formed between dysprosium and nickel (figure 6.4; ZHENG and WANG, 1982) the crystal structures of only five have been reported in the literature. Figures 7.4 and 7.5 show the subtracted Bragg peaks.

7.3.3 ABSORPTION, SELF-SHIELDING AND MULTIPLE SCATTERING CORRECTIONS.

The data from a diffraction experiment should be corrected for absorption, self-shielding and multiple scattering. Absorption is the reduction in flux due to the capture of neutrons by nuclei of the sample, self-shielding is the reduction of the primary beam by scattering as it passes through the sample, and multiple scattering is where a neutron suffers more than one scattering event. In principal these three effects cannot be separated and a full treatment of the problem requires a Monte Carlo calculation which must be repeated for every sample. However, as discussed by WRIGHT (1974), in most cases the linear absorption coefficients are such that it is a good approximation to separate the corrections.

ROUSE, COOPER, YORK and CHAKERA (1970) have used numerical integration to evaluate an approximate formula for the absorption of singly scattered neutrons within a cylindrical sample of radius R;

$$(I_m/I_t) = \exp[-(1.7133-0.0368\sin^2\theta)\mu^A R + (0.0927+0.0375\sin^2\theta)(\mu^A R)^2] \tag{7.3.1}$$

where I_m is the measured cross-section, I_t is the true cross-section (ie. that which would be measured if the absorption cross sections σ_l^A of all the elements were zero) and μ^A is the linear absorption coefficient;

$$\mu^A = \sum_l g^\circ_l \, \sigma^A_l \tag{7.3.2}$$

This formula was applied to the Dy_7Ni_3 data on the assumption that it is a good approximation to correct the multiply scattered signal with the correction factor for single scattering. The samples were treated as 7mm diameter cylinders with the effective densities ρ' given in table 7.1 . JOHNSON, WRIGHT and SINCLAIR (1983) have given a procedure by which in the small linear attenuation coefficient limit equation (7.3.1) may also be used to correct the data for self-shielding and multiple scattering. This procedure is based on the finding of ENDERBY (1968) that provided multiple scattering is small (<10%) the resultant intensity is isotropic. The cross-sections used to calculate the corrections are given in table 6.2 . Magnetic scattering was not included in the corrections since the analytic approach described above cannot be used for magnetic scattering due to the Q-dependence of the magnetic form factor f(Q).

7.3.4 SEPARATION OF SELF SCATTERING AND ABSOLUTE NORMALISATION.

The self scattering for each sample on each of the diffractometers was calculated using equation (4.1.50). In the case of D4 the detector constant γ used in the calculations was chosen to correspond to the mean efficiency f(k) of the two detectors. The reduced atomic masses (equation (4.1.51)) were calculated using the atomic masses in table 6.2 and the neutron mass in table 3.1 . The scattering cross-sections used in the calculations are given in table 6.2 and the average kinetic energy was estimated to be 25meV for both elements. The absolute normalisation was then achieved by scaling the measured diffraction patterns so that they oscillated about the calculated self scattering at high Q where the magnetic scattering $I^M(Q)$ is essentially zero. The self scattering was then subtracted from the diffraction patterns yielding $i(Q)+I^M(Q)$. Figures 7.4 to 7.6 show the calculated self scattering and the normalised experimental data.

7.3.5 SEPARATION OF MAGNETIC SCATTERING.

When a diffraction experiment is performed on an amorphous solid containing magnetic ions it is necessary to remove the magnetic scattering $I^M(Q)$ in order to obtain the distinct scattering $i(Q)$ which (as shown in section 4.1) contains the structural information. Generally $I^M(Q)$ is assumed to be totally incoherent (ie. the sample is assumed to be an ideal paramagnet - see equation 4.2.16) and calculated using values from tabulated calculations of form factors (LISHER and FORSYTH, 1971; see CLARE (1986) for an example of this approach). Alternatively an estimate of $I^M(Q)$ is made by using an ad hoc smooth curve which when subtracted from $I(Q)$ results in a $i(Q)$ of reaonable appearance (see for example WILDERMUTH, LAMPARTER and STEEB, 1985). This approach is not to be recommended for obvious reasons. For the experiments described in this Chapter a more accurate subtraction of the magnetic contribution to the scattering was achieved. This is because the diffraction pattern for the ${}^{0}Dy_7{}^{0}Ni_3$ sample provides a direct measurement of $I^M(Q)$, since it has no coherent nuclear scattering. In this way an $I^M(Q)$ curve determined under the same experimental conditions as the other spectra was subtracted. Hence any problems due to errors in tabulated form factors or due to the inapplicability of such form factors are avoided. Unfortunately the ${}^{0}Dy_7{}^{0}Ni_3$ diffraction pattern was measured on D2, and not on D4 which has the higher Q_{max}. Hence the D2 measurement of $I^M(Q)$ was extended to cover the Q-range of D4. This was achieved by joining the high Q part of the ${}^{0}Dy_7{}^{N}Ni_3$ diffraction pattern measured on D4 to the ${}^{0}Dy_7{}^{0}Ni_3$ diffraction pattern measured on D2 (figure 7.7). The justification for this procedure is that the structure in the ${}^{0}Dy_7{}^{N}Ni_3$ diffraction pattern had essentially diminished to zero by the Q_{max} of D2. It must be emphasised that the error due to using this slightly incorrect $I^M(Q)$ with the D4 data is actually very small indeed since magnetic form factors have fallen virtually to zero by the Q_{max} of D2 (~12Å^{-1}). This measurement of $I^M(Q)$ is discussed further in section 9.2 . A consequence of the use of the D2 measurement of $I^M(Q)$ in the analysis of the D4 data was that the D4 data below the Q_{min} of D2 could not be used. The final i(Q) distinct scattering curves for D4 (after the back-transform correction discussed in section 6.3.7) are shown in figure 7.8 .

7.3.6 DETERMINATION OF THE UNLIKE-ATOM DISTINCT SCATTERING.

Applying equation (4.1.24) to the present experiment yields the distinct scattering for the three coherently scattering samples as;

$$i_{ON}(Q) = 0.7\,\bar{b}_{Dy}^{2} \int_0^\infty d_{DyDy}(r)\,(\sin(Qr)/Q)\,dr \tag{7.3.3}$$

$$i_{NO}(Q) = 0.3\,\bar{b}_{Ni}^{2} \int_0^\infty d_{NiNi}(r)\,(\sin(Qr)/Q)\,dr \tag{7.3.4}$$

$$i_{NN}(Q) = i_{ON}(Q) + i_{NO}(Q) + 1.4\,\bar{b}_{Dy}\,\bar{b}_{Ni} \int_0^\infty d_{DyNi}(r)\,(\sin(Qr)/Q)\,dr \tag{7.3.5}$$

where $i_{NO}(Q)$, $i_{ON}(Q)$ and $i_{NN}(Q)$ are the distinct scattering from the ${}^{N}Dy_7{}^{0}Ni_3$, ${}^{0}Dy_7{}^{N}Ni_3$ and ${}^{N}Dy_7{}^{N}Ni_3$ samples respectively. The matrix inversion equation for the general isotopic substitution experiment (see section 5.4.1) then effectively reduces to equations (7.3.3), (7.3.4) and;

$$i_{UN}(Q) = i_{NN}(Q) - i_{NO}(Q) - i_{ON}(Q) \tag{7.3.6}$$

where $i_{UN}(Q)$ is the contribution to the distinct scattering from the $^{N}Dy_{7}{}^{N}Ni_{3}$ sample due to correlations between unlike atoms (Dy-Ni). Note that the notation used here differs from the conventional $S_{ll'}(Q)$ definitions of the partial structure factors (equation (4.1.44)). This is to emphasise the fact that the double null isotopic substitution technique yields all but one of the partial functions directly with a consequent improvement in accuracy ie. all but one of the functions compared with modelling calculations in Chapter 8 are measured directly without the need for matrix inversion.

Smooth fits for $i_{UN}(Q)$ were obtained by combining the fits to $i_{NO}(Q)$, $i_{ON}(Q)$ and $i_{NN}(Q)$ according to equation (7.3.6). The resultant fits were then compared with the corrected data to check the quality of the fit. The D2 fit was found to agree very well with the unfitted data points. In the case of the D4 data it was necessary to use the function $i_{UN}(Q)-I^{M}(Q)$ for the comparison. This is because the points of the unfitted data for $I^{M}(Q)$ had a different set of Q-values to the unfitted D4 data and so the magnetic scattering could not be subtracted from the unfitted D4 data. The D4 fit for $i_{UN}(Q)$ was not quite perfect in a few small regions and it was corrected accordingly. These slight inadequacies of the initial fit are due to the magnification of errors involved in the matrix inversion (see section 5.4.1). The final D4 $i_{UN}(Q)$ fit is shown in figure 7.8 .

7.3.7 FOURIER TRANSFORMATION

The distinct scattering curves i(Q) were extrapolated to zero Q so that they could be Fourier transformed. Since they appeared to have become essentially horizontal by the minimum experimental Q-values this was achieved simply by extending the horizontal region to Q=0 . Note that i(Q) must necessarily be horizontal at Q=0 . The distinct scattering curves were then multiplied by Q to yield Qi(Q) (see figure 7.9 for the Qi(Q) curves after the back-transform correction discussed below) and Fourier transformed according to equation (4.1.58) using FILON's quadrature (1929). The LORCH (1969) modification function M(Q) was used in the Fourier transformation so as to reduce termination ripples (see section 3.4.3). The correlation functions for the $^{N}Dy_7{}^{N}Ni_3$, $^{N}Dy_7{}^{O}Ni_3$ and $^{O}Dy_7{}^{N}Ni_3$ samples are denoted $^{NN}T'(r)$, $^{NO}T'(r)$ and $^{ON}T'(r)$ respectively. Similarly the correlation function derived from the unlike-atom contribution to the distinct scattering $i_{UN}(Q)$ is denoted $^{UN}T'(r)$. These correlation functions (after the back-transform correction discussed below) are shown in figure 7.10 .

The T'(r) curves obtained by Fourier transformation of the experimental Qi(Q) curves were found to have low-r normalisation error peaks, although they were not particularly large. Generally an investigation into the source of the normalisation error should be performed so that it can be corrected. However, in the case of Dy_7Ni_3 such an investigation was attempted but was found not to be feasible because of the additional complications introduced by the presence of magnetic scattering. Hence the data were corrected using the back-transform correction of LEVY, DANFORD and NARTEN (1966). This correction is performed by back-transforming the low-r region of T'(r) where the correlation function should be zero, subtracting the result from i(Q) and then transforming back to r-space. For

Dy_7Ni_3 the part of the T'(r) curves in the region 0<r<1Å was back-transformed. Note that this region ends considerably below the first true atom-atom peak. The back-transform correction is not generally to be recommended since it does not address the root cause of the normalisation error. However, in the case of Dy_7Ni_3 it proved to be the only practicable alternative. The effect of the correction in reciprocal-space is to at least partially counteract the effect of the normalisation error so that the i(Q) curves behave more reasonably, whilst the effect in real-space is mostly cosmetic. figure 7.11 shows the effect of the back-transform correction for for the $^{N}Dy_7{}^{N}Ni_3$ sample on D4, both in real-space and reciprocal-space.

In the process of extracting the correlation function T'(r) from the data an average density term T°(r) is added to the correlation function D'(r) which is obtained directly from the Fourier transformation (equation (4.1.58)). T°(r) was calculated according to equation (4.1.28) using the numerical values given in section 5.5 . However, it was found that below the first peak (r~1Å to 2.5Å) the correlation functions for Dy_7Ni_3 did not oscillate about the r-axis but showed various small slopes. An error in a numerical value used in the data analysis can cause such a low-r slope and in an ideal experiment it may be possible to identify which parameter has been assigned an incorrect value. An analysis to identify the cause of the low-r slopes in the Dy_7Ni_3 data was attempted, and since $^{ON}T'(r)$ did not appear to slope three possible causes were considered: An error in the coherent scattering length $\bar{b}_{Dy}$ of ^{N}Dy which would result in an incorrect T°(r) for the samples containing ^{N}Dy, an error in the total scattering cross-section σ_{Dy} of ^{N}Dy which would result in an incorrect normalisation of D′(r) for the samples containing ^{N}Dy, or an error in the atomic number density g° of Dy_7Ni_3 which would result in an incorrect T°(r) for all samples. However, when the low-r slopes of the T′(r) curves from both diffractometers were studied it was found that there was not a sufficient degree of consistency to be able to identify an error in any one parameter. Thus it was concluded that the low-r slopes are probably a result of the normalisation problems discussed previously. A consequence of this is that a limit must be placed on the accuracy of the coordination numbers obtained in Chapter 8; The magnitude of the low-r slopes indicate an accuracy of 2-3% in the peak areas obtained from the correlation functions.

The functions $t_{ll'}(r)$ were derived from the measurements of $^{NO}T'(r)$, $^{ON}T'(r)$ and $^{UN}T'(r)$ using equation (6.4.2) and these are shown in figure 7.12 .

The D4 data were also transformed with the Q_{max} of D2 (ie. with the real-space resolution of D2) and the resultant transforms were compared with the transforms of the D2 data as a consistency check. The agreement was good (see figure 7.13), with the D4 correlation functions showing slightly more structure due to the better Q-resolution of D4. (The effect of Q-resolution is the converse of the effect of atomic thermal motion - it causes a broadening in reciprocal-space which corresponds to a damping of structure in real-space. However the effect is relatively small.) Hence the modelling studies discussed in Chapter 8 were based on the D4 data since this has better real-space resolution (higher Q_{max}).

7.3.8 BHATIA-THORNTON FUNCTIONS.

The atom-atom partial structure factor and correlation function formalism used above is generally ascribed to FABER and ZIMAN (1964). However, an alternative set of partial functions for binary alloys has been proposed by BHATIA and THORNTON (1970). The Bhatia-Thornton (BT) number-concentration partial correlation functions may conveniently be defined in terms of the particle density operator $\rho_1(\underline{r},t)$ used in section 3.3.4 (cf. equation (3.3.51));

$$G_{nn}(\underline{r},t) = \frac{1}{N} \int \left\langle \left[\rho_1'(\underline{r}',0) + \rho_2'(\underline{r}',0)\right] \left[\rho_1(\underline{r}'+\underline{r},t) + \rho_2(\underline{r}'+\underline{r},t)\right] \right\rangle d\underline{r}' \tag{7.3.7}$$

$$G_{cc}(\underline{r},t) = \frac{1}{Nc_1c_2} \int \left\langle \left[c_2\rho_1'(\underline{r}',0)-c_1\rho_2'(\underline{r}',0)\right] \left[c_2\rho_1(\underline{r}'+\underline{r},t)-c_1\rho_2(\underline{r}'+\underline{r},t)\right] \right\rangle d\underline{r}' \tag{7.3.8}$$

$$G_{nc}(\underline{r},t) = \frac{1}{Nc_1c_2} \int \left\langle \left[\rho_1'(\underline{r}',0)+\rho_2'(\underline{r}',0)\right] \left[c_2\rho_1(\underline{r}'+\underline{r},t)-c_1\rho_2(\underline{r}'+\underline{r},t)\right] \right\rangle d\underline{r}' \tag{7.3.9}$$

The sum $\rho_1(\underline{r},t)+\rho_2(\underline{r},t)$ represents the local total number density whilst the combination $c_2\rho_1(\underline{r},t)-c_2\rho_1(\underline{r},t)$ represents the local deviation of concentration from the average. Thus $G_{nn}(\underline{r},t)$ represents correlations in the number density, $G_{cc}(\underline{r},t)$ represents correlations between concentration fluctuations and $G_{nc}(\underline{r},t)$ represents correlations between density and concentration fluctuations. As with the Faber-Ziman (FZ) formalism static distribution functions (t=0) may be defined and the static distribution functions of the two formalisms are related as follows;

$$t_{nn}(r) = c_1\, t_{11}(r) + c_1\, t_{12}(r) + c_2\, t_{21}(r) + c_2\, t_{22}(r) \tag{7.3.10}$$

$$t_{cc}(r) = c_2\, t_{11}(r) - c_1\, t_{12}(r) - c_2\, t_{21}(r) + c_1\, t_{22}(r) \tag{7.3.11}$$

$$t_{nc}(r) = [\ t_{11}(r) + t_{12}(r)\ ] - [\ t_{21}(r) + t_{22}(r)\ ] \tag{7.3.12}$$

Note that a reversal in the order of definition of atom types 1 and 2 causes a change in the sign of $t_{nc}(r)$. BT number-concentration partial structure factors may also be defined;

$$S_{ij}(Q) = \delta_{ij} + \int_0^\infty d_{ij}(r) \frac{\sin Qr}{Q} dr$$

with; (7.3.13)

$$t_{ij}(r) = d_{ij}(r) + t^o_j(r)$$

$$t^o_j(r) = 4\pi r\ g^o\ \delta_{jn}$$

where i and j may each be set to either n (number) or c (concentration). Note that this definition differs very slightly from that of BHATIA and THORNTON (1970) so that the structure factors oscillate about 1 or 0. The BT number-concentration partial correlation functions and partial structure factors for Dy_7Ni_3 on D4 are shown in figures 7.14 and 7.15 respectively. As with $i_{UN}(Q)$ there were slight inadequacies of the fits in a few regions of the D4 data and these were corrected with reference to the raw data and the D2 data. $t_{nn}(r)$ shows that there appear to be two principal nearest neighbour distances in Dy_7Ni_3, and $t_{cc}(r)$ shows that there is a preference for unlike atoms to be neighbours at the first of these distances and for like atoms to be neighbours at the second.

Since the partial functions of one formalism are given by a linear combination of the partial functions of the other formalism it is clear that both contain essentially the same information; they are just different ways of expressing and displaying the same information. It was decided to use the FZ partial functions for most of the modelling studies described in Chapter 8 since their meaning is more obvious and they are more clearly related to the atomic structure. In fact for Dy_7Ni_3 it would be misleading to concentrate on the BT partial correlation functions; the FZ partial correlation functions show quite clearly that there is a Ni-Ni neasrest neighbour peak at about 2.78Å which is of particular structural importance (see Chapter 8) whereas the BT functions effectively mask the occurrence of this peak. Also, since all but one of the FZ partial functions were measured directly without the need for matrix inversion, they should have smaller errors.

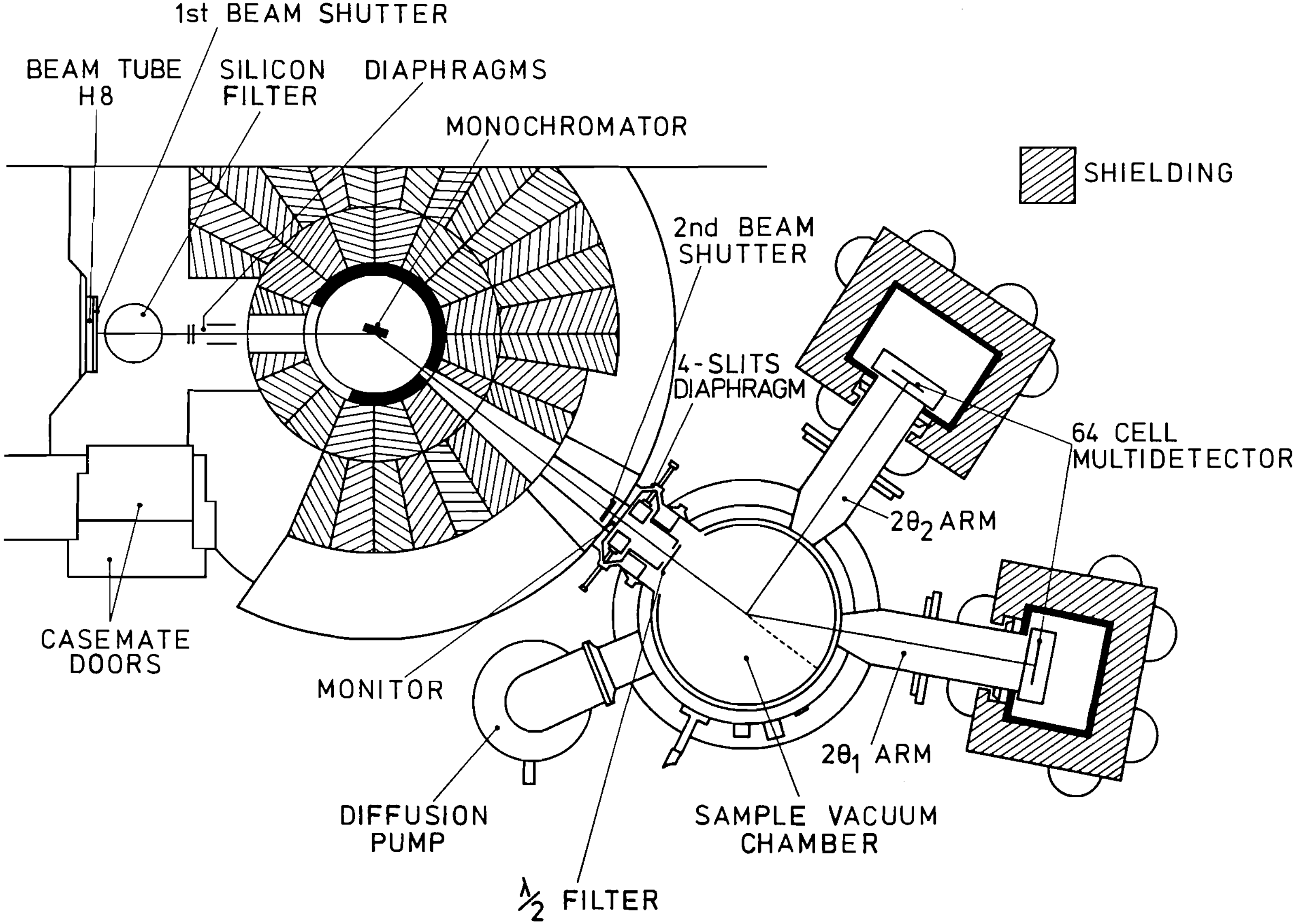

Figure 7.1 The Twin-Axis Liquids Diffractometer D4. (after CLARE (1986)

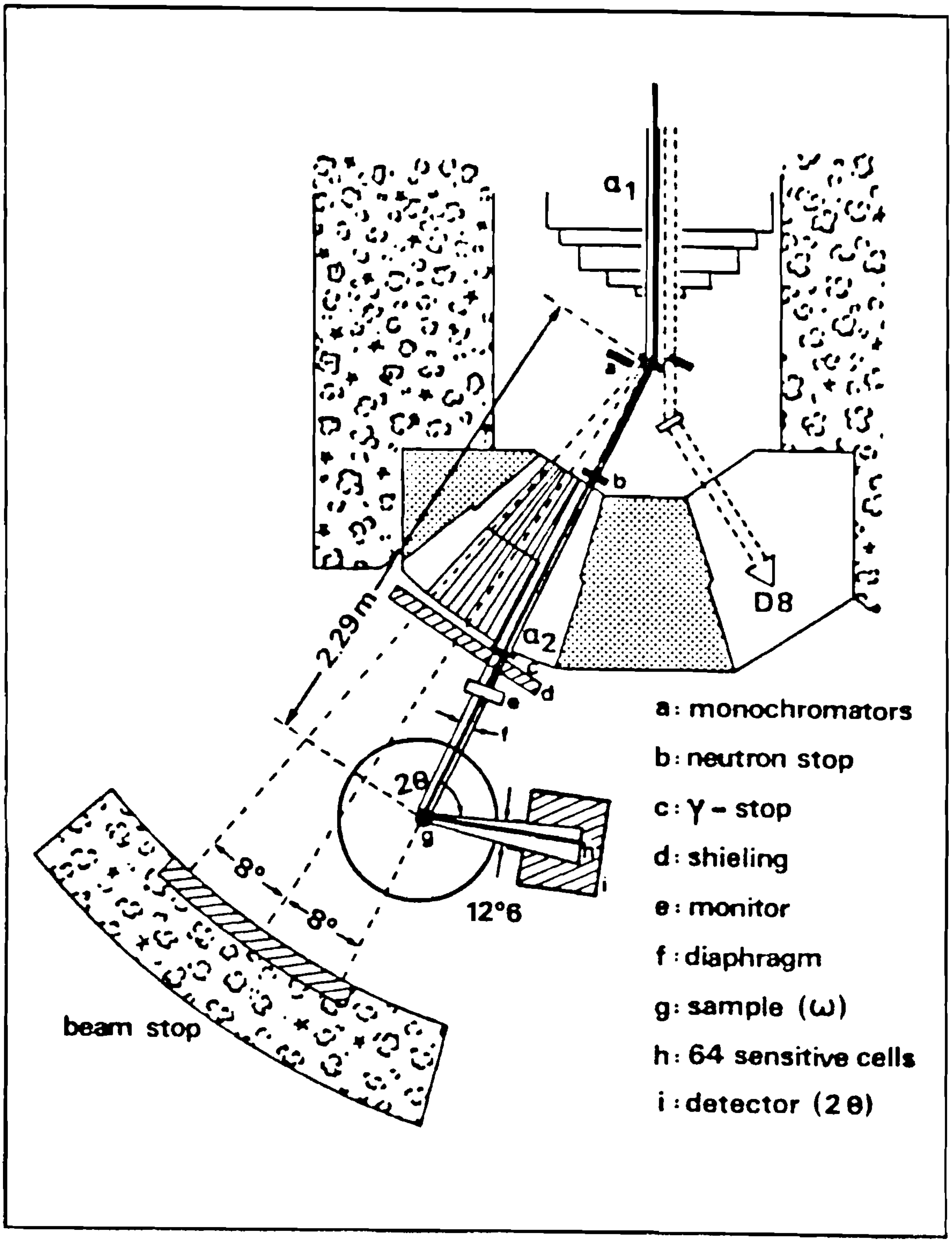

Figure 7.2 The Twin-axis Powder Diffractometer D2.

Figure 7.3

T(r) from a Neutron Diffraction Experiment

$$\underset{\text{self}}{I^S(Q)}\ \text{in}\ I(Q) = \underset{\text{self}}{I^S(Q)} + \underset{\text{distinct}}{i(Q)}$$

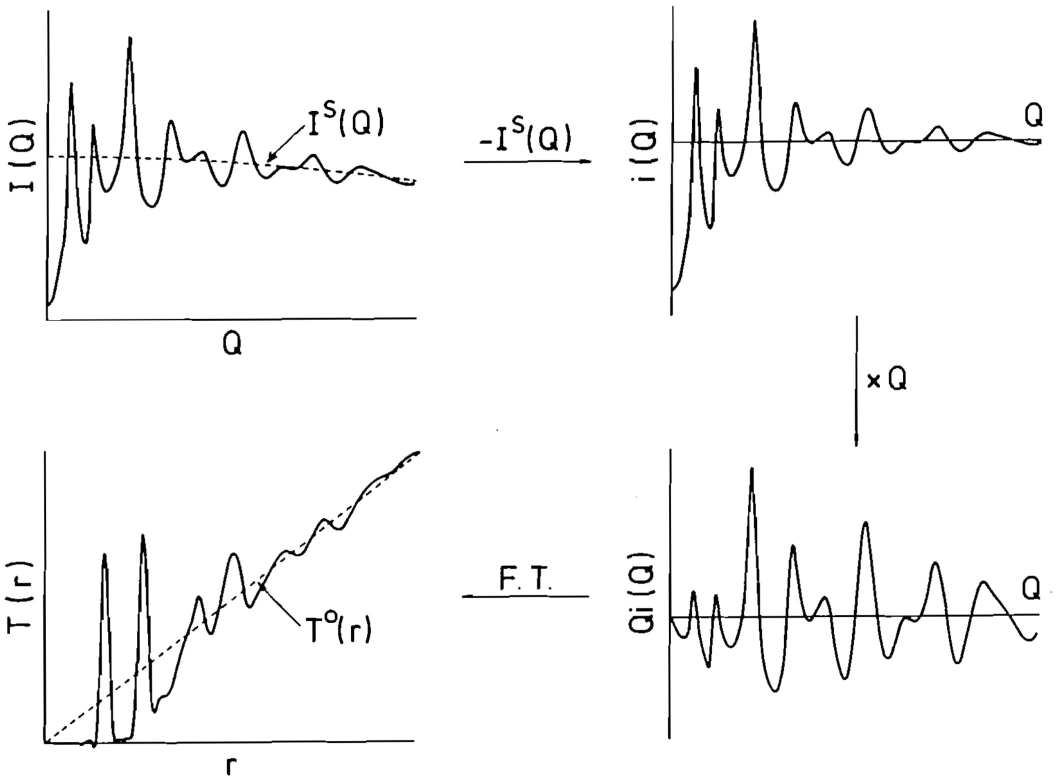

$$T(r) = T^0(r) + \frac{2}{\pi} \int_0^\infty Qi(Q)\, M(Q) \sin rQ\, dQ$$

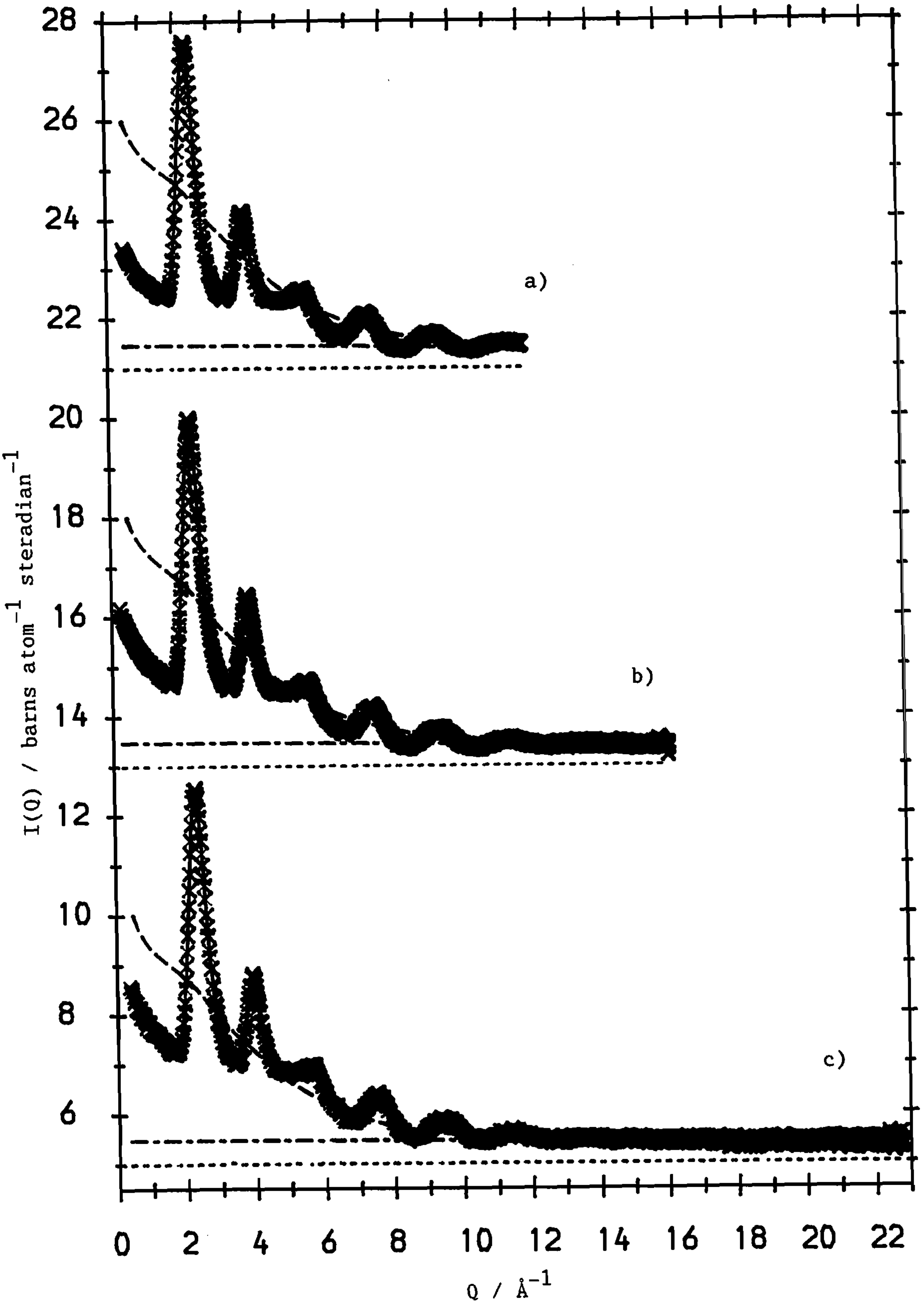

Figure 7.4 I(Q) for the $^{N}Dy_7{}^{N}Ni_3$ Sample (Points), showing the Fit to the Data (Continuous Line), the Calculated Nuclear Self Scattering (Dot-dashed Line), the Sum of the Nuclear Self Scattering and the Magnetic Scattering (Dashed Line), and the Removed Bragg Peaks (Dotted Line) {with a suitable offset}.

a) Measured on D2 {offset 16.0}

b) Measured on D4 at 0.7Å {offset 8.0}

c) Measured on D4 at 0.5Å

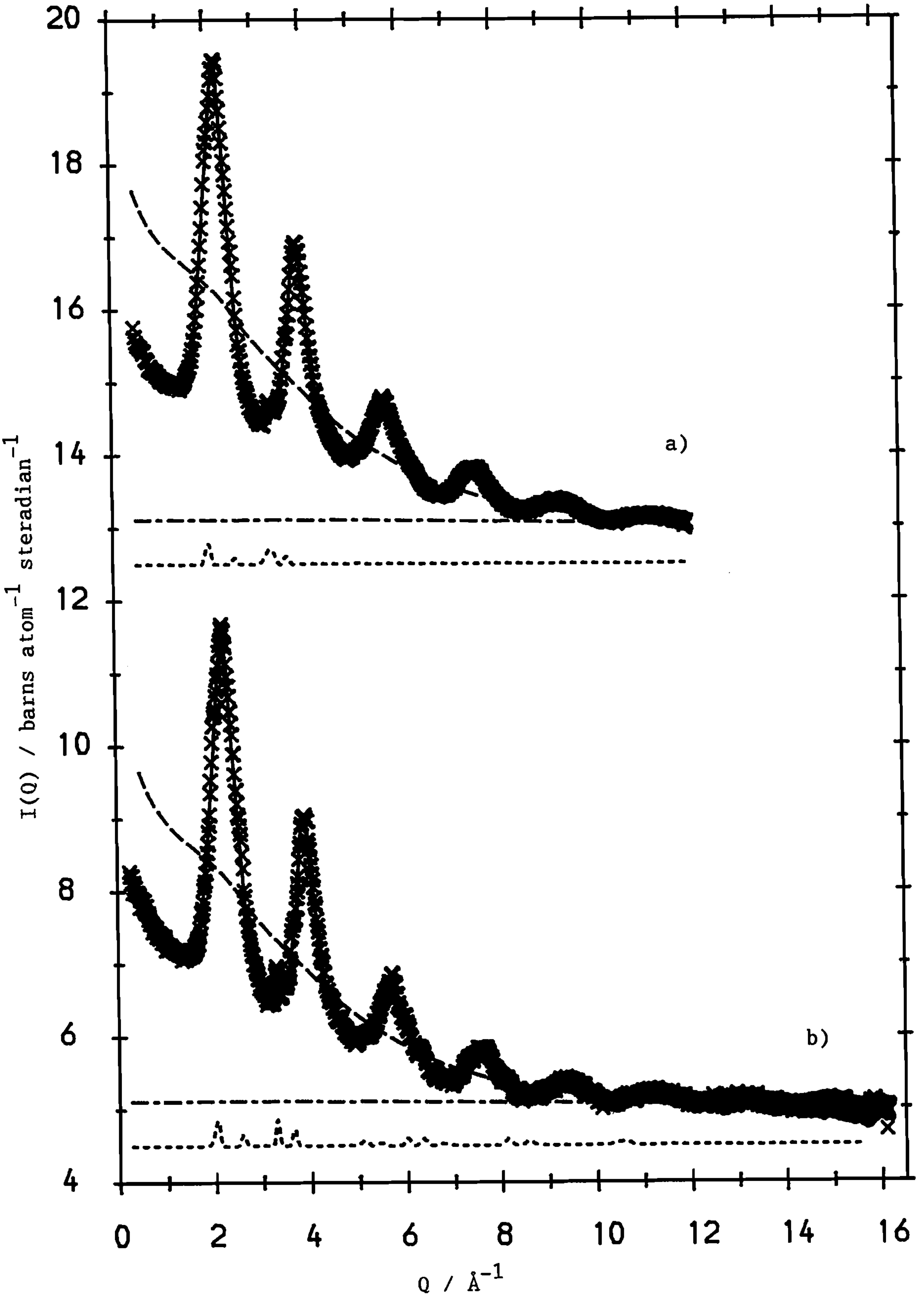

Figure 7.5 I(Q) for the $^{N}Dy_{7}{}^{0}Ni_{3}$ Sample (Points), showing the Fit to the Data (Continuous Line), the Calculated Nuclear Self Scattering (Dot-dashed Line), the Sum of the Nuclear Self Scattering and the Magnetic Scattering (Dashed Line), and the Removed Bragg Peaks (Dotted Line) {with a suitable offset}.

a) Measured on D2 {offset 8.0}

b) Measured on D4 at 0.7Å

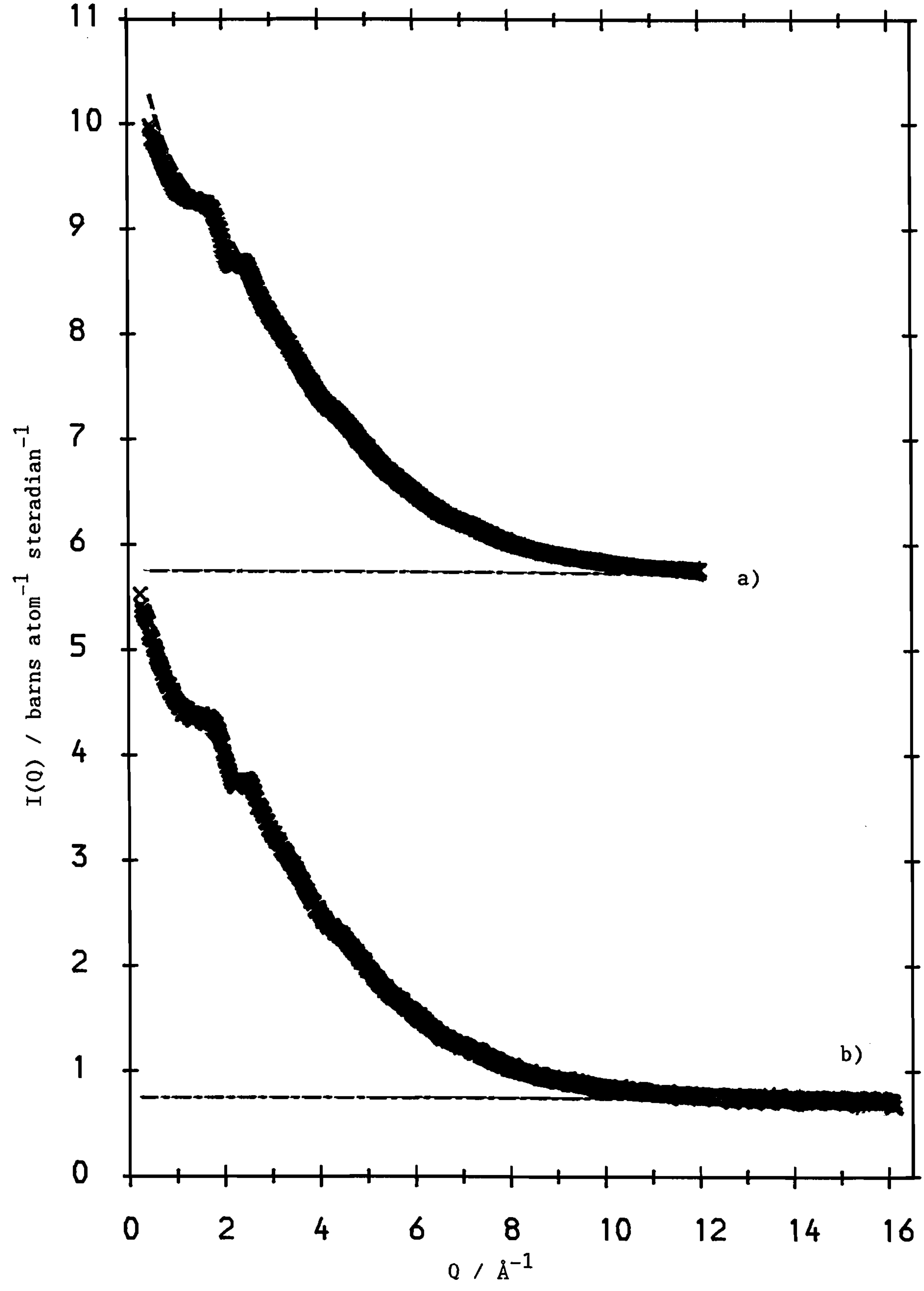

Figure 7.6 I(Q) for the ${}^{0}Dy_{7}{}^{N}Ni_{3}$ Sample (Points), showing the Fit to the Data (Continuous Line), the Calculated Nuclear Self Scattering (Dot-dashed Line) and the Sum of the Nuclear Self Scattering and the Magnetic Scattering (Dashed Line).

a) Measured on D2 {offset 5.0}

b) Measured on D4

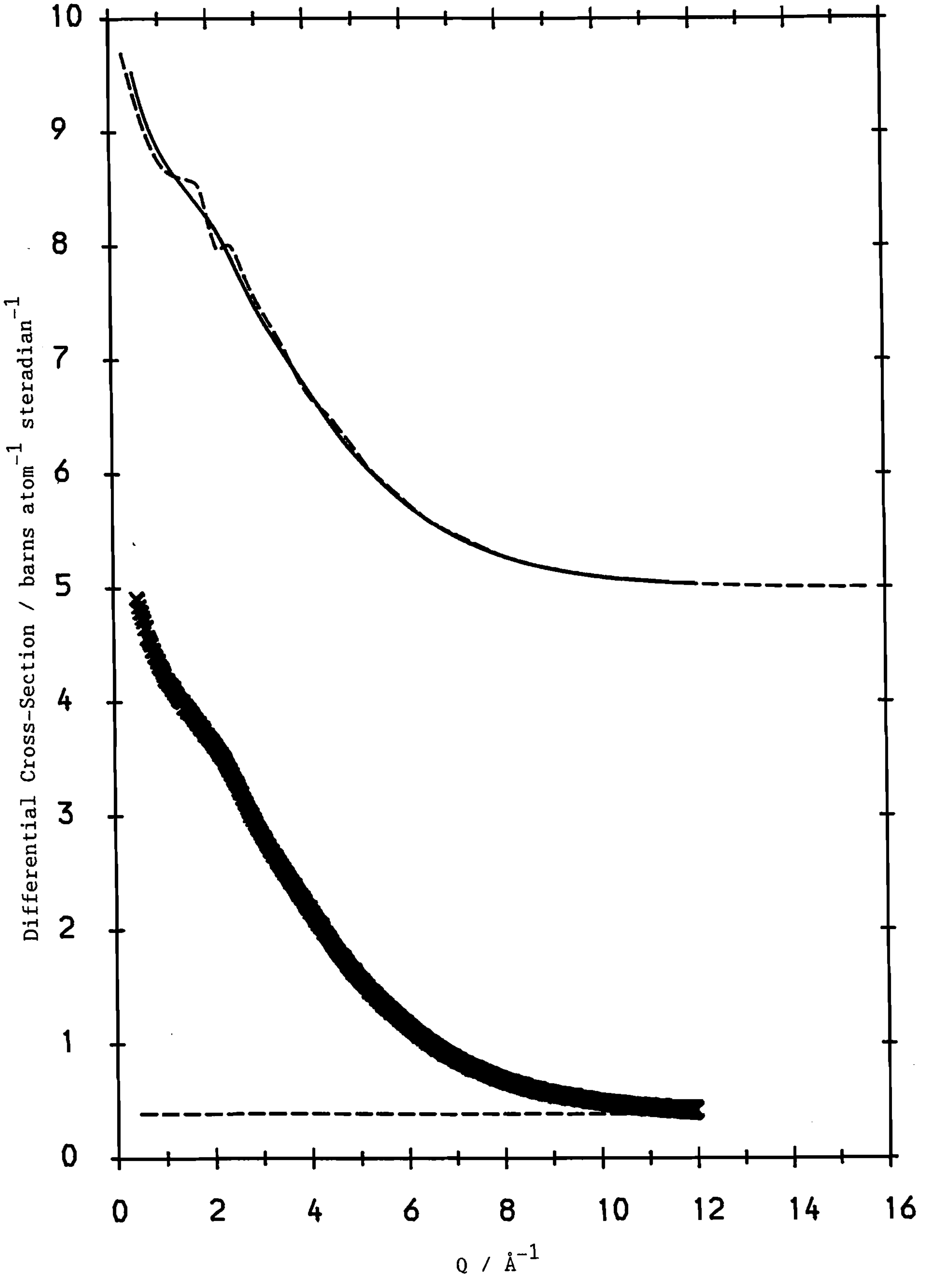

Figure 7.7 The Diffraction Pattern for the $^{0}Dy_{7}{}^{0}Ni_{3}$ Sample. The Points are the D2 Data, the Dashed Line is the Calculated Nuclear Self Scattering (for D2) and the Continuous Line {offset 5.0} is the Result of Subtracting the Nuclear Self Scattering from the Fit to the Data. The Dashed Line {offset 5.0} is the $^{0}Dy_{7}{}^{N}Ni_{3}$ D4 Measurement Used to Extend the Measurement of $I^{M}(Q)$.

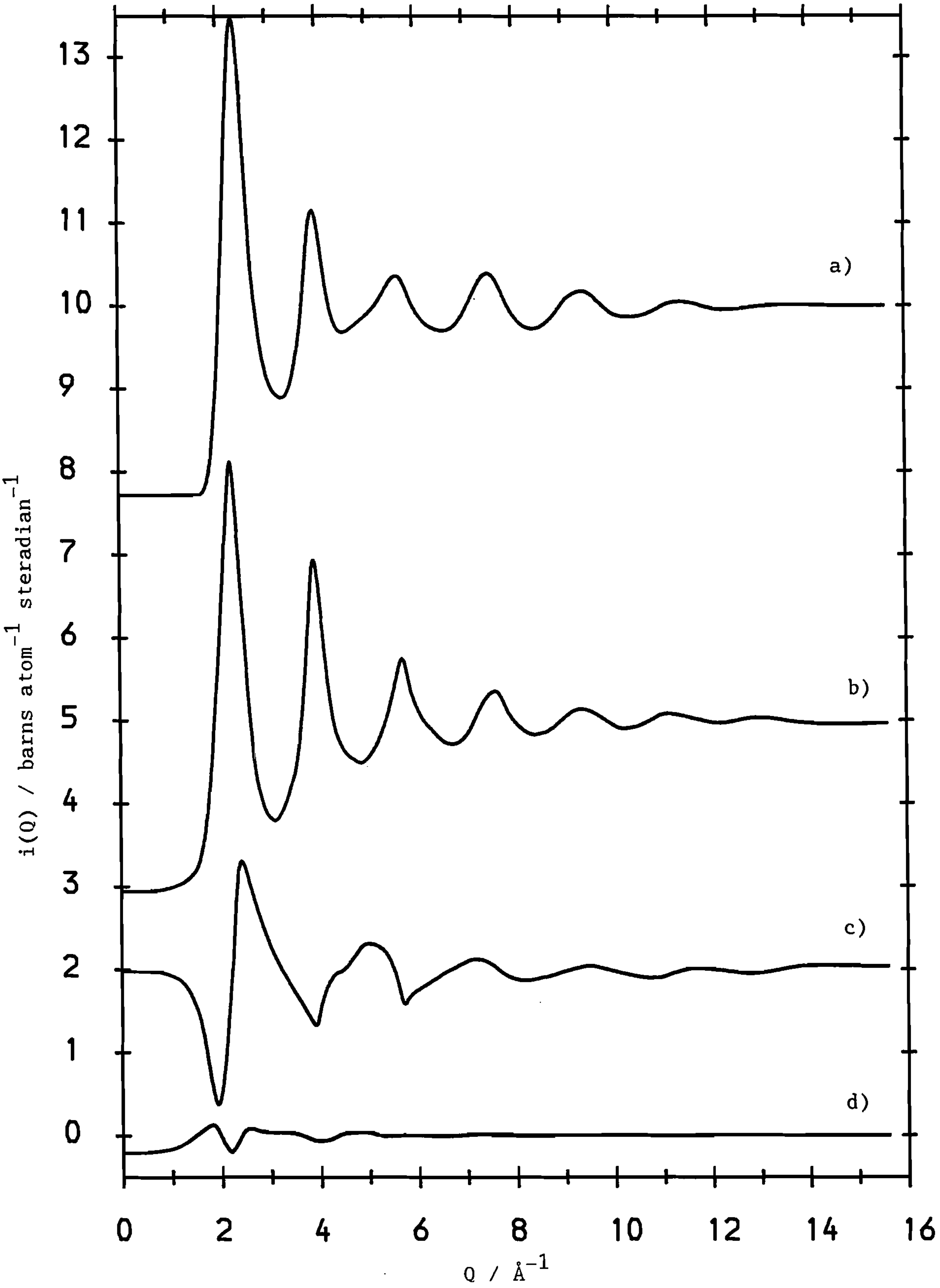

Figure 7.8 The D4 Measurements of i(Q) after the Back-transform Correction.

a) $i_{NN}(Q)$ {offset 10.0} b) $i_{NO}(Q)$ {offset 5.0}

c) $i_{UN}(Q)$ {offset 2.0} d) $i_{ON}(Q)$

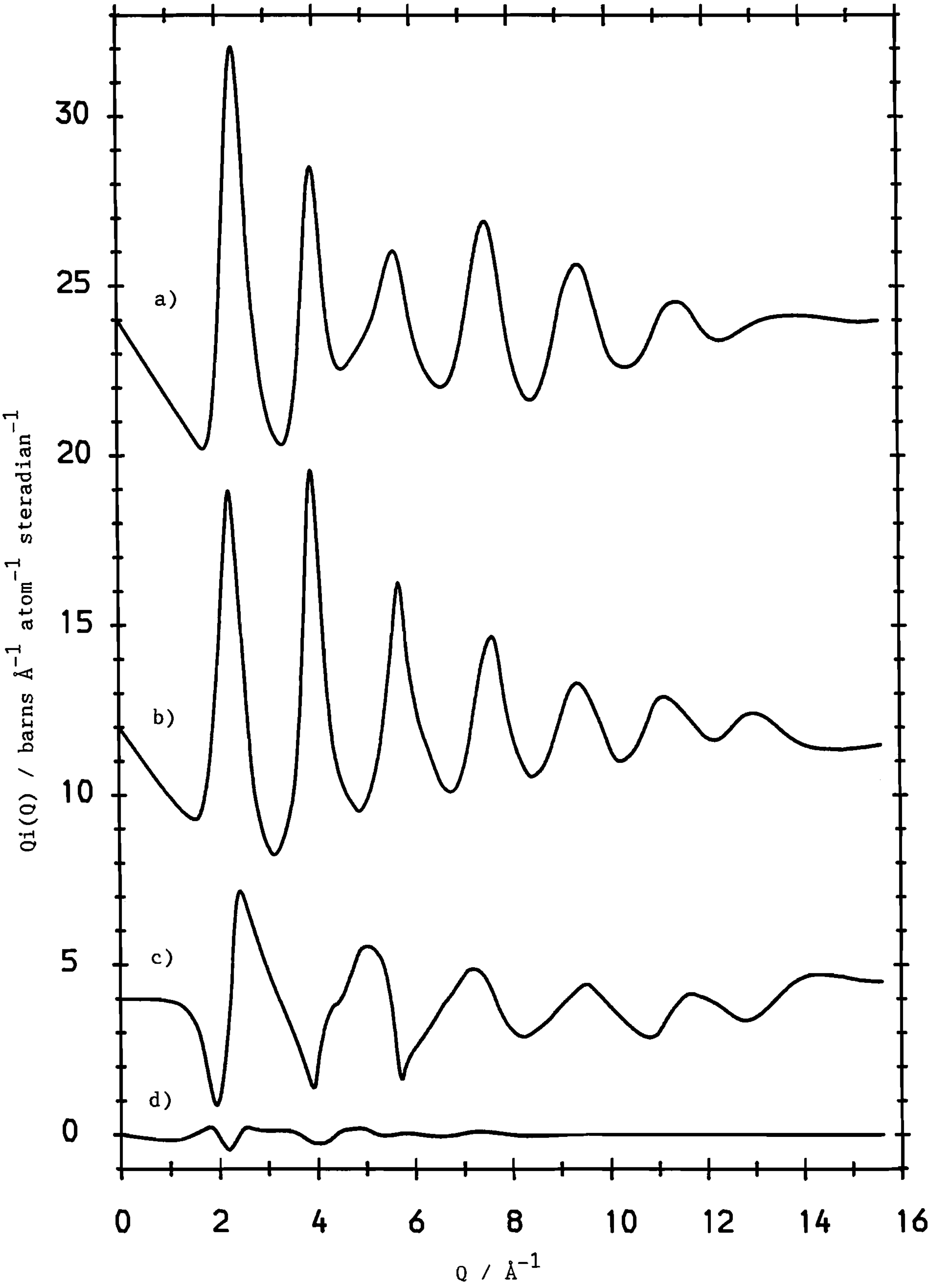

Figure 7.9 The D4 Measurements of Qi(Q) after the Back-Transform Correction.
a) $Qi_{NN}(Q)$ {offset 24.0} b) $Qi_{NO}(Q)$ {offset 12.0}
c) $Qi_{UN}(Q)$ {offset 4.0} d) $Qi_{ON}(Q)$

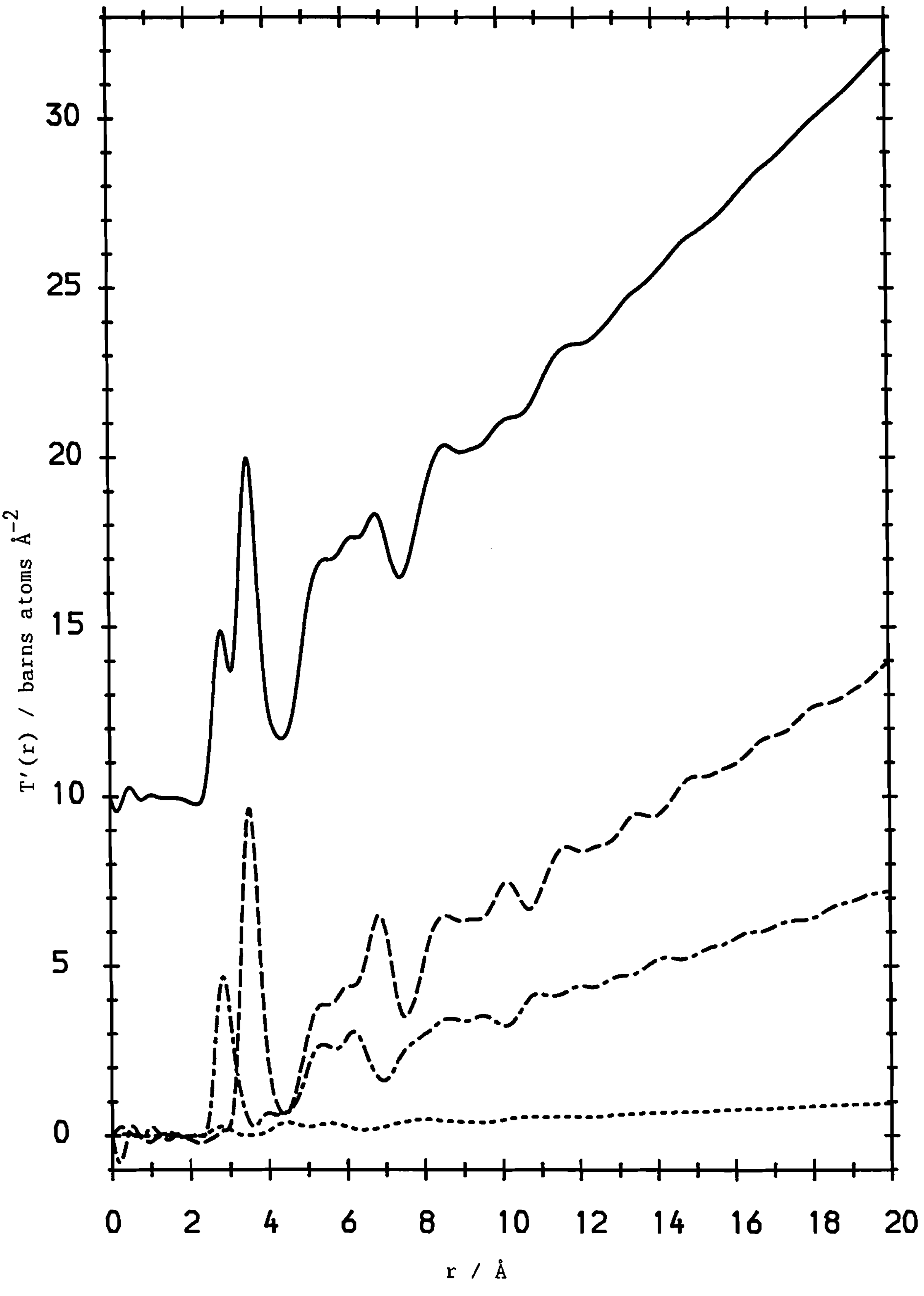

Figure 7.10 The D4 Measurements of T′(r) after the Back-transform Correction. The Continuous Line {offset 10.0} is $^{NN}T'(r)$, the Dashed Line is $^{NO}T'(r)$, the Dotted Line is $^{ON}T'(r)$ and the Dot-dashed Line is $^{UN}T'(r)$.

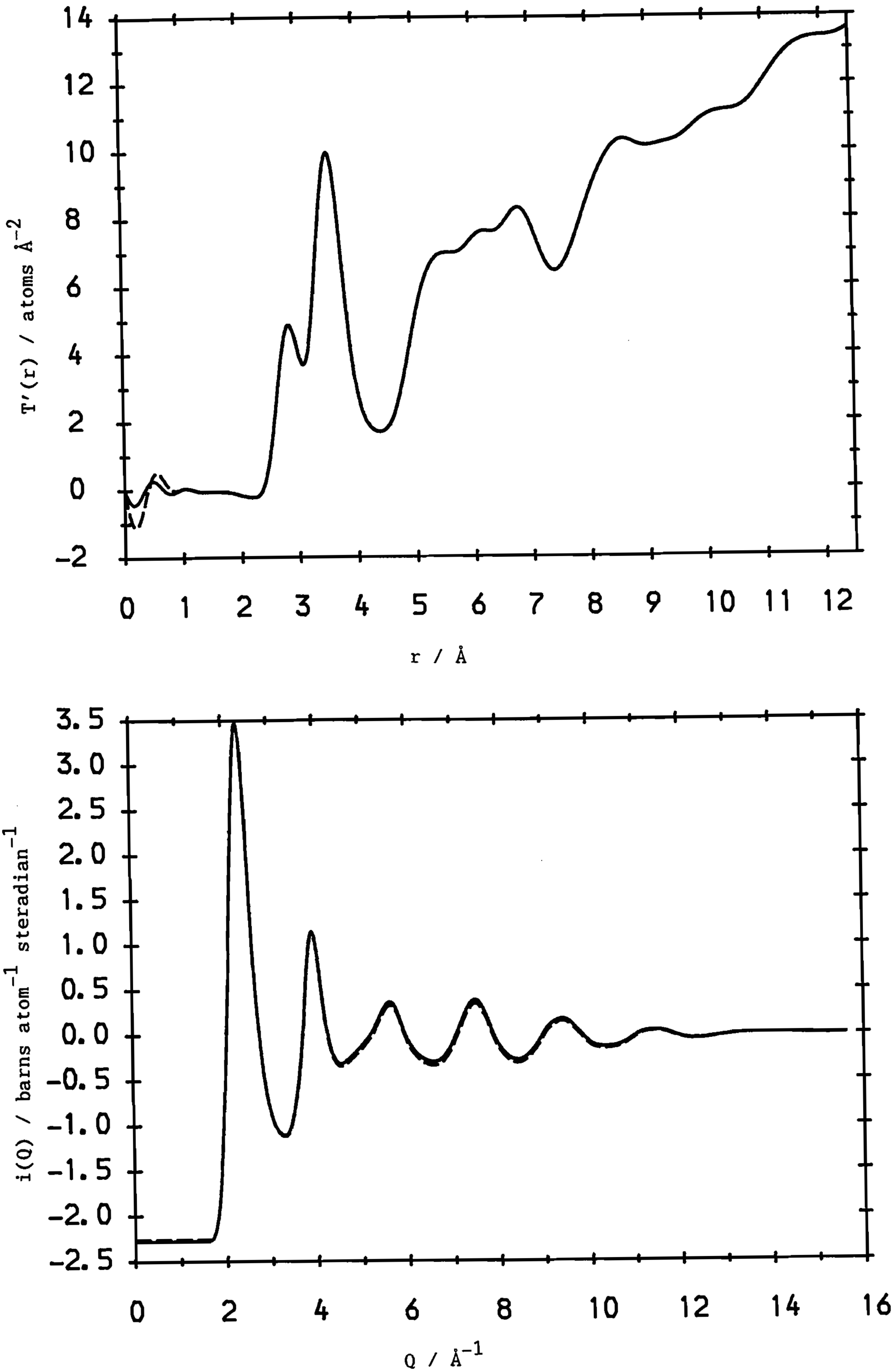

Figure 7.11 The Effect of the Back-transform Correction for the ${}^{N}Dy_7{}^{N}Ni_3$ Sample in both Real-space and Reciprocal-space. The Dashed Line shows the Data before the Correction and the Continuous Line shows the Data after the Correction.

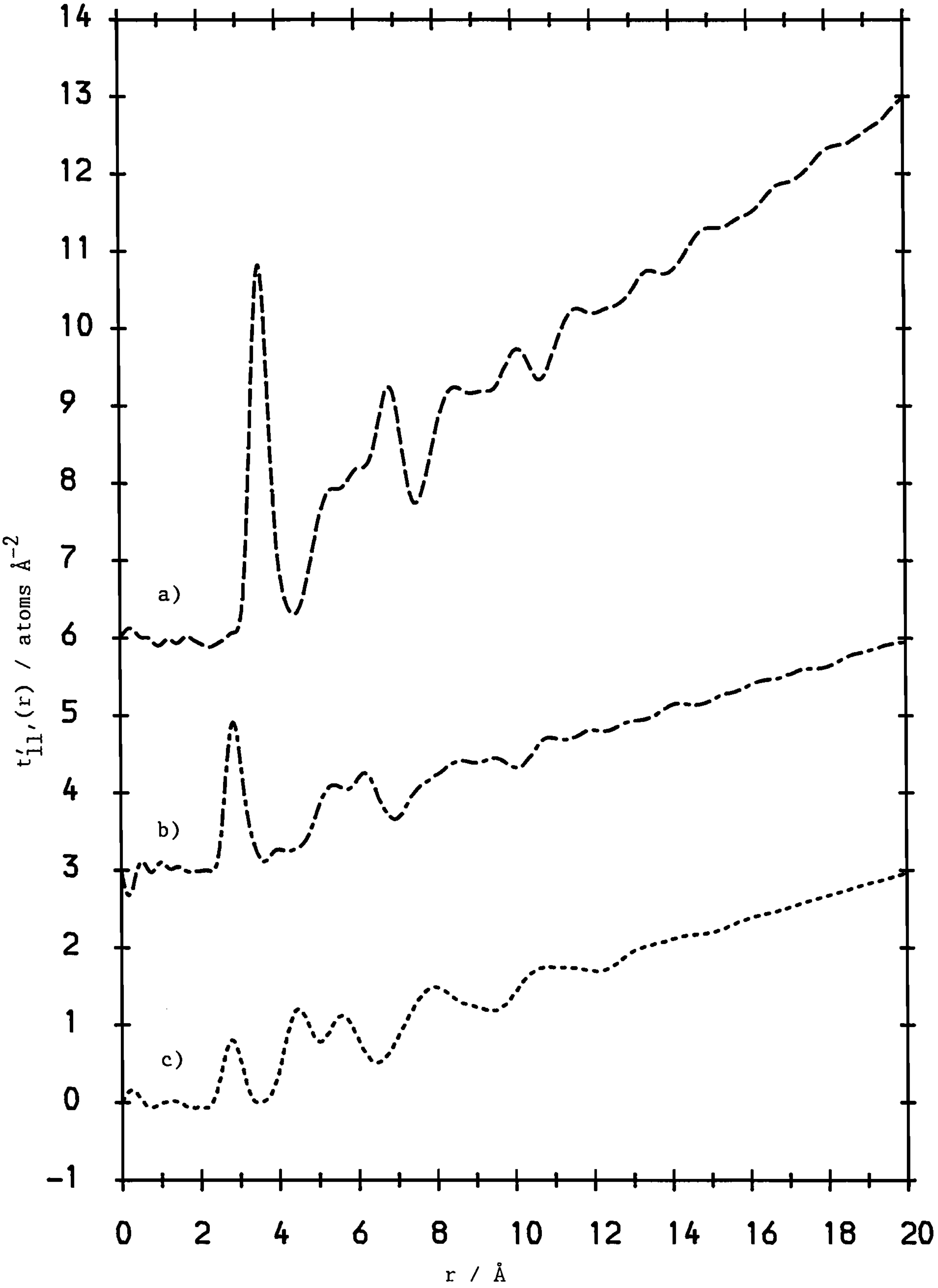

Figure 7.12 The D4 Measurements of the Partial Correlation Functions $t'_{ll'}(r)$ after the Back-transform Correction.
a) Dy-Dy {offset 6.0} b) Dy-Ni {offset 3.0}
c) Dy-Ni

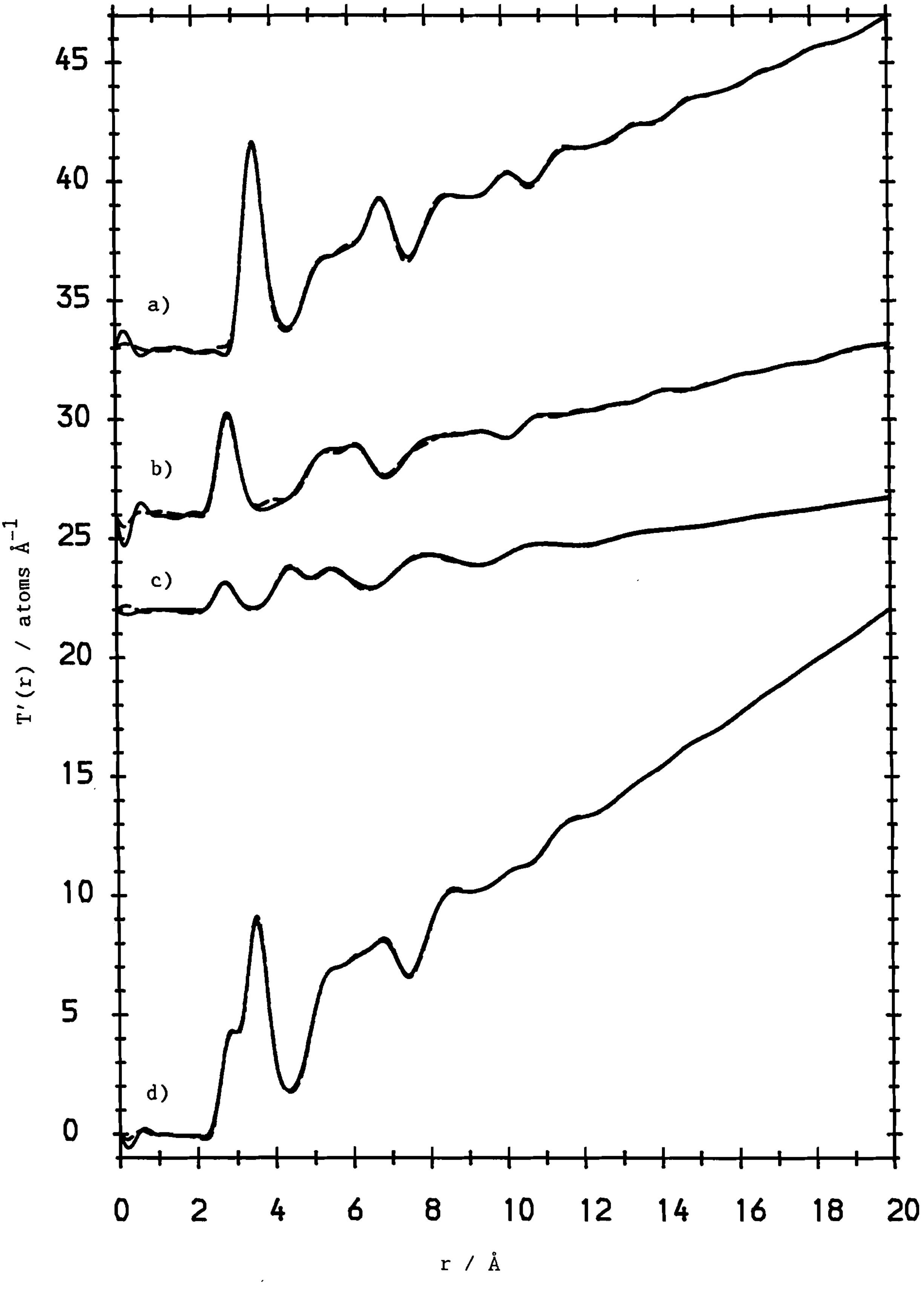

Figure 7.13 A Comparison Between The Correlation Functions T'(r) after the Back-transform Correction as Measured on D2 (Continuous Line) and as Measured on D4 (Dashed Line) Using the Q_{max} of D2.
a) $^{NO}T'(r)$ {offset 33.0} b) $^{UN}T'(r)$ {offset 26.0}
c) $^{ON}T'(r)$ {offset 22.0} d) $^{NN}T'(r)$

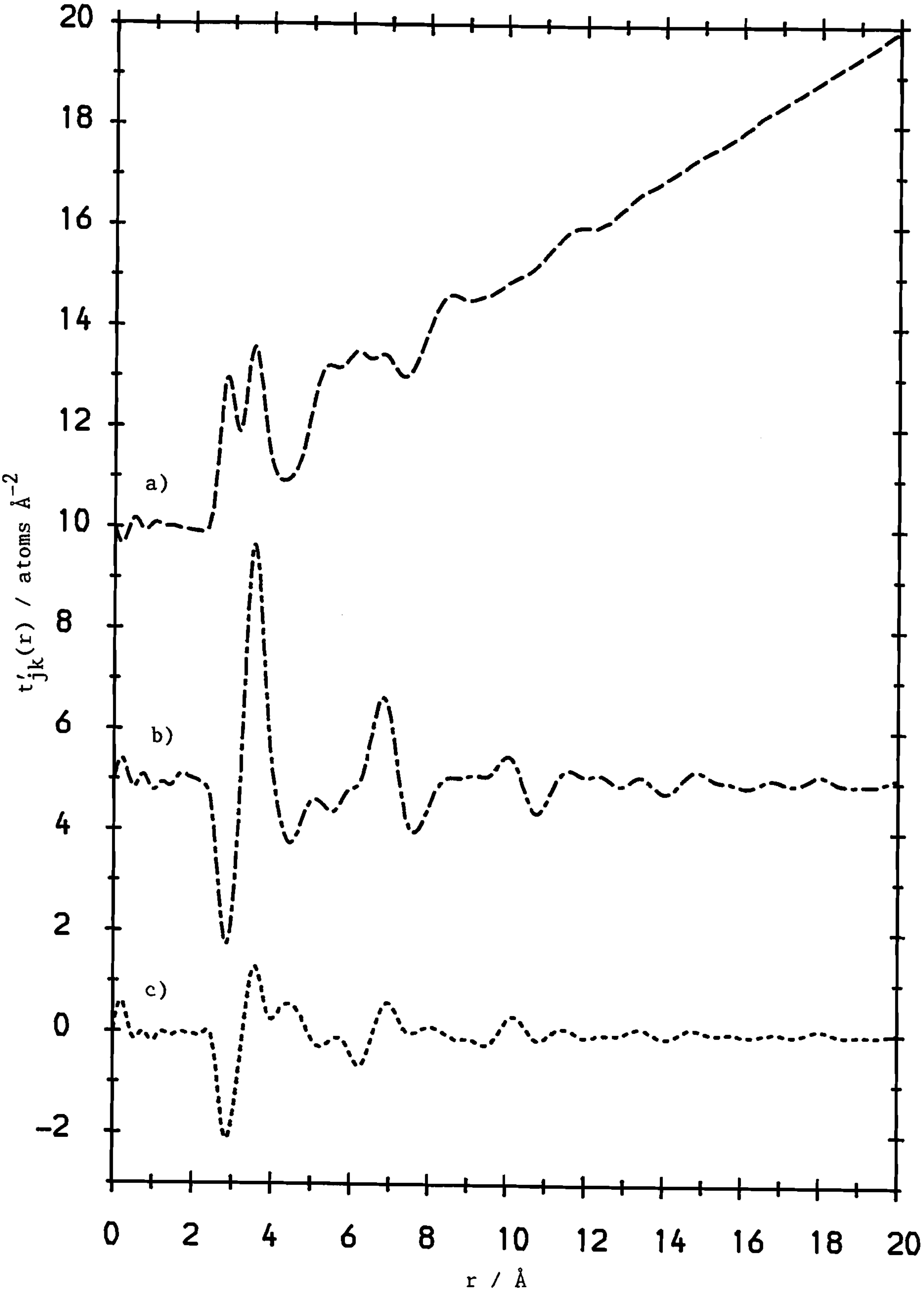

Figure 7.14 The D4 Measurements of the Bhatia-Thornton Number-concentration Partial Correlation Functions $t'_{jk}(r)$ for Dy_7Ni_3.
a) $t'_{nn}(r)$ {offset 10.0} b) $t'_{nc}(r)$ {offset 5.0} c) $t'_{cc}(r)$

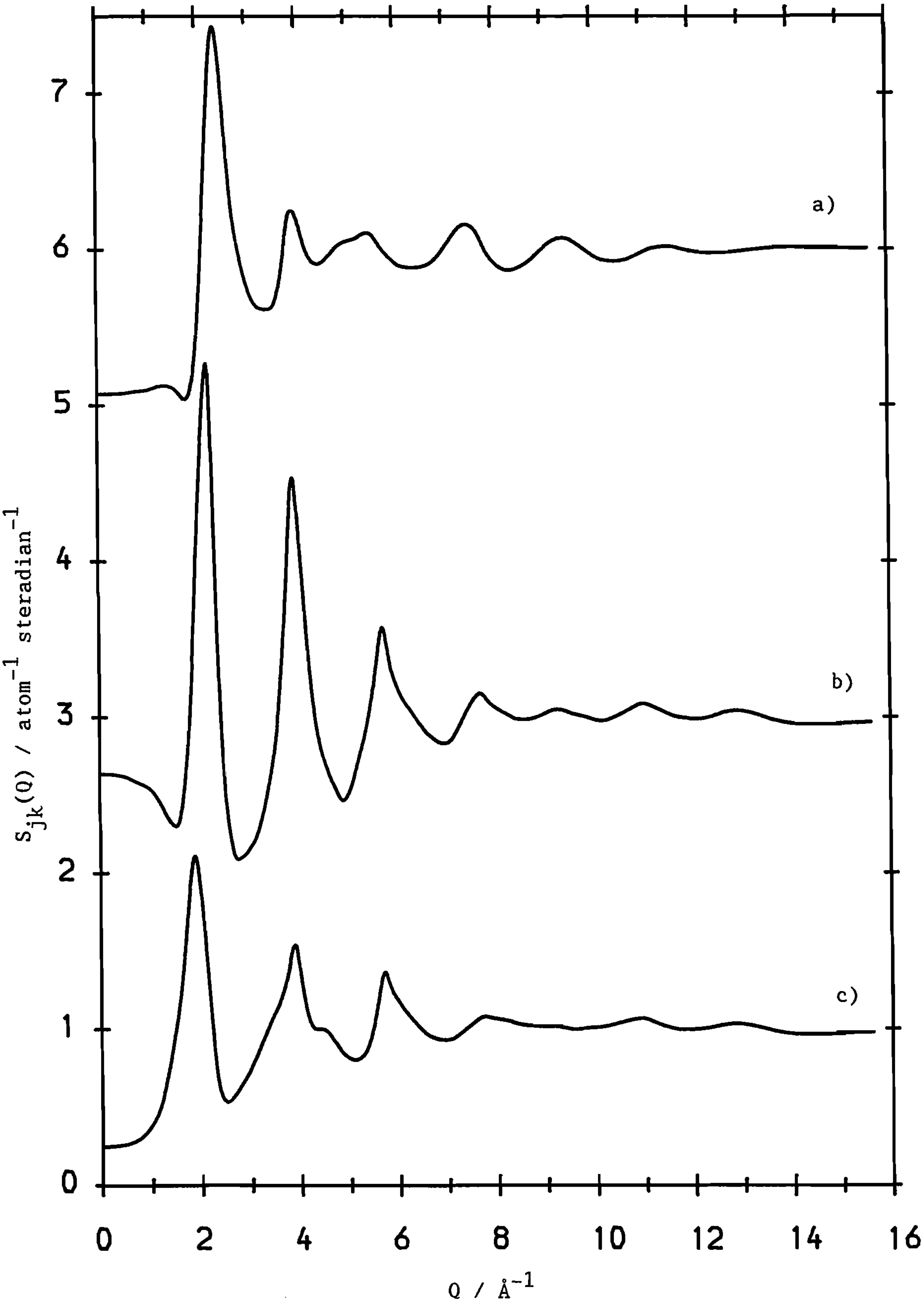

Figure 7.15 The Bhatia-Thornton Number-concentration Partial Structure Factors $S_{jk}(Q)$ for Dy_7Ni_3 as Measured on D4.
a) $S_{nn}(Q)$ {offset 5.0} b) $S_{nc}(Q)$ {offset 3.0} c) $S_{cc}(Q)$

CHAPTER 8

Dy7Ni3 - ANALYSIS AND MODELLING OF ATOMIC STRUCTURE RESULTS.

8.1 PARTIAL COORDINATION NUMBERS AND CSRO PARAMETERS.

8.1.1 PARTIAL CORRELATION FUNCTIONS.

The extraction of the three partial correlation functions $t'_{ll'}(r)$ for Dy_7Ni_3 has been discussed in Chapter 7 and these are shown in figure 7.12 (as measured on D4). For ease of reference the positions of the meaningful (ie. low-r ripples are excluded) maxima are given in table 8.1 for each partial correlation function $t'_{ll'}(r)$;

Dy-Dy	r = 3.535Å, 5.406Å, 6.830Å, 8.524Å, 9.253Å, 10.131Å, 11.662Å, 13.501Å, 15.053Å.
Dy-Ni	r = 2.845Å, 3.990Å, 5.384Å, 6.161Å, 8.640Å, 9.486Å, 10.913Å, 12.012Å, 14.199Å.
Ni-Ni	r = 2.782Å, 4.465Å, 5.565Å, 7.921Å, 10.908Å.

Table 8.1

These positions were determined by fitting a parabola to the maximum experimental data point and the two adjacent points. The first peak of $t'_{NiNi}(r)$ may be seen to occur at a very similar r-value (r_{NiNi}) to the first peak of $t'_{DyNi}(r)$ (r_{DyNi}), whereas for a RCP of hard spheres one would expect r_{NiNi} to differ from r_{DyNi} by the same amount as r_{DyNi} differs from r_{DyDy}. Hence it must be considered whether the first peak of $t'_{NiNi}(r)$ is genuine or whether it is an artefact caused by the coherent scattering length of ^{0}Dy not being exactly zero: A small non-zero $\bar{b}_{Dy}$ value for ^{0}Dy

would have the result that correlations involving dysprosium (mainly Dy-Ni because of the $\bar{b}_{Dy}^{2}$ factor for Dy-Dy correlations as opposed to the $\bar{b}_{Dy}\bar{b}_{Ni}$ factor for Dy-Ni correlations) would not be entirely absent from the correlation function measured for the ${}^{0}Dy_{7}{}^{N}Ni_{3}$ sample. A check for this was performed by subtracting a small factor times $t'_{DyNi}(r)$ from $t'_{NiNi}(r)$ so as to remove the first peak. However, a subtraction of reasonable appearance (ie. oscillating about zero with small excursions) could not be achieved and so it is concluded that the first peak of $t'_{NiNi}(r)$ is genuine and not an artefact due to a scattering length error.

8.1.2 PEAK FITTING AND COORDINATION NUMBERS.

It is usual to extract nearest neighbour distances and coordination numbers from an experimentally determined correlation function. In principle the meaning of this is clear; one can visualise the neighbours of an atom as being divided into a first coordination shell containing nearest neighbours, a second coordination shell containing second nearest neighbours, and so on. The coordination number is then the mean number of atoms in the first coordination shell and the nearest neighbour distance is the mean distance of nearest neighbours from an origin atom. Thus in principle coordination numbers may simply be obtained by integrating the RDF n'(r) (defined by equation (2.5.1)) over its first peak;

$$n = \int_{\substack{\text{first}\\\text{peak}}} n'(r)\,dr \qquad (8.1.1)$$

However, in practice the extraction and interpretation of coordination numbers and nearest neighbour distances is fraught with complications, a fact which is usually overlooked in the literature. These complications arise because of the fact that the first peak (in real-space) is a broad peak which may overlap with features at higher r, rather than a narrow and well-separated peak. The broadening in real-space is due to three effects; real-space resolution, thermal motion and static disorder. Real-space resolution is described by the peak function P(r) which is determined by the Q_{max} of the experimental data and the modification function M(Q) used in the Fourier transformation (see section 4.1.3). The measured correlation function T'(r) is the convolution of P(r) with the 'true' correlation function (ie. that which would be measured with an infinite Q_{max}). As shown in section 4.1.4, the effect of thermal motion may be described in terms of the convolution of T(r) with a Gaussian whose width is determined by the RMS deviation of the distance between two atoms $\langle u_{ll'}{}^2\rangle^{1/2}$ (see equation (4.1.78)). Static disorder is essentially a part of what is being investigated in a measurement of T'(r) and hence its form or width is not known. If it is assumed that static disorder is either very small (as it has definitively been shown to be in conventional glasses) or Gaussian in T(r) as with thermal motion, then the first peak in T'(r) can be described by the convolution of a Gaussian and P(r). JOHNSON, WRIGHT and SINCLAIR (1983) have discussed the use of this function to fit the first peak in T'(r).

In the literature it is common to find that coordination numbers have been obtained by fitting a Gaussian to the RDF with real-space resolution being totally ignored. The coordination number obtained by this method will be somewhat incorrect since the contribution to peak area included in the termination ripples is ignored. Also the nearest neighbour distance obtained by this method is somewhat incorrect since the real-space resolution function for the RDF is not a symmetric function whereas a Gaussian is a symmetric function. (Unlike the case of $T'(r)$ for which $P(r)$ is symmetric.) The use of $T'(r)$ also has the advantage that the quality of the data is readily apparent. That is to say error peaks at low r (see section 7.3.1) and a non-zero slope at low r (see section 7.3.7) which are features of normalisation and correction problems may easily be discerned. For the RDF $n'(r)$ $(=rT'(r))$ the multiplication by r has the result that these signatures of problems in the data analysis are greatly diminished.

An attempt was made to fit a single resolution-broadened Gaussian to the first peak of each of $t'_{DyDy}(r)$, $t'_{DyNi}(r)$ and $t'_{NiNi}(r)$ as measured on D4. For these measurements of the partial correlation functions table 7.4 gives a value of $15.60Å^{-1}$ for Q_{max} which results in a peak function $P(r)$ with full width at half maximum 0.349Å (see section 4.1.3) as shown in figure 8.1 . A least squares method was used to fit the convolution of $P(r)$ with a Gaussian to the first peaks, varying the position, width and height of the Gaussian. A good fit was obtained to the first peak of $t'_{NiNi}(r)$ but not to the first peak of $t'_{DyDy}(r)$ or $t'_{DyNi}(r)$. For the latter two functions a much improved fit was obtained by restricting the fitted range to include the leading edge of the first peak and only the region of the trailing edge close to the maximum of the peak. The results of these fits are shown in figures 8.2 and 8.3 and the forms of the residuals are such as to strongly suggest a second contribution to the first peaks. Consequently a second attempt was made to fit the data using more than one resolution-broadened Gaussian and the results of this are given in table 8.2;

l-l'	$r_{ll'}$/Å	$\langle u^2_{ll'}\rangle^{½}$/Å	$n_{ll'}$/atoms	$n_{l'l}$/atoms
Dy-Dy	3.531±0.005	0.170±0.005	8.85±0.15	-
	3.984±0.039	0.192±0.039	1.56±0.18	-
Dy-Ni	2.837±0.008	0.133±0.011	2.51±0.09	5.86±0.21
	3.215±0.038	0.080±0.038	0.56±0.10	1.31±0.23
	4.018±0.115	0.276±0.095	0.81±0.21	1.89±0.49
Ni-Ni	2.785±0.200	0.191±0.198	1.29±0.78	-
	4.420±0.166	0.284±0.239	3.79±1.45	-
	5.577±0.246	0.514±0.200	8.11±2.47	-

Table 8.2

The sum of two resolution-broadened Gaussians was found to fit the first peaks of $t'_{DyDy}(r)$ and $t'_{DyNi}(r)$ very much better than a single resolution-broadened Gaussian. For $t'_{NiNi}(r)$ and $t'_{DyNi}(r)$ peaks beyond the first peak were fitted as well and the fits obtained are shown in figures 8.4 to 8.6 . There is some question as to whether the third Gaussian fitted to $t'_{DyNi}(r)$ is a genuine peak since it is not obviously apparent in the D2 data (see figure 7.13). However, since the D4 data have a better real-space resolution and greater statistical accuracy the peak will be regarded here as genuine. (Note that, as discussed in section 6.4.1, the errors on $t'_{DyNi}(r)$ are greater than for the other partial functions.) As r increases beyond the first peak value the features in $t'(r)$ tend to merge together so that the process of de-convolution by the fitting of gaussians becomes increasingly difficult, and this is evident in the fit to $t'_{NiNi}(r)$. The accuracy of the partial coordination numbers obtained above is limited to 2-3% as a consequence of the normalisation problems discussed in section 7.3.7 . The question of the validity of these fits may be set in context as follows: As discussed above the broadening of the first peak of t'(r) is due to real-space resolution, thermal motion and static disorder within the first coordination shell. Whilst the broadening due to real-space resolution can be calculated explicitly, the width of the Gaussian due to thermal motion is not known and not even the functional form of the broadening due to static disorder is known. Hence in an experimental measurement of the first peak of t'(r) one cannot necessarily differentiate between the effects of thermal motion and of static disorder. For example if the static disorder is Gaussian in t(r) then its effect is totally indistinguishable from that of thermal motion. It would also be virtually impossible to differentiate these two effects if the static disorder were described by some other function symmetric in t(r). However, since thermal broadening is Gaussian and hence symmetric in t(r), and the effect of real-space resolution is also symmetric in t(r), it may definitely be said that if the first peak is asymmetric in t(r) then this must be due to static disorder within the first coordination shell. Hence an advantage of plotting t'(r), rather than the RDF n'(r) or pair distribution function g'(r), is that the presence of static disorder may easily be discerned. In the case of Dy_7Ni_3 the first peak of $t'_{11'}(r)$ is asymmetric for Dy-Dy and Dy-Ni, indicating the presence of static disorder within the first coordination shell for these two atom pairs. The fitting of two resolution-broadened Gaussians to the first peak of t'(r) can thus be regarded as an attempt to model the static disorder. Of course an attempt to deconvolute totally unresolved peaks by fitting must be regarded with caution. Specifically the fitting of two resolution-broadened Gaussians to the first peak of t'(r) models the static disorder within the first coordination shell by just two well-defined distances (or by two Gaussian distributions of distances). However, it is not clear whether this model could be differentiated from a broad asymmetric distribution of distances as predicted by the various hard sphere based models considered in later sections. Perhaps the strongest evidence in favour of the model is that for $Y_{67}Ni_{33}$ (which has structural similarities to Dy_7Ni_3 - see section 11.1) the second Gaussian component of the unlike-atom correlation function appears to have moved to higher r so that the presence of two peaks is undisputable (MARET, CHIEUX, HICTER, ATZMON and JOHNSON, 1987). Also the fact that the first peak of $t'_{NiNi}(r)$ is Gaussian lends great support to the contention that for Dy_7Ni_3 the first coordination shell atomic separations have narrow distributions about more than one well-defined distance. In order to fully establish this matter it is recommended that a low temperature experiment be performed using a neutron diffractometer on a pulsed source such as ISIS so as to obtain the necessary real-space resolution.

If partial coordination numbers are defined in terms of the total area under the first peak of $t'_{ll'}(r)$ (ie. adding the contributions from both de-convoluted gaussians where appropriate) then this yields the values given in the first row of table 8.3;

	n_{DyDy}	n_{DyNi}	n_{NiDy}	n_{NiNi}
This Work	10.41	3.07	7.16	1.29
WILDERMUTH, LAMPARTER AND STEEB, 1985.	12.4	4.9	10.8	3.0
STEEB and LAMPARTER, 1985; LAMPARTER, 1985.	14.7	4.9	11.0	3.2
Previous row corrected.	10.1	3.4	7.6	0.99

Table 8.3

where n_{DyNi} and n_{NiDy} have been related according to equation (4.1.13). The partial coordination numbers given in the second and third rows of table 8.3 are from a study of $Dy_{69}Ni_{31}$ (WILDERMUTH, LAMPARTER and STEEB, 1985; STEEB and LAMPARTER, 1985; LAMPARTER, 1985) which was performed subsequent to the work described in this thesis and also used the double null isotopic substitution technique (WRIGHT, HANNON, SINCLAIR, JOHNSON and ATZMON, 1984). The partial coordination numbers measured in this later study of $Dy_{69}Ni_{31}$ differ markedly from those obtained in the present study of Dy_7Ni_3. Unfortunately the method used to derive the partial coordination numbers for $Dy_{69}Ni_{31}$ was not given and so a comparison of the different values is difficult. However, figure 8.7 shows the partial RDFs measured for $Dy_{69}Ni_{31}$ by WILDERMUTH, LAMPARTER and STEEB (1985), STEEB and LAMPARTER (1985) and LAMPARTER (1985) and it appears that the quoted partial coordination numbers simply relate to the area under the first peaks of the partial RDFs. The definition of partial RDF used by these workers is such that they oscillate about the total macroscopic number density curve $4\pi r^2 g^\circ$, rather than about the partial number density curve $4\pi r^2 g_l^\circ$ as in the the present work. Thus the partial RDF $n^*_{ll'}(r)$ used by these workers may be related to that used in this thesis by;

$$c_{l'}n^{*}_{ll'}(r) = n'_{ll'}(r) \tag{8.1.2}$$

When this alternative definition of partial RDF is used the area under a peak of $n^{*}_{ll'}(r)$ is converted to a partial coordination number by application of a multiplying factor $c_{l'}$ (see for example MARET, CHIEUX, HICTER, ATZMON and JOHNSON, 1987). The large discrepancy between the partial coordination numbers obtained for Dy_7Ni_3 and those obtained for $Dy_{69}Ni_{31}$ may clearly be seen to be due to the omission of this factor in the studies of $Dy_{69}Ni_{31}$. In fact the value of 14.7 for n_{DyDy} obtained by STEEB and LAMPARTER (1985) is unreasonably large since the coordination number for a crystalline close packing of atoms of one size is 12 and also the largest number of spheres which it is physically possible to pack about another sphere (all one size) is 13. (Actually for Dy_7Ni_3 these considerations are complicated by the presence of nickel and the occurrence of two close but different Dy-Dy near neighbour distances. However, this does not alter the conclusion that a value of 14.7 is unreasonably large for n_{DyDy}.) The fourth row of table 8.3 gives the partial coordination numbers of STEEB and LAMPARTER (1985) and LAMPARTER (1985) corrected by the multiplying factor $c_{l'}$ of equation (8.1.2), and it may be seen that the agreement with the present work is improved. Since the method used by these workers to derive partial coordination numbers is not given, it is not possible to undertake a precise comparison with the values measured for Dy_7Ni_3.

Figure 8.8 shows the partial RDFs $n_{ll'}$ for the present work on Dy_7Ni_3 which were obtained simply by multiplying $t'_{ll'}(r)$ by r. Similarly figure 8.9 shows the partial pair distribution functions $g'_{ll'}(r)$ for Dy_7Ni_3, obtained by dividing $t'_{ll'}(r)$ by $4\pi r$ (WRIGHT, 1980b). The noise at low r below the first peak which is an indication of how well the data has been corrected and normalised is appreciably less for the partial RDFs of Dy_7Ni_3 shown in figure 8.8 than for the partial RDFs of $Dy_{69}Ni_{31}$, shown in figure 8.7 . One of the sources of error in the study of $Dy_{69}Ni_{31}$ is the method used to separate the magnetic scattering as has been discussed in section 7.3.5. Note that the error peaks in the lowest r region ($0<r<1Å$) which have been removed from the Dy_7Ni_3 $t'_{ll'}(r)$ data by a back-transform correction (see section 7.3.7) tend not to be apparent in $n'_{ll'}(r)$ because of the additional factor r ($n'_{ll'}(r) = rt'_{ll'}(r)$). In the region of r of structural significance the published data of WILDERMUTH, LAMPARTER and STEEB (1985), STEEB and LAMPARTER (1985) and LAMPARTER (1985) show a number of small features not observed in the present work: $n^*_{NiNi}(r)$ has an extra contribution to the first peak at lower r, an extra peak at about 3.5Å and a splitting of the peak at 5.6Å. Similarly $n^*_{NiDy}(r)$ has a splitting of the peak at 4.0Å and two extra peaks at about 6.8Å and 7.6Å. Whilst it cannot be absolutely ruled out that these additional features are associated with either the small difference in composition or some difference in preparation of the samples, it seems most likely that they are spurious features due to inadequate analysis of the data. Note that very little difference is to be found between the Dy_7Ni_3 partial correlation functions measured in this study on D4 and on D2 (see figure 7.13).

8.1.3 CSRO PARAMETERS.

In the measurements of the partial structure factors of binary metallic glasses reported in the literature it is common for chemical short range order (CSRO) parameters to be evaluated. Put simply a CSRO parameter is a number, derived from the partial coordination numbers, which characterises the degree of chemical order in the material ie. the extent to which contact between like atoms (or conversely unlike atoms) is preferred or avoided. The use of CSRO parameters first arose in the study of disordered crystalline alloys (see for example COWLEY (1950) or WARREN (1969)), but in recent years they have been much used in the study of the atomic structure of binary metallic glasses. WAGNER and RUPPERSBERG (1981) have generalised the WARREN (1969) CSRO parameter by defining the CSRO parameter for the first coordination shell to be;

$$\alpha_1 = 1 - n^1_{12} \,/\, (\, c_2(\, c_2 n^1_1 + c_1 n^1_2 \,)) \qquad (8.1.3)$$

where $n^1_{ll'}$ is the l-l' partial coordination number for the first coordination shell and;

$$n^1_l = \sum_{l'} n^1_{ll'} \qquad (8.1.4)$$

Similarly CARGILL and SPAEPEN (1981) have defined a CSRO parameter;

$$\eta = (\, n^1_{12}\, n^1_{nn} \,/\, c_2\, n^1_1\, n^1_2 \,) - 1 \qquad (8.1.5)$$

where n^1_{nn} is the coordination number for the first coordination shell obtained from the Bhatia-Thornton (BT) function $n'_{nn}(r)$ (=$rt'_{nn}(r)$, see section 7.3.8);

$$n^1_{nn} = \int_{\substack{\text{first}\\\text{coordination}\\\text{shell}}} n'_{nn}(r)\,dr \tag{8.1.6}$$

$$= c_1 n^1_1 + c_2 n^1_2$$

For a covalent network which is completely chemically disordered CONNELL and LUCOVSKY (1978) have shown that the partial coordination numbers are given by;

$$n^1_{11'} = c_1\,(n^1_1)^2 \;/\; (c_1 n^1_1 + c_2 n^1_2)$$

$$n^1_{12} = c_2\, n^1_1\, n^1_2 \;/\; (c_1 n^1_1 + c_2 n^1_2) \tag{8.1.7}$$

The derivation of these results depends merely upon the statistics of counting the numbers of nearest neighbours of different types. It is not necessary for covalent bonding to occur for a first coordination shell to be defined and for the statistics of the nearest neighbours within the first coordination shell to be enumerated. Hence equation (8.1.7) may be applied to metallic glasses. Substitution of these equations in equations (8.1.3) and (8.1.5) yields CSRO parameters for a completely disordered system as;

$$\alpha_1 = \eta = 0 \tag{8.1.8}$$

In the case of total phase separation n^1_{12} is zero with the result that;

$$\alpha_1 = 1 \quad \text{and} \quad \eta = -1 \tag{8.1.9}$$

For the special case of complete chemical order where there is only 1-2 contact it is found that;

$$\alpha_1 = -2c_1c_2/(c_1^2+c_2^2) \quad \text{and } \eta = 1 \tag{8.1.10}$$

For a covalent network the atomic bonding requirements result in coordination numbers n_1^1 and n_2^1 which are rigidly fixed. This has the consequence that the situation where only [illegible] is non-zero can occur at only one stoichiometry (CONNELL and LUCOVSKY, 1978) given by;

$$c_1 = n_2^1 / (n_1^1 + n_2^1) \tag{8.1.11}$$

At other stoichiometries the maximum chemical ordering that can occur is to have only one of the two like-atom partial coordination numbers equal to zero ie. to have atoms of one type surrounded only by atoms of the other type. There are thus two regimes, one which is rich in atom type 1 compared to the concentration given by equation (8.1.11), and one which is rich in atom type 2. For the 1-rich regime the maximum chemical ordering that can occur is for n_{22} to be zero and the corresponding CSRO parameters are given by (CARGILL and SPAEPEN, 1981);

$$\begin{aligned} \alpha_1^{max} &= 1 - n_2^1 / (c_1(c_2n_1^1 + c_1n_2^1)) \\ \eta^{max} &= c_2 \, n_2^1 / c_1 \, n_1^1 \end{aligned} \tag{8.1.12}$$

However, recent work by SPAEPEN and CARGILL (1985) suggests that the values given by equation (8.1.12) may be over-estimates for close-packed structures. For the 2-rich regime maximum chemical ordering occurs if $n_{11}^1=0$ and the corresponding maximum values of the CSRO parameters are given simply by exchanging 1 and 2 in equations (8.1.12). It is common to quote experimental CSRO parameter values in a renormalised form by dividing by the maximum possible value. Note that even though some of the above results were derived originally for covalent networks they may be applied to metallic glasses since they rely merely on the ability to define a first coordination shell and to count the statistics of the first neighbours contained therein. To the author's knowledge the special case of complete chemical order where there is only unlike-atom contact has never been observed in a metallic glass. (The close-packed structures of metallic glasses probably make such a situation impossible.) However, the maximum chemical order ($n_{22}^{1}=0$) has been observed to occur in dilute ($c_2 \sim 20\%$) T-M alloys such as $Ni_{81}B_{19}$. From the above discussion it may be concluded that $\eta<0$ and $\alpha_1>0$ corresponds to a preference for like-atom contact whilst $\eta>0$ and $\alpha_1<0$ corresponds to a preference for unlike-atom contact.

A prerequisite for the CSRO parameters calculated from a set of partial coordination numbers to have any meaning is that the same definition of first coordination shell has been adopted in the calculation of all of the partial coordination numbers. That is to say the maximum r-value up to which the area of each partial function is evaluated should be the same. The most reasonable definition for a single universal first coordination shell is given by the region of r below the r-value of the first deep minimum of the BT function $n'_{nn}(r)$ since this function gives the topological distribution of atoms regardless of type. Figure 8.10 shows the BT RDFs evaluated for Dy_7Ni_3 from the D4 data. The function $n'_{nn}(r)$ yields a maximum r-value of 4.245Å to define the first coordination shell. Integrating the partial RDFs between this r-value and the lower edge of the first peak yields the partial coordination numbers given in table 8.4;

n^1_{DyDy}	n^1_{DyNi}	n^1_{NiNi}	n^1_{nn}	n^1_{NiDy}	n^1_{Dy}	n^1_{Ni}
10.20	3.69	2.28	12.96	8.60	13.89	10.88

Table 8.4

The method of deriving coordination numbers by integration up to a limit is often used for systems, especially liquids, in which the coordination shells are poorly defined such that the first peak overlaps with the subsequent peaks (see BLACK and CUNDALL (1965) and MIKOLAJ and PINGS (1968)). However, it is usually overlooked that this is an approximate method and that strictly the function which should be integrated (t′(r) or n′(r)) depends upon the relative widths due to real-space resolution and thermal motion.

The n^1_1 values in table 8.4 may be used to calculate partial coordination numbers on the assumption of complete chemical disorder using equation (8.1.7);

$$n^1_{DyDy} = 10.42 \qquad n^1_{DyNi} = 3.50 \qquad n^1_{NiNi} = 2.74 \qquad (8.1.13)$$

The experimental like-atom partial coordination numbers are a little smaller than calculated on the assumption of complete chemical disorder whilst the experimental unlike-atom partial coordination number is a little larger. This indicates a small degree of chemical ordering in the first coordination shell for Dy_7Ni_3 with a preference for unlike-atom contact. The CSRO parameters defined by equations (8.1.3) and (8.1.5) may also be evaluated from the partial coordination numbers of table 8.4;

$$\alpha_1 = -0.044 \qquad \eta = 0.055 \tag{8.1.14}$$

These values also indicate a preference for unlike-atom contact. For the measured coordination numbers n^1_{Dy} and n^1_{Ni} equation (8.1.11) gives the composition at which only n^1_{12} is non-zero as c_{Dy}=0.44 (assuming no variation of total coordination numbers n^1_1 with composition). Thus for the consideration of chemical order Dy_7Ni_3 may be regarded as Dy-rich and if Dy_7Ni_3 were completely chemically ordered there would be no Ni-Ni contact. Equations (8.1.12) give the maximum CSRO parameters corresponding to the measured total coordination numbers as;

$$\alpha_1^{max} = -0.319 \qquad \eta^{max} = 0.336 \tag{8.1.15}$$

It follows that the measured renormalised CSRO parameters are;

$$\begin{aligned} \alpha_1 / \alpha_1^{max} &= 0.14 \\ \eta / \eta^{max} &= 0.16 \end{aligned} \tag{8.1.16}$$

As with coordination numbers, there are complications involved in the consideration of CSRO parameters which are usually overlooked in the literature. These arise because of the need to define a single universal first coordination shell to be used in conjunction with all of the partial RDFs. Firstly the necessary approach of integrating each partial RDF up to a maximum r-value results in partial coordination numbers which are not highly accurate because the resolution- and thermal-broadening of the 'true' partial RDFs will tend to shift area in or out of the universal first coordination shell. A second more serious problem is that when the first peaks of the partial correlation functions occur at different r-values (the so-called 'size effect') the definition of a single universal first coordination shell is of doubtful validity. The concept of CSRO parameters was first developed for the study of disordered crystalline alloys. In this case the position of an atom is always associated with a lattice site so that coordination shells may be precisely defined. For a binary crystalline alloy a particular coordination shell may contain atoms of both elements and the CSRO parameter for that coordination shell is then defined in terms of the relative number of atoms of each element in that shell. Such a picture is quite inappropriate to a binary amorhpous alloy for which the coordination shells for different atom pairs occur at different r-values. This is illustrated most clearly by the data for Dy_7Ni_3. The universal first coordination shell is defined by a maximum r-value of 4.245Å. However, for the Ni-Ni correlation function this r-value occurs well within the second peak at 4.420Å which is clearly an unreasonable definition of the first coordination shell. Following the work of LEE, JOST, WAGNER and TANNER (1985), it has been proposed (MARET, CHIEUX, HICTER, ATZMON and JOHNSON, 1987) that CSRO be characterised by the function $\alpha(R)$ which is a generalisation of the CSRO parameter of WAGNER and RUPPERSBERG (1981);

$$\alpha(R) = 1 - z_{12}(R) / (c_2(c_1 z_2(R) + c_2 z_1(R))) \tag{8.1.17}$$

where;

$$z_{11'}(R) = \int_0^R n'_{11'}(r)\, dr \tag{8.1.18}$$

$\alpha(R)$ was evaluated for Dy_7Ni_3 and is shown in figure 8.11. The function $\alpha(R)$ may be taken to be the CSRO parameter α_1 as a function of the maximum distance R chosen to define the first coordination shell. From the figure it is clear that the value obtained for the CSRO parameter depends strongly on the choice of R and in fact it is even possible to obtain values of different sign. This shows firstly that a quoted value for a CSRO parameter is meaningless unless the method used to obtain it is given. Secondly the usefulness of CSRO parameters is demonstrated to be questionable.

Since the CSRO varies continuously with different first coordination shells for the different partial RDFs one might propose the use of an alternative function to characterise CSRO;

$$\alpha'(r) = 1 - n'_{12}(r) \;/\; (\, c_2(\, c_1 n'_2(r) + c_2 n'_1(r) \,)\,) \qquad (8.1.19)$$

However, this function may be shown to reduce to;

$$\alpha'(r) = c_2\, n'_{cc}(r) \;/\; (\, c_2 n'_{cc}(r) + n'_{12}(r) \,) \qquad (8.1.20)$$

Hence it is concluded that the most reasonable way to characterise CSRO is by use of a continuous function, rather than a single parameter, and that the most appropriate function is the BT function $t'_{cc}(r)$. However, it is the opinion of this author that greater insight into the atomic structure of metallic glasses may be obtained by attempting to model the full available experimental information (ie. the three partial functions) rather than just considering a single facet of it (ie. a CSRO parameter).

8.2 HARD SPHERE MODELS OF ATOMIC STRUCTURE.

8.2.1 RCP OF HARD SPHERES.

The 12-fold coordinated Goldschmidt radii of dysprosium and nickel are

1.77Å and 1.24Å respectively (ELLIOTT, 1965). A binary RCP of hard spheres (see section 6.1.3) with these two radii would have the nearest neighbour distances given in the first row of table 8.5;

	r_{DyDy}/Å	r_{DyNi}/Å	r_{NiNi}/Å
RCP of Hard Spheres	3.54	3.01	2.48
Dy_7Ni_3	3.531	2.837	2.785

Table 8.5

A comparison of these values with the experimental values as given in the second row of the table shows that the value of r_{DyDy} for Dy_7Ni_3 is very close to that predicted by a RCP of hard spheres with the Goldschmidt radii. However, the value of r_{DyNi} for Dy_7Ni_3 is 6% smaller than predicted by this simple model, indicating a strong bonding interaction between Ni and Dy. The value of r_{NiNi} for Dy_7Ni_3 is 12% higher than for the RCP of hard spheres, indicating an avoidance of direct contact between Ni atoms. From a hard sphere viewpoint the Ni atoms may be said to be 'close but not touching'. Thus it is not clear whether the first peak of $t'_{NiNi}(r)$ should be regarded as arising from first neighbours or second neighbours, again illustrating the limitations of the 'universal coordination shell' approach to atomic structure. The experimental nearest neighbour distances r_{DyDy} and r_{DyNi} may be used to deduce atomic radii r_{Dy}=1.765Å and r_{Ni}=1.072Å. The deduced value of r_{Ni} would result in a Ni-Ni distance of 2.143Å if the nickel atoms were in contact. However, the experimental value of r_{NiNi} is considerably larger than this, again showing that on a hard sphere model the nickels are 'close but not touching'. (Note that this approach has already yielded more specific information about the structure than was obtained by the calculation of CSRO parameters.)

In order to compare the atomic structure of Dy_7Ni_3 more fully with that for a hard sphere model it is necessary to compare the partial correlation functions $t_{ll'}(r)$. To the author's knowledge there have been no MD simulations which are suitable for comparison with the Dy_7Ni_3 experimental data. The MD simulations whose parameters and approach are closest to what would be required for such a comparison is that reported by BERNU, HIWATARI and HANSEN (1985a, 1985b) and BERNU, HANSEN, HIWATARI and PASTORE (1987). In these simulations a binary soft sphere system was quenched through the glass transition for a variety of different parameters and conditions. However, a radius ratio (see section 8.3.1) of 1.4 and a mass ratio of either 2 or 4 was used for all of the simulations. These values are sufficiently at variance with the Dy_7Ni_3 values (radius ratio~1.65, mass ratio=2.77) for a comparison to be of only limited use and the two approaches described below were adopted instead.

8.2.2 THE PY EQUATION FOR A BINARY HARD SPHERE SYSTEM.

The first approach used was to calculate the partial structure factors for a binary hard sphere liquid by use of the PERCUS-YEVICK (1957) equation. The PERCUS-YEVICK (PY) equation is an approximate result used to relate the structure of a liquid to the interatomic potential. For a monatomic system the PY equation is;

$$c(r) = (1 - \exp(\phi(r)/kT)) g(r) \qquad (8.2.1)$$

where $\phi(r)$ is the interatomic potential, $g(r)$ is the pair distribution function defined by equation (4.1.6) and c(r) is a function known as 'the direct correlation function'. The direct correlation function arises in the theory of liquid structure when the total correlation between two particles is separated into two contributions;

$$g(r) - g^\circ = c(r) + \int c(|\underline{r}'|) \, (g(|\underline{r}-\underline{r}'|) - g^\circ) \, d\underline{r}' \qquad (8.2.2)$$

The first term c(r) represents correlations which are transmitted directly between two particles whilst the second term represents correlations transmitted via a third particle. Equation (8.2.2) is due originally to ORNSTEIN and ZERNIKE (1914). c(r) is defined here as a density in the same way as g(r) so that a factor of g° in the convolution term of equation (8.2.2) is unnecessary. The PY equation (8.2.1) results from neglecting terms in a cluster expansion and a detailed discussion of its derivation is beyond the scope of this thesis.

The PY equation (8.2.1) was solved by LEBOWITZ (1964) to give the partial pair distribution functions $g_{ll'}(r)$ for a binary hard sphere system. Subsequently analytic expressions for the partial structure factors were derived by ASHCROFT and LANGRETH (1967) and ENDERBY and NORTH (1968). The partial structure factors are found to be functions of only four parameters: the two hard sphere diameters, the stoichiometry and the atomic number density. The expressions for the partial structure factors are extremely convoluted algebraically and the paper of ASHCROFT and LANGRETH (1967) is to be recommended for the clearest exposition.

Considerable difficulty was encountered in obtaining a computer program to calculate the PY equation expressions for the partial structure factors for a binary hard sphere system. For example the program in WASEDA's (1980) book does not work. Eventually a program due to GILLAN (1986) was used to calculate the partial structure factors $S_{ll'}(Q)$ and thence the functions $i_{NO}(Q)$, $i_{UN}(Q)$ and $i_{ON}(Q)$ required for a direct comparison with experiment. In order to include the effects of thermal motions these were multiplied by a Debye-Waller factor (see section 4.1.4) with a value of 0.18Å for the RMS displacement of an atom $\langle u_l^2\rangle^{1/2}$ (both elements). This is equivalent to a RMS bond length variation $\langle u_{ll'}^2\rangle^{1/2}$ of 0.1470Å (equation (4.1.73)) which is roughly consistent with the experimental values in table 8.2 . In using this value it is implicitly assumed that most of the Gaussian width obtained by the fits is due to thermal motion rather than static disorder, whereas in fact some of the structural models considered in this Chapter do suggest a significant amount of static disorder. Thus it is possible that the value of 0.1470Å is somewhat of an overestimate of $\langle u_{ll'}^2\rangle^{1/2}$ and it may be that the PY equation calculations (and those of the models considered in later sections) have been broadened for the effect of thermal motion by too much. However, as discussed in section 8.1.2, the effects of static disorder and thermal motion are not easily separated and there is no straightforward solution to this problem. One might consider optimising the value of $\langle u_{ll'}^2\rangle^{1/2}$ used to simulate the effect of thermal motion so that the first peak of the correlation function agrees as well as possible with experiment, although this would sometimes result in physically unreasonable values or not be possible. The PY calculations in Q-space were Fourier transformed to obtain partial correlation functions using a Q_{max} of 15.60Å^{-1} and the LORCH (1969) modification function as with the D4 experimental data. The above procedure was repeated a number of times with different Dy and Ni hard sphere diameters so that these two parameters could be optimised empirically. The stoichiometry and the atomic number density were set to the correct values for Dy_7Ni_3 and these two parameters were not varied. Following the finding that in Dy_7Ni_3 the Ni atoms are 'close but not touching', the hard sphere diameters were optimised so that the maxima of the first peaks of the calculated $t'_{DyDy}(r)$ and $t'_{DyNi}(r)$ functions coincided with experiment. The final optimised hard sphere diameters are $d_{Dy}=3.347Å$ and $d_{Ni}=1.938Å$. These values are significantly smaller than those deduced previously. This is because the hard sphere diameters represent an absolute lower limit for interatomic distances with the result that after the partial correlation functions have been broadened their first peaks are at higher r-values than predicted by the hard sphere diameters. Figures 8.12 and 8.13 compare the calculation with experiment in reciprocal- and real-space respectively. The general form of the calculated $t'_{DyDy}(r)$ is very similar to the measured function. The experimental Dy-Dy data shows a more detailed structure than the calculation as would be expected for a solid as compared to a liquid. In particular the detailed form of the group of three peaks following the first peak in the experimental correlation function is not reproduced, although the first two troughs are reproduced well. (Note that in general the model comparisons in this Chapter will concentrate on real-space, rather than reciprocal-space, since a detailed comparison in reciprocal-space is generally only worthwhile if the SRO is at least approximately right - this is not the case for any of the models considered.) It is concluded that the Dy-Dy structure is strikingly similar to that for a hard sphere system. However, the agreement is less good for $t'_{DyNi}(r)$ and not at all good for $t'_{NiNi}(r)$. This is because the hard sphere potential does not take into account the interactions which lead to chemical ordering ie. the preference for Dy-Ni contact and the avoidance of Ni-Ni contact. Note that the high-r limits of the partial correlation functions agree because the correct stoichiometry and atomic number density were used in the calculations.

According to WAGNER (1986) the BT function $S_{nc}(Q)$ of a number of amorphous metals is found to agree surprisingly well with the hard sphere PY equation prediction. Hence figures 8.14 and 8.15 show a comparison of the Dy_7Ni_3 data in reciprocal- and real-space with the BT functions calculated according to the hard sphere PY equation. As found by WAGNER (1986) the best agreement is for the number-concentration functions which are a measure of the size effect. The number-number functions agree a little less well - a good agreement for these functions would indicate that topologically the atoms behave as hard spheres. The worst agreement is for the concentration-concentration functions, indicating the lack of chemical ordering in the model. The positive peak in the calculated $t'_{cc}(r)$ at about 2.1Å indicates a preference for like-atoms (Ni-Ni) at this distance which is in complete disagreement with experiment.

8.2.3 THE FINNEY MODEL.

A quantity frequently used in the characterisation of hand-built hard sphere RCP models is the packing density (or packing fraction) η. The packing density is simply the fraction of the total volume which is occupied by the hard spheres. A partial packing density η_1 may be defined as follows;

$$\eta_1 = c_1 \, g^{\circ} \, (4\pi/3) \, r_1^{\,3} \qquad (8.2.3)$$

where r_1 is the radius of spheres of type 1. Using the Dy atomic radius deduced from the experimental nearest neighbour distance yields a value $\eta_{Dy}=0.6354$. This value is strikingly similar to the value of 0.6366±0.0004 obtained by FINNEY (1970) for his hand-built single sphere size model (see section 6.1.3). The same value has also been obtained by SCOTT and KILGOUR (1969) for a RCP of steel spheres and it may be that this value is a fundamental geometrical property of a RCP of hard spheres. Since the experimental η_{Dy} value is so close to the model packing density the total correlation function of the FINNEY (1970) model was compared with the experimental function $t'_{DyDy}(r)$. (Note that as shown by equation (8.2.3) the value obtained for η_{Dy} is very strongly dependent on the value used for r_{Dy} and so it may be fortuitous that the experimental η_{Dy} value is so close to the model packing density.)

A central sphere of the (unrelaxed) FINNEY (1970) model containing 3500 hard spheres was used to calculate t(r) (WRIGHT, 1987) which was then corrected for the finite size of the model (equation (2.5.3)). The model t(r) was broadened in such a way as to simulate both the effect of experimental real-space resolution and of thermal motion. This was achieved by convolution with the peak function P(r) appropriate to the D4 data (equation (4.1.59)) and by convolution with a Gaussian with a width $\langle u_{11'}{}^2\rangle^{½}=0.147Å$ (equation (4.1.78)) respectively. The same procedure is also used in all of the model comparisons described below with the result that the model function compared with experiment is truly the same function; a comparison of unbroadened model functions with experiment can be misleading. The r-axis for the model was scaled so that after broadening the third peak of the model t'(r) coincided with the fourth peak of the experimental $t'_{DyDy}(r)$ at 6.830Å. After this scaling the model and the experimental first peaks were also found to occur at very similar r-values. The scaling factor used corresponds to a radius of 1.748Å for the hard spheres of the model. This compares favourably with the value of 1.765Å deduced from the resolution-broadened Gaussian fit to $t'_{DyDy}(r)$. A comparison between the model and experimental correlation functions is given in figure 8.16 .

The Finney model correlation function is quite similar to the Dy-Dy correlation function calculated according to the PY equation, as might be expected since both are based on hard spheres; the main differences are that for the Finney model the correlation function has more emphasised features and that the trough following the first peak is not as deep. When compared with the experimental Dy-Dy correlation function the Finney model predicts the first and fourth peaks very well. However, the second experimental peak is missing in the model, the third peak is too high and the trough following the first peak is not deep enough. As FINNEY (1970) has explained, the features occurring in the correlation function for a RCP of hard spheres may be interpreted qualitatively in terms of collineation of hard spheres. In a RCP of hard spheres any conceivable small group of spheres in contact will occur, and furthermore it will occur with all possible orientations between the spheres. The maximum separation between the spheres in such a group occurs when the spheres are collinear/coplanar and it follows that a decrease in the correlation function is to be expected at a distance just above this maximum separation. The groups of spheres relevant to a discussion of Dy-Dy distances in Dy_7Ni_3 are shown in figure 8.17 . Trivially a decline in the correlation function is to be expected after a distance equal to the Dy diameter (atomic configuration 1 in figure 8.17) and of course this is seen. The decrease of the model and experimental correlation functions in the region of 7.5Å may be understood in terms of atomic configuration 7. This trough is so particularly deep because atomic configuration 7 gives the largest Dy-Dy separation for any of the small groups of spheres. The smaller trough at about 6.2Å may similarly be understood in terms of atomic configuration 6. The decline of the experimental Dy-Dy correlation function at about 5.5Å is probably associated with atomic configurations 4 and 5. Since these atomic configurations involve the minority atom (Ni) their associated feature is not seen in the Finney model correlation function. (The terms minority or majority may be taken to mean an atomic concentration less than or greater than 50% respectively. In all of the work considered here the minority atoms are also the smaller atoms.) It may thus be concluded that it is necessary to explicitly include the minority atoms in a hard sphere model of Dy_7Ni_3. There is no feature in the experimental Dy-Dy correlation function which may be associated with the atomic configuration 3. Hence it is concluded that atomic configuration 3 with the four atoms coplanar does not occur in Dy_7Ni_3. This can be interpreted as evidence in favour of a more ordered model, such as the trigonal prismatic models discussed in section 8.3.2 . Atomic configuration 2 cannot occur in Dy_7Ni_3 since it would involve contact between Ni atoms which is not observed experimentally (and is also evidence in favour of a more ordered model).

Using the Ni atomic radius deduced from the experimental Dy-Ni and Dy-Dy nearest neighbour distances yields a partial packing density η_{Ni}=0.0610 and hence a total packing density η=0.6964. Thus the volume which is occupied by nickel atoms in Dy_7Ni_3 is very much smaller than that occupied by dysprosium atoms and it might be that the structural role of Ni is subsidiary to that of Dy with the Ni atoms occupying positions determined by the Dy structure. An attempt was made to investigate this hypothesis by comparing the experimental data with a previous analysis (WRIGHT, 1987) of the holes in the FINNEY (1970) model. This analysis used a central sphere of the (unrelaxed) Finney model containing 2000 hard spheres. Hard spheres with a diameter equal to half that of the original spheres were placed in all of the holes of the original packing which are large enough. A few of the larger holes were able to accept two of the small spheres. This approach was inspired by POLK's (1970) suggestion that the larger majority atoms of a metallic glass have a RCP structure with the smaller minority atoms occupying the larger holes inherent in the packing. The holes in the 2000-atom central sphere of the Finney model were found to be sufficient to accept 334 of the small atoms, corresponding to a minority atom concentration of 14.3%. This is the maximum minority atom concentration that can be achieved with a minority atom diameter equal to half the majority atom diameter. Since Dy_7Ni_3 has a minority atom concentration of 30% and the Ni diameter is larger than half the Dy diameter it is obvious that the pure RCP+interstitial structural model must be rejected. Notwithstanding this, a comparison was performed between the Dy_7Ni_3 partial correlation functions and those for the Finney model with interstitial minority atoms to investigate whether this model is able to reproduce any of the salient features of the experimental data. A complication with such a comparison is that the model has a different stoichiometry to Dy_7Ni_3. However, as with a model of the same stoichiometry the partial correlation functions $t_{11'}(r)$ were used for the comparison. This is because it is the SRO that is of interest and $t_{11'}(r)$ is the appropriate function for comparing SRO. For example if in Dy_7Ni_3 the nearest neighbour environment of Ni about Ni were as predicted by the model then the first peak of $t_{NiNi}(r)$ would be the same as the first peak of $t_{11}(r)$ for the model (1=minority atom). Of course the difference in stoichiometries has the consequence that the high r limits (equation (4.1.23)) of the model and experimental correlation functions should not be expected to agree. The partial correlation functions $t'_{11'}(r)$ were used to compare the atomic structure of Dy_7Ni_3 with all of the models discussed in the subsequent sections, regardless of stoichiometry.

The comparison between the Dy_7Ni_3 partial correlation functions and those for the Finney model with interstitial minority atoms is shown in figure 8.18 . The first peaks of the two unlike-atom correlation functions occur at different r-values merely because the model minority atoms are too small. The model allows minority atoms to come into contact, as shown by the first peak in the model 'Ni-Ni' correlation function. This disagrees with experiment. However, it might be that if larger minority atoms had been used then it would not be possible for two minority atoms to fit into any of the holes in the RCP structure. Whilst this would correctly avoid Ni-Ni contact, the first Ni-Ni peak for the model would then be at about 4.4Å which is much too high. Clearly the model in which minority atoms are interstitially positioned in a majority atom RCP structure does not even have some kind of qualitative agreement with experiment and it should be rejected outright. As predicted above by consideration of the Dy-Dy correlation function from a hard sphere viewpoint it is found to be necessary to explicitly include the minority atoms in a RCP model. The view that the atomic structure of Dy_7Ni_3 is essentially determined only by the Dy atoms is not satisfactory and in fact the Ni atoms must play an important structural role.

8.3 TRIGONAL PRISMATIC MODELS OF ATOMIC STRUCTURE.

8.3.1 COORDINATION POLYHEDRA AND HOLE FILLING.

Another quantity frequently used in the characterisation of binary hard sphere models is the radius ratio σ_r, given by the ratio of the linear dimensions of the two types of hard sphere;

$$\sigma_r = (r_l/r_L) = (2r_{lL}/r_{LL}) - 1 \qquad (8.3.1)$$

where the indices l and L refer to minority and majority atoms respectively. WRIGHT (1986) has calculated the critical radius ratio required for a smaller minority atom to occupy each of the Bernal holes (see section 6.1.3) with the larger majority atoms at the vertices. This calculation assumes that if the atom in the hole is not large enough to be simultaneously in contact with all of the majority atoms then the polyhedron is unstable. The critical radius ratio for a particular Bernal hole occurs when the atom in the hole is just large enough to be in contact with all of the majority atoms. As σ_r is increased above the critical value the polyhedron remains stable until the point is reached where an extra majority atom can be included. Note that the approach here is in a sense the converse of that described at the end of the previous section where minority atoms were placed in the holes of the Finney model; here the minority atoms disturb the majority atom structure whereas in the previous approach minority atoms were only placed in the holes if they did not disturb the majority atom structure. Some of the results of WRIGHT's (1986) calculations are given in table 8.6;

	Radius Ratio	n_{1L}	r_{1L}/r_L
Tetrahedron	0.225	4	1.225
Tetragonal Dodecahedron Dodecahedron	0.353	4	1.353
Octahedron	0.414	6	1.414
Trigonal Prism	0.528	6	1.528
Archimedean Anti-Prism	0.645	8	1.645
Dy_7Ni_3	0.607	7.16 (5.85,1.32)	1.607

Table 8.6

where the calculated value of r_{1L} assumes that the minority atom is at the centre of the Bernal hole which is itself entirely regular. The last row of table 8.6 gives experimental values for Dy_7Ni_3 as calculated from the results of the resolution broadened Gaussian fits given in table 8.2 . The radius ratio for Dy_7Ni_3 is well above the critical radius ratio for a trigonal prism but below that for an Archimedean anti-prism. Hence if a nickel atom is to be placed at the centre of a Bernal hole with dysprosium atoms at the vertices then it is the trigonal prism for which this results in a stable structure. The experimental partial coordination number and nearest neighbour distance given in table 8.6 are also between the values for a trigonal prism and an Archimedean anti-prism which supports this conclusion (see section 11.1 for a more detailed discussion).

8.3.2 GASKELL'S TRIGONAL PRISMATIC MODELS.

The hole-filling argument given above indicates that the trigonal prism is the stable Ni coordination polyhedron for Dy_7Ni_3. Hence the measured partial correlation functions for Dy_7Ni_3 were compared with the partial correlation functions for the two hand-built trigonal prismatic models discussed in section 6.1.3 . The method used to calculate the partial correlation functions of the relaxed models was as follows: First the centre of the model was determined by taking moments with equal weights for all sites. The density was then calculated as a function of diameter for a sphere with this centre. When this is done it is found that above a critical value of sphere diameter the density declines steadily. This is simply due to the surface of the sphere beginning to extend beyond the surface of the model. Only those sites within the sphere of the critical diameter were used in the analysis. the coordinates of the model were scaled with a suitable approximate scaling factor and then the partial correlation functions were calculated using the finite model size correction of equation (2.5.3). (The reason for choosing to use a spherical portion of the model is so that this correction may be applied.) These were broadened for experimental real-space resolution and thermal motion in the same way and with the same parameters as has been described for the Finney model in section 8.2.3 . A precise scaling factor for the coordinates of the model was then determined so that the first peak of $t'_{1L}(r)$ for the model (L=majority atom) would coincide exactly with the first peak of

$t'_{DyDy}(r)$. After application of the precise scaling factor the partial correlation functions were re-calculated and re-broadened. Table 8.7 gives the diameter of the spherical portion of each model used in the analysis (after precise scaling) and also the numbers of atoms involved;

Model		GASKELL (1979)	DUBOIS, GASKELL and Le CAËR (1985)
Truncation Diameter / Å		29.546	38.716
Majority Atom Diameter / Å		3.560	3.532
Radius Ratio		0.74	0.628
Original Number of Atoms	Majority	431	1456
	Minority	108	365
Final Number of Atoms	Majority	341	832
	Minority	91	211
Final c_L / %		78.94	79.77

Table 8.7

The version of the earlier model used here is that which was relaxed with constraints to maintain the trigonal prisms whilst the version of the later model used here was relaxed with unconstrained topology. For the earlier model such constraints had a significant effect, whereas the difference was minimal for the later model, and this could be associated with model size. figure 8.19 shows the density as a function of sphere diameter for the two models. For the later model the density shows more oscillatory behaviour to a higher value of sphere diameter. Possibly this is an indication of the micro-crystalline origin of the model, although surprisingly the partial correlation functions for the model show no obvious sign of micro-crystallinity. According to the original paper (DUBOIS, GASKELL and Le CAËR, 1985) only the central 400-500 atoms of the model should be used (truncation diameter~28Å when the coordinates are scaled for Dy_7Ni_3) because the polyhedra nearer the surface of the model are extensively distorted. However, in the present study the calculations were also performed with a truncation diameter of 28.260Å and no appreciable differences were apparent when the resultant correlation functions were compared with those calculated using the truncation diameter in table 8.7 . Hence the correlation functions calculated using the larger value were preferred for the comparison with the Dy_7Ni_3 experimental data. Another point arising in the consideration of this model is static disorder within the first coordination shell (see section 8.1.2). In their comparison of their model with the experimental data for $Ni_{81}B_{19}$ DUBOIS, GASKELL and LeCAËR (1985) simulate the effect of real-space resolution by broadening its correlation functions with a Gaussian. The width of this Gaussian was chosen so that the model and experimental first peaks then had the same width. This was an incorrect procedure since the model correlation functions should have been convoluted with the relevant P(r) of the correct width to simulate the effect of real-space resolution. In fact, as DUBOIS, GASKELL and LeCAËR (1985) acknowledge, the widths used in broadening the model correlation functions were only about 60% of the correct widths. If the model correlation functions had been correctly broadened it would have been found that the model correlation functions followed the experimental correlation functions more closely at higher r. It would also have been found that the contribution to the first peak width due to static disorder inherent in the model is greater that the experimentally determined peak width due to static disorder and thermal motion combined. Thus, whilst static disorder is hard to enumerate due to the difficulty in separating its effects from those of thermal motion (see section 8.1.2), it can be useful in extreme cases to indicate where the static disorder of a model is much too large. That is to say, if the static disorder width of a model is greater than the experimental width due to the combination of static disorder and thermal motion then the static disorder of the model is obviously too large. In the case of the model under consideration here the excessive static disorder may well be due to the use of a LJ potential to relax the model. It would be surprising if Lennard-Jonesium were to condense into a trigonal prismatic structure since the LJ potential is not really very different from a hard sphere potential. Thus the question is raised here as to whether the LJ potential should be used to relax trigonal prismatic models and indeed GELLATLY and FINNEY (1982) have concluded that after relaxation with a LJ potential very few of the M atoms of the GASKELL (1979) model have a trigonal prismatic coordination polyhedron. It might be better not to relax a model at all, rather than to do so with a wrong potential. Another possibility would be to use experimentally determined potentials as suggested by LI and COWLAM (1987). After scaling for Dy_7Ni_3 the model of DUBOIS, GASKELL and LeCAËR (1985) has static disorder (Dy-Dy) of FWHM~0.29Å whilst the fit values given in table 8.2 yield a combined static disorder and thermal motion FWHM of 0.40Å for the first peak of $t'_{DyDy}(r)$. Hence for Dy_7Ni_3 the model does not disobey the static disorder criterion.

Figures 8.20 and 8.21 show the comparison between the experimental Dy_7Ni_3 partial correlation functions and those of the models of $Pd_{80}Si_{20}$ (GASKELL, 1979) and of $Ni_{80}B_{20}$ (DUBOIS, GASKELL and LeCAËR, 1985) respectively. The Dy-Dy correlation functions of both of the models are very similar to those of the hard sphere models considered in section 8.2 . In the model correlation functions the trough following the first peak is not as deep as it is in the experimental data. In the model correlation functions the first peak is followed by a group of two peaks, whereas the experimental data exhibits a group of three peaks. It appears that the first of these three peaks is entirely absent from the model. Of course, since the model stoichiometries are different from that of Dy_7Ni_3, the high-r limits of the model correlation functions do not agree with the experimental data. For both models the first peak of the Dy-Ni correlation functions occurs at too high an r-value compared to the experimental data. This is simply because the models have a different radius ratio compared to the experimental value for Dy_7Ni_3 given in table 8.6 . Thus the $Ni_{80}B_{20}$ unlike-atom first peak is closer to the experimental peak because its radius ratio has a more similar value. The general form of the model unlike-atom correlation functions is roughly similar to that of the experimental Dy-Ni correlation function. However, it is when compared with the experimental Ni-Ni correlation function that the models show the most discrepancy. Both models are designed to reproduce the complete chemical order that has been observed in dilute T-M alloys (see section 6.1.3). ie. the first M-M peak of the models corresponds to second nearest neighbours. Thus the experimental first Ni-Ni peak which corresponds to atoms which are 'close but not touching' is not reproduced. Since in trigonal prismatic models there is only one minority atom in each trigonal prism, it is this third partial correlation function that is the most immediately sensitive to the manner in which the prisms are connected to each other. Hence it is concluded that a successful trigonal prismatic model for Dy_7Ni_3 would have to have at least some prisms connecting together by some other means than that used in the models considered above (Fe_3C type triangle edge sharing). This is discussed is more detail in section 11.1 .

8.4 THE ATOMIC SRO OF RELATED CRYSTALS.

As pointed out in section 2.5.3 it is frequently found that the basic structural unit in an amorphous solid is the same as in the corresponding crystalline material. Hence it can be most worthwhile to compare the measured atomic structure of an amorphous solid with the SRO of related crystals.

The chemistry of RE elements is mostly very similar indeed and many RE compounds are isostructural for different REs. For RE-TL systems the RE-rich crystal phases all have atomic structures which may be described in terms of (slightly distorted) trigonal prisms. Meanwhile the TL-rich crystal phases are found to exhibit Laves phase structures. The RE environment in the cubic RE-TL_2 Laves phase (WELLS, 1962) is illustrated in figure 8.22 . The RE atom has 12 TL nearest neighbours situated at the corners of a truncated tetrahedron. This structural unit is maintained in Laves phases with other stoichiometries, the key structural difference being the different ways that the units connect together. Dy_7Ni_3 is obviously not a TL-rich alloy and the experimentally determined value of 3.07 for n_{DyNi} is greatly at variance with the value of 12 for the Laves phase structural unit; hence Ni-rich crystal phases were not investigated as prototypes for the atomic structure of amorphous Dy_7Ni_3.

The phase diagram of the Dy-Ni system (figure 6.4; ZHENG and WANG, 1982) indicates that 10 crystalline compounds are formed between dysprosium and nickel. Of these 10 crystal phases Dy_3Ni (c_{Dy}=75%) and Dy_3Ni_2 (c_{Dy}=60%) have the closest atomic composition to amorphous Dy_7Ni_3 (c_{Dy}=70%). As predicted by the hole-filling argument at the start of section 8.3.1, both Dy_3Ni and Dy_3Ni_2 have crystal structures based upon a Dy_6Ni trigonal prismatic unit. Essentially this unit defines the Ni coordination polyhedron. Dy_3Ni has the Fe_3C cementite structure and this may be visualised in terms of layers of trigonal prisms (LEMAIRE and PACCARD, 1967) as shown in figure 8.23 . Each layer is composed of chains of trigonal prisms which are linked together through square edge sharing units. Each chain is composed of alternating triangle edge sharing trigonal prisms which are tilted relative to the chain axis. This tilting has the result that a Dy atom is positioned half-octahedrally over one of the square faces of each prism, defining the base of the next prism in the chain. This is the method of connecting prisms upon which the GASKELL (1979) model was based. Each successive layer of trigonal prisms in Dy_3Ni is shifted by half a prism unit in the direction of the chains and by one prism unit in the direction perpendicular to the chains. Unlike Dy_3Ni, Dy_3Ni_2 is not isostructural with a large number of other compounds of the same stoichiometry. The structure of Dy_3Ni_2 may be visualised in terms of 4-fold columns of trigonal prisms (MOREAU, PACCARD and PARTHÉ, 1974) as shown in figure 8.24 . Each 4-fold column can be envisioned as being composed of four single columns, where a single column is composed of triangle face sharing trigonal prisms. These single columns share square faces to form a 4-fold column. Each 4-fold column is shifted by half a trigonal prism height relative to the adjacent 4-fold columns, as indicated in figure 8.24 . This has the result that Dy atoms of one 4-fold column are positioned half-octahedrally over the square prism faces of the adjacent 4-fold columns. As is discussed in more detail in section 11.1, the trigonal prisms in Dy_3Ni_2 are irregular and consequently the nickel atoms in a 4-fold column form zig-zags perpendicular to the column length. As will be discussed below, the atomic structure of amorphous Dy_7Ni_3 was compared with the SRO in crystalline Dy_3Ni and Dy_3Ni_2. The Dy-Ni system does not form a crystal phase with a RE concentration of 70% and neither do most other RE-TL systems. However, an exception to this is the Ce-Ni system which forms Ce_7Ni_3 instead of Ce_3Ni which does not occur (ROOF, LARSON and CROMER, 1961). The SRO of crystalline Ce_7Ni_3 was also compared with the atomic structure of amorphous Dy_7Ni_3 for the sake of completeness. However, it is doubtful whether Ce_7Ni_3 provides a suitable structural prototype for Dy_7Ni_3 since the chemistry of cerium is relatively different from the other REs. The environment of a Ni atom in Ce_7Ni_3 may also be described in terms of a distorted trigonal prism, with three further Ce atoms lying outward from the square faces of the prism in half-octahedral configuration.

The SRO of the crystals Dy_3Ni, Dy_3Ni_2 and Ce_7Ni_3 was compared with the measured atomic structure of Dy_7Ni_3 by use of the quasi-crystalline model of LEADBETTER and WRIGHT (1972; see section 2.5.3 for further discussion of the model). A real-space correlation length L of 20Å was used for the quasi-crystalline calculation for all three crystals (ie. for the diameter of the single crystal - see section 2.5.3). The effect of thermal motion was included, using a value of 0.1470Å for the RMS bond length variation $\langle u_{ll'}{}^2\rangle^{½}$. The values of L and $\langle u_{ll'}{}^2\rangle^{½}$ were chosen to produce a result of similar behaviour to the experimental data (L determines the rate of decay with r of d(r) and the peak width of Qi(Q) ie. the converse of $\langle u_{ll'}{}^{2}\rangle^{1/2}$). Figures 8.25 to 8.27 show comparisons of the experimental functions $QS_{DyDy}(Q)$, $QS_{DyNi}(Q)$ and $QS_{NiNi}(Q)$ (and Qi(Q) where appropriate) with the corresponding functions for each of the three crystals as calculated by use of the quasi-crystalline model. Note that the chief advantage of using the quasi-crystalline model, as opposed to just calculating the partial correlation functions $t'_{ll'}(r)$ of the crystal, is that it enables a comparison to be performed in reciprocal-space as well as in real-space. The Qi(Q) curves calculated according to the quasi-crystalline model were Fourier transformed using the same Q_{max} as for the experimental data measured on D4, thus simulating the effect of real-space resolution. In the case of Ce_7Ni_3 there is a complication due to the fact that a cerium atom is larger than a dysprosium atom. This was taken into account by scaling the dimensions of the Ce_7Ni_3 unit cell by a factor 0.94579 so that the first peak of the calculated $t'_{CeCe}(r)$ coincided with the first peak of the experimental $t'_{DyDy}(r)$. (ie. it is assumed that the RE atom plays the dominant structural role.) Figures 8.28 to 8.30 show comparisons of the experimental partial correlation functions for Dy_7Ni_3 with those for each crystal as calculated by use of the quasi-crystalline model. The individual distances occurring in the crystals are also indicated. The partial correlation functions calculated according to the quasi-crystalline model curve upwards slightly at low r below the first peak. This is not a serious problem and may be explained as follows: the quasi-crystalline model considers a single crystal sphere embedded in a homogeneous matrix and this is achieved in practice by calculating d(r) for the crystal and then applying the MASON (1968) finite model size correction (equation (2.5.3)). Thus the negative low-r slope of d(r) is reduced with the result that when

$t^{\circ}(r)$ is added to yield $t(r)$ the result has a slight upward slope at low r.

All three crystals exhibit a RE-RE partial correlation function which is similar in form to the measured $t'_{DyDy}(r)$ ie. an asymmetric first peak followed by a deep trough, a group of three peaks and another deep trough. For $t'_{DyNi}(r)$ it is Dy_3Ni_2 which produces the best agreement since the other crystals exhibit a double second peak which is not observed in the experimental data. Similarly it is only Dy_3Ni_2 which is able to reproduce the first peak of the measured $t'_{NiNi}(r)$. However, the second peak in the Ni-Ni correlation function calculated for Dy_3Ni_2 is not observed experimentally, although the third and fourth peaks appear to agree reasonably well. Since Dy_3Ni_2 provides better agreement with experiment than Dy_3Ni or Ce_7Ni_3 this crystal is used as the starting point for the modelling discussion given in section 11.1 .

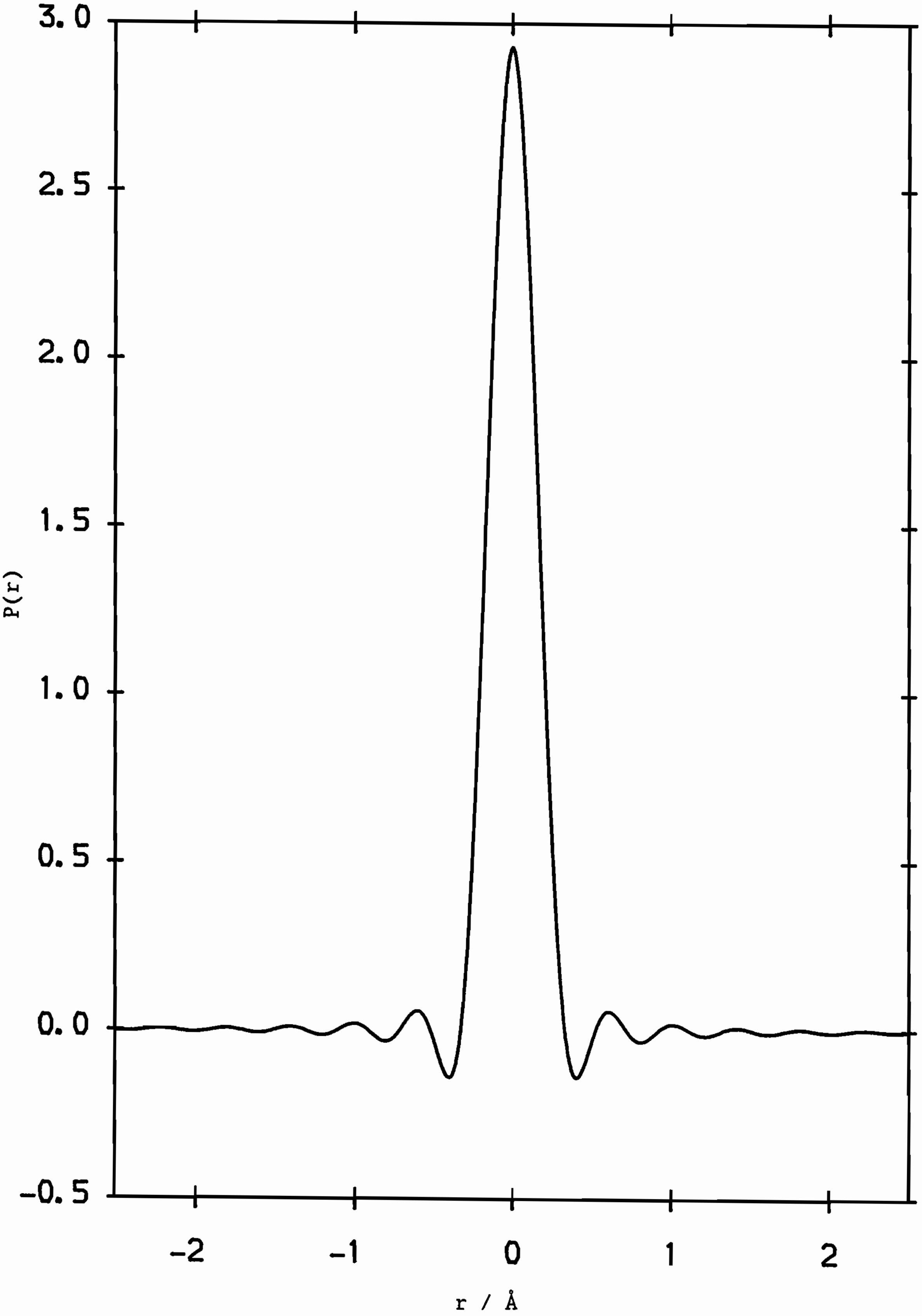

Figure 8.1 The Peak Function P(r) for the 0.7Å D4 Data.

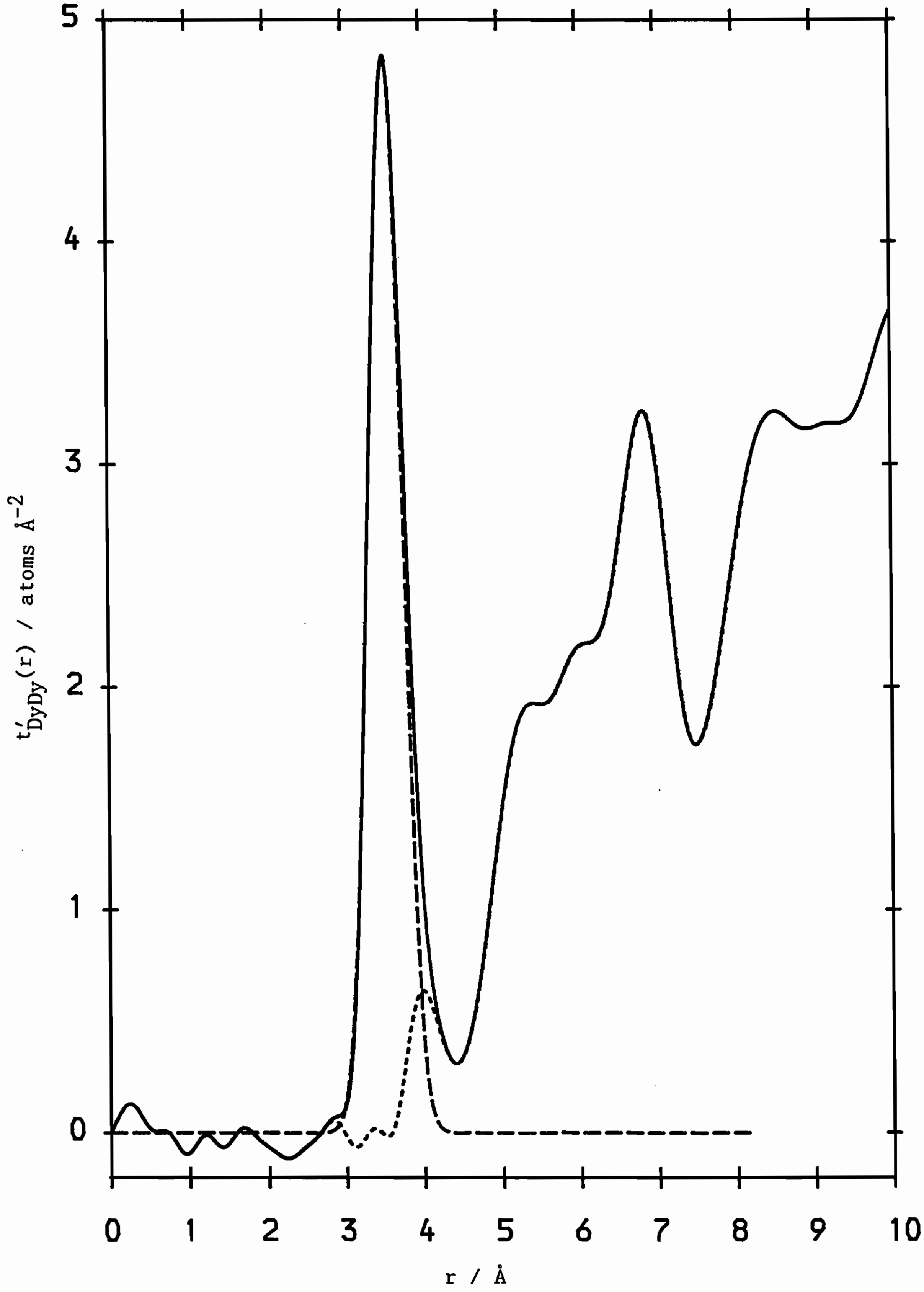

Figure 8.2 The Result of Fitting a Single Resolution-Broadened Gaussian to $t'_{DyDy}(r)$ (Continuous Line), Showing the Fit (Dashed Line) and the Residual (Dotted Line).

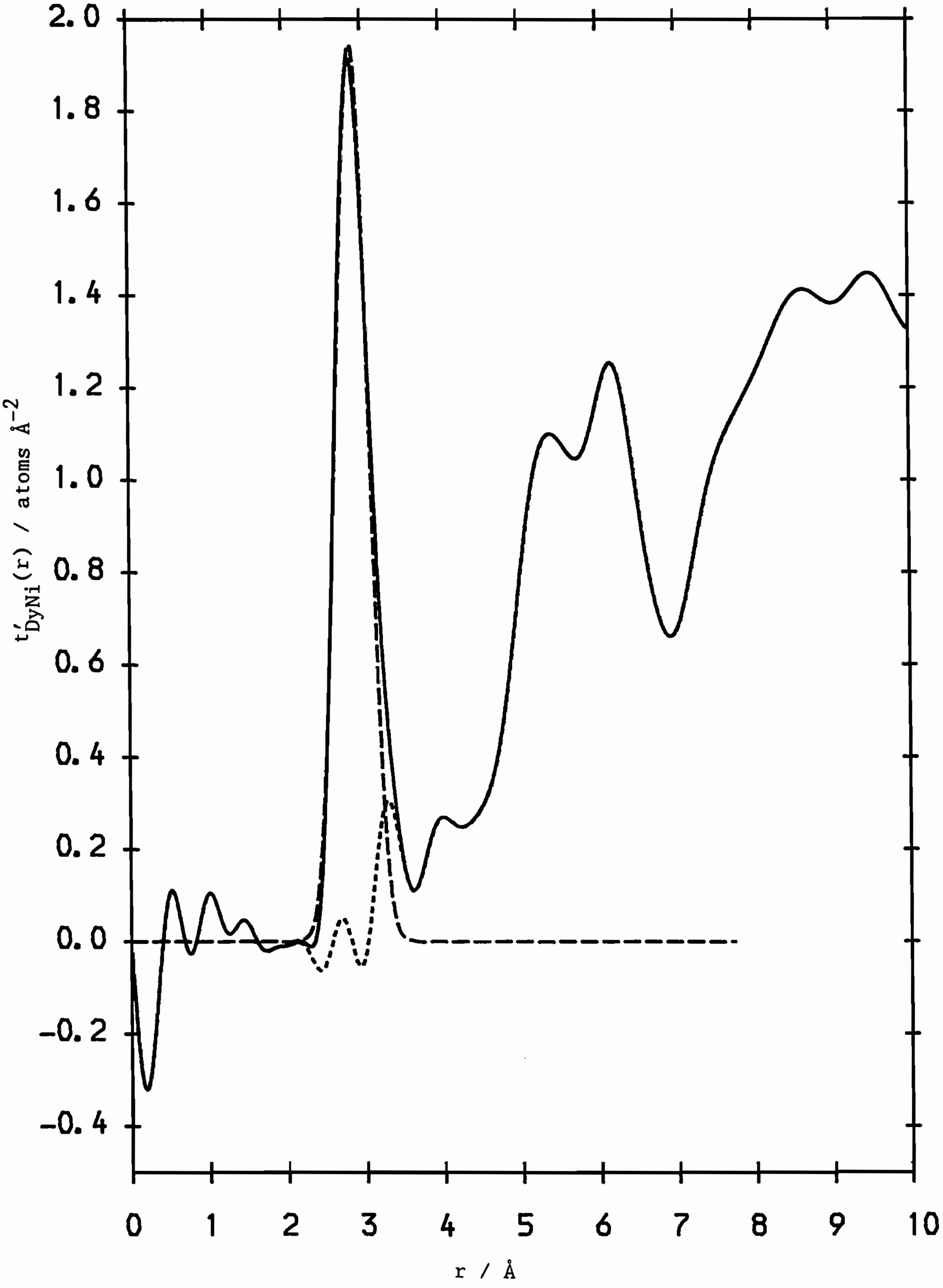

Figure 8.3 The Result of Fitting a Single Resolution-Broadened Gaussian to $t'_{DyNi}(r)$ (Continuous Line), Showing the Fit (Dashed Line) and the Residual (Dotted Line).

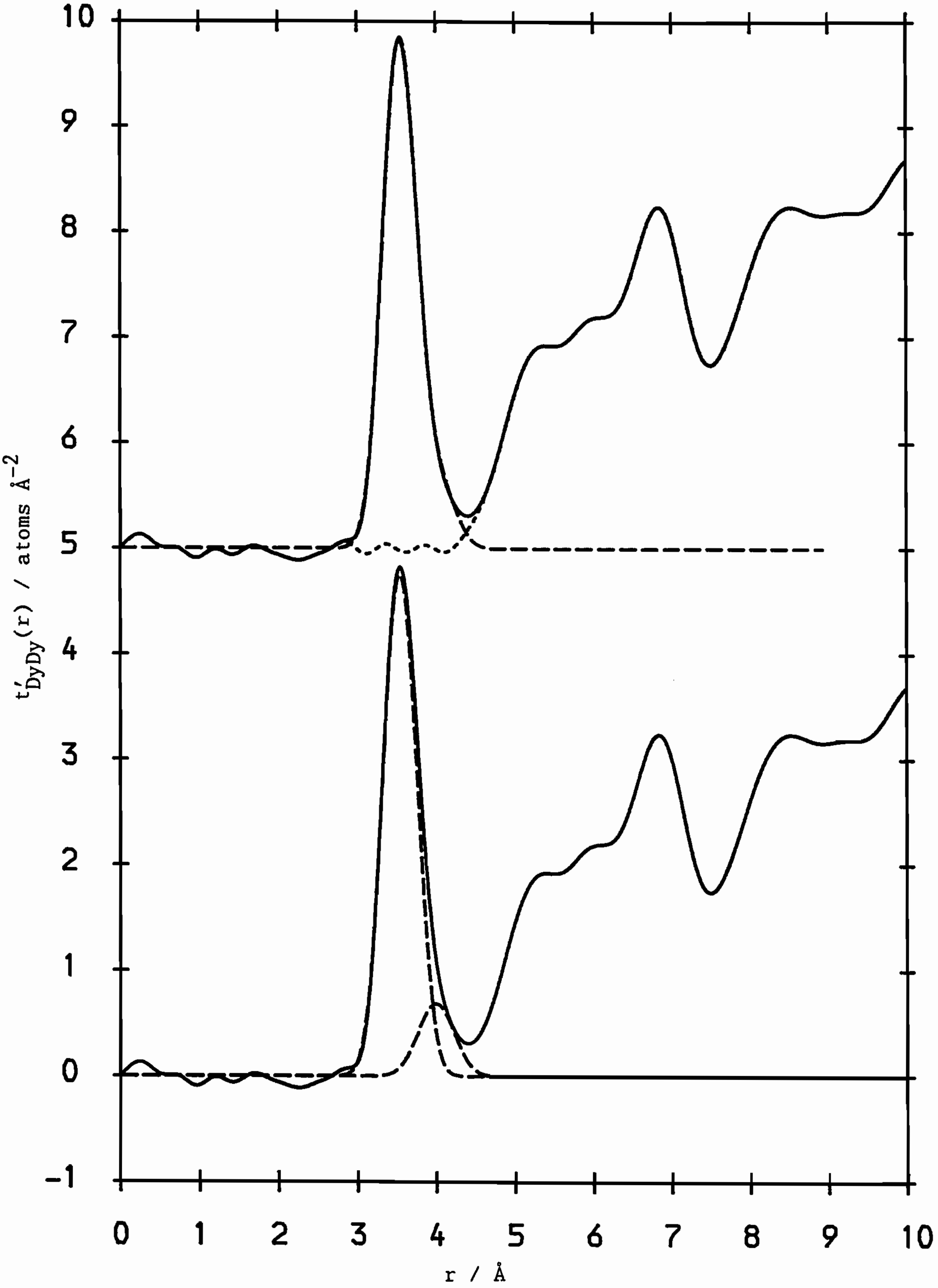

Figure 8.4 The Result of a (Resolution-Broadened) Multi-Gaussian Fit to $t'_{DyDy}(r)$ (Continuous Line).
Upper Figure {offset 5.0} Shows The Total Fit (Dashed Line) and Residual (Dotted Line).
Lower Figure Shows Individual Gaussians (Dashed Lines).

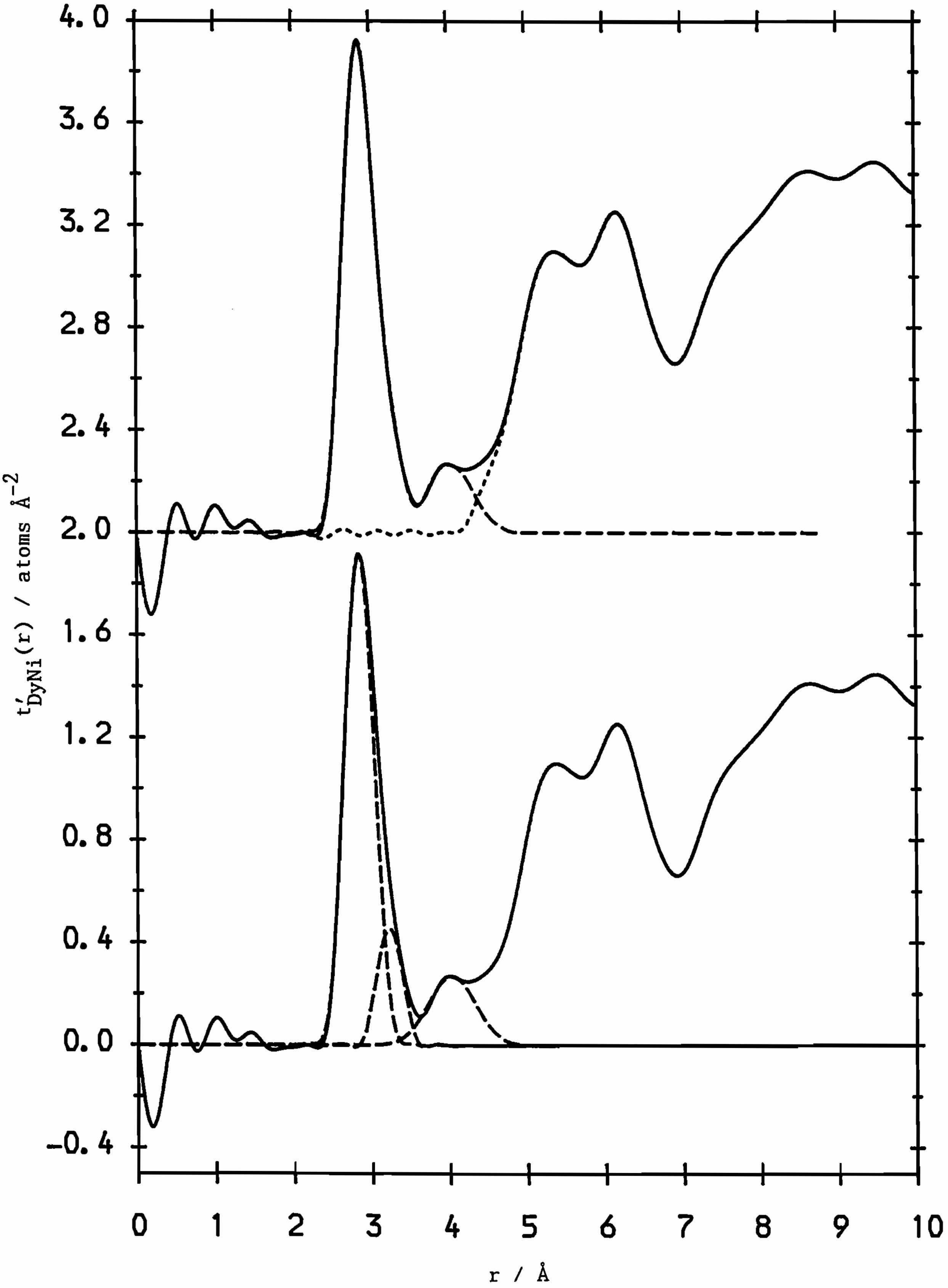

Figure 8.5 The Result of a (Resolution-Broadened) Multi-Gaussian Fit tc $t'_{DyNi}(r)$ (Continuous Line).
Upper Figure {offset 2.0} Shows The Total Fit (Dashed Line) and Residual (Dotted Line).
Lower Figure Shows Individual Gaussians (Dashed Lines).

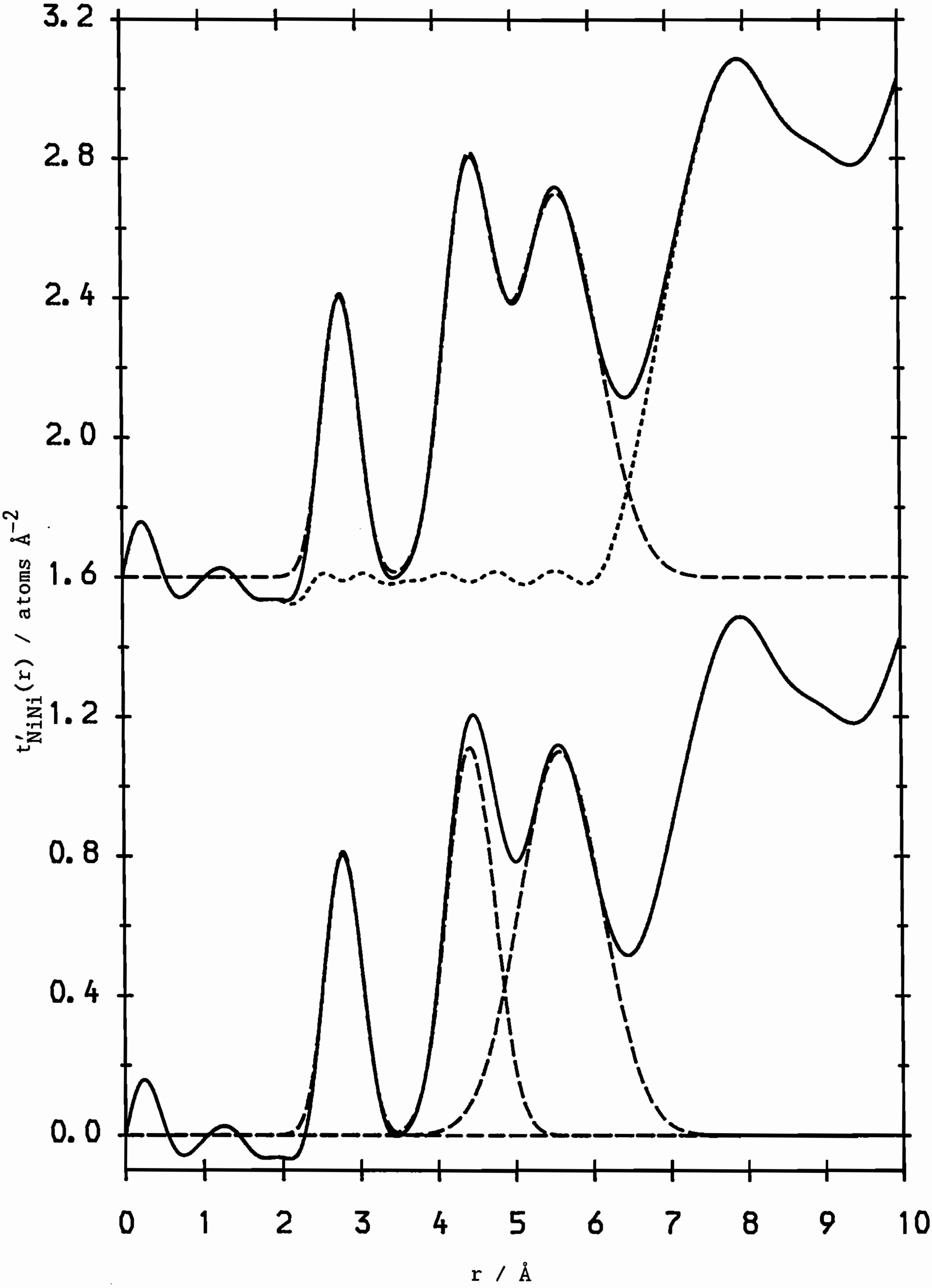

Figure 8.6 The Result of a (Resolution-Broadened) Multi-Gaussian Fit t
$t'_{NiNi}(r)$ (Continuous Line).
Upper Figure {offset 1.6} Shows The Total Fit (Dashed Line)
and Residual (Dotted Line).
Lower Figure Shows Individual Gaussians (Dashed Lines).

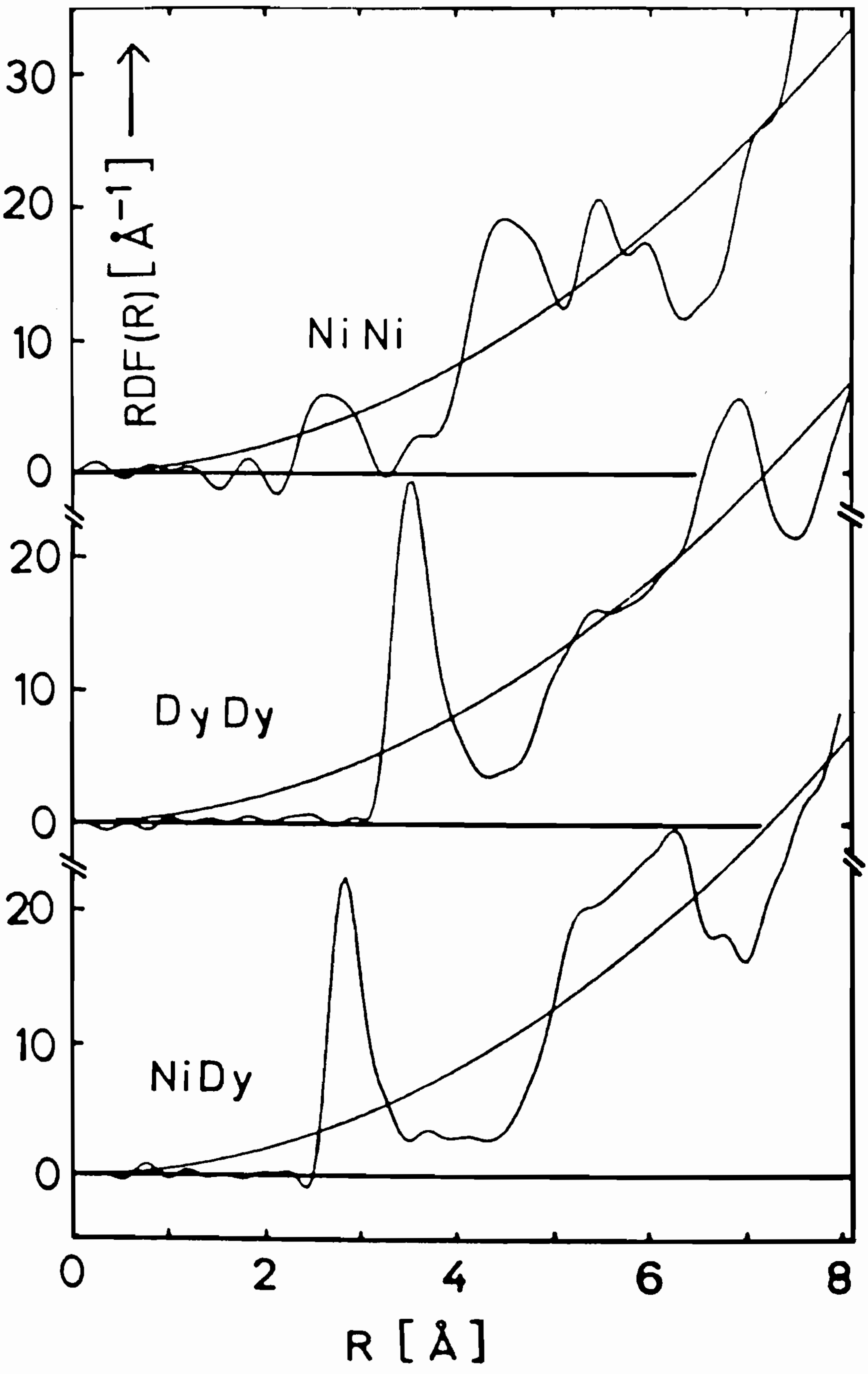

Figure 8.7 The Partial RDFs $n^*_{11'}(r)$ of $Dy_{69}Ni_{31}$ According to WILDERMUTH, LAMPARTER and STEEB (1985).

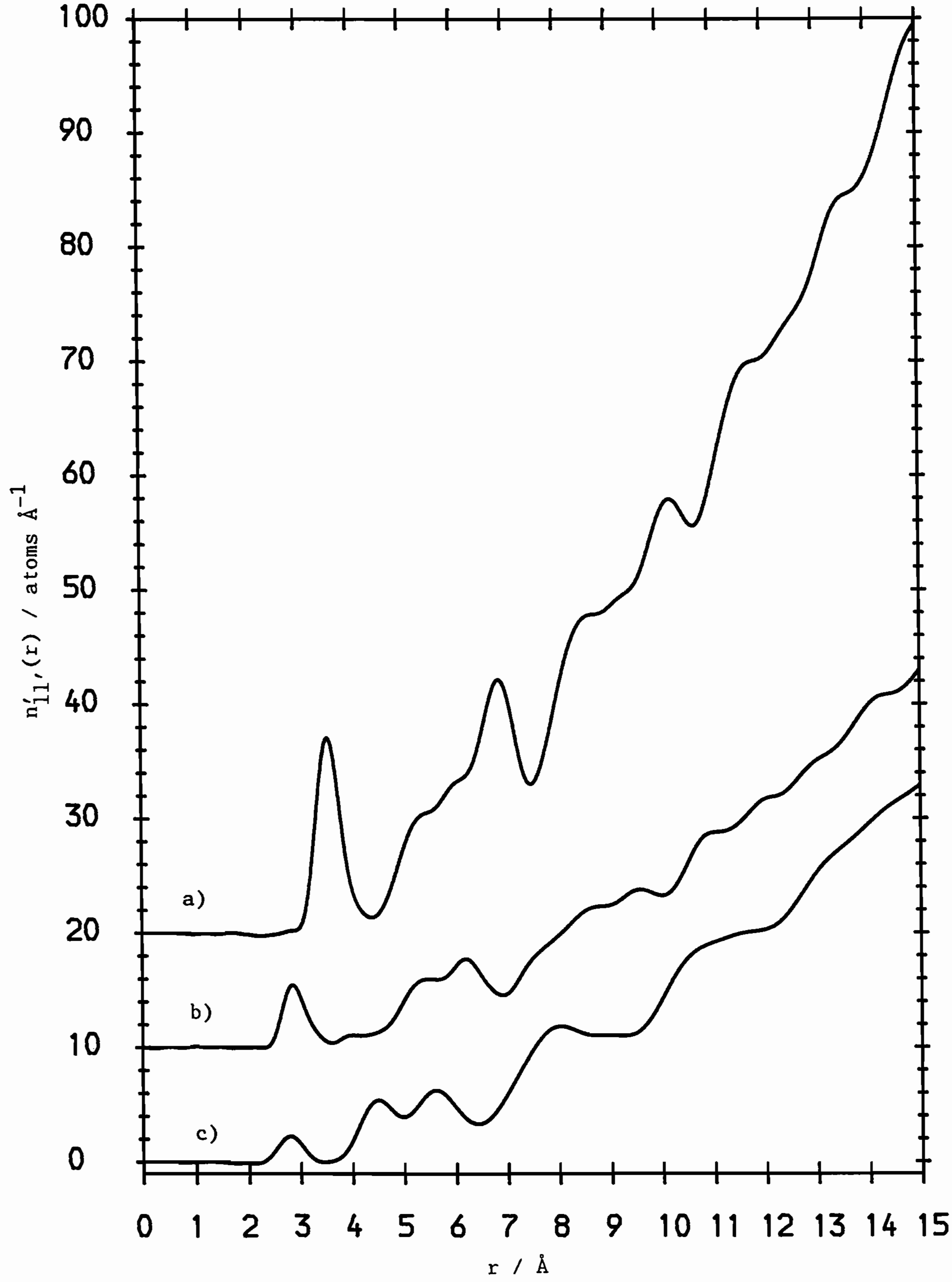

Figure 8.8 The Partial RDFs $n'_{11'}(r)$ of Dy_7Ni_3.
a) Dy-Dy {offset 20.0} b) Dy-Ni {offset 10.0} c) Ni-Ni

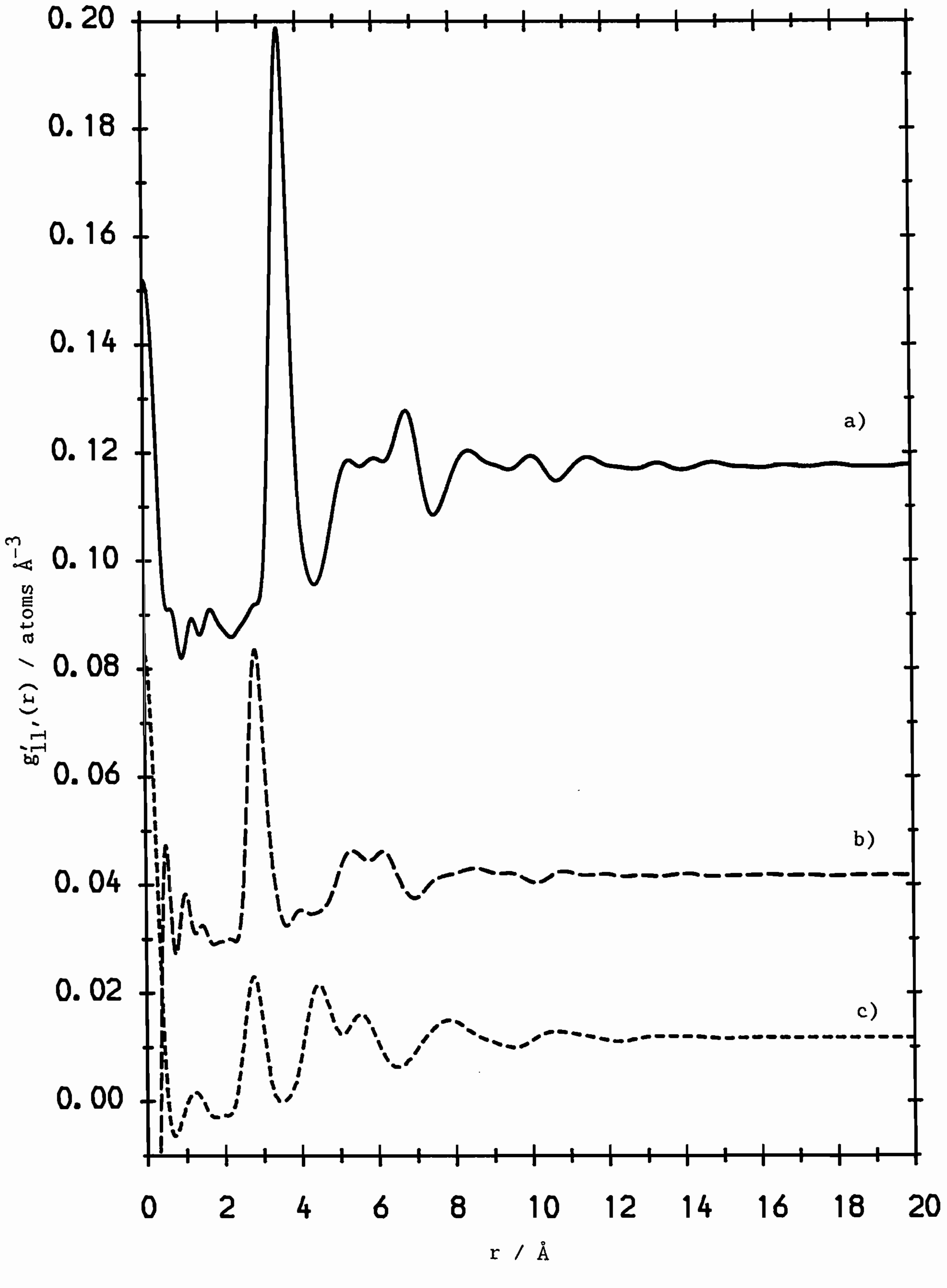

Figure 8.9 The Partial Pair Distribution Functions $g'_{11'}(r)$ for Dy_7Ni_3.
a) Dy-Dy {offset 0.09} b) Dy-Ni {offset 0.03}
c) Ni-Ni

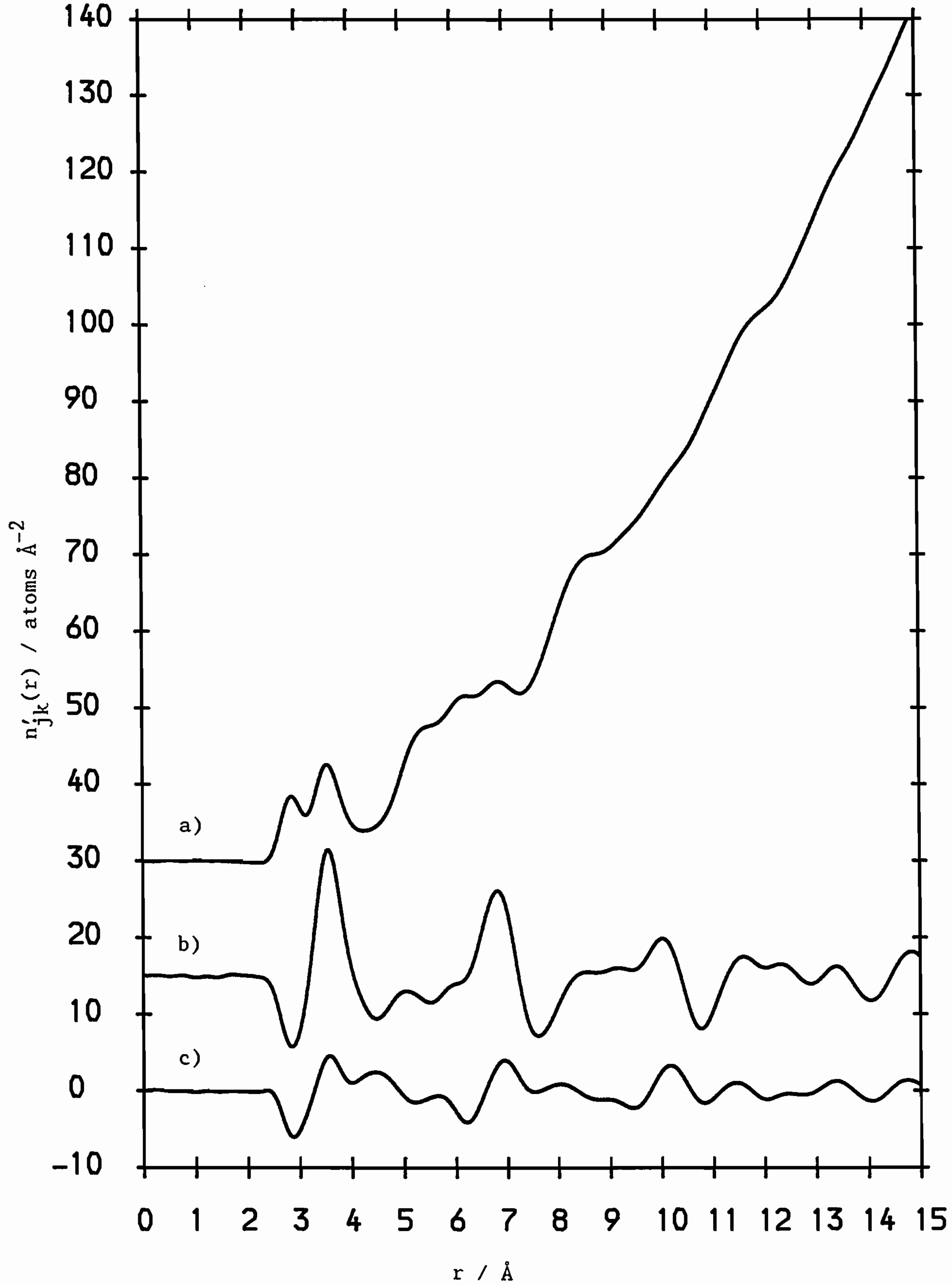

Figure 8.10 The Bhatia-Thornton Partial RDFs $n'_{jk}(r)$ for Dy_7Ni_3.
a) $n_{nn}(r)$ {offset 30.0} b) $n_{nc}(r)$ {offset 15.0} c) $n_{cc}(r)$

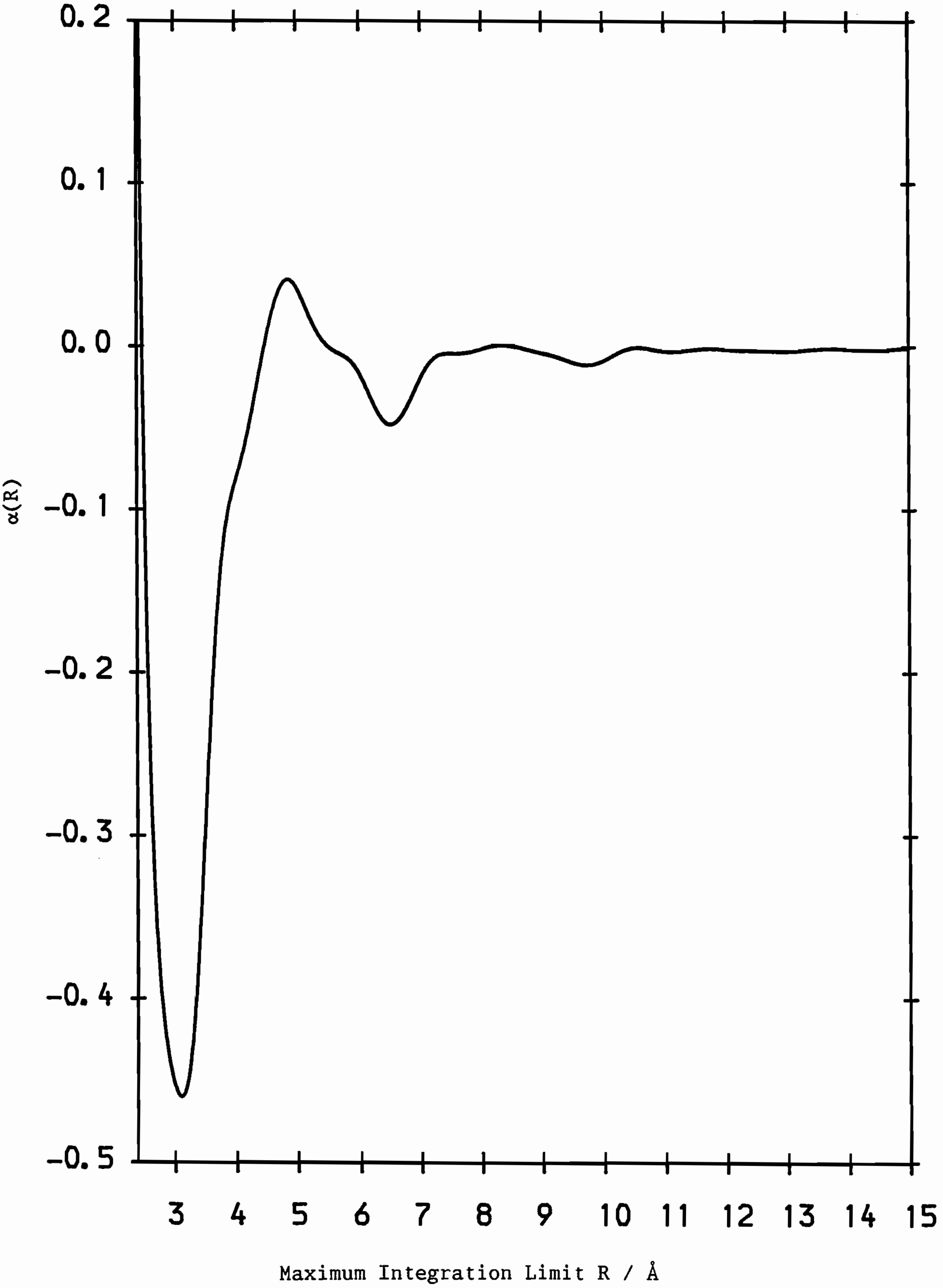

Figure 8.11 The CSRO Function α(R) for Dy_7Ni_3.

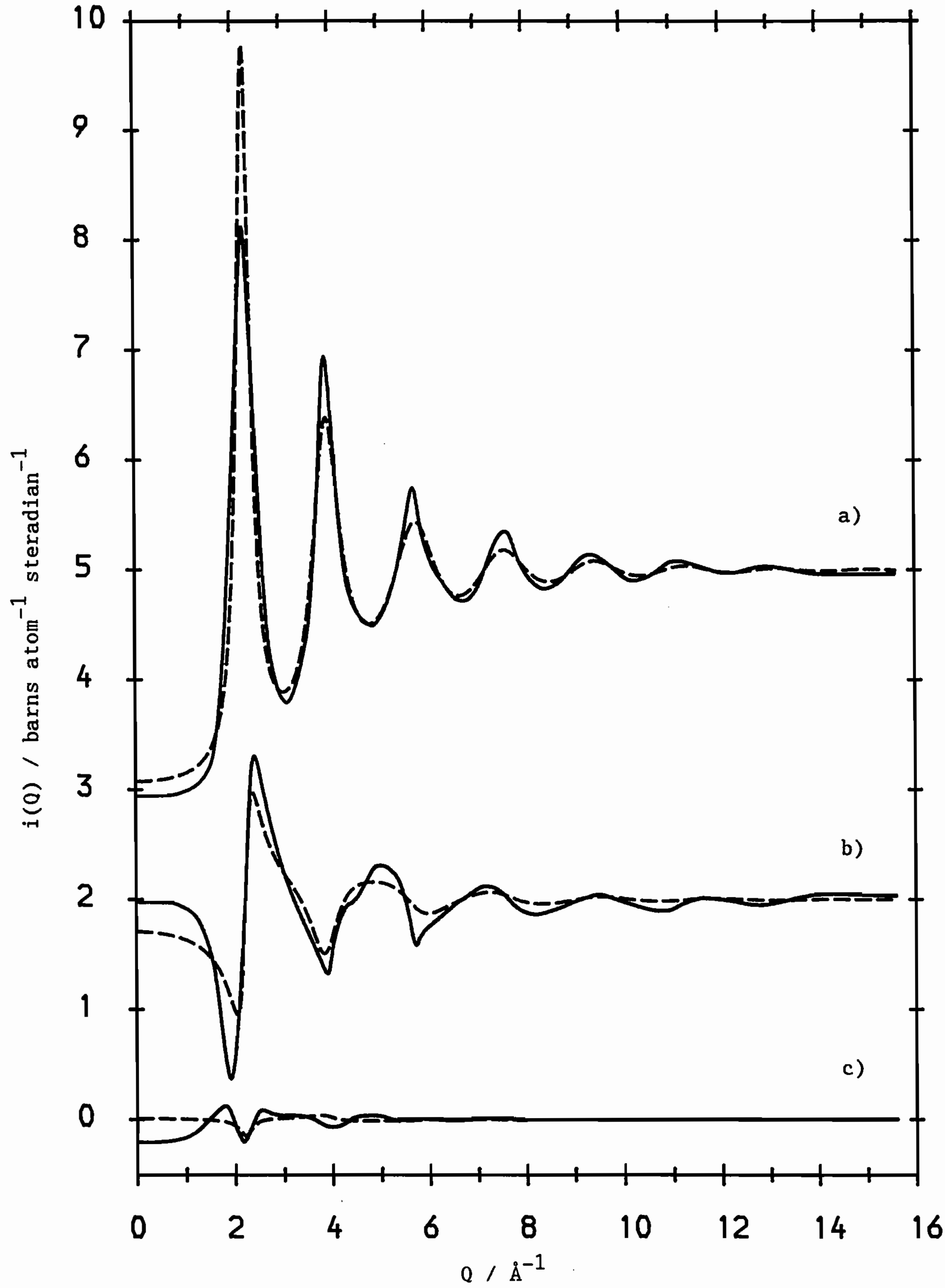

Figure 8.12 A Comparison in Reciprocal Space Between Dy_7Ni_3 (Continuous Line) and The Predictions of the PY Equation with a Hard Sphere Potential with Thermal Motions Included (Dashed Line). a) $i_{NO}(Q)$ {offset 5.0} b) $i_{UN}(Q)$ {offset 2.0} c) $i_{ON}(Q)$

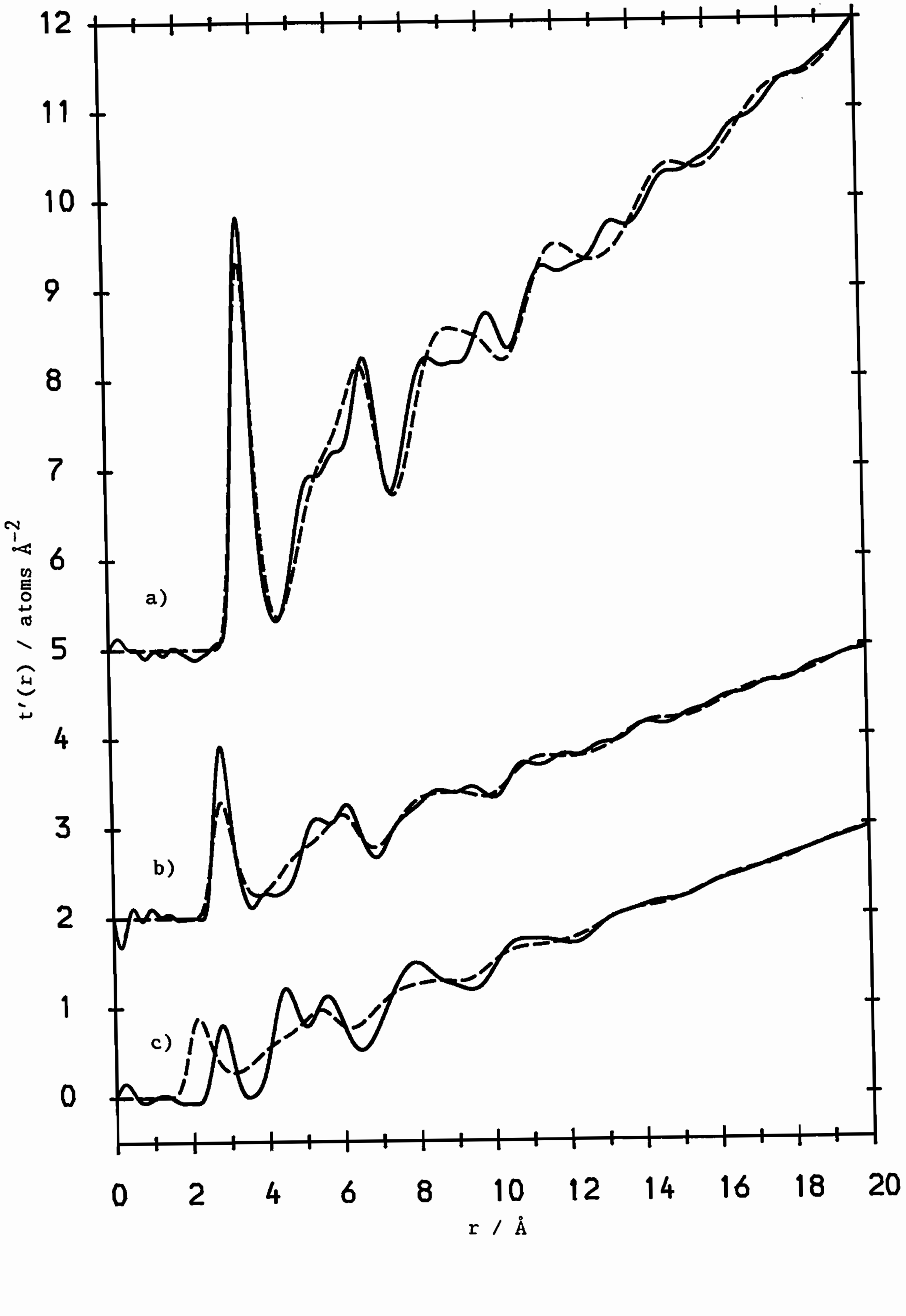

Figure 8.13 A Comparison in Real Space Between Dy_7Ni_3 (Continuous Line) and The Predictions of the PY Equation with a Hard Sphere Potential (Dashed Line).

a) $t'_{DyDy}(r)$ {offset 5.0} b) $t'_{DyNi}(r)$ {offset 2.0} c) $t'_{NiNi}(r)$

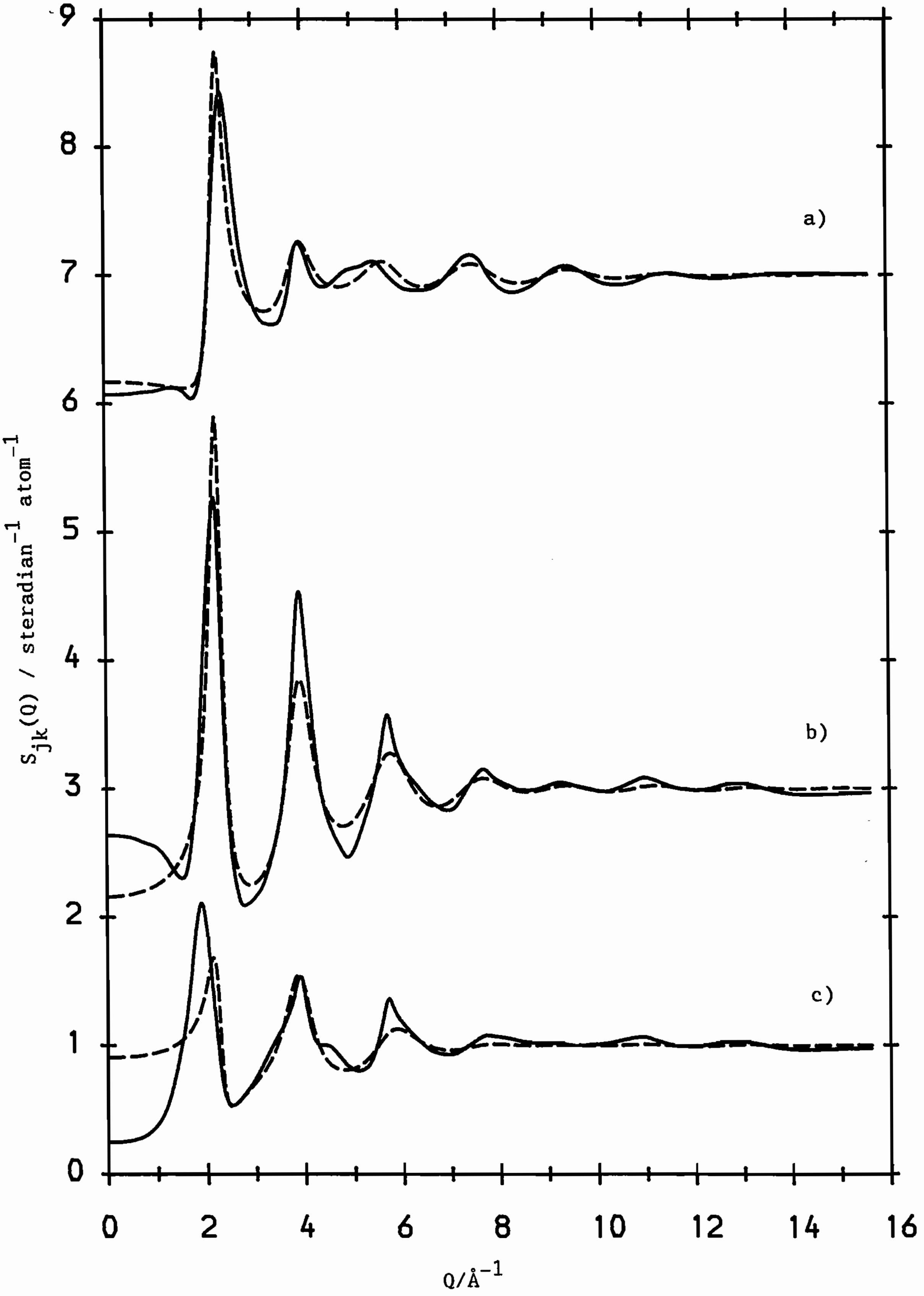

Figure 8.14 The Bhatia-Thornton Partial Structure Factors Calculated According to the PY Equation (Dashed Line) Compared with Experiment (Continuous Line).

a) $S_{nn}(Q)$ {offset 6.0} b) $S_{nc}(Q)$ {offset 3.0} c) $S_{cc}(Q)$

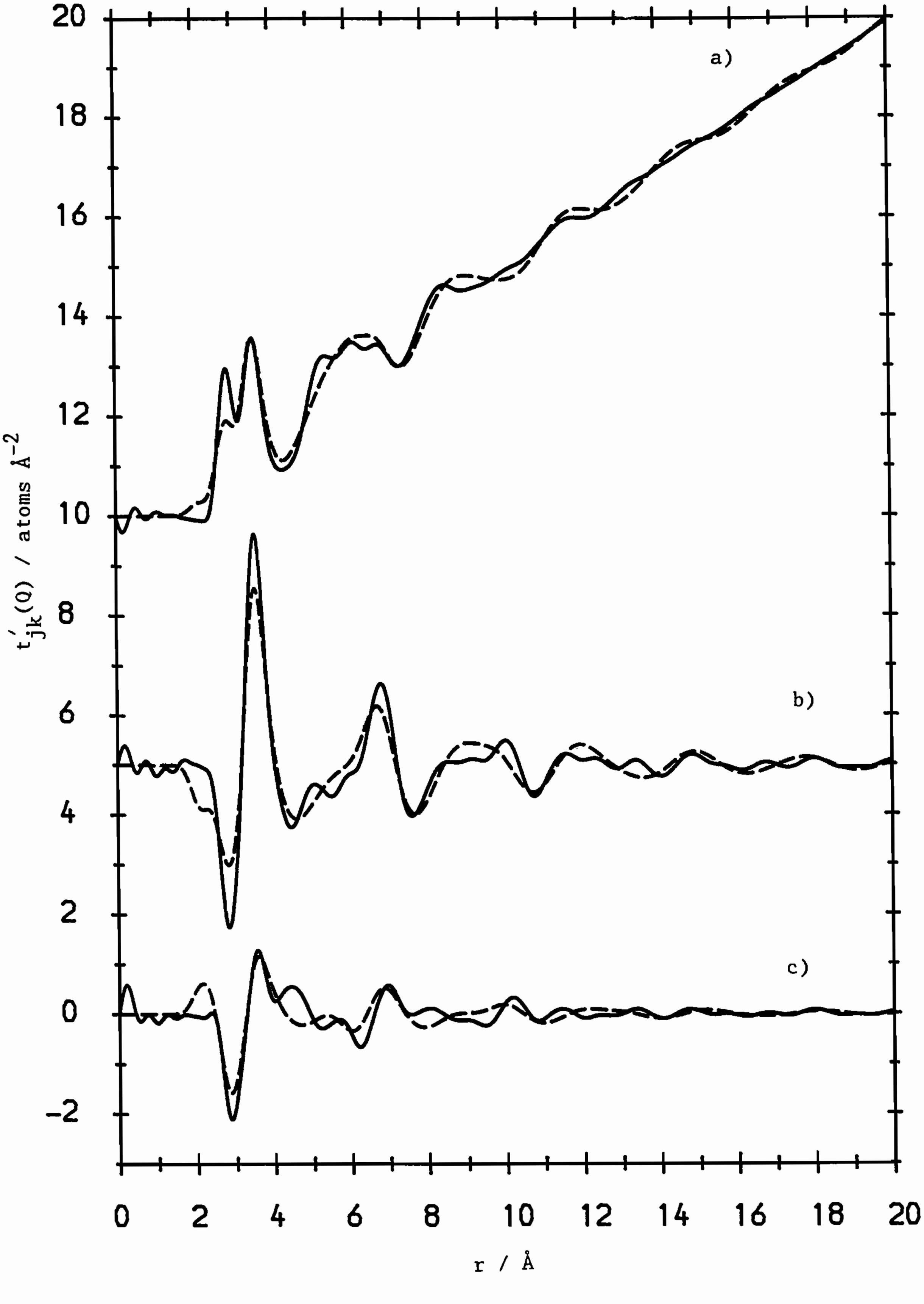

Figure 8.15 The Bhatia-Thornton Partial Correlation Functions Calculated According to the PY Equation (Dashed Line) Compared with Experiment (Continuous Line).

a) $t'_{nn}(r)$ {offset 10.0} b) $t'_{nc}(r)$ {offset 5.0} c) $t'_{cc}(r)$

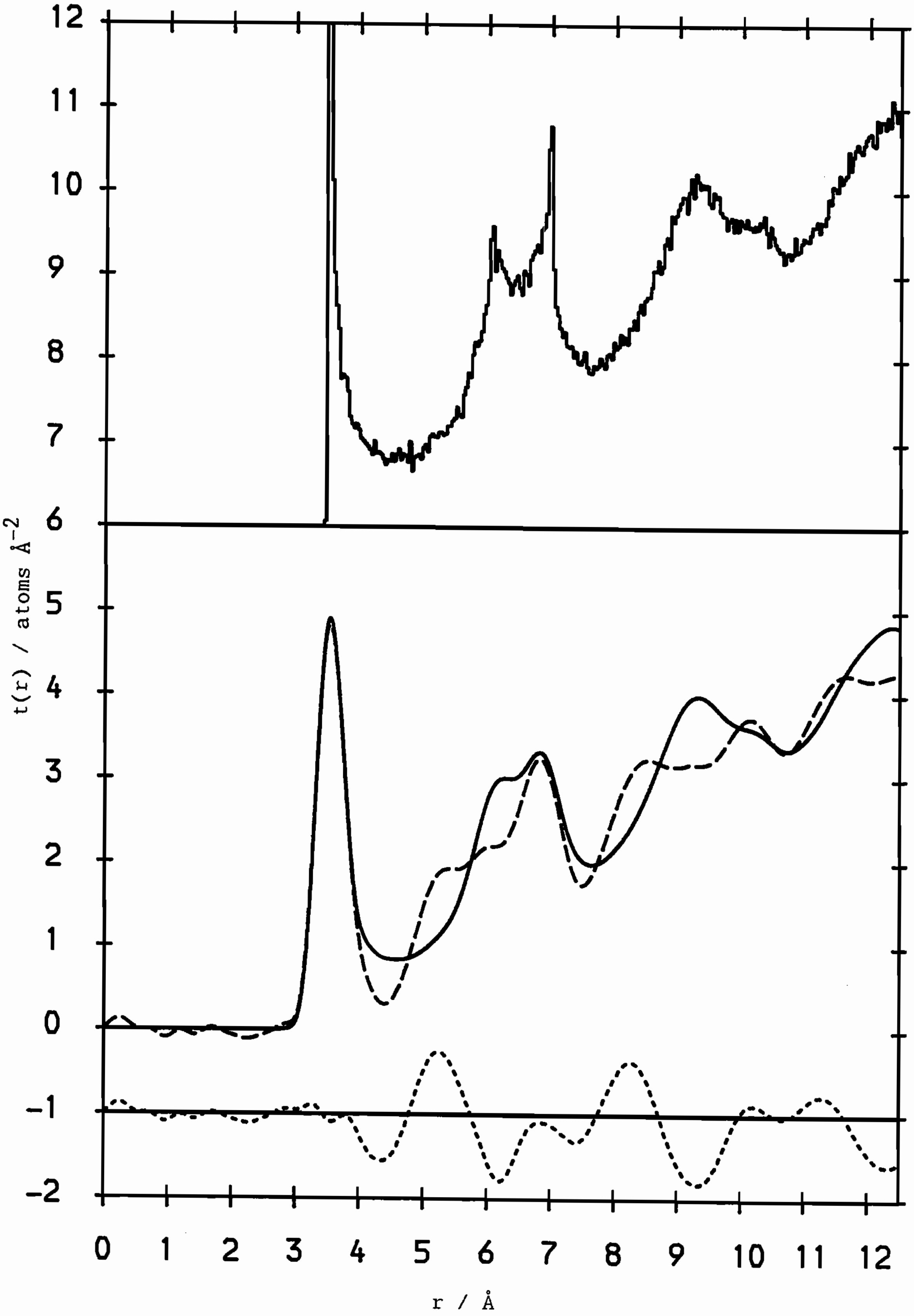

Figure 8.16 A Comparison Between $t'_{DyDy}(r)$ for Dy_7Ni_3 and t(r) for the Finney Model Showing the Unbroadened Model Correlation Function (Histogram {offset 6.0}), the Broadened Model Correlation Function (Continuous Line), the Experimental Correlation Function (Dashed Line) and the Residual (Dotted Line {offset −1.0}) between the Broadened Model Correlation Function and the Experimental Correlation Function.

	Hard Sphere Configuration	r_{DyDy}/d_{Dy}	r_{DyDy}/Å
1	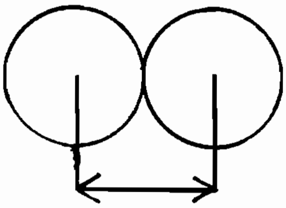	1	3.531
2	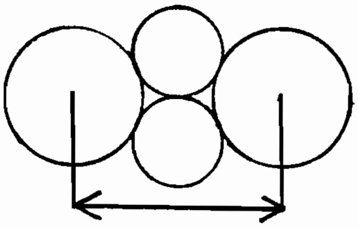	Not seen experimentally	
(σ_r=0.607) 3	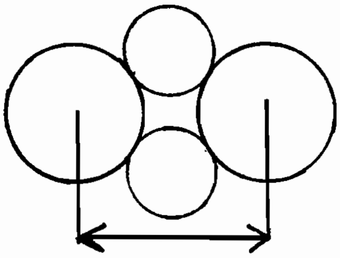	1.400	4.943
4	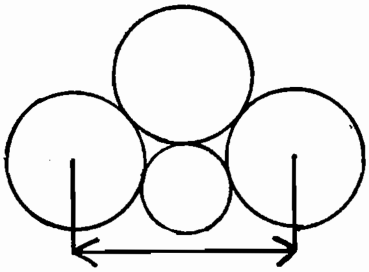	1.566	5.528
5	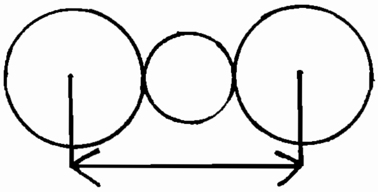	1.607	5.674
6	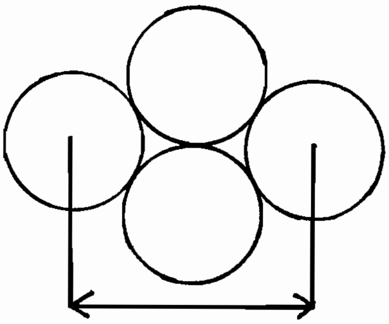	$\sqrt{3}$	6.116
7	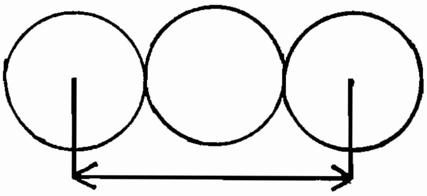	2	7.062

Figure 8.17 Hard Sphere Configurations for Dy_7Ni_3.

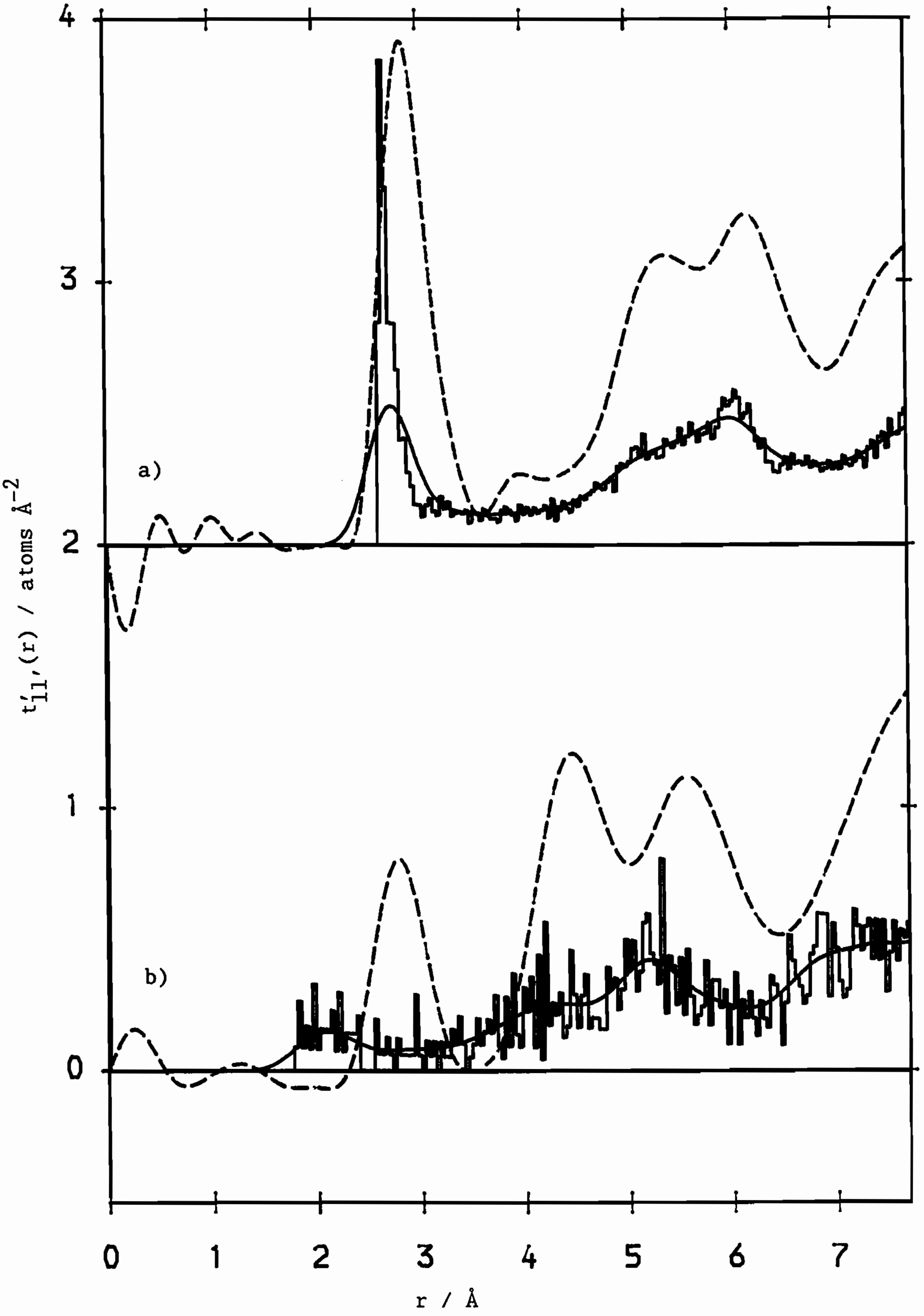

Figure 8.18 A Comparison Between the Partial Correlation Functions $t'_{ll'}(r)$ of Dy_7Ni_3 (Dashed Line) and those for the FINNEY (1970) Model with Added Minority Interstitial Atoms of Half the Majority Atom Diameter (the Histogram is before Broadening, and the Continuous Line is after Broadening).

a) Dy-Ni / Minority atom-Majority atom {offset 2.0}

b) Ni-Ni / Minority atom-Minority atom

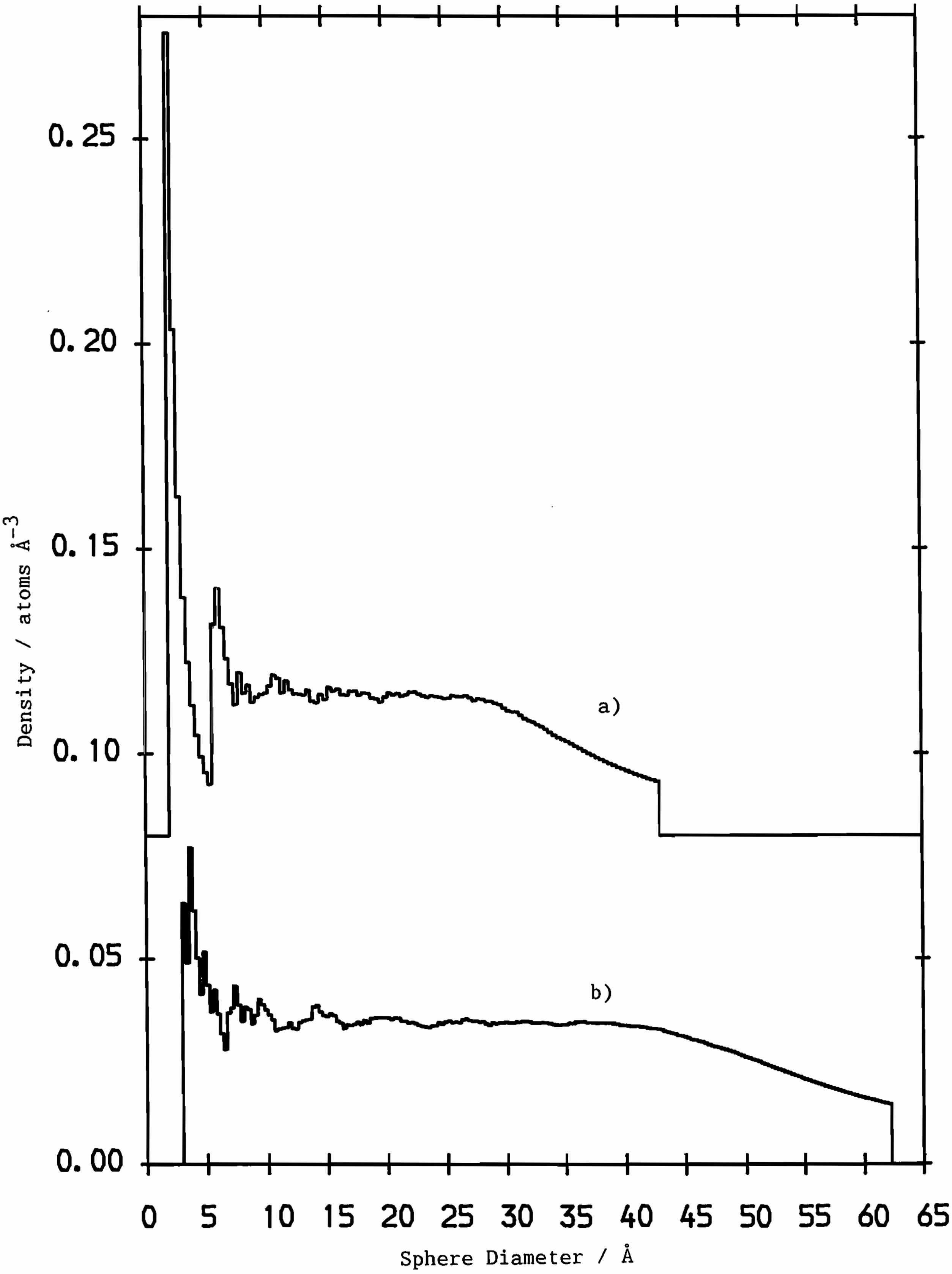

Figure 8.19 The Density of Spherical Portions of Gaskell's Trigonal Prismatic Models as a Function of Sphere Diameter.
a) GASKELL (1979) {offset 0.8}
b) DUBOIS, GASKELL and LeCAËR (1985).

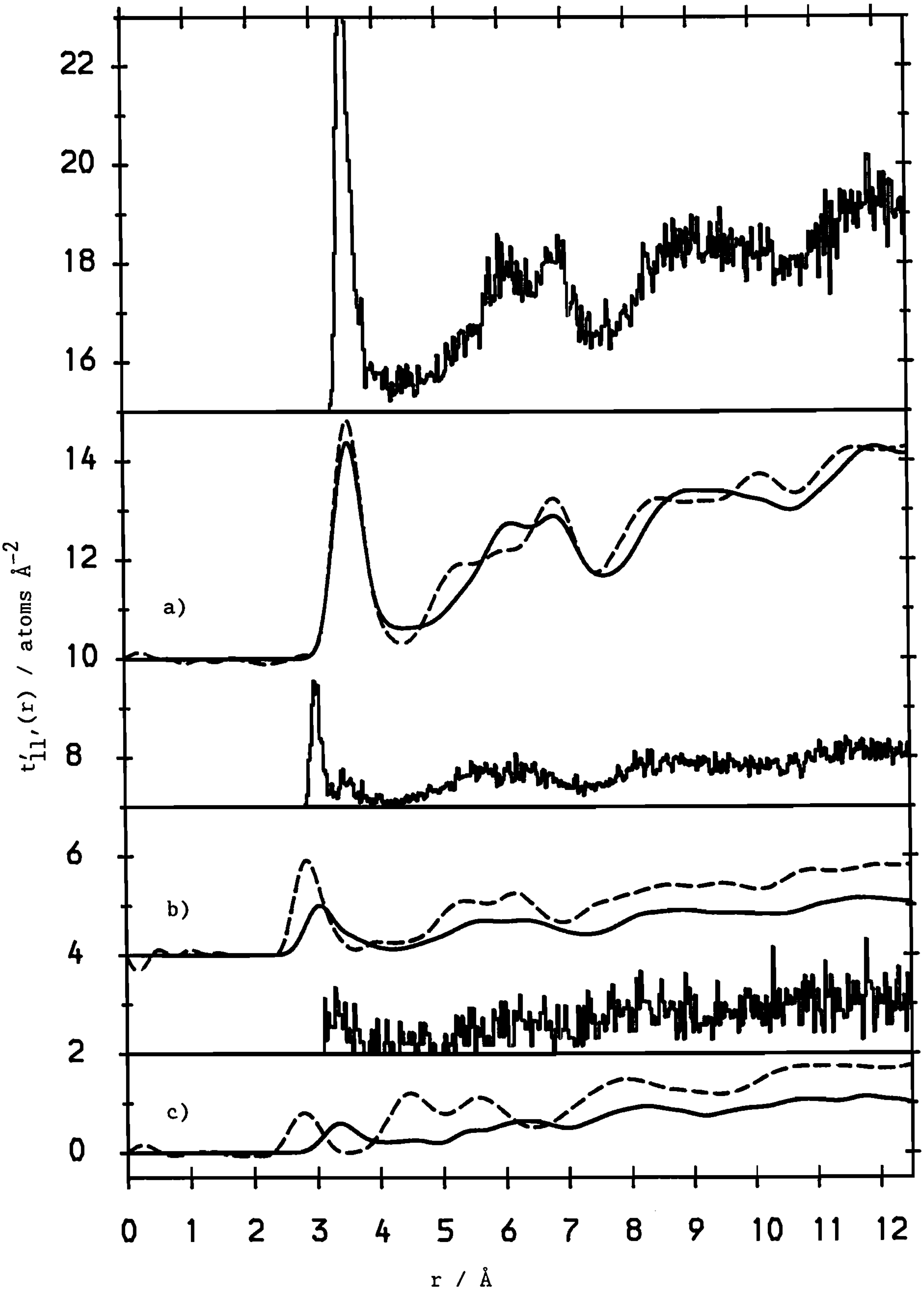

Figure 8.20 A Comparison between the Partial Correlation Functions $t'_{ll'}(r)$ of Dy_7Ni_3 (Dashed Line) and the Broadened Partial Correlation Functions (Continuous Line) for the Trigonal Prismatic Model due to GASKELL (1979). The Unbroadened Model Partial Correlation Functions (Histogram) are also shown {with suitable offsets}.
a) Dy-Dy {offset 10.0} b) Dy-Ni {offset 4.0} c) Ni-Ni

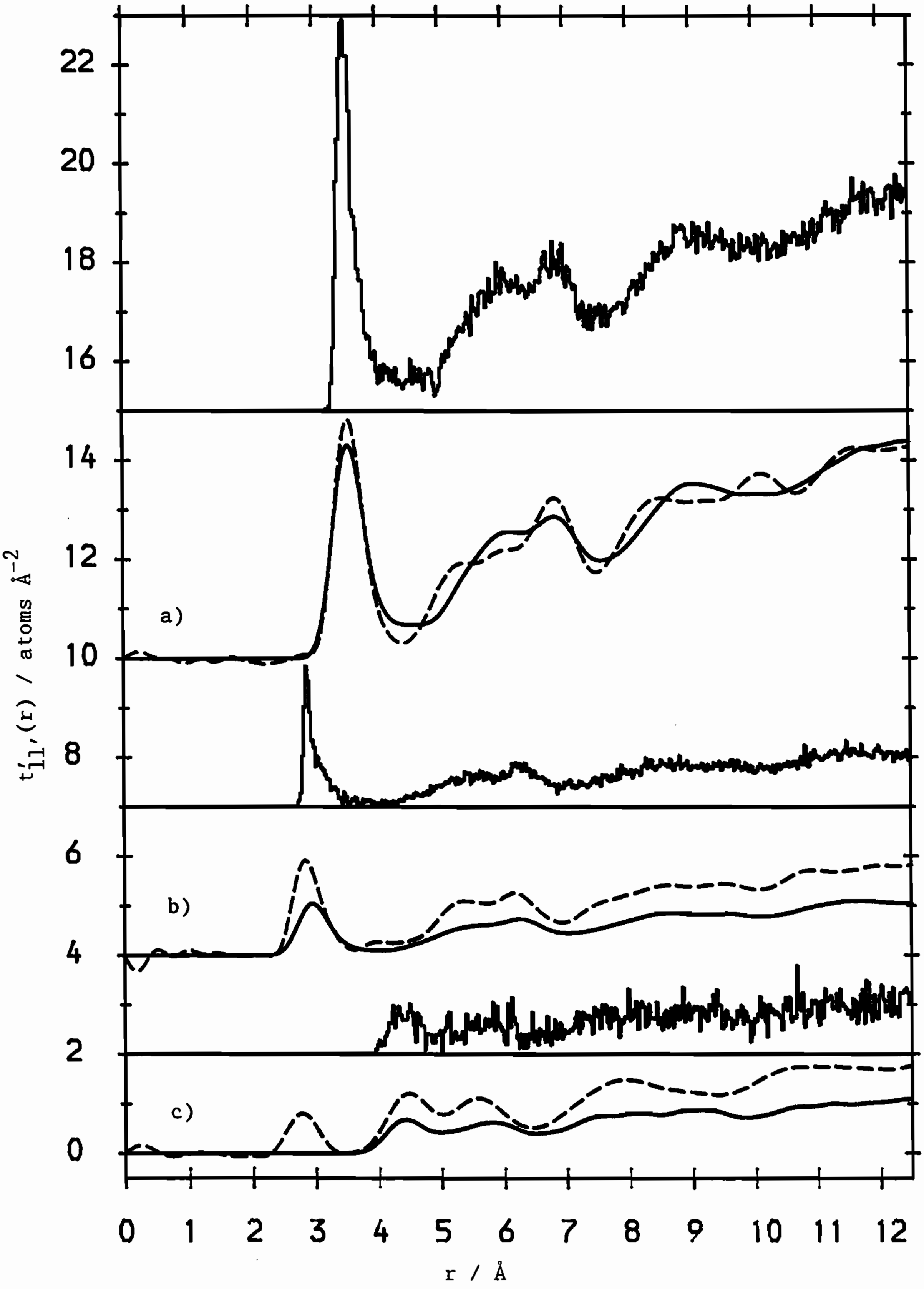

Figure 8.21 A Comparison between the Partial Correlation Functions $t'_{ll'}(r)$ of Dy_7Ni_3 (Dashed Line) and the Broadened Partial Correlation Functions (Continuous Line) for the Trigonal Prismatic Model due to DUBOIS, GASKELL and LeCAËR(1985). The Unbroadened Model Partial Correlation Functions (Histogram) are also shown {with suitable offsets}.

a) Dy-Dy {offset 10.0} b) Dy-Ni {offset 4.0} c) Ni-Ni

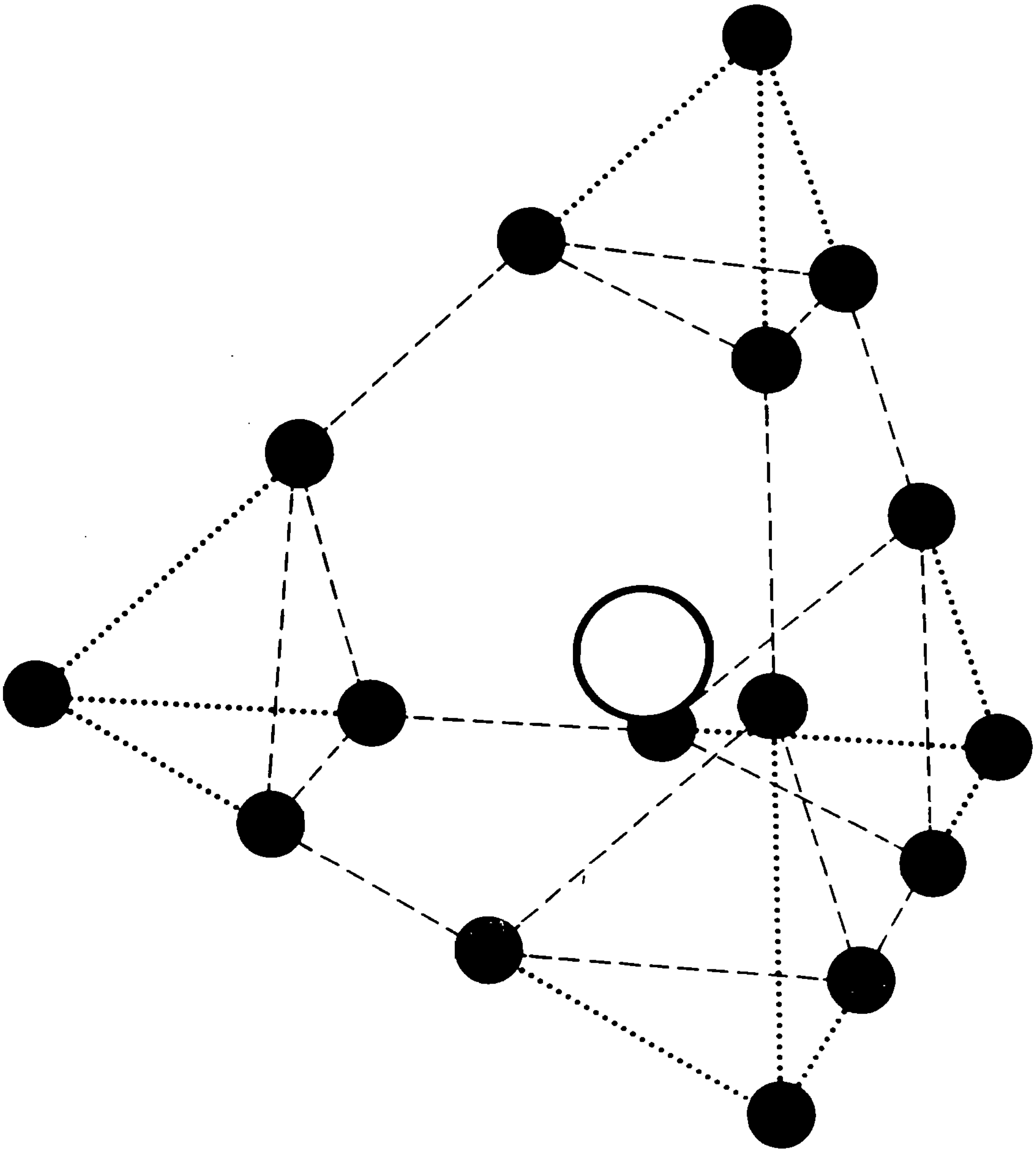

Figure 8.22 The RE Environment in a Cubic RE-TL$_2$ Laves Phase Crystal.

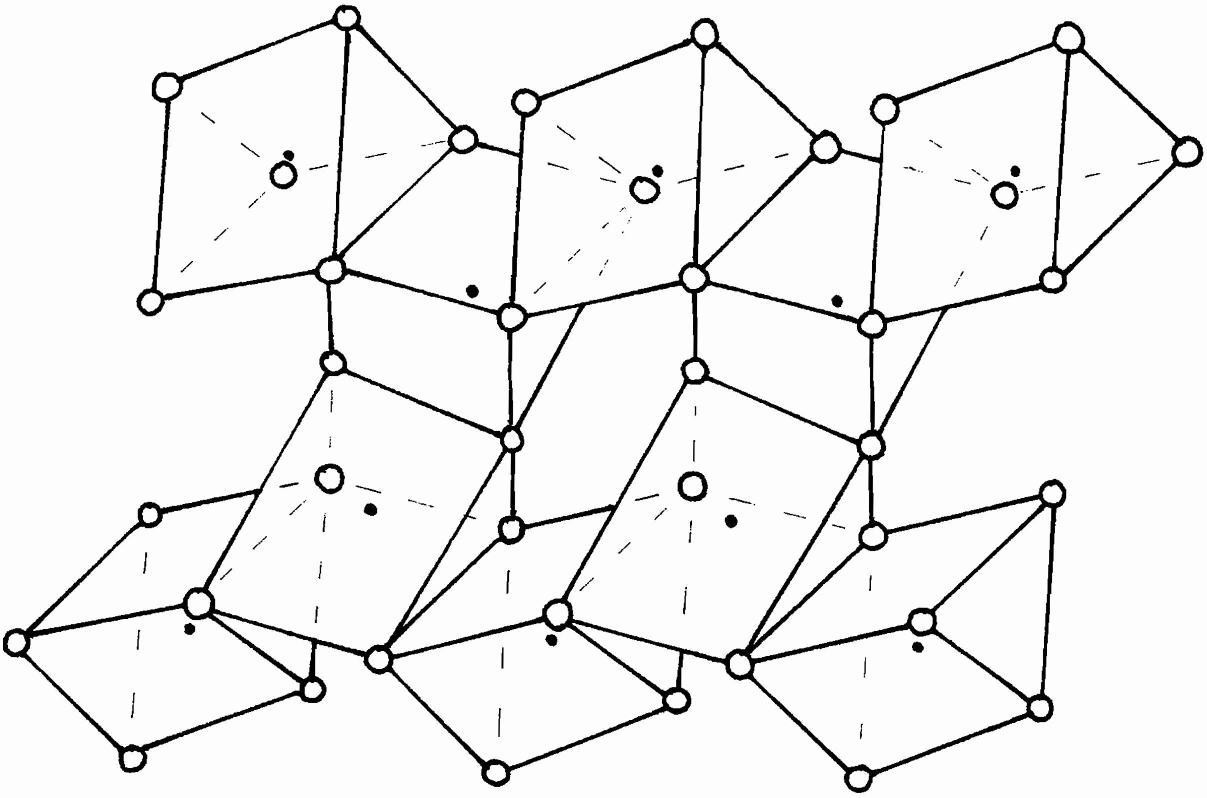

O = Dy • = Ni

Figure 8.23 A Layer of Trigonal Prisms as Found in Crystalline Dy_3Ni ($\equiv Fe_3C$).

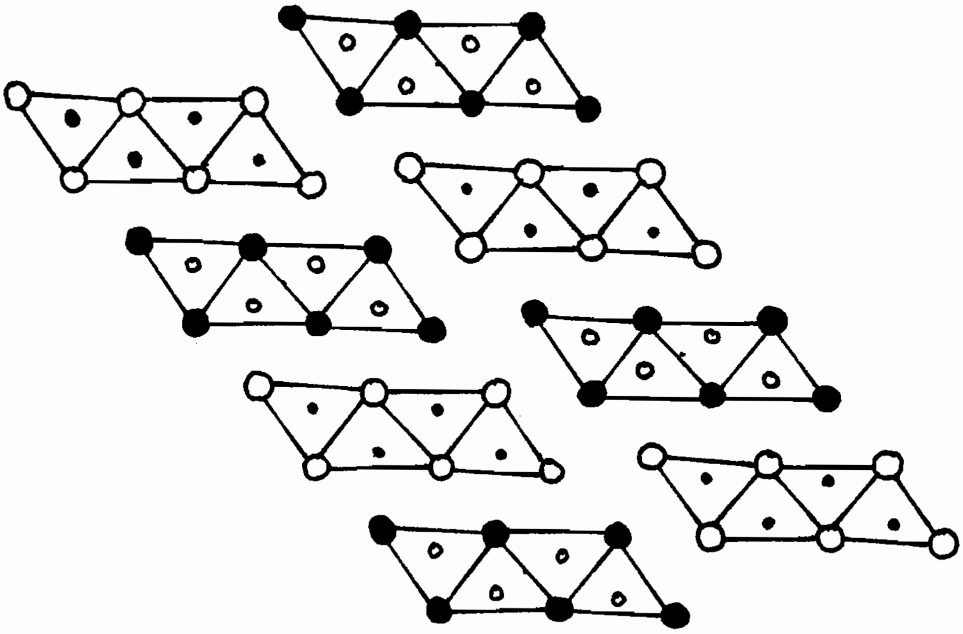

Figure 8.24 The Crystal Structure of Dy_3Ni_2. The Figure is in Projection Along the Lattice Direction Parallel to the Prism Axes with Full Black Circles at 0 and White Circles at ½. Large Circles Represent Dy Atoms, Small Circles Ni Atoms.

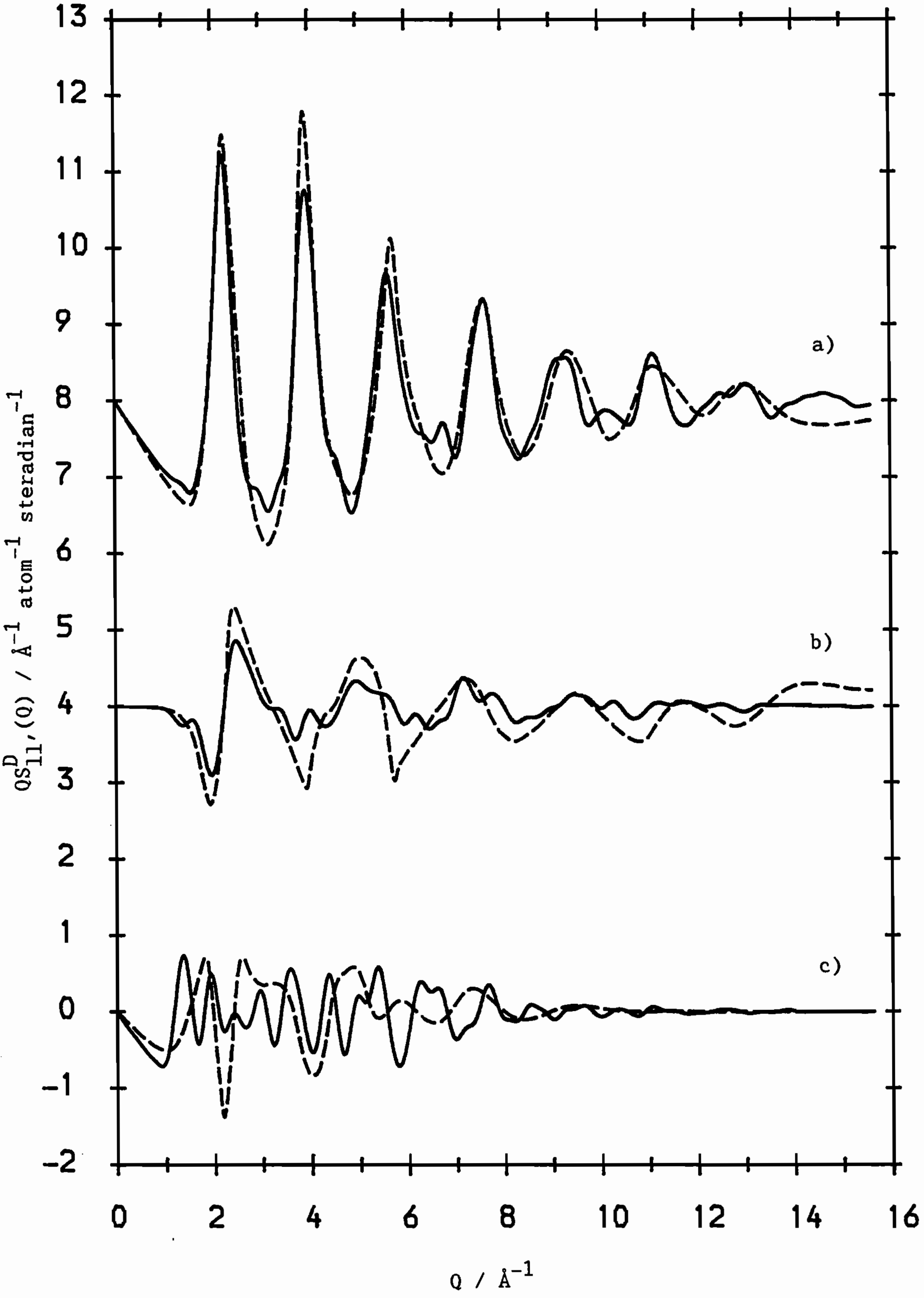

Figure 8.25 A Comparison in Reciprocal-Space Between the Quasi-crystalline Calculation for Dy_3Ni (Continuous Line) and the Experimental Data for Amorphous Dy_7Ni_3 (Dashed Line).
a) $QS^D_{DyDy}(Q)$ {offset 8.0} b) $QS^D_{DyNi}(Q)$ {offset 4.0}
c) $QS^D_{NiNi}(Q)$

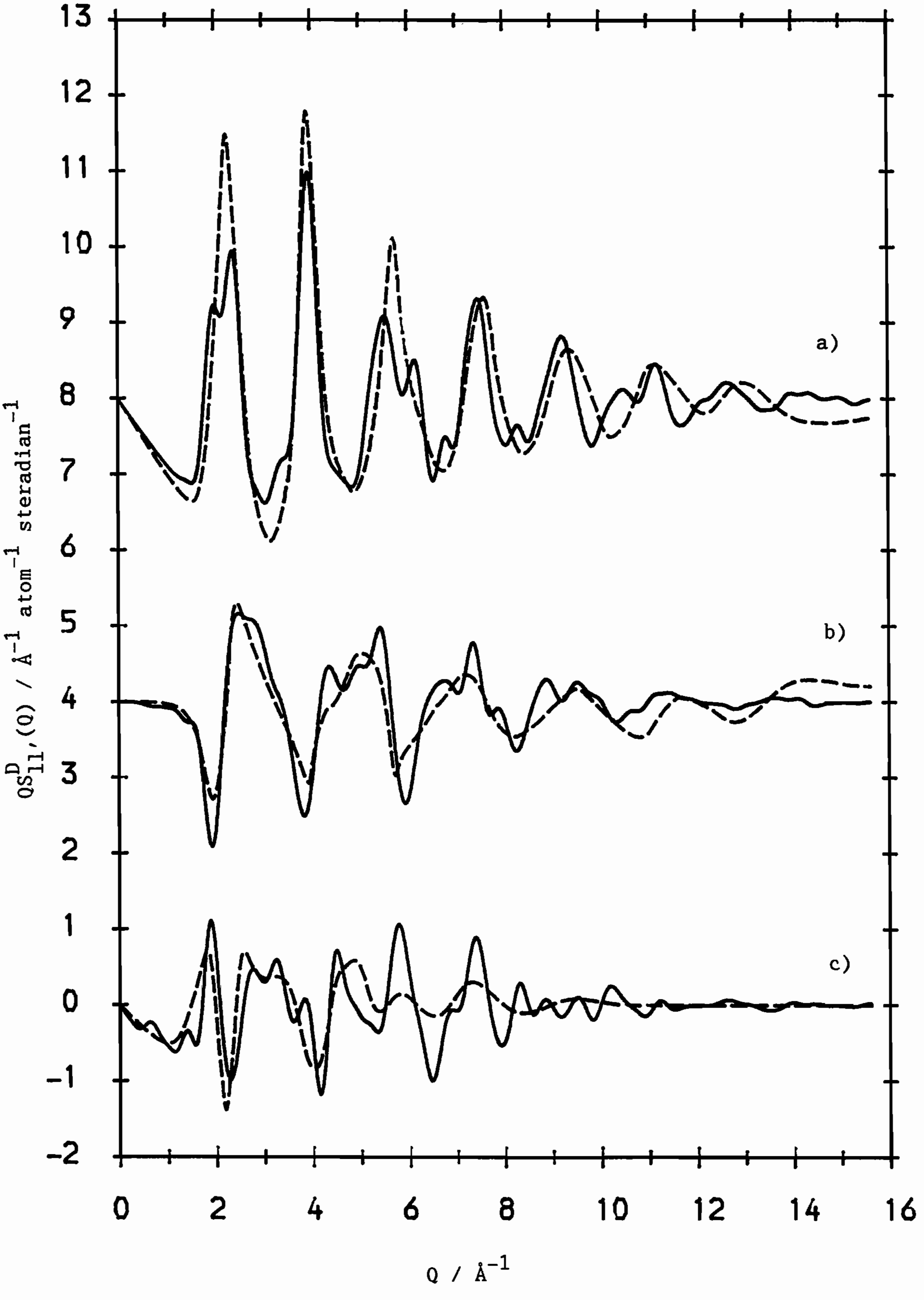

Figure 8.26 A Comparison in Reciprocal-Space Between the Quasi-crystalline Calculation for Dy_3Ni_2 (Continuous Line) and the Experimental Data for Amorphous Dy_7Ni_3 (Dashed Line).
a) $QS^D_{DyDy}(Q)$ {offset 8.0} b) $QS^D_{DyNi}(Q)$ {offset 4.0}
c) $QS^D_{NiNi}(Q)$

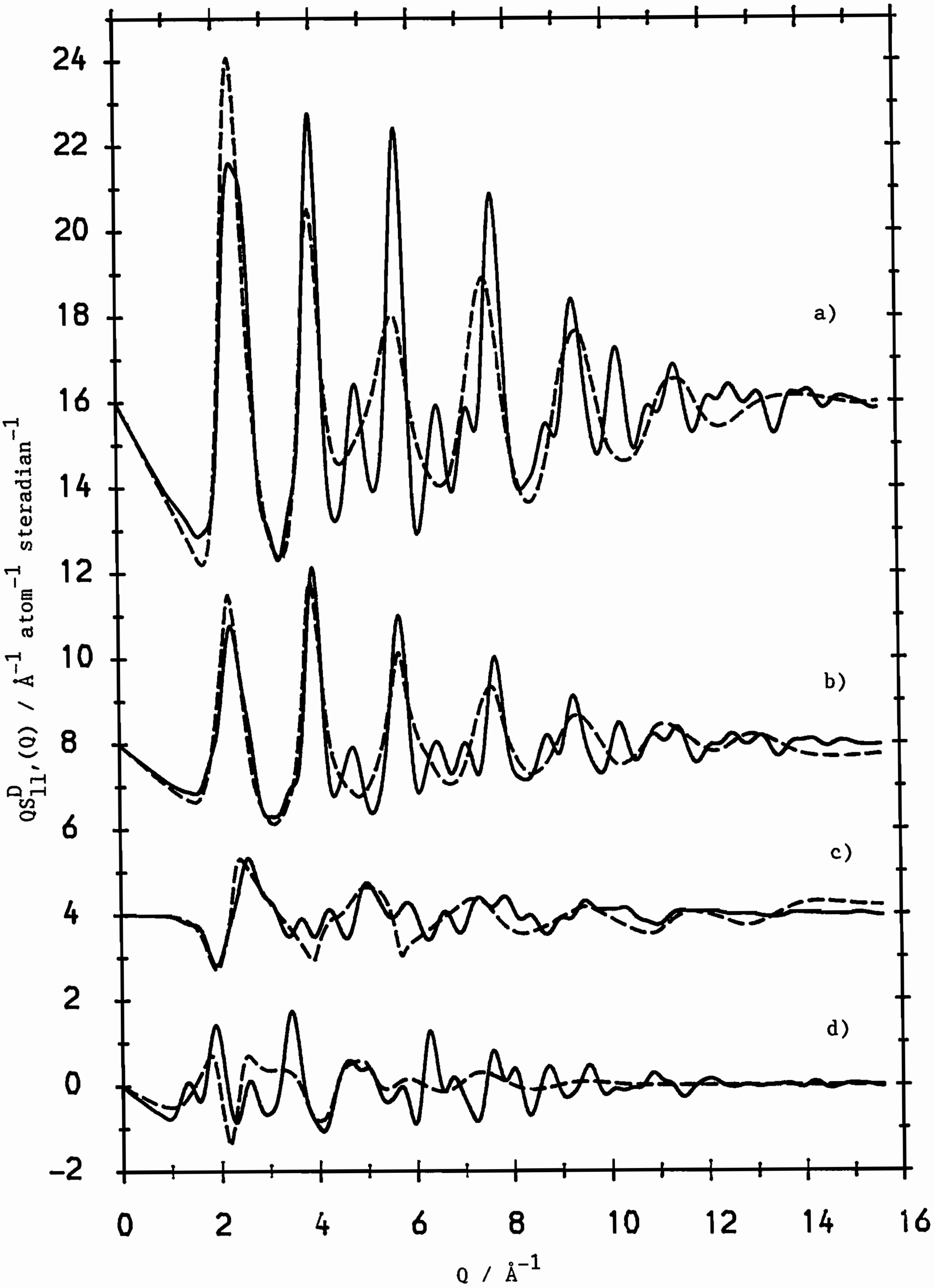

Figure 8.27 A Comparison in Reciprocal-Space Between the Quasi-crystalline Calculation for Ce_7Ni_3 (Continuous Line) and the Experimental Data for Amorphous Dy_7Ni_3 (Dashed Line).

a) Qi(Q) {offset 16.0} b) $QS^D_{DyDy}(Q)$ {offset 8.0}

c) $QS^D_{DyNi}(Q)$ {offset 4.0} d) $QS^D_{NiNi}(Q)$

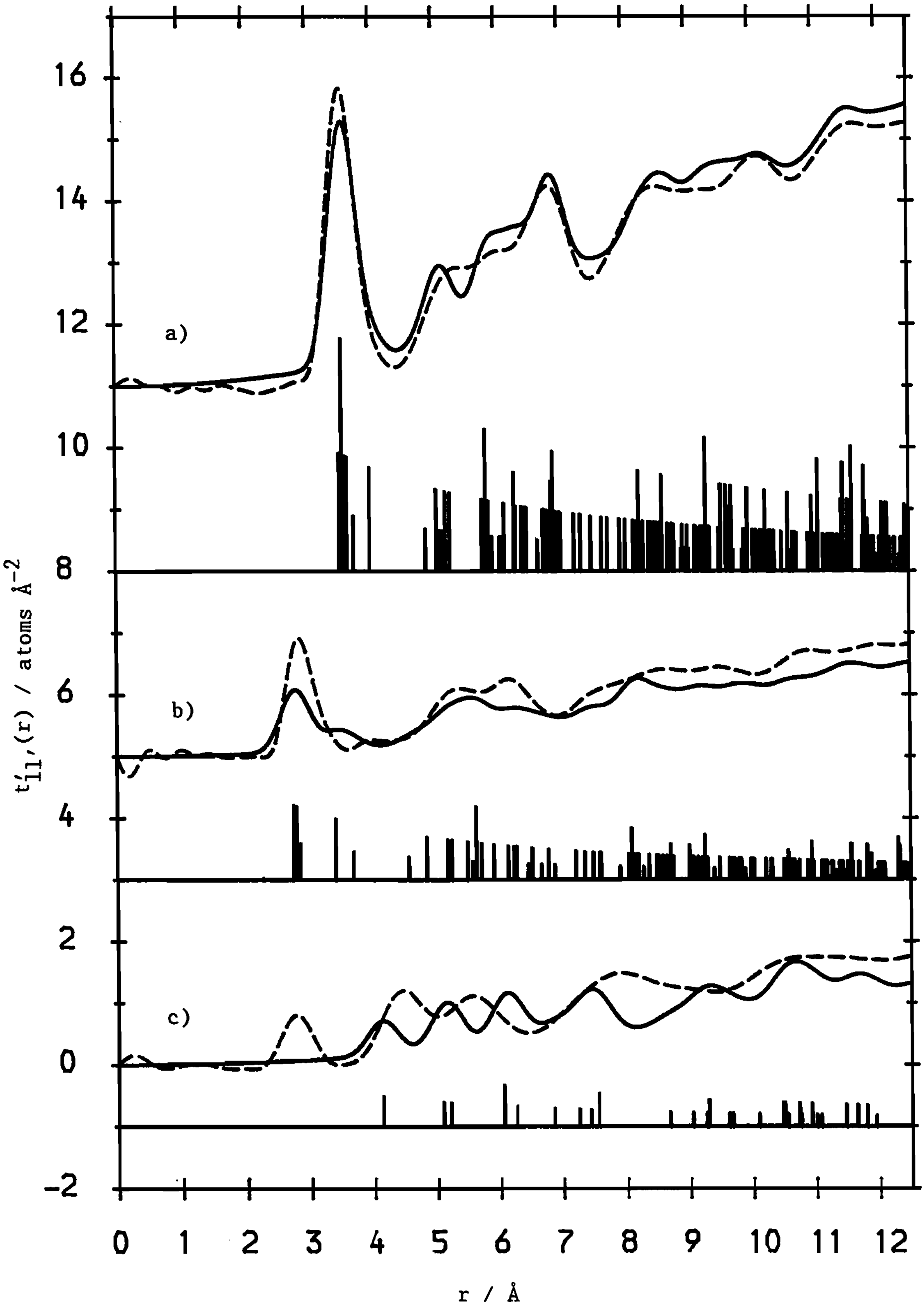

Figure 8.28 A Comparison in Real-Space Between the Quasi-crystalline Calculation for Dy_3Ni (Continuous Line) and the Experimental Data for Amorphous Dy_7Ni_3 (Dashed Line). Also shown {with suitable offsets} are the Unbroadened Partial Correlation Functions Calculated Directly from the Crystal and Reduced by Factors of 20 (Dy-Dy), 20 (Dy-Ni) and 100 (Ni-Ni).

a) $t'_{DyDy}(r)$ {offset 11.0}   b) $t'_{DyNi}(r)$ {offset 5.0}

c) $t'_{NiNi}(r)$

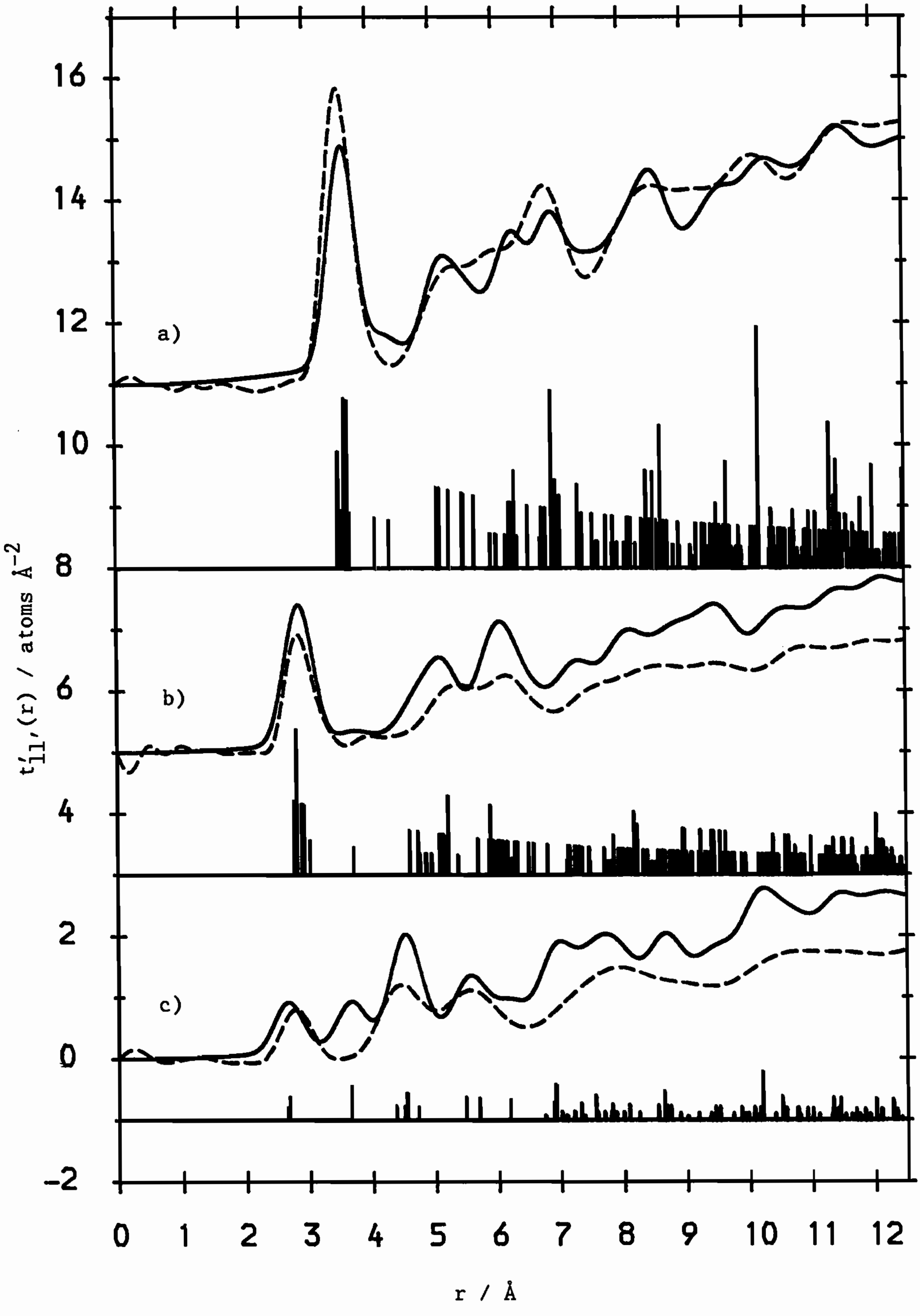

Figure 8.29 A Comparison in Real-Space Between the Quasi-crystalline Calculation for Dy_3Ni_2 (Continuous Line) and the Experimental Data for Amorphous Dy_7Ni_3 (Dashed Line). Also shown {with suitable offsets} are the Unbroadened Partial Correlation Functions Calculated Directly from the Crystal and Reduced by Factors of 20 (Dy-Dy), 20 (Dy-Ni) and 100 (Ni-Ni).

a) $t'_{DyDy}(r)$ {offset 11.0} b) $t'_{DyNi}(r)$ {offset 5.0}

c) $t'_{NiNi}(r)$

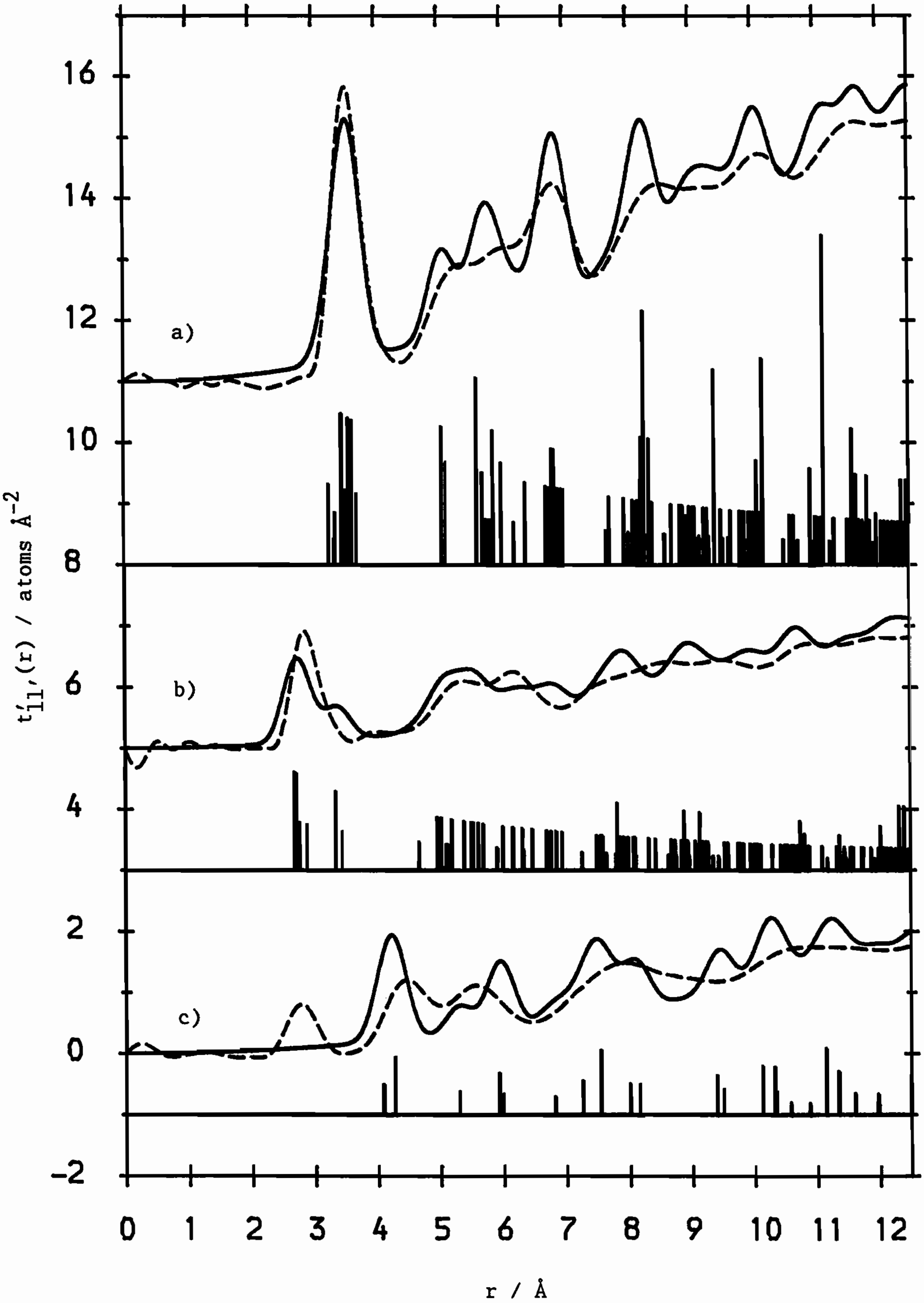

Figure 8.30 A Comparison in Real-Space Between the Quasi-crystalline Calculation for Ce_7Ni_3 (Continuous Line) and the Experimental Data for Amorphous Dy_7Ni_3 (Dashed Line). Also shown {with suitable offsets} are the Unbroadened Partial Correlation Functions Calculated Directly from the Crystal and Reduced by Factors of 20 (Dy-Dy), 20 (Dy-Ni) and 100 (Ni-Ni).

a) $t'_{DyDy}(r)$ {offset 11.0} b) $t'_{DyNi}(r)$ {offset 5.0}

c) $t'_{NiNi}(r)$

CHAPTER 9

DIFFRACTION STUDIES OF THE MAGNETIC STRUCTURE OF Dy7Ni3.

9.1 EXPERIMENTAL PROCEDURE.

Magnetic neutron diffraction experiments on Dy_7Ni_3 were performed using the powder diffractometer D2 (see section 7.1.2) on the same occasion as the studies of atomic structure described in Chapter 7. The same incident neutron wavelength of about 0.9Å was used and hence the same calibration values apply (table 7.2). The $^0Dy_7{}^0Ni_3$ sample was used for all of the magnetic diffraction experiments since this sample has no coherent nuclear scattering as has been discussed in section 6.4.2 . Ribbons of $^0Dy_7{}^0Ni_3$ were placed in a vanadium can inside the cryostat described in section 7.1.2 . Hence a separate background run was performed for the magnetic diffraction experiments. The diffraction pattern of the sample was measured at 7.2K, 44.3K and 95.8K using the same experimental procedure as for the measurements described in Chapter 7. Also short scans covering just the region of the first peak of the diffraction pattern (ie. at low angles) were performed at 7.2K, 20.1K, 32.9K, 38.0K, 52.7K, 63.6K, 95.8K and 147.7K . The temperature of the sample was measured using both carbon and platinum resistance thermometers positioned close to the sample. A preliminary report of these experiments has been given by WRIGHT, HANNON, CLARE, SINCLAIR, JOHNSON, ATZMON and MANGIN (1985).

9.2 DATA REDUCTION AND CORRECTION.

Figure 9.1 shows the short scans which cover Q-values only in the region of Q_1, the Q-value of the first peak of the diffraction pattern. The data from these scans were not smoothed with a cubic spline program (see section 7.3.2) since they only extend over a very limited Q-range which is too small for Fourier transformation to be useful. At room temperature the diffraction pattern of the ${}^{0}Dy_7{}^{0}Ni_3$ sample is smooth and virtually featureless, but as it is cooled peaks gradually appear corresponding to a steady increase in the extent of magnetic order. Figure 9.2 shows the maximum value of the short scan diffraction patterns as a function of temperature. There is no obvious indication of any change occurring at the previously reported (BUSCHOW, 1980) asymptotic Curie temperature θ_p=35K, and there is clearly magnetic order present at temperatures considerably in excess of θ_p.

The curve shown in figure 9.2 has a marked similarity to the temperature behaviour of the SANS signal, particularly in the Q-range $0.02 \rightarrow 0.03\text{Å}^{-1}$ (see Chapter 10). This raises the possibility of performing critical scattering type measurements about the first peak of the structure factor at Q_1. For amorphous solids such measurements have previously (see section 4.3) always been performed about [000] which is the only true reciprocal lattice point (equation (4.1.18)). However, in the case of a crystal critical scattering measurements may be performed about any reciprocal lattice point (see HAGEN, COWLEY, SATIJA, YOSHIZAWA, SHIRANE, BIRGENAU and GUGGENHEIM, 1983 for example) and thus for an amorphous solid it may be possible to perform critical scattering measurements about Q_1, regarding Q_1 as a pseudo reciprocal lattice point. A more detailed study would be required to establish the validity of this idea.

Figure 9.3 shows the diffraction pattern for the $^{0}Dy_7{}^{0}Ni_3$ sample measured at three low temperatures in the cryostat and also measured at room temperature without the cryostat (as described in Chapter 7). The room temperature data has the usual fall-off from low to high Q associated with a magnetic form factor indicating that at room temperature the sample is in the paramagnetic state (see section 11.2 for a further discussion of this point). As the sample is cooled an additional featured component appears in the diffraction pattern. This component is the distinct magnetic scattering (equation (4.2.21)) due to magnetic order developing in the sample.

As discussed in section 6.2.1 the usual approach used to analyse magnetic diffraction data from amorphous solids is to take a temperature difference and Fourier transform the result. There are potential problems with this approach due to the nuclear scattering: The structure in the nuclear scattering can lead to confusion and in particular the change with temperature of the nuclear scattering (as given by the Debye-Waller factor, equation (4.1.75), and also thermal expansion) is a potentially serious problem. It can be impossible to completely separate the magnetic scattering from the change with temperature of the nuclear scattering. In the case of the $^{0}Dy_7{}^{0}Ni_3$ sample the only nuclear scattering is self scattering. Hence there are no features in the nuclear scattering to cause confusion. Also, since the nuclear self scattering does not show a Debye-Waller factor temperature dependence (see section 4.1.4) or thermal expansion effects, there is no potential problem due to the nuclear scattering changing with temperature. Thus the data for the $^{0}Dy_7{}^{0}Ni_3$ sample are ideally suited to the temperature difference followed by Fourier transformation data analysis approach since the usual problems are avoided.

Note that the statement given above that nuclear self scattering is temperature independent is not strictly true because there is a temperature dependence in the Placzek expression (equation (4.1.50)) due to the mean kinetic energy $\bar{K}$. However, the terms $-8C_3\bar{K}\sin^2\theta/3\mu E_0$ and $\bar{K}/3\mu E_0$ tend to cancel each other and the temperature dependence is extremely small. A calculation of this effect shows that at the Q_{max} ($11.90Å^{-1}$) of D2 (the Placzek correction is greatest at high Q) a change in temperature from 300K to 100K produces a change in the self scattering from the ${}^{0}Dy_7{}^{0}Ni_3$ sample of only 0.04%.

All the runs at a particular temperature were added together and normalised to the monitor counts. The runs on the background were combined in a similar way and the result was then subtracted from the data for each temperature. There was found to be a loss in intensity at low angles due to the cryostat tail obstructing the scattered beam and hence the data below a Q_{min} of $0.90Å^{-1}$ was discarded. The three low temperature diffraction patterns were smoothed using the same approach as was used in the study of atomic structure (section 7.3.2). As with the nuclear scattering it was found to be necessary to add points in threes before splining to obtain a good fit at high Q. Even after this procedure the fit to the diffraction pattern at 44.3K had to be slightly corrected by hand. The fits obtained are shown in figure 9.3 together with the unfitted data. A correction was not made for absorption and self-shielding since the analytic approach discussed in section 7.3.3 cannot be used for magnetic scattering due to the Q-dependence of the magnetic form factor f(Q). The sample data was not normalised with the data from the vanadium run for the reasons discussed in section 7.3.1 and an absolute normalisation by some other means was not attempted. However, the normalisation of the data at one temperature relative to that at another temperature was consistent so that differences could successfully be taken. The temperature difference data shown in figure 9.4 were then obtained simply by subtracting the final fits to the experimental data. An advantage of the temperature difference technique is that the process of subtraction removes the nuclear self scattering, the magnetic self scattering, the background (although the background had actually been subtracted previously in the present work) and the multiple scattering so that these components of the measured diffraction pattern do not have to be explicitly subtracted. Differences were not taken between the low temperature data and the room temperature data because the room temperature data had been measured under different experimental conditions (ie. the background was different, the amount of sample in the beam was different, the sample geometry was different so that the absorption and multiple scattering were different, and also there may have been some difference in the cause of the normalisation problem discussed in section 7.3.1 and this problem cannot be corrected for in the case of magnetic scattering).

9.3 FOURIER TRANSFORMATION.

Magnetic isotropy was assumed and the low temperature data were Fourier transformed according to both approaches discussed in section 4.2.6 . The Fourier transform of $Qi^M(Q)$ with no modfication function yields a FINBAK (1949) magnetic correlation function $\Delta^i_f(r)$ whilst the Fourier transform of $Qi^M(Q)/f^2(Q)$ with a modification function yields the conventional magnetic correlation function $\Delta^{i}(r)$. These correlation functions are the magnetic equivalent of the nuclear correlation function D(r) (see equation (4.1.25)). They are used here rather than the magnetic equivalent of T(r) since a detailed knowledge of the magnetic state of the material would be required to calculate the average density term ($\sim T^{o}(r)$ - see equation (4.1.28)) which must be added to $\Delta^{i}(r)$ to obtain the magnetic equivalent of T(r).

The temperature difference data should oscillate about zero at high Q where the magnetic form factor has fallen essentially to zero. However, it was found that the temperature difference data actually oscillated about some value slightly different from zero. The causes of this are thought to include the slight temperature dependence of the nuclear self scattering mentioned above, and also a small temperature dependence of the background signal. An arbitrary but reasonable correction was made by adding a small constant to the data such that the integrand of the Fourier integral oscillated about zero at high Q. The data were extrapolated to zero Q in the same way as was used in the study of atomic structure (section 7.3.7). (The low Q extrapolations are not shown in figure 9.3 because of the additional complication due to the constant-adding correction.)

In order to obtain the magnetic correlation function $\Delta^{i}(r)$ a sharpening function $f^{2}(Q)$ (PATTERSON, 1935) is required as is shown in equation (4.2.31). In the work reported here the measured magnetic scattering from the ${}^{0}Dy_{7}{}^{0}Ni_{3}$ sample at room temperature (see section 7.3.5) was used as a sharpening function since this provides a good approximation to the magnetic form factor squared for Dy^{3+} ions in $Dy_{7}Ni_{3}$ (see also section

11.2). The modification function due to LORCH (1969) was used in the calculation of the magnetic correlation functions $\Delta^i(r)$.

A detailed examination of the temperature difference data indicated that because of the fall-off of the magnetic form factor there was not any genuine information about magnetic correlations beyond a Q of about $8Å^{-1}$ but just noise. Preliminary transforms of the data were found to be very noisy, particularly in the case of the sharpened transforms where the sharpening function magnifies noise at high Q, and hence the experimental data beyond a Q_{max} of $8.0Å^{-1}$ were not used to obtain the final transforms.

The magnetic correlation functions obtained for the three low temperature differences are shown in figure 9.5 in arbitrary units and with the Finbak magnetic correlation functions scaled to be consistent with the sharpened magnetic correlation functions. As expected the features of the sharpened magnetic correlation functions are less broad than those of the Finbak magnetic correlation functions. However, the difference in widths is quite small, indicating that the magnetic electrons are highly localised. The sharpened correlation functions show some increase in low-r normalisation error ripples. This is probably due to a difference in the cause of the normalisation problem (see section 7.3.1) between the low temperature runs with the cryostat and the room temperature run without the cryostat. A possible complication which may arise in the interpretation of magnetic correlation functions obtained from temperature difference data is that, where there is some magnetic ordering at both temperatures, the change with temperature of the mean thermal atomic displacement (~ equation (4.1.78)) could have an effect on the temperature difference magnetic correlation functions. This possible problem can be expected to be most severe for the 7.2K-44.3K difference since there is more structure in the data taken at these temperatures than in that taken at 95.8K . However, the transform obtained for 7.2K-44.3K does not show any of the features characteristic of a subtraction of peaks of differing widths. Hence it is concluded that in the temperature range of the observations the mean thermal atomic displacement for Dy_7Ni_3 does not change rapidly so that this possible problem is not significant. The interpretation of the results is discussed in section 11.3 .

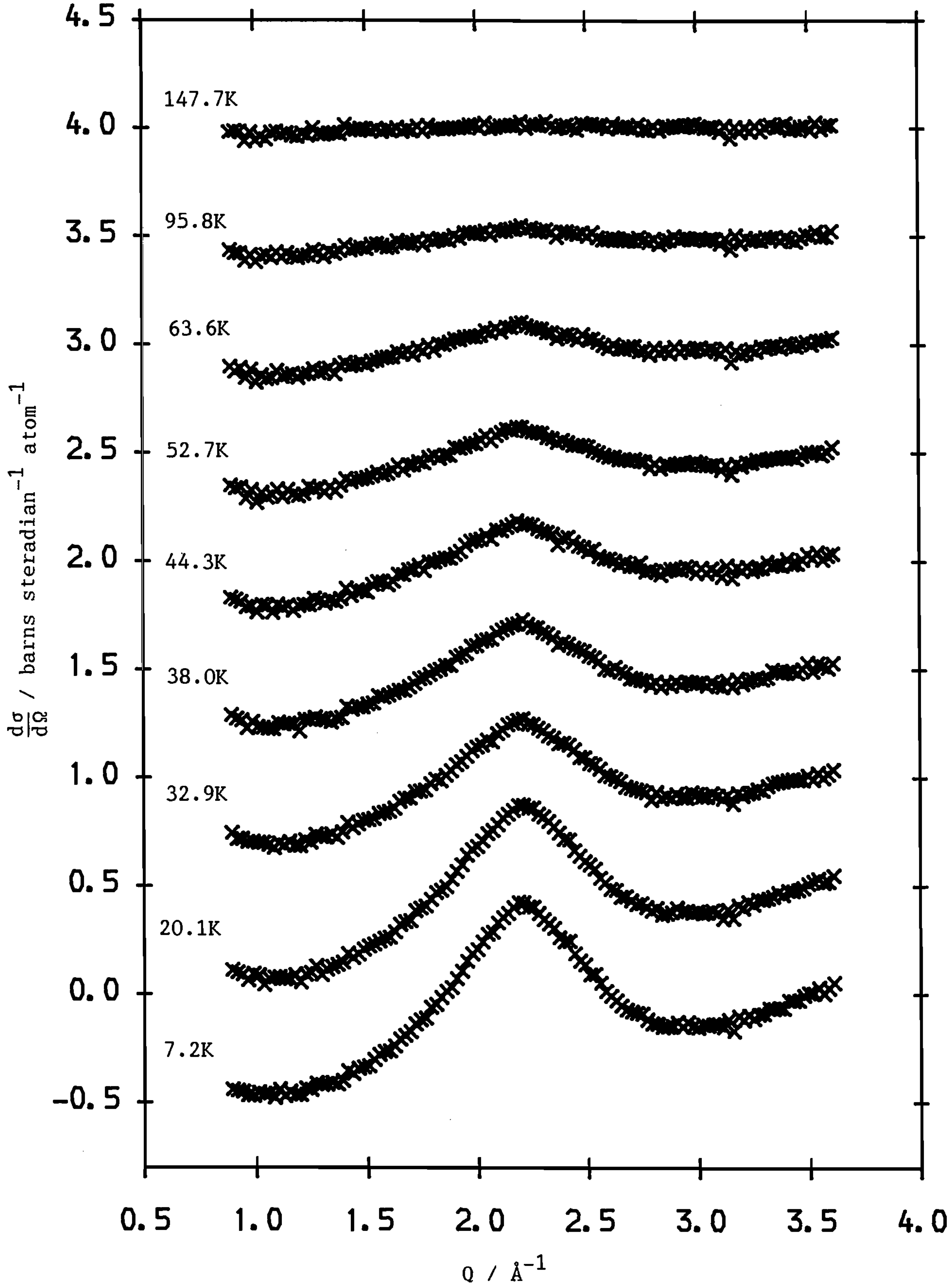

Figure 9.1 The Magnetic Diffraction Pattern of $^{0}Dy_7{}^{0}Ni_3$ in the Region of Q_1 after Subtraction of the Room Temperature Data. {offsets are in multiples of 0.5 with zero offset for 7.2K}

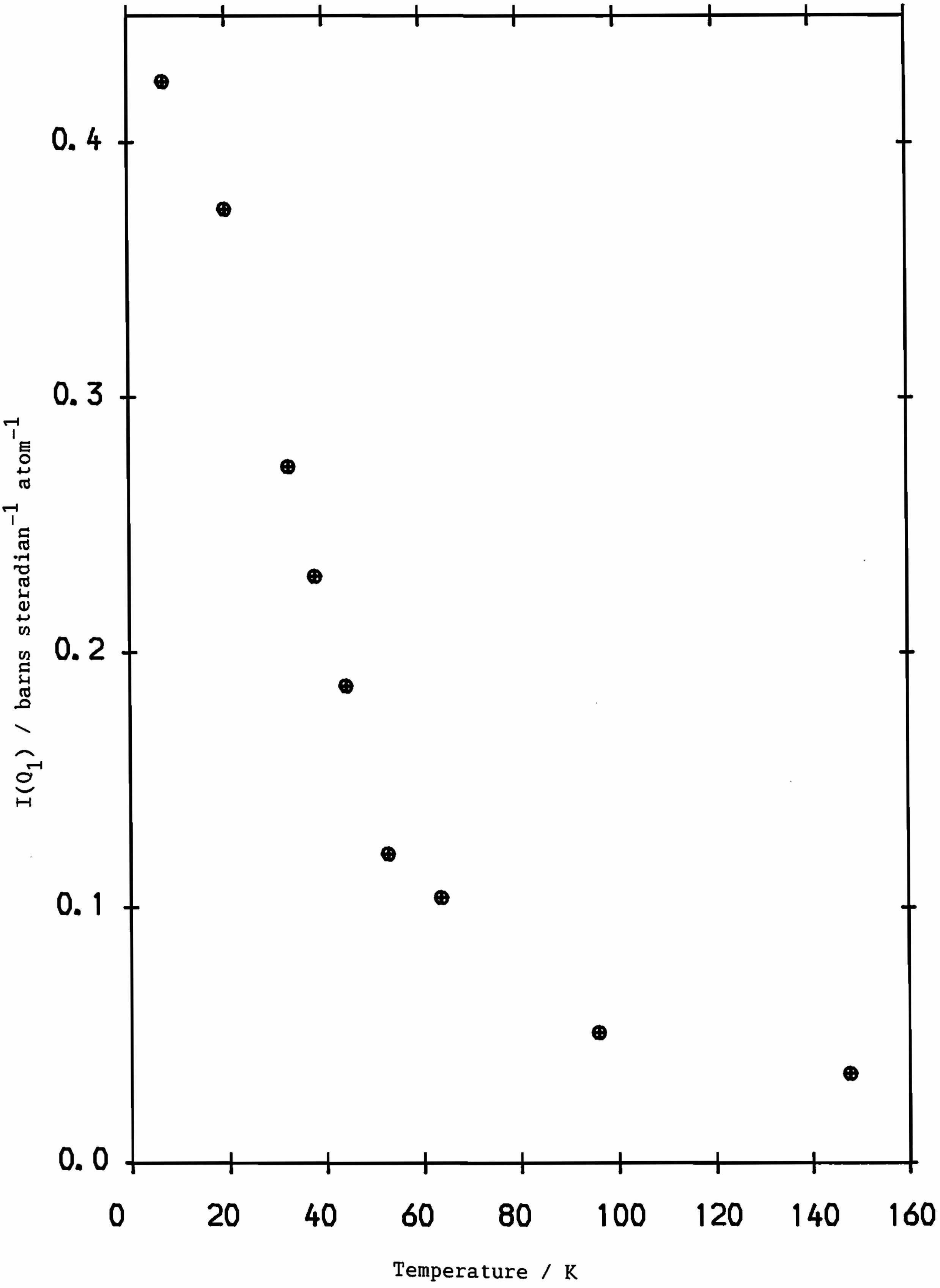

Figure 9.2 I(Q_1) for $^{0}Dy_7{}^{0}Ni_3$ as a Function of Temperature.

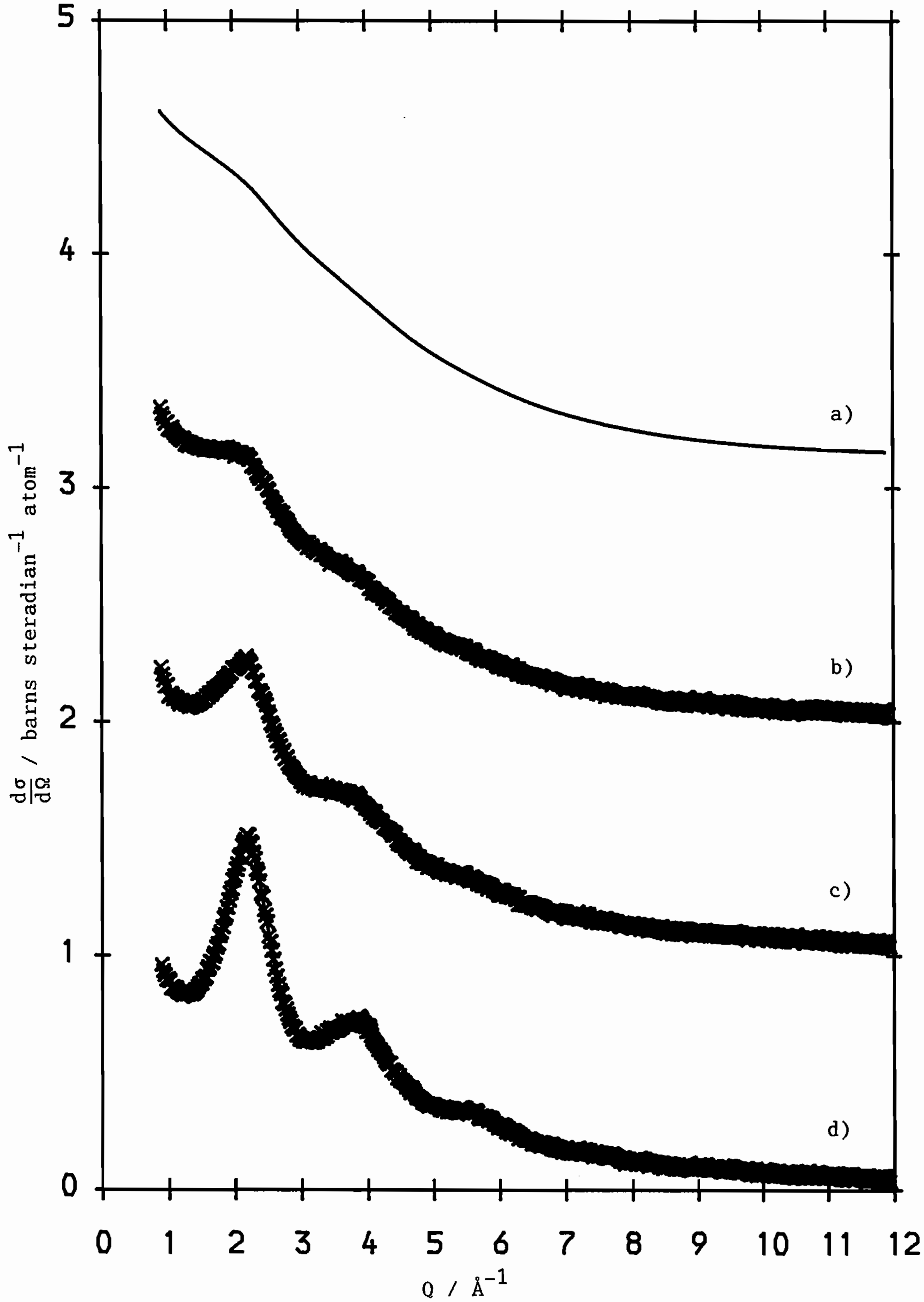

Figure 9.3 The Magnetic Diffraction Pattern of $^{0}Dy_{7}{}^{0}Ni_{3}$ at low Temperatures Showing Data Points and Fit.

a) Room Temperature {offset 3.0}

b) 95.8K {offset 2.0} c) 44.3K {offset 1.0} d) 7.2K

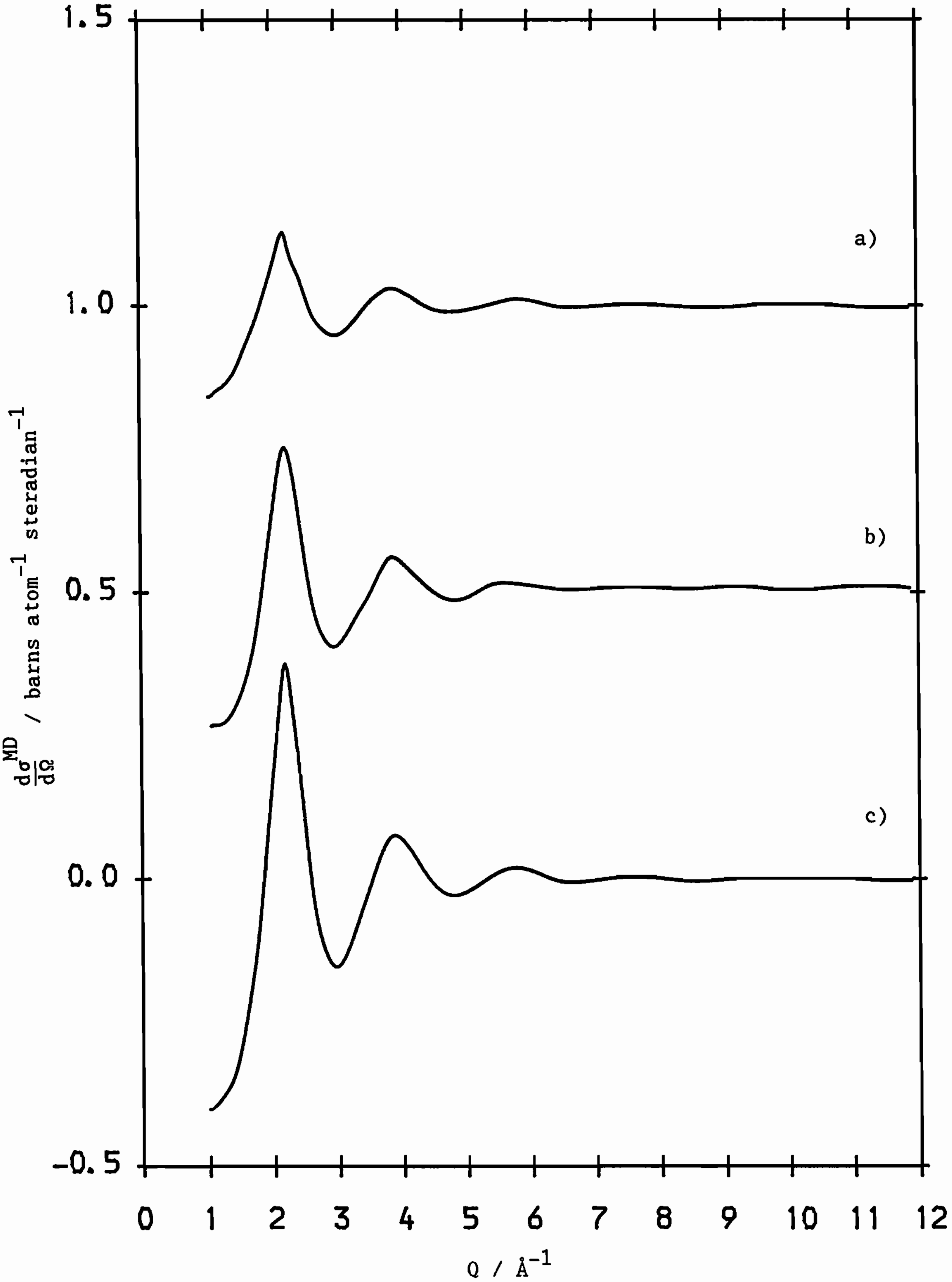

Figure 9.4 The Change with Temperature of the Diffraction Pattern of $^{0}Dy_7{}^{0}Ni_3$. a) 44.3K-95.8K {offset 1.0} b) 7.2K-44.3K {offset 0.5} c) 7.2K-95.8K

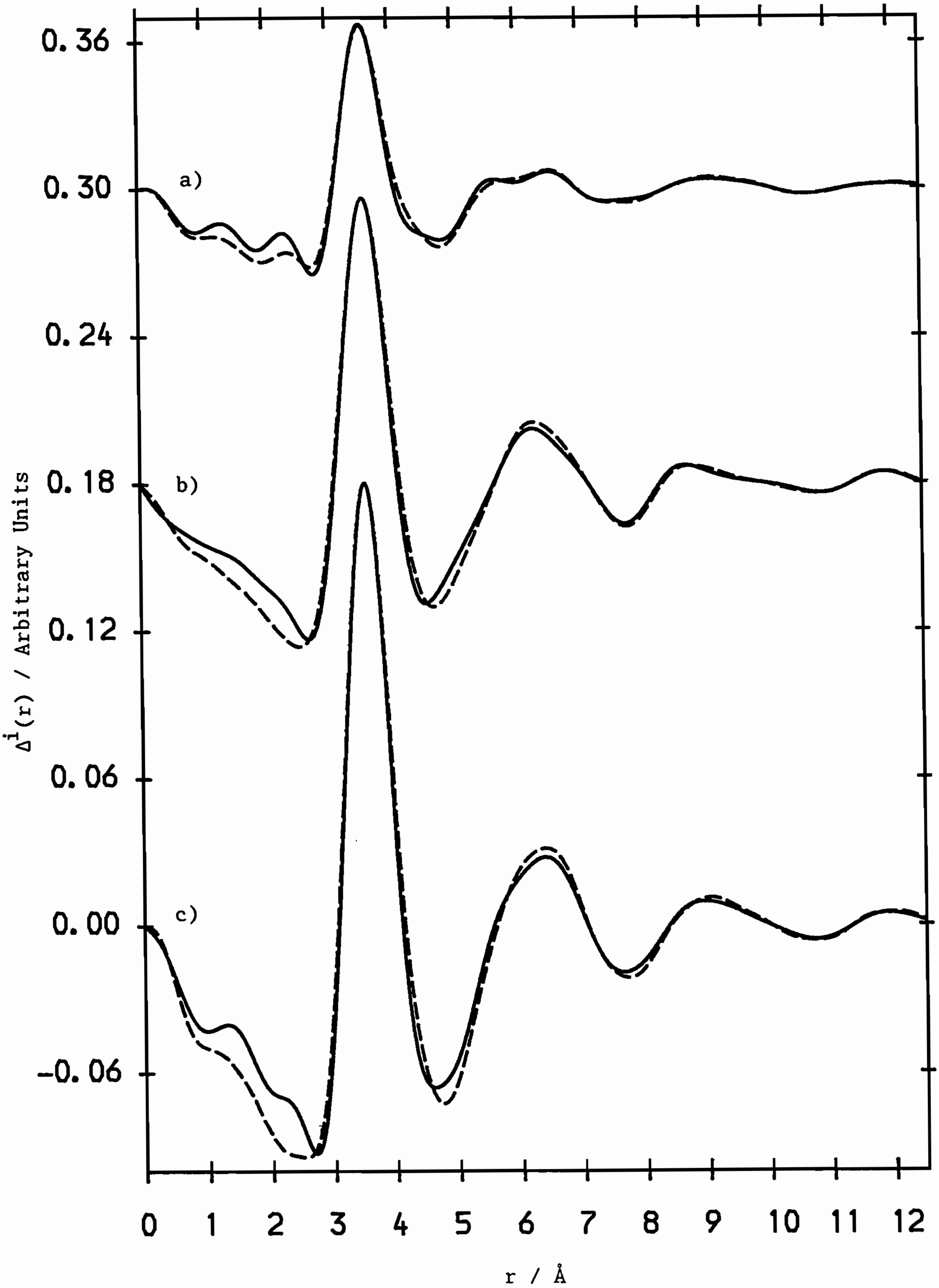

Figure 9.5 The Magnetic Correlation Functions $\Delta^i(r)$ (Continuous Line) and $\Delta^i_f(r)$ (Dashed Line). a) 44.3K-95.8K {offset 0.3} b) 7.2K-44.3K {offset 0.18} c) 7.2K-95.8K

CHAPTER 10

Dy7Ni3 - SMALL ANGLE NEUTRON SCATTERING.

10.1 THE SMALL ANGLE NEUTRON SCATTERING DIFFRACTOMETER D17.

The small angle neutron scattering (SANS) diffractometer D17 (figure 10.1) at the Institut Laue Langevin (ILL) is designed for high Q-resolution high count rate experiments measuring the low Q part of the total neutron scattering from a sample. The instrument is capable of detecting elastic Q values from 0.003$Å^{-1}$ to 1.0$Å^{-1}$, depending on the setting. It is thus designed for studying scattering from large structures with dimensions of tens or hundreds of Ångstroms (eg. phase separated regions in a solid, magnetic structures, polymer structures, biological structures, micelles, dislocations, flux lines in type II superconductors).

The instrument is installed at the exit of a curved waveguide, H17, which views a liquid deuterium source at 25K which is contained within the D_2O moderator. Thus the high flux at long wavelengths required for a SANS diffractometer is obtained. A helical slot velocity selector is used to monochromate the incident beam and any wavelength from 8Å to 20Å can be obtained. The velocity selector has a triangular wavelength distribution with a FWHM of 10%. The velocity selector is followed by an incident beam monitor. The incident beam travels along an evacuated wave guide and collimator to reach the sample position. The divergence of the incident beam can be varied by using different collimation pieces and this determines the minimum Q value observable, the lowest reasonable value being 0.003$Å^{-1}$. A wavelength of 12Å gives the maximum obtainable flux at the sample position of about 10^6 neutrons $cm^{-2}s^{-1}$.

The immediate sample position is not evacuated and various ancillary sample environment equipment can easily be installed. This includes an automatic sample changer and a standard 'orange cryostat' and temperature controller which can achieve temperatures in the range 4K to 200K. Sample sizes from 1cmx1cm to 3cmx3cm are suitable.

The scattered beam passes through a silica window into an evacuated detector tank. The detector is a BeF_3 position sensitive detector. This is a planar square matrix arrangement multidetector. The detector is 64cm by 64cm and there are 16000 cells, each 5mm by 5mm. There is a 4cm by 6cm cadmium beam stop which is used to prevent the undeviated beam from damaging the detector. However, it is usually required to measure the transmission of the sample in a SANS experiment and so an attenuator is provided. In order to measure the transmission this is placed in the incident beam and the beam stop is then removed. The sample to detector distance can be set at 0.8m, 1.4m, 2.8m or 3.5m, and the detector angle is continuously variable from 0° to 90°. A PDP 11-40 computer is used to control the collection of data and store the data.

Further information about the instrument is given in the ILL users' guide book (I.L.L., 1986), and also by KOSTORZ (1979) who describes the D11 SANS diffractometer which is similar in many respects.

10.2 EXPERIMENTAL PROCEDURE.

10.2.1 THE PERFORMANCE OF A SMALL ANGLE NEUTRON SCATTERING EXPERIMENT.

In a typical SANS experiment the first measurement to be performed is a determination of the position on the detector of the centre of the undeviated beam. This is achieved by placing the attenuator in the primary beam path, removing the beamstop and then running with an empty sample holder. This enables the beamstop to be positioned correctly and the angle, and hence the Q value, corresponding to each detector element to be determined.

The beamstop is then positioned, the attenuator removed and runs are performed on the sample, the empty sample holder, a normalisation sample, and also a cadmium sample in the case of an absorbing sample. The transmissions of the sample, T_s, and normalisation sample, T_n, are measured by placing the attenuator in the incident beam and removing the beamstop.

The normalisation sample is a sample with a strong featureless signal at low Q. This is used so as to inter-normalise detector elements of different efficiencies. Usually perspex or water is used as a normalisation sample as both of these have a large incoherent cross-section (due mainly to hydrogen) and negligible coherent small angle scattering. If an absolute normalisation is required then a further run is performed on vanadium. The purpose of the run on the cadmium sample is to measure the contribution to the background from neutrons which have not passed through the sample and from electronic noise.

If the scattering from the sample is isotropic then the data can be analysed in terms of 'radial sums'. A radial sum is the resultant intensity scan produced when the counts from detector elements at the same Q value (ie. at the same radius from the beam centre on the detector) are combined together. The final corrected SANS signal for the sample is given by;

$$I(Q) = \frac{I_s(Q) - I_c(Q) - T_s(\ I_{sb}(Q) - I_c(Q)\ )}{I_n(Q) - I_c(Q) - T_n(\ I_{nb}(Q) - I_c(Q)\ )} \qquad (10.2.1)$$

where $I_s(Q)$, $I_c(Q)$, $I_{sb}(Q)$, $I_n(Q)$ and $I_{nb}(Q)$ are the measured radial sums for the sample, cadmium, sample background, normalisation sample and normalisation sample background respectively. The transmission factors in equation (10.2.1) are necessary to account for absorption of the background signal by the sample.

10.2.2 THE EXPERIMENT ON DY7NI3.

The SANS experiment on Dy_7Ni_3, using the D17 diffractometer, was divided into two parts. For the first part measurements were performed at room temperature to investigate the nuclear homogeneity and surface defects of the samples, whilst the second part was performed at low temperatures to investigate magnetic correlations in Dy_7Ni_3. As is explained below it proved necessary to perform the measurements for the second part of the experiment on two separate occasions (denoted 'experiment I' and 'experiment II', see below). A high degree of consistency was found between the measurements from these two occasions.

For the first part of the experiment both ${}^{N}Dy_7{}^{N}Ni_3$ and ${}^{0}Dy_7{}^{0}Ni_3$ samples were used so that nuclear and magnetic contributions could be separated. Plate-like samples of approximate width 13mm were manufactured from 3cm lengths of melt-spun ribbon, using Scotch 3M tape to hold the ends together and a circular neutron beam of diameter 8mm was used. The same pieces of ribbon were used as had previously been used in the wide angle neutron scattering (WANS) studies reported in Chapters 7 and 9. In order to obtain a transmission of about 50%, which is the ideal for a SANS experiment with an absorbing sample, the ${}^{N}Dy_7{}^{N}Ni_3$ sample was 3 ribbons thick and the ${}^{0}Dy_7{}^{0}Ni_3$ sample was 6 ribbons thick. The various runs described in section 10.2.1 were performed with the three instrumental settings given in table 10.1 so as to obtain a wide range of Q;

Sample-detector Distance d/m	Detector Angle 2θ	Incident Wavelength λ/Å	Q-range / $Å^{-1}$
1.41	0.0°	8.0	0.0277→0.1983
1.41	18.0°	8.0	0.0751→0.4226
2.80	0.0°	12.0	0.0077→0.0686

Table 10.1

Water was used for the normalisation sample. A normalisation run was not performed for the detector setting with a detector angle of 2θ=18°. The count rates for the runs on Cd were virtually zero. The transmissions T measured with the detector in the straight-through position are given in table 10.2;

	Experiment I				Experiment II	
	λ=8Å		λ=12Å		λ=12Å	
	T	t/μm	T	t/μm	T	t/μm
$^{N}\mathrm{Dy}_7{}^{N}\mathrm{Ni}_3$	0.467	65.1	0.328	64.0	-	-
$^{0}\mathrm{Dy}_7{}^{0}\mathrm{Ni}_3$	0.643	146.7	0.522	144.2	0.485	160.5
Normalisation Sample	0.457	-	0.401	-	0.125	-

Table 10.2

The measured transmissions T were used together with the density (0.03938 atoms $\mathrm{Å}^{-3}$) and the cross-sections listed in table 6.2 to calculate the sample thicknesses t, also given in table 10.2 . The values obtained are consistent with a ribbon thickness of order 20μm as measured directly (see section 6.5). The variations in the values obtained for t are typical of the errors in transmission measurements made on this type of instrument. Note that magnetic scattering was ignored in the calculations of sample thickness; the purpose of the calculations is only as a check for reasonableness and consistency so that a high degree of accuracy is not required. Thus, since the inclusion of magnetic scattering in the calculations is not straightforward, it was not considered worthwhile. The effect of ignoring magnetic scattering is that the sample thickness is overestimated. The sample thicknesses calculated for the $^{0}\mathrm{Dy}_7{}^{0}\mathrm{Ni}_3$ sample show a larger discrepancy than those calculated for the $^{N}\mathrm{Dy}_7{}^{N}\mathrm{Ni}_3$ sample. This is because the $^{0}\mathrm{Dy}_7{}^{0}\mathrm{Ni}_3$ sample has smaller nuclear scattering and absorption cross-sections so that the omission of the magnetic scattering cross-section from the calculations has a greater effect.

For the second part of the experiment the $^{0}Dy_{7}{}^{0}Ni_{3}$ sample was placed in a cryostat in order to investigate magnetic correlations as a function of temperature. This sample has the advantage that it has no coherent nuclear scattering so that any SANS signal observed is entirely magnetic in origin. All of the low temperature measurements were taken with the instrumental setting given in the final row of table 10.1 . Scans were performed at a number of temperatures from 7.4K to 150K. Particular attention was given to temperatures in the region of the asymptotic Curie temperature θ_p=35K reported by BUSCHOW (1980) for $Dy_{69}Ni_{31}$. Scans were performed in this region using a temperature step of about 1.5K so that a 'weak divergence' at θ_p similar to those reported by RHYNE (1985b) for RE-Fe_2 alloys would not be missed. Hence the allocated time which remained was insufficient to obtain scans at an adequate number of higher temperatures and more higher temperature scans were performed at a later date. Where it is necessary to distinguish the data taken later this is denoted 'Experiment II' whilst the data taken on the original occasion is denoted 'Experiment I'. For Experiment II perspex was used as a normalisation sample since on this occasion all the measurements were made with a cryostat at the sample position and ice is unsuitable for this purpose due to density fluctuations. In experiment II most of the measurements were taken in the temperature range 100→170K although a few were taken at various lower temperatures to check for consistency with experiment I. The consistency was found to be good. In experiment II the sample transmission was also measured at a variety of temperatures whilst cooling in order to check for a variation as has been suggested from a quasi-elastic neutron scattering study of amorphous $Y_{33}Fe_{67}$ (MURANI and REBOUILLAT, 1982). However, the sample transmission was found to remain constant as the temperature was changed.

10.3 DATA REDUCTION AND ANALYSIS.

The programs due to GHOSH (1981) were used for the initial reduction of the data into radial sums and to obtain the corrected SANS lineshape according to equation (10.2.1). A least squares program due to HAGEN (1987) was modified for use in fitting the SANS data. This particular program was chosen since it calculates uncertainties of the fitted parameters. (If the correct function is being fitted and the points are independent and normally distributed then the uncertainty of a parameter calculated by this program represents the standard deviation of the parameter.) The agreement factor calculated by the program is defined as;

$$F = \left[(N-k)^{-1} \sum_i (I_i^{obs} - I_i^{calc})^2 E_i^{-2} \right]^{1/2} \qquad (10.3.1)$$

where N is the number of data points, k is the number of variable parameters, I_i^{obs} and I_i^{calc} are the observed and the fitted value for the i^{th} data point and E_i is the error on I_i^{obs}. An agreement factor close to unity indicates a good fit, whilst a value above one indicates a poor fit.

10.3.1 NUCLEAR HOMOGENEITY.

The room temperature data for the ${}^{N}Dy_7{}^{N}Ni_3$ and ${}^{0}Dy_7{}^{0}Ni_3$ samples were studied for evidence of anisotropy (ie. a dependence of the scattering on the direction of $\underline{Q}$) but none was found. The data for these two samples were then reduced to yield corrected SANS lineshapes, denoted $I^{NN}(Q)$ and $I^{00}(Q)$

respectively. The data taken at the three different detector settings listed in table 10.1 were scaled by suitable inter-normalisation factors so as to obtain agreement in the overlap regions. $I^{NN}(Q)$ was normalised to absolute units of barns steradian^{-1} atom^{-1} by comparison with the corrected WANS measurement made on the same sample using the D4 diffractometer with a nominal incident wavelength of 0.7Å (see Chapter 7). The overlap between the SANS data and the WANS data extends from 0.26Å^{-1} to 0.419Å^{-1}. The advantage of this normalisation method is that it yields an absolute normalisation directly. Also the radial sum which results from this normalisation procedure is implicitly corrected for absorption and self-shielding. However, it is not corrected for multiple scattering (which is known to peak in the forward direction for a plate sample of crystalline material). The alternative method for achieving an absolute normalisation of the data would be to correct for absorption using the measured transmission and to divide by the amount of sample in the beam so as to obtain the cross-section per atom. However, the results from a SANS experiment are not generally of high accuracy so that the measured transmissions and sample thicknesses are not highly accurate. In the case of Dy_7Ni_3 there is an additional complication due to the magnetic scattering as has already been mentioned in section 10.2.2 . Thus the method of normalising the SANS data by comparison with the more accurate WANS data is to be preferred. Unfortunately it was not possible to normalise the $^0Dy_7{}^0Ni_3$ SANS data by a straightforward use of this method since the only WANS data on this sample was taken on the D2 diffractometer (see section 7.2) which has a Q_{min} above the Q_{max} of the SANS data. However, it was found to be possible to normalise $I^{00}(Q)$ by an indirect use of this method as follows: The ratio of the scattering for the $^0Dy_7{}^0Ni_3$

sample to the scattering for the ${}^{N}Dy_7{}^{N}Ni_3$ sample was calculated for the low Q region of the WANS data and for the high Q region of the SANS data. In both cases this ratio was well behaved and slowly changing. Hence the ratio calculated from the WANS data was extrapolated below the Q_{min} of D2 (0.48Å^{-1}) to obtain a value of 0.60 at the Q_{max} of the SANS data (0.419Å^{-1}). This value was then used to achieve an absolute normalisation of $I^{00}(Q)$. Figure 10.3 shows the normalised room temperature SANS signals and the corresponding WANS signals in the overlap region.

The corrected and absolutely normalised $I^{NN}(Q)$ and $I^{00}(Q)$ are shown in figure 10.2 . The SANS from both samples is small (compared to the low temperature magnetic data) with an appreciable signal only below momentum transfers of about 0.025Å^{-1}. At higher Q-values the SANS becomes very small and is not discernible above the general background (ie. the low Q limit of the WANS signal). The nuclear contribution $I^{nuc}(Q)$ to the SANS was obtained simply by subtracting $I^{00}(Q)$ from $I^{NN}(Q)$. Note that this procedure does not eliminate the general background since the nuclear scattering is different for the two samples. An estimate of the general background (due to the low Q limits of the WANS signals) was subtracted from the SANS signals so that they tended to zero at higher Q. The difficulty with this general background level may be viewed as arising essentially because a glass is not in true thermodynamic equilibrium so that the low Q limit of S(Q) is not given by the compressibility as with a liquid. A constant value of 2.5 was subtracted from $I^{nuc}(Q)$ and a constant value of 5.0 was subtracted from $I^{00}(Q)$. Porod (lnI versus lnQ) and Guinier (lnI versus Q^2) plots of the 12Å measurements of the nuclear and magnetic contributions to the SANS after subtraction are shown in figures 10.4 and 10.5 respectively. The low Q regions of the Porod plots appear linear and straight lines were fitted to the data yielding;

$$\ln I^{nuc}(Q) = (-4.58\pm0.14)\ \ln Q + (-16.54\pm0.65) \qquad (F=0.63) \qquad (10.3.2)$$

$$\ln I^{00}(Q) = (-3.96\pm0.10)\ \ln Q + (-14.53\pm0.49) \qquad (F=0.84) \qquad (10.3.3)$$

The agreement factors obtained indicate good fits. The fact that $I^{nuc}(Q)$ and $I^{00}(Q)$ are proportional to a power of Q indicates that the data are in the Porod regime; for a system with non-fractal geometry the Porod approximation gives $I \propto Q^{-4}$ (equation (4.3.8)). This is a high Q approximation but the data actually deviates from it at high Q because the SANS (which has an extremely strong Q-dependence) falls to a level which is much smaller than the errors in the low Q limit of the WANS signal. Hence it is only appropriate for the low Q data to be fitted by a Porod-type equation.

As discussed in section 4.3 the Guinier approximation applies at low Q. In this approximation $I \propto \exp(-Q^2R_G^2/3)$ (equation (4.3.6)) and hence a straight line was also fitted to the low Q region of the Guinier plots (figure 10.5), although the data appear to have a significant curvature. The fits yield;

$$\ln I^{nuc}(Q) = (-1.642\pm0.051)\times10^4\ Q^2 + (6.417\pm0.060) \qquad (F=3.93) \qquad (10.3.4)$$

$$\ln I^{00}(Q) = (-1.169\pm0.029)\times10^4\ Q^2 + (5.067\pm0.040) \qquad (F=5.75) \qquad (10.3.5)$$

The agreement factors obtained show that the low Q regions of the Guinier plots are not fitted well by straight lines.

The interpretation of these results is discussed in section 11.4.1 .

10.3.2 MAGNETIC CORRELATIONS.

The low temperature data for the $^{0}Dy_7{}^{0}Ni_3$ sample were studied for evidence of anisotropy in the SANS but none was found at any temperature studied. The data were then reduced to yield a corrected SANS lineshape for each sample temperature. An absolute normalisation was not attempted since this does not produce any obvious benefit for the study of magnetic correlations.

Figure 10.6 shows the measured SANS for the $^{0}Dy_7{}^{0}Ni_3$ sample at several low temperatures and figure 10.7 shows the temperature dependence of the SANS at a selection of Q-values. The magnetic SANS for Dy_7Ni_3 exhibits the same anomalous low temperature rise as has previously been observed for RE-Fe_2 alloys (see section 6.2). At low Q the SANS rises steadily from about 150K until it starts to level off at about 20K. At high Q the SANS rises only gradually from about 150K, then rises much more sharply from about 50K and only begins to level off at the lowest temperatures (~10K). Unlike the previous measurements on RE-Fe_2 alloys (see section 6.2), there is no indication of a 'weak divergence' in the SANS for Dy_7Ni_3 at temperatures in the region of the magnetisation-determined transition temperature Θ_p=35K (BUSCHOW, 1980).

In order to further investigate the temperature dependence of the magnetism in Dy_7Ni_3 the temperature derivative of the SANS was calculated using finite differences. Figure 10.8 shows the temperature derivative of the SANS at a selection of Q-values. The temperature derivative of the total scattering at a Bragg peak has previously been used successfully to determine the critical temperature for crystalline magnetic systems (MAJKRZAK, AXE and BRUCE, 1980; HAGEN and PAUL, 1984), this method being advocated by BRUCE (1981). In the case of the present SANS study it is not possible to determine the integrated intensity since the signal is still rising sharply at the lowest experimental Q-value. However, at all but the very lowest Q-values the Q-dependent temperature derivative shown in figure 10.8 has a very strong feature at 31K and since this value is in close proximity to the asymptotic Curie temperature θ_p=35K reported by BUSCHOW (1980) for $Dy_{69}Ni_{31}$ it may be identified as a transition temperature. The temperature of this strong feature in the temperature derivative does not change with Q apart from a slight decrease at the very lowest Q-values. Also very weak features appear at 65K and 112K in the temperature derivative at the very lowest Q-values.

Following the previous work on RE-Fe_2 alloys discussed in section 6.2 a LL^2 lineshape was fitted to the SANS data at each temperature after subtraction of the room temperature data for the ${}^{0}Dy_{7}{}^{0}Ni_{3}$ sample. The justification for this subtraction is that the very small SANS signal produced by this sample at room temperature is probably surface scattering arising through the magnetic cross-section (see section 11.4). This conclusion is supported by the fact that there is virtually no change in the SANS between 170K and room temperature. However, even if this is an incorrect conclusion, the subtraction of the room temperature SANS signal actually makes very little difference since it is relatively very small. The precise function used to fit the data was;

$$I(Q) = \frac{A'}{Q^2/\kappa^2 + 1} + \frac{B'}{(Q^2/\kappa^2 + 1)^2} + D \qquad (10.3.6)$$

For the purposes of fitting this form of the LL^2 function is to be preferred to that given in equation (6.2.5) since the derivatives behave in much less singular manner. The constant D was included in order to take into account the variation with temperature of the low Q limit of the wide angle magnetic structure factor due to the evolution of magnetic SRO. The Lorentzian coefficient A′, Lorentzian squared coefficient B′, constant D, correlation length $\xi \equiv 1/\kappa$ and agreement factor (equation (10.3.1)) obtained from the fits are shown in figures 10.9 to 10.13 . At temperatures above 35K the agreement factor is close to one, indicating a good fit. The correlation length ξ falls from 220Å at temperatures in the region of 150K to 150Å in the region of 40K.

At temperatures below 35K the agreement factor obtained by fitting a LL^2 lineshape to the data rises sharply to values in the region of 3.5, indicating that the low temperature data is not fitted well by the LL^2 function. Figure 10.14 shows the residual between fit and experiment at selected temperatures below 35K. The residuals are found to be consistently positive in some Q-regions and consistently negative in other Q-regions. This would seem to indicate an inadequacy in the functional form of the fit and hence an attempt was made to fit other reasonable functions to the low temperature data. Equation (10.3.6) with either A′ or B′ set to zero gave a significantly worse fit with agreement factors of order 10. The following functions were also fitted to the low temperature data;

$$I(Q) = \frac{A'}{Q^2/\kappa^2 + 1} + \frac{B'}{(Q^2/\kappa'^2 + 1)^2} + D \qquad (10.3.7)$$

$$I(Q) = \frac{A'}{Q^2/\kappa^2 + 1} + \frac{B'}{(Q^2/\kappa^2 + 1)^2} + D + \frac{E}{Q^2/\kappa'^2 + 1} \qquad (10.3.8)$$

$$I(Q) = \frac{A'}{Q^2/\kappa^2 + 1} + \frac{B'}{(Q^2/\kappa^2 + 1)^2} + D + \frac{E}{Q^2/\kappa'^2 + 1} + \frac{F}{(Q^2/\kappa'^2 + 1)^2} \qquad (10.3.9)$$

where $\kappa' \neq \kappa$ and the additional Lorentzian could represent spin-wave scattering. All three of these functions yielded very similar agreement factors to that obtained using the LL^2 function of equation (10.3.6). A check was also made to determine whether the deterioration of the fit below 35K could be explained as being due to the points at lowest Q being unreliable; any problems with the positioning of the beamstop or with the determination of the centre of the beam would affect the reliability of the points at lowest Q and the effect could be exacerbated by the large rise of the SANS occurring at lower temperatures. The check was made by successively removing the point at lowest Q and repeating the fit. It was found that this made very little difference to the fit and hence this explanation is rejected.

The interpretation of these results is discussed in section 11.4.2 .

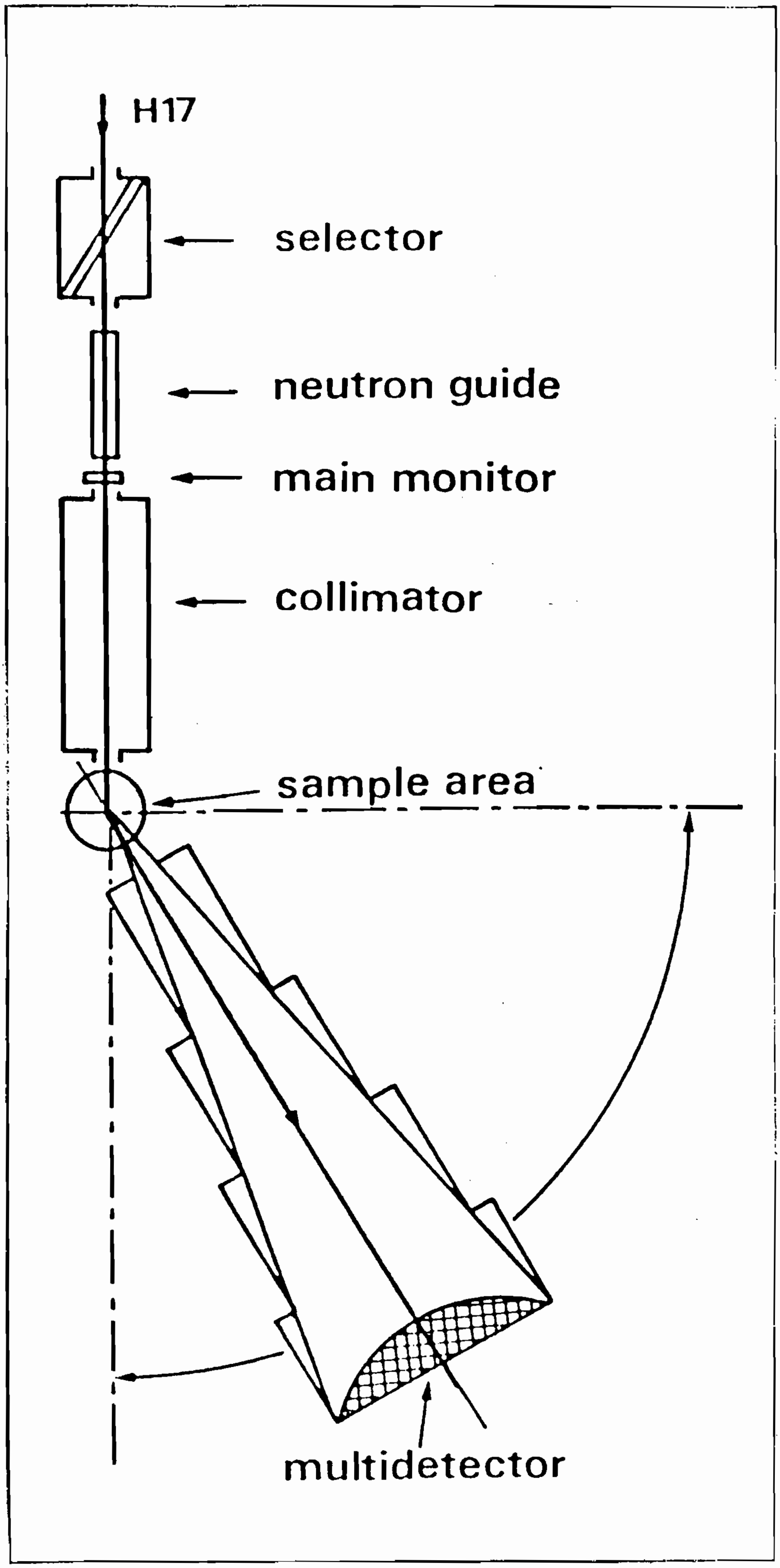

Figure 10.1 The Small Angle Neutron Scattering Diffractometer D17.

TITLE : Figure 10.2 SANS at Room Temperature for each Sample.

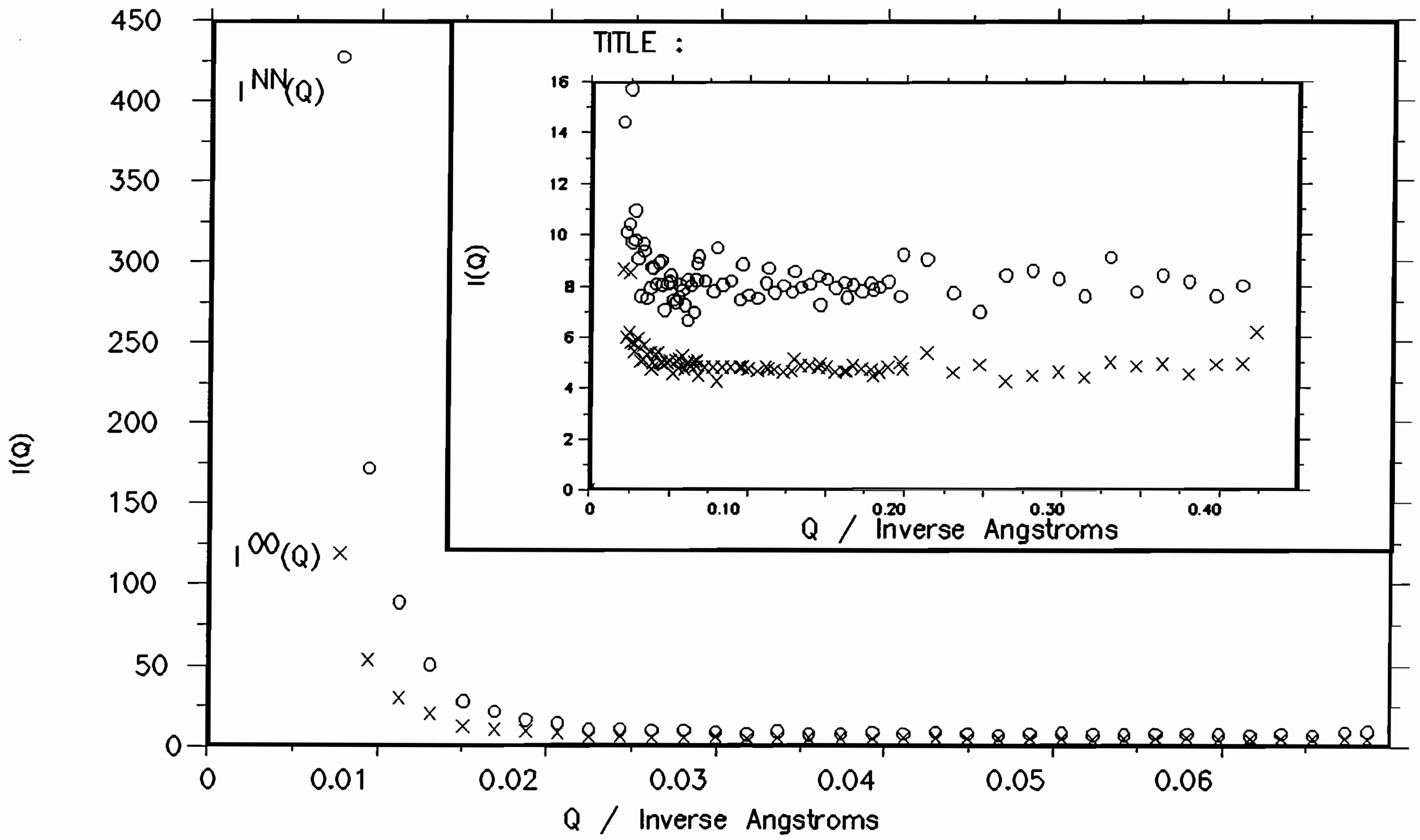

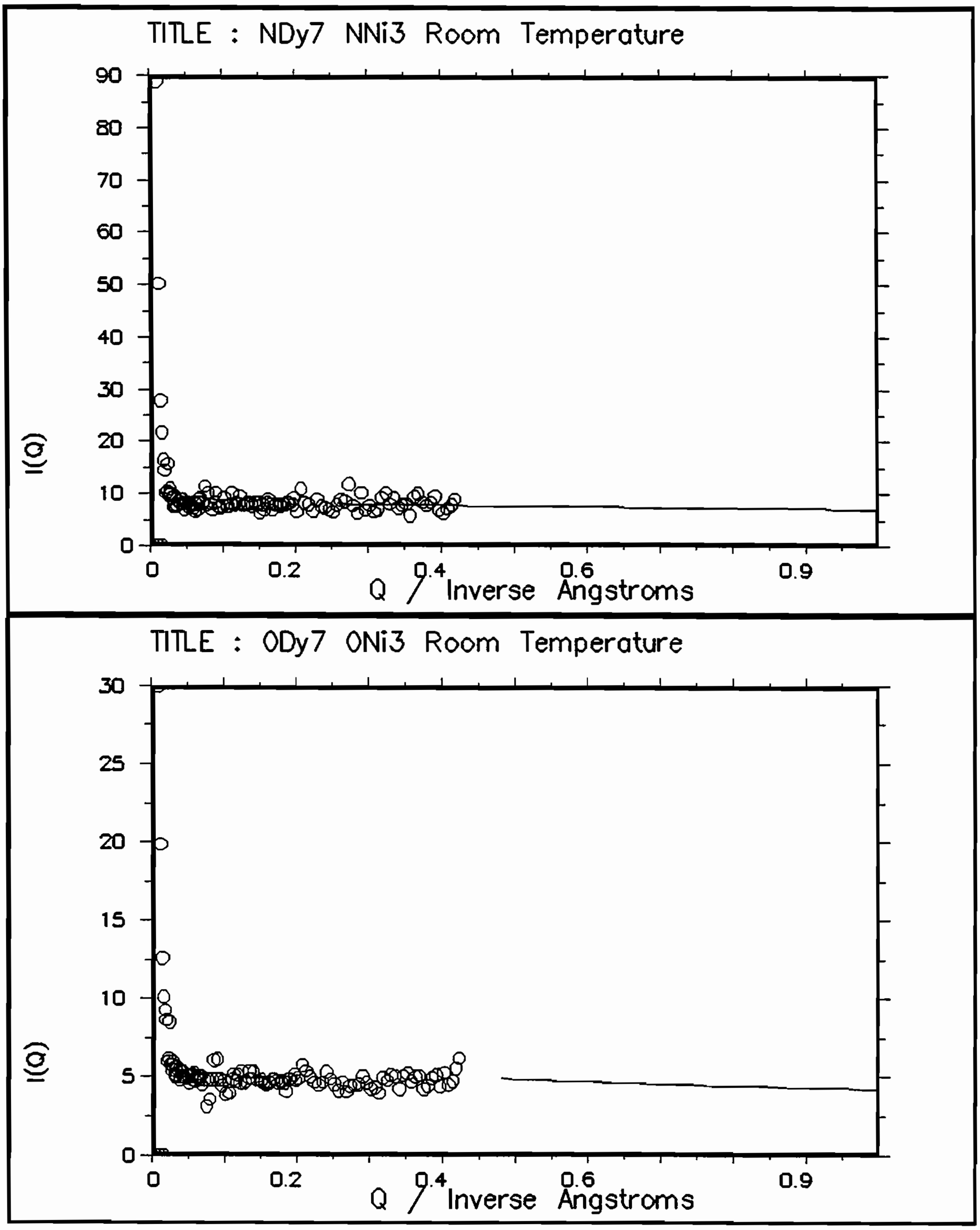

TITLE : NDy7 NNi3 Room Temperature

TITLE : ODy7 ONi3 Room Temperature

Figure 10.3 The Overlap between the Room Temperature SANS (Circular Points) and WANS (Continuous Line) for the $^{N}Dy_7{}^{N}Ni_3$ (Upper Figure) and $^{O}Dy_7{}^{O}Ni_3$ (Lower Figure) Samples.

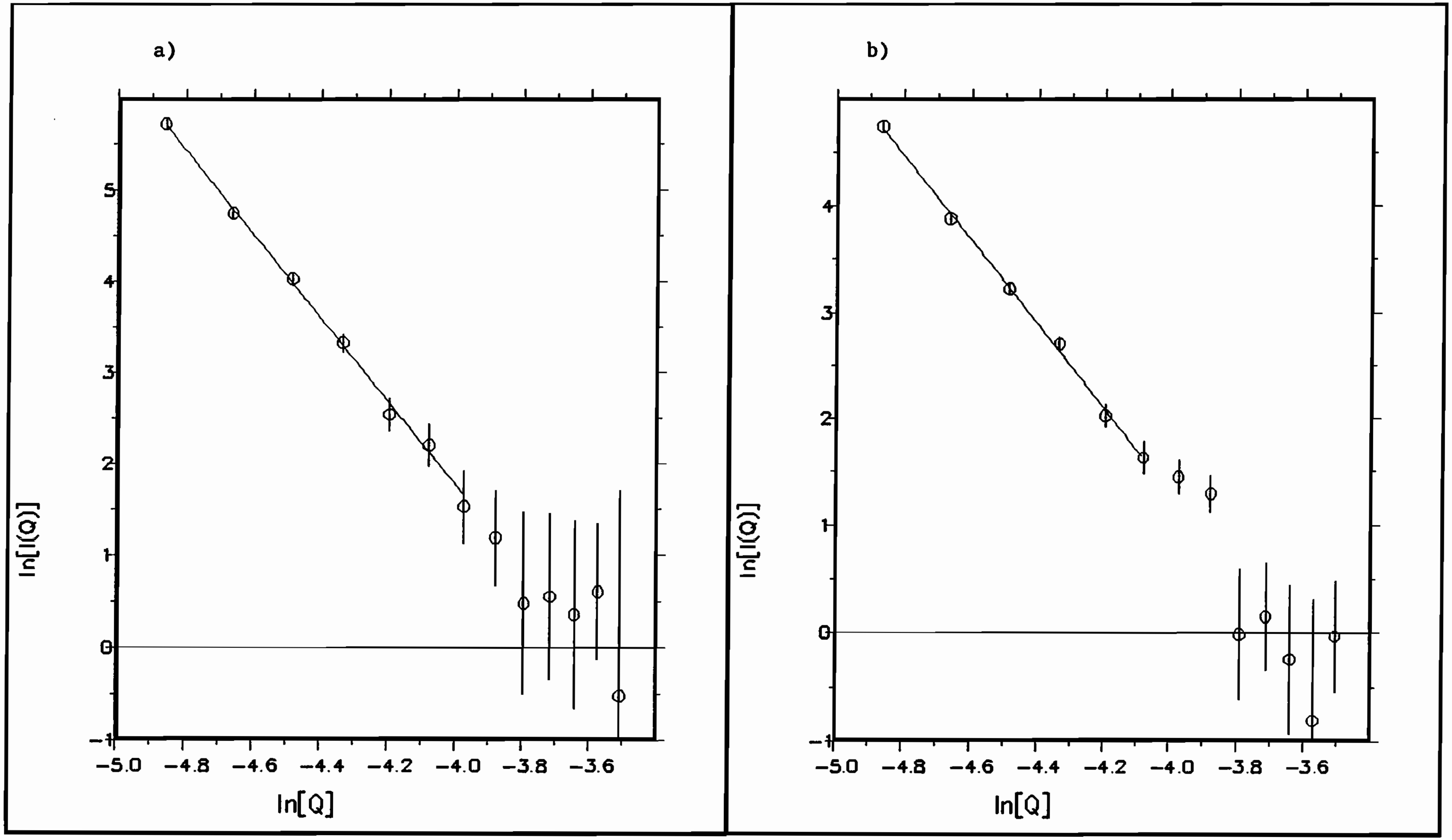

Figure 10.4 Porod Plots (lnI v. lnQ) of the Dy_7Ni_3 SANS showing the Experimental Data (Points) and the Fits to the Low Q Region (Continuous Line). a) $I^{nuc}(Q)$ b) $I^{00}(Q)$

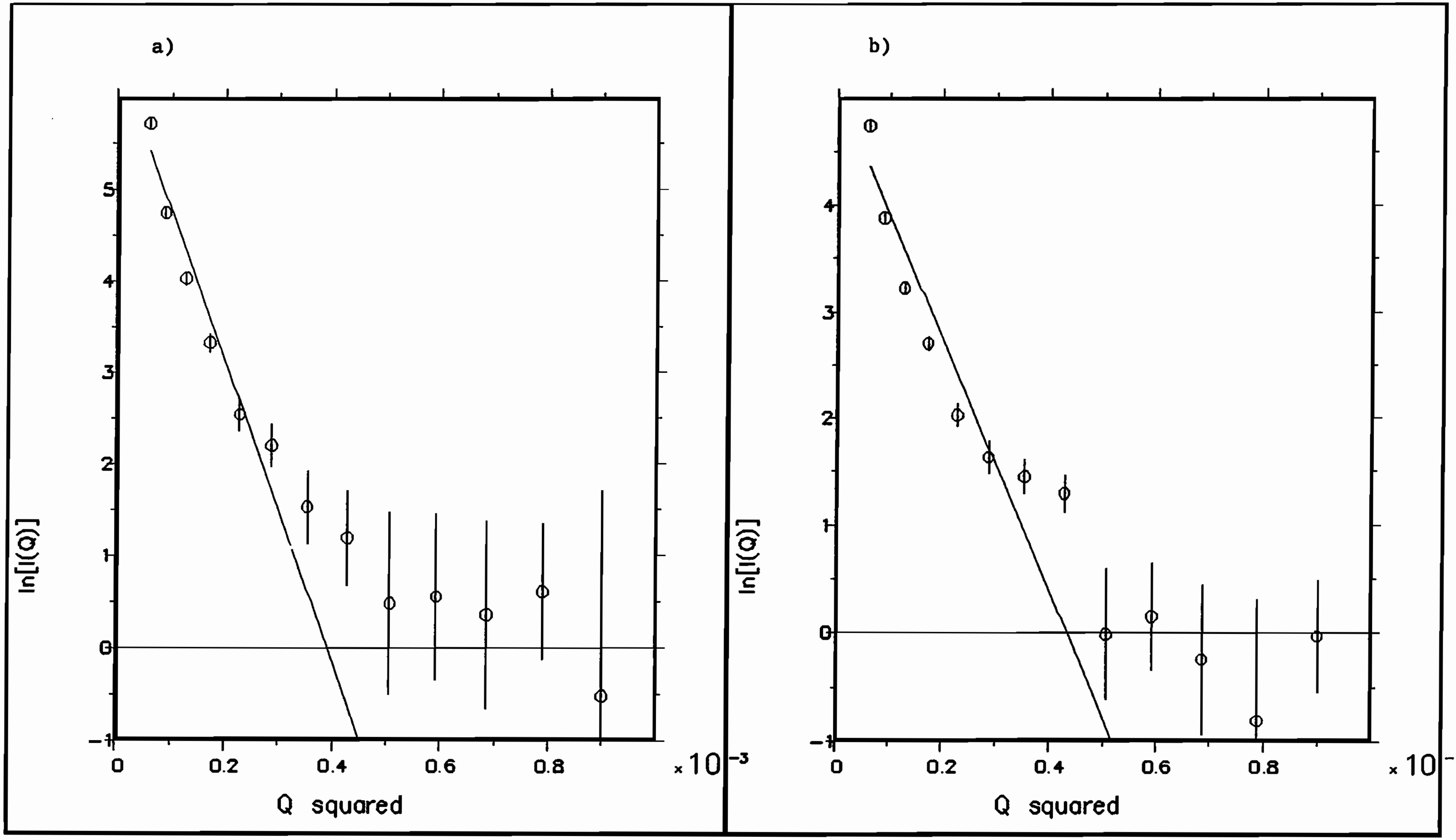

Figure 10.5 Guinier Plots (lnI v. Q^2) of the Dy_7Ni_3 SANS showing the Experimental Data (Points) and the Fits to the Low Q Region (Continuous Line). a) $I^{nuc}(Q)$ b) $I^{00}(Q)$

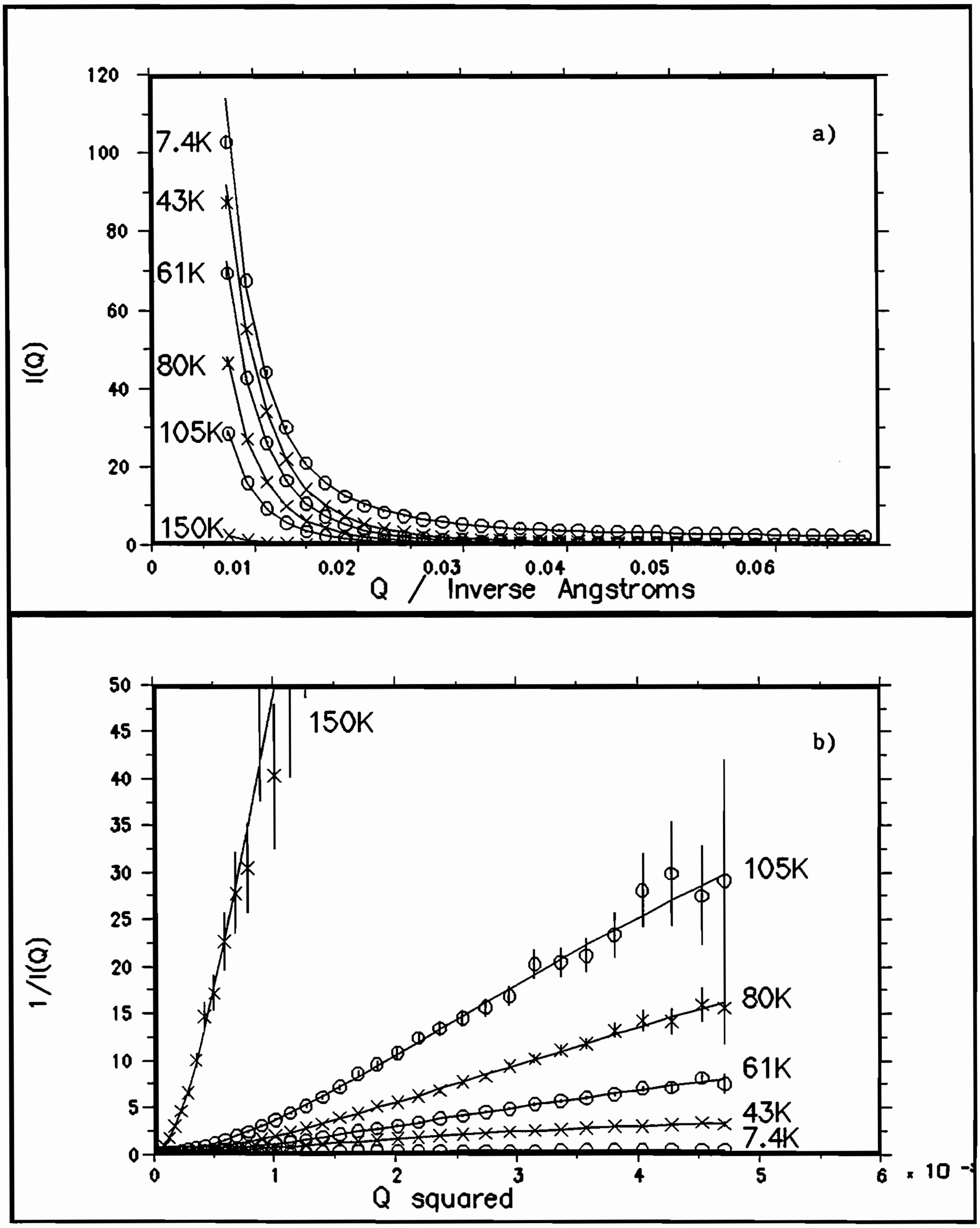

Figure 10.6 The Measured SANS for the ${}^{0}Dy_{7}{}^{0}Ni_{3}$ Sample at Several Low Temperatures (Points) Together with the Results of Fitting a LL2 Function to the Data (Continuous Line).

a) I(Q) v. Q b) 1/I(Q) v. Q^2

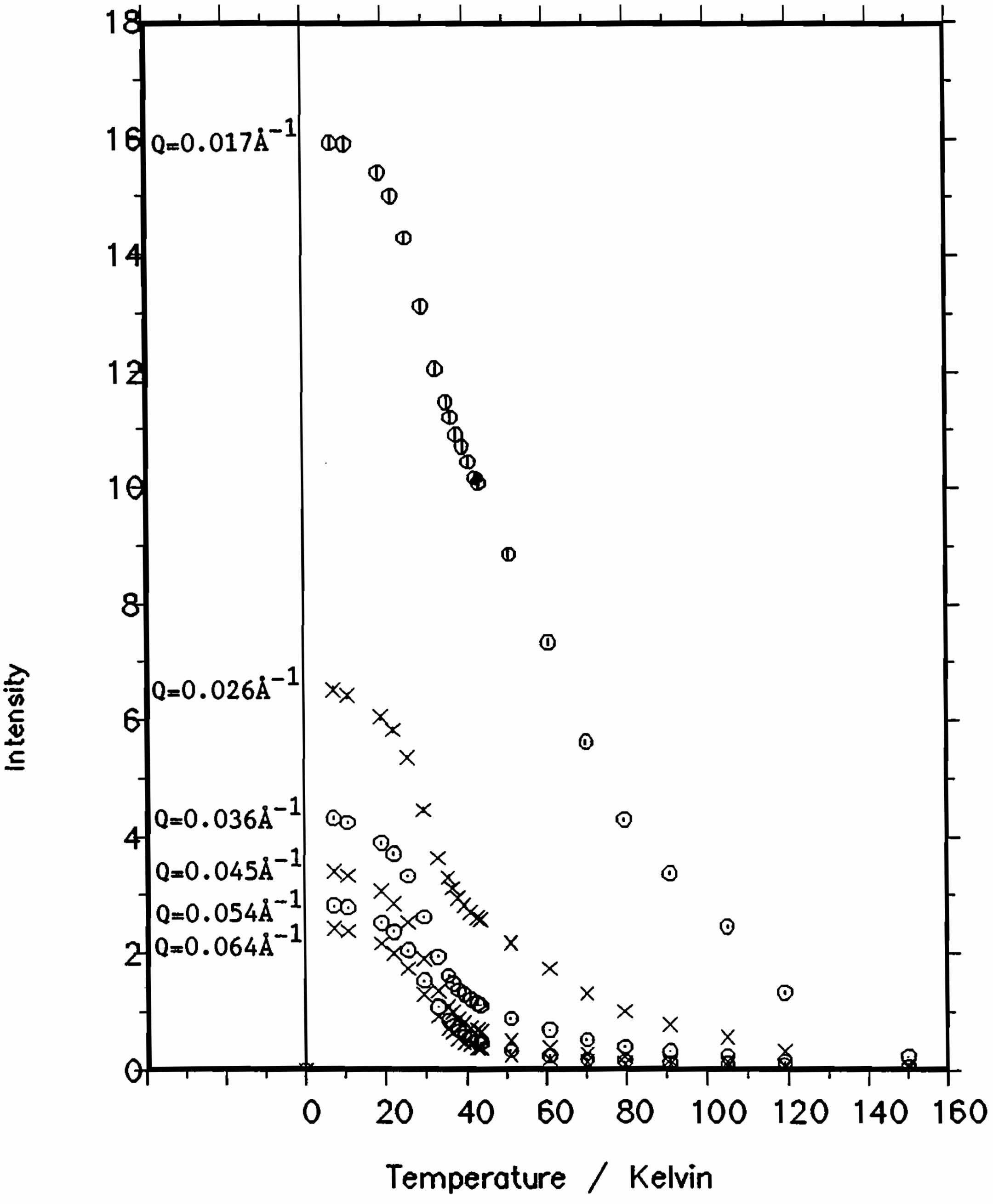

Figure 10.7 The Temperature Dependence of the SANS at a Selection of Q-values.

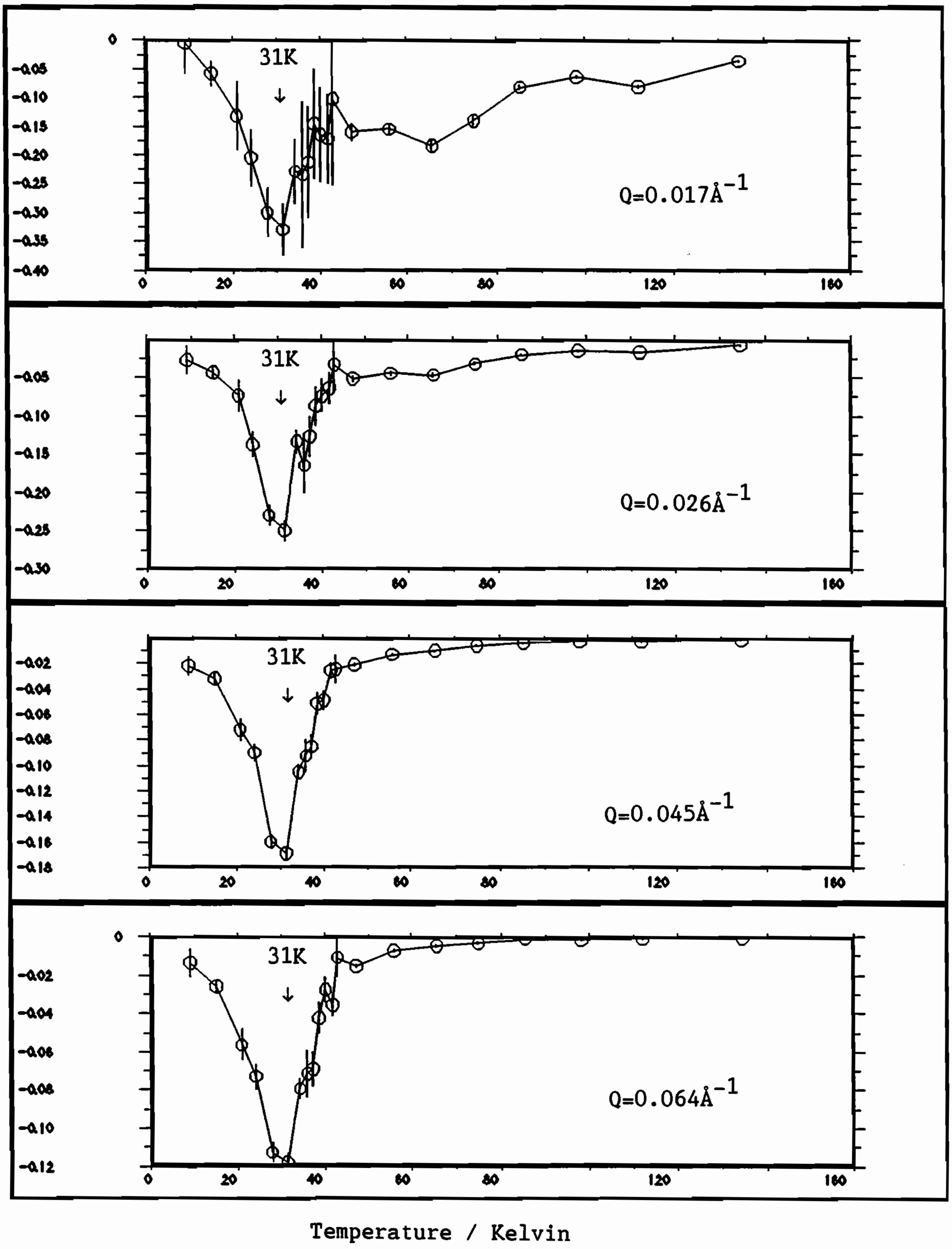

Figure 10.8 The Temperature Derivative of the SANS at a Selection of Q-values.

Figure 10.9 The Lorentzian Coefficient A′ from Fitting the SANS.

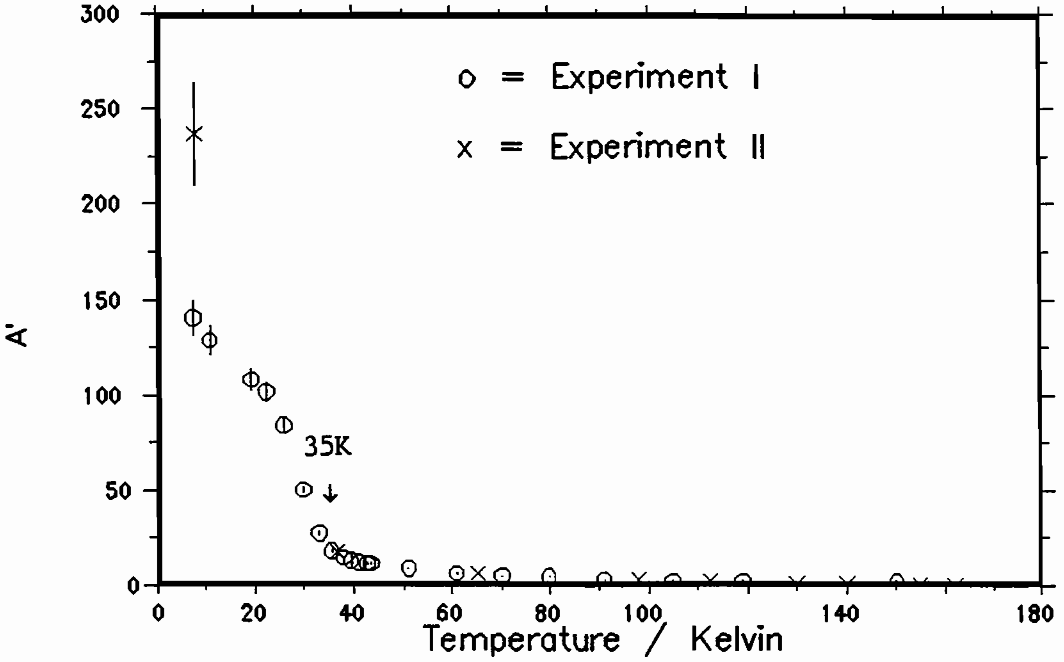

Figure 10.10 The Lorentzian Squared Coefficient B′

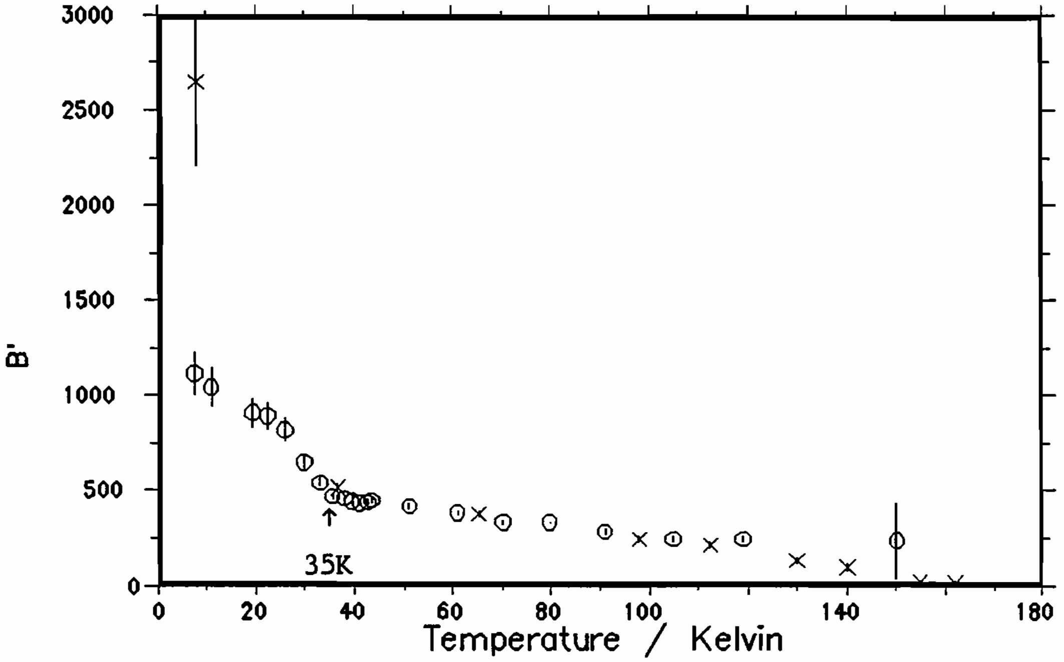

Figure 10.11 The Constant Term D from Fitting the SANS.

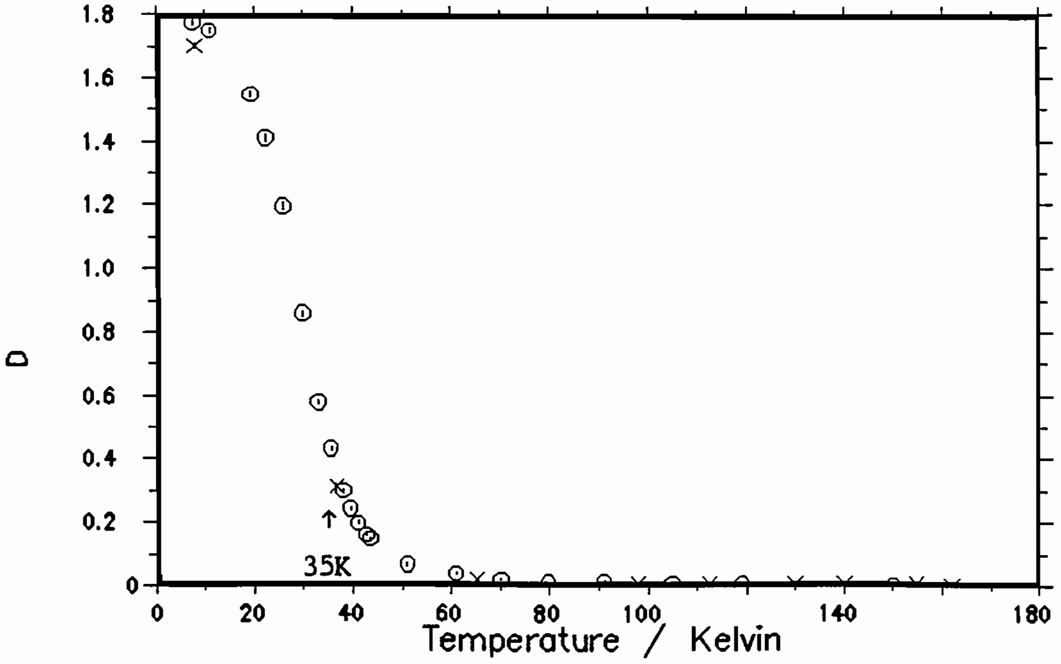

Figure 10.12 The Correlation Length ξ from Fitting LL^2 to the Dy_7Ni_3 SANS.

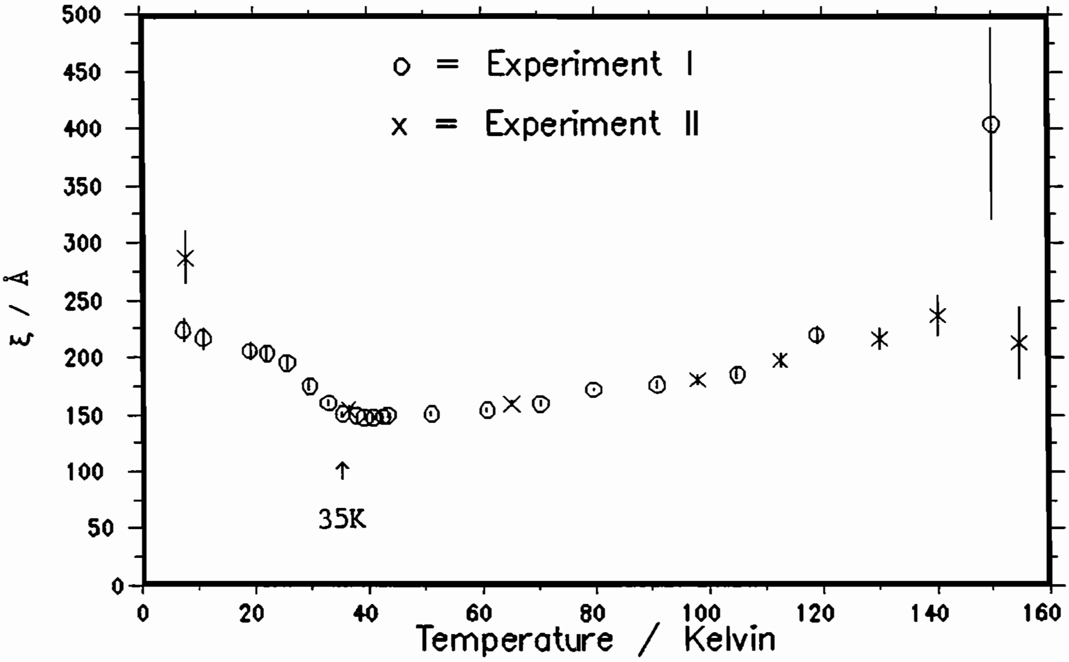

Figure 10.13 The Agreement Factor F from Fitting LL^2 to the Dy_7Ni_3 SANS.

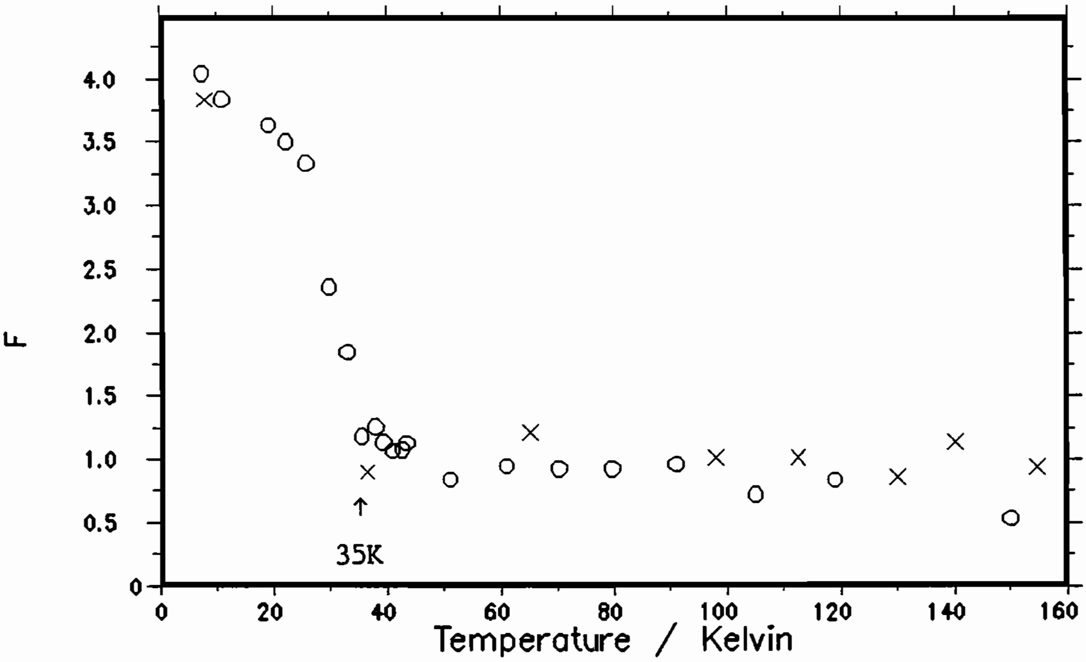

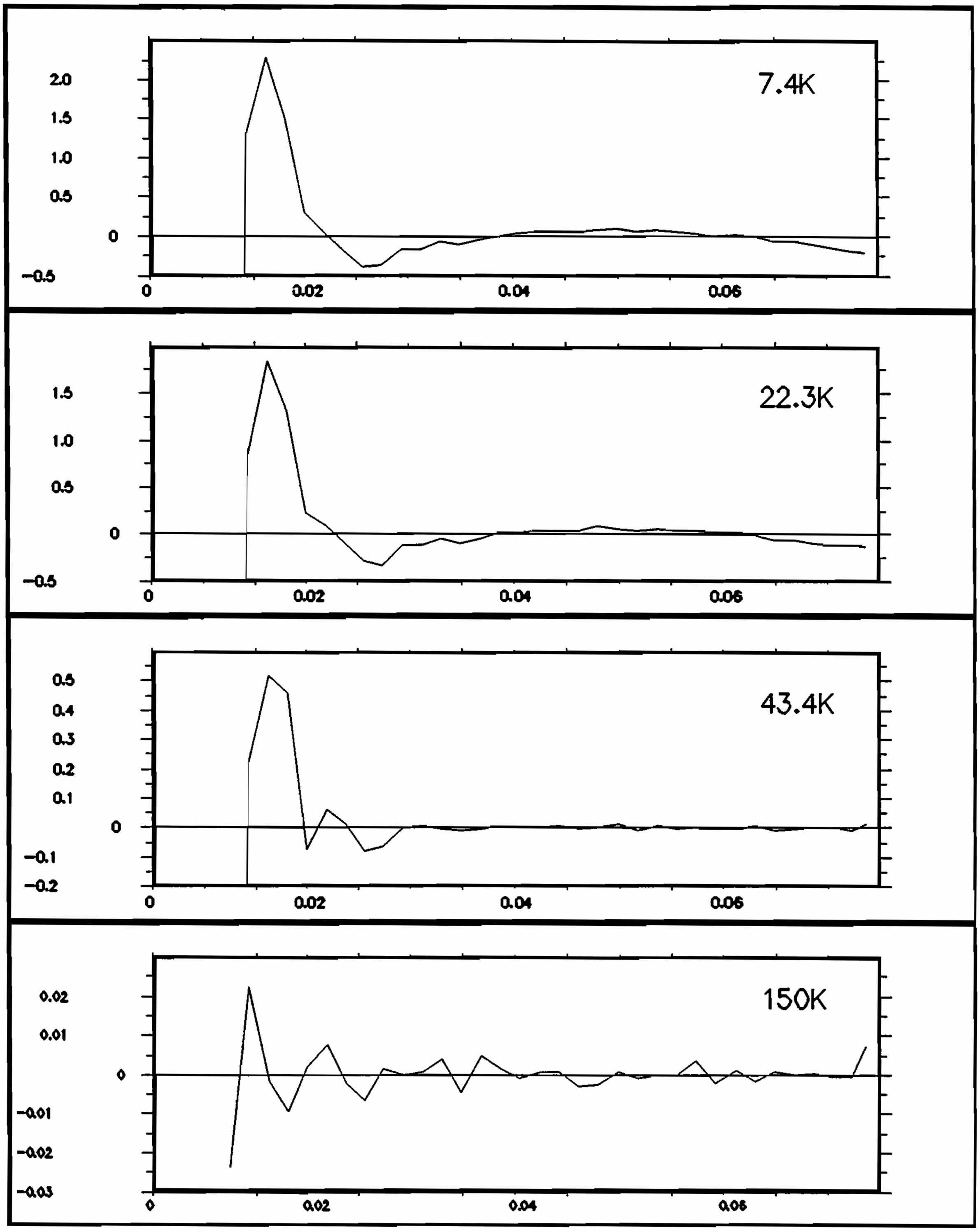

Figure 10.14 The Difference Between the SANS Experimental Data and the Result of Fitting the LL^2 Function at Several Temperatures.

CHAPTER 11

Dy7Ni3 - DISCUSSION OF RESULTS AND CONCLUSIONS.

11.1 ATOMIC STRUCTURE.

In summary the static disorder arising in Dy_7Ni_3 has been successfully modelled by a small number of well-defined atomic separations. Reasonable interatomic distances, partial coordination numbers and RMS atomic displacements have been obtained. Errors have been detected and corrected in a later similar study of $Dy_{69}Ni_{31}$. Dy_7Ni_3 has been shown to be chemically ordered. The concept of CSRO parameters was examined and found to be of dubious validity.

As discussed in section 6.1.3, most previous studies of amorphous RE-TL alloys have been of a TL-rich alloy. However, it appears that TL-rich RE-TL alloys are not chemically ordered whereas Dy_7Ni_3 is chemically ordered as has been shown in section 8.1.3 . Also a consideration of the crystal phases of RE-TL systems suggests that TL-rich amorphous RE-TL alloys will have a very different atomic structure to RE-rich alloys (see section 8.4). Hence it does not seem particularly useful to compare the measured atomic structure of Dy_7Ni_3 with that found by previous studies of TL-rich amorphous RE-TL alloys.

The only previous study of the atomic structure of a RE-rich amorphous RE-TL alloy is that of $Y_{67}Ni_{33}$ and $Y_{67}Cu_{33}$ by MARET, CHIEUX, HICTER, ATZMON and JOHNSON (1987). The partial RDFs for $Y_{67}Ni_{33}$ (see figure 11.1) are similar to those of Dy_7Ni_3, but with a number of notable differences: In

$Y_{67}Ni_{33}$ the Y-Y correlations are very similar indeed to the Dy-Dy correlations in Dy_7Ni_3 as might be expected since the RE atoms appear to behave as hard spheres. The first peak may be de-convoluted into two Gaussians at almost identical positions. However, the second Gaussian for Y-Y has about twice the coordination number found for Dy-Dy, with a corresponding reduction of the coordination number of the first Gaussian. Exactly the same features are also found at higher r for Y-Y and Dy-Dy, again with some differences in magnitudes. For $Y_{67}Ni_{33}$ the Ni-Ni RDF has a small peak which goes completely to zero before being followed by a doublet, just as in Dy_7Ni_3. In Dy_7Ni_3 the second peak of this doublet has approximately twice the coordination number of the first peak whereas the two peaks have similar coordination numbers in $Y_{67}Ni_{33}$. The total coordination number of the doublet is quite similar for the two alloys. The greatest difference for Ni-Ni correlations is that for $Y_{67}Ni_{33}$ the first peak has two components whereas there is only one component for Dy_7Ni_3. The total first peak coordination number is very similar for the two alloys. For $Y_{67}Ni_{33}$ the position of the first component is 2.47Å which is in good agreement with the value of 2.48Å calculated in section 8.2.1 for contact between hard spheres with the 12-fold coordinated Goldschmidt radius of Ni. The second component is at 2.91Å which is just a little higher than the position of the single Ni-Ni first peak found in Dy_7Ni_3 at 2.785Å. It would seem that there are structural differences between $Y_{67}Ni_{33}$ and Dy_7Ni_3 such that Ni atoms come into contact in the Y alloy with a corresponding reduction of the occurrence of the configuration which leads to close but not touching Ni atoms. A double peak for pairs of minority atoms similar to that observed in $Y_{67}Ni_{33}$ by MARET, CHIEUX, HICTER, ATZMON and JOHNSON (1987) has been reported for $Dy_{69}Ni_{31}$ (WILDERMUTH, LAMPARTER and STEEB, 1985), $Ni_{40}Ti_{60}$ (FUKUNAGA, WATANABE and SUZUKI, 1984) and $Ni_{36}Zr_{64}$ (MIZOGUCHI, YODA, AKUTSU, YAMADA, NISHIOKA, SUEMASA and WATANABE, 1985). Hence it cannot be absolutely ruled out that a double peak should have been observed for Dy_7Ni_3 but was not observed due to some problem with the data analysis. However, as has already been discussed in section 8.1.2 the data analysis for Dy_7Ni_3 presented in Chapter 7 is significantly more reliable than that for $Dy_{69}Ni_{31}$. In particular the Ni-Ni partial structure factor for $Dy_{69}Ni_{31}$ reported by WILDERMUTH, LAMPARTER and STEEB (1985) has much poorer statistics than that reported in Chapter 7. A possible interpretation is that there may be a genuine structural difference between the two Dy-Ni alloys due to sample preparation. It seems unlikely that the small difference in stoichiometry alone could produce this effect. The Y-Ni RDF for $Y_{67}Ni_{33}$ is quite similar to the corresponding Dy_7Ni_3 function. The most striking difference is that the two subsidiary Gaussian components of the first peak are shifted to higher r so that both peaks are clearly discernible in the measured function. For $Y_{67}Ni_{33}$ the position (2.89Å) of the principal Gaussian component is close to that for Dy_7Ni_3 (2.837Å). The coordination numbers are also close. In $Y_{67}Ni_{33}$ the first subsidiary component has roughly twice the coordination number of the second whereas they are approximately the same in Dy_7Ni_3. The occurrence of both subsidiary components for $Y_{67}Ni_{33}$ supports the view that the second such component is genuine for Dy_7Ni_3 (see section 8.1.2).

In the study of $Y_{67}Ni_{33}$ pre-peaks were observed in the measured S(Q)s but not in the deduced FZ partial structure factors $S_{11'}(Q)$. These pre-peaks were observed because the samples used had relatively high Ni coherent scattering lengths without the RE scattering length being zero.

Specifically the pre-peaks may be understood as arising from competition at low Q between $S_{NiNi}(Q)$ and $S_{YNi}(Q)$, and thus they do not have any especial structural significance. Such pre-peaks were not observed for Dy_7Ni_3 because the Ni coherent scattering length was either relatively small or totally dominant (the $^{0}Dy_7{}^{N}Ni_3$ sample). For $Y_{67}Ni_{33}$ a pre-peak is found to exist in the BT structure factor $S_{nn}(Q)$ which has been ascribed to a combination of a strong size effect and chemical ordering. A similar pre-peak is observed for Dy_7Ni_3 (figure 7.15) which would seem to confirm this interpretation.

In the study of $Y_{67}Cu_{33}$ it is found that the Y-Y correlation function is almost the same as for $Y_{67}Ni_{33}$. However, the Y-Cu correlation function shows more major differences and the Cu-Cu function appears very different (although it is very noisy which makes detailed interpretation difficult). The structural details of $Y_{67}Cu_{33}$ seem to be considerably different from those of $RE_{67}Ni_{33}$ type alloys and they have been interpreted in terms of a structure with complete chemical disorder.

It would be most appealing to be able to conclude this section with a statement to the effect that one of the models considered for the atomic structure of amorphous Dy_7Ni_3 is 'better' than the others. However, none of the models considered agrees well with the experimental data and it is probably more useful to explore the potential for improving the agreement of each of the models.

An important key to understanding the atomic structure of Dy_7Ni_3 would appear to be the unusual position of the first Ni-Ni peak which corresponds to atoms which are 'close but not touching'. Whilst this is not the first metal-metal alloy to exhibit nearest neighbour distances which are not evenly separated (as would be the case for a RCP of hard spheres), the effect in Dy_7Ni_3 is much more pronounced than has hitherto been observed. A straightforward RCP of hard spheres is unlikely to reproduce the measured positions of the three first peaks in Dy_7Ni_3 because of the unusual Ni-Ni first peak position. However, the use of the PY equation with a binary hard sphere potential has produced surprisingly good results and it could be worthwhile to pursue this approach with a better interatomic potential. The unexpected degree of success obtained by this approach can perhaps be understood as resulting from the fact that an amorphous metal is produced by very rapid quenching of the liquid. Thus it could be worthwhile to further investigate the use of liquid structure models to describe the structure of amorphous metals. In the case of the PY equation one possibility might be to investigate the feasibility of a charged hard sphere potential. It could be that the use of suitable charges (Dy^{3+}, Ni^{2+}) might cause an increase in the nearest neighbour Ni-Ni separation. Such a potential could be justified by considering the system to be positive ions in a uniform distribution of conduction electrons. The conduction electrons are obviously required to ensure charge neutrality and to prevent the positive ions from flying apart and their effect is included implicitly in such a model by constraining the density. Another possibility might be to use a hard sphere pair potential but with the hard sphere radii being different for interactions between different pairs of atoms (ie. r_{Ni} for $\phi_{NiNi}(r)$ not equal to r_{Ni} for $\phi_{DyNi}(r)$). An advantage of this approach is that a Dy atom for example would 'look different' to a Ni atom or another Dy atom. Hence there would probably be a greater chance of reproducing the chemical order that is observed experimentally. In section 8.2.3 the approach where minority atoms are interstitially positioned in a hand-built RCP of ball bearings has been shown to be unable to account for the first Ni-Ni distance. It is also shown that a hard sphere RCP model would have to include the Ni atoms explicitly. However, it seems certain that a suitable hand-built RCP of two sizes of ball bearings would also be unable to account for the first Ni-Ni distance. Similarly the more chemically ordered trigonal prismatic models considered in section 8.3.2 are unable to produce a first Ni-Ni peak at the correct position. It is proposed that this is due to a different method of connecting the prisms being required for Dy_7Ni_3.

The only model of all those considered which produces a Ni-Ni first peak of approximately the correct r-value is the quasi-crystalline calculation for Dy_3Ni_2 discussed in section 8.4 . Thus the structure of this crystal may be used as the starting point for an attempt to indicate how a model of the type constructed by GASKELL (1979) could be devised specifically for Dy_7Ni_3. In Dy_3Ni_2 the Ni coordination polyhedra are Dy trigonal prisms which connect together by sharing both triangular and square faces. The triangular face sharing configuration results in a Ni-Ni distance between adjacent trigonal prisms of 3.662Å. This distance is equal to the height of a prism and as such also represents an important Dy-Dy distance. For Dy_7Ni_3 the correlation function $t'_{NiNi}(r)$ shows no sign of a peak either at 3.662Å or at any other distance equal to a Dy-Dy distance. Hence it is concluded that triangular face sharing would not be a suitable configuration for a trigonal prismatic model of Dy_7Ni_3. The square face sharing configuration results in Ni-Ni distances between adjacent trigonal prisms of 2.64Å and 2.68Å. Hence the sharing of square faces would appear to be the way for the model to reproduce the position of the first Ni-Ni peak.

As shown by the values in table 8.6 the measured distances r_{DyDy} and r_{DyNi} for Dy_7Ni_3 are not consistent with Ni atoms being positioned at the centre of regular (ie. all sides of equal length and angles of 90° between square and triangular faces) Dy trigonal prisms. However, crystal studies of metallic structures with trigonal prisms show that in general the prisms are distorted (PARTHÉ, CHABOT and HOVESTREYDT, 1983). This may be understood simply in terms of the hole filling argument presented at the start of section 8.3.1; if the radius ratio is larger than the critical value this has the effect of forcing the majority atoms apart and thus a distorted polyhedron can easily occur. In the case of Dy_3Ni_2 the effect is to open out one of the square faces of the trigonal prism (b>a in figure 6.2). The height of the prisms and the lengths of the two short triangle edges (a in figure 6.2) are all a little above 3.5Å (3.502Å, 3.537Å, 3.584Å and 3.662Å) whilst the long triangle edges (b in figure 6.2) are found to be either 4.103Å or 4.332Å. The results of the resolution-broadened Gaussian fits given in table 8.2 show two Dy-Dy distances of 3.531Å and 3.984Å in Dy_7Ni_3. Clearly these may be interpreted as the two dimensions (a and b) of a distorted trigonal prism of the type found in Dy_3Ni_2. Even if one were to reject the modelling of the static disorder by a small number of well-defined distances it would still be possible to interpret the static disorder inherent in the asymmetric first peak of $t'_{DyDy}(r)$ in terms of irregular Ni coordination polyhedra.

If a regular trigonal prism is constructed with its edge length equal to the Dy-Dy nearest neighbour distance in Dy_7Ni_3 (3.531Å), a geometrical calculation shows that the centre of the prism is a distance 2.697Å from the vertices. This differs from the fitted value for the Dy-Ni nearest neighbour distance of 2.837±0.008Å by 5%. However, if a distorted trigonal prism is constructed with the dimensions obtained from the fit to $t'_{DyDy}(r)$ for Dy_7Ni_3 then the calculated distance from a vertex to a point equidistant from all vertices is 2.773Å. This differs from the measured Dy-Ni distance by only 2%. Hence the first two Dy-Dy distances and the first Dy-Ni distance may be seen to be consistent with the presence of distorted trigonal prisms in Dy_7Ni_3. The first partial coordination number n_{NiDy} would be 6.0 for an ideal trigonal prismatic structure and obviously the fitted value of 5.86±0.21 gives great support to this model. The two fitted values of n_{DyDy} also seem reasonable for a model containing the distorted trigonal prisms discussed above.

In Dy_3Ni_2 the trigonal prisms share small square faces and not the large rectangular faces. Sharing of the rectangular faces could be expected to result in too small a Ni-Ni distance compared to the Ni-Ni distance in Dy_7Ni_3. The measured Dy_7Ni_3 partial coordination number $n_{NiNi}=1.29\pm0.78$ may be interpreted as the average number of shared small square faces per prism. In Dy_3Ni_2 there are rows of four small square face sharing prisms. However, a group of three or more small square face sharing prisms results in the occurrence of a Ni-Ni distance equal to the long prism edge. The measured correlation function $t'_{NiNi}(r)$ for Dy_7Ni_3 does not have a peak in the region of 3.984Å (nor any other peaks coinciding with Dy-Dy peaks) and hence a trigonal prismatic model for Dy_7Ni_3 should not have more than two square face sharing prisms in a group. This results in a maximum value of

1.0 for n_{NiNi} which is reasonably consistent with experiment.

Clearly square face sharing trigonal prisms alone are not a sufficient ingredient for the construction of a 3D non-crystalline model and some other way for the prisms to connect is required: In both Dy_3Ni_2 and Dy_3Ni dysprosium atoms are to be found positioned over the square (or rectangular) faces of the trigonal prisms, forming a half-octahedron. If a Dy atom is positioned over the small square face of a distorted trigonal prism (with the dimensions derived from the fit to $t'_{DyDy}(r)$ for Dy_7Ni_3) such that its distance from the adjacent Dy atoms in the prism is 3.531Å, then this results in a Dy-Ni distance of 3.703Å. The same configuration with a Dy positioned over a large rectangular face of a distorted prism results in a Dy-Ni distance of 3.196Å. The fit to $t'_{DyNi}(r)$ for Dy_7Ni_3 yields a Dy-Ni distance of 3.215Å and hence a trigonal prismatic model for Dy_7Ni_3 should have Dy atoms in half-octahedral configuration over the large rectangular faces of the prisms, but not over the small square faces. Since the distorted prisms of the type found in the crystal Dy_3Ni_2 have only one large rectangular face, the measured Dy_7Ni_3 second partial coordination number $n_{NiDy}=1.31\pm0.23$ seems a little large. However, it is quite likely that if distorted trigonal prisms are the correct structural unit for describing the SRO in Dy_7Ni_3 then they may well not be exactly identical to those in the crystal Dy_3Ni_2; for example if at least some prisms were to have two large rectangular faces then the measured second Ni-Dy coordination number would be most reasonable. In crystalline Dy_3Ni half-octahedrally positioned Dy atoms form part of a second trigonal prism which shares a triangle edge with the first prism (see figure 6.2). (This is the edge sharing Fe_3C cementite arrangement which is used to connect the trigonal prisms in the GASKELL (1979) model.) Thus the sharing of triangle edges is an appropriate way for a trigonal prismatic model of the atomic structure of Dy_7Ni_3 to achieve 3D connectivity. However, it is not clear whether all of the half-octahedrally positioned Dy atoms in such a model should be part of a triangle edge sharing prism.

The larger distances (ie. above 4Å) implied by the atomic configurations discussed above have not been compared in detail with the experimental data. These distances include the Dy-Dy diagonal distances for a distorted trigonal prism (4.994Å, 5.324Å), the additional Dy-Dy and Dy-Ni distances occurring when two prisms share a square face and the additional distances of all three types which occur when two prisms share a triangle edge. The reason for this is that at larger r the number of different distances proliferates very quickly, as can be seen from the distances occurring in the crystals shown in figures 8.28 to 8.30 . Above about 4Å the crystals have distances due to trigonal prisms which are not directly connected. Thus it would probably be necessary to actually construct a model to test whether the ideas presented above can achieve any kind of agreement at higher r.

11.2 DY^{3+} MAGNETIC FORM FACTOR.

Magnetic form factors f(Q) (as defined in section 3.4) are usually measured by studying the integrated intensities of magnetic reflections from single crystals (see for example NATHANS and PICKART, 1963, or FORSYTH, 1977). Polarised neutrons are generally used so as to achieve a separation between the magnetic and nuclear contributions to intensities. A disadvantage of this technique is that values for f(Q) are only obtained at the discrete Q-values of the Bragg peaks and thus f(Q) is not measured as a continuous function of Q. Magnetic form factors may be measured as a continuous function of Q by a study of paramagnetic scattering or of diffuse scattering from a disordered alloy. The purpose of measuring magnetic form factors is to provide an experimental determination of the wavefunctions of the unpaired electrons which are responsible for the magnetic properties of materials.

As is discussed in sections 6.2.2 and 11.3, the magnetism in Dy_7Ni_3 is due entirely to the Dy moments since the Ni moments are completely quenched. It follows that the magnetic self scattering (equation (4.2.16)) for Dy_7Ni_3 reduces to;

$$\frac{d\sigma^{MS}}{d\Omega} = \frac{2}{3}\,(\gamma r_o)^2\, c_{Dy}\, \langle \underline{\mu}_{Dy}^2 \rangle\, |f_{Dy}(Q)|^2 \qquad (11.2.1)$$

Thus a measurement of the magnetic self scattering for Dy_7Ni_3 yields the square modulus of the magnetic form factor for Dy in Dy_7Ni_3. Furthermore if the sample is at a sufficiently high temperature that it behaves as an ideal paramagnet with no correlations between the moments (see below for further discussion of this point) then the magnetic distinct scattering will be zero and the magnetic self scattering (equation (11.2.1)) will be the only magnetic contribution to the scattering. Hence a measurement of the total magnetic contribution to the scattering from Dy_7Ni_3 at elevated temperatures yields the Dy form factor as a continuous function of Q. The problem with such a measurement is that the magnetic scattering must be separated from the nuclear scattering. This problem was overcome by making the measurement (see section 7.3.5) with the $^{0}Dy_7{}^{0}Ni_3$ sample since the only nuclear scattering for this sample is self scattering (see section 6.4.2) and this may be calculated according to equation (4.1.50). The total scattering for the $^{0}Dy_7{}^{0}Ni_3$ sample is shown in figure 7.7 together with the calculated nuclear self scattering. The measured diffraction pattern for $^{0}Dy_7{}^{0}Ni_3$ was scaled so as to be equal to the calculated nuclear self scattering at the highest Q-values on the assumption that the magnetic scattering has fallen essentially to zero at high Q due to the fall-off of the magnetic form factor (see below for further discussion of this point). Figure 11.2 shows the measurement of the magnetic scattering obtained by subtracting the calculated self scattering from the diffraction pattern for the $^{0}Dy_7{}^{0}Ni_3$ sample. Note that this procedure results in an absolutely normalised measurement. As with the diffraction studies of the magnetic structure of Dy_7Ni_3, corrections were not made for absorption, self-shielding and multiple scattering because of the Q-dependence of magnetic scattering (see section 9.2).

As mentioned above, magnetic form factors are of interest since they provide experimental information about the wavefunctions of unpaired electrons and there has been a substantial effort to perform theoretical calculations of magnetic form factors. Figure 11.2 shows a calculation of the magnetic scattering from Dy_7Ni_3 using equation (11.2.1) and the theoretical expression for the spherical contribution to the Dy^{3+} magnetic form factor given by LISHER and FORSYTH (1971);

$$f(Q) = A \exp(-ax^2) + B \exp(-bx^2) + C$$

where; (11.2.2)

$x = Q/4\pi$

$A = 0.2214$	$a = 11.65$
$B = 0.8014$	$b = 3.371$
$C = -0.0229$	

The values for these parameters were obtained by a least sqaures fitting of the analytic expression (11.2.2) to the numerical results of a theoretical calculation (BLUME, FREEMAN and WATSON, 1962) based on Hartree-Fock wavefunctions. The aspherical contribution to the calculated Dy^{3+} magnetic form factor was not included in the calculation shown in figure 11.2 because of the isotropic nature of an amorphous solid. According to a simple 'Hund rules' calculation the magnetic moment of a free Dy^{3+} ion is $10.63\mu_B$ and a value of $\sim 10.6\mu_B$ is found experimentally (KITTEL, 1976). A value of $10.6\mu_B$ was used for $\langle \underline{\mu}_{Dy}{}^2 \rangle^{1/2}$ in the calculation shown in figure 11.2 . The very similar magnitudes of the calculation and experiment indicate that this experimental measurement is consistent with the view that the magnetism in Dy_7Ni_3 is due to localised moments on the dysprosium ions only of approximately $10.6\mu_B$. Carefully normalised conventional magnetic measurements would also be of value in confirming the magnitude of the Dy moment in amorphous Dy_7Ni_3.

The measured magnetic scattering was square-rooted according to equation (11.2.1) and a value of $10.6\mu_B$ was used for the Dy magnetic moment to yield the experimental Dy^{3+} magnetic form factor shown in figure 11.3 together with the theoretical form factor calculated according to LISHER and FORSYTH (1971). The experimental measurement extends to higher Q than the theoretical calculation which signifies that the unpaired 4f electrons of

Dy in Dy_7Ni_3 are more highly localised than predicted by the Hartree-Fock wavefunctions (BLUME, FREEMAN and WATSON, 1962). The experimental measurement shows a very slight feature in the 1→3$Å^{-1}$ region which is not apparent in the theoretical calculation. Also at low Q the calculation levels off to a constant value whereas the experimental measurement continues to rise. Thus consideration was given as to whether these features of the experimental measurement are genuine. The first possibility considered was that the slight structure apparent in the experimental data could be due to a slight persistence of correlations, either nuclear or magnetic: If there had been an error in the zeroing of the coherent nuclear scattering lengths of the $^0Dy_7{}^0Ni_3$ sample then a small amount of distinct nuclear scattering would be observed. Alternatively a persistence of magnetic correlations at room temperature (see section 11.3) would cause a slight structure to be seen in the magnetic scattering. To test for this possibility various small fractions f times the diffraction pattern of the $^NDy_7{}^0Ni_3$ sample (and also the $^NDy_7{}^NNi_3$ sample) was subtracted from the diffraction pattern for the $^0Dy_7{}^0Ni_3$ sample. The justification for this is that in the case of nuclear scattering an error in $\bar{b}_{Dy}$ would be far more significant, and in the case of magnetic scattering only the Dy ions possess a magnetic moment. It was found that if f was made sufficiently large to appreciably decrease the structure in the 1→3$Å^{-1}$ region then additional structure was introduced at higher Q, particularly in the region of the second peak of $i_{NO}(Q)$. Hence this possibility was rejected and it was concluded that the experimental measurement of the magnetic scattering possessed structure at low Q only. Another possibility considered was that the rise at low Q could be due to SANS. However, the measurements of section 10.3.1 show that for the $^0Dy_7{}^0Ni_3$ sample at room temperature the

SANS is only appreciable at momentum transfers below about 0.025Å^{-1} (see figure 10.3) with a very strong Q-dependence (~Q^{-4}). Hence the rise at low Q of the measured diffraction pattern of the $^{0}Dy_7{}^{0}Ni_3$ sample at room temperature cannot possibly be due to SANS (see also figure 9.1). It was concluded that the measurement of the magnetic scattering shown in figure 11.2 is genuine and that there are no observable magnetic correlations in Dy_7Ni_3 at room temperature.

The rise in the form factor at low Q and the slight structure around 2Å^{-1} can be explained if there is an additional contribution to the form factor besides that due to the 4f electrons. Since this contribution occurs at low Q it must be due to electrons which are less highly localised in real-space than the 4f electrons. Two phenomena which can give rise to an additional contribution to a magnetic form factor at low Q have been proposed in the literature: HUBBARD and MARSHALL (1965) have shown theoretically that covalent bonding produces an additional contribution at low Q to the form factor due to a mixing of magnetic ion wavefunctions with those of a nominally non-magnetic ligand ion. MOON, KOEHLER, CABLE and CHILD (1972) have measured the magnetic form factor of metallic gadolinium and observed a rise at low Q and structure similar to that reported here for Dy_7Ni_3. It was found that the data for gadolinium could be explained in terms of an additional contribution to the form factor due to conduction electron polarisation. A rise in the form factor at low Q due to conduction electron polarisation has also been observed for a number of other RE-containing metals (BOUCHERLE, GIVORD and SCHWEIZER, 1982), but is not observed for non-metallic Gd_2O_3 (MOON and KOEHLER, 1975). The second of these proposals is probably more appropriate to amorphous Dy_7Ni_3 because of the type of bonding involved. However, to the author's knowledge this is the first time that the form factor of Dy^{3+} has been measured in any material, metallic or non-metallic, and so there is no previous data with which a direct comparison can be made. MOON, KOEHLER, CABLE and CHILD (1972) were able to separate the 4f electron and the conduction electron polarisation contributions to the magnetic form factor for metallic gadolinium by making use of the periodicity of the crystal lattice. However, such a separation was not attempted for Dy_7Ni_3 since the isotropic nature of an amorphous solid results in a considerable reduction in the available information as compared to a single crystal and it is not clear how a separation could be achieved. Even in the case of a crystal such a separation would be significantly more complicated for the H-state Dy^{3+} ion than for the isotropic S-state Gd^{3+} ion.

An additional difference between the calculated and measured Dy^{3+} magnetic form factors shown in figure 11.3 is that the calculated form factor is very slightly negative at high Q whilst the measured form factor is not negative. It is generally found that both measured and calculated form factors are slightly negative at high Q and thus it is concluded that there is a slight error in the measured form factor due to the procedure used to subtract the nuclear scattering and normalise the data. This error arises from the assumption that the form factor is essentially zero at high Q. Note that if the magnetic form factor becomes negative at high Q then this will result in the magnetic scattering (equation (11.2.1)) rising again, although this effect will be very small since the magnetic scattering depends on the square modulus of the form factor. No indication of the magnetic scattering rising at high Q was observed when the nuclear scattering was subtracted. Thus polarised neutrons would be required to achieve a significantly improved separation of magnetic and nuclear contributions to the scattering. Since the experimental data falls off less rapidly with Q than the calculation it may be that the true magnetic form factor for Dy in Dy_7Ni_3 crosses the Q-axis at a higher Q-value than the Q_{max} of the experimental data. One possibility that was considered is that the difference in the rate at which the experimental and calculated form factors fall off could be due in part to the normalisation problem encountered in the diffraction studies of the atomic structure of Dy_7Ni_3. However, as discussed in section 7.3.1, it appears that this problem arises only for the vanadium data and not for the sample data. Hence the difference in the rate at which the experimental and calculated form factors fall off is thought to be genuine.

The experimental form factor was multiplied by Q and extrapolated linearly to the origin. The SANS measured for the ${}^{0}Dy_7{}^{0}Ni_3$ sample was not used for this extrapolation firstly because the Q_{min} of D2 is higher than the Q_{max} of the SANS data so that there is no overlap (see figure 10.3) and secondly because the higher Q part of the measured SANS is not of high statistical accuracy since the signal is very small compared to those typically observed in SANS experiments. After extrapolation to the origin the data were Fourier transformed according to equation (3.4.8) to yield the function $4\pi r g_{mDy}(r)$ where $g_{mDy}(r)$ is the radial density function for the unpaired 4f electrons in the Dy^{3+} ions in Dy_7Ni_3. Surprisingly it was found to be necessary to use a modification function (LORCH, 1969) to avoid substantial termination ripples. The measured electron distribution function is shown in figure 11.4 together with that obtained from the calculated (LISHER and FORSYTH, 1971) form factor. Note that since the magnetic form factor is a very slowly changing function of Q the use of a modification function has the result that the normalisation of the electron distribution functions shown in figure 11.4 is not reliable. The very slight ripples in the electron distribution functions shown in figure 11.4 almost certainly arise from the process of Fourier transformation. The experimental distribution function shows an extremely small feature in the region of 3.5Å. This probably indicates a very slight persistence of correlations, either nuclear or magnetic, which is too small to have been detected by the method used above. The greater magnitude of the experimental distribution function would seem to indicate that the magnetic moment of Dy in Dy_7Ni_3 must be larger than the value of $10.6\mu_B$ used above. The experimental function has a peak at a distance of 0.228Å whereas the calculated function has a peak at 0.265Å which shows that, as has already been concluded from the reciprocal-space data, the 4f electrons of Dy in Dy_7Ni_3 are more highly localised than predicted by the Hartree-Fock wavefunctions (LISHER and FORSYTH, 1971). The experimental electron distribution function doea not appear to have any feature which can be ascribed to the additional contribution to the form factor at low Q. It may thus be concluded that the conduction electron polarisation is small but that its effect becomes more apparent in the reciprocal-space data because of the factor of Q in the integrand of equation (3.4.8).

11.3 MAGNETIC STRUCTURE.

Figure 11.5 shows a comparison between the three magnetic correlation functions $\Delta^i(r)$ whose measurement is discussed in Chapter 9 and the atomic partial correlation function $D_{DyDy}(r)$. The atomic Dy-Dy correlation function shown in figure 11.5 was calculated from the D2 data using a Q_{max} of $8.0Å^{-1}$ as with the magnetic correlation functions. For ease of comparison $D_{DyDy}(r)$ was also scaled arbitrarily by making the height of the first peak the same as for the magnetic correlation functions. The first peak of the magnetic correlation functions is seen to occur at very nearly the same r-value as the first peak of the atomic Dy-Dy correlation function at about 3.5Å. There is no indication of a peak in the magnetic correlation functions in the 2.8→2.9Å region where the Dy-Ni and Ni-Ni nearest neighbour peaks are found in the atomic partial correlation functions. Thus it may be concluded that, as discussed in section 6.2.2, the nickel moments are quenched to essentially zero and the moments are only on the dysprosium ions. The similarity of the magnetic correlation functions to the atomic Dy-Dy correlation function shows that, as one would expect with RE ions, the magnetism in Dy_7Ni_3 is due to localised moments on the ions, rather than some kind of itinerant electron magnetism.

As has been discussed by WEDGEWOOD and WRIGHT (1976), the fact that the nearest neighbour peak of the magnetic correlation functions is a positive peak is a clear indication that the interaction between nearest neighbour Dy ions is ferromagnetic. The shape of the nearest neighbour peak of the magnetic correlation functions appears to be very similar to that of the atomic Dy-Dy correlation function which indicates that there is little variation in the degree of alignment over the range of r covered by the nearest neighbour peak. As the sample is cooled the alignment between moments on neighbouring ions increases resulting in a growth of the nearest neighbour peak in the magnetic correlation functions. The detailed study of the first peak of the structure factor as a function of temperature (see figure 9.2) indicates that there is a persistence of magnetic correlations at temperatures considerably in excess of the reported (BUSCHOW, 1980) asymptotic Curie temperature θ_p=35K, with no indication of any particular effect occurring at θ_p. However, a persistence of magnetic correlations into the paramagnetic region has been observed before in crystalline materials (see for example MOON and KOEHLER, 1975) and so this observation is not in itself unique. In the region of r beyond the nearest neighbour peak there is still a general similarity of form between the magnetic correlation functions and the atomic Dy-Dy correlation function, but the detailed structure of the atomic correlation function appears to be smoothed out in the magnetic correlation functions. In particular the peak in the atomic Dy-Dy correlation function at about 6.8Å does not appear to be significant for the magnetic correlation functions. The reason for this smoothing out of detail is not clear but it may be associated with either the variation of magnetic correlations with distance or the neglection of magnetic anisotropy which is discussed below. The 5→6Å region of the 44.3K-95.8K magnetic correlation function possibly suggests that at higher temperatures correlations at this shorter distance may be more important than at lower temperatures. With this data it would be desirable to be able to discriminate between different proposed models for the magnetic structures which may occur in RAM systems. In particular it would be useful to be able to discriminate between the proposed CSM structure (CHUDNOVSKY and SEROTA, 1983) in which there is a smooth gradual rotation of the magnetisation over a magnetic correlation length (see section 6.2.2) and a SG-like SM in which the moments are strongly locked to their local anisotropy axes but with a preference for neighbouring moments to be locked in the orientation which is closer to being parallel than anti-parallel. Without an absolute normalisation of the data it is very difficult to draw such conclusions. However, the fact that the magnetic correlation functions obtained by ignoring magnetic anisotropy are so similar to the nuclear Dy-Dy correlation function may be taken as strong circumstantial evidence that the anisotropy is small. This is consistent with the conclusions of the SANS study of magnetic correlations given in section 11.4 .

A drawback of the magnetic diffraction data analysis method used in Chapter 9 is that, whilst the results may be interpreted qualitatively as above, it is not clear how they may be interpreted in a precise and quantitative manner. Also, in order to Fourier transform the data, it is necessary to assume that local magnetic anisotropy is negligible and it is not entirely clear whether this is a satisfactory assumption. For example, in crystalline Dy it is found (NATHANS and PICKART, 1963) that in the magnetically ordered states the magnetisation is constrained to lie in the hexagonal planes of the hcp structure due to a strong magnetic anisotropy interaction. Hence the assumption that local magnetic anisotropy can be ignored must be questioned (although the fact that ignoring anisotropy yields correlation functions which appear reasonable may indicate that the anisotropy term is actually quite small) and the alternative data analysis method (NÄGELE, KNORR, PRANDL, CONVERT and BUEVOZ, 1978) discussed in section 6.2.1 should be considered. This method, which so far has hardly ever been used, does not ignore the local magnetic anisotropy term $\Delta^{a}(r)$ in equation (4.2.21). Hence it is not possible to Fourier transform the data and instead least squares fitting is used to fit equation (4.2.21) to the reciprocal space data. The drawback with this method is that some kind of a model assumption must be made in order to do the fitting. The most reasonable assumption is to divide the ions into coordination shells (BLECH and AVERBACH, 1964) with no variation within a shell of the degree of alignment (a(r) and b(r) of equations (4.2.27) and (4.2.28)) between the moments in the shell and the moment at the centre of the shell. In the case of Dy_7Ni_3 this should not prove a serious drawback (the modelling of the atomic static disorder given in section 11.1.2 might be used to define the shells) and a use of this alternative data analysis method could form the basis of a worthwhile further study. The work discussed above has shown that the magnetism in Dy_7Ni_3 arises from magnetic moments on the Dy ions and the fact that the atomic Dy-Dy partial correlation function has also been measured (Chapter 7) is an almost unique advantage for the application of this data analysis method. The great similarity of the nearest neighbour peaks of the atomic and magnetic correlation functions indicates that there is little variation of the degree of alignment of moments over the range of r covered by this peak and hence the model assumption where the ions are divided into coordination shells is reasonable. It would be advantageous if an absolute normalisation of the magnetic diffraction data could be achieved, and this may be possible by comparison with the form factor measurement. Then a consideration of the nearest neighbour peak (together with the Dy-Dy coordination number from the study of atomic structure and the magnetic moment of a Dy^{3+} ion) of the data at 7.2K (at which temperature the increase in magnetic order has almost levelled off) should show definitively whether the nearest neighbours of a moment are nearly aligned as one would expect in a CSM, or whether there is just a slight preference for alignment as expected for a SG-like SM.

11.4 DISCUSSION OF RESULTS AND CONCLUSIONS FROM SANS EXPERIMENT.

11.4.1 NUCLEAR HOMOGENEITY AND SURFACE DEFECTS.

As has been shown in section 10.3.1 the nuclear SANS for Dy_7Ni_3 is roughly consistent with the Porod approximation, but not with the Guinier approximation. Thus it may immediately be concluded that $Ql \gg 1$ (see section 4.3) for the range of Q over which the measurements were made (see table 10.1). Hence the nuclear SANS is due to structures with a characteristic length l which is large in comparison with $1/Q_{min}$, where Q_{min} is the minimum experimental momentum transfer;

$$l \gg 140\text{Å} \qquad (11.4.1)$$

The gradient of the linear fit to the low Q region of the Guinier plot of the nuclear SANS yields a radius of gyration (equations (4.3.6) and (4.3.7));

$$R_G = (\ 222.0 \pm 3.5\ )\ \text{Å} \qquad (11.4.2)$$

Since the Guinier plot was not linear, even at low Q, this value cannot be regarded as accurate. However, it may provide a lower limit on the size of the structures giving rise to the nuclear SANS. In order to further understand the nuclear SANS from Dy_7Ni_3 it is worthwhile first to discuss previous nuclear SANS measurements on amorphous metals:

SANS has frequently been used as a technique for studying phase separation and concentration fluctuations in metallic glasses (see for example STEEB and LAMPARTER, 1985). However, recently there has been a body of experimental evidence showing that for ordinary melt-spun amorphous alloys the surface state is responsible for a large proportion of the SANS intensity (see for example JANOT and GEORGE, 1985; RODMACQ, MANGIN and CHAMBEROD, 1985). In these experiments the technique of contrast variation was used so as to identify the contribution to the SANS due to the surface. This technique involves placing the sample in a liquid of the same scattering length density as the surface material of the sample. The surface contribution to the SANS is then eliminated. For the amorphous alloy $Fe_{70}Cr_{5}P_{15}C_{10}$ JANOT and GEORGE (1985) have shown that the bulk atomic scattering may be as small as 2% of that due to the surface (which in turn is less than 5% of that arising from magnetic fluctuations). The surface scattering is relatively large for melt-spun ribbons simply because they are thin, typically of order 20μm, and hence the surface to volume ratio is high. The surface scattering observed in SANS experiments is not due to the overall dimensions of the ribbons (~1mm) since this corresponds to Q-values of order $10^{-6}Å^{-1}$ which is very much smaller than the Q-range covered in a SANS experiment (typically $Q>10^{-3}Å^{-1}$). Instead the surface scattering may be understood in terms of surface defects. These surface defects are due to gas bubbles which become trapped between the solidifying ribbon and the cold spinning copper wheel during the manufacturing process (YAVARI, DESRE and CHIEUX, 1985). They may be observed directly by studying the ribbon surface with a scanning electron microscope.

Since the work discussed above demonstrates quite clearly that the nuclear SANS for ordinary melt-spun amorphous alloys is due almost entirely to surface defects, it is now considered whether the nuclear SANS $I^{nuc}(Q)$ for the Dy_7Ni_3 ribbons can be interpreted as surface scattering. ROTH

(1977) has shown that SANS from surface features may be treated in terms of the Porod approximation. ie. according to the theory discussed in section 4.3 surface scattering should give rise to a SANS signal proportional to Q^{-4} (equation (4.3.8)). However, this simple theory ignores the recent development of the theory of fractal geometry (MANDELBROT, 1982). In fact the SANS measured in the Porod regime is only given by Q to the power of -4 when the structures involved are compact and smooth. A more general result for the Porod regime is (SCHAEFER, 1988);

$$I(Q) \propto Q^{P} \qquad (11.4.3)$$

where the Porod slope is given by;

$$P = -2D_M + D_S \qquad (11.4.4)$$

D_M is the mass fractal dimension ($D_M \leq 3$) and D_S is the surface fractal dimension ($2 \leq D_S \leq 3$). Compact ($D_M=3$) objects with a smooth surface $D_S=2$ scatter according to the Porod equation $P=-4$. For mass fractal objects $D_S=D_M$ so that $P=-D_M$ and hence $P \geq 3$. For compact objects with rough surfaces $D_M=3$ so that $P=-6+D_S$ and hence $-4 \leq P \leq -3$. It may thus be concluded that a Porod slope between zero and -3 is indicative of mass fractal objects whilst a Porod slope between -3 and -4 is indicative of surface fractal objects. The magnitude of the Porod slope is never greater than 4. Inspection of the results of the previous SANS studies of amorphous metallic ribbons (see above) shows that the Porod slopes obtained were always in the region of -4, but not exactly equal to -4. The Porod slope obtained from the measured nuclear SANS $I^{nuc}(Q)$ for Dy_7Ni_3 was -4.58 ± 0.14 (equation (10.3)). It is thus concluded that this value is more consistent with an interpretation in terms of surface defects, rather than bulk defects, although its magnitude is somewhat larger than theory predicts as possible. However, there are practical factors which can affect the magnitude of the experimentally-determined Porod slope: the SANS experiments on Dy_7Ni_3 were optimised for a study of the evolution of magnetic correlations with the study of nuclear inhomogeneities being a secondary interest. Hence the measured nuclear SANS signal was very small with only a very few points of the Porod plot (figure 10.4) being available for fitting. When the SANS signal is so small it is inevitable that the extracted Porod slope is quite sensitive to the estimated value used for the general background level (the low Q limit of the WANS signal) as well as to any experimental factors. The effect is most severe at higher Q where a point may go negative after the subtraction of the general background value so that it does not appear on the Porod plot and hence the fit becomes biased. The Porod fit to the nuclear SANS from Dy_7Ni_3 was performed by fitting a straight line to the Porod plot. An alternative approach might have been to fit the Porod law equation (11.4.3) directly to $I^{nuc}(Q)$, including a constant term for the general background. However, it was concluded that the quality of the data did not justify this more sophisticated approach. (Also there is some question as to whether this approach would be mathematically well-behaved because of the problem mentioned above of points going negative at higher Q after subtraction of the general background level.)

A possible alternative explanation for the small nuclear SANS observed for Dy_7Ni_3 is that it could be due to the small concentration of crystallites which was observed in the nuclear diffraction experiments (see section 7.3.2). However, since the concentration of these crystallites is small it is quite possible that the pieces of ribbon used for the SANS experiments happened to have no crystallites. Furthermore the magnitude of the Porod slope (and the lack of a linear Guinier plot) is such as to suggest surface defects rather than bulk defects as the cause of the nuclear SANS. Hence this explanation was rejected.

Equation (4.3.8) shows that the intercept of the straight line fitted to the Porod plot of the nuclear SANS (equation (10.3)) may be used to determine the surface area N_pA_p of the surface defects. This is the reason for the absolute normalisation of the room temperature SANS data as discussed in Chapter 10. The scattering length density of $^{N}Dy_7{}^{N}Ni_3$ was calculated to be 0.058755×10^{-14}m/Å^3 and it was assumed that there is no change in scattering length density at the surface of the sample since efforts had been made to avoid surface contamination (see section 6.5). It was also assumed that the scattering length density of the air surrounding the sample is negligible. For a piece of ribbon LÅ long and WÅ wide (20µm thickness) the defect surface area was then calculated to be;

$$N_pA_p = (0.024 \pm 0.012)LW \text{ Å}^2 \qquad (11.4.5)$$

This value should not be regarded as highly accurate because of the difficulty of estimating the general background level as discussed above. If it is assumed that the surface defects are only on one side of the ribbon as would be expected if they are due to interaction with the cold spinning copper wheel used in the manufacturing process then it may be concluded that they have a surface area which is (2.4±1.2)% of the ribbon area. (However, it is possible that the sanding of the samples mentioned in section 7.2.2 may have introduced surface defects of a size which is observable by SANS.) Note that this analysis yields the total surface area of the defects but does not yield any information concerning the area of an individual defect (but see equation (11.4.2)). Also, since the scattering vector Q lies almost exactly in the plane of the ribbons, the surface area detected may be regarded as lying parallel to the ribbons. The value obtained in equation (11.4.5) is reasonably consistent with a contrast variation study of melt-spun amorphous $Pd_{80}Si_{20}$ (RODMACQ, MANGIN and CHAMBEROD, 1985) in which the surface defects were found to have a surface area which was 6% of the ribbon area. In order to confirm absolutely that the nuclear SANS from Dy_7Ni_3 is due to surface defects it would be necessary to perform a contrast variation SANS experiment. However, since the nuclear SANS is reasonably consistent with the results of the previous contrast variation experiments, both in exhibiting a Porod-type form and in being of the expected magnitude, there can be little doubt that this conclusion is correct. In view of this it may be concluded that the bulk of the sample is highly homogeneous with little variation in either density or composition.

The room temperature magnetic scattering $I^{00}(Q)$ observed for Dy_7Ni_3 has been shown to follow a Porod form (equation (10.4)). It is thus tentatively suggested that this scattering may also be surface scattering, but arising via the magnetic scattering length density (see also section 10.3.2).

11.4.2 MAGNETIC CORRELATIONS.

A preliminary report of the SANS study of magnetic correlations in amorphous Dy_7Ni_3 has been given by HANNON, CYWINSKI, SINCLAIR, GRIMLEY and

WRIGHT (1988).

When a ferromagnet is cooled the temperature dependence of the SANS at a particular Q-value shows a cusp at the Curie temperature. However, the SANS from Dy_7Ni_3 (see figure 10.7) does not show a cusp in the region of the reported asymptotic Curie temperature θ_p=35K (BUSCHOW, 1980). From the lack of a cusp in the SANS together with its monotonic rise at low temperatures it may immediately be concluded that Dy_7Ni_3 is not ferromagnetic. Thus the transition temperature of 31K deduced in section 10.3.2 by studying the temperature derivative of the SANS does not represent the Curie temperature of a ferromagnet. This immediate conclusion is consistent with the theoretical studies showing that ferromagnetism is impossible in a RAM system in less than four dimensions (see section 6.2.2).

The SANS measured for Dy_7Ni_3 is markedly different in detail to that observed in the previous studies of amorphous RE-Fe alloys (RHYNE, 1985b). In these previous studies it was found that the SANS undergoes a 'weak divergence' at the magnetisation-determined critical temperature T_c. ie. the SANS has a slight hump at T_c. However, there is no sign of such a divergence in the Dy_7Ni_3 SANS (figure 10.7) and it appears that the only connection between the SANS and the asymptotic Curie temperature θ_p reported by BUSCHOW (1980) is that the SANS has its greatest change with temperature at a temperature roughly equal to θ_p. In the previous RE-Fe studies it was found that above T_c the SANS lineshape was closely Lorentzian and that below T_c the lineshape could be represented by the LL^2 function (equation (10.7)). This is to be contrasted with the finding for Dy_7Ni_3 (see section 10.3.2) that above the reported Curie temperature (35K) the data are fitted well by the LL^2 function (the inclusion of the Lorentzian squared term is essential), whilst below the reported Curie temperature the data are not fitted well by the LL^2 function or any other function considered. The correlation length ($\xi \equiv \kappa^{-1}$) obtained by fitting to the SANS lineshape of RE-Fe alloys has always been found to be very small (~10Å) at high temperatures, to rise to a maximum close to T_c and then to fall to a constant value (~50Å→100Å) at lower temperatures. The correlation length obtained by fitting to the Dy_7Ni_3 data behaves quite differently (see figure 10.12); at temperatures above the reported Curie temperature ξ is found to have a high value (~175Å) which decreases as the sample is cooled (note however that $\xi <<$ the minimum sample dimension 20μm). At no temperature at which the SANS is large enough to be measured does ξ appear to fall to a low value (~10Å). There is perhaps a slight indication of a 'weak divergence' in the correlation length at about 150K. However, the SANS signal is very small indeed by this temperature so that the errors in the fitted parameters are correspondingly large. Hence it is not possible to draw a definite conclusion concerning the possible presence of a 'weak divergence' of the correlation length at 150K. Because the SANS is so small at these temperatures the counting time required to settle this question is prohibitively high. A 'weak divergence' of ξ at a temperature completely different to T_c has not been observed in any of the previous work in this field. There are also hints of complexities in the detailed behaviour of ξ between 150K and 35K. As the sample is cooled below 35K the LL^2 fit to the Dy_7Ni_3 data yields a correlation length which rises again (more sharply than it falls above 35K), stabilising at a value roughly equal to its high temperature value. This behaviour is also quite unlike that seen in RE-Fe alloys, although the fit results below 35K should be treated with caution since the LL^2 function no longer fits the data well. Two possible factors which may be connected with the surprisingly large difference between the magnetic ordering occurring in Dy_7Ni_3 and that observed previously in other amorphous alloys by other workers are as follows: Firstly Dy_7Ni_3 has only one magnetic species, a RE, whereas all of the previous studies have been of RE-TL alloys with a magnetic moment on TL sites. Secondly all of the previous studies have been of TL-rich alloys whereas Dy_7Ni_3 is a RE-rich alloy and as is discussed in section 6.1.2 and section 8.4 these form very different atomic structures.

The agreement factor (figure 10.13) obtained by fitting the LL^2 function (equation (10.7)) to the Dy_7Ni_3 SANS data shows a marked deterioration below a temperature of 35K. The implication is that below 35K the LL^2 function is no longer an adequate description of the SANS lineshape. However, the question must be raised as to whether this deterioration of the fit is significant. One suggestion is that this can be viewed merely as a breakdown of what is essentially a linear response theory result (the LL^2 function). This suggestion is rejected for the following reasons: Firstly the deterioration of the agreement factor is almost step-like and quite unlike the temperature behaviour of the SANS at any Q-value (figure 10.7). A step in the agreement factor is more suggestive of a change in the functional form of the SANS lineshape. Also the behaviour below 35K of the residual between experiment and fit (figure 10.14) is such as to suggest an inadequacy of the functional form of the fit. Secondly the fact that the deterioration of the agreement factor occurs exactly at the reported asymptotic Curie temperature (BUSCHOW, 1980) would seem to indicate a genuine physical phenomenon. Thirdly it appears that the LL^2 function fits the SANS data for RE-Fe alloys successfully at all temperatures with no evidence of a breakdown. (Unfortunately the previous workers who have fitted the LL^2 function to the SANS from RAM systems have not given a clear indication of the quality of the fit, as is given by the agreement factor used here.) Hence it is concluded that some new functional form is required to explain the Dy_7Ni_3 SANS lineshape below 35K. None of the variants of the LL^2 function considered in Chapter 10 (equations (10.8) to (10.10)) were found to fit the data any better than the LL^2 function. Whilst the LL^2 function does have some theoretical backing, it is essentially a phenomenological result. Hence future attempts to find a better function for describing the low temperature SANS from Dy_7Ni_3 could be based either on the trial and error fitting of reasonable functions (as in section 10.3.2) or on some new function suggested by theoretical studies. One possibility that might be considered is a fractal-type approach.

Equations (6.2.2) and (6.2.3), derived by CHUDNOVSKY and SEROTA (1982; 1983), may be combined to express the spin correlation length for a RAM system in 3D as;

$$\xi \simeq (J_o/D_o)^2 \; (a/R_c)^4 \; R_c \qquad (11.4.6)$$

where a is the atomic spacing and R_c is the spatial correlation of easy axes (~3a→5a). The study of magnetic SRO described in section 11.3 indicates that the magnetic moments in amorphous Dy_7Ni_3 are only on the Dy atoms and the study of atomic SRO described in section 8.1.2 shows that these have a nearest neighbour distance of a=3.531Å (table 8.2). A reasonable value may be estimated for the spatial correlation of easy axes to be R_c~12Å (by inspection of the Dy-Dy correlation function - see figure

7.6). At temperatures above 35K where the LL^2 function fits the Dy_7Ni_3 SANS well the extracted correlation length is $\xi \sim 175 Å$ and equation (11.4.6) shows that this corresponds to an anisotropy to exchange ratio $D_0/J_0 \sim 0.023$. This value differs considerably from the value of 0.95±0.30 for amorphous $DyNi_{1.32}$ obtained from high field magnetisation measurements (BARBARA and DIENY, 1985). The question thus arises as to whether the present work is consistent with the results previously obtained for amorphous alloys in the series $Dy_zGd_{1-z}Ni_x$ ($x \sim 1$) using conventional magnetic measurements (see section 6.2.2 for a full list of references). A direct comparison is difficult because of the additional presence of Gd which has a magnetic moment due to spin angular momentum only and also because of the stoichiometry difference. However, the following points may be made: In the work on $Dy_zGd_{1-z}Ni_x$ alloys ($x \sim 1$) it is found that increasing z from 0 to 1 causes J_0 and the critical temperature to decrease whilst D_0 increases and then decreases again. Also the anisotropy to exchange ratio D_0/J_0 is found to increase as z increases. Thus the critical temperature decreases asD_0/J_0 increases. The critical temperature of $DyNi_{1.32}$ is 13.9K which compares with a value of 35K for Dy_7Ni_3 and hence it is to be expected that Dy_7Ni_3 will have the lower value of D_0/J_0. This is what has been found and consequently it is concluded that (insofar as a comparison is possible) the D_0/J_0 value deduced for Dy_7Ni_3 is consistent with the work on $Dy_zGd_{1-z}Ni_x$ alloys ($x \sim 1$). Further tentative conclusions may be drawn regarding amorphous alloys in the series $Dy_{1-x}Ni_x$ as follows: The alloy $DyNi_3$ is reported (ARRESE-BOGGIANO, CHAPPERT, COEY, LIÉNARD and REBOUILLAT, 1976) to have a critical temperature of 47K and to have much stronger anisotropy than exchange interactions. Since the work on $Dy_zGd_{1-z}Ni$ alloys shows that the critical temperature follows J_0 it is proposed that for $Dy_{1-x}Ni_x$ alloys the exchange interaction J_0 is low for intermediate x and high for low or high x. Furthermore it appears that D_0/J_0 increases with x and hence that D_0 also increases with x (see figure 11.6).

The value $D_0/J_0 \sim 0.023$ obtained above implies that Dy_7Ni_3 is a system with low (but non-zero) anisotropy. This agrees with the finding of section 11.3 that the magnetic correlation function extracted on the assumption of zero anisotropy is very similar to the Dy-Dy nuclear correlation function. For RAM systems with low anisotropy the appropriate model for the magnetic structure appears to be that of the correlated speromagnet (CSM - see section 6.2.2) in which the magnetisation undergoes a smooth rotation over a correlation length ξ, with $\xi >> a$. This is to be contrasted with $DyNi_{1.32}$ for which the measured D_0/J_0 value of 0.95 may be used in equation (11.4.6) (together with the values for a and R_c deduced for Dy_7Ni_3) to yield a spin correlation length $\xi \sim 0.1$Å. In this case $\xi << a$ which may be interpreted as meaning each Dy moment is strongly locked onto its local easy axis with very little correlation between adjacent moments. Hence the appropriate model for the magnetic ordering occurring in RAM systems such as $DyNi_{1.32}$ with large anisotropy is that of the spin glass-like speromagnet which has $\xi << a$.

In terms of a CSM model for the magnetic structure the observed small temperature variation of ξ may simply be explained as being due to the temperature dependence of either or both of D_0 and J_0 (CHUDNOVSKY, SASLOW and SEROTA, 1986). The steady rise of the SANS as the temperature is reduced may be explained in terms of a change with temperature of the fluctuations of directions of moments; as the sample is cooled the correlation length ξ changes little but there is a decrease in the fluctuations of the moment directions away from their ordered directions. Thus as the temperature is reduced there is an increase in the effective moment involved in the structure and hence a corresponding increase in the magnitude of the SANS. The magnetic ordering in Dy_7Ni_3 can then be viewed as a progressive 'freezing' of the moments into the CSM structure.

In order to obtain a complete picture of the magnetic order occurring in Dy_7Ni_3 it would be necessary to interpret the SANS data in conjunction with other measurements relevant to magnetic ordering. A quasi-elastic neutron scattering study, such as has previously been performed for amorphous $Y_{33}Fe_{67}$ (MURANI and REBOUILLAT, 1982), would be most useful in investigating whether the magnetic correlations observed in the SANS from Dy_7Ni_3 are static or dynamic and in observing the gradual freezing of moments suggested above. Also it would be worthwhile to perform conventional magnetic measurements on Dy_7Ni_3 in low fields. It is well known that for magnetic materials showing cluster-glass behaviour the efect of a high magnetic field is to totally obscure the features observed by conventional magnetic measurements using a low magnetic field. For example see the work of SHIGA and NAKAMURA (1983) who have measured the magnetisation and ac susceptibility of the crystalline cluster glass $Fe_{65}(Ni_{0.74}Mn_{0.26})_{35}$ at a large number of different applied fields, showing the effect most clearly. The minimum magnetic field used by BUSCHOW (1980) in studying $Dy_{69}Ni_{31}$ was 3kOe whereas a more suitable field for studying this type of system would be of order 100Oe or less and when they are compared with the results of SHIGA and NAKAMURA (1983) it is clear that BUSCHOW's (1980) results are very strongly affected by the use of an excessively high magnetic field. Hence conventional magnetic measurements in low field could help considerably to understand the Dy_7Ni_3 SANS results. Another suggestion for further work relating to magnetic correlations in Dy_7Ni_3 would be to perform an investigation of the dependence of the SANS on an applied magnetic field. There are theoretical studies which could be compared with the results of such an experiment. For example CHUDNOVSKY, SASLOW and SEROTA (1986) have shown that the behaviour of a CSM should become increasingly like that of a ferromagnet as the applied field is increased.

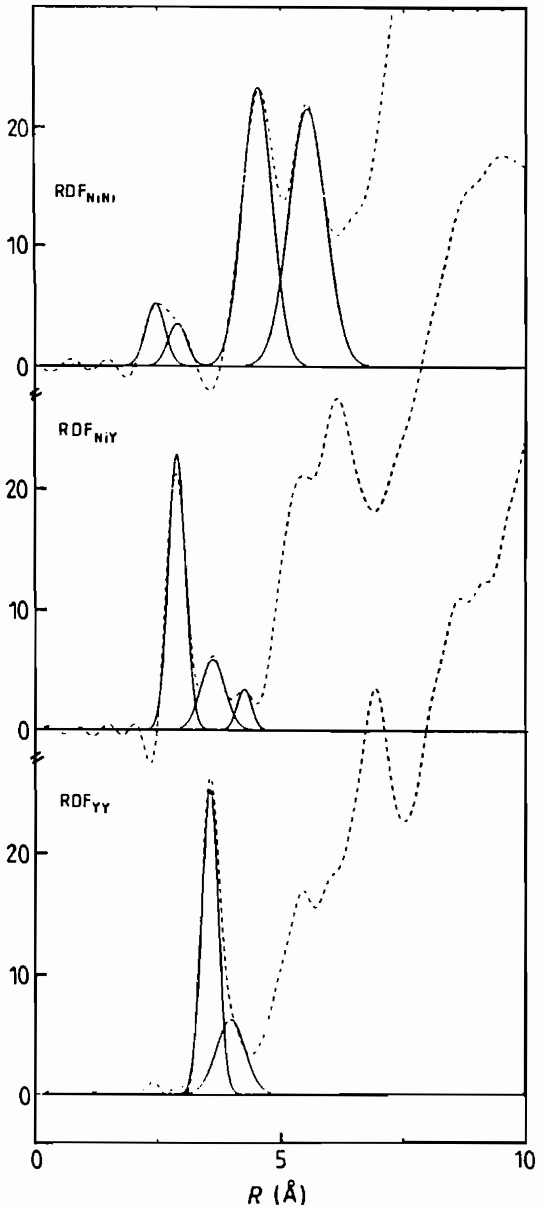

Partial radial distribution functions of $Ni_{33}Y_{67}$ glass and gaussian components of the nearest-neighbour regions.

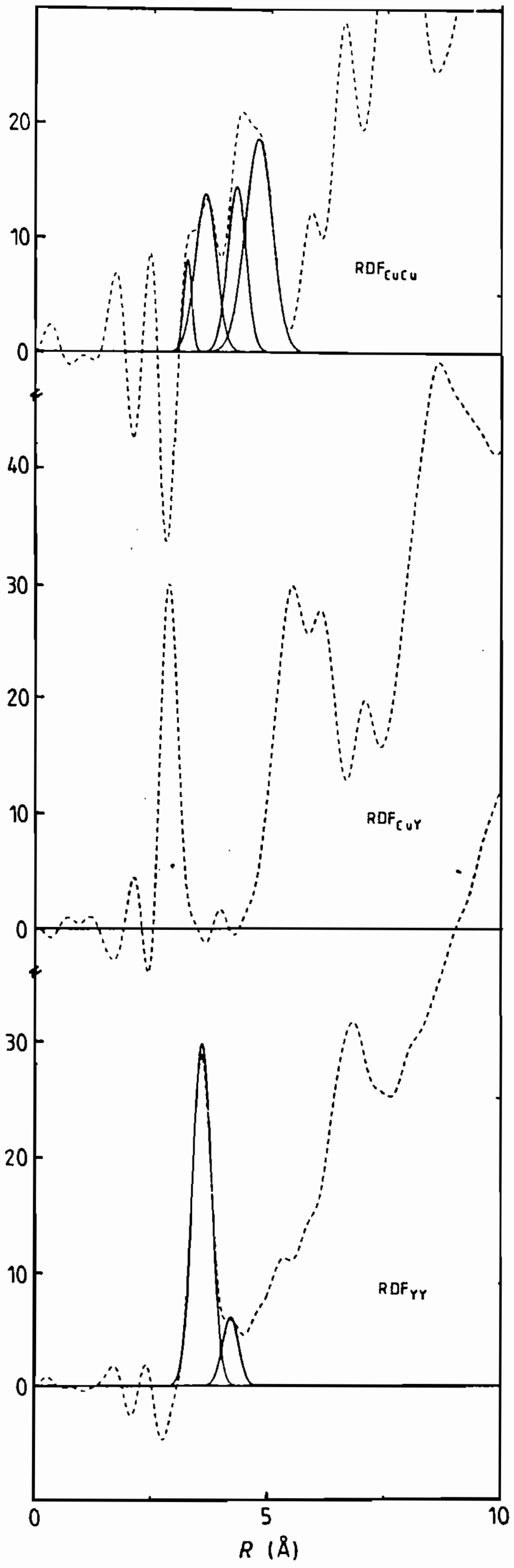

Partial radial distribution functions

$Cu_{33}Y_{67}$ glass and gaussian components of t

nearest-neighbour regions.

Figure 11.1 The Partial RDFs $n^*_{11'}(r)$ of $Y_{67}Ni_{33}$ and $Y_{67}Cu_{33}$ (MARET, CHIEUX, HICTER, ATZMON and JOHNSON, 1987).

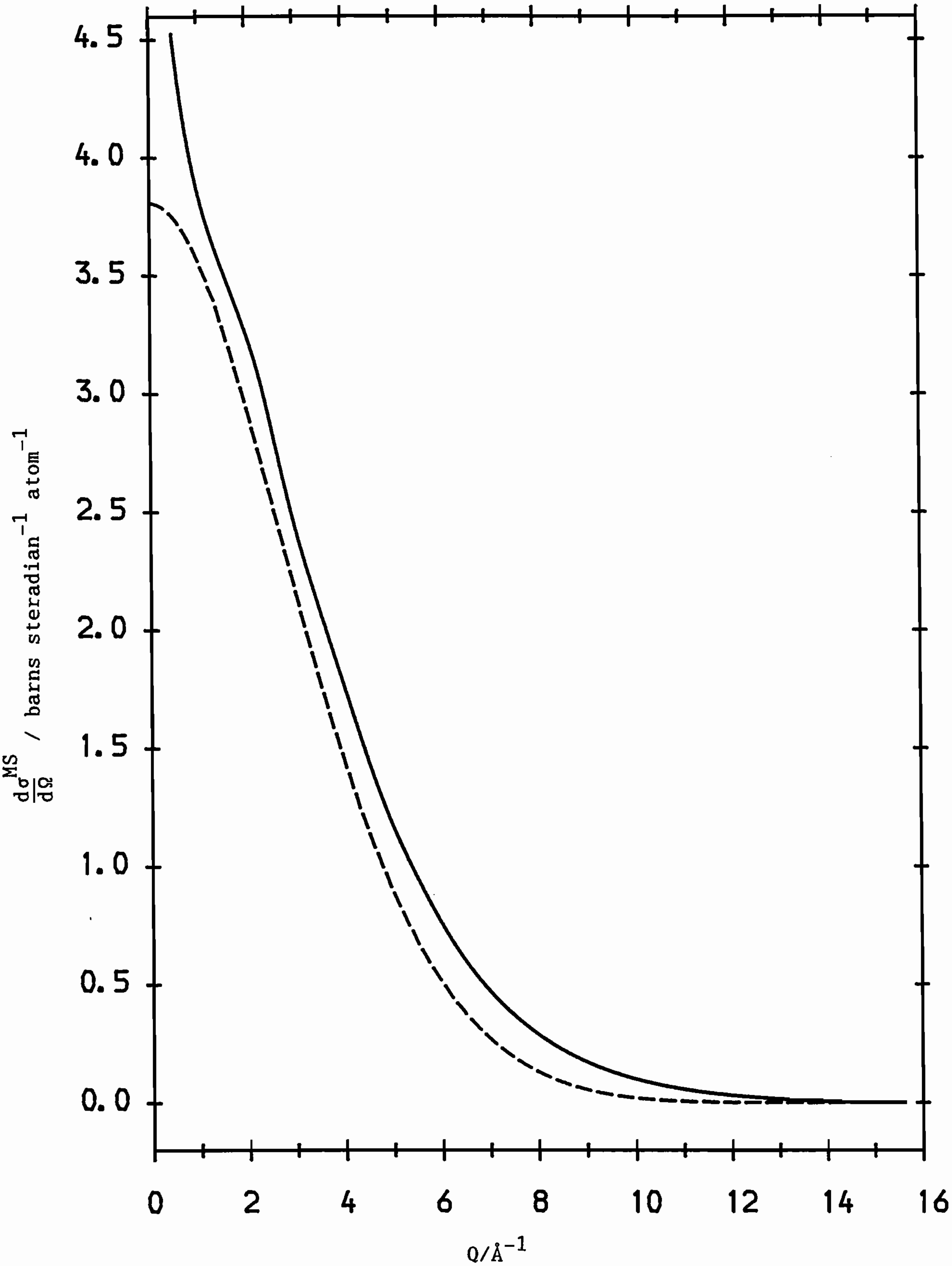

Figure 11.2 The Measured (Continuous Line) and Predicted (Dashed Line) Magnetic Self Scattering for Dy_7Ni_3.

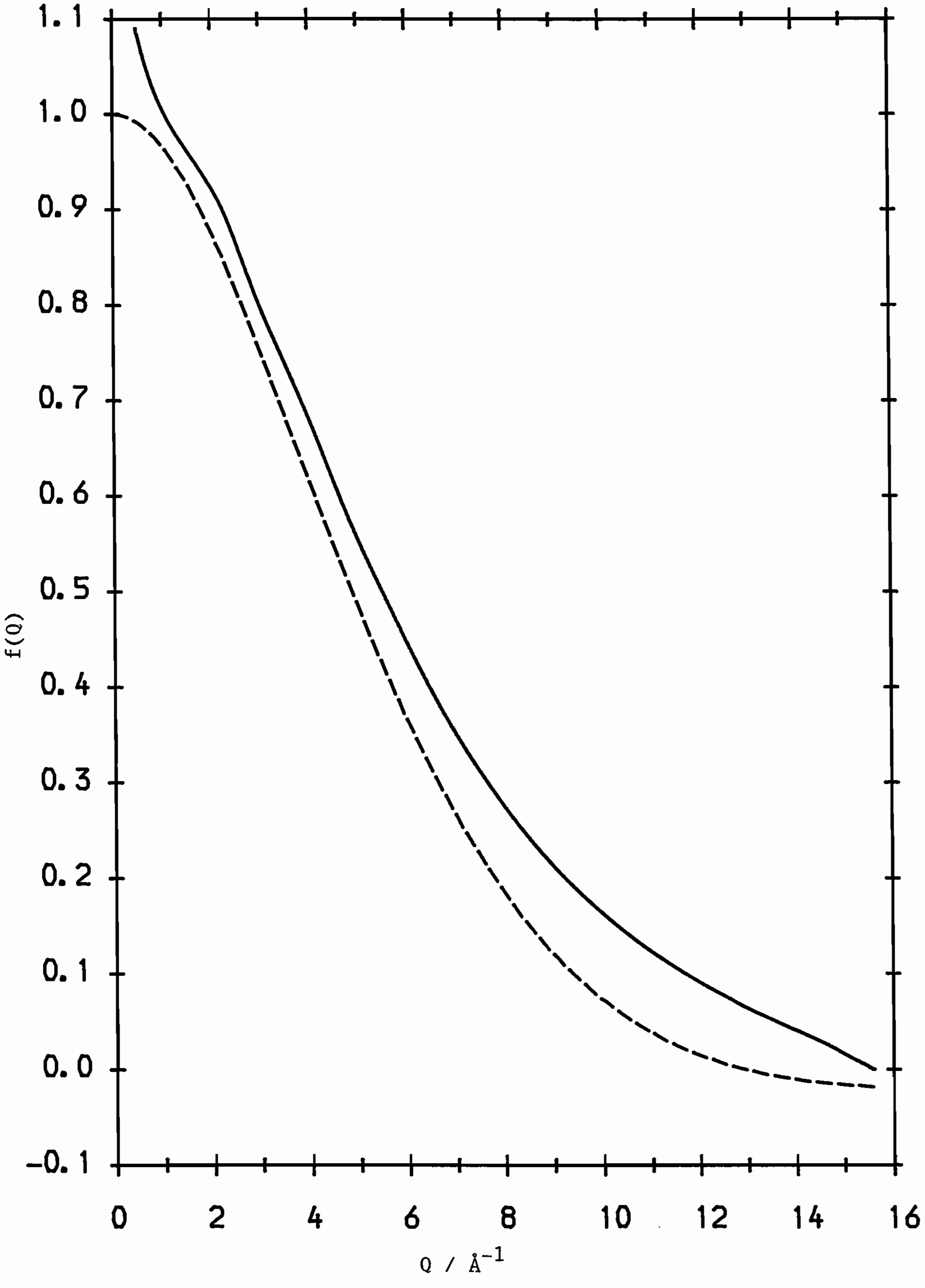

Figure 11.3 The Measured (Continuous Line) and Predicted (Dashed Line) Dy^{3+} Form Factor.

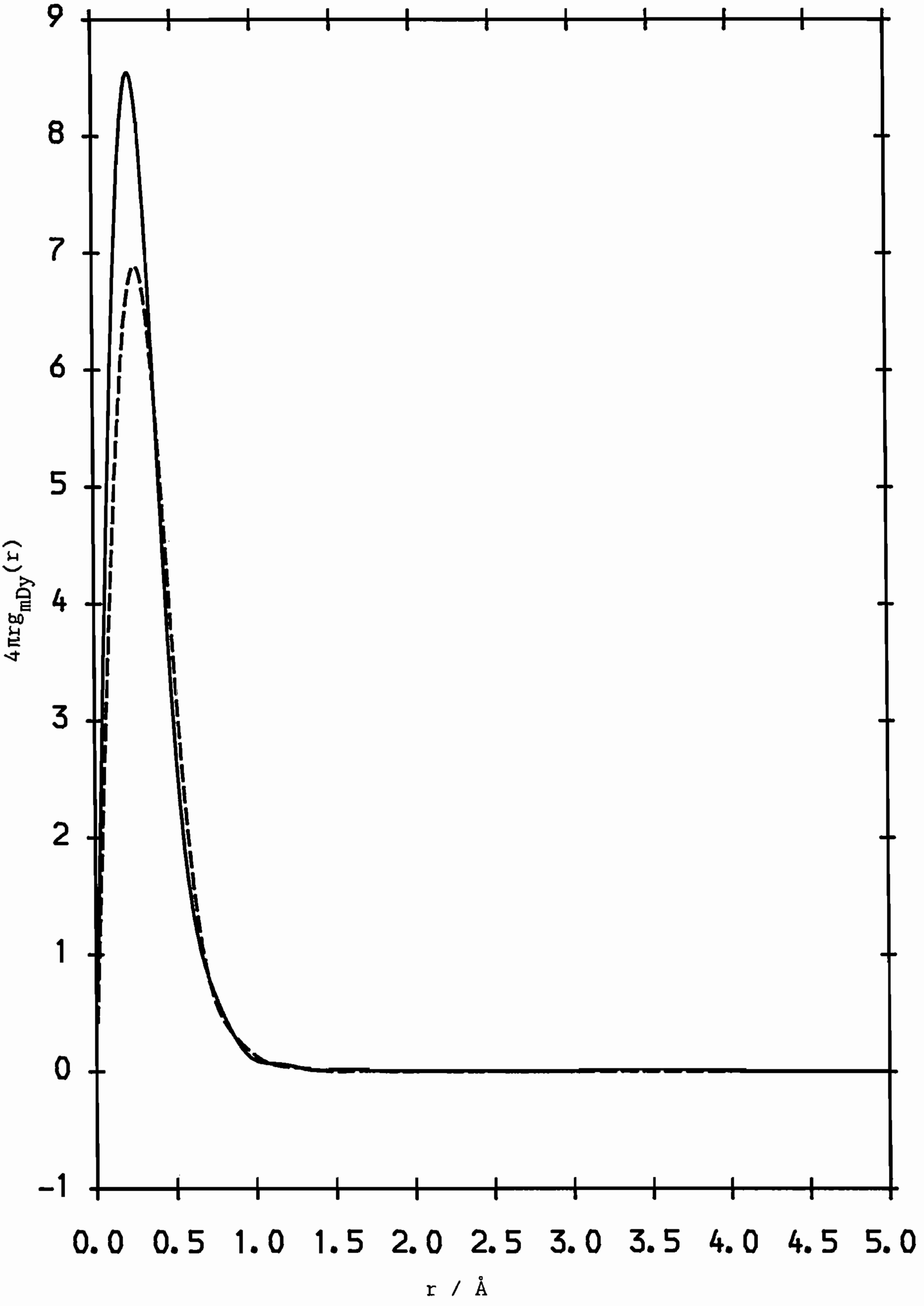

Figure 11.4 The Measured (Continuous Line) and Predicted (Dashed Line) Dy^{3} Normalised Real-Space Unpaired Electron Distribution $4\pi rg_{mDy}($

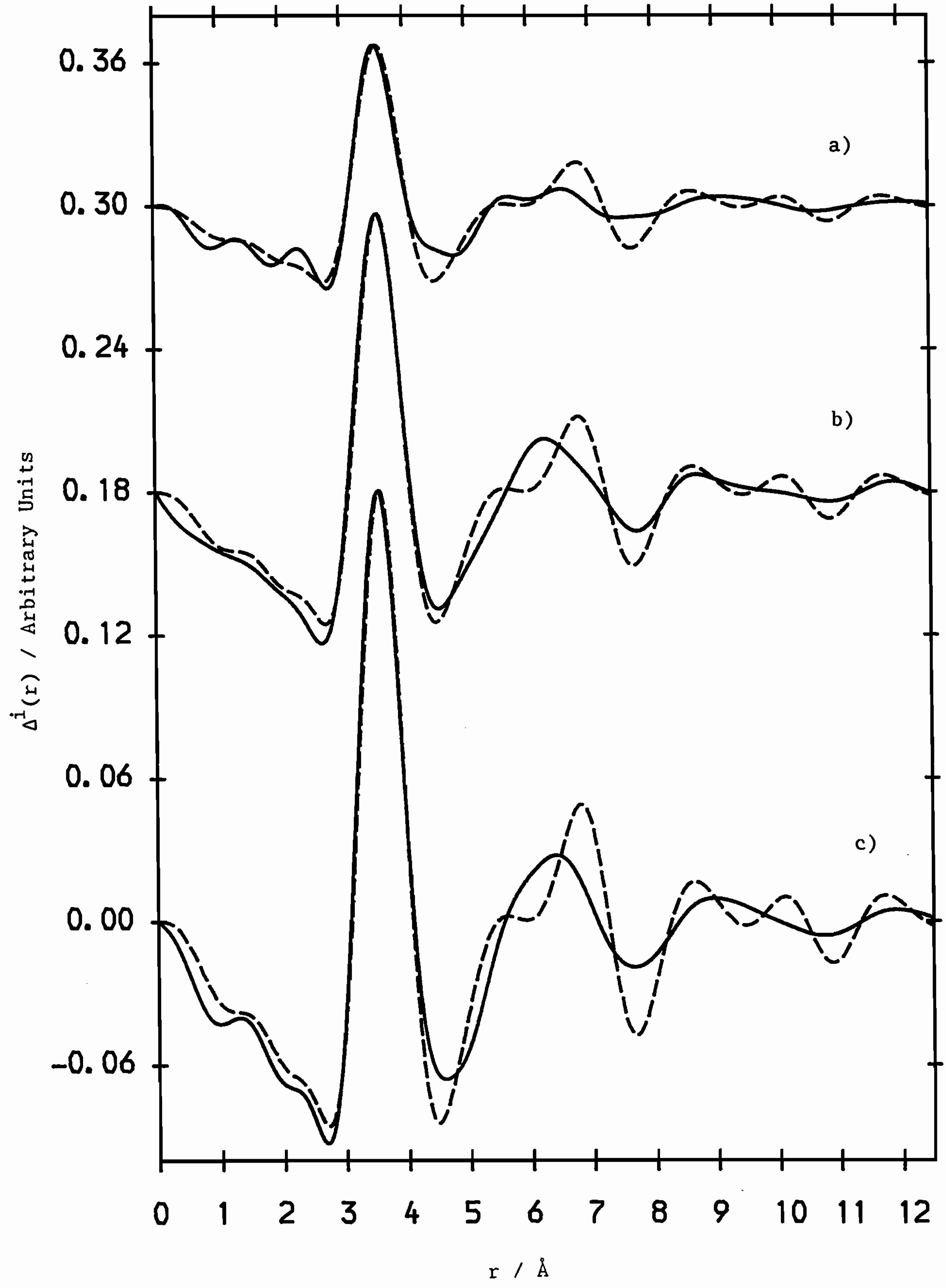

Figure 11.5 The Magnetic Correlation Functions $\Delta^i(r)$ (Continuous Line) Compared with $D_{DyDy}(r)$ (Dashed Line).

a) 44.3K-95.8K {offset 0.3}

b) 7.2K-44.3K {offset 0.18}

c) 7.2K-95.8K

$Dy_{1-x}Ni_x$

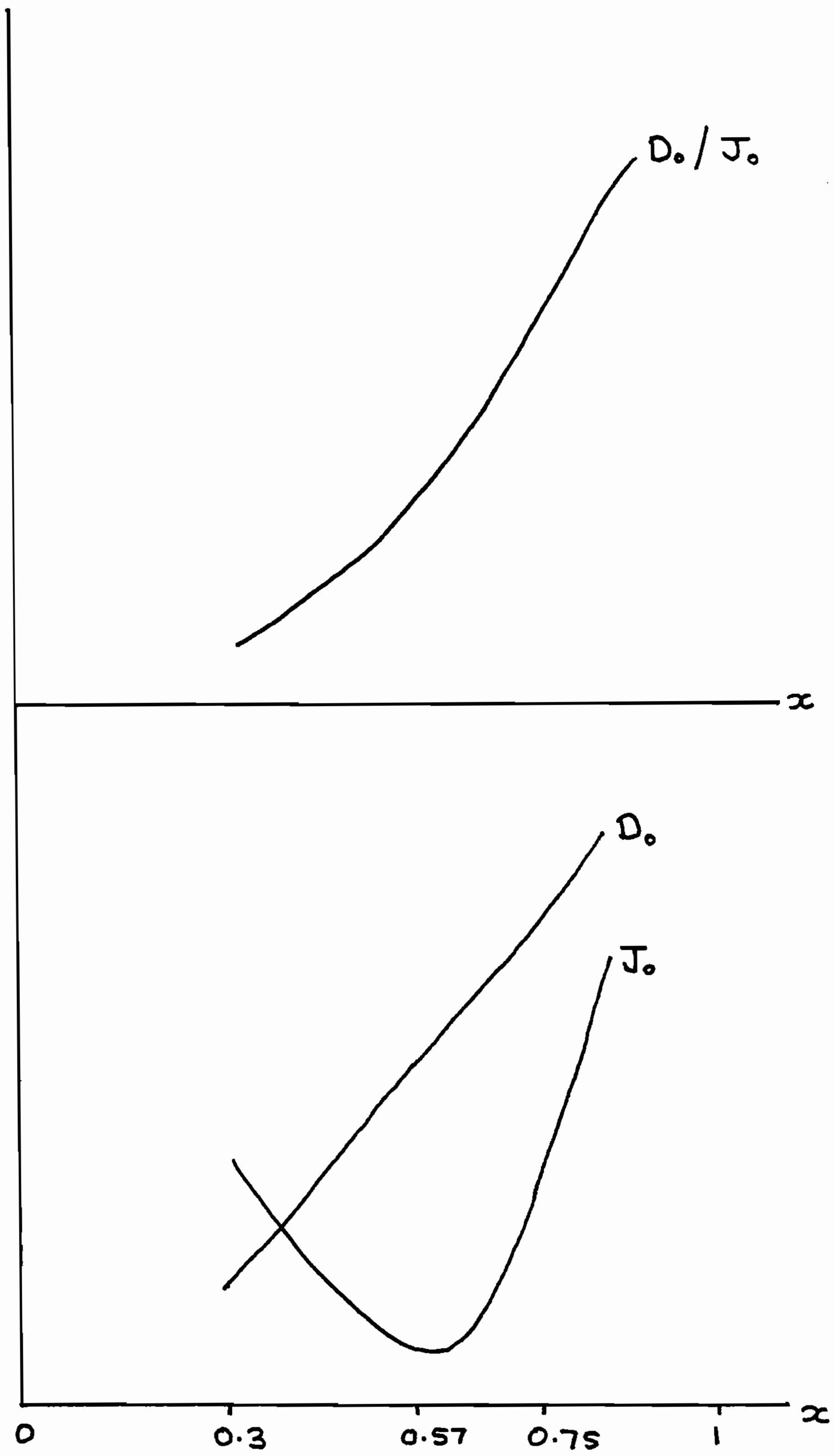

Figure 11.6 The Postulated Behaviour of D_o/J_o, D_o and J_o for Amorphous $Dy_{1-x}Ni_x$ Alloys as a Function of x.

CHAPTER 12

B2O3 - THE BOROXOL RING CONTROVERSY.

12.1 THE ZACHARIASEN CRN MODEL.

In his celebrated paper ZACHARIASEN (1932) proposed what is now the generally accepted basic model of the atomic structure of vitreous boric oxide, B_2O_3. In this model B_2O_3 is viewed as a CRN composed of corner-linked BO_3 triangles. Experimental evidence strongly supporting this proposal was provided by WARREN, KRUTTER and MORNINGSTAR (1936). The X-ray diffraction pattern of B_2O_3 was measured and Fourier transformed to obtain the RDF. The positions and areas of the low r peaks in the RDF were then found to be consistent with a CRN with three-coordinated boron atoms and two-coordinated oxygen atoms, and with each boron atom at the centre of an equilateral triangle of oxygen atoms. The random nature of this structure arises from the distribution of orientations of one triangle to another. Figure 2.6 shows a 2D representation of such a structure. Additional evidence from nuclear magnetic resonance (NMR) studies (SILVER and BRAY, 1958; SVANSON, FORSLIND and KROGH-MOE, 1962; SVANSON and JOHANSSON 1969) strongly suggests that each boron atom is at the centre of an equilateral triangle of oxygen atoms. Since ZACHARIASEN's proposal (1932) there have been quite a number of alternative proposals for the atomic structure of vitreous B_2O_3. However, none of these have been found to be as successful when compared with the experimental data as the CRN of corner-linked BO_3 triangles proposed by ZACHARIASEN (1932). (This excludes the modification of the ZACHARIASEN model discussed in the rest of this Chapter.) Reference should be made to the review by KROGH-MOE (1969) or the review section of the paper by JOHNSON, WRIGHT and SINCLAIR (1982) for further details of these alternative structural models.

12.2 THE BOROXOL RING MODEL.

In 1953 GOUBEAU and KELLER showed that the three principal features of the Raman spectrum of B_2O_3 are quite similar to the Raman spectra of a number of molecules, all of which contain a planar three-fold ring known as a boroxol ring. It was later suggested by KROGH-MOE (1958; 1965) that the structure of B_2O_3 should be described by a CRN of corner-linked BO_3 triangles which includes a significant concentration of B_3O_6 boroxol rings (see figure 12.1), thus explaining the principal features of the Raman spectrum. In particular the Raman spectrum of B_2O_3 (see figure 12.2) exhibits a highly polarised and extraordinarily intense and sharp line at $808cm^{-1}$ (≡100.2meV). Since this line is so highly polarised, and also does not appear in the IR spectrum, it must be due to a totally symmetric vibration. A BO_3 triangle cannot maintain a totally symmetric vibration and hence an acceptable structural model for B_2O_3 must contain a large proportion of some larger structural unit which can support a totally symmetric vibration. In fact the mode of vibration thought to give rise to the $808cm^{-1}$ Raman line is a symmetric stretch motion of the boroxol ring, known as a breathing mode, and this is illustrated in figure 12.1 . This mode involves an in-phase movement of the oxygen atoms in and out of the ring. There is no movement of the boron atoms and thus the mode is localised to one ring. The extreme narrowness of the Raman line is then due to the localisation of the mode to one particularly well-defined structural feature. It must be emphasised that the term 'boroxol ring' denotes a ring of three triangular units which is rigidly planar due to delocalised π-bonding, and not just any ring of three triangular units with random torsion angles. Thus, as WRIGHT, SUMNER and CLARE (1982) have pointed out, according to this model B_2O_3 may be considered as a CRN with two structural units. However, the frequency of occurrence of boroxol rings cannot be reliably determined from the Raman spectrum due to the difficulty in calculating the Raman scattering matrix element for amorphous solids and there has been considerable controversy as to the importance of boroxol rings in the atomic structure of B_2O_3. The purpose of this Chapter is to briefly consider the evidence relating to the issue of boroxol rings in B_2O_3 with particular emphasis on vibrational properties since the studies on B_2O_3 reported in Chapters 13 to 15 involve the phonon spectrum, although some discussion of other properties is required too. Reference should be made to the review by KROGH-MOE (1969) for a discussion of some of the properties not mentioned here, such as heat capacity and viscosity.

12.3 RELATED STRUCTURES.

B_2O_3 is one of the classic oxide glasses and in fact it has never been observed to crystallise at atmospheric pressure (UHLMANN, HAYS and TURNBULL, 1967). However, if the melt is cooled under a modest pressure (~4kbar) a crystal phase B_2O_3-I can be formed. The structure of B_2O_3-I, first determined correctly by STRONG and KAPLOW (1968), consists of ribbons of interconnected BO_3 triangles and this provides additional evidence for the Zachariasen model of vitreous B_2O_3 described in section 12.1 . B_2O_3-I does not contain boroxol rings. However, the density of B_2O_3-I (2.56 gcm^{-3}) is considerably greater than that of the glass (1.84 gcm^{-3}) and this can be ascribed to the presence of boroxol rings in the glass since these will result in a relatively open structure of low density. Indeed it may well be that the presence of highly stable planar boroxol rings is in part responsible for the inhibition of crystallisation. A second crystalline polymorph, B_2O_3-II, is obtained at higher pressures (~20kbar) and this has a structure which is comprised of BO_4 tetrahedra (PREWITT and SHANNON, 1968). Whilst the crystalline polymorphs of B_2O_3 do not contain boroxol rings, it has been found that the crystal structure of B_2S_3 does contain borsulphol rings (DIERCKS and KREBS, 1977). B_2Se_3 is thought to have a crystal structure similar to that of B_2S_3 (HUTCHINSON and EICK, 1962) and furthermore boroxol rings do occur in many borate crystals (GRISCOM, 1978). Also GALEENER, LUCOVSKY and MIKKELSEN (1980) have shown that there is considerable correspondence between the Raman spectrum of B_2O_3 and that of the orthorhombic form of metaboric acid $H_3B_3O_6$ which does contain boroxol rings. Thus, whilst the crystalline phases of B_2O_3 do not have boroxol rings, many other related materials do have such rings.

12.4 IDENTIFICATION OF THE BOROXOL RING BREATHING MODE.

There is considerable evidence confirming the identification of the $808cm^{-1}$ (≡100.2meV) Raman line with the breathing mode of a boroxol ring. BRONSWIJK and STRIJKS (1977) have shown that the Raman spectrum of crystalline B_2O_3 does not contain such a line. Furthermore it was shown that crystalline cesium enneaborate $Cs_2O(B_2O_3)_9$ which includes boroxol rings has sharp, highly polarised Raman lines at 806 cm^{-1} and 815 cm^{-1}, whilst crystalline cesium triborate $Cs_2O(B_2O_3)_3$ which does not include boroxol rings does not have such Raman lines. Also sodium metaborate

$Na_3B_3O_6$ and potassium metaborate $K_3B_3O_6$ which are isomorphous and contain isolated $B_3O_6^{3-}$ anions both give rise to a Raman line at $806cm^{-1}$. A detailed analysis of the Raman spectra of these materials has been given by BRIL (1976) who concludes that the $806cm^{-1}$ line is due to the breathing mode of the boroxol ring. GALEENER, LUCOVSKY and MIKKELSEN (1980) have measured the IR reflectivity and the IR dielectric constant of B_2O_3 as well as the polarised Raman spectra. An analysis in terms of a central force model showed that a CRN of BO_3 triangles is inadequate for an explanation of the phonon spectra of B_2O_3. Further details of this analysis are discussed in section 12.7 . GALEENER, LUCOVSKY and MIKKELSEN (1980) concluded that inelastic neutron scattering data were needed to complete the data desirable for a definitive vibrational analysis. Such neutron scattering data are reported in Chapter 13. It was also concluded to be desirable to have a realistic ball-and-stick model calculation of the dynamics for both the triangle and boroxol ring network models. Such calculations are reported in Chapter 14. GALEENER and GEISSBERGER (1982) have performed Raman studies on B_2O_3 making use of $^{10}B \rightarrow {}^{11}B$ (ie. ^{10}B replaces ^{11}B) isotopic substitution. It was found that, whilst most features in the spectrum were shifted to varying extents, both the 808 cm^{-1} and 470 cm^{-1} lines were unshifted, indicating that they are associated with modes which involve little or no motion of the boron atoms. The sharp $808cm^{-1}$ line is interpreted as being due to the breathing mode of a boroxol ring. The sharpness of the line is ascribed to the motion being localised to a single ring and to the small spread of angles in the rings. The broad $470cm^{-1}$ line is interpreted as being due to an in-phase motion of the bridging oxygens. The breadth of the line is ascribed to the motion being extended and to the distribution of bridging oxygen B-O-B angles outside the rings. Further Raman studies by WINDISCH and RISEN (1982a) in which $^{18}O \rightarrow {}^{16}O$ isotopic substitution was used as well as boron isotopic substitution have concluded that there is both highly localised vibrational motion characteristic of boroxol rings and network motion characteristic of such rings randomly connected in a network. For a $^{11}B_2{}^{16}O_{1.5}{}^{18}O_{1.5}$ sample the 808cm^{-1} line was found to have split into four unbroadened lines with intensities in the ratio 1:3:3:1 , and this is very strong evidence that the 808cm^{-1} line is due to a localised motion of the oxygen atoms in a boroxol ring. Evidence for boroxol rings was also found in a Raman study of B_2O_3 films (WINDISCH and RISEN, 1982b). Clearly there can be little doubt that the 808 cm^{-1} Raman line is due to boroxol rings in the glass. Furthermore the anomalous sharpness of the line is a strong indication that the rings are highly planar. Thus the Raman data on B_2O_3 would seem to suggest that boroxol rings play an important role in the atomic structure of B_2O_3. However, WILLIAMS and ELLIOTT (1982b) have suggested the possibility that Raman scattering (and also NMR) could be particularly sensitive to these rings (see also ELLIOTT (1987)) and that in fact they may only be present in a small proportion as one of a distribution of ring sizes (and presumably it is also suggested that planar boroxol rings are only present as part of a wide distribution of torsion angles within three-fold rings).

12.5 EXPERIMENTAL STUDIES OF THE ATOMIC STRUCTURE OF B2O3.

In 1970 MOZZI and WARREN performed an X-ray diffraction experiment on B_2O_3. The measured real space correlation function was compared with a model correlation function which included all the fixed distances occurring in a CRN composed entirely of boroxol rings together with the first inter-ring B-B distance assuming a bond angle on the bridging oxygen atom between rings of 130°. The model was found to predict all the peaks in the experimental correlation function out to 6Å. However, the structure in the model curve was a little too pronounced, indicating that not all the BO_3 triangles are in boroxol rings. NMR experiments by JELLISON, PANEK, BRAY and ROUSE (1977) on ^{17}O in B_2O_3 have provided evidence for two types of oxygen environment, one of which is ascribed to oxygen atoms in boroxol rings and the other of which is ascribed to oxygen atoms outside boroxol rings but in BO_3 triangles. From the results of these experiments it is deduced that the fraction of boron atoms in boroxol rings is 0.82 ± 0.08 (ie. ~1.52 boroxol rings to each independent BO_3 triangle). The fraction f of boron atoms in boroxol rings may easily be shown to be related to the ratio r of the number of boroxol rings to the number of independent BO_3 triangles by;

$$f = 3r / (1+3r) \qquad (12.5.1)$$

JELLISON, PANEK, BRAY and ROUSE (1977) were also able to determine the B-O-B angle at bridging oxygens outside boroxol rings to have a narrow distribution (RMS deviation = 1.7°) centred around either 134.6° or 128.1°, although it was not possible to distinguish which of these two values is the correct value. This angle agrees well with that used by MOZZI and WARREN (1970). Also the B-O-B angles in B_2O_3-I are found to range from 128.3° to 133.4° with a mean value of 130.7°. JOHNSON, WRIGHT and SINCLAIR (1982) have performed a neutron diffraction experiment on B_2O_3. An analysis of the results, similar to that of MOZZI and WARREN (1970) but considering a CRN of both boroxol rings and BO_3 triangles, indicated that the fraction of boron atoms in a boroxol ring is 0.6 ± 0.2 (ie. r=0.5). In particular the correlation function measured by neutron diffraction exhibits a peak at about 3.6Å which is exceptionally well-defined for such a large distance compared to the nearest neighbour distance. This peak would seem to suggest that there is a particularly high degree of IRO in B_2O_3, and in the boroxol ring model it is ascribed to correlations between boron atoms within the ring and oxygen atoms which are outside the ring but bonded to one of the other boron atoms in the ring (d in figure 12.1) . Recently GRIMLEY (1987) has also performed a neutron diffraction experiment on B_2O_3 (figure 12.3) and obtained a figure of 0.86±0.1 for the fraction of boron atoms in boroxol rings (ie. r~2.04). There has also been a recent X-ray study of samples of B_2O_3 which were densified by annealing at 300°C under high pressure (CHASON and SPAEPEN, 1988). The data were analysed in terms of a model consisting of planar ribbons of BO_3 triangles as in B_2O_3-I from which the authors concluded that boroxol rings were not essential for an explanation of their results.

As discussed by KROGH-MOE (1969), there is considerable evidence from studies of the temperature dependence of Raman scattering, X-ray diffraction, density, heat capacity and viscosity which suggests that a structural change takes place progressively with temperature. WALRAFEN, HOKMABADI, KRISHNAN, GUHA and MUNRO (1983) have shown that for molten B_2O_3 the integrated intensity of the $808cm^{-1}$ (≡100.2meV) Raman line decreases with increasing temperature over a wide range of temperatures. This was interpreted as being due to a decrease in boroxol ring concentration, yielding an energy of formation of boroxol rings from BO_3 triangles of 5.0 Kcal/mol.

12.6 MODELLING STUDIES OF THE ATOMIC STRUCTURE OF B2O3.

Several large ball-and-stick models of the atomic structure of vitreous B_2O_3 of the type described in section 2.5.3 have been constructed. In 1978 ELLIOTT used computer procedures to make a topological transformation of the coordinates of two already-existing models of three-coordinated arsenic (GREAVES and DAVIS, 1974) and thus produce two random network models for the atomic structure of B_2O_3 composed of BO_3 triangles. These models did not contain any boroxol rings whatsoever and yet it was found that they were able to reproduce the positions of the peaks at higher r in the RDF measured by X-ray diffraction. Previously MOZZI and WARREN (1970) had used these peaks as evidence for the presence of boroxol rings. The density of the models was about 35% too low and this was ascribed to constraints imposed on the structure through modification of a model originally built to simulate a different material. Hence a ball-and-stick model with no boroxol rings was constructed (WILLIAMS and ELLIOTT, 1982a; 1982b) specifically to simulate the structure of B_2O_3, the density of which was 17% above that of the real material. This model also reproduced the positions of the peaks in the experimental correlation function, although after broadening with the relevant experimental peak function P(r) the model correlation function peaks seem to have somewhat different shapes to the experimental correlation function peaks as determined by X-ray and neuton diffraction. In particular the peak at ~3.6Å in the model correlation function is not as narrow as the experimental peak, suggesting that torsion angles in the model are not sufficiently constrained.

BELL and CARNEVALE (1981) have constructed four ball-and-stick type models for B_2O_3. A random network model composed of BO_3 triangles was constructed by a topological tranformation of the GREAVES and DAVIS (1974) As model using ELLIOTT'S method (1978). A second model composed of BO_3 triangles was constructed from the BELL and DEAN (1972) SiO_2 model. A topological transformation was used to produce a mixed SiO_2-B_2O_3 model with equal numbers of Si and B atoms, and then the SiO_2 portions were discarded. Hence this model had large empty spaces and a density which was about 54% too low. Two more models composed entirely of boroxol rings were constructed by replacing the BO_3 triangles of the first two models with B_3O_6 boroxol rings and re-scaling. The densities of the resultant models were reduced by a factor 3/8, worsening the comparison with the density of B_2O_3. The model RDFs were calculated using a Lorentzian of arbitrary width, rather than the correct experimental peak function (see section 4.1.3), and compared with the X-ray RDF of MOZZI and WARREN (1970). It was concluded that the models with boroxol rings were marginally to be preferred and it was speculated that a locally layered random network model with boroxol rings might improve the agreement. In this model boroxol rings would be found parallel to each other, but rotated by 60°. However, in view of the physical inadequacies of this study discussed above it is perhaps questionable how much importance can be attached to the conclusions. Also JOHNSON, WRIGHT and SINCLAIR (1982) have shown that a layered structure of the type proposed by BELL and CARNEVALE (1981) cannot readily be reconciled with the measured density of B_2O_3.

AMINI, MITRA and HOCKNEY (1981) have performed a molecular dynamics (MD) study of B_2O_3 and the simulated glass was found to contain planar BO_3

triangles. This is somewhat surprising since a purely ionic force law was used, whereas , MOZZI and WARREN (1970) have shown that the bonding in B_2O_3 is predominantly covalent, and it may be that the triangular coordination is a fairly inevitable result of the radius ratio and stoichiometry. The distribution of bridging oxygen angles in the simulated glass was very broad with an average of 154°, which is much too large, and no evidence for a boroxol ring structure was found. However, there must be some doubt as to whether the results of this study would remain unchanged if a more realistic force law were to be used.

There has recently been an upsurge of interest in performing MD calculations for borate glasses. SOPPE, van der MAREL, van GUNSTEREN and den HARTOG (1988), XU, KAWAMURA and YOKOKAWA (1988) and TETER (1988) have all performed MD calculations in which boroxol rings were not reproduced in the structure of vitreous B_2O_3. However, in another MD calculation performed by INOUE, AOKI and YASUI (1987) boroxol rings were reproduced in the structure of B_2O_3. The calculated bond angles were found to be closer to the observed values than for earlier MD simulations and this was ascribed to the use of three-body potentials. The concentration of boroxol rings in the model was less than indicated by experiment but this has been attributed to the quench rate for the calculation being unrealistically high. TANAKA and KATAYAMA (1988) have also found evidence for the presence of a high concentration of boroxol rings in vitreous B_2O_3 by comparing the results of 'liquid cluster' calculations with the experimental neutron and X-ray structure factors.

WRIGHT, SUMNER and CLARE (1982) have also constructed two ball-and-stick models for B_2O_3. These models contained equal numbers of boroxol rings and independent BO_3 triangles (ie. r=1.0 and f=0.75) , one model with the units arranged at random and the other with an alternate arrangement of units. The density of the alternate model was found to be unstable and the correlation function did not agree with experiment. The density of the random model was 17% below that of vitreous B_2O_3, suggesting that the model contained somewhat too large a proportion of boroxol rings. The comparison of the random model correlation function with that measured by neutron diffraction appears quite favourable, and in particular the peak at ~3.6Å seems to be reproduced quite well.

12.7 MODELLING STUDIES OF THE NETWORK DYNAMICS OF B2O3.

BELL, CARNEVALE, KURKJIAN and PETERSON (1980) have computed the optical spectra of the two models of B_2O_3 derived from the BELL and DEAN (1972) SiO_2 model which are discussed in section 12.6 . A comparison was made with the IR spectrum and with an unspecified combination of the polarised and depolarised Raman components. It was concluded that the network of boroxol rings gave a satisfactory account of the optical spectra whilst the network of triangles did not. However, the models were extremely small for this type of work, the boroxol rings model containing only four boroxol rings, and because of this together with the density problems discussed in section 12.6 the results obtained cannot be regarded as conclusive.

The analytic central force methods which were introduced by SEN and THORPE (1977) for SiO_2 and generalised to several other topologies by THORPE and GALEENER (1980) have been extended to B_2O_3 by GALEENER and

THORPE (1983). These methods ignore non-central forces and assume that it is sufficient to consider a single angle θ at the bridging oxygens (using the notation of GALEENER and THORPE (1983)). The end result is a calculation of the energies of the band edges of the VDOS as a function of θ. GALEENER and THORPE (1983) have performed a central force calculation for a network of planar BO_3 triangles. The calculation was fitted to the high frequency region of the Raman spectrum (GALEENER, LUCOVSKY and MIKKELSEN, 1980). It was found that the only symmetric motion in the calculated results then occurred at $567cm^{-1}$ which does not agree well with the $808cm^{-1}$ line which is known to be due to a symmetric motion (see section 12.2). Also the general form of the calculated results was much less structured than the experimental data. However, the fit did yield a value of 120° for θ which is suggestive of boroxol rings. The central force methods were developed to treat networks of small regular rings of bonds and a calculation was performed for a network of three-fold rings of planar BO_3 triangles, assuming θ to be the same both inside and outside rings. The general form of the calculated VDOS was much more structured and more similar to the Raman spectrum of B_2O_3. In particular it exhibited a gap similar to that in the Raman spectrum (see figure 12.2) with a delta-function at the low energy edge of the gap similar to the $808cm^{-1}$ Raman line. A calculation was also performed for the generalised problem of a network of three-fold rings of puckered XO_3 triangles with different bridging oxygen X-O-X angles inside and outside the rings : the specific problem with planar XO_3 triangles and a bridging oxygen angle of 120° inside the rings then corresponds to a network of boroxol rings. The general form of the VDOS was the same as for the network of three-fold rings of planar triangles apart from some increase in structure above the energy gap. The results for a network of boroxol rings were then fitted to the Raman spectrum of B_2O_3. The fitting method is duscussed further in Chapter 14. A value of 130° was obtained for the bridging oxygen angle outside the rings which agrees well with the values obtained by other methods. The peaks above the energy gap were found to occur at energies which were too low and an ad hoc gap expansion of $140cm^{-1}$ (which is a shift in energy of the modes above the gap of roughly 15%) was introduced to draw attention to similarities between the calculation and the Raman spectrum. It was suggested that this gap expansion could be accounted for by a difference between the central force constant inside and outside the boroxol rings. The results of the calculation for a network of three-fold rings of planar BO_3 triangles were compared with the experimental isotope shifts in the Raman spectrum (see section 12.4). This is also discussed further in Chapter 14. It was concluded that the network of boroxol rings showed improved agreement with experiment over the network of BO_3 triangles. The discrepancies which remained were ascribed to the need to include non-central forces in the calculation. Non-central forces are included in the calculations reported in Chapter 14 and indeed there is a considerable improvement in agreement with experiment. There are also conclusions regarding some of the assumptions made by GALEENER and THORPE (1983).

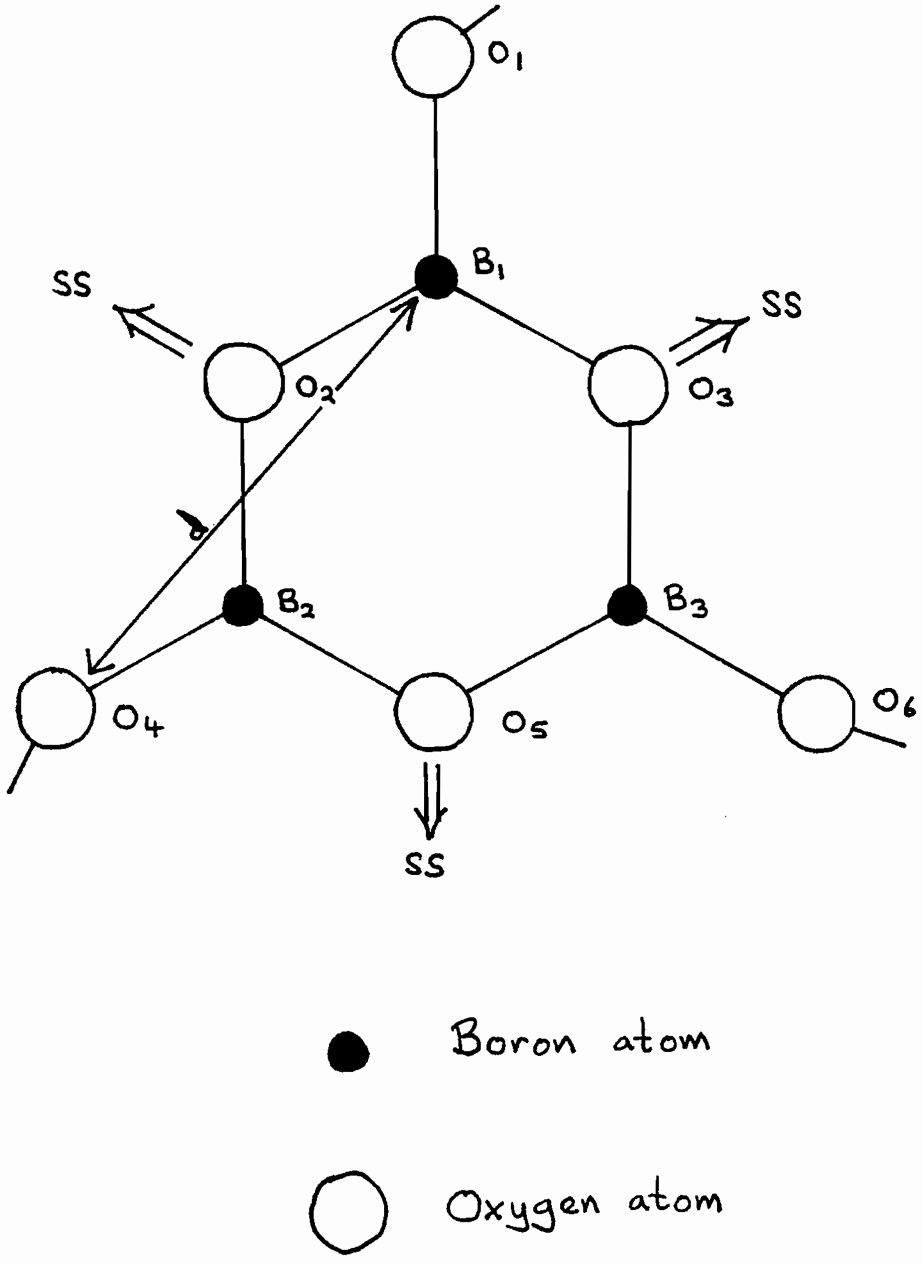

Figure 12.1 A B_3O_6 Boroxol Ring, Showing the Breathing Mode (SS).

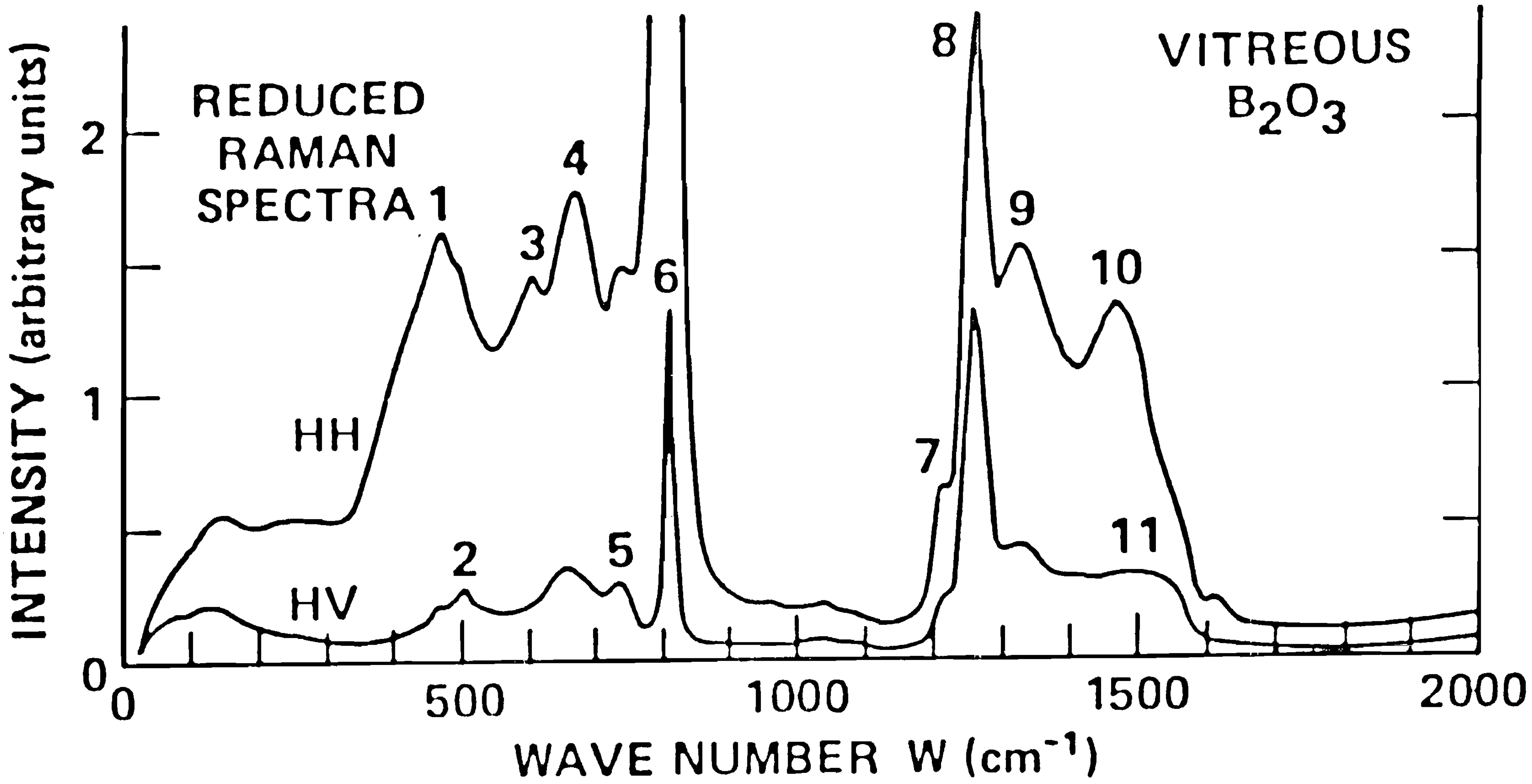

Figure 12.2 The Reduced Raman Spectra of Vitreous B_2O_3 {after GALEENER and THORPE, 1983}.

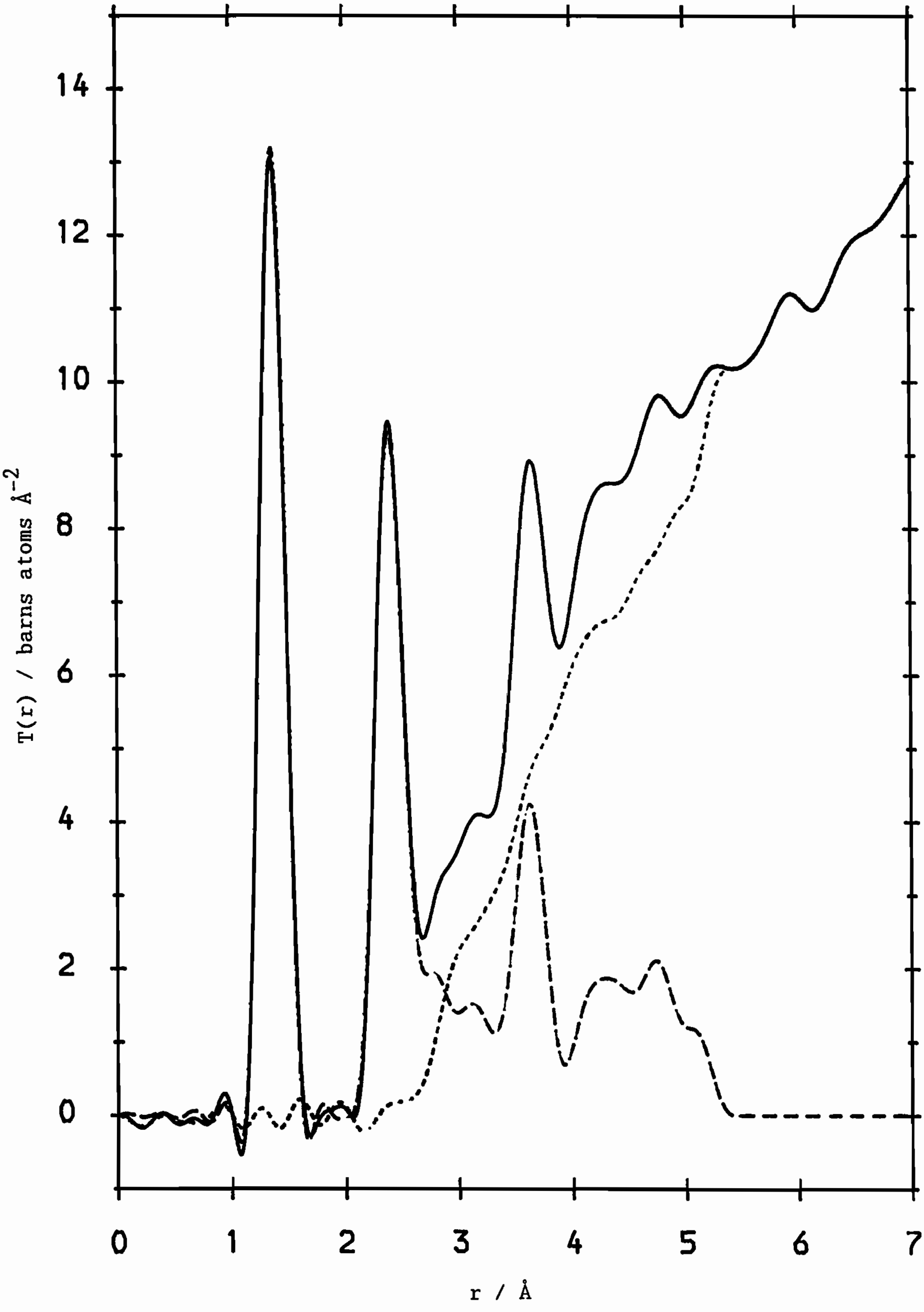

Figure 12.3 The Experimental (Continuous Line) Neutron Scattering Length Weighted Correlation Function T′(r) of Vitreous B_2O_3 (GRIMLEY, 1987) together with a Model Correlation Function (Dashed Line) for the Smaller Distances Occurring in a CRN with 86% of the Boron Atoms in Boroxol Rings and the Residual Between Experiment and Model (Dotted Line).

CHAPTER 13

B203 - INELASTIC NEUTRON SCATTERING.

13.1 CHOPPER SPECTROMETERS.

The VDOS of B_2O_3 was studied using the Low Resolution Medium Energy Chopper Spectrometer (LRMECS) and the High Resolution Medium Energy Chopper Spectrometer (HRMECS) at the Intense Pulsed Neutron Source (IPNS) at Argonne National Laboratory, Chicago (PRICE, CARPENTER, PELIZZARI, SINHA, BRESOF and OSTROWSKI, 1982). LRMECS was used for a medium resolution (ie. energy resolution) study of the VDOS over the whole energy range whilst HRMECS was used for a high resolution study of the VDOS at energies in the region of the boroxol ring breathing mode (100.2meV). The measurement performed using HRMECS has already been reported briefly in the literature by SINCLAIR (1985) and PRICE (1986).

The neutron source at IPNS (CARPENTER, PRICE and SWANSON, 1978) is a pulsed source (see section 3.1.1) in which neutrons are produced 30 times a second by a burst of 500MeV protons colliding with a uranium target. LRMECS and HRMECS both receive neutrons via beam tubes which at the time of the experiments viewed high density polyethylene moderators at a temperature of about 50°C (LOONG, IKEDA, CARPENTER and PRICE, 1987). As with all instruments at pulsed sources, LRMECS and HRMECS rely on the time of flight (TOF) technique to determine neutron energies. The basic principle of the TOF technique is simply to measure the time that neutrons take to travel a fixed flight path and hence evaluate the neutron energy by Newtonian mechanics (relativistic corrections are negligible). Clearly the energy resolution of TOF spectrometers depends upon the length of the flight path, with longer spectrometers having finer resolution. Both LRMECS and HRMECS are direct geometry chopper spectrometers and the significant differences between them may be described in terms of layout and emphasis. Hence the two spectrometers will be discussed together.

For a direct geometry inelastic neutron scattering spectrometer the incident energy E is fixed by some means so that mono-energetic pulses of neutrons are incident on the sample. The scattered neutrons are then detected as a function of TOF so that the energy $\hbar\omega$ and the momentum $\hbar\underline{Q}$ transferred to the sample may be determined. In the case of LRMECS and HRMECS the incident energy is defined by a chopper. This is a rotating mechanical device which transmits neutrons only when it is in a particular orientation relative to an incident beam. The chopper is situated at a distance d_1 from the pulsed source of neutrons (see figure 13.1 for the general layout of the chopper spectrometers) and is rotated in phase with the source so that it transmits neutrons at a time t_1 after the neutrons have left the source. Thus the chopper defines the incident neutron energy to be;

$$E = (1/2)\ m\ (d_1/t_1)^2 \tag{13.1.1}$$

By these means a pulse of neutrons of energy E arrives at the sample position at a time $t_1(d_1+d_2)/d_1$ after the neutrons have left the source, where d_2 is the flight path from the chopper to the sample. If a neutron with total TOF t is detected by a detector at a distance d_3 from the sample its final energy E′ may then be determined by;

$$E' = (1/2)\ m\ [d_3/(t-t_1(d_1+d_2)/d_1)]^2 \tag{13.1.2}$$

where t_1 is obtained from the incident energy according to equation (13.1.1). It is then trivial to determine the energy transferred to the sample $\hbar\omega$ (equation (3.3.4)). The momentum transferred to the sample $\hbar Q$ may be evaluated from E and E′ together with the scattering angle 2θ of the detector and equation (4.1.34). Thus a chopper spectrometer is ideally suited for a measurement of the double differential cross-section $d^2\sigma/d\Omega d\varepsilon$ of an amorphous solid as a function of ε and Q. A more detailed discussion of choppers and their use in direct geometry inelastic neutron scattering spectrometers has been given by WINDSOR (1981).

The specifications of the two chopper spectrometers are given in table 13.1;

	LRMECS	HRMECS
d_1/m	6.2	12.8
d_2/m	0.6	1.1
d_3/m	2.5	4.0
Approximate Energy Resolution	6→8%	3→4%
Scattering Angle Range	-10°→+120°	-20°→+20°
Maximum Q-Range/Å^{-1}	0.1→30	0.3→9
Beam Size/cm²	5.08x10.16	7.62x10.16

Table 13.1

The dimensions of HRMECS are of order twice those of LRMECS (see figures 13.2 and 13.3) and hence HRMECS has a finer resolution than LRMECS and a correspondingly smaller count rate. The flight paths of both spectrometers are evacuated to remove air scattering of the neutrons. The walls of the vacuum vessels are lined with absorbing material to reduce secondary scattering. Low efficiency BF_3 monitor detectors are placed in the incident beam to enable the incident energy E and the incident flux to be determined. The scattered neutrons are detected by ^3He detectors positioned on an arc with its centre at the sample position.

13.2 EXPERIMENTAL PROCEDURE.

13.2.1 THE PERFORMANCE OF A DIRECT GEOMETRY INELASTIC NEUTRON SCATTERING EXPERIMENT.

The most important adjustable parameter in a direct geometry inelastic neutron scattering experiment is the incident energy E. This must be chosen so as to obtain a satisfactory energy transfer range and resolution. To maximise the resolution at a particular energy transfer the value of the incident energy should be close to but larger than the energy value of interest. This is because a neutron which transfers to the sample an amount of energy equal to the energy of interest will then have a small final velocity so that its TOF, and hence its final energy, can be determined very accurately. Note that in an experiment of this type it is the so-called 'down-scattering' part of the inelastic signal (ie. that in which the neutrons transfer energy to the sample) that is of interest. WINDSOR (1981) has given an analytic expression for the energy resolution of an idealised chopper spectrometer;

$$\Delta\hbar\omega/E = 2\delta_m/(d_1+d_2)\ [\ 1 + (\Delta t_r/\Delta t_m)^2(1+(1-\hbar\omega/E)^{3/2}(d_1+d_2)/d_3)^2\ ]^{1/2} \qquad (13.2.1)$$

where δ_m is the effective moderator thickness, Δt_r is the opening time of the chopper and Δt_m is the pulse width of the source. A more realistic analysis of the energy resolution of a chopper spectrometer has been given by LOONG, IKEDA, CARPENTER and PRICE (1987). In practice there is a limit on how close E can be to the energy of interest because if it is too close the scattered neutrons will be so slow and spread out in time that the count rate tends to zero. The Q-range required must also be considered in the choice of incident energy, although a spectrometer which covers a reasonable range of scattering angle will generally have an adequate range of Q at any reasonable incident energy. For a chopper spectrometer the required incident energy is selected by adjusting the chopper phasing relative to the source.

In an experiment of this type the sample should be cooled so as to minimise multiphonon scattering since it is the single-phonon cross-section that is of interest (see section 4.4). The count rates are generally very low so that long counting times are required to obtain adequate statistics. Runs must be performed on the sample of interest, on the sample background, on a vanadium sample and on the vanadium background. The purpose of the run on vanadium is to normalise the data by taking advantage of the fact that the scattering from vanadium is almost entirely incoherent as has already been discussed in section 7.2.1 . The precise value of the incident energy is determined from the spectra obtained from the monitor detectors. The data are then transformed from being a function of TOF and 2θ to being a function of ε and Q by use of the measured incident energy, the dimensions of the spectrometer and the angles of the detectors (equations (13.1.2) and (4.1.34)). In this way a measurement of the double differential cross-section $d^2\sigma/d\Omega d\varepsilon$ is obtained. However, the cross-section which is measured directly includes multiple scattering and multiphonon scattering which contribute a smooth slowly-varying background to the single-phonon scattering (the quantity of interest) and a lengthy correction process is required to remove these contributions.

13.2.2 THE EXPERIMENTS ON B2O3.

The sample used in the experiments was isotopically enriched so that it contained mostly ^{11}B. A later isotopic analysis (FOSTER, 1985), performed at Harwell Laboratory, found that the sample contained (0.43±0.01)% ^{10}B and (99.57±0.01)% ^{11}B. The reason for the use of an isotopically enriched sample is that ^{10}B has a very high neutron absorption cross-section (see table 13.2), and so the absorption of neutrons by a sample containing natural boron (20.0% ^{10}B) would be prohibitively high. The values of cross-sections used in this study are given in table 13.2 (the source used for these values is SEARS, 1986);

	Total Bound Atom Scattering Cross-Section /barns	Incoherent Bound Atom Scattering Cross-Section /barns	Absorption Cross-Section for 2200ms^{-1} neutrons /barns
^{10}B	3.1	3.0	3837
^{11}B	5.78	0.22	0.0055
Natural O	4.232	$<10^{-3}$	0.00019
$\sim^{11}B_2O_3$	24.23	0.464	33.0
Vanadium	5.205	5.187	5.08

Table 13.2

The sample was manufactured by the author at Reading University by quenching from the melt in a platinum boat. The sample was cast as a 9.6cm×4.6cm plate. The thickness of the plate varied considerably due to surface tension effects in the molten state, with an average thickness ~4mm being obtained from micrometer measurements. The mass of the sample was 30.38g and use of this value together with a value of 1.823gcm^{-3} for the density of $^{11}B_2O_3$ yields an average thickness of 3.77mm. Prior to the experiment the sample was stored in a sealed container with silica gel because the surface of a B_2O_3 sample tends to take on water, becoming cloudy in appearance. It is especially undesirable that the sample becomes contaminated with water because the very high incoherent scattering cross-section of hydrogen (79.90 barns) means that a small number of vibrational modes involving hydrogen will result in a large contribution to the inelastic signal. In its initial state the sample has very little water contamination because the heat of the manufacturing process tends to drive off any water.

The experimental parameters relating to the two experiments on B_2O_3 are given in table 13.3;

	LRMECS	HRMECS
Incident Energy/meV	278.15	199.58
Approximate Resolution/meV	15	5
Mask Size/cm²	3.0x9.0	5.08x10.16
Angle of Sample to Beam	42°	90°
Temperature of Sample/K	15.0	11.0
Number of B_2O_3 Units in Beam	0.2276×10^{24}	0.2631×10^{24}
Vanadium Plate Size/cm³	0.108x7.8x12.8	0.1575x7.93x11.16
Number of Vanadium Atoms in Beam	0.2902×10^{24}	0.5542×10^{24}

Table 13.3

Raman measurements (GALEENER, LUCOVSKY and MIKKELSEN, 1980, see figure 12.2) show that the VDOS of B_2O_3 extends to about $1600cm^{-1}$ (~200meV). Hence an incident energy of 278.15meV was chosen for the experiment on LRMECS so as to cover the whole range of the VDOS with as fine a resolution as possible. With this incident energy the energy resolution of LRMECS is approximately 15meV (PRICE, 1985). For HRMECS an incident energy of 199.58meV was selected to maximise the resolution in the region of the boroxol ring breathing mode at 100.2meV. The energy resolution of HRMECS is approximately 5meV with this incident energy (PRICE, 1985).

For each spectrometer the various runs described in section 13.2.1 were performed. The sample was held in the beam in a thin aluminium foil case, suspended beneath a Displex closed cycle refrigerator. The sample was also surrounded by a thin aluminium heat shield. A boron nitride mask was placed in front of the sample so as to define the precise area exposed to the beam. The sample was run for 5 days for the LRMECS experiment and for 8 days for the HRMECS experiment.

The precise values of the incident energy given in table 13.3 were determined from the monitor spectra. The final monitor spectra from the sample and background runs were used to evaluate the measured transmissions given in table 13.4;

	Measured Transmission	Calculated Transmission
B_2O_3 on LRMECS	78.2%	75.1%
B_2O_3 on HRMECS	90.9%	80.7%
Vanadium on LRMECS	95.1%	93.0%
Vanadium on HRMECS	91.6%	92.5%

Table 13.4

The calculated transmissions in table 13.4 were evaluated from the values for the various parameters given in the earlier tables of this Chapter. Apart from the transmission of B_2O_3 on HRMECS the calculated and measured values agree quite well. The reason for the discrepancy with B_2O_3 on HRMECS is not known. However, it is thought that the measured transmission for B_2O_3 on HRMECS is in error since the parameter values used to evaluate the calculated transmission were successfully used to normalise the $S(Q,\varepsilon)$ data (see section 13.3). Possibly the cause of the error was a temporary fault with the monitor detector on HRMECS during either the sample or sample background run, but which did not occur during the vanadium or vanadium background runs.

For both experiments it was necessary to divide the detectors into groups at similar angles and then to combine together the TOF spectra of all the detectors within a group. This increases the effective count rate and reduces the data storage requirement. There is however a small degradation of Q resolution, but not of energy resolution.

13.3 DATA ANALYSIS.

13.3.1 DATA REDUCTION.

The data were reduced by running the programs of PRICE and LOONG (1985) at IPNS (see figure 13.4). The vanadium and vanadium background data for both spectrometers were normalised to the relevant monitor counts. The vanadium background data were not smoothed since they appeared to have sufficient statistical accuracy to make this unnecessary. It was also decided not to subtract time-independent backgrounds from the data (see section 13.3.2 for further discussion of this point). The vanadium background data were corrected for attenuation by the sample using the energy-independent expression for the attenuation $A(2\Theta)$ due to an infinite plate (WINDSOR, 1981);

$$A(2\theta) = \frac{\exp(-\mu_A t\sec\alpha) - \exp(-\mu_A t\sec(2\theta-\alpha)}{\mu_A t[\sec(2\theta-\alpha) - \sec\alpha]} \qquad \text{for transmission geometry}$$

and; (13.3.1)

$$A(2\theta) = \frac{1 - \exp(-\mu_A t(\ \sec\alpha - \sec(2\theta-\alpha)\ )}{\mu_A t[\sec\alpha - \sec(2\theta-\alpha)]} \qquad \text{for reflection geometry}$$

where α is the angle between the beam and the normal to the sample, t is the thickness of the sample and μ_A is the linear attenuation coefficient. The value used for $\mu_A t$ was obtained from the measured transmissions (table 13.4). The corrected vanadium background was then subtracted from the vanadium data. Note that the vanadium data were taken at room temperature with the same incident energy as for the sample. The background-subtracted vanadium data were integrated over an elastic energy range and compared with a calculation (COPLEY, PRICE and ROWE, 1973) for a thin vanadium plate based on VINEYARD's (1954) approximation and the cross-section in table 13.2 . A ratio was taken of the calculated elastic scattering and the measured elastic scattering to yield detector efficiency factors which were then used in the analysis of the sample data.

The data for the sample runs and for the sample background runs on each spectrometer were combined and normalised to the relevant monitor counts and detector efficiency factors. The background data were not smoothed as this did not appear to be necessary. Also time-independent backgrounds were not subtracted from the data (see section 13.3.2 for further discussion of this point). The background data were corrected for attenuation by the sample using equation (13.3.1) and then subtracted from the sample data for each spectrometer. At this stage it was necessary to run an additional program for the HRMECS data to account for the fact that this spectrometer has detectors at two slightly different distances from the sample position. The data were corrected for the energy-dependence of detector efficiency (equation (4.1.55)) and the incident and final energies were used to obtain the scattering function $S(Q,\varepsilon)$ where;

$$\frac{d^2\sigma}{d\Omega d\varepsilon} = \frac{k'}{k} S(Q,\varepsilon) \tag{13.3.2}$$

figure 13.5 shows the $S(Q,\varepsilon)$ obtained from LRMECS, including the elastic region (ε=0). As predicted by equation (4.4.12) the elastic region shows great similarity to the diffraction pattern of B_2O_3 (figure 13.6 shows the diffraction pattern of B_2O_3 at room temperature as measured on D4 (GRIMLEY, 1987)). In the inelastic region of the LRMECS measurement of $S(Q,\varepsilon)$ two broad non-dispersive bands are apparent at about 85meV and about 170meV. figure 13.7 shows the $S(Q,\varepsilon)$ obtained from HRMECS. The elastic region has not been included in this figure since the higher resolution of HRMECS leads to measured $S^{el}(Q)$ values which totally overwhelm the measured inelastic $S(Q,\varepsilon)$ values. Again there is a broad non-dispersive band at about 85meV.

The elastic region of the LRMECS data covers a range of Q from 0.76Å^{-1} to 19.63Å^{-1}. However, the data from any particular detector group are not at constant Q but rather at constant scattering angle 2θ. Thus each group of detectors measures a cut of $S(Q,\varepsilon)$ taken along a constant-2θ locus in Q-ε-space as given by equation (3.3.34). As a result of this the Q-range covered by the experimental data decreases with increasing energy transfer ε, as is apparent in figure 13.5 . For the present experiment the maximum useful energy transfer on LRMECS was about 240meV. In order to obtain data at constant ε and also at constant Q which is more useful for further calculation and analysis the program INTERP (PRICE and LOONG, 1985) was used on the constant-2θ LRMECS data. This program operates by fitting a cubic spline as a function of Q to the constant-2θ data and then interpolating. The elastic region of the HRMECS data covers a range of Q from $0.3Å^{-1}$ to $3.4Å^{-1}$. As with LRMECS, the Q-range decreases with increasing energy transfer ε. Hence the Q-range becomes very small at intermediate and high ε and it was found that there were insufficient data points along a rectilinear cut of S(Q,ε) for interpolation to work successfully. Hence the HRMECS data were analysed as constant-2θ data only. For the present work the maximum useful energy transfer on HRMECS was about 140meV.

S(Q,0) was obtained from the LRMECS constant-Q interpolated data and compared with the neutron diffraction pattern of B_2O_3 (GRIMLEY, 1987) so as to yield a value for the Debye-Waller factor $\exp(-2\overline{W})$ as follows: The Q-values, $Q_{D=0}$, at which the distinct scattering contribution i(Q) to the diffraction pattern I(Q) is zero were determined;

$$i(Q_{D=0}) = 0 \qquad\qquad I(Q_{D=0}) = I^S(Q_{D=0}) \qquad (13.3.3)$$

Following the approach of equation (4.4.22) the relation between elastic scattering and total scattering (equation (4.4.12)) may be expressed;

$$\frac{d\sigma^{el}}{d\Omega} = S^{el}(Q) = I(Q) - I^S(Q) + \overline{\langle b^2\rangle} \exp(-Q^2\overline{\langle u^2\rangle}/3) \qquad (13.3.4)$$

At $Q=Q_{D=0}$ this becomes;

$$S^{el}(Q_{D=0}) = \overline{\langle b^2 \rangle} \exp(-Q^2_{D=0}\overline{\langle u^2 \rangle}/3)$$

$$\ln[S^{el}(Q_{D=0})] = \ln[\overline{\langle b^2 \rangle}] - Q^2_{D=0}\overline{\langle u^2 \rangle}/3 \qquad (13.3.5)$$

Thus $\ln[S^{el}(Q)]$ was plotted against Q^2 (see figure 13.8) and the points on this curve corresponding to $Q=Q_{D=0}$ were determined. A straight line was drawn through the $Q=Q_{D=0}$ points and a value for the average RMS atomic displacement $\overline{\langle u^2 \rangle}^{1/2} = 0.081$Å was obtained from the gradient of the line. This method for extracting a value for the Debye-Waller factor from the elastic self scattering is due to PRICE (1985). Note that it is insensitive to possible errors in the normalisation of $S(Q,\varepsilon)$.

JOHNSON, WRIGHT and SINCLAIR (1982) have obtained a value of 0.07Å for the RMS (root mean square) bond length variation in B_2O_3 at room temperature for all pairs of atoms except B-O nearest neighbours. This value was obtained by fitting the distances for a CRN of both boroxol rings and independent BO_3 triangles to the neutron diffraction pattern. Equation (4.1.73) shows that on the assumption of isotropy (and equivalence of atom types) a RMS bond length of 0.07Å corresponds to a value $\overline{\langle u^2 \rangle}^{1/2} = 0.086$Å. This value is not expected to be precisely the same as the value obtained above from the LRMECS data for four reasons: Firstly the lower temperature of the LRMECS experiment will result in a lower value for $\overline{\langle u^2 \rangle}^{1/2}$ being obtained from the elastic scattering (see equation (13.3.6)). Secondly the inadequacy of the assumption of uncorrelated thermal motions has the result that different values of $\overline{\langle u^2 \rangle}^{1/2}$ are obtained from total diffraction and from elastic scattering; as has been discussed by WRIGHT and SINCLAIR (1985), this may be understood by considering that total diffraction is related to $G(\underline{r},0)$ (see section 4.1) and is insensitive to zone-centre acoustic phonons, whilst elastic scattering is related to $G(\underline{r},\infty)$ (see section 4.4) and is sensitive to all phonons. Hence the value of $\overline{\langle u^2\rangle}^{1/2}$ obtained by elastic scattering will tend to be larger than that obtained by total diffraction. Thirdly the value $\overline{\langle u^2\rangle}^{1/2}$ obtained from elastic scattering is due only to thermal motion whereas the value obtained from total diffraction can include a contribution due to static disorder as well (see section 8.1.2). The effect of this is to make the diffraction value larger than the elastic scattering value. Fourthly anisotropy in the atomic displacements will cause the two values to differ since total diffraction involves the RMS variation of bond lengths whereas elastic scattering involves the RMS atomic displacements (in all directions). Consequently the value of 0.081Å obtained from the elastic scattering measured by LRMECS is consistent with the value of 0.086Å obtained by total diffraction (JOHNSON, WRIGHT and SINCLAIR, 1982). Furthermore these two values are such as to suggest that static disorder in B_2O_3 is small (since the total diffraction value is only a little higher than the elastic scattering value).

The Debye-Waller factor obtained above was used to convert the LRMECS constant-ε data for $S(Q,\varepsilon)$ to the generalised density of states $G(Q,\varepsilon)$ defined according to equation (4.4.22). Multiple scattering and multiphonon scattering were ignored at this stage. A value $\bar{M}$=13.540amu is appropriate for the $^{\sim 11}B_2O_3$ sample used in these experiments. $G(Q,\varepsilon)$ was then averaged over Q, following equation (4.4.28), to yield an initial measurement of the effective VDOS $g_{eff}(E)$ (uncorrected for multiple scattering and multiphonon scattering).

13.3.2 MULTIPLE SCATTERING AND MULTIPHONON CORRECTIONS.

At this stage it was necessary to correct the experimental data for multiple scattering and multiphonon scattering so as to obtain the single-scattering single-phonon scattering function and hence a corrected measurement of the effective VDOS $g_{eff}(E)$. The data from both spectrometers were corrected for multiple scattering using the Monte Carlo program MSCAT (COPLEY, 1975). The version of MSCAT used (PRICE, CARPENTER, COPLEY, LOONG and SOKOL, 1985) had been adapted for use with data from the IPNS chopper spectrometers and also to include continuous coherent elastic scattering as with an amorphous solid. To calculate the multiple scattering this program requires a $S(Q,\varepsilon)$ to be input as a kernel for the calculation. In order to correct the experimental data over its whole range of Q and ε the kernel must cover a larger range of Q and ε. Hence the experimental data itself is not adequate and a model $S(Q,\varepsilon)$ was calculated from the experimental data for use as a kernel for the multiple scattering calculation. Two separate contributions were used to calculate the model $S(Q,\varepsilon)$. The first contribution was a theoretical calculation of $S(Q,\varepsilon)$ for a harmonic solid in the incoherent approximation. This was calculated from the initial LRMECS measurement of $g_{eff}(E)$ using the program SAB which operates as follows: the one-phonon scattering is calculated from $g_{eff}(E)$ using a procedure based on the equations given in section 4.4, the two-phonon scattering is calculated using a similar set of equations for two-phonon processes and the higher multiphonon terms are calculated using an approximation due to SJÖLANDER (1958). For this calculation the region of

$g_{eff}(E)$ below 50meV was not used so as to avoid including the contribution due to elastic scattering. Instead the Debye theory result $g(E) \propto E^2$ was used to extend the measured $g_{eff}(E)$ from 50meV to the origin. The program SAB also calculates a value for the Debye-Waller factor from the input $g_{eff}(E)$ according to the following equation;

$$\overline{\langle u^2\rangle} = (3\hbar^2/2\bar{M}) \int \langle 2n+1\rangle \, g_{eff}(E) \, E^{-1} \, dE \qquad (13.3.6)$$

This equation may be derived (SQUIRES, 1978) from the normal mode expansion of equation (4.4.13). A value of $\overline{\langle u^2\rangle}^{1/2}$=0.070Å was obtained which is consistent with the room temperature diffraction value of 0.086Å. Unfortunately the exponential factors in the program SAB diverged using the true sample temperature and hence it was necessary to use the fictitious value of 30K for the temperature. However, at a temperature of 15K the mean thermal energy kT=1.3meV with the result that at either 15K or at 30K only those modes with very low energies are appreciably populated. There are very few modes at energies this low ($g(E) \sim E^2$) and the inelastic scattering which they give rise to is totally obscured by the elastic scattering. Hence the error due to the use of the fictitious temperature 30K is entirely negligible. The value for $\overline{\langle u^2\rangle}^{1/2}$ from the program SAB was used to calculate the second contribution to the model $S(Q,\varepsilon)$ to be used as the kernel for the multiple scattering calculation. This second contribution was the elastic scattering which was calculated from the diffraction pattern (GRIMLEY, 1987) using equation (13.3.4). The Debye-Waller factor value from the program SAB was preferred to the earlier value obtained by comparing the elastic scattering with the diffraction pattern so that the elastic region of the model $S(Q,\varepsilon)$ would be consistent with the inelastic region.

The program MSCAT was used to calculate the multiple scattering for LRMECS and for HRMECS from the model scattering function. For each spectrometer the Monte Carlo calculations were carried out for a total of 10^5 scattering events. The total CPU time required to perform these calculations on a VAX-11/780 computer was about 70 hours for the LRMECS calculation and about 120 hours for the HRMECS calculation. The sample container was neglected in the calculations since it does not contribute greatly to the scattering.

The calculated multiple scattering was interpolated and then subtracted from the constant-2θ $S(Q,\varepsilon)$ data for each spectrometer. A self-shielding correction was performed using the total cross-section as a function of energy which is also calculated by the program MSCAT. Furthermore MSCAT calculates the transmission of the sample and this may be used as a consistency check on the multiple scattering calculation. A value of 76.7% was calculated for the LRMECS experiment which agrees well with the value in table 13.4 . In the case of HRMECS a value of 81.1% was calculated by MSCAT which agrees with the calculated value in table 13.4, supporting the conclusion that the measured value is in error. For the LRMECS experiment the multiple sattering calculation was found to have converged to an adequate statistical accuracy as is apparent from the figures relating to the subsequent data analysis. However, in the case of the HRMECS experiment it was found that the multiple scattering calculation had not converged to an adequate statistical accuracy. An effective VDOS $g_{eff}(E)$ was calculated from the constant-2θ HRMECS data both before and after subtraction of the calculated multiple scattering and these are shown in figures 13.9 and

13.10 respectively. Clearly the effect of subtracting the calculated multiple scattering is to introduce statistical fluctuations. However, whilst the corrected $g_{eff}(E)$ is not useful for identifying sharp features in the VDOS of B_2O_3 because of these fluctuations, it does serve to indicate that $g_{eff}(E)$ is zero in the region from about 100meV to about 150meV as found by Raman scattering (figure 12.2). A prohibitive amount of computer CPU time would have been required to calculate the multiple scattering for the HRMECS experiment with sufficient statistical accuracy to yield a corrected $S(Q,\varepsilon)$ which could usefully be further analysed.

The LRMECS constant-2θ $S(Q,\varepsilon)$ data, corrected for multiple scattering, were converted to constant-Q data using the program INTERP. The zeroth moment of $S(Q,\varepsilon)$ was calculated as a function of Q (equation (4.1.41)) and this was compared with the diffraction data (GRIMLEY, 1987) to check the normalisation of the LRMECS data - one should obtain the same S(Q) from either integrating the inelastic data at constant Q or from measuring the diffraction pattern and applying the Placzek correction. The LRMECS data were found to be correctly normalised to within an estimated margin of 3%.

A least squares fitting program was used to fit the sum of a Gaussian and a straight line to the elastic region of the constant-Q cuts of the LRMECS $S(Q,\varepsilon)$ data. The best fit was obtained by fitting to the region from ε=-50meV to an energy roughly 4meV above the centre of the elastic peak. The fitted Gaussians were then subtracted from $S(Q,\varepsilon)$ in attempt to remove the elastic scattering prior to correcting the data for multiphonon scattering. The resultant inelastic single-scattering function is shown in figure 13.11 . (The dip at about 40meV in the cut at lowest Q is thought to be spurious - this region where the elastic scattering has been subtracted is not reliable, see below.)

The multiple scattering-corrected LRMECS measurement of $S(Q,\varepsilon)$, after subtraction of elastic scattering, was corrected for multiphonon scattering using the following iterative prodecure: an initial estimate for $g_{eff}(E)$ was obtained by converting $S(Q,\varepsilon)$ (which still includes multiphonon scattering) to $G(Q,\varepsilon)$ and averaging over Q, the multiphonon scattering was calculated from $g_{eff}(E)$ using the same method as used by the program SAB (see above), this was subtracted from the data to provide an improved estimate of $S(Q,\varepsilon)$, and so on. In practice this procedure was found to have converged by the second iteration and the final $g_{eff}(E)$ obtained after multiple scattering and multiphonon scattering correction of the LRMECS data, and also attempted removal of the elastic scattering, is shown in figure 13.12 .

The interpretation of the results of these experiments will be discussed in Chapter 15. However, deficiencies in the LRMECS measurement will be discussed in this Chapter: The Raman spectrum of B_2O_3 (figure 12.2) shows that the VDOS has a maximum energy of about 200meV and thus $g_{eff}(E)$ should ideally go to zero at energies above this cut-off energy. However, whilst the final $g_{eff}(E)$ (figure 13.12) does diminish considerably at about 203meV, it does not fall to zero and furthermore it starts to rise again at higher energies. Also the final $g_{eff}(E)$ does not fall completely to zero in the region from about 110meV to about 140meV whereas the Raman spectrum and the HRMECS measurement (and also the calculations of Chapter 14) indicate that there is a gap in the VDOS at these energies. One possible cause of these two deficiencies in the LRMECS measurement may be the decision not to subtract a time-independent background: It is often the practice with neutron scattering data from a pulsed accelerator source to subtract a time-independent component from the data for each run. The object of this procedure is primarily to remove the contribution to the background due to delayed neutrons from the target (CARPENTER, 1980). The variation with time of this contribution is much slower than the source frequency so that it may be treated as time-independent. In general this contribution to the background is not completely removed by the standard background subtraction procedure because the precise long-time behaviour of the neutron source from one run to another is not reproducible. The effect of a time-independent background may be seen by combining equation (13.3.2) with equations (13.1.1) and (13.1.2) to give;

$$S(Q,\varepsilon) = (d_3/2) \left(\frac{mE}{2}\right)^{\frac{1}{2}} \frac{1}{(E-\varepsilon)^2} \frac{d^2\sigma}{d\Omega dt} \qquad (13.3.7)$$

A time-independent signal gives a constant contribution to the cross-section $d^2\sigma/d\Omega dt$ and equation (13.3.7) shows that this will cause $S(Q,\varepsilon)$ to diverge quadratically as ε approaches E. A time-independent background was not subtracted in the initial stages of the data analysis because there was no obvious sign of the divergence at high energy transfers ε predicted by equation (13.3.7). However, the rise in the final $g_{eff}(E)$ at high energies is not that great and it is possible that it is due to a time-independent background which should have been subtracted. In the region from 110meV to 140meV where, as discussed above, $g_{eff}(E)$ is expected to fall to zero it is found that the final $g_{eff}(E)$ is gradually decreasing. Hence it would seem unlikely that this deficiency in the final

$g_{eff}(E)$ is due to a time-independent background since equation (13.3.7) shows that a time-independent background introduces a monotonically increasing contribution to $S(Q,\varepsilon)$ and hence to $G(Q,\varepsilon)$. Thus it may be that the deficiencies in the final LRMECS measurement of $g_{eff}(E)$ are due to some as yet unidentified experimental artifact, and in fact similar problems were encountered with other measurements made on LRMECS at about the same time (PRICE, 1985). One possibility that has been pointed out by PRICE and CARPENTER (1987) is that there may be an additional source of multiple scattering, although this is probably more important at low energies. Another possible cause of a time-independent background could be the thermalisation of fast neutrons in the chopper.

An additional deficiency of the final LRMECS measurement of $g_{eff}(E)$ is the low energy region where an attempt was made to remove the elastic contribution to the scattering. At zero energy transfer (and also at small energy transfer once energy resolution is taken into account) the elastic scattering totally overwhelms the inelastic scattering and hence any attempt to subtract the elastic scattering is likely to be unreliable. Some difficulty was encountered in fitting to the elastic region of the LRMECS data and an abortive attempt to fit to the elastic region of the HRMECS data proved most problematic. Thus it is not possible to draw conclusions about the low energy features in the VDOS from these measurements.

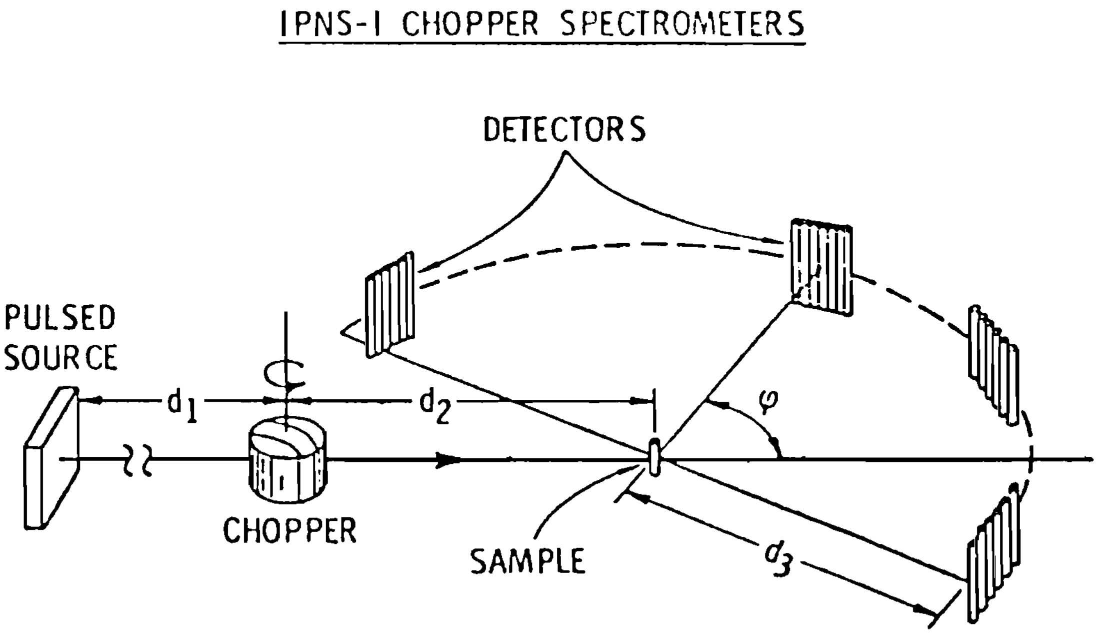

	d_1	d_2	d_3	$\Delta E/E_0$	φ
LRMECS	6.2 m	0.6 m	2.5 m	6-8%	-10° to +120°
HRMECS	12.8 m	1.1 m	4.0 m	3-4%	-20° to +20°

Figure 13.1 The General Layout of a Direct Geometry Inelastic Scattering Chopper Spectrometer {after PRICE et al, 1982}.

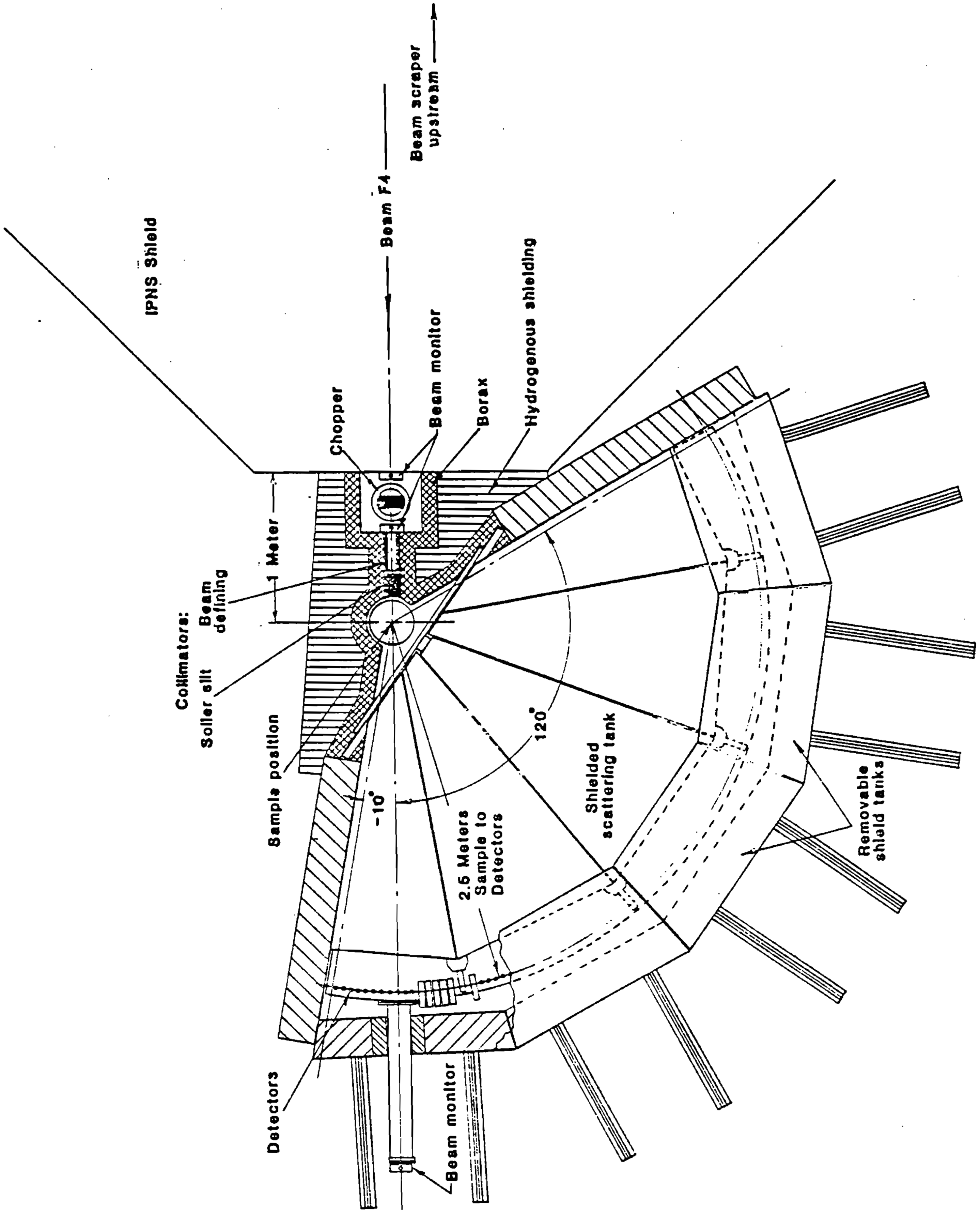

Figure 13.2 - Low-Resolution Medium-Energy Chopper Spectrometer

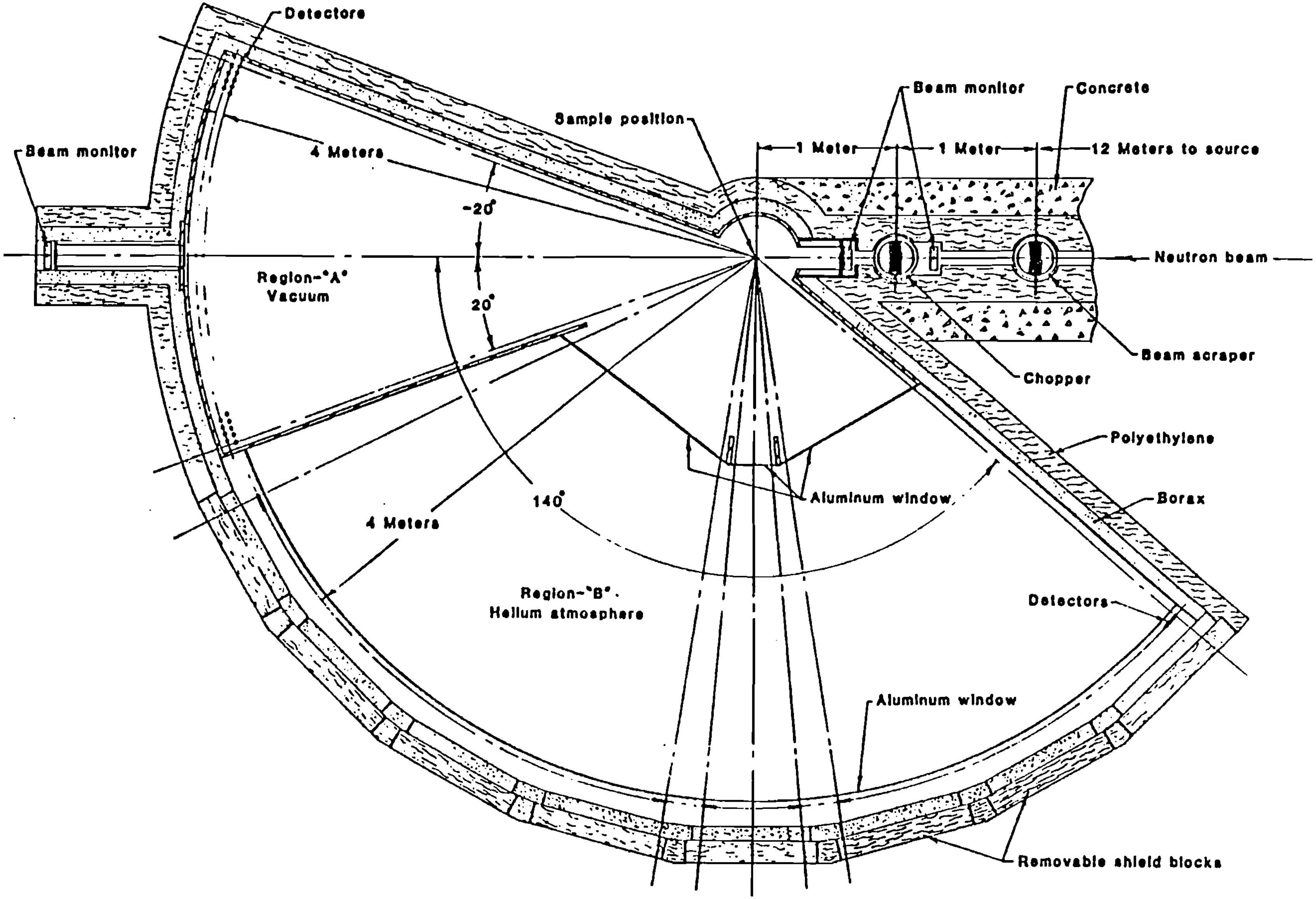
Detectors
Beam monitor
Concrete
Sample position
1 Meter
1 Meter
12 Meters to source
Beam monitor
4 Meters
-20°
Neutron beam
Region-"A"
Vacuum
20°
Beam scraper
Chopper
Polyethylene
Aluminum window
140°
Borax
4 Meters
Region-"B"
Helium atmosphere
Detectors
Aluminum window
Removable shield blocks

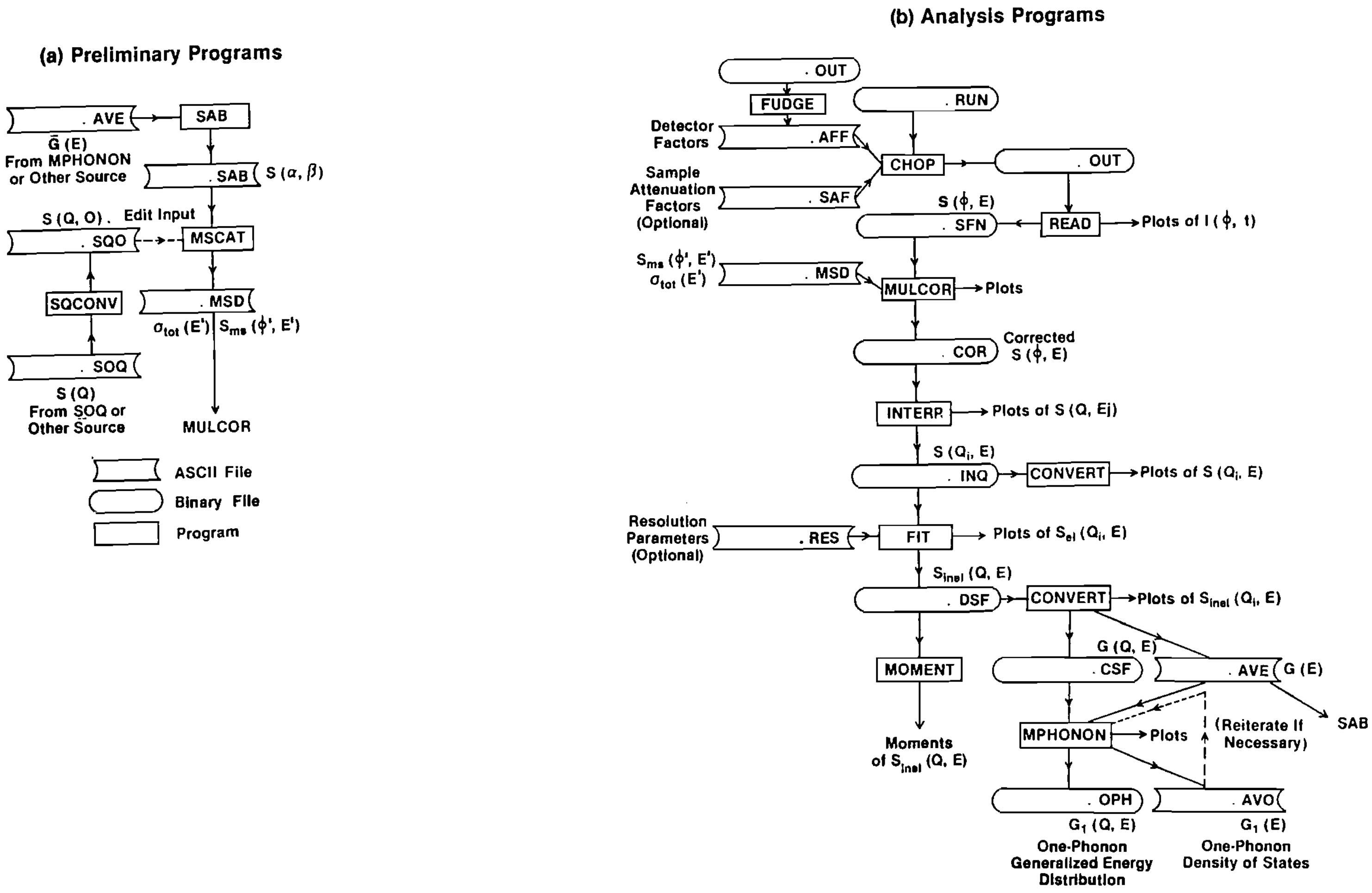
(a) Preliminary Programs

(b) Analysis Programs

Figure 13.4 The Computer Programs Used to Reduce and Analyse the B_2O_3 Inelastic Neutron Scattering Data (after PRICE and CARPENTER, 1987)

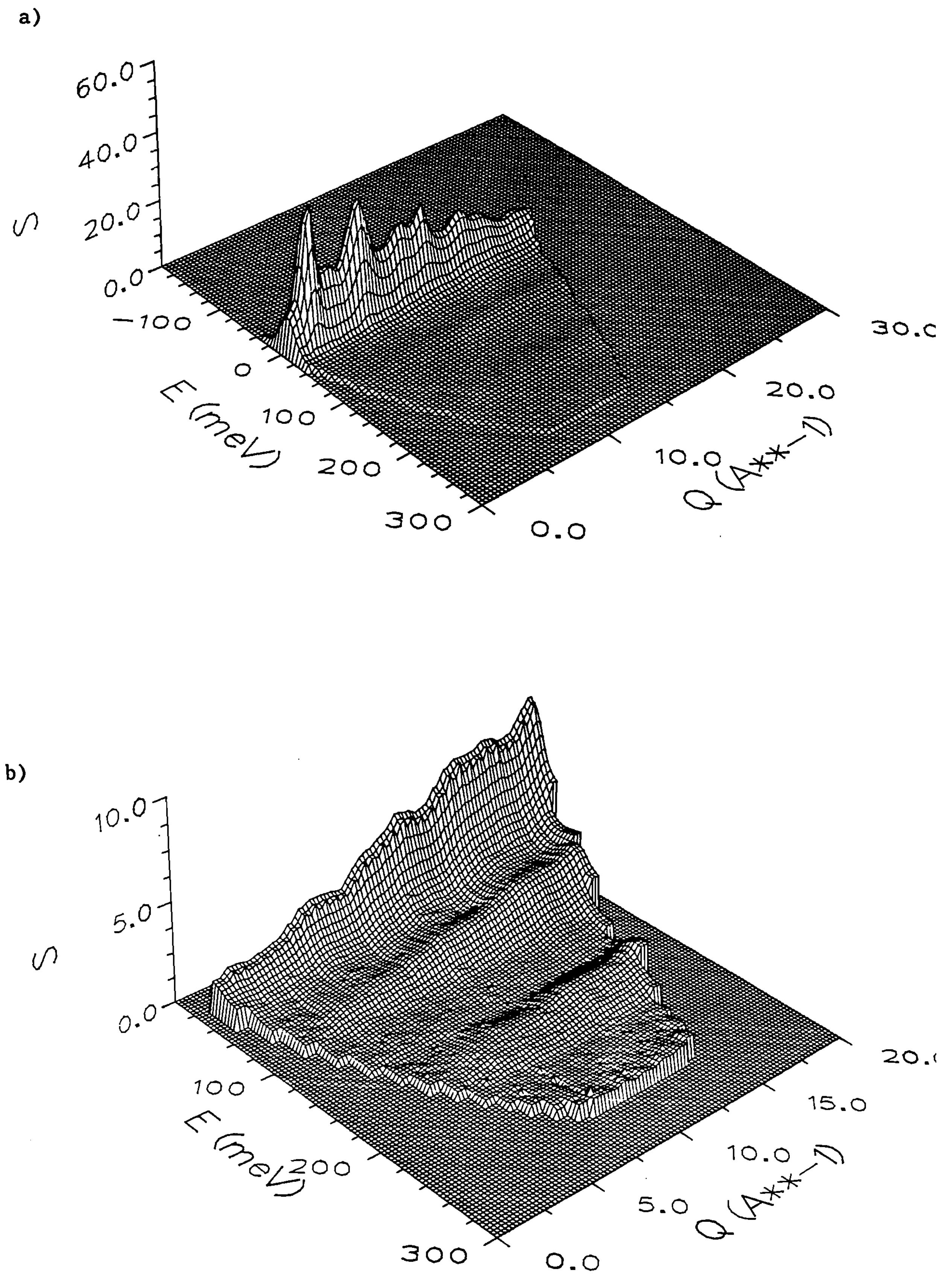

Figure 13.5 S(Q, ε) for B_2O_3 as Measured on LRMECS.
a) Including the Elastic Region (ε=0).
b) For Energy Transfers ε Greater than 25meV.

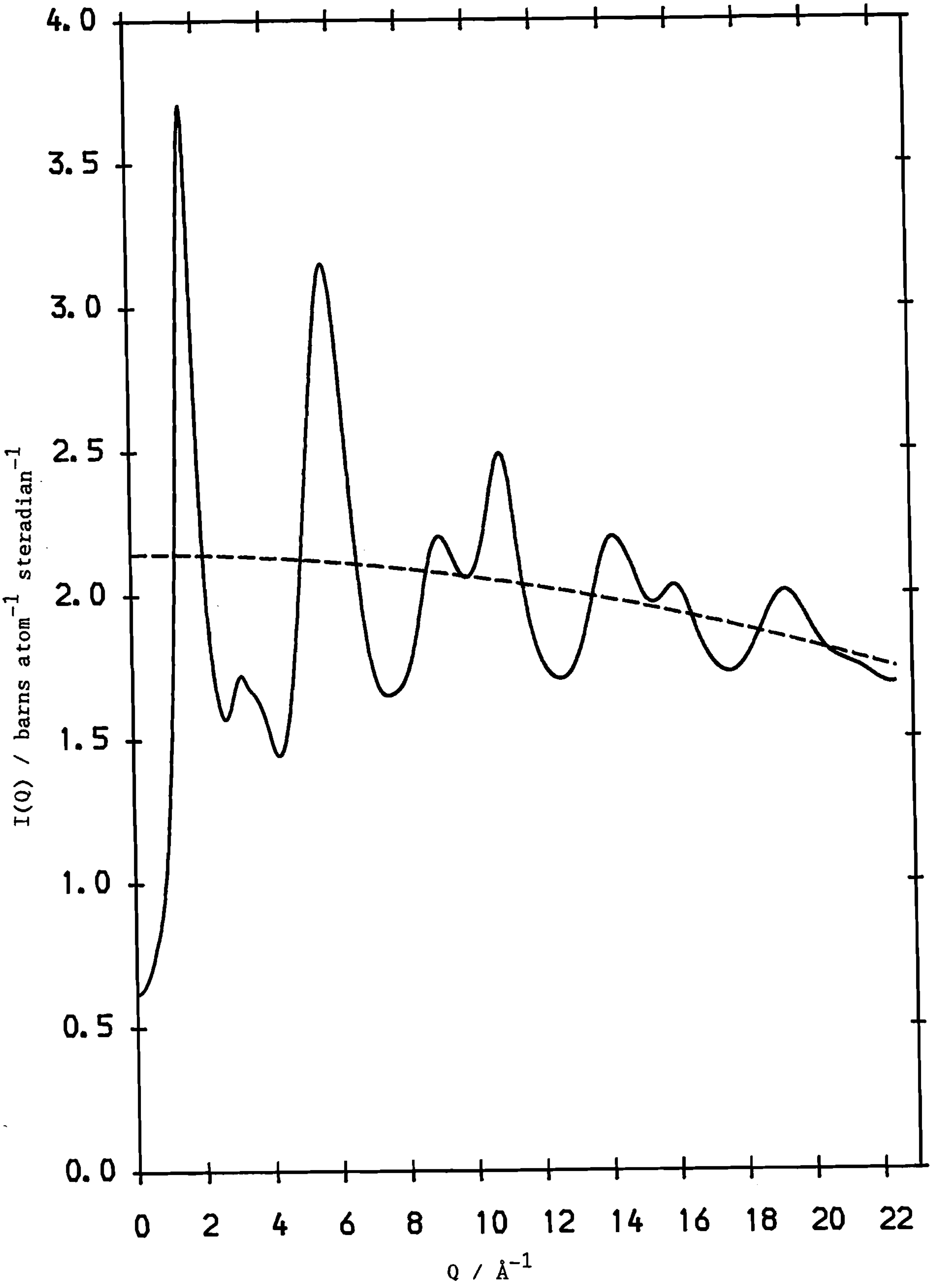

Figure 13.6 The Diffraction Pattern I(Q) of B_2O_3 at Room Temperature (GRIMLEY, 1987). The Dashed Line is the Calculated Self Scattering.

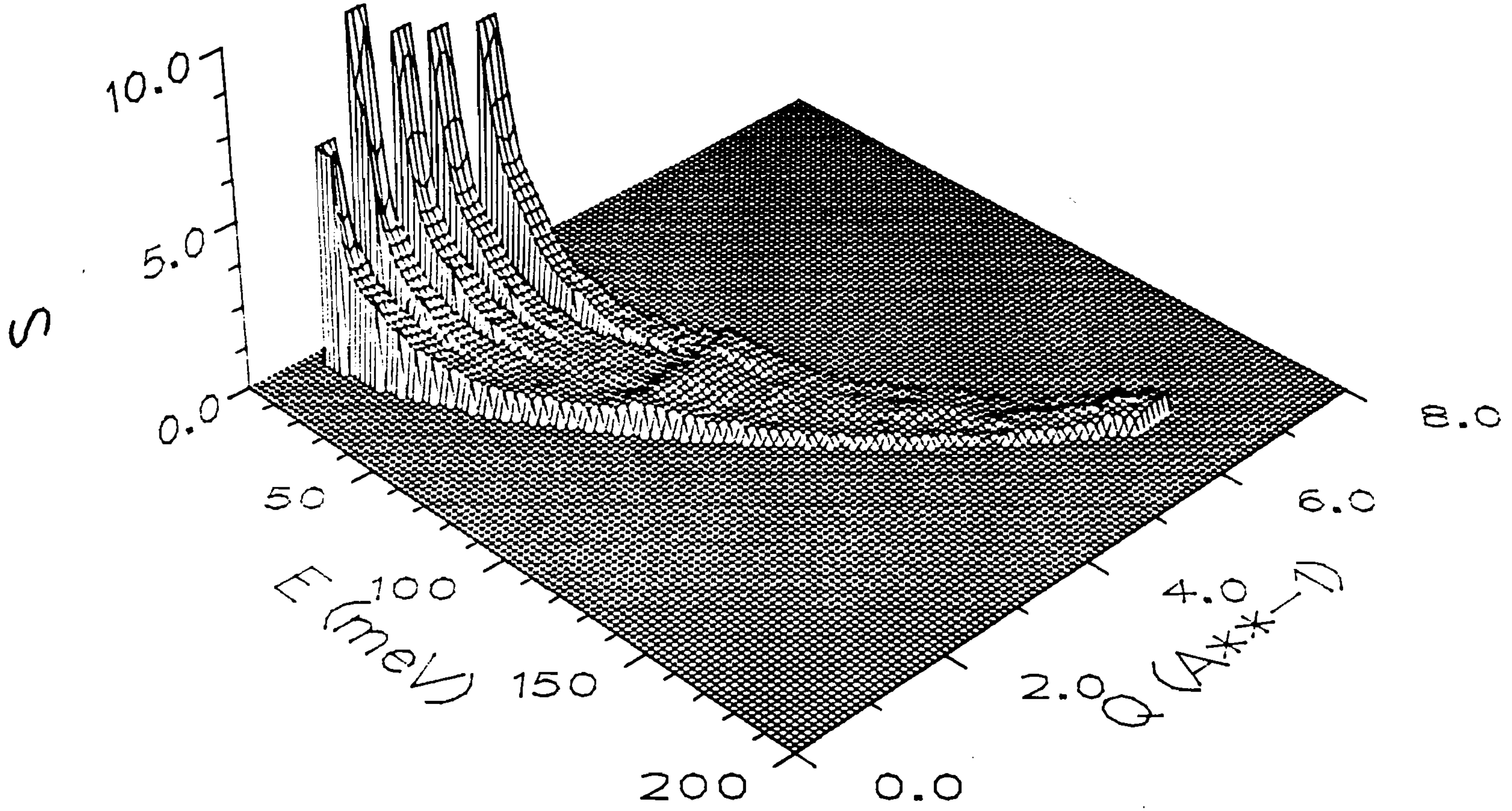

Figure 13.7 S(Q,ε) for B_2O_3 as Measured on HRMECS, not including the Elastic Region.

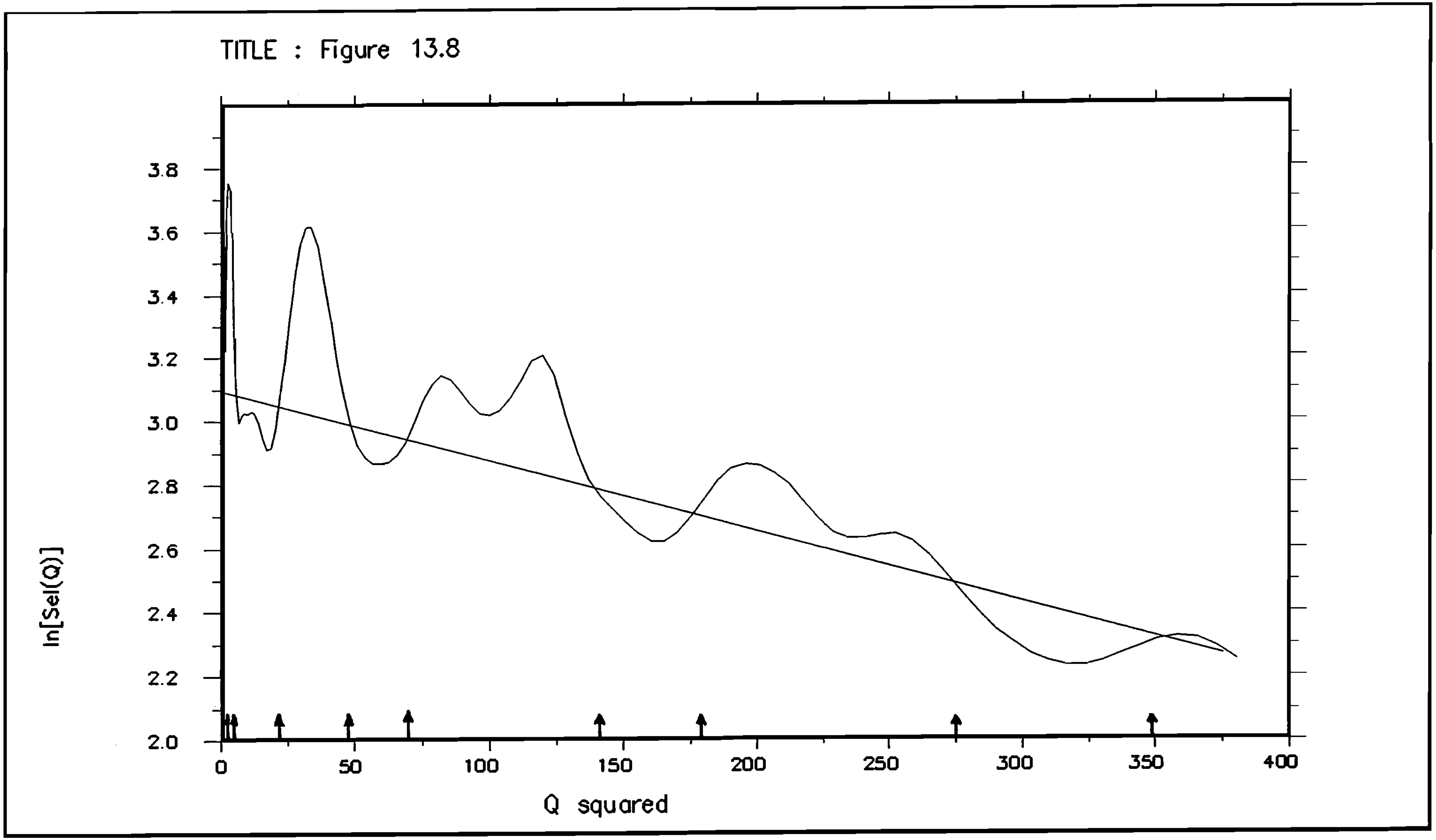

Figure 13.8 ln[S^{el}(Q)] v. Q^2 for B_2O_3 as Measured on LRMECS. The Straight Line Corresponds to a Debye-Waller Factor with $\overline{\langle u^2\rangle}^{1/2}$ = 0.081Å, and the Arrows Indicate the Q-Values $Q_{D=0}$.

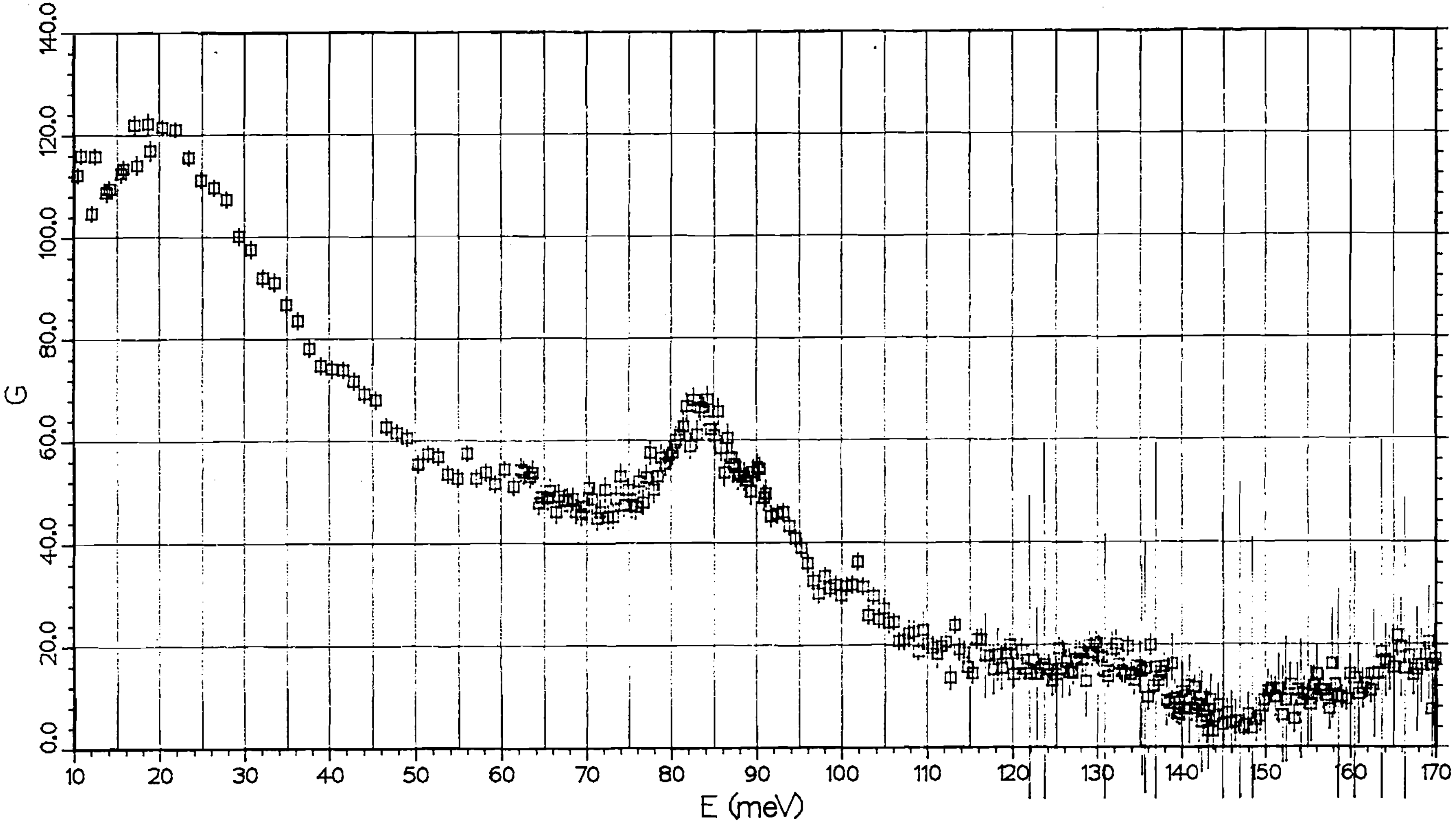

Figure 13.9 The Effective VDOS $g_{eff}(E)$ for B_2O_3 Calculated from the HRMECS Data without Subtraction of the Calculated Multiple Scattering Contribution.

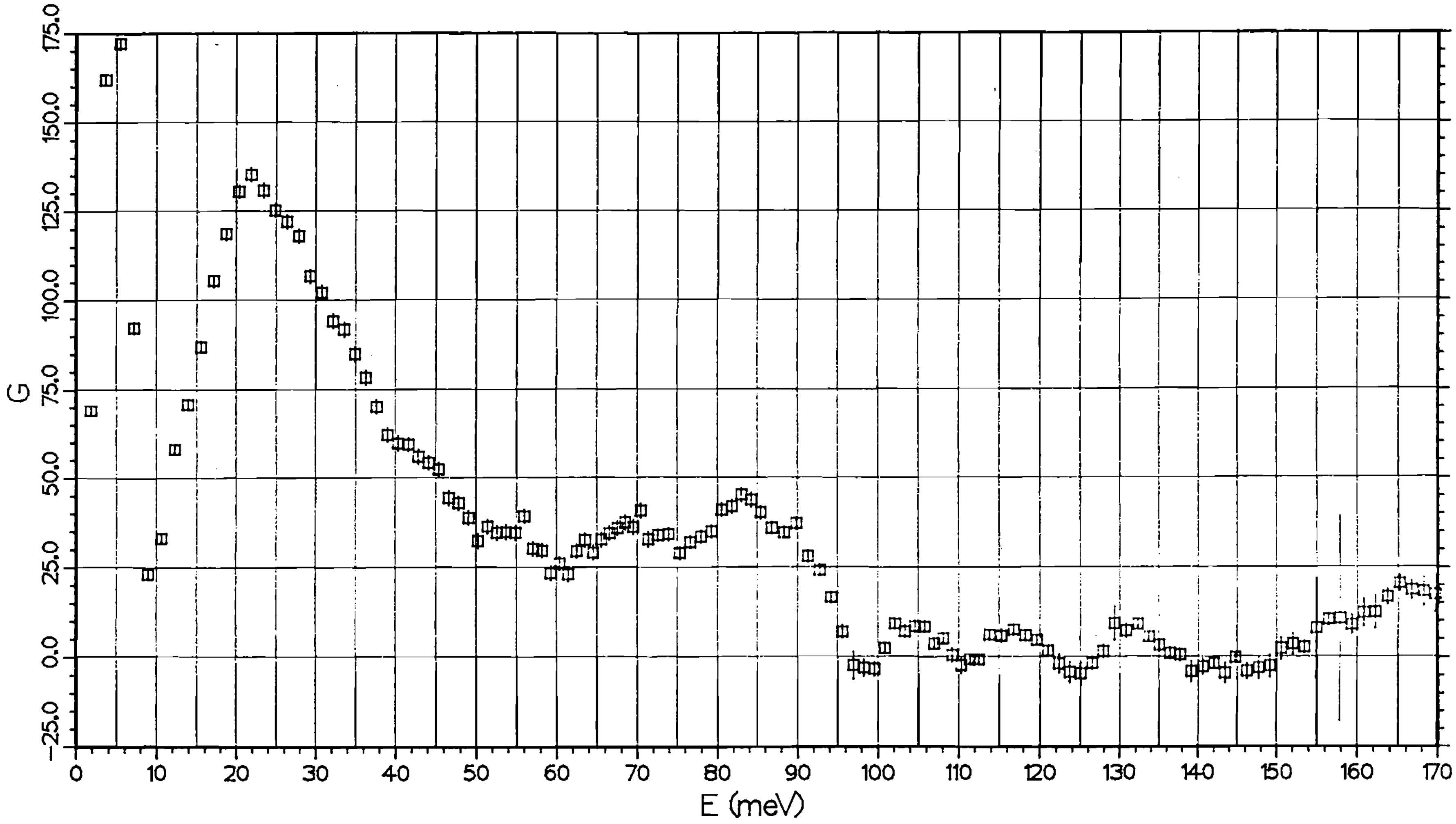

Figure 13.10 The Effective VDOS $g_{eff}(E)$ for B_2O_3 Calculated from the HRMECS Data after Subtraction of the Calculated Multiple Scattering Contribution.

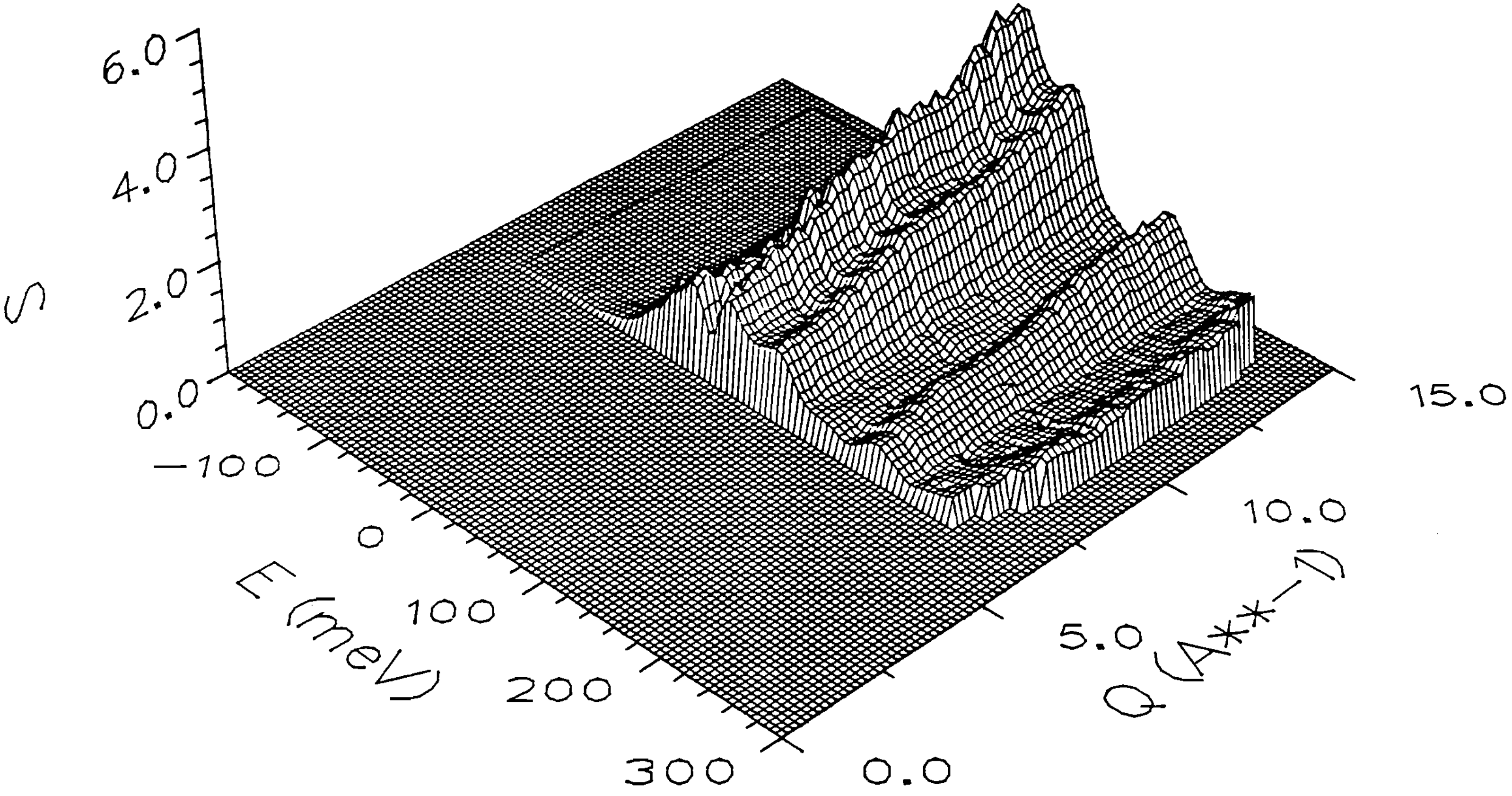

Figure 13.11 The One-Phonon Scattering Function of B_2O_3.

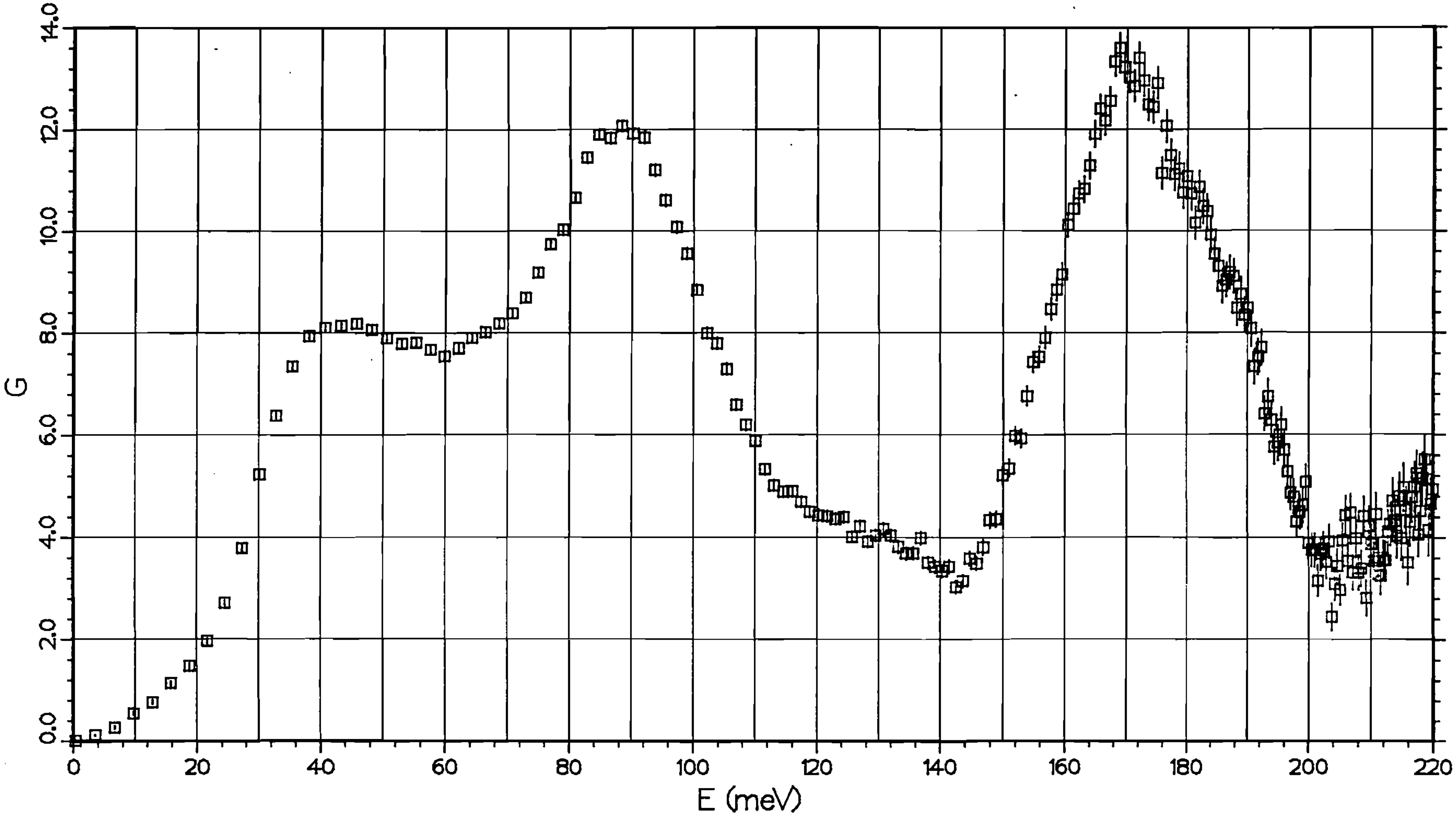

Figure 13.12 The Effective VDOS of B_2O_3 Calculated from the LRMECS Data after Correction for Multiple Scattering, Multiphonon Scattering and Elastic Scattering.

CHAPTER 14

B203 - NUMERICAL CALCULATIONS OF NETWORK DYNAMICS.

14.1 THE METHOD.

The ball-and-stick models used to characterise the structure of amorphous solids typically contain between a few hundred and a few thousand atoms (eg. the Polk model for amorphous silicon (POLK and BOUDREAUX, 1973) contains 519 atoms). For such a system the 3N×3N dynamical matrix $\underline{\underline{W}}$ is very large and it is clearly impractical to find the eigenvalues analytically. In any case it is the spectrum of the eigenvalues that is of interest, rather than the individual eigenvalues, and the following method has been used in the study reported in this Chapter:

A force model is adopted in which interactions between atoms which are not nearest neighbours are ignored. Thus the dynamical sub-matrix $\underline{\underline{w}}_{ij}$ is set to zero if atoms i and j are not nearest neighbours. The result of this is that a large majority of the elements of $\underline{\underline{W}}$ are zero; $\underline{\underline{W}}$ is a sparse matrix. The method which has been used makes use of the fact that $\underline{\underline{W}}$ is sparse. A package of Fortran subroutines known as Sparspak (GEORGE, LIU and NG, 1980) and provided by the University of Waterloo in Canada was adapted (BLACKMAN, 1984) for this problem. Since $\underline{\underline{W}}$ is sparse it is of great advantage to re-order the problem so that the non-zero elements of $\underline{\underline{W}}$ are as close to the diagonal as possible, and this is done using the method of nested dissection (GEORGE and LIU, 1981). Then $\underline{\underline{W}}$ is factorised into the form $\underline{\underline{W}} = \underline{\underline{L}}\,\underline{\underline{D}}\,\underline{\underline{L}}^{-1}$ where $\underline{\underline{L}}$ is a lower triangular matrix and $\underline{\underline{D}}$ is a diagonal matrix. Now the negative eigenvalue theorem (NET) of DEAN and MARTIN (1960) states that the number of negative eigenvalues of $\underline{\underline{L}}\ \underline{\underline{D}}\ \underline{\underline{L}}^{-1}$ is equal to the number of negative elements of $\underline{\underline{D}}$. Thus the number of negative eigenvalues of $\underline{\underline{W}}$ (which is of course zero) can be calculated just by examining the elements of $\underline{\underline{D}}$. Now consider the matrix $\underline{\underline{W}} - \omega_o^2\underline{\underline{I}}$, where ω_o is a constant and $\underline{\underline{I}}$ is the appropriate unit matrix. Calculating the eigenvalues of this matrix is effectively the same as shifting the zero for the eigenvalues ω^2 of $\underline{\underline{W}}$ ie. calculating the number of negative eigenvalues of $\underline{\underline{W}} - \omega_o^2\underline{\underline{I}}$ is equivalent to calculating the number of ω^2 less than ω_o^2 . It follows that, by using different values of ω_o, a histogram of the spectrum of eigenvalues may be built up.

A Fortran program named BORN was written to use the Sparspak subroutines to perform the calculations described above and this program is listed in Appendix B. The program was run on the Reading University Amdahl 370 mainframe computer which runs the CMS operating system and it was compiled using the FORTVS Fortran77 compiler. The models studied contained around 1300 atoms, leading to a dynamical matrix of about 15 million elements, and 4Mbyte of memory was found to be just sufficient to run the program. A calculation of the VDOS for one of these models required about 650 seconds of CPU time.

The program BORN was written to calculate the VDOS for a ball-and-stick model on the assumption of nearest neighbour only Born forces, rather than Keating or valence forces, for the reasons discussed in section 5.3.3 . As written the program does not allow for any disorder in the force constants and thus there is just one value of λ^c (central force constant - see

Chapter 5) and one value of λ^{nc} (non-central force constant) for all bonded pairs of atoms. Hence the program is only applicable to either monatomic systems or completely chemically ordered diatomic systems with only one type of bond between the atoms of the two elements. However, it can easily be adapted for more complicated systems

The program was written to calculate the VDOS of a model subject to free end boundary conditions. BELL and DEAN (1970) have performed similar calculations on a 334 atom model of SiO_2 for both free end and fixed end boundary conditions and it was found that 'the change of boundary condition from the fixed end to the free end condition made relatively little difference to the computed atomic vibrational properties and the form of the spectrum over most of the frequency range' . This conclusion should be even more true for the work reported here since the models studied were considerably larger (~1300 atoms) than the model studied by BELL and DEAN (1970). Furthermore the 334 atom SiO_2 model of BELL and DEAN (1970) had 62 non-bridging oxygen atoms at the surface (19% of the atoms) whereas the the 1262 atom random B_2O_3 model of WRIGHT, SUMNER and CLARE (1982), which is one of the models studied in the work reported here, had only 24 non-bridging oxygen atoms at the surface (1.9% of the atoms). This difference is primarily a consequence of the lower connectivity of the B_2O_3 network and has the result that the surface should be of very little importance in the calculations for the B_2O_3 models.

In plotting the results of the calculations a histogram is generally used as the most appropriate method except where some other format serves better to illustrate a particular aspect. The binning of the histograms is performed such that a mode ω_i is contained in the bin (ω_n, ω_{n+1}) if $\omega_n \leq \omega_i < \omega_{n+1}$. This seems the most logical approach since a mode of zero frequency is then contained in the first positive bin, rather than the first negative bin which would give an unphysical appearance to the results. In the plots of the results three zero frequency modes have been subtracted from the calculated distribution. These three modes correspond to macroscopic translation of the model along the three Cartesian directions and they are subtracted since in the VDOS of the real material they are entirely negligible. As discussed in section 5.3.2 the Born force is not rotationally invariant and so the calculated VDOS does not have any zero frequency modes corresponding to rotations of the model.

14.2 PRELIMINARY CALCULATIONS.

As a demonstration of the method, the VDOS for an ordered chain of identical atoms was calculated using a 1D version of the program (figure 14.1). The chain consisted of 1000 atoms, and nearest neighbour only harmonic forces were used. For such a simple arrangement there is an analytic expression for the VDOS (ELLIOTT and GIBSON, 1974);

$$g(\omega) = (2N/\pi)\,(\omega_m{}^2 - \omega^2)^{-1/2} \qquad \text{for} \quad 0 < \omega < \omega_m \qquad (14.2.1)$$

$$= 0 \qquad \text{otherwise}$$

where N is the number of atoms and;

$$\omega_m = 2\,(\lambda/m)^{1/2} \qquad (14.2.2)$$

in which λ is the force constant for the harmonic force between neighbouring atoms and m is the atomic mass. From the figure it can be seen that the histogram agrees very well with this expression.

A second demonstration of the method was performed, this time in 3D, by calculating the VDOS for the 519 atom POLK model of silicon (POLK and BOUDREAUX, 1973). One of the difficulties involved in a calculation of the VDOS of an amorphous solid is to determine values for the force constants. Molecular spectroscopy or lattice dynamics results may be used to suggest values for the force constants, but it has been found that better agreement between calculation and experiment is usually obtained if larger values are used (see for example BELL, BIRD and DEAN (1968)). It is generally accepted that non-central force constants are of order 0.2 times central force constants (WRIGHT, 1987) and a value of $0.2\lambda^c$ was used for λ^{nc} in the calulation of the VDOS of the Polk model. The calculated distribution was compared with the inelastic neutron scattering data of KAMITAKAHARA, SHANKS, McCLELLAND, BUCHENAU, GOMPF and PINTSCHOVINS (1984) and a value of $154Nm^{-1}$ for λ^c was found to give quite good agreement (figure 14.2). The VDOS of the monatomic tetrahedral network shows very few features compared to the VDOS of B_2O_3 and this is an indication of the higher degree of IRO in B_2O_3.

14.3 CALCULATIONS FOR B203.

14.3.1 INITIAL CALCULATIONS ON B203 MODELS.

In this study calculations of the VDOS have been performed for three different large ball-and-stick models of the atomic structure of vitreous B_2O_3, as given in table 14.1;

Model	Number of atoms	Relaxed	Reference
No Boroxol Rings	1344	No	ELLIOTT, 1978. model II
Random	1262	Yes	WRIGHT, SUMNER and CLARE, 1982 .
Alternate	1249	No	

Table 14.1

These models are discussed in more detail in Chapter 12. To the author's knowledge they are the largest ball-and-stick models for which the VDOS has been calculated.

For the calculations reported in this Chapter there are two adjustable parameters, λ^{c} and λ^{nc}, since the program does not allow for any variation of force constants with atomic environment as discussed in sections 5.3 and 14.1 . However, it was found to be more convenient to use the parameters λ^{c} and r, where the force constant ratio r is defined by;

$$r = \lambda^{nc} / \lambda^{c} \qquad (14.3.1)$$

Since vibrational frequencies scale as $(\lambda/m)^{1/2}$ for harmonic forces the calculations were performed as a function of a dimensionless normal frequency defined by;

$$\omega' = (\mathrm{amu(Kg)}/\lambda)^{1/2}\ \omega(\mathrm{rad\ s^{-1}}) \qquad (14.3.2)$$

This enables the atomic masses to be expressed in atomic mass units and the force constant λ^{c} to be set to one for the calculations. The absolute magnitude of the force constants appropriate to the solid is not known and this may be involved at a later stage simply by scaling the energy-axis according to;

$$E(\mathrm{meV})/1000 = (\hbar/e)\ (\lambda/\mathrm{amu}(\mathrm{Kg}))^{1/2}\ \omega' \tag{14.3.3}$$

$$E(\mathrm{meV}) = 16.1526\ \lambda^{1/2}\ \omega' \tag{14.3.4}$$

Since the energies of the modes scale as $(\lambda/m)^{1/2}$ it is to be expected that vibrational modes for which boron (m_B ~ 11 amu) motion predominates will tend to be at higher energies whilst modes for which oxygen (m_0 ~ 16 amu) motion predominates will tend to be at lower energies. The higher connectivity of the boron atoms means that they are more rigidly held than the oxygen atoms and this also has the effect that modes for which boron motion predominates will tend to be at higher energy.

Initial calculations (figure 14.3) were performed for each model with a value of 0.2 for r and with boron and oxygen masses of 11 amu and 16 amu respectively (for the sample studied in Chapter 13 the exact masses were 11.005021 amu and 15.9994 amu). The general form of the calculated distributions is quite similar; they all exhibit two bands of modes followed by a gap and another band. The Raman scattering and neutron scattering experimental data also have this form and the energy gap is a particularly distinctive feature of the phonon spectrum of B_2O_3. It may thus be concluded that this general form is associated with the SRO in the form of BO_3 triangles. The random and alternate models have particularly similar phonon spectra, indicating that the additional topological order of the alternate model has little effect on the VDOS beyond a slight sharpening of the peaks, whilst the model with no boroxol rings has a spectrum which differs to a greater extent. The differences between the model with no boroxol rings and the other two models can be ascribed to the difference in IRO. Figure 14.4 shows a comparison of the calculated VDOS for the no boroxol rings model and the random model. The random model has a feature (6) at the low energy edge of the gap which the no boroxol rings model does not have. Since the boroxol ring breathing mode is found experimentally at the low energy edge of the gap, this feature in the VDOS of the random model may be tentatively identified as the boroxol ring breathing mode. One possible objection to this identification is that the boroxol ring breathing mode is found experimentally to be very narrow whereas the feature in the VDOS of the random model is fairly broad. However, this difference can readily be explained as being due to the potential used to relax the random model: The potential did not differentiate between bonds inside and outside boroxol rings and could not be expected to maintain the high planarity of the boroxol rings. Thus the relaxation procedure degraded the planarity of the boroxol rings and this is the cause of the broadening of the mode in the VDOS of the random model. Further evidence of this is obtained from the calculation for the alternate model. This model was not relaxed (as is apparent from the small number of modes in the gap which are probably highly localised 'defect' modes) and hence it can be expected that the boroxol rings are more highly planar than in the random model. Figure 14.3 shows that the feature at the low energy edge of the gap in the VDOS of the alternate model is indeed considerably narrower than for the random model.

14.3.2 IDENTIFICATION OF MODES FOR THE RANDOM MODEL.

In a calculation of the type reported here a direct identification of the nature of the modes in a paricular peak of the VDOS is difficult since only the eigenvalues are calculated, and not the eigenvectors. Hence two calculational techniques were developed in this study which enable information about the atomic motions associated with the modes to be deduced. The first of these techniques involves a variation of the parameter r. Figures 14.5 and 14.6 show the effect of this for the random and no boroxol rings models respectively. The r=0.0 calculations show great similarity to the central force calculations of GALEENER and THORPE (1983) for a CRN of boroxol rings and a CRN of triangles respectively.

The second calculational technique developed for studying atomic motions has been to vary the atomic masses in imitation of the Raman scattering experiments in which isotopic substitution was used to probe atomic motions (GALEENER and GEISSBERGER, 1982; WINDISCH and RISEN, 1982). Figures 14.7 to 14.10 show the results of these calculations for the random and no boroxol rings models with values of 0.2 and 0.0 for r. Figures 14.7 and 14.8 show the effect on the random model VDOS of $^{10}B \rightarrow {}^{11}B$ substitution and $^{18}O \rightarrow {}^{16}O$ substitution respectively. Similarly figures 14.9 and 14.10 show the effect on the no boroxol rings model VDOS of $^{10}B \rightarrow {}^{11}B$ and $^{18}O \rightarrow {}^{16}O$ substitution.

Figure 14.7 shows that the feature 6 in the VDOS of the random model which is tentatively identified above as the boroxol ring breathing mode has zero shift for boron substitution. Hence the modes in this peak involve motion of the oxygen atoms only. The Raman isotopic substitution experiments have shown that the $808cm^{-1}$ (≡100.2meV) boroxol ring breathing mode has zero shift for boron substitution and therefore the identification of the feature 6 in the random model VDOS as the boroxol ring breathing mode is confirmed. Figure 14.9 shows that the no boroxol rings model VDOS does not have a peak which involves oxygen motion only (or otherwise) at the lower edge of the energy gap. The neutron scattering results of Chapter 13 show that the boroxol ring breathing mode contributes a significant peak to the VDOS of vitreous B_2O_3 at the lower edge of the energy gap at 100meV and hence it may be concluded that the random model reproduces this region of the VDOS of the real material whilst the no boroxol rings model does not.

Since the random model reproduces the boroxol ring breathing mode in the VDOS of B_2O_3 it is worthwhile to consider the results of the two calculational techniques for this model in more quantitative detail across the whole energy range. Figure 14.11 shows the r-dependence of the positions of the peaks in the random model VDOS. With central forces only (r=0.0) there are two bands of modes in the VDOS. The isotopic substitution calculations show that the lower band contains modes which involve oxygen motion only whilst the modes in the upper band involve motion of atoms of both elements. The frequencies of these modes changes only slightly as r is increased from zero. With central forces only there is also a delta function of modes at $\omega'=0.0$. An explanation of this delta function is given in section 5.3.1 , although the number of modes involved is actually slightly greater than the theoretical figure of 9N/5 due to the lower coordination of the surface atoms of the model. As r is increased from zero the modes in the delta function spread out quite rapidly into two bands. As with the central force bands, the isotopic substitution calculations show that the lower band contains modes which involve oxygen motion only whilst the modes in the upper band involve motion of both atoms.

The peaks in the calculated VDOS have been labelled 0 to 6 and a to e, as shown in the figures, so that the identification of the modes is consistent with the numbering scheme of GALEENER and THORPE (1983). The shifts with isotopic substitution of the positions of the peaks in the VDOS of the random model are given in table 14.2;

		$^{10}B\rightarrow{}^{11}B$ Substitution		$^{18}O\rightarrow{}^{16}O$ Substitution	
Feature	ω'(natural)	$\omega'(^{10}B)$	$\Delta\omega'_B/\omega'(^{10}B)$	$\omega'(^{18}O)$	$\Delta\omega'_O/\omega'$(natural)
0	0.0458	0.0474	-0.033	0.0458	0
1	0.1420	0.1420	0	0.1373	-0.033
2	0.1623	0.1623	0	0.1521	-0.063
3	0.2217	0.2217	0	0.2069	-0.067
4	0.2522	0.2624	-0.039	0.2522	0
5	0.2773	0.2874	-0.035	0.2718	-0.020
6	0.3070	0.3070	0	-	-
a	0.4321	0.4524	-0.045	0.4321	0
b	0.4524	0.4673	-0.032	0.4470	-0.012
c	0.4618	0.4775	-0.033	0.4571	-0.010
d	0.4923	0.5072	-0.029	0.4822	-0.021
e	0.5072	0.5267	-0.037	0.4970	-0.020

Table 14.2

where ω'(natural) is the normal frequency at which the mode occurs for the natural atomic masses (m_B = 11 amu and m_O = 16 amu), $\omega'(^{10}B)$ is the normal frequency at which the mode occurs for $^{10}B_2{}^{16}O_3$ and $\omega'(^{18}O)$ is the normal frequency at which the mode occurs for $^{11}B_2{}^{18}O_3$. The isotope shifts are then defined by;

$$\Delta\omega'_B = \omega'(\text{natural}) - \omega'(^{10}B) \qquad (14.3.5)$$

$$\Delta\omega'_O = \omega'(^{18}O) - \omega'(\text{natural}) \qquad (14.3.6)$$

The uncertainties in the calculated shifts are determined by the width used for the histogram bins. The minimum value for the bin width for reasonable results is determined by the size of the model and a width $\delta\omega'=0.005$ was found to be small enough to reveal the structure of the VDOS of the models without the finite size of the model becoming apparent or the computation time becoming prohibitive. For this bin width the uncertainty in the calculated shifts is estimated to be less than or of order ±0.02 . The experimental isotopic substitution shifts given by GALEENER and THORPE (1983) are summarised in table 14.3;

Feature	Energy/cm^{-1}	Energy/meV	$\Delta\omega_B/\omega(^{10}B)$	$\Delta\omega_O/\omega$(natural)
1	470	58.3	-0.002	-0.053
2	502	62.2	-0.004	-0.056
3	602	74.6	-0.005	-0.058
4	660	81.8	-0.029	-0.006
5	732	90.7	-0.031	-
6	809	100.3	0	-0.059
7	1212	150.3	-0.022	-0.026
8	1261	156.3	-0.020	-0.020
9	1327	164.5	-0.032	-0.007
10	1467	181.9	-0.030	-0.010
11	1510	187.2	-0.029	-

Table 14.3

The uncertainty in the experimental fractional isotope shifts is of order ±0.004 . (The calculated and experimental fractional isotope shifts are given in separate tables since, as is discussed below, not all of the peaks have been definitely identified and also some of the identified peaks are not in the same order in experiment and calculation.)

As can be seen from tables 14.2 and 14.3, the isotopic substitution data strongly indicates an identification of the peaks 1 to 6 of the model VDOS with the experimental peaks 1 to 6: Peak 4 of the model VDOS shows zero shift with $^{18}O \rightarrow {}^{16}O$ substitution and the experimental peak 4 shows an oxygen shift which is almost zero. Thus both peaks relate to modes which involve boron motion only, and hence peak 4 of the model VDOS can be identified with the experimental peak 4. Peak 6 of the model VDOS has already been identified with the experimental peak 6, the boroxol ring breathing mode. On oxygen substitution peaks 5 and 6 merge so that peak 6 cannot be discerned in the model VDOS. However, in the Raman data it is peak 5 which cannot be discerned due to the great enhancement of peak 6. The shift with boron substitution seems to confirm the identification of the peak 5 of the model VDOS with the experimental peak 5. In the model VDOS peak 5 does not show LO/TO splitting which is found experimentally. This is because the force model used in the calculation does not include the long range Coulomb force which is the cause of LO/TO splitting (GALEENER and LUCOVSKY, 1976; DE LEEUW and THORPE, 1985). Peaks 1, 2 and 3 of the model VDOS show zero shift with boron substitution and they can thus be identified with the experimental peaks 1, 2 and 3 which show very small shifts with boron substitution. The shifts of these peaks with oxygen substitution confirm this identification, and the lack of a boron shift indicates that they correspond to modes which involve oxygen motion only. The behaviour with isotopic substitution of peaks below 1 has not been reported. However, peak 0 of the model VDOS can probably be identified with the Raman peaks at $130cm^{-1}$ (≡16.1meV) and $145cm^{-1}$ (≡18.0meV). Thus below the energy gap the random model has a VDOS which reproduces the peaks of modes of B_2O_3 with great success. Figure 14.11 can then be used to determine a reasonable value for r: When r=0.15 peaks 3 and 4 are merged, whilst peaks 5 and 6 are merged when r=0.25. Since peaks 3, 4, 5 and 6 are found experimentally to be clearly separated and to occur in the order in which they are numbered, the correct value of r must lie between these two values. Hence a value of r of 0.2 is seen to be ideal.

GALEENER and THORPE (1983) have identified five peaks, labelled 7 to 11, above the energy gap in the Raman data, although peak 11 appears to be very broad and ill-defined. The model VDOS also has five peaks above the energy gap, labelled a to e, although it is perhaps questionable whether b and c really represent two separate peaks of modes. The main evidence suggesting that b and c are separate peaks is the VDOS of the alternate model in which they appear as two quite distinct features. They are almost merged in the VDOS of the random model because of deficiencies in the relaxation potential, as has been discussed above in connection with the boroxol ring breathing mode 6. A comparison of the model and experimental oxygen isotopic substitution data suggests that the model peak a should be identified with the experimental peak 9 since both show very small shifts. This identification may seem surprising since the peak a is at the edge of the energy gap whilst the peak 9 is in the middle of the band of modes above the energy gap. However, a reasonable justification may be obtained from a consideration of the force model as is discussed below. The oxygen substitution results suggest that a tentative identification may also be made between the calculated peak c and the observed peak 10.

14.3.3 CONSIDERATION OF THE FORCE MODEL.

Each of the identified peaks may be used to yield a value for the central force constant λ^c according to equation (14.3.4);

Feature	1	2	3	4	5	6	a	c
(E/ω')/meV	414	387	340	327	330	329	384	397
$\lambda^c/\mathrm{Nm}^{-1}$	657	574	442	410	417	416	565	605

Table 14.4

The peak positions are discussed in terms of E/ω' ($E/\omega' \propto \lambda^{c1/2}$), rather that λ^c, since they are relatively insensitive to λ^c; a discussion in terms of λ^c would exaggerate differences in the energy-axis scaling factor required to make calculated peaks coincide with experimental peaks. The positions of the peaks 3 to 6 are all consistent with a value of about 330meV for E/ω' ($\lambda^c \sim 420\mathrm{Nm}^{-1}$). However, this force constant value results in peaks 1 and 2 of the model occurring at too low an energy. A value of about 390meV for E/ω' ($\lambda^c \sim 580\mathrm{Nm}^{-1}$) is required for the model peaks 1 and 2 to occur at the correct energy (the value from peak 2 is to be preferred since peak 1 is quite broad). Peaks a and c of the model also occur at the correct energy if a value of about 390meV is used for E/ω'. Thus a consideration of the peak positions suggests that a force model with two different values of λ^c should be used. GALEENER and THORPE (1983) have previously proposed that a higher value should be used for λ^c for bonds which are outside boroxol rings than for bonds within boroxol rings. It was suggested that this would improve the agreement above the energy gap between their central forces calculation and experiment. A calculation with two values of λ^c was not performed because the omission of non-central forces was thought to be just as important. However, the work reported here shows that the addition of non-central forces has very little effect above the energy gap apart from introducing a slight splitting between peaks d and e. Hence a central force calculation would be of value in understanding the modes above the energy gap. The study of peak positions described above supports GALEENER and THORPE's proposal (1983), as does the earlier consideration of the potential used to relax the random model. It is thus proposed that the use of a more realistic force model would result in all the peaks delow the energy gap occurring at the correct energy and also in the closure of the narrow gap at about $\omega'=0.2$ in the calculated VDOS of the random model - such a gap is not observed experimentally. Furthermore the agreement above the energy gap could well be improved by a better force model. It is suggested that the pair of peaks a and c would swap positions with the pair of peaks d and e, with the force constant value $\lambda^c=420\text{Nm}^{-1}$ being associated with the peaks d and e and the value 580Nm^{-1} associated with the peaks a and c. A tentative identification of the calculated peaks d and e with the experimental peaks 7 and 8 leads to E/ω' values of 308meV and 311meV respectively. These values are reasonably consistent with the figure of about 330meV obtained above. However, a calculation using a force model with different central force constants inside and outside the boroxol rings would have to be performed to substantiate these tentative identifications.

Since the feature 6 has been identified as the boroxol ring breathing mode the central force constant value $\lambda^c \sim 420 \mathrm{Nm}^{-1}$ must be associated with bonds within boroxol rings and the value $580 \mathrm{Nm}^{-1}$ with bonds outside the boroxol rings. It must be pointed out that the discussion above assumes that a value of 0.2 for r applies to bonds both within and outside the boroxol rings, whereas it may well be that the non-central forces also show different behaviour inside and outside the boroxol rings. A force model which differentiated between motions in the plane of a boroxol ring and perpendicular to the ring, as BELL, CARNEVALE, KURKJIAN and PETERSON (1980) appear to have used, would probably be more realistic.

The above analysis of peak positions in terms of central force constants may be too simplistic since the energies of all but the most localised of modes can be expected to depend on both of the two central force constants to some extent. However, many of the modes are in fact highly localised, as is shown below, and so the conclusions and values deduced above provide a useful starting point for a calculation based on a more realistic force model, which would be necessary to confirm the ideas proposed above.

The values for λ^c obtained by previous workers are summarised in table 14.5;

Reference	$\lambda^c/\mathrm{Nm}^{-1}$	(E/ω')/meV	Comment
GALEENER, LUCOVSKY and MIKKELSEN (1980)	612	400	CRN of triangles
GALEENER and THORPE (1983)	470	350	CRN of boroxol rings
BELL, CARNEVALE, KURKJIAN and PETERSON (1980)	350	302	CRN of triangles
	350	302	CRN of boroxol rings
This work	420	330	inside boroxol rings
	580	390	outside boroxol rings

Table 14.5

The value obtained by GALEENER, LUCOVSKY and MIKKELSEN (1980) for a CRN composed solely of triangles agrees quite well with the value found in the present work to apply outside the rings. The value obtained by GALEENER and THORPE (1983) for a CRN composed solely of boroxol rings does not agree as well with that found in the present work to apply inside the boroxol rings. However, this is to be expected since, as is discussed below, GALEENER and THORPE (1983) incorrectly identified one of the two features which were used to fit the model parameters. The central force constants obtained by BELL, CARNEVALE, KURKJIAN and PETERSON (1980) do not appear to agree particularly well with the present work. However, a full acount of this work does not appear to have been published and hence a detailed comment on the disagreement cannot be made.

In their central force calculations GALEENER and THORPE (1983) chose to fit to features 1 and 6 in order to determine the two parameters of the calculation. However, the work reported here shows that non-central forces are essential in describing the motion associated with the peak labelled 1, since it occurs at zero frequency for the central forces only calculation (r=0.0). The band edge in GALEENER and THORPE's calculated (1983) VDOS which was fitted to peak 1 of the Raman spectrum becomes a significant peak on the addition of non-central forces and should have been fitted to peak 3. A good agreement was obtained between the isotope shifts of the experimental peaks 1, 2 and 3 and the low energy peaks of the central force VDOS. However, according to the present work this agreement was fortuitous since the peaks were incorrectly identified and furthermore peaks 1 and 2 cannot be explained at all by a model involving central forces only. A more realistic central forces calculation should be able to explain peaks 3, 6 and 7 to 11, contrary to GALEENER and THORPE's conclusion (1983) that a correct explanation of features 7 and 8 requires non-central forces. However, peaks 0, 1, 2, 4 and 5 can only be understood if non-central forces are included.

Figures 14.12 and 14.13 show comparisons of the VDOS of the random model calculated for r=0.2 and λ^c=420Nm^{-1} with the Raman data of GALEENER, LUCOVSKY and MIKKELSEN (1980) and the neutron data of Chapter 13 respectively.

14.3.4 MOLECULAR UNITS AND LOCALISATION.

The program BORN has also been used to study the vibrations of two simple molecular units in order to investigate the question of localisation and provide additional information relating to the network dynamics of B_2O_3. The zero frequency modes corresponding to translations or rotations in the three Cartesian directions have not been subtracted from the results of these calculations. The first unit studied was a perfect B_3O_6 boroxol ring, the coordinates of which are given in Appendix C. Figure 14.14 shows the vibrational modes of a B_3O_6 boroxol ring subject to Born forces for different values of r, and figure 14.15 shows how the energies of these modes change as r is varied. The spectrum exhibits an energy gap similar to that of B_2O_3, and the four modes immediately below the gap behave as r is varied in a very similar way to the peaks 3, 4, 5 and 6 of the random model VDOS. However, whereas a value of 0.2 for r leads to these peaks being well separated in the VDOS of the random model, a value of about 0.175 is required for the B_3O_6 boroxol ring. This is just an effect of the reduced connectivity of the B_3O_6 ring. $^{10}B \rightarrow {}^{11}B$ and $^{18}O \rightarrow {}^{16}O$ isotopic substitution calculations were performed for the B_3O_6 boroxol ring with a value of 0.175 for r (figure 14.16) and the results of these calculations are given in table 14.6;

		$^{10}B\rightarrow{}^{11}B$ Substitution		$^{18}O\rightarrow{}^{16}O$ Substitution	
Feature	ω'(natural)	$\omega'(^{10}B)$	$\Delta\omega'_B/\omega'(^{10}B)$	$\omega'(^{18}O)$	$\Delta\omega'_O/\omega'$(natural)
i	0.0747	0.0747	0	0.0724	-0.031
ii	0.0974	0.0974	0	0.0919	-0.056
iii	0.1170	0.1170	0	0.1123	-0.040
iv	0.1349	0.1349	0	0.1279	-0.052
v	0.1521	0.1576	-0.035	0.1474	-0.031
3	0.2225	0.2225	0	0.2069	-0.070
4	0.2374	0.2475	-0.041	0.2374	0
5	0.2569	0.2671	-0.038	0.2522	-0.018
6	0.2773	0.2773	0	0.2624	-0.054
a/b/c	0.4493	0.4649	-0.034	0.4423	-0.016
d/e	0.4900	0.5048	-0.029	0.4798	-0.021

Table 14.6

A comparison of table 14.6 with table 14.2 shows that the four modes of the B_3O_6 boroxol ring below the energy gap have the same isotope shifts as the peaks 3, 4, 5 and 6 of the random model VDOS. Clearly there is a very strong connection between the modes of the ring and of the network in this energy region, and this is best explained if the peaks 3, 4, 5 and 6 correspond to vibrational modes which are localised to a single B_3O_6 structural unit. Indeed it has already been pointed out in Chapter 12 that the boroxol ring breathing mode (6) is localised to one boroxol ring since the boron atoms do not move in this mode of vibration. The peaks of the random model at energies below that of 3 are obviously derived from the low energy modes of the boroxol ring since both show zero shift on $^{10}B \rightarrow {}^{11}B$ substitution and hence involve oxygen motion only. However, there is no clear relation between the two sets of modes (the number of features is not even the same), and this can be explained as being due to modes of vibration involving oxygen atoms outside the ring becoming smeared out extended modes of vibration of the bridging oxygens in the network. Similarly there is no clear relation between the modes of the B_3O_6 boroxol ring above the gap and the peaks of the random model VDOS above the gap. Hence these peaks in the random model VDOS probably also correspond to extended modes of vibration. These conclusions appear to be in agreement with the results of the molecular calculations of WINDISCH and RISEN (1982a). However, a direct comparison could not be performed since WINDISCH and RISEN (1982a) used a different force model and only calculated totally symmetric modes whilst in the present work all modes were calculated and eigenvectors were not accessible.

The second simple molecular unit studied was a perfect BO_3 triangle, the coordinates of which are given in Appendix C. Figure 14.17 shows the vibrational modes of a BO_3 triangle subject to Born forces for different values of r, and figure 14.18 shows how the energies of these modes change as r is varied. Isotopic substitution calculations were performed with a value of 0.15 for r (figure 14.19), since the modes are then well separated, and the results of these calculations are given in table 14.7;

		$^{10}B\rightarrow^{11}B$ Substitution		$^{18}O\rightarrow^{16}O$ Substitution	
Feature	ω'(natural)	$\omega'(^{10}B)$	$\Delta\omega'_B/\omega'(^{10}B)$	$\omega'(^{18}O)$	$\Delta\omega'_O/\omega'$(natural)
A	0.0974	0.0974	0	0.0919	-0.056
B	0.1224	0.1224	0	0.1123	-0.083
C	0.2225	0.2319	-0.041	0.2225	0
X	0.2522	0.2522	0	0.2374	-0.059
D/E	0.4626	0.4775	-0.031	0.4571	-0.012

Table 14.7

The boron shifts show that the modes labelled A and B involve oxygen motion only, as with the low energy modes of the B_3O_6 boroxol ring and of the random model. However, there is no clear correspondence between A and B and any particular mode of the other models. This is not surprising since these appear to be extended modes of vibration for the CRN. The oxygen shift data indicates strongly that mode C corresponds to peak 4 since both have a shift of zero, and also both features require non-central forces. Hence peak 4 would seem to be associated with modes which involve motion which can be understood in terms of a single triangle. The mode D/E above the gap is obviously associated with the modes above the gap of the other models, but again these modes appear to be extended for the CRN and there is no exact correspondence. The mode X is unusual in that its energy is totally unaffected by λ^{nc}. The isotope shift data indicates that it correcponds to either peak 3 or peak 6. It would be surprising if the mode X did correspond to peak 6 since peak 6 has been identified previously as the boroxol ring breathing mode and a further consideration of the no boroxol rings model is required to address this issue.

Figure 14.20 shows the behaviour of the positions of the peaks of the no boroxol rings model VDOS as r is varied. A comparison of this figure and figure 14.6 with the relevant figures for the calculations on the BO_3 triangle shows that the mode X of the triangle becomes broadened into a featureless band when BO_3 triangles are connected together to form a CRN. Hence the mode X of the BO_3 triangle cannot explain the peak 6 observed just below the energy gap in the phonon spectrum of B_2O_3. There is quite a detailed correspondence between the modes of the BO_3 triangle and the peaks of the no boroxol rings model VDOS. The mode D/E becomes spread out into two peaks, labelled D and E, whilst the modes A, B, and C appear to carry over from the isolated BO_3 triangle to the CRN. The effective disappearance of the mode X is the only major difference between the two calculated phonon distributions. The VDOS of a CRN composed entirely of BO_3 triangles is thus shown to have a simple form with five main features. Such a form is at variance with the richness of features found in experimental measurements of the phonon spectra, and this leads to the conclusion that a CRN structure for B_2O_3 based only on BO_3 triangles is inconsistent with the experimental vibrational spectra.

14.3.5 CONSIDERATION OF THE NO BOROXOL RINGS MODEL.

The calculated isotope shifts for the peaks in the VDOS of the no boroxol rings model are given for completeness in table 14.8;

		$^{10}B\rightarrow{}^{11}B$ Substitution		$^{18}O\rightarrow{}^{16}O$ Substitution	
Feature	ω'(natural)	$\omega'(^{10}B)$	$\Delta\omega'_B/\omega'(^{10}B)$	$\omega'(^{18}O)$	$\Delta\omega'_O/\omega'$(natural)
A	0.0771	0.0771	0	0.0724	-0.061
B	0.1576	0.1576	0	0.1474	-0.065
C	0.2718	0.2820	-0.036	0.2671	-0.017
X	0.4172	0.4376	-0.047	0.4165	-0.001
D/E	0.5220	0.5369	-0.028	0.5072	-0.028

Table 14.8

The isotope shifts for peaks A to E of the no boroxol rings model are very much the same as for the modes of the BO_3 triangle. Figure 14.4 shows that as well as being unable to reproduce the boroxol ring breathing mode (6), the no boroxol rings model is unable to reproduce peaks 3 and 5 (peak C corresponds to peak 4). Hence peaks 3, 5 and 6 may be regarded as signatures of the presence of boroxol rings. Furthermore the no boroxol rings model is unable to split peaks 1 and 2 (~B), and it appears to have an insufficient number of features above the energy gap.

At this stage it is worthwhile to consider the hypothesis that highly planar boroxol rings are only present in the B_2O_3 network of BO_3 triangles at a very low concentration but that they are observed because both Raman scattering and NMR are peculiarly sensitive to their presence. If it is assumed that this great sensitivity of both techniques to boroxol rings can be explained then the success in fitting the random model VDOS to the Raman data is not necessarily inconsistent with this hypothesis. However, the central force constant for outside boroxol rings obtained from comparing the random model VDOS with the Raman data should then be the central force constant which applies throughout the bulk of the CRN of BO_3 triangles. Using this central force constant value together with the VDOS of the no boroxol rings model will then yield the true VDOS of B_2O_3. Table 14.9 gives the energies of the features of the no boroxol rings model VDOS calculated using the central force constant $580Nm^{-1}$ (E/ω'=390meV) for outside boroxol rings;

Feature	A	B	C	lower edge of energy gap	D	E
ω'	0.0771	0.1576	0.2718	0.3398	0.4172	0.5220
E/meV	30	61	106	133	163	204

Table 14.9

These features (see also figure 14.21a) should then be compared with the results for inelastic neutron scattering from B_2O_3 since, as discussed in Chapter 13, this provides a good measure of the true VDOS and is unlikely to show the great enhancement for a particular mode that can occur with optical measurements. The VDOS for B_2O_3 measured with LRMECS (figure 13.12) does not agree well with the figures in table 14.9 : The band of modes above the energy gap centred at about 170meV does not appear to be related to two well-separated peaks such as D and E, and in particular E occurs at too high an energy to be consistent with this band of modes. The peak C at 106meV does not occur in the experimental data, whilst the experimental peak at about 88meV does not occur in the calculated distribution. The lower energy region also shows a lack of agreement, although this region of the experimental data is less reliable. Of course it could be argued that the central force constant value obtained from studying the random model VDOS is not representative of the CRN of BO_3 triangles away from the very occasional boroxol rings and that use of a different value would improve the agreement. However, there are two objections to this argument : Firstly a lower value is required to improve the agreement whereas the indications are that the central force constant appropriate to a CRN of BO_3 triangles would be higher than the value of $580Nm^{-1}$ (E/ω'=390meV). The study of the VDOS of the random model shows that a higher central force constant applies for triangles near boroxol rings than applies for boroxol rings, and by extrapolation one would expect triangles far from boroxol rings to have a higher value again if indeed there is a difference. The central force constant value of $612Nm^{-1}$ obtained by GALEENER, LUCOVSKY and MIKKELSEN (1980) for a CRN composed solely of BO_3 triangles would seem to support this conjecture. Secondly the use of an ad hoc central force constant value together with the VDOS calculated for the no boroxol rings model does not produce satisfactory agreement : If the band of modes centred at about 170meV in the LRMECS data is identified with the band of modes including peaks D and E (ignoring the lack of two separate peaks in the experimental data) which is centred at $\omega' \sim 0.46$ this yields a central force constant value of about $525Nm^{-1}$ ($E/\omega' \sim$ 370meV). Use of this value together with the r=0.2 calculation for the no boroxol rings model (see figure 14.21b) places the peak C at 101meV which is not consistent with the experimental peak at about 88meV. Whilst the positions of D and E depend very little on r, the position of C is strongly affected by r, and an unexpectedly low value of about 0.16 causes C to coincide with the 88meV experimental peak (see figure 14.21c). However, the peak B is then found at 52meV and such a peak is not found in the experimental data. Since similar work on systems with a single simple structural unit has shown good agreement with the inelastic neutron scattering results (see for example BELL (1982)) it must be concluded that a structural model for B_2O_3 comprising a CRN of BO_3 triangles with an insignificant concentration of boroxol rings is inappropriate.

14.3.6 COMPARISON WITH EXPERIMENT.

In performing a comparison of a calculated VDOS with experiment the calculated distribution should ideally be used to calculate the function actually measured (BELL (1982)), taking into account the experimental resolution. This has not been done in the work described in this Chapter owing to the problems involved. To calculate the Raman spectrum one needs to know the polarisability of the modes and to calculate the inelastic neutron scattering signal one needs to know the amplitudes of vibration for the modes (diffraction experiments only yield an average amplitude at best). Since the calculations described in this Chapter do not yield eigenvectors, but only eigenvalues, these properties are not readily calculable. Furthermore the calculations for B_2O_3 are still at too crude a stage for inclusion of the experimental resolution to be worthwhile. That is to say it is much more important to be able to reproduce the correct peaks at the correct energies than it is to be able to reproduce the experimental resolution. The use of a realistic force model in relaxing a ball-and-stick model and in calculating its VDOS is much more important than including the experimental resolution; as the work described in this Chapter shows, the use of an unrealistic relaxation potential can significantly broaden the peaks of the calculated VDOS.

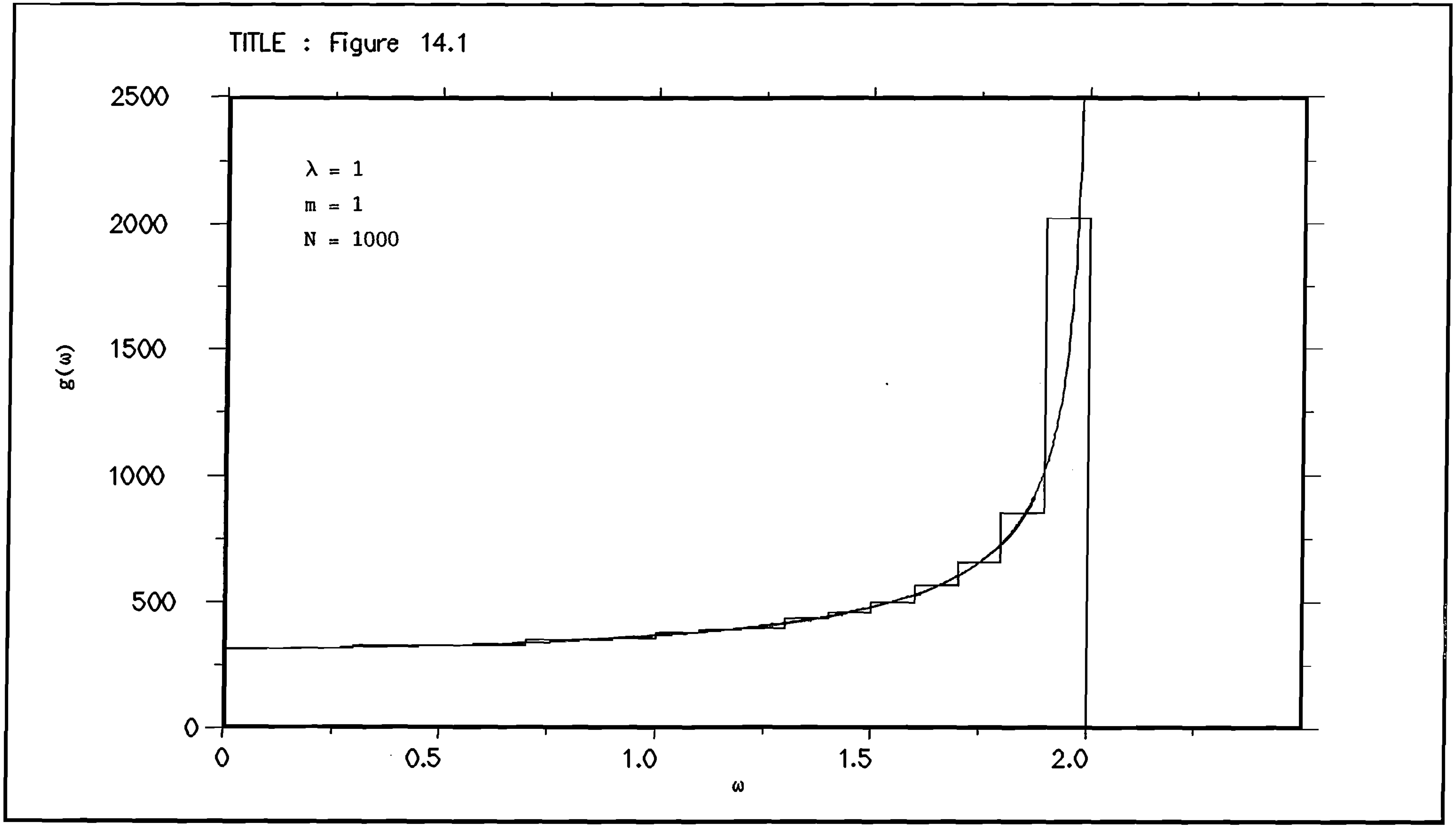

Figure 14.1 The VDOS of a Regular Monatomic Chain Calculated Analytically (Continuous Line) and Using the Numerical Computer Program (Histogram).

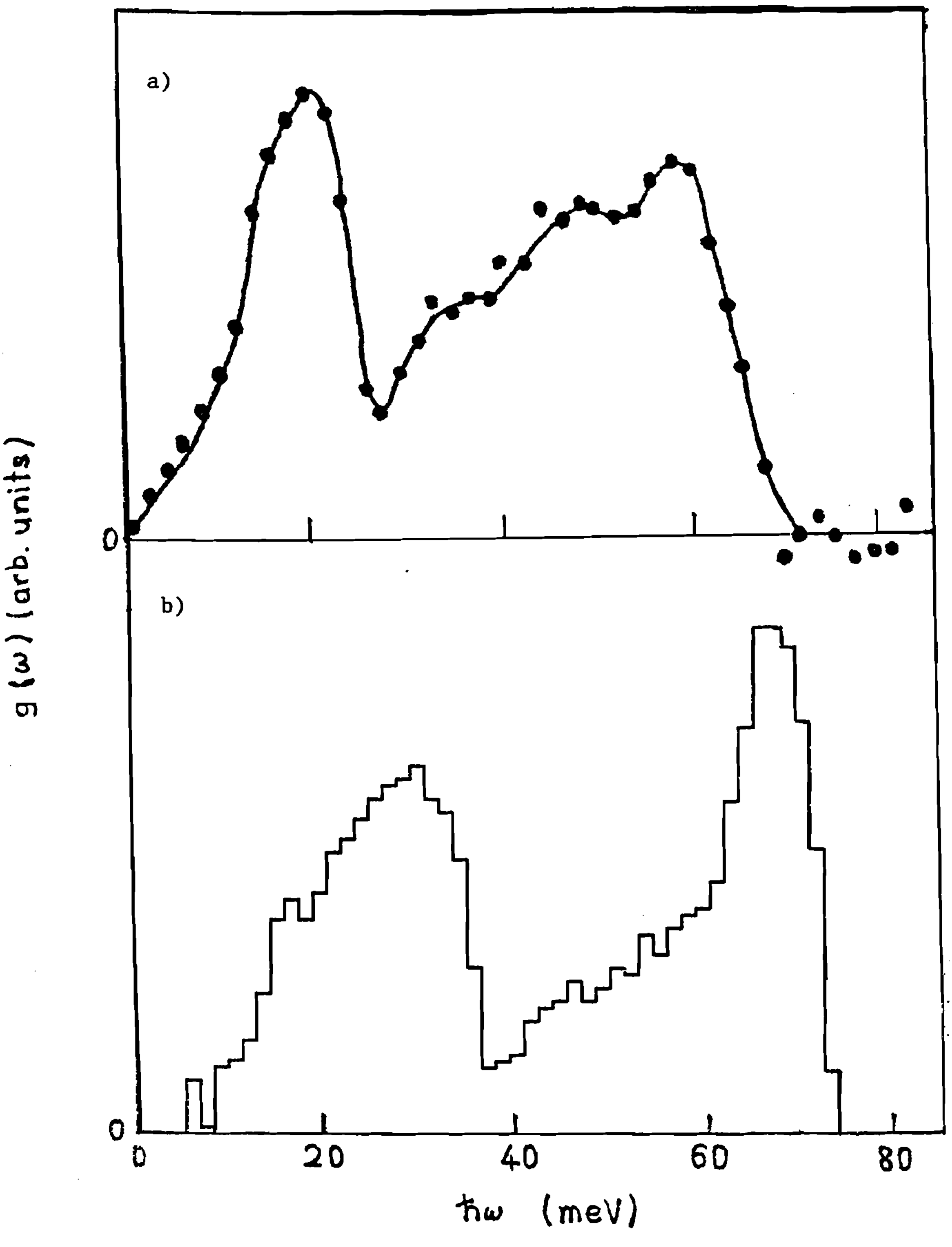

Figure 14.2 a) The VDOS of Amorphous Silicon as Measured by Inelastic Neutron Scattering (KAMITAKAHARA, SHANKS, McCLELLAND, BUCHENAU, GOMPF and PINTSCHOVINS, 1984).
b) The VDOS of the Polk (POLK and BOUDREAUX, 1973) Model of Amorphous Silicon as Calculated by the Program BORN.

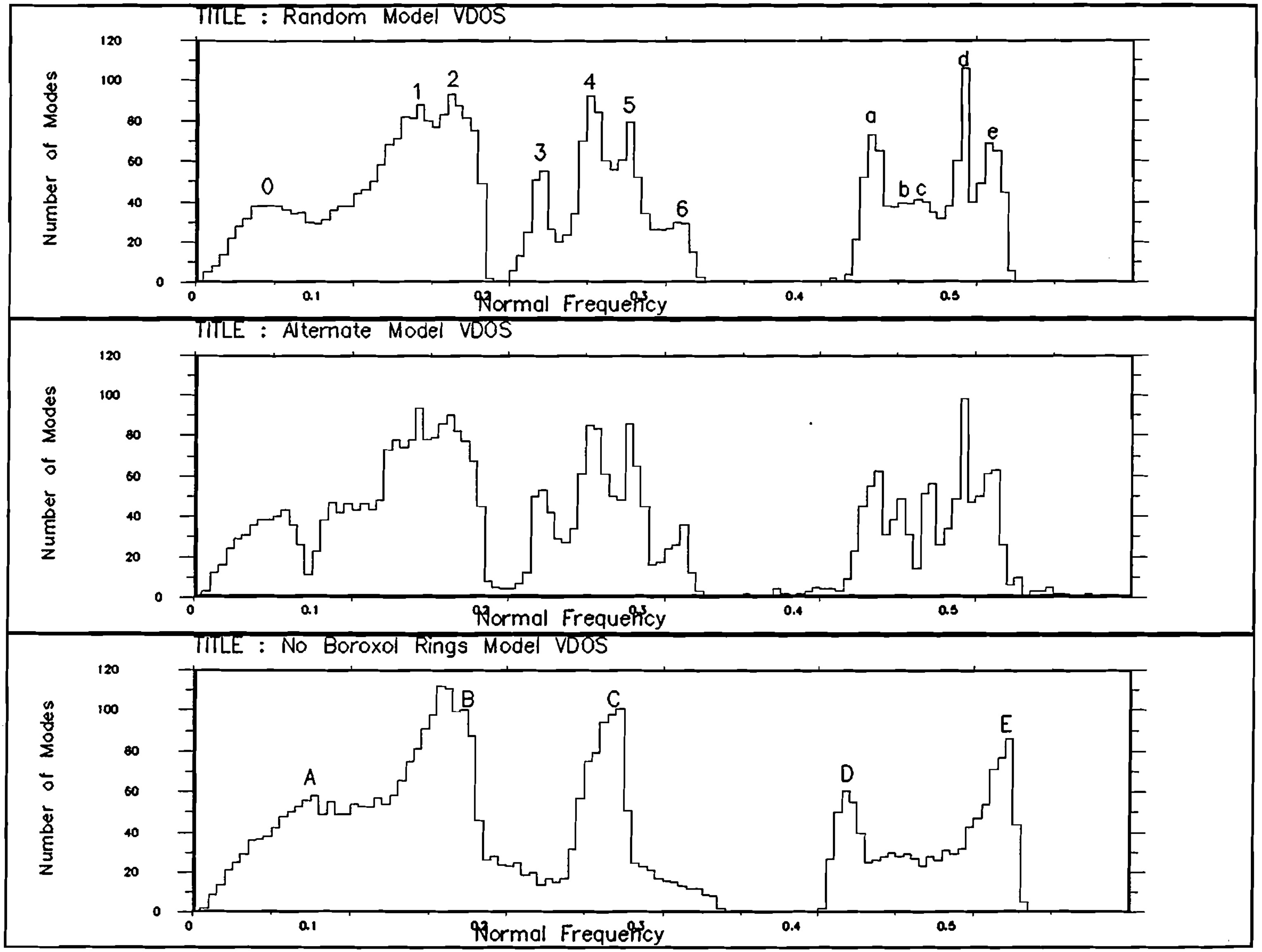

Figure 14.3 The VDOS of each of the Three Models Calculated with r=0.2 .

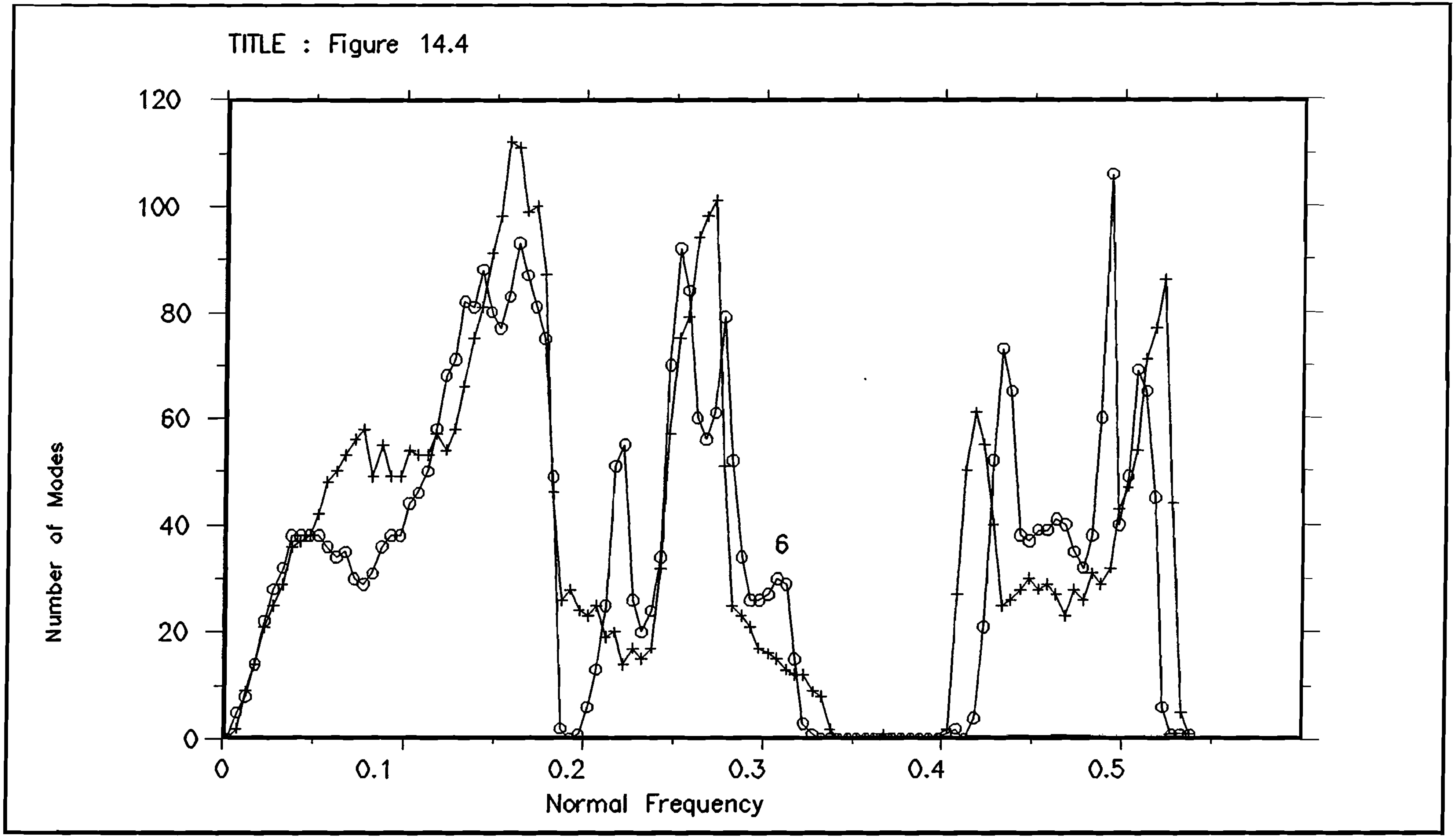

Figure 14.4 A Comparison Between the Random Model VDOS (Circles) and the No Boroxol Rings Model VDOS (Plus Signs).

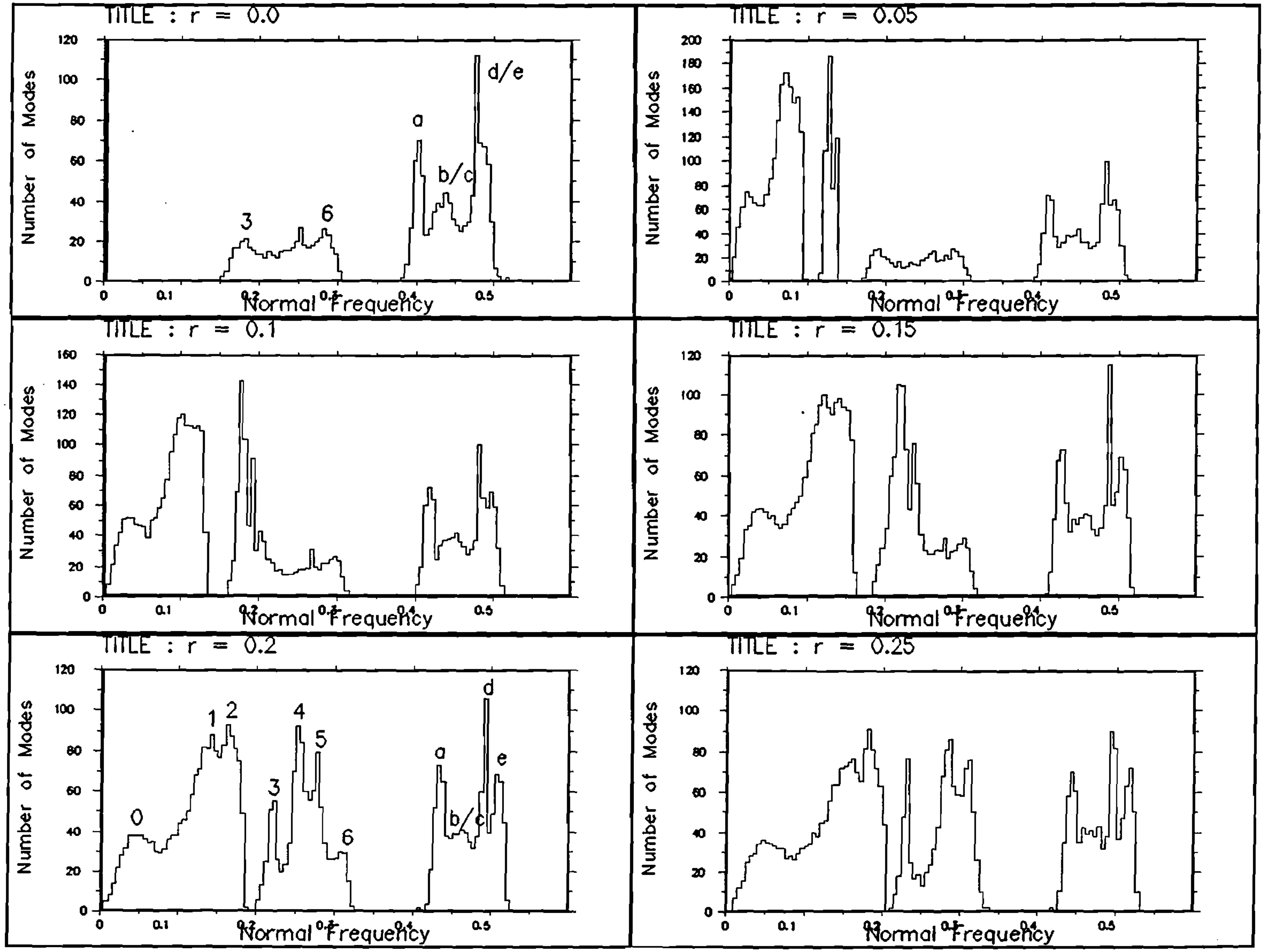

Figure 14.5 The VDOS of the Random Model for Different Values of r.

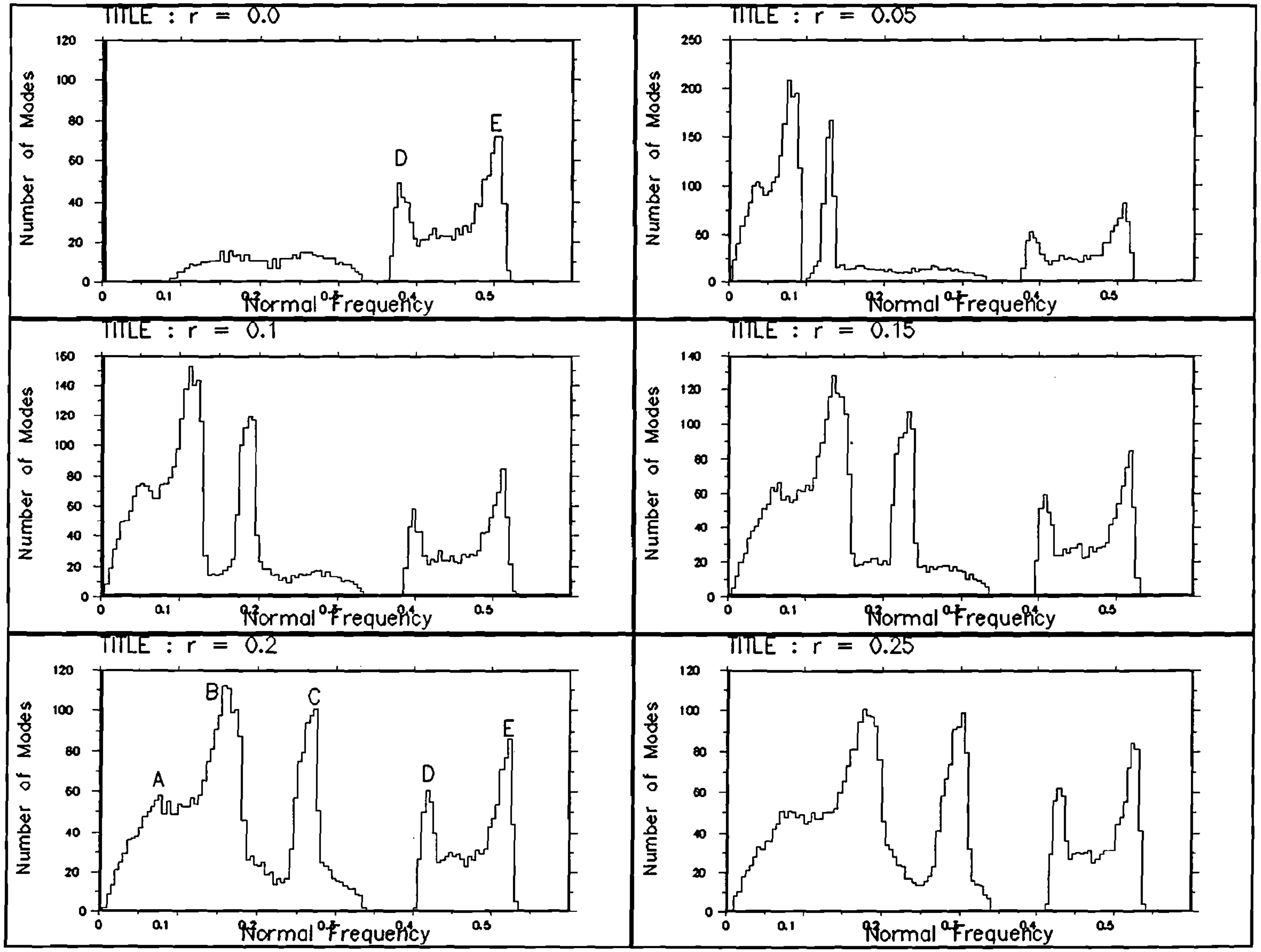

Figure 14.6 The VDOS of the No Boroxol Rings Model for Different Values of r.

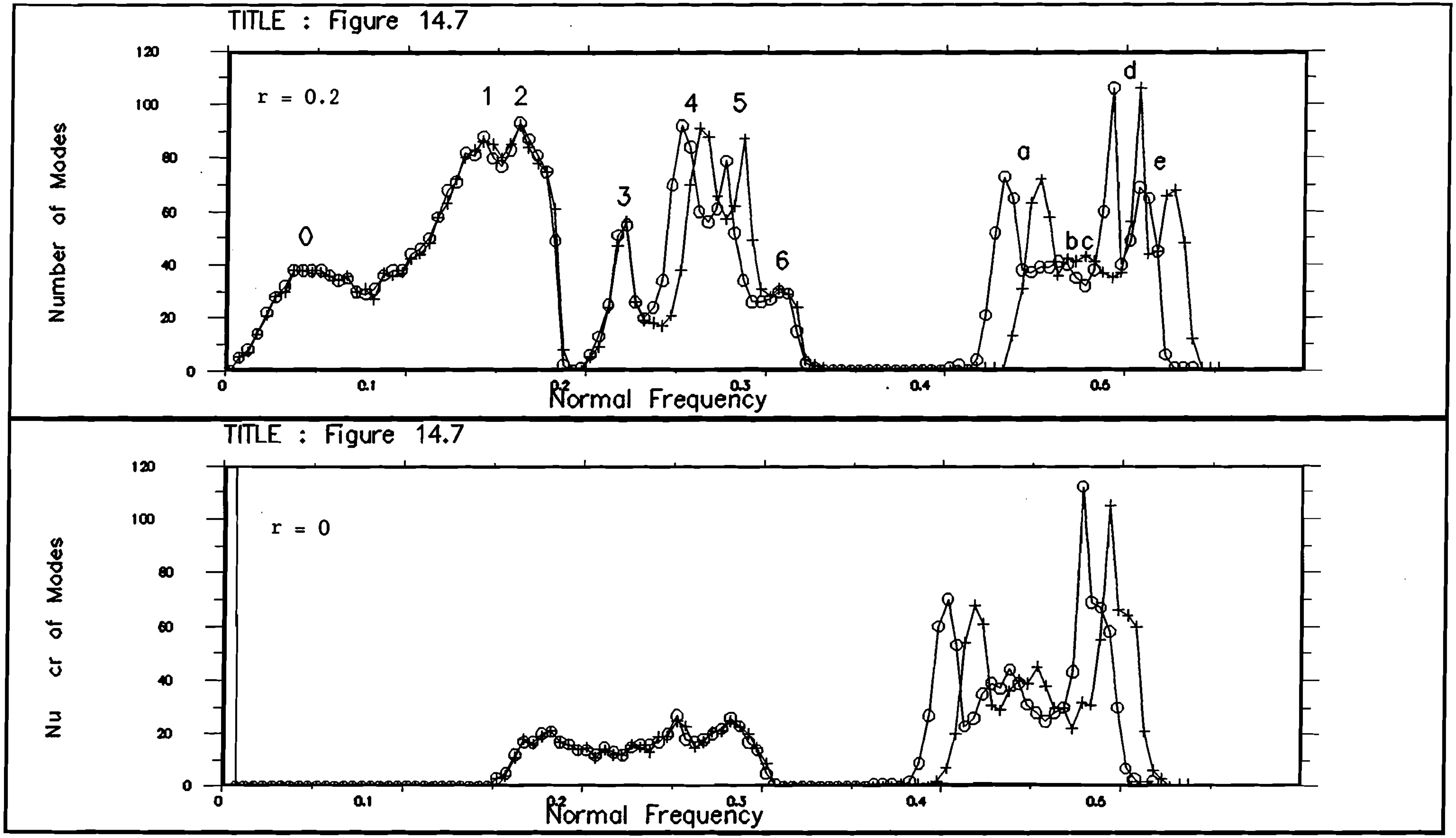

Figure 14.7 The Effect of Boron Isotopic Substitution on the Random Model VDOS. Circles are for ^{11}B and Plus Signs are for ^{10}B.

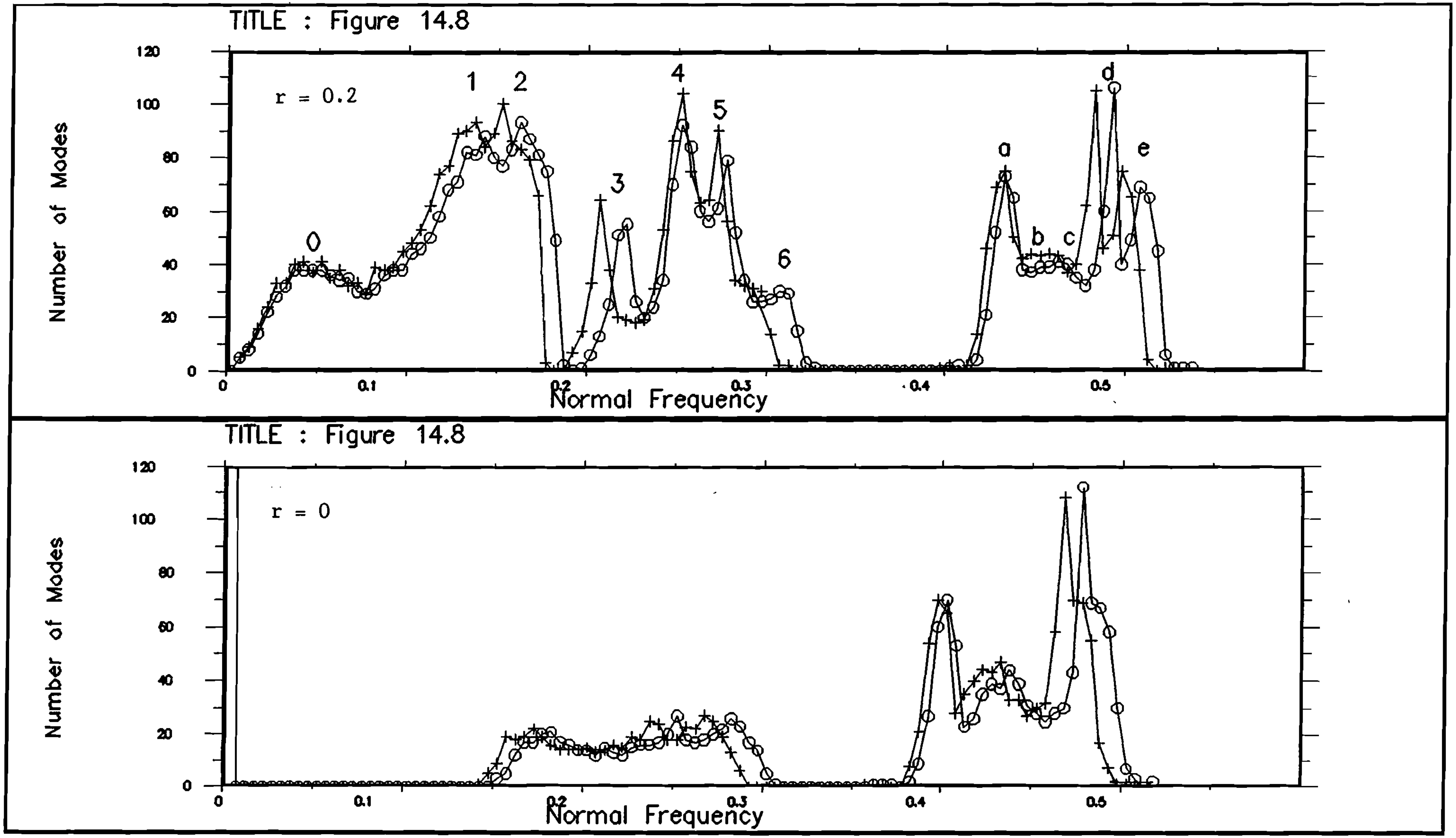

Figure 14.8 The Effect of Oxygen Isotopic Substitution on the Random Model VDOS. Circles are for ^{16}O and Plus Signs are for ^{18}O.

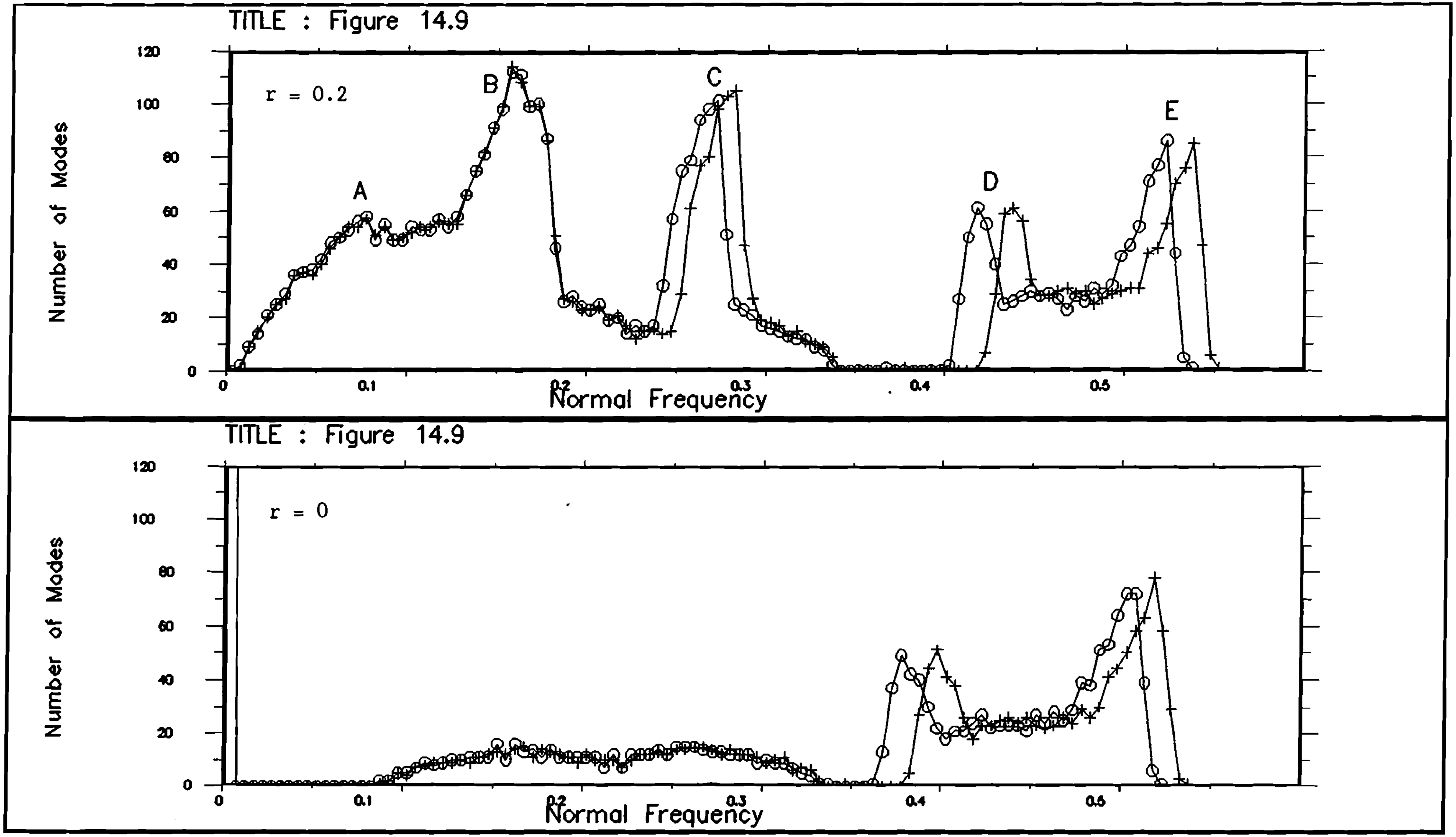

Figure 14.9 The Effect of Boron Isotopic Substitution on the No Boroxol Rings Model VDOS. Circles are for ^{11}B and Plus Signs are for ^{10}B.

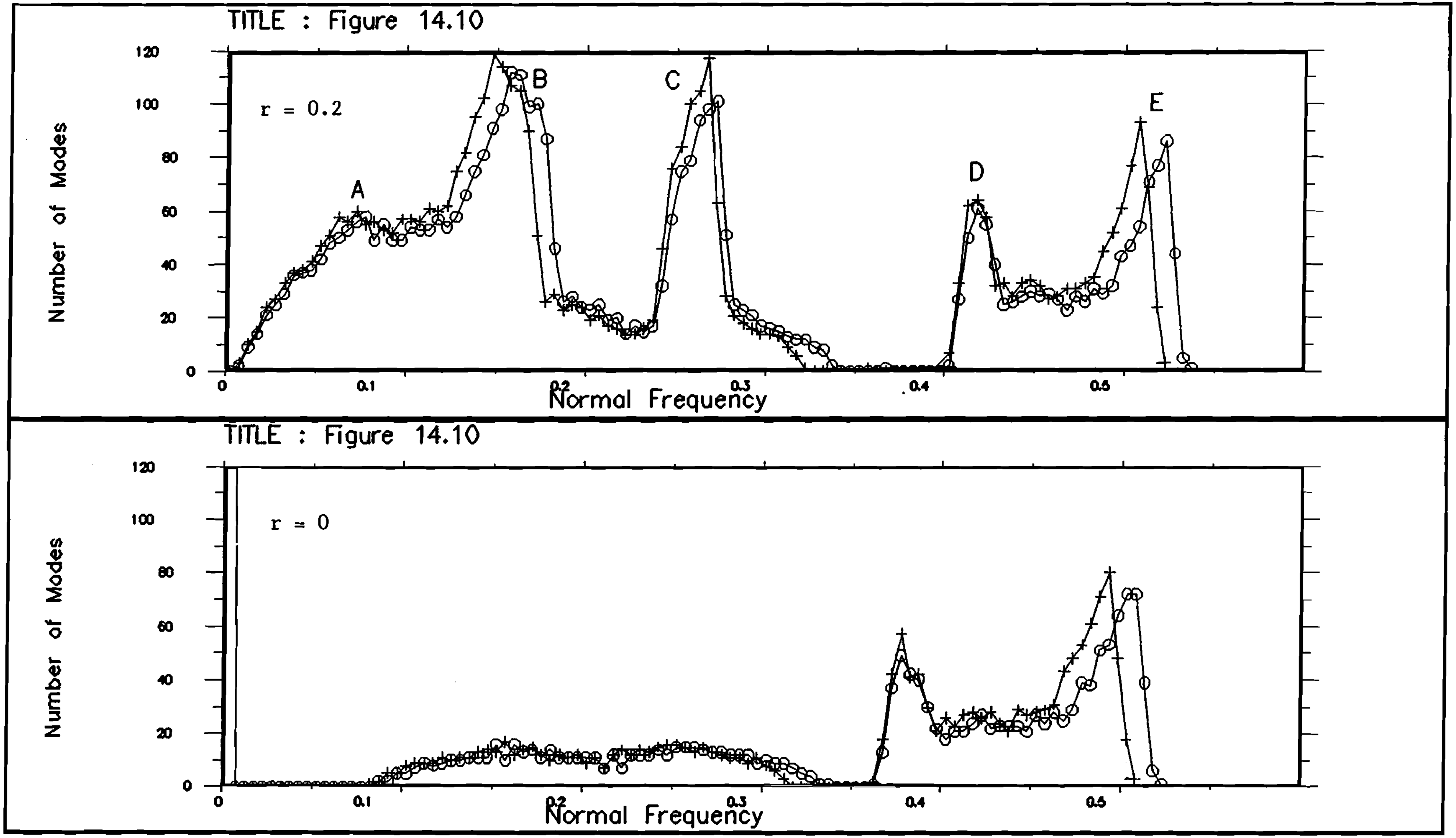

Figure 14.10 The Effect of Oxygen Isotopic Substitution on the No Boroxol Rings Model VDOS. Circles are for ^{16}O and Plus Signs are for ^{18}O.

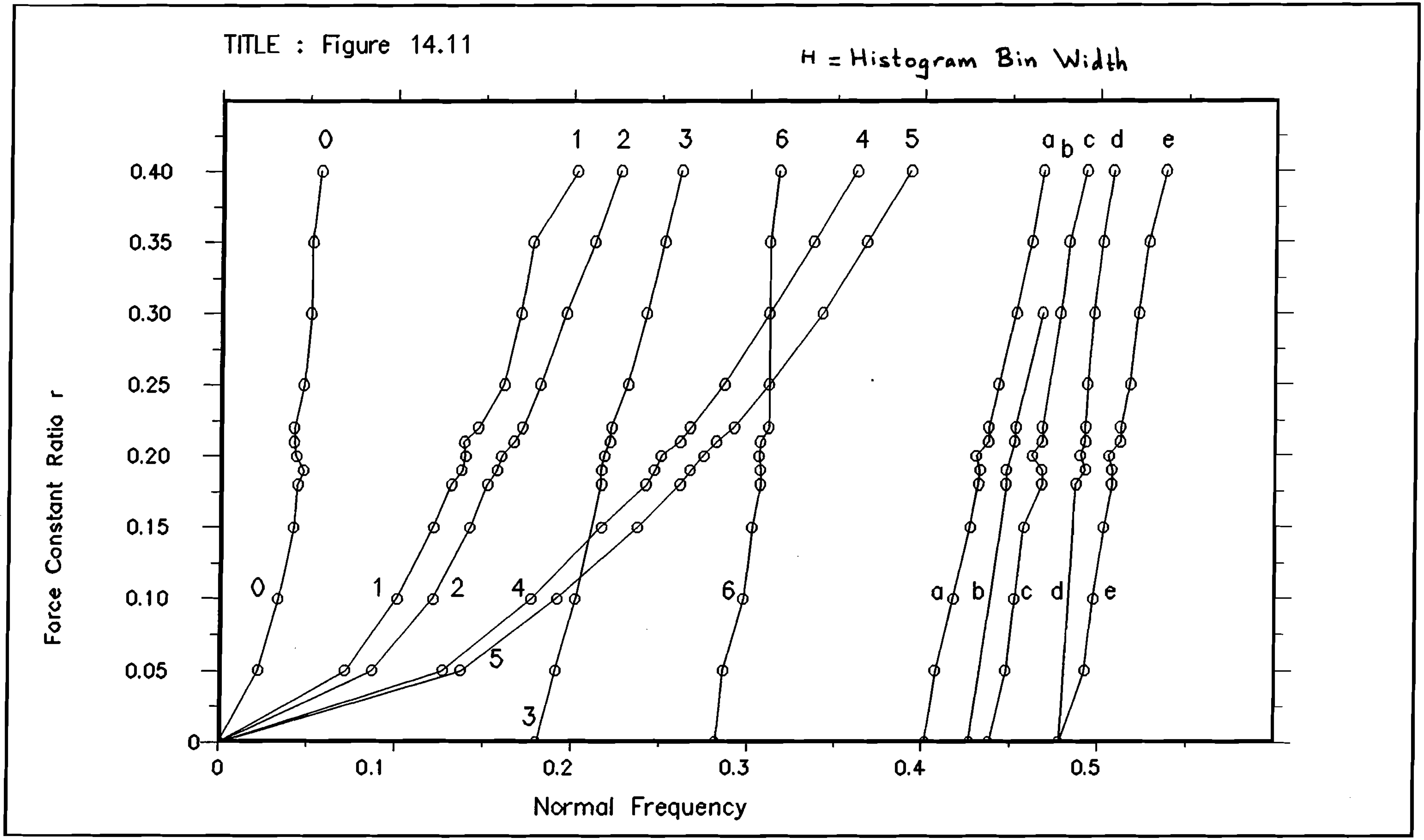

Figure 14.11 The Behaviour of the Peaks in the Random Model VDOS as r is Varied.

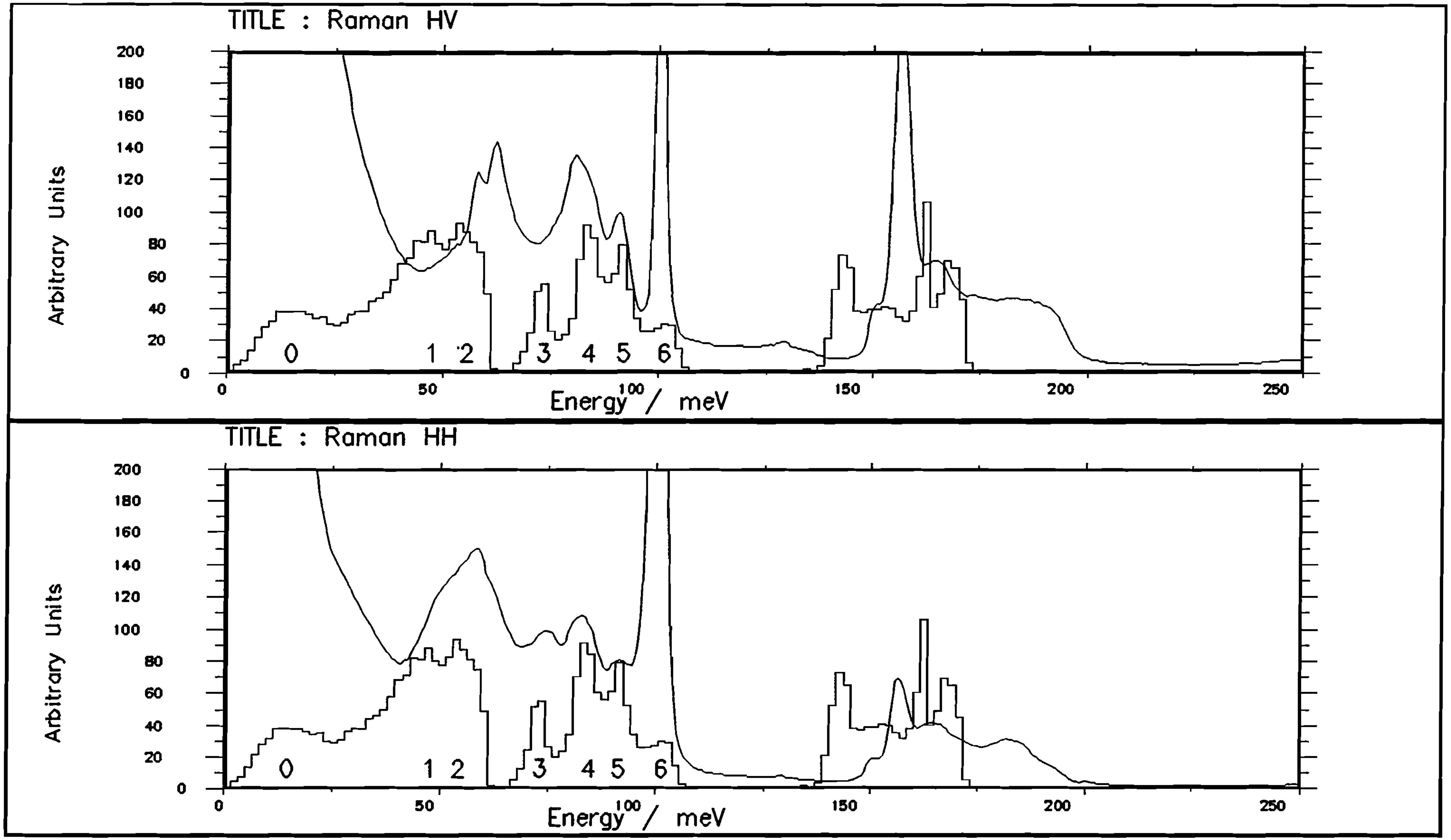

Figure 14.12 A Comparison Between the VDOS (r=0.2 and λ^c=420Nm^{-1}) of the Random Model (Histogram) and the Raman Spectra (without Removal of the Exciting Line) of B_2O_3 (Continuous Line).

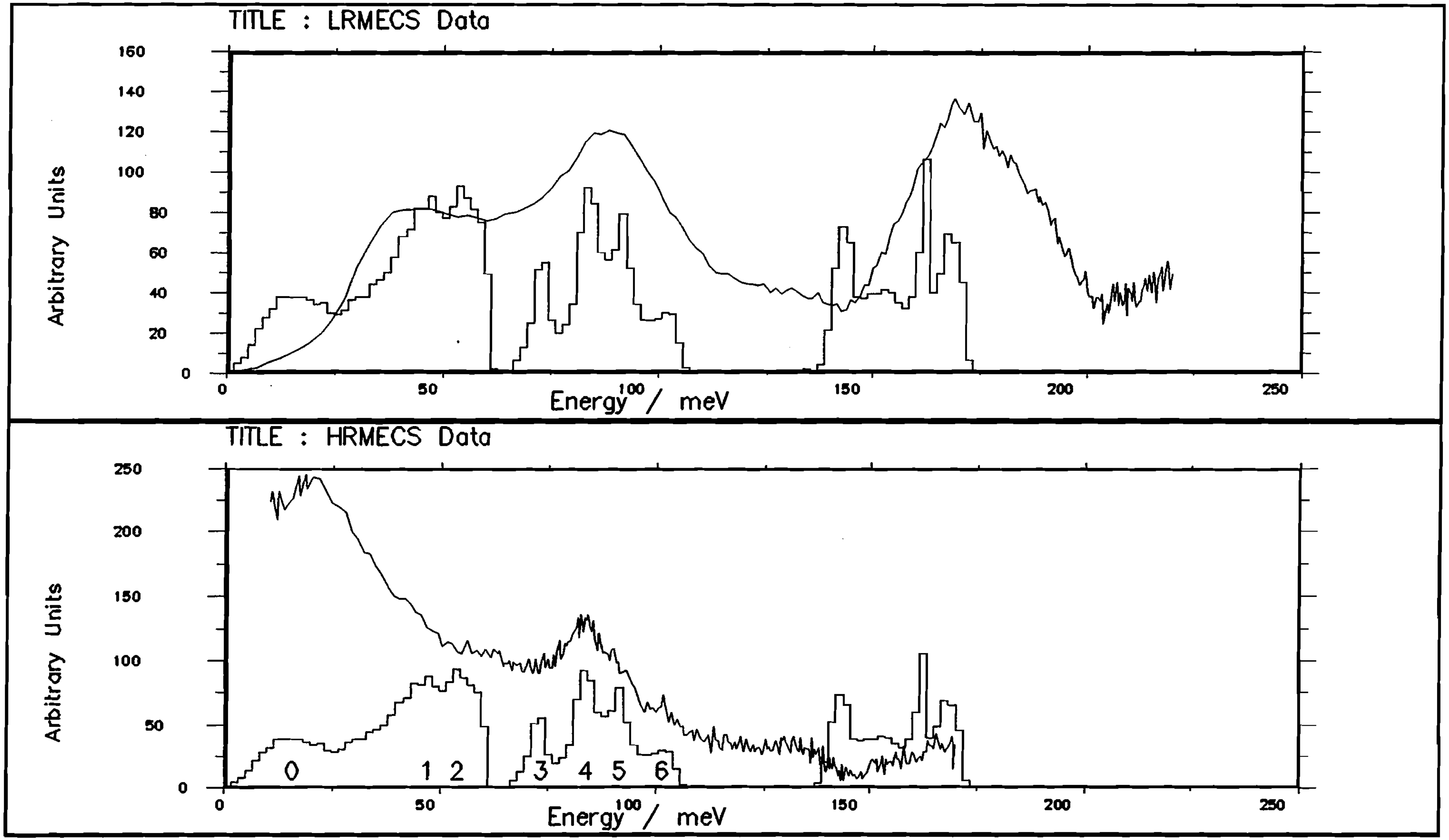

Figure 14.13 A Comparison Between the VDOS ($r=0.2$ and $\lambda^c=420Nm^{-1}$) of the Random Model (Histogram) and the VDOS of B_2O_3 as Measured by Inelastic Neutron Scattering (Continuous Line).

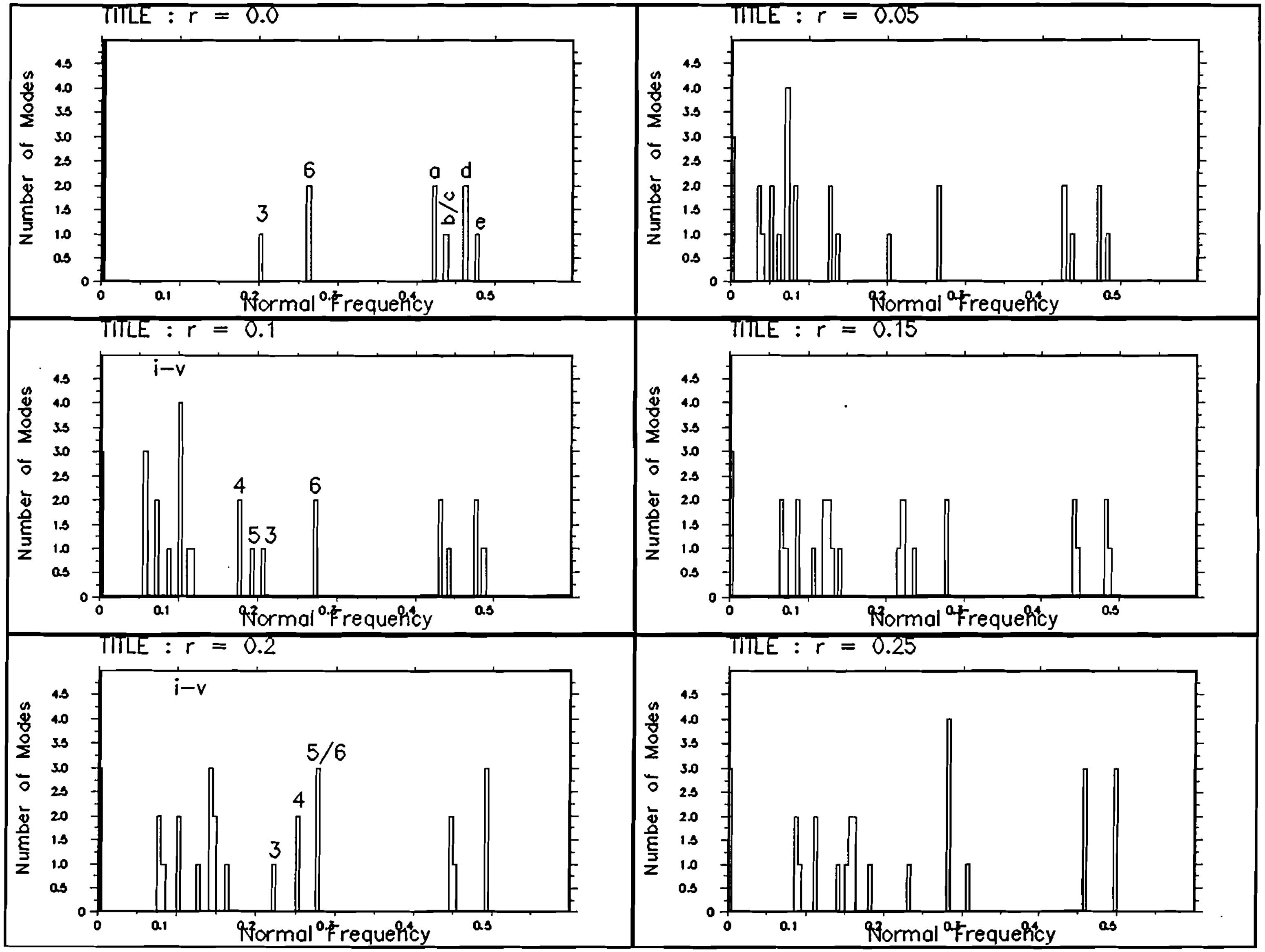

Figure 14.14 The Vibrational Modes of a B_3O_6 Boroxol Ring for Different Values of r.

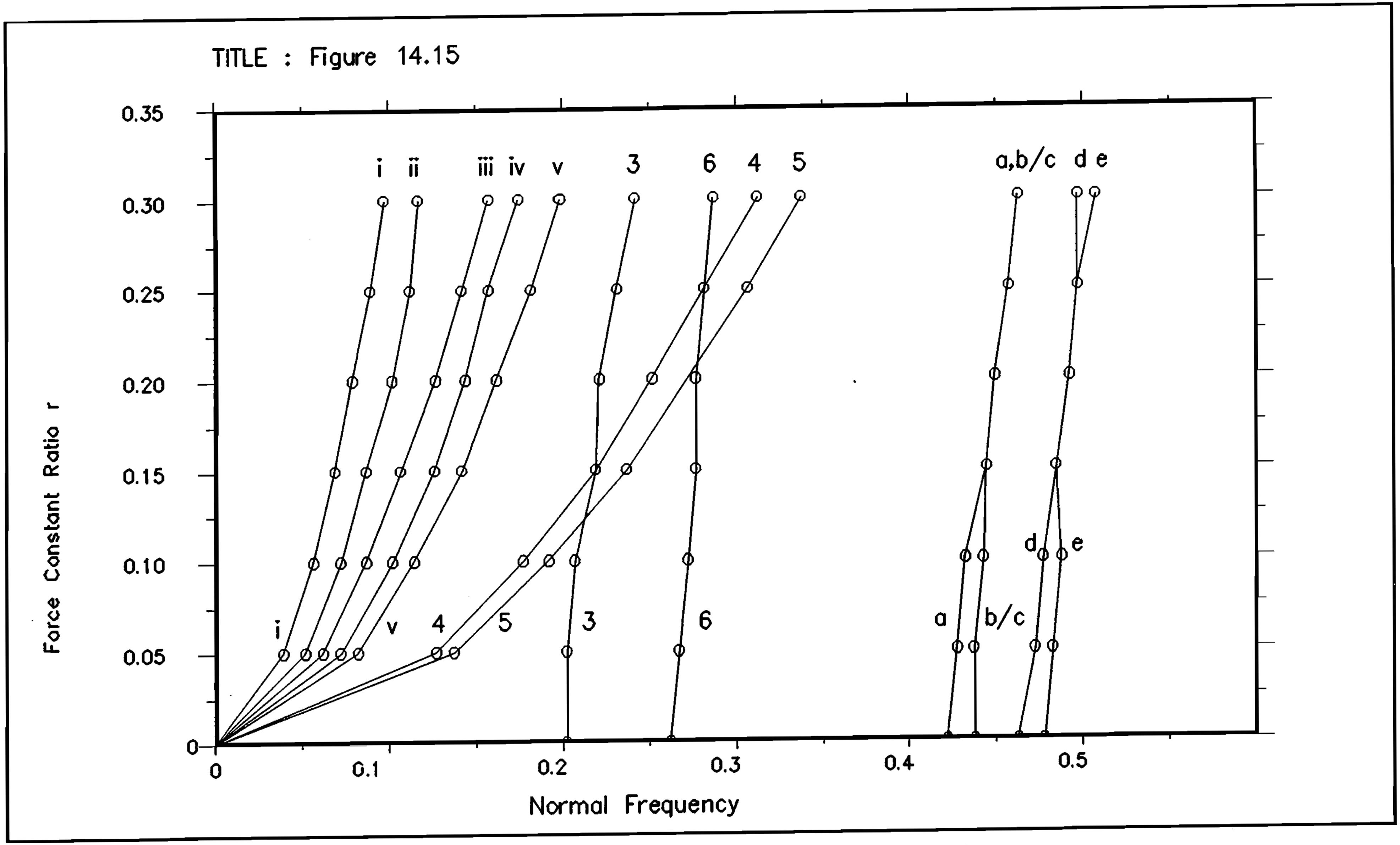

Figure 14.15 The Behaviour of the Vibrational Modes of a B_3O_6 Boroxol Ring as r is Varied.

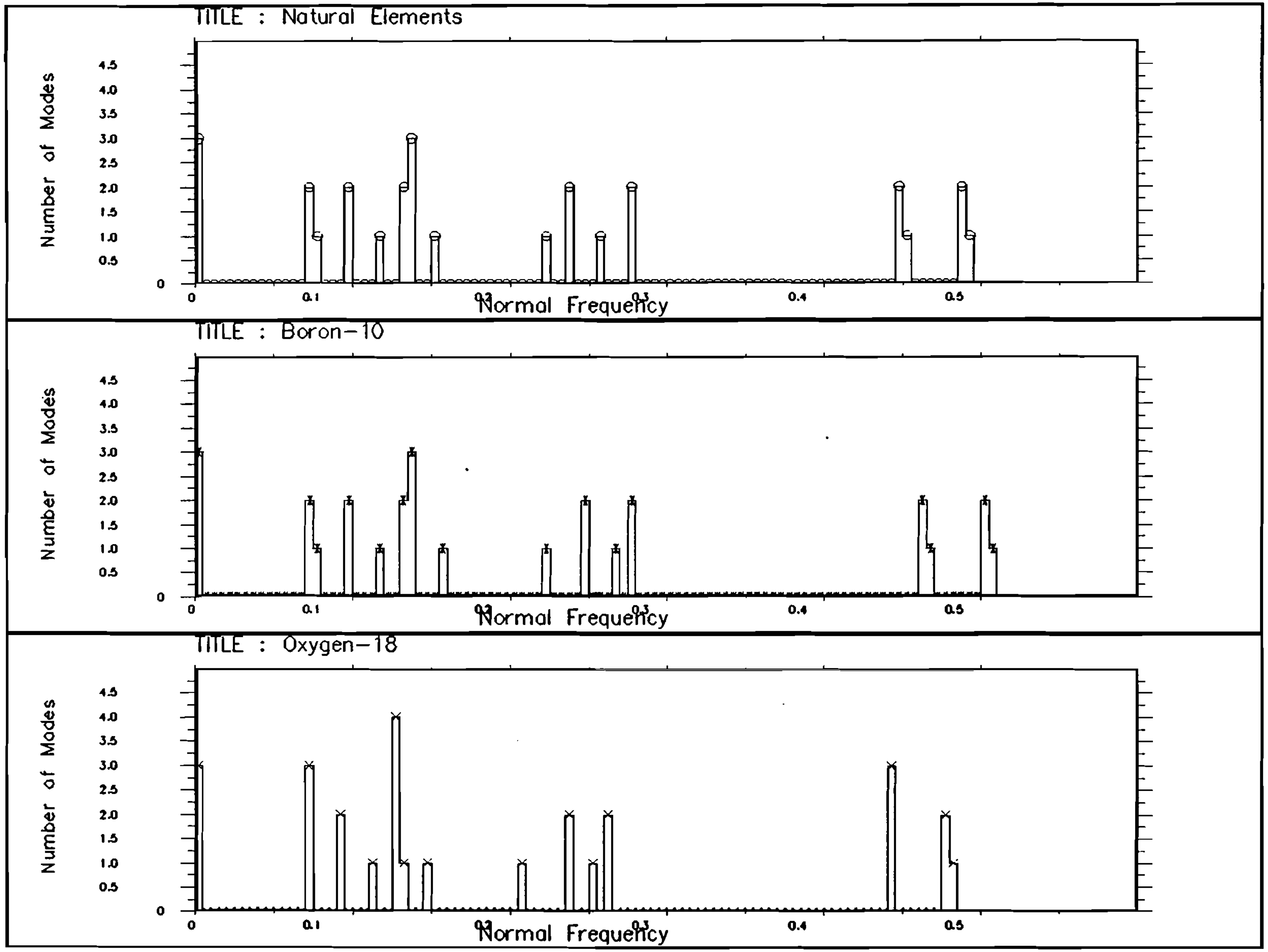

Figure 14.16 The Effect of Isotopic Substitution on the VDOS of a B_3O_6 Boroxol Ring (r=0.175). Circles are for Natural Elements, Stars for ^{10}B and Crosses for ^{18}O.

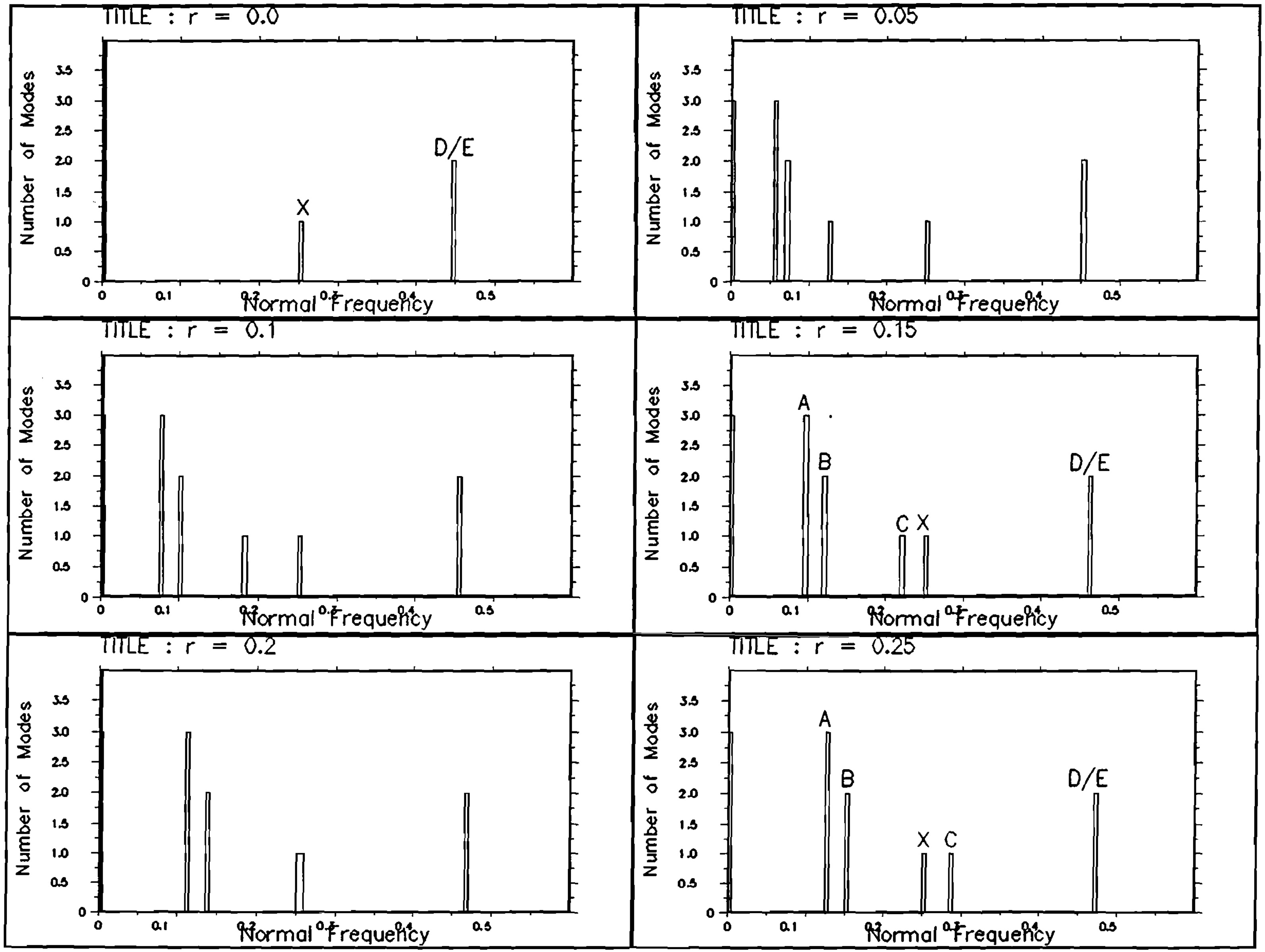

Figure 14.17 The Vibrational Modes of a BO_3 Triangle for Different Values of r.

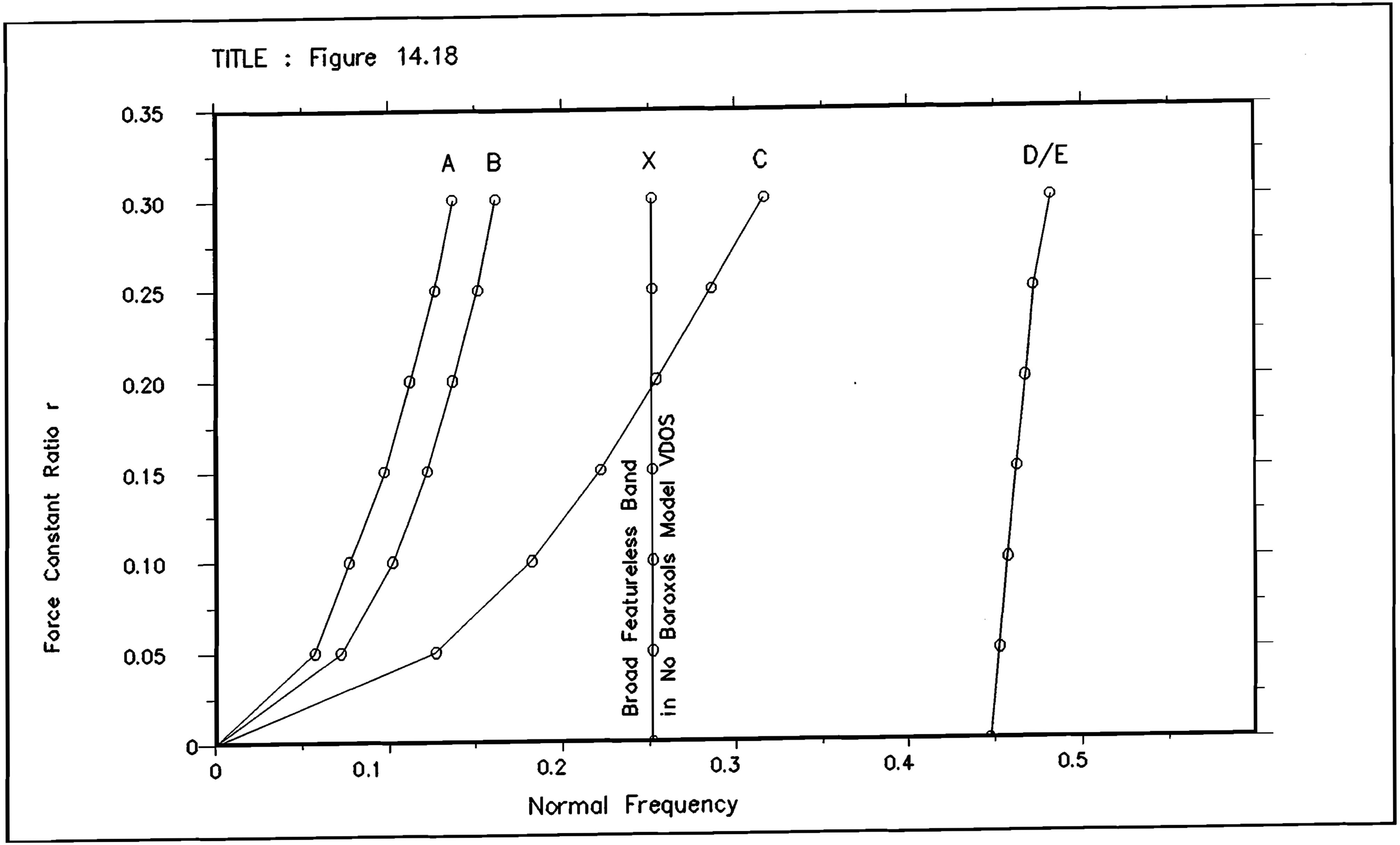

Figure 14.18 The Behaviour of the Vibrational Modes of a BO_3 Triangle as r is Varied.

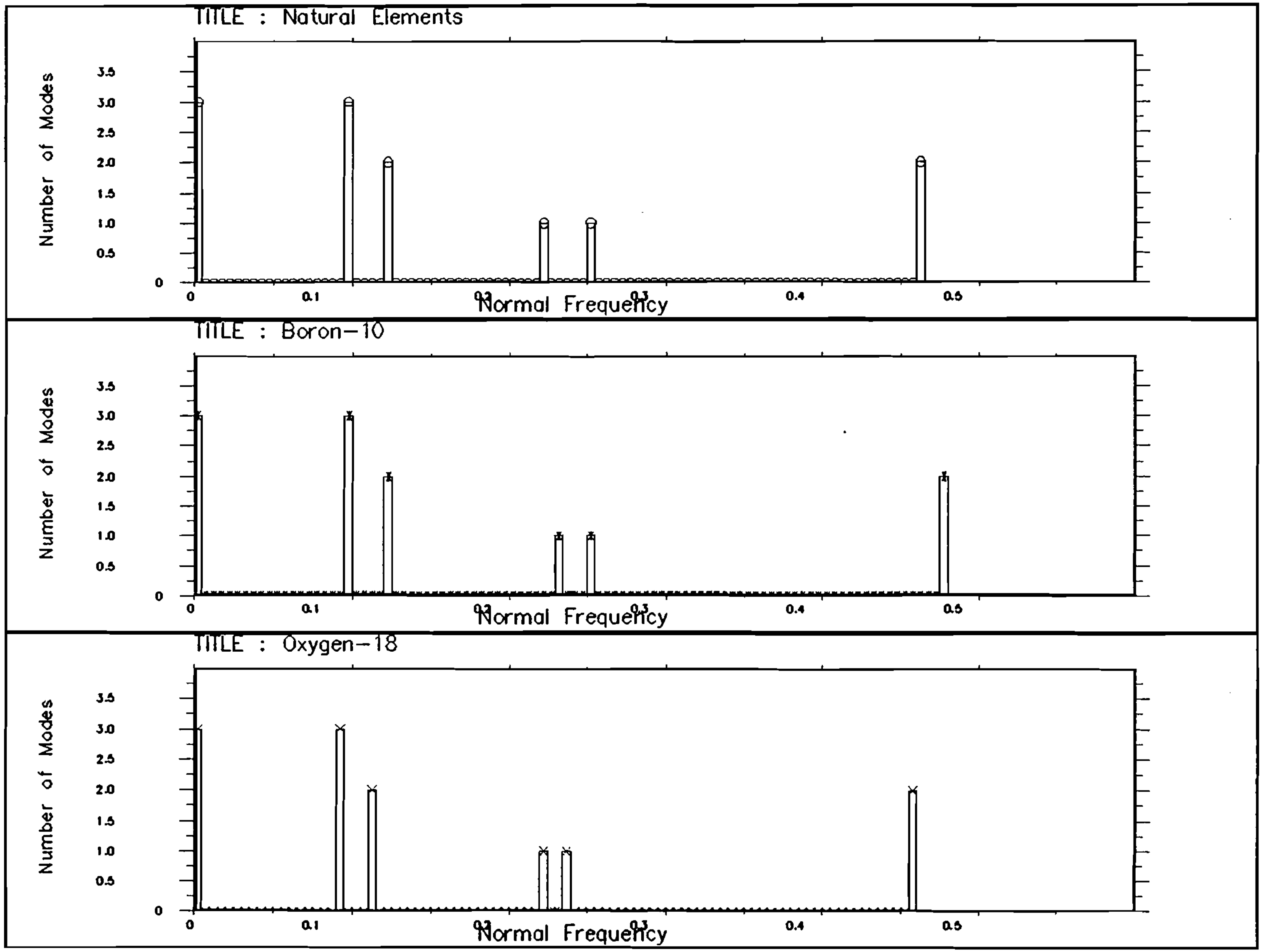

Figure 14.19 The Effect of Isotopic Substitution on the VDOS of a BO_3 Triangle with r=0.15. Circles are for Natural Elements, Stars for ^{10}B and Crosses for ^{18}O.

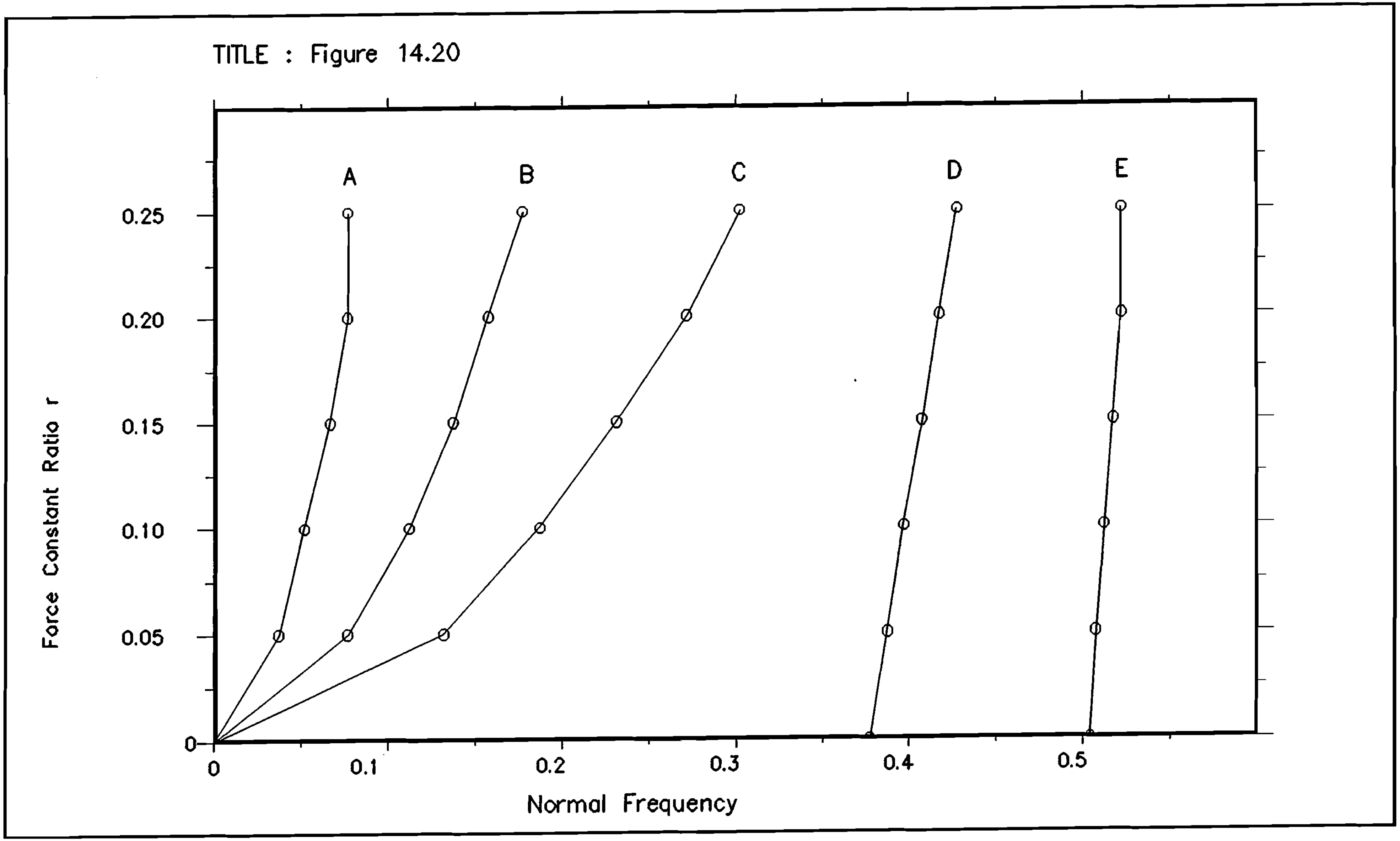

Figure 14.20 The Behaviour of the Peaks in the No Boroxol Rings Model VDOS as r is Varied.

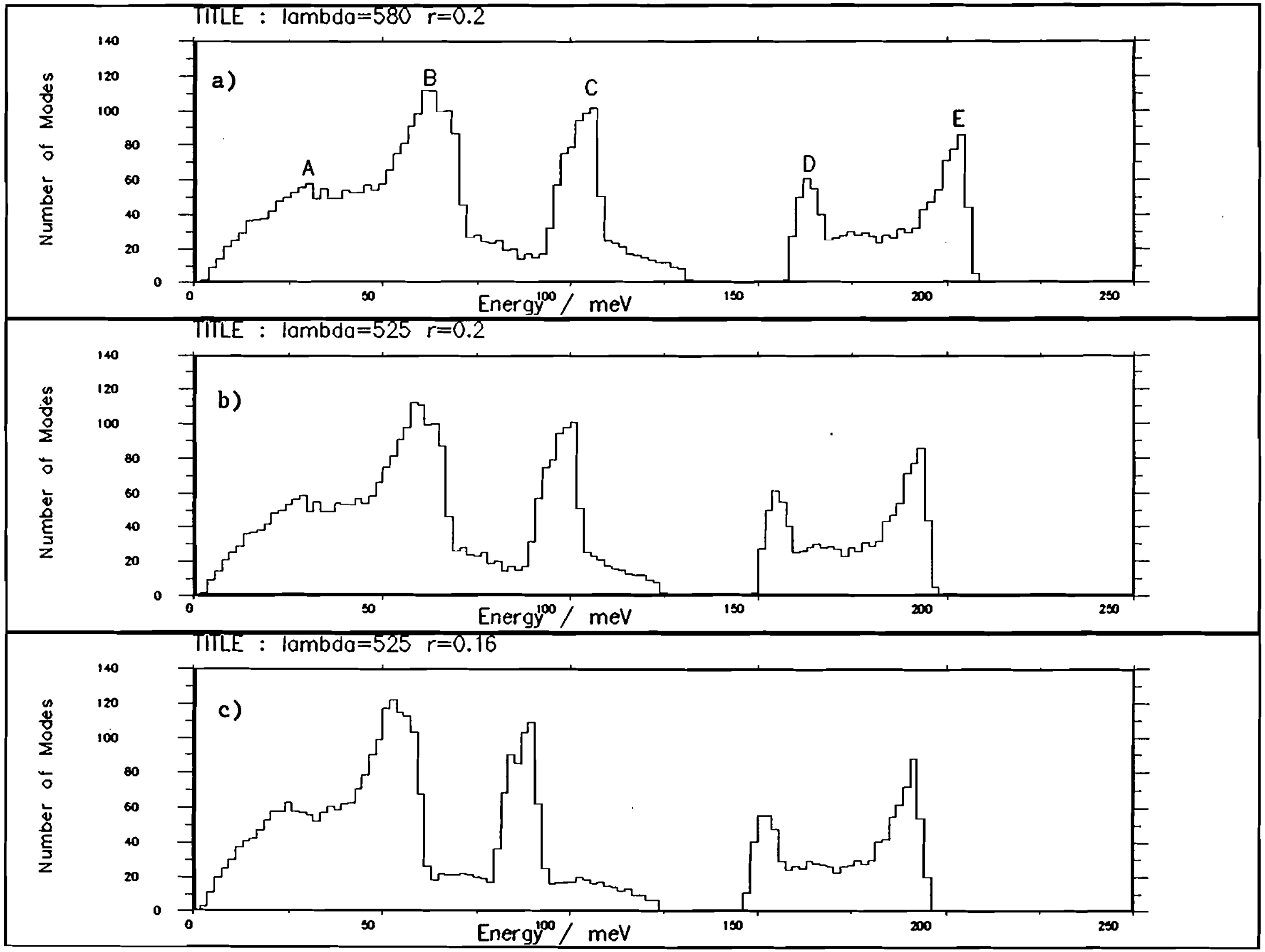

Figure 14.21 The No Boroxol Rings Model VDOS. a) Calculated with r=0.2 and λ^c=580Nm^{-1} b) Calculated with r=0.2 and λ^c=525Nm^{-1} c) Calculated with r=0.16 and λ^c=525Nm^{-1}.

CHAPTER 15

B203 - CONCLUSIONS.

A preliminary report of the work described in Chapters 13 and 14 has been given in the literature by HANNON, SINCLAIR, BLACKMAN, WRIGHT and GALEENER (1988).

15.1 NEUTRON SCATTERING - RESULTS.

The effective VDOS $g_{eff}(E)$ of B_2O_3 has been measured with a resolution of approximately 15meV using the inelastic neutron scattering spectrometer LRMECS (figure 13.12). Also the inelastic neutron scattering spectrometer HRMECS has been used to measure $g_{eff}(E)$ below an energy of about 140meV with a resolution of approximately 5meV (figure 13.9). The deficiencies of these measurements are discussed in Chapter 13. The measurements indicate that the general form of the VDOS can be described as two bands of modes followed by a gap and another band (this is the same general form as found in the calculations of Chapter 14). At high energies the LRMECS measurement shows a broad band of modes centred at 170meV which extends from 145meV to 205meV. There are no sharp outstanding features in this band such as are observed in the Raman spectrum (figure 12.2). The intense feature 8 at 1261cm^{-1} (≡156.3meV) in the Raman spectrum (using the feature-labelling scheme of GALEENER and THORPE (1983) as in Chapter 14) does not appear to be present in the neutron measurement. However, the resolution of LRMECS is sufficiently broad that a feature such as 8 could be a fairly significant feature of the VDOS without being readily apparent in the measured $g_{eff}(E)$. As discussed in Chapter 13, the indications are that there is a gap in the

VDOS between 110meV and 145meV. There is then another band of modes in the LRMECS measurement of $g_{eff}(E)$ which is centred at 88meV and extends from 60meV to 110meV. There are also indications of a broad band of modes at lower energies, but the precise position of this band is obscured by the presence of elastic scattering. As with the high energy band of modes, there are no sharp outstanding features in the LRMECS measurement of the band centred around 88meV. However, definite features may be discerned in this region of the narrower resolution HRMECS measurement. Thus the point made above that the lack of sharp features in the high energy region of the LRMECS measurement is due to insufficient energy resolution is confirmed. In the HRMECS measurement the band of modes is centred at 83meV. It is not clear why this value is slightly lower than for the LRMECS measurement but it may be due in part to the difference in resolution (LOONG, IKEDA, CARPENTER and PRICE, 1987). The feature at 83meV in the neutron $g_{eff}(E)$ may be identified with the feature 4 at 670cm^{-1} (≡83.1meV) in the Raman spectrum. Of particular interest for B_2O_3 is the feature 6 of the Raman spectrum, the boroxol ring breathing mode at 808cm^{-1} (≡100.2meV). In the HRMECS measurement of $g_{eff}(E)$ there is a small feature at 102meV which may be identified as the boroxol ring breathing mode. However, the relative magnitude of this feature is vastly reduced compared to the Raman spectrum, indicating that this particular mode is greatly enhanced in the Raman spectrum. The polarisability and hence the Raman matrix element of the boroxol ring breathing mode must be very much greater than for most of the other vibrational modes of the B_2O_3 network. Thus there is a considerable variation in Raman matrix element over the range of the VDOS which is perhaps greater than has previously been realised. Conversely if a greatly enhanced Raman matrix element is a general feature for vibrational modes isolated to one regular ring then it may be concluded that Raman scattering is an experimental technique ideally suited to the detection of regular rings in a CRN. The HRMECS measurement of $g_{eff}(E)$ also appears to have two smaller features at 90meV and 93meV, and these may be identified with feature 5 of the Raman spectrum which the IR spectra (GALEENER, LUCOVSKY and MIKKELSEN, 1980) indicate to be split into a TO mode ($720cm^{-1} \equiv 89.3meV$) and a LO mode ($740cm^{-1} \equiv 91.7meV$). There is also some indication of a slight feature around 60meV which may be associated with features 1 and 2 of the Raman spectrum. However, the feature 3 of the Raman spectrum at $610cm^{-1}$ ($\equiv 75.6meV$) is not readily apparent in the HRMECS measurement of $g_{eff}(E)$. A possible explanation for this could be that the Raman matrix element for this mode is greatly enhanced as with the boroxol ring breathing mode. However, the calculations of Chapter 14 indicate that the feature 3 should be of a similar order of magnitude to the feature 6 and hence the reason for the apparent absence of feature 3 from the neutron $g_{eff}(E)$ is not clear. Possibly the explanation for this may involve the force model; figure 14.5 shows that the apparent importance of feature 3 increases strongly as the force constant ratio r is increased.

A comparison of the elastic scattering for B_2O_3 with the neutron diffraction data has been used to deduce a value of 0.081Å for the average RMS displacement from equilibrium of an atom $\overline{\langle u^2 \rangle}^{1/2}$.

The occurrence of the boroxol ring breathing mode in the neutron $g_{eff}(E)$ is clear evidence for the presence of boroxol rings in B_2O_3. However, it might be argued that the concentration of boroxol rings is very low but that the boroxol ring breathing mode appears to be significant in the neutron $g_{eff}(E)$ because this mode is also enhanced for neutron scattering. The equations of section 4.4 show that such enhancement could occur if the amplitude of vibration for this mode were exceptionally large. The boroxol ring breathing mode involves the motion of oxygen atoms in and out of the ring and it could be argued that the restoring force for this motion is principally the smaller non-central force and hence that the amplitude of vibration is particularly large for this mode. In fact this is not the case since the calculations of Chapter 14 (see figure 14.11) show that the boroxol ring breathing mode occurs with central forces only and is only weakly affected by the non-central force constant. Thus it is unreasonable to suppose an exceptionally large amplitude of vibration for the boroxol ring breathing mode and it must be concluded that this mode is not enhanced in the neutron $g_{eff}(E)$. In fact GALEENER, LEADBETTER and STRINGFELLOW (1983) have attempted to calculate coupling coefficients for various modes in the inelastic neutron scattering spectra of several tetrahedral glasses and most of the coupling coefficients are found to be near to unity, with the greatest enhancement or diminution being of order 50%. Thus a more precise conclusion regarding the presence of the boroxol ring breathing mode in $g_{eff}(E)$ is that there may be some enhancement or diminution of the mode but that the extent of the effect cannot be a gross distortion as is the case with the Raman spectrum. A comparison of the HRMECS measurement of $g_{eff}(E)$ (figure 13.9) with the calculation of the VDOS for the random model (figure 14.13) shows features 4 and 6 have approximately the same relative magnitudes in both cases. Hence it may be concluded that the concentration of boroxol rings in the random model (equal numbers of boroxol rings and independent BO_3 triangles) is approximately the same as for the real material B_2O_3.

15.2 NEUTRON SCATTERING - FURTHER WORK.

Since the resolution of HRMECS was only just sufficient to observe the boroxol ring breathing mode it would be worthwhile to confirm the findings of this work by repeating the measurement with a higher resolution spectrometer such as at the new ISIS neutron source. This would also enable the form of the VDOS at lower energies to be determined. The calculations of Chapter 14 also suggest that a higher resolution study of the high energy region of the VDOS would be helpful in determining the force constants inside and outside the boroxol rings.

15.3 MODELLING - RESULTS.

The VDOS has been calculated for three ball-and-stick models of the B_2O_3 network, one composed solely of BO_3 triangles and two containing equal numbers of independent BO_3 triangles and B_3O_6 boroxol rings. Born forces were assumed and the calculations were performed for a range of different force constant values. No topological variation in force constant values was allowed. The models containing boroxol rings were found to reproduce the richness of the measured phonon spectra whilst the model without boroxol rings did not. Isotopic substitution calculations were performed and compared with the isotopic substitution Raman data. A detailed correspondence was found between the peaks of the VDOS of one of the models with boroxol rings and the experimental peaks. A force constant ratio of 0.2 was found to be consistent with the experimental data, and non-central forces were found to be essential in explaining a number of the peaks.

Evidence of inadequacies in the force model was obtained, and a more realistic force model is suggested with central force constant values of about 420Nm^{-1} inside the boroxol rings and about 580Nm^{-1} outside the boroxol rings. An attempt was made to maximise the agreement between the model with no boroxol rings and experiment, but despite adjusting all available parameters good agreement was not obtained. The conclusion of this work is that a significant concentration of boroxol rings in the B_2O_3 network is required in order to explain the experimental phonon spectra. Thus this work is a prime example of the value of studying vibrational excitations as a means of investigating the extent of IRO in amorphous solids. In particular isotopic substitution is shown to be a most valuable technique. To the author's knowledge this is the first time that isotopic substitution calculations have been performed for a ball-and-stick model. The question of localisation has also been addressed in this study and a number of the modes of B_2O_3 are demonstrated to be localised to a single boroxol ring. An additional finding of this work is that ball-and-stick models must be relaxed with a realistic potential. In the case of B_2O_3 a realistic potential would be one which maintained the high degree of planarity of the boroxol rings. It is suggested that a very high force constant for out of plane non-central forces would achieve this. Another alternative might be to relax the ball-and-stick model using the Keating potential with a very high equilibrium bond angle for the boroxol rings so as to maintain planarity. However, there is no clear physical justification for this and the adapted Born force model is to be preferred.

15.4 MODELLING - FURTHER WORK.

There are a number of further modelling studies of the VDOS of B_2O_3 which could usefully be performed. In particular a calculation of the VDOS of a ball-and-stick model with boroxol rings based on a force model which differentiates between boroxol rings and isolated triangles should be performed in order to confirm whether this produces the predicted improvement in agreement with experiment. Also a calculation for a ball-and-stick model containing only boroxol rings would show whether network dynamics studies can differentiate between a CRN containing only boroxol rings and a CRN of boroxol rings and BO_3 triangles. Such a model could be constructed by a topological transformation of the model with no boroxol rings. The density of the resultant model would be considerably different from the density of B_2O_3, but this would probably not matter much for an initial calculation of the VDOS. The calculations performed on simple molecular units suggest that a calculation of the eigenvectors for these units could be most useful in understanding the nature of the atomic motions associated with the vibrational modes of B_2O_3. Ideally the eigenvectors for the vibrational modes of the ball-and-stick models should be calculated but this appears to require more computational power than is available. If such a calculation could be performed one could envisage being able to calculate the experimental function corresponding to a ball-and-stick model, and it might even be possible to study the distinct part of the scattering function (see for example WALTER, PRICE, SUSMAN and VOLIN (1988) or ARAI, PRICE, SUSMAN, VOLIN and WALTER (1988)). It might also be worthwhile to perform some calculations to confirm assumptions made in the work described in Chapter 14 : It was assumed that the effect of the surface was not important and calculations performed with different boundary conditions would confirm this. The assumption that it is a good approximation to use Born forces for B_2O_3 is based on the findings of previous workers when studying tetrahedral materials and calculations based on the Keating potential or possibly the valence force field could be performed to confirm whether this is so.

CHAPTER 16

FINAL CONCLUSIONS.

A complete exposition of the theory of neutron scattering from amorphous solids has been given. This has enabled the neutron scattering experiments discussed in subsequent chapters to be analysed with a high level of confidence and comprehension. Furthermore data analysis errors in the work of some other authors have been identified, explained and corrected. Also the theory of atomic vibrations has been presented using a non-standard form which is particularly well suited to numerical calculations of vibrational properties.

The partial structure factors and correlation functions of the amorphous metal Dy_7Ni_3 have been extracted by use of the neutron diffraction double null isotopic substitution technique. This experiment is one of the most well-conditioned partial structure factor measurements ever undertaken, although the data analysis proved exceptionally complicated due to instrumental difficulties and the presence of magnetic scattering. However, the use of the double null isotopic substitution technique enabled the magnetic scattering to be separated in a uniquely exact way.

The first peaks of the Dy-Dy and Dy-Ni partial correlation functions of Dy_7Ni_3 were found to exhibit a marked asymmetry which was ascribed to static disorder. For each of these partial correlation functions the static disorder within the first coordination shell was successfully modelled by two well-defined distances. No such asymmetry was found in the first peak of the Ni-Ni partial correlation function which was modelled by a single distance. The nearest neighbour distances, partial coordination numbers and RMS variations of interatomic distances are not given here since it is misleading to quote these out of context. There was clear evidence for a small degree of chemical ordering in the alloy. Chemical short range order parameters were considered and shown to be of doubtful value.

When interpreted from a hard sphere viewpoint the nearest neighbour distances of Dy_7Ni_3 indicate that the Ni atoms are 'close but not touching'. Thus the three nearest neighbour distances disagree fundamentally with a random close packing of hard spheres. However, it was shown that the features of the Dy-Dy partial correlation function can be interpreted successfully in terms of hard sphere configurations. The need to explicitly include the Ni atoms in a model of the atomic structure of Dy_7Ni_3 was also demonstrated. The nearest neighbour distances were used to deduce atomic radii r_{Dy}=1.765Å and r_{Ni}=1.072Å, leading to a radius ratio σ_r=0.607 and a total packing density η=0.6964 . A hole-filling argument was found to be useful and this indicated the trigonal prism as the stable Ni coordination polyhedron.

The measured partial functions of Dy_7Ni_3 were compared with the following structural models from the literature: the Percus-Yevick equation solved for a binary hard sphere potential, a hand-built random close packing of hard spheres of a single size together with interstitial minority atoms, trigonal prismatic models and crystal-based models. None of the models were found to explain the data at all well. However, the possibility of improving each of the models was considered. It was predicted that any model based on a pure hard sphere approach will be unable to explain the data. However, a modified potential could show more promise. The model which has the most scope for improvement is the trigonal prismatic model. The Dy_3Ni_2 crystal structure was used as a basis to indicate a possible improved trigonal prismatic model. Such a model would have distorted trigonal prisms, a large number of groups of two square face sharing prisms and Dy atoms in half-octahedral configuration, probably as part of the Fe_3C triangle side sharing configuration.

Whilst the presence of magnetic neutron scattering from Dy_7Ni_3 was a complication for the study of atomic structure, it had the advantage that it enabled some particularly elegant magnetic neutron scattering experiments to be performed by further use of the double null isotopic substitution technique. A particularly accurate study of the magnetic diffraction pattern as a function of temperature was performed without the usual interference from distinct nuclear scattering. It was found that there is a persistence of short range magnetic correlations at temperatures considerably in excess of the reported asymptotic Curie temperature 35K. The data were Fourier transformed on the assumption of zero magnetic anisotropy and the resultant magnetic correlation functions were found to be similar to the Dy-Dy partial nuclear correlation function. Following this it was concluded that the magnetic moments are on the Dy ions only (the Ni moments are quenched) and that the nearest neighbour interaction is ferromagnetic in character. Also the indications are that magnetic anisotropy is small.

The double null isotopic substitution technique also enabled a unique measurement to be made of the spherical contribution to the Dy^{3+} magnetic form factor in amorphous Dy_7Ni_3 as a continuous function of Q. This was compared with a theoretical Hartree-Fock calculation and the unpaired 4f electrons of Dy^{3+} in Dy_7Ni_3 were found to be more highly localised than predicted theoretically. The magnitude of the Dy moments was shown to be close to the free ion value. The experimental form factor exhibits a rise at low Q and this is thought to be due to a conduction electron polarisation. An electron distribution function was extracted from the experimental form factor and this was found to peak at 0.228Å.

The homogeneity of the melt-spun amorphous Dy_7Ni_3 ribbons was studied by small angle neutron scattering. The signal at room temperature was found to be very small and was shown to be reasonably consistent with the idea that it is due to surface scattering. It is thus concluded that the bulk of the sample is highly homogeneous. The evolution of magnetic order in Dy_7Ni_3 as a function of temperature was also studied by small angle neutron scattering. The behaviour was found to be markedly different from that observed by other workers for Fe-rich RE-Fe amorphous alloys. Above the transition temperature of 35K the lineshape was found to be well described by the sum of a Lorentzian and a Lorentzian squared. However, a successful fit to the data below 35K was not achieved and the indications are that a new functional form is required. The spin correlation lengths obtained by fitting were typically of order 175Å with a slight decrease occurring as the temperature is decreased. A value for the anisotropy to exchange ratio $D_o/J_o \sim 0.023$ was deduced from the typical spin correlation length. The magnetic anisotropy in Dy_7Ni_3 is thus low but non-zero, consistent with the findings of the conventional magnetic diffraction experiment. The appropriate model for the magnetic structure of the random anisotropy magnet Dy_7Ni_3 is the correlated speromagnet.

The second material studied in this thesis is vitreous B_2O_3. The vibrational spectra of B_2O_3 have been used to provide new insight into the controversy regarding the presence of B_3O_6 boroxol rings in the atomic structure. It has been shown that when used in conjunction the results of inelastic neutron scattering and of Raman scattering provide considerable information about the atomic vibrations of glasses and hence information about the atomic structure. Inelastic neutron scattering provides a good experimental measure of the vibrational density of states whilst Raman scattering yields an effective denisty of states in which the modes of highly regular structures are greatly accentuated. Inelastic neutron scattering has been used to measure the vibrational density of states of B_2O_3 at high resolution in the region of the boroxol ring breathing mode (~100meV) and at medium resolution over the whole energy range (0→200meV). It was found that the vibrational density of states has a band of modes from 205meV to 145meV, a gap between 145meV and 110meV, a band of modes centred at 83meV and another band of modes at lower energies. The boroxol ring breathing mode at about 100meV was found to only produce a small barely discernible feature in the vibrational density of states and hence the Raman matrix element for this mode was shown to be exceptionally large. The elastic neutron scattering yielded a value of 0.081Å for the RMS displacement of an atom from equilibrium.

Detailed theoretical calculations of the vibrational density of states have been performed for two of the best available structural models for vitreous B_2O_3, one containing only independent BO_3 triangles and the other including a high concentration of boroxol rings. Born forces were assumed. It was found that both non-central forces and the presence of boroxol rings are required to explain the complexity of the observed phonon spectra. Two methods have been developed for use with calculations of the vibrational density of states whereby the relative magnitude of non-central forces is varied and Raman isotopic substitution data are simulated respectively. A non-central to central force constant ratio of 0.2 gave good consistency with experiment and a high level of agreement was found between the calculated isotope shifts and those measured by Raman scattering. However, evidence was found for a more sophisticated force model with a central force constant of about $420 Nm^{-1}$ inside the boroxol rings and about $580 Nm^{-1}$ outside the boroxol rings. It was concluded that, despite the fact that the boroxol rings breathing mode only contributes a small feature to the vibrational density of states, the phonon spectra of B_2O_3 are consistent with a structural model containing a high proportion of boroxol rings.

APPENDIX A.

OUTER PRODUCTS.

If $\underline{w}$ and $\underline{v}$ are two conformable vectors one may form an object $T_{ij}=w_i v_j$ with nine components, known as the outer product of the two vectors. The second rank tensor $\underline{\underline{T}}$ is sometimes represented by a symbol called a dyad, $\underline{w}\ \underline{v}$ (MATHEWS and WALKER, 1970). Note that the order of vectors in a dyad is important.

The notation of dyads enables the expression $(\underline{u}.\underline{v})\ \underline{w}$ to be written in a form particularly useful for the calculations discussed in chapters 4 and 12. In 3D;

$$
\begin{aligned}
(\underline{u}.\underline{v})\ \underline{w} &= (u_x v_x + u_y v_y + u_z v_z) \begin{pmatrix} w_x \\ w_y \\ w_z \end{pmatrix} \\
&= \begin{pmatrix} v_x w_x, & v_y w_x, & v_z w_x \\ v_x w_y, & v_y w_y, & v_z w_y \\ v_x w_z, & v_y w_z, & v_z w_z \end{pmatrix} \begin{pmatrix} u_x \\ u_y \\ u_z \end{pmatrix} \\
&= \underline{\underline{T}}\ \underline{u}
\end{aligned}
$$

ie;

$$(\underline{u}.\underline{v})\ \underline{w} = (\underline{w}\ \underline{v})\ \underline{u} \qquad \text{(A.1)}$$

This expression is most useful as it enables $(\underline{u}.\underline{v})\ \underline{w}$ to be 'projected' onto $\underline{u}$.

APPENDIX B.

```
      PROGRAM BORN
C
C **************************************************************************
C * A PROGRAM TO CALCULATE THE VDOS OF A CLUSTER MODEL SUBJECT TO BORN     *
C * FORCES AND WITH FREE BOUNDARY CONDITIONS.                              *
C * COPYRIGHT A.C.HANNON 1988.                                             *
C **************************************************************************
C
C INPUT/OUTPUT UNITS ARE DEFINED BY THE CMS FILEDEF COMMAND AS FOLLOWS:
C 96 = file VLIST   (DIAGNOSTIC OUTPUT FROM SPARSPAK)
C 97 = file VDATA   (INPUT PARAMETERS FOR THE RUN)
C 98 = file SPDATA  (OUTPUT RESULTS)
C 99 = model COORDS (COORDINATES AND NEAREST NEIGHBOUR TABLE OF THE MODEL)
C (FORMATS OF THESE FILES ARE DESCRIBED IN THE RELEVANT INPUT/OUTPUT
C  SUBROUTINE.)
C
C SPARSPAK SUBROUTINES REQUIRED BY THE PROGRAM ARE AS FOLLOWS:
C ADAIJ5      BUILD          DTIME          EMSG1          EMSG2
C EMSG3       EMSG4          EMSG5          ERRMSG         FMADJY
C FNDSEP      FNROOT         GENND          GSFCT          GSSLV
C IJBEGN      IJEND          INAIJ5         INIJ           INVRSE
C ORDRA5      PERMRV         PICTUR         PRNTLS         PRNTRV
C PRTIVL      PRTIVS         PRTPIC         PSTATS         RCOPYL
C REORGZ      REVRSE         ROOTLS         SMBFCT         SOLVE5
C SPRSPK      ZEROLS         ZERORV
C
C THE SUBROUTINE ERRSET IS ALSO REQUIRED TO PATCH OVER ERRONEOUS UNDERFLOW
C ERRORS.
C
      IMPLICIT DOUBLE PRECISION (A-H,O-Z),
     +         INTEGER (I-N)
      DIMENSION S(180000)
      DIMENSION NTABLE(2000,12), NUMNN(2000), ITYPE(2000), INEG(0:200)
      DIMENSION COORDS(2000,3), AMASS(10)
      DIMENSION ELMENT(3,3), DIAGEL(3,3)
      INTEGER*4 IA(1)
      INTEGER*4 ICPAD, IERR, IPRNTE, IPRNTS, MAPPTR, MAXS
      INTEGER*4 MSGLVL, MXUSED, NUSER, STAGE
      INTEGER*2 IB(1)
      REAL RATIOL, RATIOS, SVALUE, TIME
      EQUIVALENCE (S,IA,IB)
      COMMON /BLK1/ COORDS
      COMMON /BLK2/ NTABLE, NN, NUMNN, ITYPE
      COMMON /BLK3/ WMIN, WMAX, DELTAW, AMASS, NTYPES
      COMMON /BLK4/ CCENTL, CNONCL
      COMMON /WHY/ NSKIP
      COMMON /SPKUSR/ MSGLVI, IERR, MAXS, NEQNS
      COMMON /SPKSYS/ IPRNTE, IPRNTS, RATIOS, RATIOL, TIME
      COMMON /SPKCON/ STAGE, MXUSED, ICPAD(12)
```

```
      COMMON /SPKMAP/ MAPPTR(15)
      COMMON /SPKDTA/ SVALUE(10)
  101 FORMAT(I8)
  102 FORMAT(A3)
C
C----START--------------------------------------------------------------
      CALL ERRSET(208,256,-1,1,0,0)
C THIS ROUTINE CAUSES THE PROGRAM TO IGNORE ERRONEOUS UNDERFLOW ERRORS.
C
       CALL PARAMS(97,NN)
       CALL READM(99,N,NSKIP)
       WRITE(IPRNTE,103) N
       WRITE(6,103) N
  103  FORMAT(1X,18HNUMBER OF ATOMS N=,I4)
       CALL SPRSPK
       MAXS = 180000
C *****NOTE: IF MAXS IS CHANGED THEN IT IS IMPERATIVE THAT THE DIMENSION
C            OF S IS ALSO CHANGED.
      DO 96 I=1,MAXS
   96 S(I) = 0.0
      MSGLVL = 4
      WZERO = WMIN
      INGOLD = 0
      SMALL = 1.0D-12
      EPS = WZERO*WZERO - SMALL
C
C----INPUT LOCATIONS----------------------------------------------------
      CALL IJBEGN
      DO 31 I=1,N
C FIRST INPUT LOCATION OF DIAGONAL AND SUB-DIAGONAL ELEMENTS
C OF THE SELF SUB-MATRIX OF ATOM I.
      DO 32 I2=3*I-2,3*I
      DO 32 J2=3*I-2,3*I
      IF (I2.LE.J2) GOTO 32
      CALL INIJ(I2,J2,S)
   32 CONTINUE
C
C LOOP OVER NEAREST NEIGHBOURS OF ATOM I.
C
      DO 31 K=1,NUMNN(I)
      J = NTABLE(I,K)
C
C ONLY NEED INPUT SUB-DIAGONAL ELEMENTS OF DYNAMICAL MATRIX,
C SINCE IT IS SYMMETRIC, SO GO ON TO NEXT NEAREST NEIGHBOUR OF
C ATOM I IF (I,J) IS NOT SUB-DIAGONAL.
      IF (I.LT.J) GOTO 31
C
C NOW INPUT THE LOCATION OF THE SUB-MATRIX LINKING ATOMS I AND J
      DO 31 I2=3*I-2,3*I
      DO 31 J2=3*J-2,3*J
      CALL INIJ(I2,J2,S)
   31 CONTINUE
      CALL IJEND(S)
```

```
C----END OF LOCATION INPUT---------------------------------------------
C
C NOW LOCATIONS OF NON-ZEROS ARE KNOWN, REORDER THE PROBLEM.
       CALL ORDRA5(S)
C
C----START OF INPUT OF NUMERICAL VALUES---------------------------------
      M = 0
   69 CONTINUE
      M = M + 1
      DO 80 I=1,N
      CALL MAT3F(DIAGEL,0.0D0)
      DO 46 K=1,NUMNN(I)
      J = NTABLE(I,K)
      CALL CALCEL(I,J,ELMENT)
      IF (I.LT.J) GOTO 43
C INPUT SUB-DIAG ELEMENTS HERE
      DO 90 IIA=1,3
      DO 90 IIB=1,3
      COEFF = SQRT(AMASS(ITYPE(I))*AMASS(ITYPE(J)))
      VALUE = ELMENT(IIA,IIB)/COEFF
   90 CALL INAIJ5(3*I+IIA-3,3*J+IIB-3,VALUE,S)
   43 DO 46 INT1=1,3
      DO 46 INT2=1,3
   46 DIAGEL(INT1,INT2) = DIAGEL(INT1,INT2) - ELMENT(INT1,INT2)
C INPUT SELF ELEMENTS HERE
      DO 80 IIA=1,3
      DO 80 IIB=1,3
      IF (IIA.LT.IIB) GOTO 80
      SHIFT = 0.0D0
      IF (IIA.EQ.IIB) THEN
          SHIFT = EPS
      ENDIF
      COEFF = AMASS(ITYPE(I))
      VALUE = DIAGEL(IIA,IIB)/COEFF
      CALL INAIJ5(3*I+IIA-3,3*I+IIB-3,VALUE-SHIFT,S)
   80 CONTINUE
      CALL LDUND5(S)
C
C IF BY CHANCE HAVE HIT AN EIGENVALUE DIRECTLY (MOST UNLIKELY IN PRACTICE)
C THEN SHIFT ORIGIN VERY VERY VERY SLIGHTLY
      IF (IERR.NE.53) GOTO 68
      IERR = 0
      EPS = EPS - SMALL
      GOTO 69
   68 CONTINUE
C===START OF EIGENVALUE CALCULATION
              IP = MAPPTR(4)
              WRITE(IPRNTE,500) WZERO
              WRITE(6,500) WZERO
  500        FORMAT(/1X,5HWZERO,F8.3)
              IQ = IP + ICPAD(2) - 1
              INEG(M) = 0
              IPOS = 0
```

```
             IZER = 0
                DO 400 JJ=IP,IQ
                IF(S(JJ).GT.0.0D0) GO TO 401
                IF(S(JJ).LT.0.0D0) GO TO 402
                IZER = IZER + 1
                GO TO 400
  401          IPOS = IPOS + 1
                GO TO 400
  402          INEG(M) = INEG(M) + 1
  400          CONTINUE
         INEGD = INEG(M) - INGOLD
         INGOLD = INEG(M)
             WRITE(6,26) INEG(M), IZER, IPOS
   26        FORMAT(1X, 12HNEG ZER POS ,3I5)
        WZERO = WZERO + DELTAW
      EPS = WZERO*WZERO
        IF (IPOS.EQ.0) GOTO 67
        IF (WZERO.LE.WMAX) GOTO 69
C===END OF EIGENVALUE CALCULATION
   67  CALL SPDATA(N,M,DELTAW,INEG)
       CALL PSTATS
       END
C
C-----------------------------------------------------------------------
C
      SUBROUTINE MAT3F(ARRAY,FACTOR)
C
C MULTIPLY A 3X3 MATRIX BY A FACTOR (WHICH CAN BE ZERO TO NULL THE MATRIX)
C
      IMPLICIT DOUBLE PRECISION (A-H,O-Z),
     +         INTEGER (I-N)
      DIMENSION ARRAY(3,3)
      DO 70 IS2=1,3
      DO 70 IS3=1,3
   70 ARRAY(IS2,IS3) = ARRAY(IS2,IS3)*FACTOR
      END
C
C-----------------------------------------------------------------------
C
      SUBROUTINE CALCEL(I,J,ELMENT)
C
C CALCULATE THE STRUCTURAL PART OF THE DYNAMICAL SUB-MATRIX LINKING
C ATOMS I AND J WHERE (I.NE.J)
C
      IMPLICIT DOUBLE PRECISION (A-H,O-Z),
     +         INTEGER (I-N)
      DIMENSION COORDS(2000,3), ELMENT(3,3)
      DIMENSION SEPVEC(3)
      COMMON /BLK1/ COORDS
      COMMON /BLK4/ CCENTL, CNONCL
      SEPSQ = 0.0D0
      DO 60 IS1=1,3
      SEPVEC(IS1) = COORDS(I,IS1) - COORDS(J,IS1)
```

```
   60 SEPSQ = SEPSQ + SEPVEC(IS1)*SEPVEC(IS1)
      CALL DYAD(SEPVEC,SEPVEC,ELMENT)
      CALL MAT3F(ELMENT,-(CCENTL-CNONCL)/SEPSQ)
      DO 61 L1=1,3
   61 ELMENT(L1,L1) = ELMENT(L1,L1) - CNONCL
      END
C
C----------------------------------------------------------------------
C
      SUBROUTINE READM(M,N,NSKIP)
C
C THIS ROUTINE READS IN THE NTABLE AND COORDS OF A CLUSTER MODEL,
C ALSO RETURNING THE NUMBER OF ATOMS N.
C
C INPUT FILE = model COORDS
C FORMAT IS:
C NSKIP LINES OF COMMENTS
C ONE RECORD FOR EACH ATOM : INDEX NUMBER OF ATOM, TYPE OF ATOM,
C COORDINATES OF ATOM, NEAREST NEIGHBOUR TABLE OF ATOM.
C
      IMPLICIT DOUBLE PRECISION (A-H,O-Z),
     +         INTEGER (I-N)
      DIMENSION COORDS(2000,3)
      DIMENSION NTABLE(2000,12), NUMNN(2000), ITYPE(2000)
      COMMON /BLK1/ COORDS
      COMMON /BLK2/ NTABLE, NN, NUMNN, ITYPE
C
      DO 51 IR=1,NSKIP
   51 READ(M,*)
C
      N = 0
   52 N = N + 1
      READ(M,*,END=53) NR, ITYPE(N), (COORDS(N,JR),JR=1,3),
     +                 (NTABLE(N,IR),IR=1,NN)
      GOTO 52
   53 N = N - 1
      DO 55 IR=1,N
      NUMNN(IR) = NN + 1
   54 NUMNN(IR) = NUMNN(IR) - 1
      IF (NTABLE(IR,NUMNN(IR)).EQ.0) GOTO 54
   55 CONTINUE
      END
C
C----------------------------------------------------------------------
C
      SUBROUTINE PARAMS(M,NN)
C
C READ IN THE INPUT PARAMETERS FOR THE CALCULATION FROM file VDATA.
C FORMAT IS:
C NAME OF PROGRAM TO BE RUN, NAME OF COORDS FILE
C NUMBER OF ENTRIES IN NEAREST NEIGHBOUR TABLE, NUMBER OF ATOM TYPES, NSKIP
C MINIMUM NORMAL FREQUENCY, MAXIMUM NORMAL FREQUENCY, NORMAL FREQUENCY STEP
C MASSES
```

```
C FORCE CONSTANTS
C
-     IMPLICIT DOUBLE PRECISION (A-H,O-Z),
     +         INTEGER (I-N)
      DIMENSION AMASS(10)
      COMMON /BLK3/ WMIN, WMAX, DELTAW, AMASS, NTYPES
      COMMON /BLK4/ CCENTL, CNONCL
      COMMON /WHY/ NSKIP
      READ(M,*)
      READ(M,*) NN, NTYPES, NSKIP
      READ(M,*) WMIN, WMAX, DELTAW
      READ(M,*) (AMASS(IP),IP=1,NTYPES)
      READ(M,*) CCENTL, CNONCL
      END
C
C---------------------------------------------------------------------------
C
      SUBROUTINE SPDATA(N,M,DELTAW,INEG)
C
C OUTPUT THE RESULTS OF THE CALCULATION TO file SPDATA
C FORMAT IS:
C TEXT LINE
C NUMBER OF ATOMS, MAXIMUM NORMAL FREQUENCY OF CALCULATED VDOS, NORMAL -
C - FREQUENCY STEP
C TEXT LINE
C A NUMBER OF RECORDS COVERING THE NORMAL FREQUENCY RANGE:
C NORMAL FREQUENCY, NUMBER OF NEGATIVE EIGENVLAUES, CHANGE IN NUMBER OF -
C - NEGATIVE EIGENVALUES
C
      IMPLICIT DOUBLE PRECISION (A-H,O-Z),
     +         INTEGER (I-N)
      DIMENSION INEG(0:200)
      WRITE(98,100) 'N      WMAX      DELTAW'
      WRITE(98,14) N, M*DELTAW, DELTAW
   14 FORMAT(I5,2F8.3)
      WRITE(98,100) 'WZERO   INEG     DELTAINEG'
  100 FORMAT(A)
      INEGD = 0
      DO 88 IS=0,M-1
      INEGD = INEG(IS+1) - INEG(IS)
   88 WRITE(98,17) IS*DELTAW, INEG(IS+1), INEGD
   17 FORMAT(F8.3,2I5)
      END
C
C---------------------------------------------------------------------------
C
      SUBROUTINE DYAD(V,W,OUTPRD)
C
C THIS ROUTINE CALCULATES THE OUTER PRODUCT OF THE TWO VECTORS V AND W.
C THIS IS USEFUL WHEN WE HAVE THE FORM (U.V)W {U IS ALSO A VECTOR}
C AS THIS IS EQUAL TO OUTPRD U.
C
      IMPLICIT DOUBLE PRECISION (A-H,O-Z),
```

```
     +          INTEGER (I-N)
      DIMENSION V(3), W(3), OUTPRD(3,3)
      DO 89 ID=1,3
      DO 89 JD=1,3
   89 OUTPRD(ID,JD) = V(ID)*W(JD)
      END
C
C---------------------------------------------------------------------------
C
         SUBROUTINE LDUFCT (NEQNS,XLNZ,LNZ,XNZSUB,NZSUB,DIAG,
     1                      LINK,FIRST,TEMP,IFLAG)
C
C MODIFIED VERSION OF THE SPARSPAK SUBROUTINE GSFCT TO PERFORM THE
C LDU FACTORISATION.
C BY J.A.BLACKMAN.
C
         DOUBLE PRECISION COUNT,OPS
         COMMON /SPKOPS/ OPS
         DOUBLE PRECISION DIAG(1),LNZ(1),TEMP(1),
     1           DIAGJ,LJK
         INTEGER*2 LINK(1),NZSUB(1)
         INTEGER*4 FIRST(1),XLNZ(1),XNZSUB(1),
     1           I,IFLAG,II,ISTOP,ISTRT,ISUB,J,
     1           K,KFIRST,NEQNS,NEWK
         DO 100 I=1,NEQNS
         LINK(I)=0
         TEMP(I)=0D0
  100    CONTINUE
         DO 600 J=1,NEQNS
         DIAGJ=0.0D0
         NEWK=LINK(J)
  200    K=NEWK
         IF(K.EQ.0)GO TO 400
         NEWK=LINK(K)
         KFIRST=FIRST(K)
         LJK=LNZ(KFIRST)
C **********  CHANGE FROM GSFCT
         DIAGJ=DIAGJ+LJK*LJK*DIAG(K)
         OPS=OPS+1.0D0
         ISTRT=KFIRST+1
         ISTOP=XLNZ(K+1)-1
         IF(ISTOP.LT.ISTRT)GO TO 200
         FIRST(K)=ISTRT
         I=XNZSUB(K)+(KFIRST-XLNZ(K))+1
         ISUB=NZSUB(I)
         LINK(K)=LINK(ISUB)
         LINK(ISUB)=K
         DO 300 II=ISTRT,ISTOP
         ISUB=NZSUB(I)
C **********  CHANGE FROM GSFCT
         TEMP(ISUB)=TEMP(ISUB)+LNZ(II)*LJK*DIAG(K)
         I=I+1
  300    CONTINUE
```

```
        COUNT=ISTOP-ISTRT+1
        OPS=OPS+COUNT
        GO TO 200
  400   DIAGJ=DIAG(J)-DIAGJ
        IF(DIAGJ.EQ.0.0D0)GO TO 700
C***********  CHANGE FROM GSFCT
         DIAG(J)=DIAGJ
         ISTRT=XLNZ(J)
        ISTOP=XLNZ(J+1)-1
        IF(ISTOP.LT.ISTRT)GO TO 600
        FIRST(J)=ISTRT
        I=XNZSUB(J)
        ISUB=NZSUB(I)
        LINK(J)=LINK(ISUB)
        LINK(ISUB)=J
        DO 500 II=ISTRT,ISTOP
        ISUB=NZSUB(I)
        LNZ(II)=(LNZ(II)-TEMP(ISUB))/DIAGJ
        TEMP(ISUB)=0.0D0
        I=I+1
  500   CONTINUE
        COUNT=ISTOP-ISTRT+1
        OPS=OPS+COUNT
  600   CONTINUE
        RETURN
  700   IFLAG=1
        RETURN
        END
```

APPENDIX C.

COORDINATES OF B2O3 STRUCTURAL UNITS.

The coordinates of a BO_3 triangular structural unit and of a B_3O_6 boroxol ring (see figure 10.1) are given in units of one bond length for the case where the unit lies in the x-y plane:

BO3 TRIANGLE.

B	(0,0)
O_1	(0,1)
O_2	(-0.8660,-0.5)
O_3	(0.8660,-0.5)

All z=0.

B3O6 BOROXOL RING.

B_1	(0,0)
B_2	(-0.8660,-1.5)
B_3	(0.8660,-1.5)
O_1	(0,1)
O_2	(-0.8660,-0.5)
O_3	(0.8660,-0.5)
O_4	(-1.7321,-2)
O_5	(0,-2)
O_6	(1.7321,-2)

All z=0.

APPENDIX D.

LIST OF ABBREVIATIONS.

BORN	Fortran Program to Calculate the VDOS of a Cluster Model.
BT	BHATIA and THORNTON, 1970.
CON	Chemically Ordered Network.
CRN	Continuous Random Network.
CSM	Correlated Speromagnet.
CSRO	Chemical Short Range Order.
EXAFS	Extended X-Ray Absorption Fine Structure.
FZ	FABER and ZIMAN, 1964.
HPZ	HARRIS, PLISCHKE and ZUCKERMANN, 1973.
HRMECS	High Resolution Medium Energy Chopper Spectrometer.
ILL	Institut Laue Langevin.
IPNS	Intense Pulsed Neutron Source.
IR	Infrared Absorption.
IRO	Intermediate Range Order.
LJ	Lennard-Jones.
LL^2	Sum of a Lorentzian and a Lorentzian Squared.
LO	Longitudinal Optic.
LRMECS	Low Resolution Medium Energy Chopper Spectrometer.
LRO	Long Range Order.
M	Metalloid.
MD	Molecular Dynamics.
NET	Negative Eigenvalue Theorem.
NMR	Nuclear Magnetic Resonance.

ORNL	Oak Ridge National Laboratory.
PY	PERCUS and YEVICK, 1957.
RAM	Random Anisotropy Magnetism.
RCN	Random Covalent Network.
RCP	Random Close Packing.
RDF	Radial Distribution Function.
RE	Rare Earth.
RE-TL	Rare Earth-Late Transition Metal (Alloy).
RMS	Root Mean Square.
SANS	Small Angle Neutron Scattering.
SAS	Small Angle Scattering.
SG	Spin Glass.
SM	Speromagnet.
SRO	Short Range Order.
T	Transition Metal.
T-M	Transition Metal-Metalloid (Alloy).
TE-TL	Early Transition Metal-Late Transition Metal (Alloy).
TO	Transverse Optic.
TOF	Time Of Flight.
VDOS	Vibrational Density of States.
WANS	Wide Angle Neutron Scattering.
1D	One Dimension, One Dimensional.
2D	Two Dimensions, Two Dimensional.
3D	Three Dimensions, Three Dimensional.

APPENDIX E.

LIST OF SYMBOLS.

a	atomic spacing
a_s, a_s^+	annihilation and creation operators for mode s
a(r)	isotropic function for magnetic diffraction
$\underline{\underline{A}}$	inversion matrix for separation of partials
$\lvert A \rvert_E$	Euclidean norm
$A(2\Theta)$	attenuation factor for an infinite plate
A_p	particle surface area
b	scattering length
$\bar{b}$	coherent nuclear scattering length
$\overline{b^2}$	mean square scattering length
$\langle\overline{b^2}\rangle$	averaged mean square scattering length
$b^{+/-}$	scattering length for $I\pm\frac{1}{2}$ compound nucleus
b(r)	anisotropic function for magnetic diffraction
c_1	composition variable for element 1
c(r)	direct correlation function
cc	(subscript) Bhatia-Thornton concentration-concentration function
coh	(superscript) coherent
C_1, C_2, C_3	detector constants
d_1	moderator-chopper distance
d_2	chopper-sample distance
d_3	sample-detector distance
$\underline{d}_{jj'}$	interatomic bond
$d_{ll'}(r)$	(differential) partial pair correlation function

D	(superscript) distinct
D_i	anisotropy interaction parameter
D_M	mass fractal dimension
D_S	surface fractal dimension
D_0	average anisotropy interaction parameter
$D(r)$	total (differential) correlation function
$\underline{D}_{ijk}$	atomic coordinates vector
$\underline{e}_i$	atomic displacement in normal coordinates
$\underline{e}_j^s$	polarisation vector of atom j in mode s
eff	(subscript) effective
E, E'	initial and final neutron energy
E_i	error on data point
E_λ	energy of the state $\|\lambda\rangle$
f	fraction of boron atoms in B_2O_3 in boroxol rings
$f(k')$	detector efficiency
$f(\underline{Q})$	magnetic form factor
f_i	abundance of isotope i
f_n	n^{th} derivative of $f(k')$ with respect to k', evaluated at $k=k'$
F	agreement factor from fit
$\underline{F}$	force
$g(\omega)$	vibrational density of states (VDOS)
$g_{ll'}(r)$	partial pair distribution function
$g^{eq}(r)$	equilibrium pair distribution function
$g_m(r)$	normalised density of unpaired electrons
g^0	macroscopic atomic number density
$g_{+/-}(r)$	charge density of electron spin state +/- in ion
$G(\underline{r},t)$	Van Hove correlation function

$G(\underline{Q},\omega)$	generalised phonon density of states
h	Planck's constant
$\hbar$	$h/2\pi$
H	Hamiltonian
i	index for isotopes
$i(Q)$	distinct scattering cross-section
inc	(superscript) incoherent
I	nuclear spin
$\underline{\underline{I}}$	unit matrix
I^m	measured cross-section
I^t	true cross-section
$I(Q)$	total diffraction cross-section
I^S	self scattering diffraction cross-section
j, j'	index for nuclei in the sample
J_{ij}	exchange interaction parameter
J_o	average exchange interaction parameter
k	number of variable parameters in fit
$\underline{k}, \underline{k}'$	initial and final neutron wavevector
l	characteristic length for variation of $\rho_b(\underline{r})$
l, l'	index for elements in sample
l/L	index for minority/majority atoms
L	model diameter, ribbon length
m	neutron mass
m_e	electron rest mass
m_p	proton rest mass
M	(superscript) magnetic

$\bar{M}$	averaged atomic mass
M_l	mass of nucleus of element l
M(Q)	modification function
$\underline{M}(\underline{r})$	magnetisation density
$\underline{n}_i$	local easy axis
$\langle n_s \rangle$	population factor of mode s
$n_{ll'}$	partial coordination number
$n_{ll'}(r)$	partial radial distribution function (RDF)
$n^{*}_{ll'}(r)$	partial RDF - alternative definition
nc	(subscript) Bhatia-Thornton number-concentration function
nn	(subscript) Bhatia-Thornton number-number function
nuc	(superscript) nuclear contribution for the $^{N}Dy_7{}^{N}Ni_3$ sample
N	number of atoms in sample, number of data points in fit
N_p	number of particles
N_u	number of composition units in sample
NN	(superscript/subscript) $^{N}Dy_7{}^{N}Ni_3$ sample
NO	(superscript/subscript) $^{N}Dy_7{}^{0}Ni_3$ sample
$\underline{p}$	electron momentum
$\underline{p}_l$	momentum of atom of element l
p_λ	probability of state $\|\lambda\rangle$
p_σ	probability distribution of polarisation of incident neutrons
P	Porod slope
P(r)	peak function
$\underline{q}$	phonon wavevector
$\underline{Q}$	momentum transferred to sample
Q_0	magnitude of $\underline{Q}$ for elastic scattering

Q_1	Q-value of first peak in S(Q)
r	ratio of number of boroxol rings in B_2O_3 to number of independent triangles, force constant ratio
$\underline{r}$	distance vector
r_1	hard sphere radius
r_0	classical electron radius
R	radius of cylindrical sample
$\underline{R}$	position vector of a nucleus in the sample
R_c	spatial correlation of easy axes
R_G	radius of gyration
$\underline{s}$	electron spin operator
sa	(subscript) static approximation
S	(superscript) self
$\underline{S}$	ionic angular momentum
S(Q)	structure factor
$S_n(Q)$	nth moment of scattering function
$S(\underline{Q},\omega)$	scattering function
$S^{el}(Q,\omega)$	elastic scattering function
$S^m(Q_0,\omega)$	mth derivative of $S(Q,\omega)$ with respect to Q^2, evaluated at $Q=Q_0$
$S^p(Q,\omega)$	p-phonon scattering function
t	time, thickness of plate sample
t_1	time at which chopper is open
Δt_m	pulse width of source
Δt_r	opening time of chopper
$t_{ll'}(r)$	partial pair correlation function
T	Turing's number, transmission, temperature
T_f, T_g, T_m	fictive-, glass-, melting- temperature

$T(r)$	total correlation function
$T^{0}(r)$	constant density contribution to total correlation function
$\underline{u}$	atomic displacement
$\langle u_l{}^2 \rangle$	mean square atomic displacement for element l
$\overline{\langle u^2 \rangle}$	averaged mean square atomic displacement
$\langle u_{l\alpha}{}^2 \rangle$	mean square atomic displacement in a specified direction for element l
$\langle u_{ll'}{}^2 \rangle^{1/2}$	RMS bond length variation
UN	(superscript/subscript) unlike-atom contribution for the $^{N}Dy_7{}^{N}Ni_3$ sample
$\underline{\underline{v}}_{ij}$	sub-matrix
$V(\underline{r})$	potential describing the interaction between a neutron and the sample
V_p	particle volume
$\underline{\underline{w}}_{ij}$	dynamical dub-matrix
W	ribbon width
$\underline{\underline{W}}$	dynamical matrix
$\exp(-W_{ll'})$	Debye-Waller factor
x	$Q/4\pi$, composition variable
$\underline{y}$	atomic displacements vector
z	composition variable
$z_{ll'}(R)$	partial integrated coordination number
ON	(superscript/subscript) $^{0}Dy_7{}^{N}Ni_3$ sample
OO	(superscript/subscript) $^{0}Dy_7{}^{0}Ni_3$ sample
α	index for Cartesian directions, Keating bond stretch force

	constant, angle between neutron beam and normal to a plate sample
α_l	Wagner and Ruppersberg's CSRO parameter
$\alpha(R)$	CSRO function
β	index for Cartesian directions, Keating bond bend force constant
δ_m	effective moderator thickness
$\delta(x)$	Dirac delta-function
$\delta_{jj'}$	Kronecker delta
Δ	$Q^2-Q_0^2$
$\Delta^a_{ll'}(r)$	anisotropic magnetic correlation function
$\Delta^i_{ll'}(r)$	isotropic magnetic correlation function
$\Delta^i_f(r)$	Finbak magnetic correlation function
ε	energy transferred to sample
γ	detector efficiency constant
$\Gamma(\underline{r},t)$	Van Hove magnetic correlation function
κ	inverse spin correlation length
$\bar{\kappa}_l$	average kinetic energy of atom of element l
$\|\lambda\rangle$	scattering system state
λ^c	central force constant
λ^{nc}	non-central force constant
Λ_r	parameter for magnetic structure
μ	reduced mass of nucleus-neutron system
μ_A	linear absorption coefficient
μ_l	M_l/m
$\underline{\mu}$	ionic magnetic moment
$\underline{\mu}_\perp$	component of $\underline{\mu}$ perpendicular to $\underline{Q}$
μ_B	Bohr magneton

μ_N	nuclear magneton
η	Cargill and Spaepen's CSRO parameter
η_1	partial packing density
ω	$\varepsilon/\hbar$
ω'	dimensionless normal frequency of modes
$\Delta\omega'$	isotope shift of a mode
$\Delta\hbar\omega$	energy resolution width
ω_s	angular frequency of mode s
Ω	solid angle
Π	parallel
ϕ	azimuthal angle
$\phi(r)$	interatomic potential
Φ	neutron flux
ψ_{sc}	scattered neutron wavefunction
ρ	density
ρ'	effective density
$\rho(\underline{r},t)$	particle density operator
$\rho_b(\underline{r})$	scattering length density
ρ_b^o	average scattering length density
$\rho_b'(\underline{r})$	deviation of scattering length density from average
ρ_{bm}	matrix scattering length density
ρ_{bp}	particle scattering length density
σ, σ'	initial and final neutron spin
$\underline{\sigma}$	neutron Pauli spin operator
σ_r	radius ratio
σ_{total}	total cross-section for an interaction between a neutron and the

	sample.
$\frac{d\sigma}{d\Omega}$	differential cross-section
$\frac{d^2\sigma}{d\Omega d\varepsilon}$	double differential cross-section
2θ	scattering angle
V	sample volume
ζ	displacement variable
ξ	spin correlation length
$\perp$	perpendicular

APPENDIX F.

LIST OF FIGURES.

CHAPTER 2

CHAPTER 4

CHAPTER 5

CHAPTER 6

CHAPTER 7

CHAPTER 8

CHAPTER 9

CHAPTER 10

CHAPTER 11

CHAPTER 12

CHAPTER 13

CHAPTER 14

REFERENCES.

C.J.ADKINS, Equilibrium Thermodynamics, Second edition (McGraw-Hill(UK), London, 1975)p.245.

B.K.AGRAWAL, J. Non-Crystalline Solids 72(1985)191.

A.AHARONY, Phys. Rev. B 12(1975)1038.

A.AHARONY and E.PYTTE, Phys. Rev. B 27(1983)5872.

R.ALBEN, D.WEAIRE, J.E.SMITH Jr. and M.H.BRODSKY, Phys. Rev. B 11(1975)2271.

R.ALBEN, J.J.BECKER and M.C.CHI, J. Appl. Phys. 49(1978)1653.

H.A.ALPERIN, S.J.PICKART and J.J.RHYNE, J. Appl. Cryst. 11(1978)648.

M.AMINI, S.K.MITRA and R.W.HOCKNEY, J. Phys. C 14(1981)3689.

M.ARAI, D.L.PRICE, S.SUSMAN, K.J.VOLIN and U.WALTER, Phys. Rev. B 37(1988)4240.

R.ARRESE-BOGGIANO, J.CHAPPERT, J.M.D.COEY, A.LIÉNARD and J.P.REBOUILLAT, J. Phys. Colloque C6(1976)771.

N.W.ASHCROFT and D.C.LANGRETH, Phys. Rev. 156(1967)685.

M.ATZMON, K.M.UNRUH, C.POLITIS and W.L.JOHNSON, in: Rapidly Solidified Alloys and Their Mechanical and Magnetic Properties (Mater. Res. Soc., Pittsburgh, 1985)p.27.

M.ATZMON, 1986, Private Communication.

J.D.AXE and R.M.NICKLOW, Physics Today January(1985)27.

B.BARBARA and B.DIENY, Physica 130B(1985)245.

B.BARBARA, B.DIENY, A.LIÉNARD, J.P.REBOUILLAT, B.BOUCHER and J.SCHWEIZER, Solid State Commun. 55(1985)463.

B.BARBARA, M.COUACH and B.DIENY, Europhys. Lett. 3(1987)1129.

R.A.BARRIO, F.L.GALEENER and E.MARTINEZ, Phys. Rev. Lett. 52(1984)1786.

D.BEEMAN and R.ALBEN, Adv. Phys. 26(1977)339.

J.BELL and B.JOHNSTONE, New Scientist 21st March 1985 p36.

R.J.BELL, N.F.BIRD and P.DEAN, J. Phys. C 1(1968)299.

R.J.BELL and P.DEAN, Disc. Faraday Soc. 50(1970)55.

R.J.BELL and P.DEAN, Phil. Mag. 25(1972)1381.

R.J.BELL, A.CARNEVALE, C.R.KURKJIAN, and G.E.PETERSON, J. Non-Crystalline Solids 35&36(1980)1185.

R.J.BELL and A.CARNEVALE, Phil. Mag. B 43(1981)389.

R.J.BELL in: Excitations in Disordered Systems, ed. M.F.Thorpe (Plenum Press, New York, 1982)p. 347.

J.D.BERNAL, Nature 183(1959)141.

J.D.BERNAL, Nature 185(1960)68.

J.D.BERNAL, Proc. Roy. Soc. A 280(1964)299.

J.D.BERNAL, I.A.CHERRY, J.L.FINNEY and K.R.KNIGHT, J. Phys. E 3(1970)388.

B.BERNU, J.P.HANSEN, Y.HIWATARI and G.PASTORE, Phys. Rev. A 36(1987)4891.

B.BERNU, Y.HIWATARI and J.P.HANSEN, J. Phys. C 18(1985a)L371.

B.BERNU, Y.HIWATARI and J.P.HANSEN, J. Phys. Colloque C8(1985b)323.

F.BETTS, A.BIENENSTOCK and S.R.OVSHINSKY, J. Non-Crystalline Solids 4(1970)554.

A.B.BHATIA and D.E.THORNTON, Phys. Rev. B 2(1970)3004.

P.J.BLACK and J.A.CUNDALL, Acta Cryst. 19(1965)807.

J.A.BLACKMAN, 1984, Private Communication.

J.S.BLAKEMORE, Solid State Physics (Cambridge University Press, Cambridge, 1969) p.1.

I.A.BLECH and B.L.AVERBACH, Physics 1(1964)31.

M.BLUME, A.J.FREEMAN and R.E.WATSON, J. Chem. Phys. 37(1962)1245.

M.BORN, Annln. Phys. 44(1914)605.

B.BOUCHER, A.LIÉNARD, J.P.REBOUILLAT and J.SCHWEIZER, J. Phys. F 9(1979a)1421.

B.BOUCHER, A.LIÉNARD, J.P.REBOUILLAT and J.SCHWEIZER, J. Phys. F 9(1979b)1433.

B.BOUCHER, P.CHIEUX, P.CONVERT, R.TOURBOT and M.TOURNARIE, in: Proc. 5th Int. Conf. on Rapidly Quenched Metals, (Elsevier, Amsterdam, 1985) p.1169.

B.BOUCHER, P.CHIEUX, P.CONVERT, R.TOURBOT and M.TOURNARIE, J. Phys. F 16(1986)1821.

J.X.BOUCHERLE, D.GIVORD and J.SCHWEIZER, J. Phys. Colloque C7(1982)199.

D.S.BOUDREAUX and J.M.GREGOR, J. Appl. Phys. 48(1977)152.

T.W.BRIL, Philips Res. Repts. Suppl. 2(1976).

J.P.BRONSWIJK and E.STRIJKS, J. Non-Crystalline Solids 24(1977)145.

A.D.BRUCE, J. Phys. C 14(1981)193.

S.K.BURKE, R.CYWINSKI and B.D.RAINFORD, J. Appl. Cryst. 11(1978)644.

K.H.J.BUSCHOW, J. Magn. Magn. Mater. 21(1980)97.

G.S.CARGILL III, J. Appl. Phys. 41(1970)2249.

G.S.CARGILL III, AIP Conf. Proc. 18(1974)631.

G.S.CARGILL III, Solid State Physics 30(1975)227.

G.S.CARGILL III and S. KIRKPATRICK, AIP Conf. Proc. 31(1976)339.

G.S.CARGILL III, in: Diffraction Studies on Non-Crystalline Substances, eds. I.Hargittai and W.J.Orville-Thomas (Elsevier, Amsterdam, 1981)p.781.

G.S.CARGILL III and F.SPAEPEN, J. Non-Crystalline Solids 43(1981)91.

J.M.CARPENTER and C.A.PELIZZARI, Phys. Rev. B 12(1975)2397.

J.M.CARPENTER, D.L.PRICE and N.J.SWANSON (eds.), 'IPNS - A National Facility for Condensed Matter Research', Argonne Laboratory Report

ANL-78-88, Illinois, 1978.

J.M.CARPENTER, Nucl. Instr. and Meth. 175(1980)287.

J.M.CARPENTER, G.H.LANDER and C.G.WINDSOR, Rev. Sci. Instrum. 55(1984)1019.

J.M.CARPENTER and D.L.PRICE, Phys. Rev. Lett. 54(1985)441.

J.CHADWICK, Proc. Roy. Soc. A 136(1932)692.

E.CHASON and F.SPAEPEN, J. Appl. Phys. (1988) in press.

P.CHAUDHARI and D.TURNBULL, Science 199(1978)4324.

E.M.CHUDNOVSKY and R.A.SEROTA, Phys. Rev. B 26(1982)2697.

E.M.CHUDNOVSKY and R.A.SEROTA, J. Phys. C 16(1983)4181.

E.M.CHUDNOVSKY, W.M.SASLOW and R.A.SEROTA, Phys. Rev. B 33(1986)251.

A.G.CLARE, PhD Thesis, University of Reading(1986).

J.M.D.COEY and P.W.READMAN, Nature 246(1973)478,
also see Nature 246(1973)445.

J.M.D.COEY, J.CHAPPERT and T.S.WANG, Phys. Rev. Lett. 36(1976)1061.

M.H.COHEN and D.TURNBULL, Nature 203(1964)964.

G.A.N.CONNELL and G.LUCOVSKY, J. Non-Crystalline Solids 31(1978)123.

J.R.D.COPLEY, D.L.PRICE and J.M.ROWE, Nucl. Instr. and Meth. 107(1973)501.

J.R.D.COPLEY, Comp. Phys. Comm. 9(1975)59.

J.M.COWLEY, J. Appl. Phys. 21(1950)24.

R.A.COWLEY, L.D.CUSSEN and N.COWLAM, To be published, 1988.

M.F.DANIEL, A.J.LEADBETTER, A.C.WRIGHT and R.N.SINCLAIR, J. Non-Crystalline Solids 32(1979)271.

L.B.DAVIES and P.J.GRUNDY, Phys. Stat. Sol. (a)8(1971)189.

L.B.DAVIES and P.J.GRUNDY, J. Non-Crystalline Solids 11(1972)179.

E.A.DAVIS, H.WRIGHT, N.J.DORAN and C.M.M.NEX, J. Non-Crystalline Solids 32(1979)257.

P.DEAN and J.L.MARTIN, Proc. Roy. Soc. A 259(1960)409.

P.DEAN and M.D.BACON, Proc. Phys. Soc. 81(1963)642.

P.DEAN, Rev. Mod. Phys. 44(1972)127.

S.W.DE LEEUW and M.F.THORPE, Phys. Rev. Lett. 55(1985)2879.

B.DIENY and B.BARBARA, J. Physique 46(1985)293.

B.DIENY and B.BARBARA, Phys. Rev. Lett. 57(1986)1169.

H.DIERCKS and B.KREBS, Angew. Chem. 89(1977)327.

M.DIXON, A.C.WRIGHT and P.HUTCHINSON, Nucl. Instr. and Meth. 143(1977)379.

J.M.DUBOIS, P.H.GASKELL and G.LeCAËR, Proc. Roy. Soc. Lond. A 402(1985)323.

J.S.DUGDALE, D.PAVUNA and P.RHODES, Phys. Bull. 35(1984)64.

R.J.ELLIOTT and A.F.GIBSON, An Introduction to Solid State Physics and its Applications (Macmillan Press, London, 1974) p.57.

R.P.ELLIOTT, Constitution of Binary Alloys, McGraw-Hill Series in Materials Science and Engineering 1st suppl. (McGraw-Hill, New York, 1965)p.678.

S.R.ELLIOTT, Phil. Mag. B 37(1978)435.

S.R.ELLIOTT, Physics of Amorphous Materials (Longman, London, 1983) p.331.

S.R.ELLIOTT, J. Non-Crystalline Solids 97&98(1987)159.

J.E.ENDERBY, D.M.NORTH and P.A.EGELSTAFF, Phil. Mag. 14(1966)961.

J.E.ENDERBY, in: Physics of Simple Liquids, eds. H.N.V.Temerley, J.S.Rowlinson and G.S.Rushbrooke (North-Holland, Amsterdam, 1968) Chap. 14.

J.E.ENDERBY and D.M.NORTH, Phys. Chem. Liq. 1(1968)1.

T.E.FABER and J.M.ZIMAN, Phil. Mag. 11(1964)153.

J.L.FELDMAN, F.CARTER, E.F.SKELTON and D.FORESTER, in: The Rare Earths in Modern Science and Technology, eds. G.J.McCarthy and J.J.Rhyne (Plenum Press, New York, 1978)p. 375.

J.FILIPPI, B.DIENY and B.BARBARA, Solid State Commun. 53(1985)523.

L.N.G.FILON, Proc. Roy. Soc. (Edinburgh) 49(1929)38.

C.FINBAK, Acta. Chem. Scand. 3(1949)1279.

J.L.FINNEY, Proc. Roy. Soc. A 319(1970)479.

P.J.FLORY, Science 188(1975)1268.

D.W.FORESTER, N.C.KOON, J.H.SCHELLENG and J.J.RHYNE, J. Appl. Phys. 50(1979)7336.

J.B.FORSYTH, Physica Scripta 15(1977)69.

E.FOSTER, 1985, Private Communication.

T.FUKUNAGA, W.WATANABE and K.SUZUKI, J. Non-Crystalline Solids 61&62(1984)343.

F.L.GALEENER and G.LUCOVSKY, Phys. Rev. Lett. 37(1976)1474.

F.L.GALEENER, Phys. Rev. B 19(1979)4292.

F.L.GALEENER, G.LUCOVSKY and J.C.MIKKELSEN Jr., Phys. Rev. B 22(1980)3983.

F.L.GALEENER and A.E.GEISSBERGER, J. Phys. Colloque C9(1983)343.

F.L.GALEENER, A.J.LEADBETTER and M.W.STRINGFELLOW, Phys. Rev. B 27(1983)1052.

F.L.GALEENER and M.F.THORPE, Phys. Rev. B 28(1983)5802.

F.L.GALEENER, R.A.BARRIO, E.MARTINEZ and R.J.ELLIOTT, Phys. Rev. Lett. 53(1984)2429.

F.L.GALEENER, J. Non-Crystalline Solids 75(1985)399.

P.P.GARDNER and N.COWLAM J. Phys. F 15(1985)2553.

P.H.GASKELL, Phil. Mag. 32(1975)211.

P.H.GASKELL, J. Non-Crystalline Solids 32(1979)207.

P.H.GASKELL, Nature 289(1981)474.

B.J.GELLATLY and J.L.FINNEY, J. Non-Crystalline Solids 50(1982)313.

P.G.De GENNES, in: Magnetism Vol.III, ed. O.T.Rado and H.Suhl (Academic Press, New York, 1963)p.115.

A.GEORGE, J.W.LIU and E.NG, University of Waterloo, Reasearch Report

CS-78-30, (1980).

A.GEORGE and J.W.LIU, Computer Solution of Large Sparse Definite Systems (Prentice-Hall, 1981).

R.GHOSH, A Computing Guide for Small-Angle Scattering Experiments (ILL, Grenoble, 1981).

M.R.J.GIBBS, Chemistry in Britain 9(1983)837.

M.J.GILLAN, 1986, Private Communication.

L.F.GLADDEN and S.R.ELLIOTT, Phys. Rev. Lett. 59(1987)908.

D.T.GOLDMAN, in: American Institute of Physics Handbook, 3rd edition, ed. D.E.Gray (McGraw-Hill, New York, 1972)p.8-6.

C.H.L.GOODMAN, in: The Structure of Non-Crystalline Materials 1982, eds. P.H.Gaskell, J.M.Parker and E.A.Davis (Taylor and Francis, London, 1982)p.151.

J.GOUBEAU and H.KELLER, Z. Anorg. Allg. Chem. 272(1953)303.

C.GRANT and R.McKIM, New Scientist 94(1982)637.

G.N.GREAVES and E.A.DAVIS, Phil. Mag 29(1974)1201.

R.GRIGOROVICI and R.MANAILA, J. Non-Crystalline Solids 1(1969)371.

D.L.GRISCOM, in: Borate Glasses eds L.D.Pye, V.D.Fréchette and N.J.Kreidl (Plenum, New York, 1978)p.11.

D.I.GRIMLEY, 1987, Private Communication.

A.GUINIER, Ann. Phys. 12(1939)161.

M.HAGEN, R.A.COWLEY, S.K.SATIJA, H.YOSHIZAWA, G.SHIRANE, R.J.BIRGENAU and H.J.GUGGENHEIM, Phys. Rev. B 28(1983)2602.

M.HAGEN and D.McK.PAUL, J. Phys. C 17(1984)5605.

M.E.HAGEN, 1987, Private Communication.

H.HALBAN and P.PREISWERK, C. R. Acad. Sci. Paris 203(1936)73.

O.HALPERN and M.H.JOHNSON, Phys. Rev. 55(1939)898.

A.C.HANNON, R.CYWINSKI, R.N.SINCLAIR, D.I.GRIMLEY and A.C.WRIGHT, Physica B (1988) in press.

A.C.HANNON, R.N.SINCLAIR, J.A.BLACKMAN, A.C.WRIGHT and F.L.GALEENER, J. Non-Crystalline Solids (1988) in press.

R.HARRIS, M.PLISCHKE and M.J.ZUCKERMANN, Phys. Rev. Lett. 31(1973)160.

R.HARRIS, J. Phys. F 10(1980)2545.

R.HOSEMANN, J. Phys. Colloque C8(1985)379.

J.HUBBARD and W.MARSHALL, Proc. Phys. Soc. 86(1965)561.

W.E.HUTCHINSON and H.A.EICK, Inorg. Chem. 1(1962)434.

T.ICHIKAWA, Phys. Stat. Sol. (a)19(1973)707.

I.L.L., Neutron Research Facilities At The ILL High Flux Reactor (Institut Laue Langevin, Grenoble, 1983).

Y.IMRY and S.MA, Phys. Rev. Lett. 35(1975)1399.

H.INOUE, N.AOKI and I.YASUI, J. Am. Ceram. Soc. 70(1987)622.

ISIS, User Guide - Experimental Facilities at ISIS (RAL, Chilton, 1988).

C.JANOT and B.GEORGE, J. Physique Lett. 46(1985)L85.

G.E.JELLISON Jr., L.W.PANEK, P.J.BRAY and G.B.ROUSE Jr., J. Chem. Phys. 66(1977)802.

E.R.JETTE and F.FOOTE, J. Chem. Phys. 3(1935)605.

J.D.JOANNOPOULOS and F.YNDURAIN, Phys. Rev. B 10(1974)5164.

P.A.V.JOHNSON, A.C.WRIGHT and R.N.SINCLAIR, J. Non-Crystalline Solids 50(1982)281.

P.A.V.JOHNSON, A.C.WRIGHT and R.N.SINCLAIR, J. Non-Crystalline Solids 58(1983)109.

G.O.JONES, Glass, Second edition. Revised by S.Parke. (Chapman and Hall, 1971).

W.A.KAMITAKAHARA, H.R.SHANKS, J.F.McCLELLAND, U.BUCHENAU, F.GOMPF and

L.PINTSCHOVIUS, Phys. Rev. Lett. 52(1984)644.

W.KAUZMANN, Chem. Rev. 43(1948)219.

P.N.KEATING, Phys. Rev. 145(1966)637.

C.KITTEL, Introduction to Solid State Physics, 5th edition (Wiley, New York, 1976) p.442.

W.KLEMENT Jnr., R.H.WILLENS and P.DUWEZ, Nature 187(1960)869.

G.KOSTORZ and S.W.LOVESEY, in: Treatise on Materials Science and Technology, vol. 15, Neutron Scattering, ed. G.Kostorz (Academic Press, New York, 1979)p.1.

G.KOSTORZ, in: Treatise on Materials Science and Technology, vol. 15, Neutron Scattering, ed. G.Kostorz (Academic Press, New York, 1979) p.227.

J.KROGH-MOE, Ark. Kemi 12(1958)475.

J.KROGH-MOE, Phys. Chem. Glasses 6(1965)46.

J.KROGH-MOE, J. Non-Crystalline Solids 1(1969)269.

P.LAMPARTER, W.SPERL, S.STEEB and J.BLÉTRY, Z. Naturf. 37a(1982)1223.

P.LAMPARTER, S.STEEB and E.GRALLATH, Z. Naturforsch. 38a(1983)1210.

P.LAMPARTER, in: Atomic Transport and Defects in Metals by Neutron Scattering, eds. C.Janot, W.Petry, D.Richter and T.Springer (Springer-Verlag, Berlin, 1985) p.49.

R.B.LAUGHLIN and J.D.JOANNOPOULOS, Phys. Rev. B 16(1977)2942.

R.B.LAUGHLIN and J.D.JOANNOPOULOS, Phys. Rev. B 17(1978)2790.

A.J.LEADBETTER and A.C.WRIGHT, J. Non-Crystalline Solids 7(1972)23.

A.J.LEADBETTER, in: Chemical Applications of Thermal Neutron Scattering, ed. B.T.M.Willis (Oxford University Press, Oxford, 1973) p.146.

H.J.LEAMY, G.H.GILMER, and A.G.DIRKS, in: Current Topics in Materials Science Vol.6, ed. E.Kaldis (North-Holland, 1980) p.309.

A.A.LEBEDEV, Trudy Gosud. Optichesk. Inst. 2(1921)51
(Trans. State Optical Inst.).

J.L.LEBOWITZ, Phys. Rev. 133(1964)A895.

A.E.LEE, G.ETHERINGTON and C.N.J.WAGNER, J. Non-Crystalline Solids 61&62(1984)349.

A.E.LEE, S.JOST, C.N.J.WAGNER and L.E.TANNER, J. Phys. Colloque C8(1985)181.

A.E.LEE, G.ETHERINGTON and C.N.J.WAGNER, in: Proc. 5th Int. Conf. on Rapidly Quenched Metals, (Elsevier, Amsterdam, 1985)p.491.

S.LEFEBVRE, A.QUIVY, J.BIGOT, Y.CALVAYRAC and R.BELLISSENT, J. Phys. F 15(1985)L99.

R.LEMAIRE and D.PACCARD, Bull. Soc. franç. Minéral. Cristallogr. 90/XC(1967)311.

H.A.LEVY, M.D.DANFORD and A.H.NARTEN, U.S.A.E.C. Rept ORNL-3960 (1966).

J.LI and N.COWLAM, Phys. Chem. Liq. 17(1987)29.

E.J.LISHER and J.B.FORSYTH, Acta. Cryst. A 27(1971)545.

A.LIÉNARD and J.P.REBOUILLAT, J. Appl. Phys. 49(1978)1680.

A.K.LIVESEY and P.H.GASKELL, in: Proc. 4th Int. Conf. on Rapidly Quenched Metals, vol.1 (Japan Institute of Metals, Sendai, 1982) p335.

C.-K.LOONG, S.IKEDA, J.M.CARPENTER and D.L.PRICE, Nucl. Instr. and Meth. A 260(1987)381.

E.LORCH, J. Phys. C 2(1969)229.

C.F.MAJKRZAK, J.D.AXE and D.BRUCE, Phys. Rev. B 22(1980)5278.

B.B.MANDELBROT, The Fractal Geometry of Nature, (Freeman, San Francisco, 1982).

M.MARET, A.SOPER, G.ETHERINGTON and C.N.J.WAGNER, J. Non-Crystalline Solids 61&62(1984)313.

M.MARET, P.CHIEUX, P.HICTER, M.ATZMON and W.L.JOHNSON, in: Proc. 5th Int. Conf. on Rapidly Quenched Metals, (Elsevier, Amsterdam, 1985)p.521.

M.MARET, PhD Thesis, University of Grenoble(1986).

M.MARET, P.CHIEUX, P.HICTER, M.ATZMON and W.L.JOHNSON, J. Phys. F 17(1987)315.

W.MARSHALL and S.W.LOVESEY, Theory of Thermal Neutron Scattering, (Oxford University Press, Oxford, 1971) p.7.

G.MASON, Nature 217(1968)733.

J.MATHEWS and R.L.WALKER, Mathematical Methods of Physics (Benjamin Inc., New York, 1970).

P.E.MEEK, Phil. Mag. 33(1976)897.

D.F.R.MILDNER and A.C.WRIGHT, J. Non-Crystalline Solids 42(1980)97.

P.G.MIKOLAJ and C.J.PINGS, Phys. Chem. Liq. 1(1968)93.

D.P.MITCHELL and P.N.POWERS, Phys. Rev. 50(1936)486.

T.MIZOGUCHI, T.KUDO, T.IRISAWA, N.WATANABE, N.NIIMURA, M.MISAWA and K.SUZUKI, in: Proc. 3rd Int. Conf. on Rapidly Quenched Metals, vol.2 (Metals Society, London, 1978) p.384.

T.MIZOGUCHI, S.YODA, N.AKUTSU, S.YAMADA, J.NISHIOKA, T.SUEMASA and N.WATANABE, in: Proc. 5th Int. Conf. on Rapidly Quenched Metals, (Elsevier, Amsterdam, 1985)p.483.

R.M.MOON, W.C.KOEHLER, J.W.CABLE and H.R.CHILD, Phys. Rev. B 5(1972)997.

R.M.MOON and W.C.KOEHLER, 11(1975)1609.

J.M.MOREAU, D.PACCARD and E.PARTHÉ, Acta. Cryst. B30(1974)2583.

R.L.MOZZI and B.E.WARREN, J. Appl. Cryst. 3(1970)251.

A.P.MURANI and J.P.REBOUILLAT, J. Phys. F 12(1982)1427.

W.NÄGELE, K.KNORR, W.PRANDL, P.CONVERT and J.L.BUEVOZ, J. Phys. C

11(1978)3295.

R.NATHANS and S.J.PICKART, in: Magnetism, vol.III eds. G.T.Rado and H.Suhl (Academic Press, New York, 1963) Chapter 5.

W.P.O'LEARY, J. Phys. F 5(1975)L175.

L.ORNSTEIN and F.ZERNIKE, Proc. Acad. Sci. Amsterdam 17(1914)793.

E.PARTHÉ, B.CHABOT and E.HOVESTREYDT, Acta. Cryst. B39(1983)596.

A.L.PATTERSON, Z. Krist. 90(1935)517.

R.A.PELCOVITS, E.PYTTE and J.RUDNICK, Phys. Rev. Lett. 40(1978)476.

R.A.PELCOVITS, E.PYTTE and J.RUDNICK, Phys. Rev. Lett. 48(1982)1297.

J.K.PERCUS and G.J.YEVICK, Phys. Rev. 110(1957)1.

J.C.PHILLIPS, J. Non-Crystalline Solids 43(1981)37.

S.J.PICKART, J.J.RHYNE and H.A.ALPERIN, Phys. Rev. Lett. 33(1974)424.

S.J.PICKART, J.J.RHYNE and H.A.ALPERIN, AIP Conf. Proc. 24(1975)117.

S.J.PICKART, Amorphous Magnetism II, eds. R.A.Levy and R.Hasegawa (Plenum Press, New York, 1977) p.479.

S.J.PICKART, H.A.ALPERIN and J.J.RHYNE, Phys. Lett. 64A(1977)337.

G.PLACZEK, Phys. Rev. 86(1952)377.

D.E.POLK, Scr. Met. 4(1970)117.

D.E.POLK and D.S.BOUDREAUX, Phys. Rev. Lett. 31(1973)92.

E.A.PORAI-KOSHITS, The Structure of Glass (Consultants Bureau, New York, 1958)p.25.

G.POROD, Kolloid-Zeitschrift 124(1951)83.

C.T.PREWITT and R.D.SHANNON, Acta. Cryst. B 24(1968)869.

D.L.PRICE, J.M.CARPENTER, C.A.PELIZZARI, S.K.SINHA, I.BRESOF and G.E.OSTROWSKI, in: Proc. Sixth Meeting on International Collaboration on Advanced Neutron Sources, Argonne National Laboratory, June 1982, Report No' ANL-82-80, p.207.

D.L.PRICE, 1985, Private Communication.

D.L.PRICE, J.M.CARPENTER, J.R.D.COPLEY, C.-K.LOONG and P.E.SOKOL, 1985, 'Multiple Scattering Corrections To Chopper Spectrometer Data At IPNS', Unpublished Report.

D.L.PRICE and C.-K.LOONG, 1985, 'IPNS Chopper Data Analysis Programs', Unpublished Report.

D.L.PRICE, Physica 136 B (1986)25.

D.L.PRICE and K.SKÖLD, in: Neutron Scattering, Part A, eds. K.Sköld and D.L.Price (Academic Press, Orlando, 1986)p.1.

D.L.PRICE and J.M.CARPENTER, J. Non-Crystalline Solids 92(1987)153.

B.D.RAINFORD, C.CORNELIUS, S.KILCOYNE and K.A.MOHAMMED, 1988, Private Communication.

J.T.RANDAL, H.P.ROOKSBY and B.S.COOPER, Nature 125(1930)458.

J.P.REBOUILLAT, A.LIÉNARD, J.M.D.COEY, R.ARRESE-BOGGIANO and J.CHAPPERT, Physica 86-88 B (1977)773.

A.L.RENNINGER, M.D.RECHTIN and B.L.AVERBACH, J. Non-Crystalline Solids 16(1974)1.

J.J.RHYNE, S.J.PICKART and H.A.ALPERIN, Phys. Rev. Lett. 29(1972)1562.

J.J.RHYNE, S.J.PICKART and H.A.ALPERIN, in: Amorphous Magnetism, eds. H.O.Hooper and A.M.de Graaf (Plenum Press, New York, 1973)p.373.

J.J.RHYNE, S.J.PICKART and H.A.ALPERIN, AIP Conf. Proc. 18(1974)563.

J.J.RHYNE, S.J.PICKART and H.A.ALPERIN, J. Appl. Phys. 49(1978)1691.

J.J.RHYNE and C.J.GLINKA, J. Appl. Phys. 55(1984)1691.

J.J.RHYNE, Physica 130 B (1985a)253.

J.J.RHYNE, IEEE Trans. Magn. (Proc. of the 1985 Intermag Conf.) MAG-21(1985b)1990.

B.RODMACQ, P.MANGIN and A.CHAMBEROD, J. Phys. Colloque C8(1985)499.

R.B.ROOF Jr., A.C.LARSON and D.T.CROMER, Acta. Cryst. 14(1961)1084.

J.H.ROOT, P.A.EGELSTAFF and B.G.NICKEL, Inst. Phys. Conf. Ser. 81 (Institute of Physics, Bristol, 1986)p.71.

M.ROTH, J. Appl. Cryst. 10(1977)172.

K.D.ROUSE, M.J.COOPER, E.J.YORK and A.CHAKERA, Acta. Cryst. A 26(1970)682.

M.A.RUDERMAN and C.KITTEL, Phys. Rev. 96(1954)99.

J.F.SADOC and J.DIXMIER, Mat. Sci. Eng. 23(1976)187.

J.H.SCHACHTSCHNEIDER and R.G.SNYDER, Spectrochim. Acta 19(1963)117.

D.W.SCHAEFER, MRS Bulletin 13(1988)22.

G.D.SCOTT and D.M.KILGOUR, J. Phys. D 2(1969)863.

P.N.SEN and M.F.THORPE, Phys. Rev. B 15(1977)4030.

D.SHECHTMAN, I.BLECH, D.GRATIAS and J.W.CAHN, Phys. Rev. Lett. 53(1984)1951.

V.F.SEARS, in: Neutron Scattering, Part A, eds. K.Sköld and D.L.Price (Academic Press, Orlando, 1986)p.521.

D.J.SELLMYER and S.NAFIS, J. Appl. Phys. 57(1985)3584.

M.SHIGA and Y.NAKAMURA, J. Magn. Magn. Mater. 31-34(1983)1411.

A.H.SILVER and P.J.BRAY, J. Phys. Chem. 29(1958)984.

R.N.SINCLAIR, J. Non-Crystalline Solids 76(1985)61.

A.SJÖLANDER, Ark. Fysik 14(1958)315.

A.K.SOPER, 1988, Private Communication.

W.SOPPE, C.van der MAREL, W.F.van GUNSTEREN and H.W.den HARTOG, J. Non-Crystalline Solids 103(1988)201.

T.F.SOULES, J. Chem. Phys. 73(1980)4032.

J.B.SOUSA, J.M.MOREIRA, V.S.AMARAL, M.M.AMADO, M.E.BRAGA, B.BARBARA, B.DIENY and J.FILIPPI, J. Phys. F 17(1987)2377.

F.SPAEPEN and G.S.GARGILL III, in: Proc. 5th Int. Conf. on Rapidly Quenched

Metals, (Elsevier, Amsterdam, 1985)p.581.

M.L.SPANO and J.J.RHYNE, J. Appl. Phys. 57(1985)3303.

M.L.SPANO and J.J.RHYNE, J. Magn. Magn. Mater. 54-57(1986)300.

M.R.SPIEGEL, Fourier Analysis (McGraw-Hill, New York,1974)p.82.

G.L.SQUIRES, Introduction to the Theory of Thermal Neutron Scattering (Cambridge University Press, Cambridge, 1978).

S.STEEB and P.LAMPARTER, J. Phys. Colloque C8(1985)247.

S.L.STRONG and R.KAPLOW, Acta. Cryst. B 24(1968)1032.

E.SVÁB, G.MÉSZÁROS, G.KONCZOS, S.N.ISHMAEV, S.L.ISAKOV, I.P.SADIKOV and A.A.CHERNYSHOV, J. Non-Crystalline Solids 104(1988)291.

S.E.SVANSON, E.FORSLIND and J.KROGH-MOE, J. Phys. Chem. 66(1962)174.

S.E.SVANSON and R.JOHANSSON, Acta. Chem. Scand. 23(1969)635.

Y.TANAKA and M.KATAYAMA, J. Phys. Soc. Japan 57(1988)543.

M.TETER, J. Non-Crystalline Solids (1988) in press.

M.F.THORPE, Phys. Rev. B 8(1973)5352.

M.F.THORPE, in: Physics of Structurally Disordered Solids ed. S.S.Mitra (Plenum, New York, 1976) p.623.

M.F.THORPE and F.L.GALEENER Phys. Rev. B 22(1980)3078.

V.F.TURCHIN, Slow Neutrons (Israel Program for Scientific Translations, Jerusalem, 1965) Chapter V.

A.M.TURING, Quart. J. Mech., and Appl. Math. 1(1948)287.

D.TURNBULL and M.H.COHEN, J. Chem. Phys. 34(1961)120.

D.TURNBULL and M.H.COHEN, J. Chem. Phys. 52(1970)3038.

D.R.UHLMANN, J.F.HAYS and D.TURNBULL, Phys. Chem. Glasses 8(1967)1.

L.VAN HOVE, Phys. Rev. 95(1954a)249.

L.VAN HOVE, Phys. Rev. 95(1954b)1374.

G.H.VINEYARD, Phys. Rev. 96(1954)93.

C.N.J.WAGNER, N.HEIMAN, T.C.HUANG, A.ONTON and W.PARRISH, AIP Conf. Proc. 29(1976)188.

C.N.J.WAGNER and H.RUPPERSBERG, Atomic Energy Rev. 1(1981)101.

C.N.J.WAGNER, in: Amorphous Metals and Semiconductors, eds. P.Haasen and R.I.Jaffee (Pergamon, Oxford, 1986)

G.E.WALRAFEN, M.S.HOKMABADI, P.N.KRISHNAN, S.GUHA and R.G.MUNRO, J. Chem. Phys. 79(1983)3609.

U.WALTER, D.L.PRICE, S.SUSMAN and K.J.VOLIN, Phys. Rev. B 37(1988)4232.

B.E.WARREN, H.KRUTTER and O.MORNINGSTAR, J. Am. Ceram. Soc. 19(1936)202.

B.E.WARREN, J. Appl. Phys. 8(1937)645.

B.E.WARREN and J.BISCOE, J. Am. Ceram. Soc. 21(1938)49.

B.E.WARREN, Chem. Rev. 26(1940)237.

B.E.WARREN, X-Ray Diffraction, Addison-Wesley, Reading, Mass., 1969, p.229.

Y.WASEDA, The Structure of Non-crystalline Materials (McGraw Hill, 1980).

J.WASER and V.SCHOMAKER, Rev. Mod. Phys. 25(1953)671.

D.WEAIRE and R.ALBEN, Phys. Rev. Lett. 29(1972)1505.

F.A.WEDGEWOOD and A.C.WRIGHT, J. Non-Crystalline Solids 21(1976)95.

A.F.WELLS, Structural Inorganic Chemistry (OUP, Oxford, 1962).

A.WILDERMUTH, P.LAMPARTER and S.STEEB, Z. Naturforsch. 40 a(1985)191.

S.J.WILLIAMS and S.R.ELLIOTT, Proc. Roy. Soc. Lond. A 380(1982a)427.

S.J.WILLIAMS and S.R.ELLIOTT, in: The Structure of Non-Crystalline Materials 1982, eds. P.H.Gaskell, J.M.Parker and E.A.Davis (Taylor and Francis, London, 1982b)p.407.

C.F.WINDISCH Jr. and W.M.RISEN Jr., J. Non-Crystalline Solids 48(1982a)307.

C.F.WINDISCH Jr. and W.M.RISEN Jr., J. Non-Crystalline Solids 48(1982b)325.

C.G.WINDSOR, Pulsed Neutron Scattering, Taylor and Francis, London, 1981.

A.C.WRIGHT, Adv. Struct. Res. Diffr. Meth. 5(1974)1.

A.C.WRIGHT and A.J.LEADBETTER, Phys. Chem. Glasses 17(1976)122.

A.C.WRIGHT, J. Non-Crystalline Solids 40(1980a)325.

A.C.WRIGHT, Nucl. Instr. and Meth. 176(1980b)623.

A.C.WRIGHT, D.J.SUMNER and A.G.CLARE, in: The Structure of Non-Crystalline Materials 1982, eds. P.H.Gaskell, J.M.Parker and E.A.Davis (Taylor and Francis, London, 1982)p.395.

A.C.WRIGHT, A.C.HANNON, R.N.SINCLAIR, W.L.JOHNSON and M.ATZMON, J. Phys. F 14(1984)L201.

A.C.WRIGHT and R.N.SINCLAIR, J. Non-Crystalline Solids 76(1985)351.

A.C.WRIGHT, D.I.GRIMLEY, R.N.SINCLAIR, K.J.RAO and B.G.RAO, J. Phys. Colloque C8(1985)305.

A.C.WRIGHT, R.N.SINCLAIR and A.J.LEADBETTER, J. Non-Crystalline Solids 71(1985)295.

A.C.WRIGHT, A.C.HANNON, A.G.CLARE, R.N.SINCLAIR, W.L.JOHNSON, M.ATZMON and P.MANGIN, J. Phys. Colloque C8(1985)299.

A.C.WRIGHT, in: Proc. NATO ARW on Halide Glasses For Infrared Fiberoptics, ed. R.M.Almeida (Martinus Nijhoff, Dordrecht, 1986).

A.C.WRIGHT, 1987, Private Communication.

Q.XU, K.KAWAMURA and T.YOKOKAWA, J. Non-Crystalline Solids 104(1988)261.

J.L.YARNELL, M.J.KATZ, R.G.WENZEL and S.H.KOENIG, Phys. Rev. A 7(1973)2130.

R.YAVARI, P.DESRE and P.CHIEUX, in: Atomic Transport and Defects in Metals by Neutron Scattering, eds. C.Janot, W.Petry, D.Richter and T.Springer (Springer-Verlag, Berlin, 1985) p.42.

H.YOSHIZAWA, R.A.COWLEY, G.SHIRANE, R.J.BIRGENAU, H.J.GUGGENHEIM and H.IKEDA, Phys. Rev. Lett. 48(1982)438.

W.H.ZACHARIASEN, J. Am. Chem. Soc. 54(1932)3841.

J.ZHENG and C.WANG, Acta Phys. Sinica 31(1982)668.

W.H.ZINN, Phys. Rev. 71(1947)752.